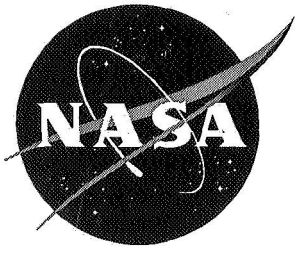

NASA Conference Publication 3274
Part 2

FAA/NASA International Symposium on Advanced Structural Integrity Methods for Airframe Durability and Damage Tolerance

Edited by
Charles E. Harris

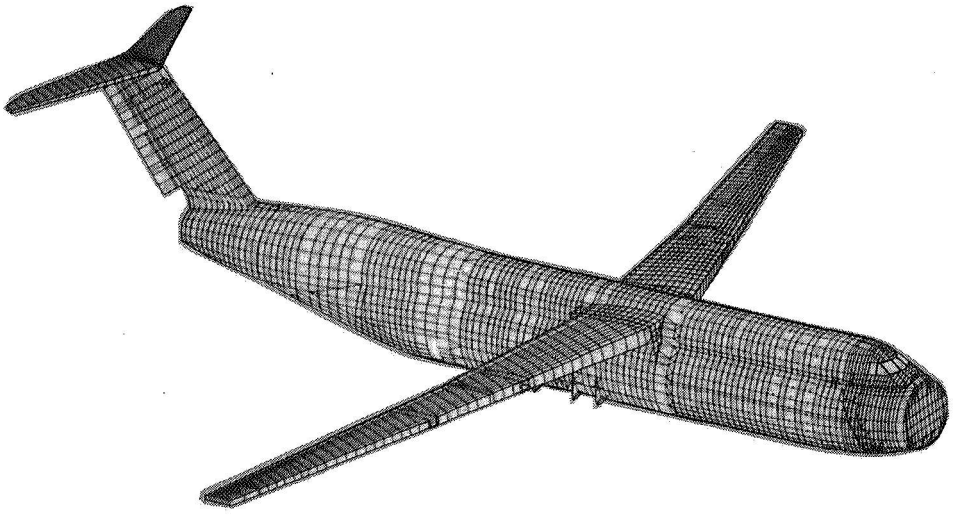

Proceedings of a symposium jointly sponsored by the Federal Aviation Administration, Washington, DC, and the National Aeronautics and Space Administration, Washington, DC, and held in Hampton, Virginia
May 4–6, 1994

September 1994

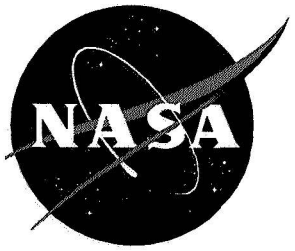

P.9

NASA Conference Publication 3274
Part 2

FAA/NASA International Symposium on Advanced Structural Integrity Methods for Airframe Durability and Damage Tolerance

Edited by
Charles E. Harris
Langley Research Center • Hampton, Virginia

Proceedings of a symposium jointly sponsored by the Federal Aviation Administration, Washington, DC, and the National Aeronautics and Space Administration, Washington, DC, and held in Hampton, Virginia
May 4–6, 1994

National Aeronautics and Space Administration
Langley Research Center • Hampton, Virginia 23681-0001

September 1994

The use of trade names of manufacturers in this report does not constitute an official endorsement of such products or manufacturers, either expressed or implied, by the National Aeronautics and Space Administration.

Preface

The need to design ultra lightweight airframe structures that are both durable and damage tolerant has historically been a major motivation for the engineering and research community. More recently, transport aircraft are being kept in service well beyond their original design economic life goals. Advanced technologies are under development that will enable the structural engineers to design longer life aircraft and to extend the life of high time aircraft currently in the commercial and military fleets. These technologies include better corrosion prevention, more accurate residual strength and life prediction methodologies, more durable materials, and more reliable and economical in-service inspection techniques. In order to advance civil aviation and to promote continuous airworthiness, the United States Federal Aviation Administration and the National Aeronautics and Space Administration co-sponsored this symposium to review recent research developments and to stimulate the exchange of technical ideas within the international aeronautical engineering community. The focus of the symposium was on advanced durability and damage tolerance methodology for metallic airframe structures.

Technical papers were selected for presentation at the symposium after a review of extended abstracts received by the Organizing Committee from a general call-for-papers. Keynote addresses were given in the opening Plenary Session by Mr. Harvey Safeer, Director of the FAA Technical Center, and Mr. Ray Hood, Manager of the NASA Advanced Subsonic Technology Program. Mr. Safeer gave the FAA perspective on the role of advanced technology in improving aircraft safety and Mr. Hood reviewed NASA's technology development programs for the next generation subsonic and supersonic aircraft. Technical papers were presented in oral briefings or posters on the following topics:

Structural Concepts for Enhanced Durability, Damage Tolerance, and Maintainability
New Metallic Alloys and Processing Technology
Fatigue Crack Initiation and Small Crack Effects
Fatigue Crack Growth Models
Fracture Mechanics Failure Criteria for Ductile Materials
Structural Mechanics Methodology for Residual Strength and Life Prediction
Development of Flight Load Spectra for Design and Testing
Advanced Approaches to Resist Corrosion and Environmentally Assisted Fatigue

Full-length manuscripts were solicited from the authors of papers presented in both oral briefings and posters. These papers are included in the proceedings.

The members of the Symposium Organizing Committee are as follows:

Charles E. Harris, NASA Langley Research Center, Symposium Chairman
Chris C. Seher, FAA Technical Center, Symposium Co-Chairman
Satya N. Atluri, Georgia Institute of Technology
Arij de Koning, National Aerospace Laboratory NLR, The Netherlands
Walter F. Jones, USAF AFOSR, Bolling Air Force Base
John W. Lincoln, USAF ASD/ENFS, Wright-Patterson Air Force Base
Matthew Miller, Boeing Commercial Airplane Group
James C. Newman, Jr., NASA Langley Research Center
Tom Swift, FAA National Resource Specialist

Approximately 300 research scientists and practicing engineers attended the symposium. The affiliations of the participants included 25% from government agencies, 31% from academia, and 44% from industry.

Charles E. Harris
NASA Langley Research Center

CONTENTS

* Part 1 is presented under separate cover.

PART 2

* This paper was not included in the Table of Contents for Part 1.

FLIGHT PARAMETERS MONITORING SYSTEM FOR TRACKING STRUCTURAL INTEGRITY OF ROTARY-WING AIRCRAFT

Jamshid Mohammadi and Craig Olkiewicz
Systems & Electronics, Inc.
Elk Grove Village, IL

SUMMARY

Recent developments in advanced monitoring systems used in conjunction with tracking structural integrity of rotary-wing aircraft are explained. The paper describes: (i) an overview of rotary-wing aircraft flight parameters that are critical to the aircraft loading conditions and each parameter's specific requirements in terms of data collection and processing; (ii) description of the monitoring system and its functions used in a survey of rotary-wing aircraft; and (iii) description of the method of analysis used for the data. The paper presents a newly-developed method in compiling flight data. The method utilizes the maneuver sequence of events in several pre-identified flight conditions to describe various flight parameters at three specific weight ranges.

INTRODUCTION

Flight data monitoring has proven to be an effective method for the evaluation of structural integrity of aircraft. A successful monitoring program requires a comprehensive effort involving data gathering, analysis and engineering evaluation and interpretation of all parameters that influence the aircraft loading conditions. Specifically, the flight parameters data in the form of time history and/or frequency of occurrence of peaks and valleys are needed for implementation in the analysis of structural integrity of the aircraft. Examples of such parameters include the normal acceleration (N_Z), roll, pitch, gross weight, rotor speed, etc. During a flight operation, an immense amount of data on the flight parameters is gathered so that nearly all possible values of the key parameters, that influence the load conditions of the aircraft, can be captured. This calls for an advanced system capable of (i) handling the volume of incoming flight data, and (ii) processing the data on a real-time basis.

This paper focuses on recent developments in advanced monitoring systems used in conjunction with tracking structural integrity of rotary-wing aircraft. In particular, the paper describes the experiences of Systems & Electronics, Inc. (SEI) in design and application of such systems. The paper presents: (i) an overview of rotary-wing aircraft flight parameters that are critical to the aircraft loading conditions and each parameter's specific requirements in terms of data collection and processing; (ii) description of SEI's monitoring system and its functions. This includes the system's operational capabilities and recording capacity; and, (iii) description of the method of analysis used for the data. In this regard, the paper describes that the analysis is partially done by the recorder on a real-time basis. Additional processing and development of flight parameters histories, maneuver recognition, flight maneuver sequence of events and frequency of occurrence of peaks and valleys of key parameters are performed upon downloading the recorder onto a personal computer.

The research has been in progress for the past three years. With the current system in operation, flight data aboard several aircraft types are being compiled and processed. The paper specifically discusses that: (i) Flight maneuver sequence of events recording, as adopted in this project, provides a detailed information on aircraft various operations during the flight. This also allows for recording of various key flight parameters at each flight condition and at each event; (ii) Development of a built-in data quality assurance procedure provides a means to verify the expected ranges of flight parameters. To a limited extent, this procedure is effective in identifying problem areas that may occur during the data acquisition process; and (iii) The processed data can be used as an input to development of a comprehensive structural integrity evaluation. The peak and valley data and the item-by-item sequence of events data recording are specially helpful in tracking the structural integrity of the aircraft in a more refined manner by identifying flight conditions that are more severe to the aircraft structure.

The paper also presents samples of aircraft data compiled and processed via SEI's system.

AIRCRAFT FLIGHT PARAMETERS

The selection of flight parameters depends on the type of aircraft and the configuration of its structural components. Furthermore, the selection of desired parameters depends on the flight condition for which the data is being compiled. A multi-parameter data acquisition system is used and configured to accommodate the aircraft's requirements and intended flight conditions. Flight parameters selected in the survey of CH-46 and AH-1W aircraft are described in this paper.

In the CH-46 application, twenty (20) parameters were selected for the survey by SEI. These parameters are: (1) normal acceleration; (2) roll angle; (3) pitch angle; (4) heading angle; (5) rotor RPM; (6) outside air temperature; (7) longitudinal speed; (8) rudder pedal position; (9) weight on wheels; (10) rotor brake; (11) collective stick position; (12) airspeed; (13) altitude; (14) fuel quantities (left and right); (15) cruise guide indicator; (16) lateral speed (doppler); (17) engine torques (left/right); (18) cargo hook strain; (19) longitudinal stick position; and (20) lateral stick position.

The system employed to monitor CH-46 consists of the following equipment:

- Recorder Converter, RD-601/ASH-37 (RC)
- Memory Unit, MU-983/ASH-37 (MU)
- Motional Pick-up Transducer, TR-354/ASH-37 (MPT)
- Signal Data Converter, CV-4193/ASH-37 (SDC)
- Data Entry Keyboard, KY-941/ASH-37 (DEK)
- Temperature probe for the outside air temperature
- Recorder Reproducer, RD-608/ASH-37 (RR)

The Recorder Converter, Memory Module and Motional Pick-up Transducer make up the components of the structural data recording set (SDRS). Figure 1 shows the process of data

acquisition using SDRS.

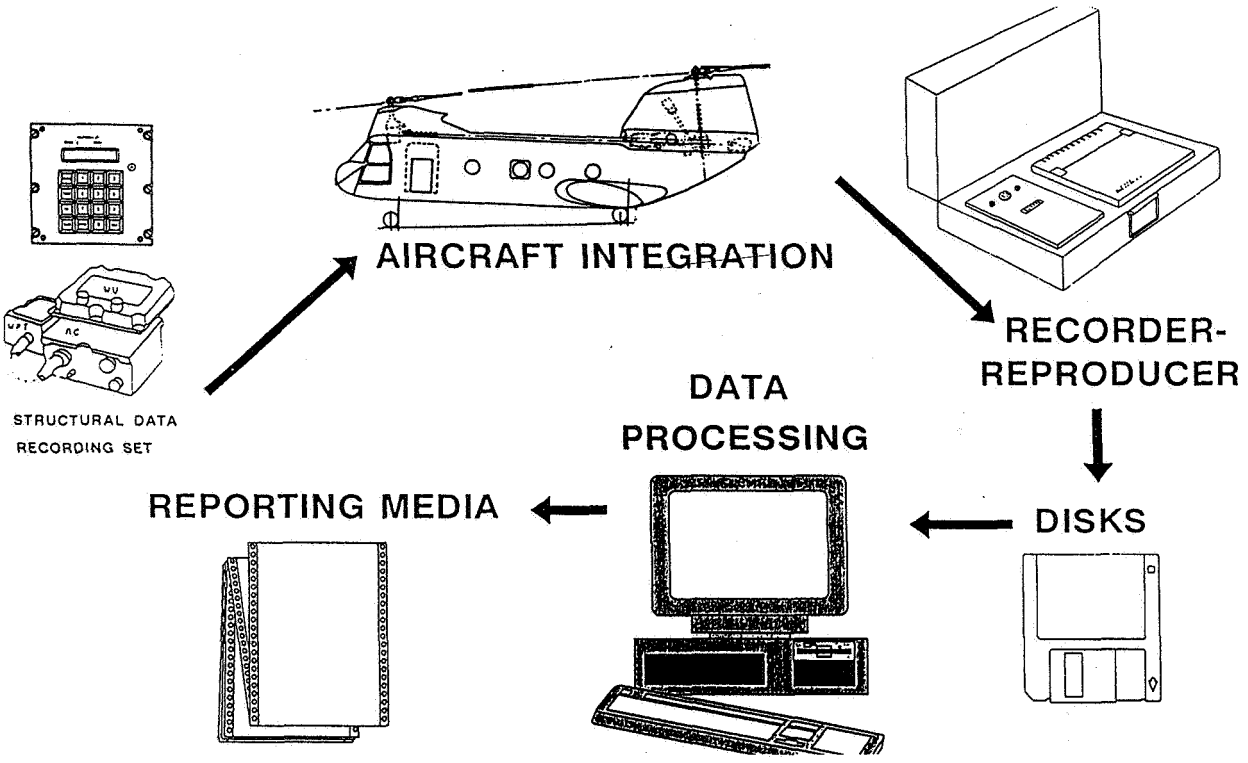

Fig. 1 SDRS Recording Procedure

The CH-46 aircraft parameters were acquired as follows:

1) Normal acceleration was obtained from the MPT which was installed on floor board at FS 254.

2) Air data (pitot and static pressure) was obtained from the aircraft pitot, static system. These pressures were then supplied to the pressure transducers internal to the RC and aircraft. The indicated airspeed and altitude values were derived from these pressures.

3) Roll angle, pitch angle and heading were obtained from the aircraft attitude heading reference system. These signals were then conditioned by the SDC and supplied to the RC.

4) Rotor RPM was obtained from the aircraft rotor tach generator. This signal was then conditioned by the SDC and provided to the RC.

5) Left and right engine torques were obtained from the co-pilot's torque indicator. These signals were conditioned in the SDC and then supplied to the RC.

6) Outside air temperature (OAT) was obtained from the OAT probe installed on the forward left side of the aircraft.

7) Pedal, longitudinal stick, lateral stick and collective stick positions signals were obtained from the roll, pitch and yaw control and collective stick transducer. These signals were conditioned by the SDC and then input into the RC.

8) The cruise guide indication was obtained from the cruise guide indicator located in the cockpit. This signal was conditioned by the SDC and input into RC.

9) The lateral and longitudinal velocities were obtained from the radar navigation set, AN/APN-21F. These signals were conditioned by the SDC and then input into the RC.

10) The right and left tank fuel quantities were obtained from the cockpit fuel quantity indicator. These signals were then combined to provide a total fuel quantity signal by the SDC and then input into the RC.

11) The external load was obtained from a strain sensor mounted to the external cargo hook. This signal was conditioned by the SDC and then input to the RC.

12) The weight-off-wheels signal was obtained from the left main gear squat switch. This signal was conditioned by the SDC and then input to the RC.

13) The rotor brake signal was obtained from the rotor brake and blade fold control box. This signal was conditioned by the SDC and input into the control box. The signal was then conditioned by the SDC and supplied to the RC.

In the AH-1W application the flight parameters recorded are mainly the same as those in the CH-46 application. Among these parameters included (1) the normal acceleration, (2) airspeed, (3) roll and pitch attitudes, (4) engine torque, (5) rotor speed, (6) lateral and longitudinal stick positions, (7) pedal position, and (8) rate of descent. Figure 2 shows the data acquisition block diagram in the AH-1W application.

PROCESSING THE DATA

The processing of the data is partially performed by the recorder. Additional analyses are then performed upon downloading the data onto a PC. The data recording process used in RC is a maneuver recognition algorithm. Using this algorithm, all input parameters to the SDRS are monitored for identification of various sequence of events and specific maneuvers experienced by the aircraft during the flight. The sequence of events that define a maneuver is determined from the flight spectrum specified by the aircraft manufacturer. In the AH-1W application, a total of 293 uniquely definable flight conditions were incorporated in the RC data processing algorithm. Each defined flight condition is, in turn, separated into three gross weight ranges. These are:

- The low weight range defined by a gross weight of less than 12,500 lbs;
- The medium range defined by a gross weight of between 12,500 and 13,500 lbs; and,
- The heavy weight range defined by those in excess of 13,500 lbs.

Table I presents two samples of the sequences of events that uniquely identify a specific

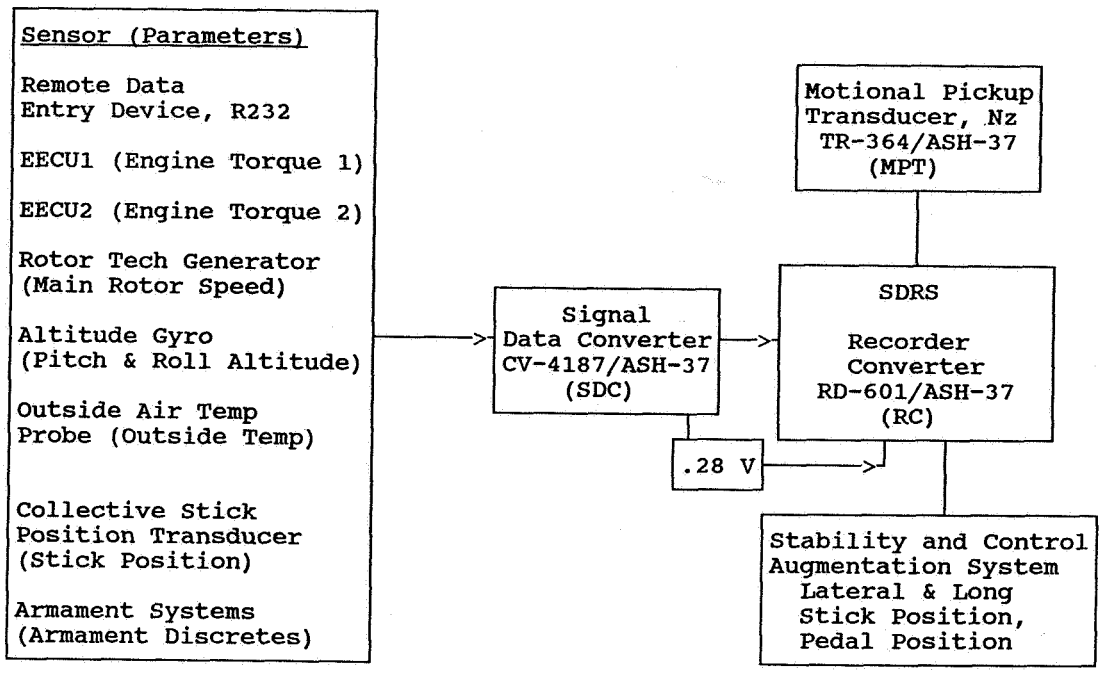

Fig. 2 AH-1W SDRS Block Diagram

maneuver in the AH-1W application. A similar process is also adapted in the CH-46 application. However, this process can be tailored to meet the specific data acquisition needs of each type of aircraft.

The SDRS executes the maneuver recognition algorithm on a real-time basis starting from aircraft power up to power down. The final product at the conclusion of each operation is a complete history of the flight with (i) the time of occurrence of each maneuver; (ii) the time spent in each maneuver; and (iii) the values of all parameters that show a change. Furthermore, the weight ranges in which the maneuver occurs is identified and marked. If a flight condition that is not previously defined is encountered, the system automatically assigns an "unrecognized mode" recording. Simultaneously, the system logs a record of each flight parameter's band, thereby compiling the data on the parameter's range. Each time a parameter's value changes into a new band, the system logs the parameter that experienced the change and the corresponding new band value. This type of recording continues until one of several pre-identified built-in "recognized" flight conditions is encountered.

The data compiled for an unrecognized mode of recording provides a detailed description of those flight parameters that are significantly affected. If an unrecognized mode is repeated over a period of time, then the system will treat the mode as a new flight regime and will add it to the aircraft's flight spectrum.

At the conclusion of each flight data acquisition session, the compiled data is summarized describing the period of time spent (i) in each flight regime pre-defined by the aircraft's flight spectrum, and (ii) in regimes labeled as unrecognized modes. For certain flight parameters, additional analyses and data summary can also be conducted to suit the specific requirements by

a given type of aircraft. For example, in most applications, the frequency of various levels of the normal acceleration (N_Z) encountered during the flight is desired. Such data include the number of times a specific N_Z level has been experienced either as a peak or valley acceleration. The system can also be configured to adopt any desired cycle counting method for this purpose. The current algorithm is based on counting the rising and dropping N_Z (peaks) or dropping and rising N_Z (valley) as it crosses various thresholds predetermined and built in the system. Other cycle counting algorithms (ref. 1) including the ASTM rainflow method (ref. 2) can easily be configured and implemented in the system.

With current applications, more than thirty flight hours of data are typically recorded in less than 100K bytes of nonvolatile memory. Samples of AH-1W data are presented in Table II.

DATA QUALITY ASSURANCE

To assure the quality of the incoming data on a continuous basis, a rigorous program of data inspection and analysis will be needed. As it is expected, flight data are subject to variations. The purpose of the quality assurance (QA) procedure adopted for use in conjunction with the flight parameters data acquisition of rotary-wing aircraft is merely to limit these variations to those that arise from such factors as:

- Uncertainty associated with the method of data acquisition process. Marginal errors in predicting various thresholds and bands for flight parameters are among uncertainties inherent in the method of data acquisition process. In most parts the estimates for a flight parameter's bands are derived on the basis of the aircraft's previous flight records which are subject to variabilities.

- Errors associated with various sensors' sensitivities.

- Marginal errors encountered during installations, initial readings, tests and calibrations.

The QA procedures are intended to provide a safeguard against recording erroneous data that generally do not fall within the expected norms. Although a total elimination of errors is not feasible, certain measures can be taken to minimize their occurrence and recurrence during the data acquisition process. The QA process adopted in the flight survey of aircraft is a three-step procedure. The first step is conducted by the system as a self-test type of approach. The second step consists of a rigorous statistical analysis of the data to establish data trends and to identify any discrepancies in the data that may be an indication of a potential deviation from the norms. The final step involves the identification of the source of the problem and development of an appropriate corrective measure to remedy the potential problem areas. Figure 3 presents a schematic diagram of the QA procedure activities. A brief description of the three steps involved in the QA procedure is provided below.

As described earlier, the system is initially introduced with several pre-identified flight conditions. As the data compilation continues, the system recognizes the occurrence of these pre-defined flight conditions. The values of the flight parameters within each flight condition are regularly checked against the expected limits. Any discrepancies are flagged for further investigations. If the system does not recognize a flight condition, with all parameters being within their respective acceptable ranges, a new flight condition will be added provided that the

unrecognized condition is repeated (as described earlier). This constitutes Step 1 in the QA process.

As flight data are compiled, batches of data are selected for detailed statistical analyses. The purpose of such analyses is to investigate:

- Any statistical correlation that is expected between two or more parameters.
- A trend or pattern in the distribution of a parameter or groups of parameters.
- Consistency among blocks of data compiled for a given flight parameter for the same aircraft or for several identical aircraft.
- Consistency of the data when compared with published results, design values and norms indicated in the aircraft's manual.

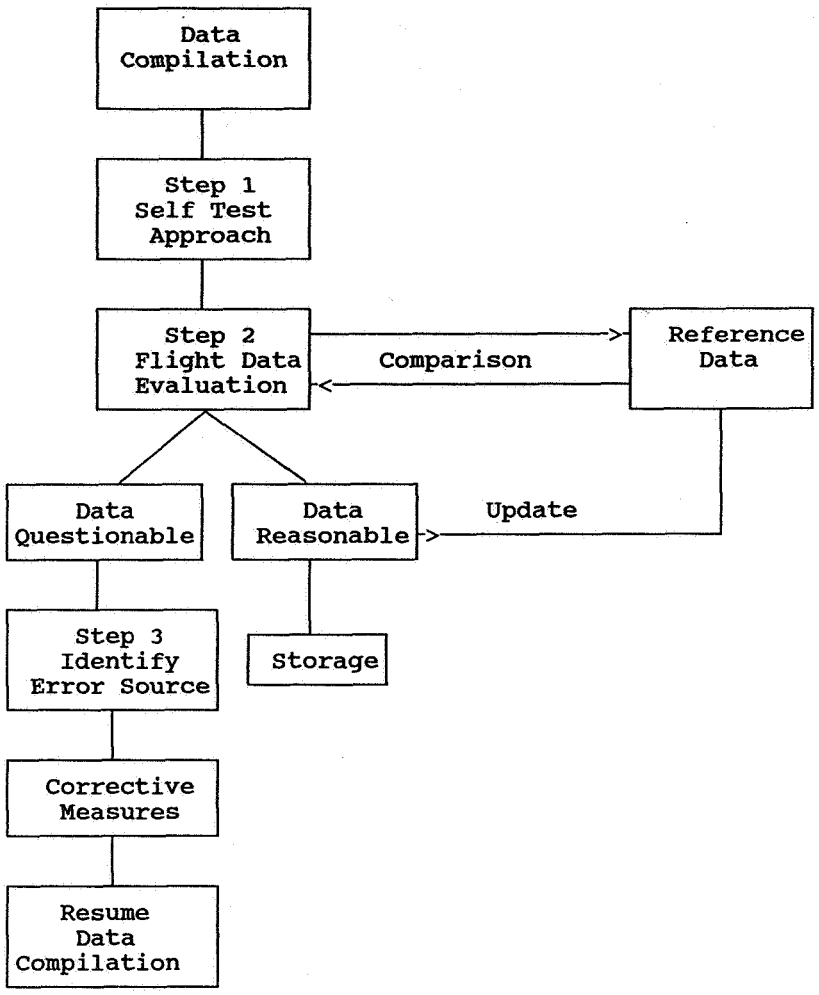

Fig. 3 Flight Data QA Procedure

An inventory of qualified data or published results are maintained for a reference. The reference data is periodically updated and revised, if necessary, as new data becomes available. Dramatic changes occurring in the data are carefully investigated to identify any potential problem area associated with the data acquisition process. This constitutes Step 2 in the QA process.

Corrective measures are taken only if a problem area has been identified and proven to be the source of error or dramatic change in the data. Appropriate measures could consist only of a few adjustments in the previously-selected expected thresholds for a parameter; a re-calibration of sensors; an added feature to the previously-identified flight conditions; a replacement of a faulty sensor; a reconfiguration of the system; or replacement of the data acquisition system. In most applications the replacement of a sensor or the entire data acquisition system is rarely needed. Most often the problem area can be corrected with a few changes in the system configuration. This constitutes Step 3 in the QA procedure.

MONITORING AIRCRAFT STRUCTURAL INTEGRITY

A major application of the results of aircraft flight surveys is in tracking the structural integrity of the aircraft. This section briefly discusses the process via which the structural integrity evaluation of the aircraft can be achieved using flight data. No specific method has been established by SEI for this purpose. The following discussion is intended only for describing the effort needed to develop a method for evaluating the integrity of the airframe structure based on the type of flight data compiled for rotary wing aircraft.

The peak and valley statistics compiled for the normal acceleration are crucial to the structural analysis of the aircraft. These statistics provide the input data needed for estimating the damage induced in various structural components of the aircraft. The peak and valley statistics of N_Z constitute the distribution of the frequency of load application on the structure. These statistics can be used directly to estimate the remaining useful life of various critical components of the aircraft. In this regard, the aircraft manufacturer's data on the damage tolerance of a given structural component will then be needed and used along with the load statistics to estimate the damage accumulated by the component as a result of the load applied for the duration of flight for which the load data was compiled. In rotary wing aircraft, the damage tolerance data is often described in terms of the total number of load cycles of specific ranges needed to cause a complete failure of the component.

Alternatively, the load data can be used in a detailed structural analysis of the aircraft to arrive at stress distributions at a critical structural component. This information can then be used along with the fatigue or fracture mechanics approach to arrive at the damage accumulated by the component and thus to estimate the remaining useful life of the component. This method has been mainly used in other types of structures (ref. 3) and especially to fixed wing aircraft. The basic requirement for this method is that the fatigue characteristics of the component in the form of S-N relation (stress versus the number of load cycles to failure) be known so that a crack initiation analysis can be conducted. If a crack growth analysis is the method of choice, then crack growth characteristics of the structural component will be needed (see, for example, refs. 1 and 4). Such data for various structural components can be found in ref. 5. The data in ref. 5, however, has been mainly used in fixed wing aircraft applications.

The flight maneuver sequence of events compiled for rotary wing aircraft, as described in this paper, provide the data on specific flight conditions. This type of data is especially useful in identifying the damage potentials of the applied load at various operations during the flight. The data specific to each operation can be used to estimate the percent of a component's life expended as a result of that flight operation. This information is critical to the structural integrity of the aircraft and development of a more efficient planning for inspection and maintenance of the aircraft. The data is especially useful to ascertain the significance of various flight operations on tear and wear of structural and mechanical components of the aircraft.

CONCLUSIONS

The process of flight data acquisition for rotary wing aircraft is explained in this paper. The paper describes various elements of this process and the type of flight data compiled in conjunction with tracking the structural integrity of aircraft. The presented method groups flight data in three weight categories and lists them by a series of pre-identified flight conditions (regimes). Major conclusions of the study are:

- The item-by-item sequence of events data recording is helpful in providing a more refined and more descriptive way of summarizing the flight data.

- The self-test mechanism and automatic upgrading of flight spectrum as conducted by the data acquisition system are features that are especially helpful in assuring the quality of the incoming flight data.

- The system offers an efficient mechanism to compile up to 30 hours of flight data in one download. An ample amount of information on the aircraft parameters is acquired and summarized by the system in each flight.

- The results of the survey using the system described in this paper can be used as an input to a comprehensive structural tracking program for rotary wing aircraft.

It is anticipated that the results of this study will enhance the process of tracking the structural integrity of rotary-wing aircraft. Possible future research in this area is expected in automated condition assessment of aircraft structural components and estimation of their potential accumulated damage on a flight-by-flight basis. An advanced system capable of conducting the needed structural analysis should have a built-in module containing the fatigue properties of critical structural components. Furthermore the system will need a direct communication link with the current SEI's monitoring system so that it can receive the flight data for the purpose of structural analyses.

REFERENCES

1. Broek, D., *The Practical use of Fracture Mechanics,* Kluwer Academic Publishers, The Netherlands, 1989.

2. American Society for Testing and Materials, *Annual Book of ASTM Standards*, Section 3, Volume 03.01, Designation: E 1049, 1987.

3. Mohammadi, J. and Polepeddi, R., "Application of Field Data to Fatigue Life Estimation of Structures," *Proceedings, Society for Experimental Mechanics Conference*, held in Los Vegas, Nevada, 1992.

4. Barsom, J.M., and Rolfe, S.T., *Fracture & Fatigue Control in Structures, Applications of Fracture Mechanics*, Second Edition, Prentice Hall, Englewood Cliffs, N.J., 1987.

5. Gallagher, J.P., et al, *USAF Damage Tolerant Design Handbook, Rept. #AFWA L-TR-82-3073,* University of Dayton Research Institute, Dayton, OH, May 1984.

TABLE I Samples of AH-1W Sequence of Events

MANEUVER	PARAMETER RANGES	SEQUENCE OF EVENTS
NORMAL TURN @ 0.7 Vh	$1.3g \leq N_z < 1.8g$ $0.55Vh \leq$ AIRSPEED < 0.75 Vh ROLL ATTITUDE $> \|10^{\circ}\|$ -500 FEET PER MINUTE $\leq$ RATE OF DESCENT $<$ 500 FEET PER MINUTE. $-35^{\circ} <$ PITCH ATTITUDE $< 35^{\circ}$. ENGINE TORQUE 1 $<$ 405 FT. -LBS. ENGINE TORQUE 2 $<$ 405 FT. -LBS. MAIN ROTOR SPEED $<$ 326 RPM. $0\% \leq$ LATERAL STICK POSITION $<$ 100%. $0\% \leq$ LONGITUDINAL STICK POSITION $<$ 100%. $0\% \leq$ PEDAL POSITION $<$ 100%. COLLECTIVE STICK POSITION $>$ 10%.	ROLL ATTITUDE EXCEEDS 10° ANGLE OF BANK. THEN N_z EXCEEDS 1.3g BUT DOES NOT EXCEED 1.8g. THEN N_z GOES BACK BETWEEN 1g AND 1.3g. THEN ROLL ATTITUDE GOES LESS THAN 10° ANGLE OF BANK. THEN YOU WAIT FOR POSSIBLE SUBSEQUENT ROLL EXCURSIONS. WHEN THEY ARE COMPLETED THE TURN IS OVER. LOG AMOUNT OF TIME IN TURN AND ENTER A NEW REGIME.

TABLE I (continued)

AIRCRAFT: AH-1W MANEUVER	PARAMETER RANGES	SEQUENCES OF EVENTS
STRAIGHT AND LEVEL FLIGHT 0.5 Vh	$0.5g \leq N_z < 1.3g$ 0.4 Vh $\leq$ AIRSPEED < 0.55 Vh ROLL ALTITUDE < $\|10^{\circ}\|$ -500 FEET PER MINUTE $\leq$ RATE OF DESCENT < 500 FEET PER MINUTE. $-13^{\circ} \leq$ PITCH ATTITUDE < 7° 30 FT. -LBS. $\leq$ ENGINE TORQUE 1 < 405 FT. -LBS. 30 FT. -LBS. < ENGINE TORQUE 2 < 405 FT -LBS. MAIN ROTOR SPEED < 326 RPM 0% $\leq$ LATERAL STICK POSITION < 100% 0% $\leq$ LONGITUDINAL STICK POSITION < 100% 0% $\leq$ PEDAL POSITION < 100% COLLECTIVE STICK POSITION > 10%	IF THIS COMBINATION OF PARAMETER VALUES OCCURS FROM ANY OTHER FLIGHT REGIME THEN THIS REGIME IS ENTERED.

TABLE II Samples of AH-1W Flight Data

Peak Nz Counts:		Valley Nz Counts:	
-1.00g to -0.75g	0	-1.00g to -0.75g	0
-0.75g to -0.50g	0	-0.75g to -0.50g	0
-0.50g to -0.25g	0	-0.50g to -0.25g	0
-0.25g to 0.00g	0	-0.25g to 0.00g	0
0.00g to 0.25g	0	0.00g to 0.25g	0
0.25g to 0.50g	0	0.25g to 0.50g	6
0.50g to 0.75g	4	0.50g to 0.75g	0
0.75g to 1.00g	3	0.75g to 1.00g	0
1.00g to 1.25g	0	1.00g to 1.25g	0
1.25g to 1.50g	0	1.25g to 1.50g	0
1.50g to 1.75g	0	1.50g to 1.75g	0
1.75g to 2.00g	0	1.75g to 2.00g	0
2.00g to 2.25g	0	2.00g to 2.25g	0
2.25g to 2.50g	0	2.25g to 2.50g	0
2.50g to 2.75g	0	2.50g to 2.75g	0
2.75g to 3.00g	0	2.75g to 3.00g	0
3.00g to 3.25g	0	3.00g to 3.25g	0
3.25g to 3.50g	0	3.25g to 3.50g	0
3.50g to 3.75g	0	3.50g to 3.75g	0
3.75g to 4.00g	0	3.75g to 4.00g	0
4.00g to 4.25g	0	4.00g to 4.25g	0
4.25g to 4.50g	0	4.25g to 4.50g	0
> 4.5g	0	> 4.5g	0

####	FCC	ELAP. TIME	MANV. TIME	FCC DESCRIPTION	ROTOR	ALTITUDE
1	267	00:02:38.1		Rotor Start/Stop (Low wgt)	280<rtr<295	alt<3k
2	0	00:09:36.7		Normal Takeoff (Low wgt)	295<rtr<326	alt<3k
3	6	00:09:53.2	00:00:16.5	Steady Hover (Low wgt)	295<rtr<326	alt<3k
4	51	00:09:56.1	00:00:02.9	Forward Flt < .3Vh (Low wgt)	295<rtr<326	alt<3k
5	562	00:10:00.1	00:00:04.0	Asc Hover/Forward Flight below .3 VH (Low wgt)	295<rtr<326	alt<3k
6	51	00:10:03.2	00:00:03.1	Forward Flt < .3Vh (Low wgt)	295<rtr<326	alt<3k
7	261	00:10:03.2		Normal Landing (Low wgt)	295<rtr<326	alt<3k
8	3	00:12:12.6		Jump Takeoff (Low wgt)	295<rtr<326	alt<3k
9	562	00:12:18.1	00:00:05.5	Asc Hover/Forward Flight below .3 VH (Low wgt)	295<rtr<326	alt<3k
10	6	00:12:49.1	00:00:31.0	Steady Hover (Low wgt)	295<rtr<326	alt<3k
11	532	00:12:50.1	00:00:01.0	Desc Hover/Forward Flight below .3 VH (Low wgt)	295<rtr<326	alt<3k
12	6	00:12:52.1	00:00:02.0	Steady Hover (Low wgt)	295<rtr<326	alt<3k
13	562	00:12:54.1	00:00:02.0	Asc Hover/Forward Flight below .3 VH (Low wgt)	295<rtr<326	alt<3k
14	6	00:13:21.1	00:00:27.0	Steady Hover (Low wgt)	295<rtr<326	alt<3k
15	562	00:13:23.1	00:00:02.0	Asc Hover/Forward Flight below .3 VH (Low wgt)	295<rtr<326	alt<3k
16	6	00:13:46.6	00:00:23.5	Steady Hover (Low wgt)	295<rtr<326	alt<3k
17	51	00:13:47.4	00:00:00.8	Forward Flt < .3Vh (Low wgt)	295<rtr<326	alt<3k
18	36	00:13:49.0	00:00:01.6	Left Sideward Flt (Low wgt)	295<rtr<326	alt<3k
19	370	00:13:49.8	00:00:00.8	Low Speed Maneuver below .3 VH (Low wgt)	295<rtr<326	alt<3k
20	51	00:13:50.1	00:00:00.3	Forward Flt < .3Vh (Low wgt)	295<rtr<326	alt<3k
21	532	00:13:52.1	00:00:02.0	Desc Hover/Forward Flight below .3 VH (Low wgt)	295<rtr<326	alt<3k
22	832	00:13:53.9		Maximum Band Threshold Crossing (Low wgt)		
				Offending Value(s): ROT - 4		

FATIGUE LOADS SPECTRA DERIVATION FOR THE SPACE SHUTTLE-SECOND CYCLE

Raphael Ortasse
Member of the Technical Staff, Engineering Specialist
Rockwell - Space Systems Division
Downey, California

113054

N95-19470

P.27

359189

SUMMARY

Some of the environments and loads experienced by the Space Shuttle or future reusable space vehicles are unique, while others are similar to those encountered by commercial and/or military aircraft.

Prior to the Space Transportation System (STS) flights, fatigue loads spectra were generated for the Space Shuttle based on anticipated environments and assumptions that were shown not to be applicable to the actual flight environments the vehicle experienced. This resulted in the need to generate a new cycle of fatigue loads spectra, which was based on measured flight data as well as mission profiles, reflecting the various types of service and operations the vehicle and payloads experienced.

1. INTRODUCTION

This paper presents the environment fatigue criteria defined for the purpose of deriving the fatigue loads spectra for the Integrated Vehicle Baseline Configuration (IVBC-3) third cycle, the methodology used to generate the fatigue loads spectra for each segment of the flight, and the elements for which the fatigue loads spectra were generated.

1.1 Baseline Vehicle Configuration

The baseline vehicle, also known as Configuration No. 6 Vehicle 6.0, consists of the Orbiter, the External Tank (ET), and two Solid Rocket Boosters (SRBs).

The relative locations of the Orbiter, External Tank and Solid Rocket Boosters are shown in Figure 1. This configuration is pertinent to the pre-launch, liftoff and the initial ascent phases of the Orbital mission. The orbiter vehicle is launched in a vertical attitude by means of the Space Shuttle main engines (SSME) and two SRBs. The orbiter lands horizontally similar to conventional aircraft. The configuration for the descent and landing phase is presented in Figure 2. Figure 3 summarizes a typical sequence of events of the Space Shuttle mission.

The ferry flight from Edwards Air Force Base in California to Florida requires the Orbiter be mated with a Boeing 747 Carrier Aircraft. This mated configuration is shown in Figure 4. It should be noted that an aerodynamically shaped fairing (Tail Cone) is attached to the aft section of the Orbiter in order to reduce base drag and other aerodynamic disturbances during the ferry flight.

1.2 Payloads Weights

The design maximum payload capability of the Space Shuttle is 65,000 pounds for an easterly launch from the Eastern Test Range (ETR) at Kennedy Space Center (KSC). Figure 5 shows the weight of the payloads for 30 flights used in present analysis, and Figure 6 shows the payloads for the next 12 flights. Mission 51L and seven DOD payloads are not included in those figures.

The maximum payload carried at liftoff to date was 49,999 lbs., the Ulysses, on STS-41. The minimum weight carried aloft at liftoff was 10,823 lbs., on STS-1. The average payload of 30 flights (excluding DOD flights) used in the present analysis is 35,716 lbs., and the average payload weight of the next anticipated 12 flights is 34,218 lbs, which indicates the same trend. On the basis of the data presented a variety of payloads were used in IVBC-3 fatigue loads spectra derivation wherever the payload was a significant parameter.

2. DEFINITION OF MISSION/FLIGHT FOR FATIGUE ANALYSIS

As stated in the introduction, in order to carry out an appraisal of the potential life of the Space Shuttle Vehicle on the basis of the missions/flights carried out to date and the IVBC-3 load cycle, the loading that is considered must reflect the various types of missions/flights that have and will be experienced.

Three types of missions/flights have been experienced by the Space Shuttle Vehicle.

1. Approach and Landing Test (ALT) Flights. 2. Ferry Flights. 3. Orbital Missions.

The Approach and Landing Test Flights were carried out on the Orbiter vehicle Enterprise only and was not considered in our present fatigue analysis.

2.1 Definition of Approach And Landing Test (ALT) Flights

There were two types of ALT Flights: (1) Captive and (2) Captive with separation.

1. In the case of the Captive Approach and Landing Test flights, both manned and unmanned configurations, a flight is defined as follows: The interval between the time when the Shuttle Carrier Aircraft's (SCA) landing gears lift off and the time when they lift off again for the next flight. The flight includes landing and the ground activities that occur between landing and the liftoff of the subsequent flight.
2. In the case of the Approach and Landing Test flights where separation occurred a flight is defined as follows: The interval from the time when the Shuttle Carrier Aircraft landing gears lift off, through the time when the Orbiter's landing gears touch down and lift on the orbiter is reduced to essentially zero, through the ground operations, until the time when the SCA's landing gears lift off for the subsequent flight.

2.2 Definition Of Ferry Flights

The ferry flights are carried out for the purpose of transporting the Orbiter to and from the launch sites or maintenance, testing or refurbishing facilities. Aside from the variation in the distance between the two points to which the Orbiter is transported, all ferry flights are anticipated to be practically the same and have the same configuration (Figure 4). The

main difference between the ferry flights is the number of hops that are carried out between the initial ferry flight and the final destination. Therefore, there is a need here to define both: (1) A Ferry Flight and (2) A Hop.

1. A ferry flight is defined as: A flight when the Orbiter is ferried by means of piggyback attachments (Ferry kit) to a 747 aircraft from the landing site to the launch site, or from the launch site to a maintenance, testing or refurbishing facility. A ferry flight may consist of 2 or more hops.
2. A ferry flight hop is defined as: The interval from the time when the Shuttle Carrier Aircraft's landing gears lift off, through SCA landing gear touchdown, and when lift on the carrier aircraft and shuttle is reduced to essentially zero, until the carrier aircraft's gears lift off for the next hop. The hop includes all the ground activities that occur between the touchdown of the SCA and its liftoff in the subsequent flight.

2.3 Definition Of an Orbital Mission

The launch vehicle configuration for the Orbital Mission consists of the Orbiter (which carries a crew and payload), External Oxygen and Hydrogen Tank (ET) and two Solid Rocket Boosters (SRB's).

An orbital mission is made up of nine basic segments. They are: (1) Ground Operations, (2) Pre-Launch, (3) Buildup and Liftoff, (4) Ascent*(5) Space Operations (6) Entry (7) Descent and Landing Approach (Atmospheric Flight) (8) Landing Impact or splashdown and (9) Landing Rollout.

2.3.1 Ground Operations

Ground Operations is defined as all the events that take place from when the vehicle comes to a full stop on the runway in the completion of an Orbital Mission until it is readied for hoisting for piggyback ferry on the Carrier Aircraft and after landing of the carrier aircraft and as it is placed on the taxiway and then readied for next launch.

The ground operations include the following activities:

- Tow Orbiter from runway to OPF (Orbiter Processing Facility)
- Safe vehicle
- Jack vehicle to level position of carrier A/C (with gears off ground and retracted and with residual RCS/OMS fuel still on board
- Attach to carrier aircraft
- Demate from Carrier Aircraft and lower to taxiway
- Tow to Orbiter Processing Facility (OPF)
- Jack
- Prepare Orbiter for next mission
- Change jacks
- Lower from jacks
- Tow to mating building (VAB)
- Install payload
- Jack to level
- Hoist to mate
- Erecting
- Tow to Launch Pad by means of crawler
- Pressurize
- Fuel

*Note: The Ascent segment consists of several sub-segments. They are 4a) Roll Maneuver, 4b) Hi-Q, 4c) Pre-SRB Separation, 4d) Post SRB Staging, 4e) Orbiter Burn Max Load Factor, 4f) Orbiter Main Engine Shut Down, 4g) External Tank Separation, 4h) Orbit Insertion.

2.3.2 Pre-Launch

Pre-Launch is defined as the interval beginning with completion of vehicle transportation and installation on the launch pad and terminating with the commencement of final countdown.

The events that need to be considered for this segment are:

- Wind exposure ET Empty
- Wind exposure ET Full

2.3.3 Buildup And Liftoff

Buildup and liftoff together are the segment usually called liftoff. It begins at first SSME fire, approximately 6.611 sec. before SRB ignition. It continues for 14 seconds, approximately until the beginning of the roll maneuver segment. The dividing line between buildup and liftoff is at 6.5 sec. after SSME ignition. This represents the time just before SRB ignition.

The buildup and liftoff conditions include the effects of the following events:
- Orbiter main engine (SSME) thrust buildup (Symmetric & unsymmetric)
- SRB engines thrust buildup (symmetric & unsymmetric)
- SRB internal pressure buildup
- Wind loads
- Simulated Control system response
- SRB ignition over pressure
- Holddown bolt release

2.3.4 Ascent

Ascent is defined as the interval beginning at the instant of vertical liftoff or holddown release and terminating with the decay of thrust cut-off transients at insertion into orbit for the Orbiter and at SRB separation for the Booster.

The ascent conditions include the effects of the following events:

- Roll Maneuver
- High Dynamic Pressure - Subsonic speed
- High Dynamic Pressure - Supersonic speed
    - Flight Controls (,)
    - High and low performance of SRB's
    - SSME thrust variation
    - Alternate rotational accelerations - pitch, roll, yaw
- Rocket Booster Burn - Max Load Factor
    - High/Low SRB Thrust
- Pre-SRB Staging (Pre-SRB Separation)
    - Heavy/Light ET Configuration

    - High/Low SSME Thrust
    - Low/High Orbiter Payload Weight
    - Thrust Mismatch
- Post SRB Separation (Pre-Staging)
    - Heavy/Light ET Configuration
    - High/Low SSME Thrust
    - High/Low SSME Thrust
    - Low/High Orbiter Payload Weight
    - SSME Trim in Pitch and Yaw
- Orbiter End Burn - (Pre ET Separation)
    - High/Low SSME Thrust
    - Low/High Orbiter Payload Weight
    - SSME Trim in Pitch and Yaw
- Orbiter Main Engine Shutdown (MECO)
- External Tank Separation
- Orbital Insertion

2.3.5 Space Operation

Space operation is defined as the interval beginning with the decay of thrust cutoff transients at orbit insertion and terminating with initiation of de-orbit retro impulse. The space operations operation phase includes transfer and mechanical operations in space.

2.3.6 Entry

Entry for the Orbiter is defined as the interval beginning with the initiation of de-orbit retro-impulse and terminating after the transition of the Orbiter to aerodynamically controlled flight. For the booster, it is defined as the interval beginning at the instant of separation from the Orbiter and terminating after the transition of the booster to aerodynamically controlled flight.

2.3.7 Descent And Landing Approach

Descent and Landing Approach (Atmospheric Flight) is defined as the interval beginning with transition of the Orbiter or in the case of the booster to aerodynamically controlled flight and termination at touchdown or splash down respectively.

2.3.8 Landing Impact or Splashdown

Landing Impact for the Orbiter is defined as the interval beginning with the main landing gear touching down on the runway and terminating with the nose gear touchdown. For the Booster splashdown, it is defined as the interval beginning with the initial contact with the water and terminating when the whole Booster is in contact with the water.

2.3.9 Landing Rollout

Landing Rollout is defined as the interval beginning with nose landing gear contact with the runway and terminating with the full stop of the vehicle on the runway.

2.4 Definition Of Ground - Ascent - Orbit Dock Cycle And Deorbit Descent - Ground Cycle

In the case of the Approach and Landing Test and Ferry Flights, the definition of the G-A-G cycle is essentially the same as it is defined for an airplane. However, for the Orbital mission it is necessary to modify the definition of the G-A-G cycle. During the Orbital mission, the Orbiter will experience two equivalent Ground-Air-Ground cycles during a completed Orbital flight. Therefore, the Orbiter will experience two distinct load buildup cycles. These two cycles are identified herein as:
G-A-O/G-A-D cycle or Ground-Ascent-Orbit/Ground-Ascent-Dock Cycle and
D-D-G /U-D-G or De-Orbit-Descent-Ground Cycle/Undock-Descent-Ground Cycle

An aborted mission will experience only one equivalent G-A-G cycle, identified herein as: G-A-G, Ground-Ascent-Ground cycle.

3. ENVIRONMENT

There are three types of environments that need to be considered in the derivation of the fatigue loads spectra for the Space Shuttle Vehicle. Some of these environments are unique to the Space Shuttle and others are similar to those encountered by commercial and/or military aircraft.

The three types of environments are: (1) Natural Environment, (2) Man-made Environment, and (3) Induced Environment.
1. NATURAL ENVIRONMENT - is defined as those external conditions that exist in nature independent of the vehicle. Examples: temperature, pressure, radiation, winds, gusts, precipitation, meteoroids, and dust.
2. MAN-MADE ENVIRONMENT - is defined as those external conditions that are man-made and that exist independent of the vehicle. Examples: sonic booms, explosions, air contaminants, and debris in space.
3. INDUCED ENVIRONMENT - is defined as those conditions created by the vehicle or its systems, or by response of the vehicle to the natural environment. Examples: aerodynamic pressures and forces, aerodynamic heating, rocket exhaust pressures and heating, wind induced bending loads, and differential pressure such as experienced during ascent.

3.1 Wind Definition And Criteria

Ground and in-flight winds and gust are among the natural environments that are considered significant parameters when design and fatigue loads are generated for the Space Shuttle Vehicle structure. Wind design requirements are divided into five separate sets of wind data, each of which corresponds to one of the segments of the orbital and ferry flights. These are winds experienced during (1) On-Pad, Pre-launch, (2) Ascent, (3) Orbiter Entry, Descent and Landing, (4) Ferry Flights, (5) Transportation, and (6) Winds considered for support Facilities. For the purpose of fatigue loads derivation, the above winds are grouped into two categories. They are: (1) Ground Winds data, and (2) In-flight winds data.

1. Ground winds data are defined as those winds which are experienced at heights of 10 to 15 .3 meters (32.8 to 500 ft.) above the ground.
2. In flight winds data are defined as those winds which are experienced at heights of 152.4 meters to 80 kilometers (500 ft to 262,400 ft) above the ground.

Wind design requirements are normally specified in terms of a horizontal wind velocity with an azimuth and with or without gust. Criteria of wind design as defined in Section 5.0 of Reference 1 are applicable for at least one flight of the fatigue life of 100 Orbital flights.

3.1.1 Ground Winds

Ground winds, experienced from various azimuths and acting on the Integrated Space Shuttle vehicle in the fueled and unfilled configurations, are the primary load source when the Shuttle is on the launch pad in the pre-launch condition. The criteria and the number of occurrences of the fueled and unfueled configurations are discussed in Sections 1.6.2.1 through 1.6.2.4 and 4.1 of Reference 3.

3.1.1.1 Ground Winds Used For Pre-Launch IVBC-3 Analysis

To generate the IVBC-3 fatigue loads spectra, measured ground winds at KSC, taken from July 1967 through April 1968, are used. The specifics of the measured data are as follows: The measured wind data (velocity and azimuth) were received from NASA /MSFC . The wind measurements (velocity and azimuth) were taken at 3, 18, 30, 60, 120 and 150 meter elevations. The units of velocity and azimuth were in meters/sec and in degrees, respectively. Measurements were recorded every tenth of a second. A total of 50 measurements, each approximately 10 to 13 minutes long, were analyzed for fatigue analysis. The 18 meter (60 feet) is the reference height at KSC for ground winds; therefore, wind data for each month at 18 meter is used for analysis.

3.1.2 In-Flight Wind

In-flight wind is the largest contributor to structural loads during the first stage of ascent. During the descent phase of the Orbital mission, the wind contributes significantly to structural loads during landing impact.

3.1.2.1 Ascent

Because of the large contribution of the wind to structural loads during the first-stage of ascent, extensive analysis was performed to assess the effects of various wind conditions on the IVBC-3 generic trajectories. A large matrix of synthetic wind cases was run for each of the missions studied. The ascent GN&C trajectory simulation includes a wind model that is capable of generating synthetic wind profiles representing any statistical probability for a given launch month and wind azimuth. Shear buildups of any probability level and different magnitudes of gust were inserted in the probability wind at a specified altitude. The types of synthetic winds used in the IVBC-3 analyses are described in Reference 2 Section 6.3.2, Pages 6-10.

The use of the synthetic winds in combination with gust is not adequate for fatigue analysis for two reasons. First, this approach does not yield a continuous time history of the load response. Second, this approach combines the load due to wind shear and gust, while for fatigue there is a need to have the loads due to wind shear and gust separately, since they are two separate phenomena. The approach taken in fatigue analysis is to consider the load due to wind shear having its own cycle, and the occurrence of the cyclic load due to gust as being superimposed on the load due to wind shear. Therefore, for fatigue analysis, it was necessary to make use of the measured wind profile taken by NASA/MSFC during a period of two years. These measurements were taken at various altitudes for each of the 12 months of the year. NASA provided Rockwell with 1800 measured wind profiles, 150 for each month of the year. These wind measurements consist of both wind velocity and

azimuth. Since 1800 wind cases would be too large of a number to handle and expensive, there was a need to reduce the number of the cases to an acceptable minimum number. The method and procedure used to reduce the number of wind cases to 100 (the number of missions the Space Shuttle Vehicle is certified to) is presented in Section 5.1.4 of Reference 3.

3.2 Gust - Definition And Criteria

Per Reference 5, discrete gusts are specified in an attempt to represent, in a physically reasonable manner, characteristics of small-scale motions associated with vertical wind velocity profiles. Gust structure usually is quite complex and is not always understood. For vehicle design studies, discrete gusts are usually idealized because of their complexity and in order to enhance their utilization.

Gusts may be defined in the form of sharp-edged and repeated sinusoidal waves. They are important types, since they can influence the design of space vehicles. Quasi-square-wave gusts with amplitudes of approximately 9 m/sec have been measured. These gusts are frequently referred to as embedded jets or singularities in the vertical profile. By definition, Reference 5, a gust is a wind speed in excess of the defined steady-state value; therefore, these gusts are employed on top of the steady-state wind profile values. Discrete gusts may vary in length from 60 to 300 meters, thus having different frequencies in addition to varying velocity.

3.2.1 Ground Gust - Velocity and Azimuth

In the present IVBC-3 fatigue analysis a spectrum more representative and reflective of the gust turbulence that the Space Shuttle Vehicle actually sees and responds to was used. Actual measured wind profiles obtained from MSFC for all months of the year were used. These measured winds included gust occurrences. The wind measured profiles were converted into a forcing function and applied to the Vehicle at discrete nodes of the math model ,on the ET, the Orbiter and the SRB/SRM .

The load simulation methodology used to generate the fatigue loads spectra due to the 100 ground wind and gust conditions for the Pre-launch is consistent with that used to generate critical design conditions cases for Pre-launch.

The procedure used to select the segments of the measured winds on each of the components is described in Reference 3 Section 5.1.1and Reference 4. The length of stay on the launch pad for each mission is given in Reference 3 Section 1.3.2.1. The minimum, maximum and average stay on the launch pad are 14, 180 and 47.5 days, respectively.

3.2.2 In-flight Gust - Velocity And Azimuth

In-flight winds were defined in Section 3.1.2. Although the In-Flight winds and gust are treated separately in fatigue, they are, nonetheless, interrelated in that the wind shear is considered as the Quasi-Steady state about which the gust is oscillating.

The aerodynamic loads during ascent flight can be viewed as following one of these general ground rules:

1. Quasi-Steady state and repeatable airloads are due to steering trajectories which program a selected profile of angle of attack in both pitch and yaw planes. Pitch plane program is selected to bias airloads to a favorable range, which involves in a bias to negative angle of attack during the Hi-Q region of Ascent. Yaw steering program is selected to account for

prevailing crosswinds for a given trajectory and minimize excursions of yaw angles of attack due to winds from a nominal trajectory.
2. Random load oscillations due to wind shears (change in wind speed vs. altitude) during Ascent.
3. Random load oscillations due to gusts (abrupt change in wind speed with altitude) during Ascent.

Discrete gusts are a simplified representation of atmospheric turbulence, which can be characterized as a continuous random process. There are two forms of representing atmospheric turbulence:

1. A turbulence spectra for Horizontal flight, such as observed by aircraft.
2. A turbulence spectra for Vertical flight, such as observed by sounding rocket, Jim-Sphere, and Space Shuttle Vehicle.

In this section the latter will be discussed with the procedure followed to generate the gust turbulence velocity and number of occurrences at the mach numbers of interest.

3.2.2.1 Gust Turbulence For Vertically Flying Vehicles

Reference 6, Section 8.4.8, defines the power spectrum recommended for use in elastic body studies for small scale motion by the following expression:

$$E(K) = \frac{683.4\ (4000k)1.62}{1 + 0.0067\ (4000K)^{4.05}}$$

where the spectrum E(K) is defined so that integration over the domain 0<K<a yields the variance of the turbulence. In the above equation E(K) is the power spectral density [$(M/sec)^2$/cycles per Meter] at wave number K (cycles per meter). This function represents the 99 percentile scalar wind spectra for small-scale motions.

The above turbulence spectra were converted to a synthesis of discrete gust exceedance spectra in the following manner:

1. The spectrum (over normalized frequency range of .00001 to .025 cycles/meter) is divided into 7 frequency band widths.
2. The numerical integration of turbulence power spectral density over each frequency band width is carried out to yield increment of variance. The square root of this quantity is calculated and gives the RMS gust velocity over a given frequency band.
3. Distribution of gust cycles, frequency vs. velocity, is assumed to be represented by a normal distribution function.
4.A representative flight path distance of 10.0 km/mission for 100 missions is used as the basis for total number of gust occurrences.
5. Gust occurrences from various frequency bands are superimposed by RSS combination (similar to ground wind turbulence approach for the IVBC-2) and gust velocity exceedance curves are developed in a similar manner.

3.3 Buffeting

Certain flight regimes and configurations will experience buffeting. These effects are accounted for in the derivation of the fatigue loads spectra where they are significant. Buffet load occurrences are assumed to be a function of the component's natural frequency

and the time spent in the buffet environment. The primary components that are subjected to a significant buffet and their natural frequency are:

Vertical Tail $f_n = 3.7$ cps for Mx , $f_n = 8.1$ cps for My
Inboard Elevon $f_n = 10$ cps Outboard Elevon $f_n = 12.5$ cps
Body Flap $f_n = 13.4$ cps
Upper Rudder $f_n = 30.6$ cps Lower Rudder $f_n = 32.8$ cps

3.4 Temperature And Temperature Cycle

The Orbiter undergoes one temperature cycle during the ascent segment of an Orbital mission, one temperature cycle per orbit during space operations, and one temperature cycle during the descent and landing segment of the Orbital mission.

The Orbiter can fly in a number of different modes which affect temperature management. The typical mode is one where the Orbiter rotates for an even exposure to the sun. The most extreme mode is when one side (usually the bottom of the Orbiter) faces the sun during the whole exposed part of the orbit. Temperature measured data is available from STS-1 through STS-5. However stresses due to on-orbit temperature cycles were determined to be negligible.

4 MISSION AND FLIGHT PROFILES

4.1 Orbital Mission Profiles

The launch vehicle configuration and the definition of an Orbital mission are given in sections 1 and 2. Figure 3 illustrates a typical Space Shuttle Vehicle Orbital Mission Profile.

In the fatigue appraisal of commercial and military aircraft, the various types of flight or mission profiles are grouped into several categories based on the aircraft usage. These mission profiles, grouped into several categories, contain rational definitions of airplane loading and usage, such as external/internal store configuration (which may impact the loading on the aircraft) and take-off/landing weights for evaluation of ground handling loads and ground-air-ground load cycles. The flight or mission significant parameters are also defined in order to be able to derive the fatigue loads spectra for each segment of the flight.

A similar approach to commercial and military aircraft was taken in defining the mission profiles of the Space Shuttle Vehicle which are different than those for airplanes. The Space Shuttle Vehicle mission consists of many flight segments which are short in duration.. Furthermore, the significant parameters that affect the load response at each segment are different and in some segments numerous.

In the following paragraphs each segment of the Ascent mission profile is discussed.

4.1.1 Ground Operations

Definition of the events that take place during ground operations are given in section 2.3.1

4.1.2 Prelaunch

The definition of the Prelaunch segment is given in section 2.3 The primary load source for Prelaunch is ground winds from various directions experienced by the Space Shuttle Vehicle (SSV) while it is on the launch pad in the unfueled and fueled configurations. The number of wind velocity occurrences during the unfueled and fueled configurations is based on measurements of ground wind conditions at KSC. Wind exposure is affected by the length of time the Space Shuttle Vehicle is on the launch pad. The length of stay of the Space Shuttle Vehicle on the launch pad is compiled from orbital missions STS-1 through STS-40. There were forty-one shuttle missions from the initial flight of April 12, 1981 through May 24, 1991 when STS-40 was flown.

Figure 7 shows the time on the launch pad for each mission in the order that they were flown. Figure 8 shows the number of Shuttle launches occurring in each month of the year. Figure 9 presents the number of all the 100 launches based on the 41 missions distribution and used in the present analysis.

Figure 10 shows the probability of a stay on the launch pad exceeding a given length of time. This probability is derived from the 41 missions considered in the present analysis. In addition Figure 10 shows an exponential probability curve fitted through the measured data of the number of days stay on the launch pad.

To summarize, the criteria used to define the Pre-launch mission profile, based on analysis of the Shuttle stay on the launch pad for flights STS-1 through STS-40, are as follows:

1. The distribution of the stay on the launch pad in the unfueled condition will correspond to the distribution of stay on the launch pad experienced by STS-1 through STS-40.
2. The total number of days of stay on the launch pad for each month of the year that the SSV is projected to experience in 100 missions is given in Table 1.4.1.2-11 of Reference
3. The length of stay on the launch pad is given in terms of number of days, of hours and of seconds.
3. The fueled configuration is on the launch pad for 10 hrs. per mission or 1000 hrs. per 100 missions. To date, there has been an average of 1.7 tankings per mission. The same was applied in the IVBC-3 analysis, i.e., 1700 hrs. of on-pad exposure in the fueled configuration in 100 missions .

4.1.2.1 Methodology Of Developing Prelaunch Mission Profiles

Prelaunch mission profiles for SRB and Orbiter are constructed with the following parameters:

1. The number of days on launch pad 2. Wind Intensity Distribution Each Month:
3. Distribution of Wind Directions at KSC

Each wind segment was applied from the cardinal directions North (0 degrees), East (90 degrees), and South (180 degrees). (No wind is applied from the west since the service structure was considered to effectively block all wind from that direction.) The occurrences were distributed by direction according to MSFC recommendations.

4.1.3 Liftoff Mission Profile

The load cases used for fatigue liftoff were generated by the same system that is used for Design Certification Review (DCR) and Flight Readiness Review (FRR) liftoff loads

cases. The one hundred basic liftoff cases were defined by randomly deriving values for the input parameters.

The input parameters are as follows:

1. Payload (Model) Effect unpredictable so use all models available and assume equal probability except one zero payload and one 65K payload in 100 missions. (Also, some design cases have P0K or STS61G). 2. SRB Temperature. 3. SSME Thrust. 4. SSME Buildup Time. 5. SSME Thrust Misalignment. 6. SSME Side loads. 7. Flight Control Commands to aero surfaces. Measured data from 10 flights were used. 8. Wind Force of ground wind on structure. Measured wind data chosen by launch month. 9. SRB Thrust Misalignment. Angle from axis of SRB. Direction - equal probability of each possible direction. 10. SRB Thrust Offset distance from center axis of SRB. Direction - equal probability of each possible direction. 11. Mu for SRB Case Growth . 12. SRB Ignition Timing . 13. SRB Thrust Mismatch. Delta thrust between SRB's. 14. SRB Performance . SRB steady state thrust. 15. SRB Ignition Interval between signal to ignite and actual ignition. 16. SRB Rise Rate Slope of SRB thrust rise. 17. SRB Internal Pressure Buildup Profile. Use measured data with an equal probability of each. 18. Over pressure Scale Factor. 19. SRB Over pressure Timing . How shock wave of over pressure rises along vehicle. 20. Bolt Release Timing . 21. Structural Mismatch (Stacking Misalignment). 22. Engine Out (Yes/No) Input to the program since engine-out causes a design case. If an engine is out, randomly determine which one is out. 23. Engine Out Timing.

4.1.4 Roll Maneuver

In establishing the Roll Maneuver mission profile, use was made of the prelaunch and liftoff data. Essentially the significant parameters for the Roll Maneuver are: degree of inclination, payload weight, engine temperature, rotational acceleration, SRB gimbal angle, SRB internal pressure and SRB thrust. The roll maneuver is divided into two segments of load periods. The two time periods considered are different in that certain parameters maximize in each segment. The first segment occurs approximately 7 to 12 seconds at which time maximum negative rotational acceleration about x-axis and maximum SRB gimbal angles are experienced. The second segment occurs approximately 12 to 18 seconds at which time maximum positive rotational acceleration about x-axis, maximum SRB internal pressure and maximum SRB thrust are experienced. Since the variation in the loads experienced by the Space Shuttle Vehicle is not large during roll maneuver, only four cases were generated from trajectories which are considered as representative and were used to construct the 100 mission profiles. All the four cases used have a 65k payload. Three of the cases are trajectories with 28.5 degree inclination and the Propellant Mean Bulk Temperature (PMBT) was nominal, hot and cold. The one case with 57 degree inclination was used with nominal PMBT. The dynamic pressure was constant for both segments of the roll maneuver.

4.1.5 Hi-Q

In establishing the Hi-Q ascent mission profiles, the pre-launch and liftoff data from STS-1 through STS-40 was used to define parameters common to all segments of the orbital missions. In addition to common parameters, there are several other parameters that define the ascent profile segments of the Orbital flight. These are:

1. The Environment - Month of Launch, which defines what measured profiles to use.
2. Mass Properties - Vehicle Gross weight and Model
3. Aerodynamic Pressure Distribution

4. Angle of Inclination
5. Trajectory Data
   a. Dynamic Pressure
   b. Pitch and Yaw Angles
   c. Elevon Deflection Schedule (Inboard and Outboard)
   d. Propulsion (Thrust-SRM, SSME, OMS, RCS)
   e. Gimbal Angles

A discussion on each of the above parameters follows:

1. Environment - The 150 winds measured for each month of the year were used. The 2850 winds for two inclinations 28.5 and 57.0 degrees were used in the TRAKR program to generate the rigid load response . Out of all the TRAKR response cases, 100 cases representing 100 missions were selected to give a desired statistical distribution.
2. Mass Properties - The mass properties used in TRAKR representing the 100 mission profiles are given below for M=0.6 and M=2.20, respectively.
Gross weights at M=0.6
Orbiter G. W. = 255,000 lbs. ET G. W. = 1,913,015 lbs.
SRB/L+R G. W. 1,469,888 lbs. Total G. W. = 3,637,000 lbs.

X c.g . =11.21.8 in Yc.g. = 0.50 in Z c.g. = 380.90 in
Ixx = 11,442,300 lb-sec^2-in Iyy = 86,805,200 lb-sec^2-in Izz = 90,196,200 lb-sec^2-in
Ixy = 55,644 lb-sec^2-in Ixz =2,995,500 lb-sec^2-in Iyz = 18,672 lb-sec^2-in

Gross weight at M = 2.20
Orbiter G. W. = 255,000 lbs. ET G. W. = 965,173 lbs.
SRB/L+R G. W. 1,282,719 lbs. Total G. W. = 2,502,892 lbs.

3. Aerodynamics Pressure Distribution - The IVBC-3 integrated vehicle aerodynamic pressure distribution was used as defined in References 7 through 9.
4. Angle of Inclination - For the present fatigue analysis and definition of the mission profiles, two Inclinations were used, 28.5 and 57 degrees.
5. Trajectory Data - The trajectory data is developed by the Guidance, Navigation, and Control (GN&C) Group, and it is given in the time domain. Each wind profile has its own trajectory, since the program used to generate these trajectories is sensitive to the wind azimuth. The six-degree-of-freedom continuous system modeling program (CAMP) generates high-fidelity ascent trajectories incorporating an accurate representation of GN&C related avionics systems, rigid body equations of motion, vehicle propulsion models, aerodynamic models, mass properties, slosh dynamics, and wind and atmosphere models.

Table 1.4.1.4.2-2 of Reference 3 presents trajectory data for one wind (January Wind No. 1) used in the fatigue analysis for an Inclination of 28.5 degrees. It defines the following parameters at eight mach Numbers, M =0.6, 0.9, 1.05, 1.10, 1.25, 1.40, 1.8 and 2.20.

(a) Dynamic Pressure (PSF), (b) Pitch Angle (, degrees), and Yaw Angle (, degrees);
(c) Elevon Deflections, (degrees) for inboard and outboard elevons.
(d) Propulsion - thrust (lbs) for SSME engines 1, 2, & 3 and RSRB/LSRB engines 4, 5.

The 100 wind cases were selected so that they represent the best statistical representation for derivation of the fatigue loads spectra. Figures 11 and 12 illustrate the distribution of Q-alpha and Q-beta within the squatcheloid envelope for the eight mach numbers.

4.1.6 Post Hi-Q Profile

Post Hi-Q segment of the flight contains the following events:

1. SRB burn - maximum load factor. 2. Pre SRB separation. 3. Post SRB staging. 4. SSME burn - Orbiter maximum load factor. 5. SSME end burn.

Since there is little variation in the post Hi-Q segment of flight , the cases run for design were also used for the fatigue loads spectra evaluation.

SRB Burn - Maximum Load Factor consists of the following configurations:

1. High/low SRB thrust. 2. High/low SSME thrust 3. High/low ET weight. 4. High/low Orbiter weight.

Ten conditions were generated for this flight segment which are repeated 10 times to obtain 100 mission profiles.

Pre SRB Separation - is based upon following configurations:

1. Heavy/light ET configuration. 2. High/low SSME thrust. 3. Low/high Orbiter payload weight. 4. Thrust mismatch (maximum mismatch 710,000 lbs).

Five conditions were generated for the pre SRB separation segment which are sequentially repeated to obtain 100 mission profiles.

Post SRB Separation - is based on the following configuration:

1. Heavy/light ET configuration. 2. High/low SSME thrust. 3. Low/high Orbiter payload weight.

Four conditions were generated for this flight segment which are sequentially repeated to obtain 100 mission profiles.

SSME Burn - Orbiter Maximum Load Factor - the following configurations are considered:

1. High/low SSME thrust. 2. Low/high Orbiter payload weight. 3. SSME trim in pitch and yaw.

Three conditions were generated for the Orbiter maximum burn segment which are repeated sequentially to obtain 100 flight missions.

SSME End Burn - SSME end burn case also consists of the following configuration:

1. High/low SSME thrust. 2. Low/high Orbiter payload weight. 3. SSME trim in pitch and yaw.

Three conditions were generated for the SSME end burn segment which are sequentially repeated to obtain 100 missions.

4.2 Ferry Flight Profiles

Ferry flights of the mated Orbiter/747 CA configuration are performed to transport the Orbiter vehicle and its cargo from the post orbital mission landing site back to the KSC launch site. Occasional flights occur from KSC to the Rockwell plant in Palmdale for scheduled Orbiter maintenance, testing and refurbishing activities. This analysis considers a two hop flight for an Orbiter weight of 220,000 lbs. and a four hop flight for an Orbiter weight of 240,000 lbs.

An aerodynamically shaped tail cone is attached to the aft face of the Orbiter (Figure 4) to reduce the drag caused by the exposed SSME's and to smooth out the airflow to the 747 vertical tail surface. The added weight of the tail cone structure and other ferry flight kit items are slightly offset by the drainage of fluids and removal of personnel and other flight related equipment items. Boeing 747-100 aircraft is used to ferry the Orbiter from landing to launch site. The Orbiter incidence angle relative to the 747 body axis is 3.0 degrees. For all ferry flights, the Orbiter control surfaces are set to zero degrees except the body flap which is deflected - 11.7 degrees. This results in a nested configuration of the body flap with the attached tail cone.

5. METHODOLOGY

The methodology used in generating the fatigue loads spectra for IVBC-3 load cycle differs in a number of ways from the approach used in generating the IVBC-2 load cycle. One of the basic differences, is that the current fatigue loads spectra are generated on the basis of mission profiles and flight-by-flight events. It also reflects actual experience and utilization of the Space Shuttle Vehicle from STS-1 to STS-40, and fatigue load spectra generated reflects future anticipated utilization of the Space Shuttle Vehicle within IVBC-3.

The methodology of generating the fatigue loads spectra for each segment of the orbital flight ascertained the loads being generated by the models, and the definition of the environment, reflect the loads experienced by the Space Shuttle Vehicle.

Figure 13 is a flow chart diagram describing step by step the methodology used in generating the IVBC-3 fatigue loads spectra cases. Figure 14 is a flow chart diagram of the programs used to generate the fatigue loads spectra for the critical locations defined in Reference 3 Section 6.

The first block marked with Roman numeral I and Ia shows the various loads simulation programs available to the user to calculate loads for different segments of the Orbital flight. For example, lift off uses the FORTIE, ULTIMATE, and LIFTOFF programs and for Hi-Q wind shear environment the TRAKR program is used. On the other hand, flight measured data can be used in the fatigue spectra generation process if it is first converted to F-Arrays format, only then can it be handled by subsequent programs in this process. Block II shows the PRERASSP process described in detail in Section 7.2 of Reference 3. The purpose of this program is to pick peaks and valleys of a continuous time history and the time consistent loads or accelerations of the remaining degrees of freedom at each respective structural location. Block III shows the process of storing all peaks and valleys on direct access files for subsequent use in the spectrum generation. Block IV is the SALSA program which links together the peaks and valleys from different segments of flight environments at a specific location on the SRB/SRM or Orbiter. This program is further described in detail in Reference 3 Section 7.4. The output format of this program is described in Reference 3 Section 8.0.

Figure 15 is the Fatigue Loads Process Flow diagram.

6. COMPUTER PROGRAMS USED IN DERIVING FATIGUE LOADS SPECTRA

6.1 RASSP

The Rockwell Automated Stress Spectrum Program (RASSP) was developed to generate load and stress spectra and to perform fatigue and fracture mechanics analysis, primarily on the B1-B Bomber. The RASSP was developed by the El Segundo Division of Rockwell, and modified RASSP to accept the unique parameters and format of the Space Shuttle fatigue loads. Figure 16 is a flow diagram of the spectrum generation portion of RASSP. This figure shows the databases that RASSP accesses in order to generate a fatigue spectrum. During the IVBC-3 Fatigue Loads Analysis it became apparent that RASSP could not track time consistent loads, which were necessary for Fatigue/Fracture Damage Assessment. Because of this requirement to track time consistent loads, a program called Shuttle Automatic Loads Spectra Analyzer was developed to generate the fatigue loads spectra which tracks time consistent loads. SALSA was developed as a spectra generator only. It does not perform the fatigue and fracture analysis that RASSP performs:

1. Fatigue Program (Miner's Rule)
2. Non-linear Fatigue Program (YSAFE)
3. Crack Growth Program (EFFGRO)
4. Crack Growth Program (CRKGRO)

A description of SALSA is found in section 7.4 of Reference 3.

6.2 Prerassp

The PRERASSP program was developed to select load or acceleration peaks and valleys from time histories at selected locations on the Space Shuttle Vehicle (SSV) and the time consistent loads at the other Degrees of Freedom (DOF) at each respective location. This is accomplished by reading ASCENT, TRAKR, LIFTOFF, or F-ARRAY cases, and from this large set of loads/accelerations a smaller subset is selected. The time histories of peaks and valleys are then stored into files which will be stored on direct access files for use by SALSA. Following will be a short description of the inputs to the program and the different run options available to the user.

6.2.1 Prerassp Flow Chart

Shown in Figure 17 is a block diagram of the program PRERASSP and its accompanying routines. The purpose of this diagram is to give the user of this program some knowledge as to how the PRERASSP peak selection routine operates and to give the programmer an idea of where to look in case of future size errors or problems which may arise.

6.2.2 Other Programs

Other programs were developed for the purpose of generating the fatigue loads spectra for the various segments and also for storing the data generated. They are described in detail in Reference 3 section 7.0 .

7.0 CONCLUSIONS

1. The IVBC-3 generated fatigue loads spectra reflect the current usage and utilization of the Space Shuttle.

2. The fatigue environment defined for generating the IVBC-3 fatigue loads spectra reflects that experienced by the Space Shuttle.

3. Based on the discussion of the requirements for time consistent loads and analysis presented in Reference 3 , it would be more efficient for future reusable space vehicles to develop a finite element model and compute the voluminous data generated.

4. One of the main features of the post processing program developed is that it enables the structures engineer to directly read any fatigue spectrum generated into the fracture mechanics analysis program. This feature is discussed and illustrated in Reference 3.

ACKNOWLEDGMENT

The author would like to acknowledge the valuable contribution of Mr. Jack Barneburg of NASA/JSC for his technical review and comments as the Loads and Dynamics Panel Chairman and the team at Rockwell who worked diligently on this task. They are: Judith Goldish, Saroj Gupta, Brent Mann, Perwez Obaid and Rick Stauf.

REFERENCES

1. Structural Design Loads Data Book, Vol. 1, Baseline Vehicle Design Criteria and Missions, Report No. STS85-0169-1 dated October 1989.

2. Structural Design Loads Data Book, Vol. 1, Baseline Vehicle Design Criteria and Missions, Report No. STS85-0169-1, Vol. 1, dated February 1988.

3. STS85-0169-6 Structural Fatigue Loads Spectra Data Book, Vol. 6, ORBITER/RSRB/RSRM dated May 1993.

4. Definition of Prelaunch Wind Environment for Space Shuttle Fatigue Loads Spectra (Paper to be published October 31, 1994)

5. NASA TM 78118, "Terrestrial Environment (Climatic) Criteria Guidelines for use in Aerospace Vehicle Development", dated 1977.

6. NASA TMX-65767, "Terrestrial Environment (Climatic) Criteria Guidelines for use in Aerospace Vehicle Development", dated 1973.

7. Aerodynamic Design Data Book, Vol. 2, Launch Vehicle, Space Transportation System Division, Rockwell International, SD72-SH-0060-2M, dated August, 1983.

8. Documentation of the Aerodynamic Data Base for IVBC-3 Trajectory Analysis, Space Division, Rockwell International, Internal Letter SAS/AERO/82-676 dated December 7, 1982.

9. Shuttle Operational Data Book, Vol. 1, Johnson Space Center, JSC-08934 dated September 1982.

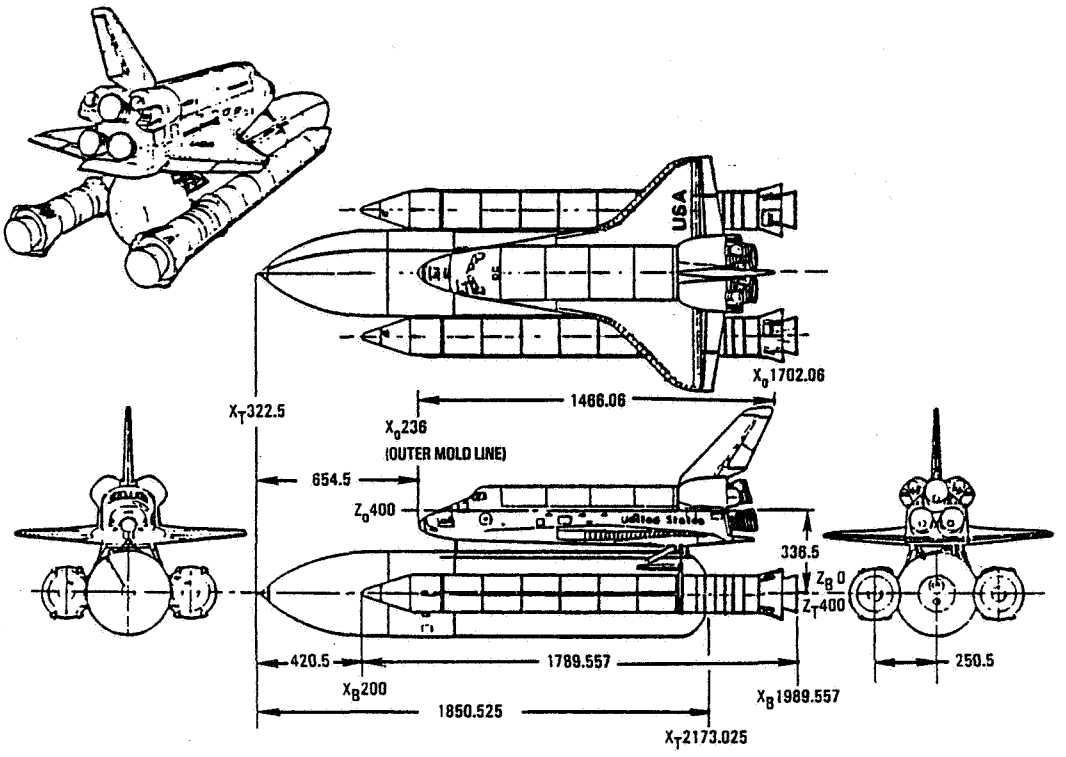

1. Launch Vehicle Geometry

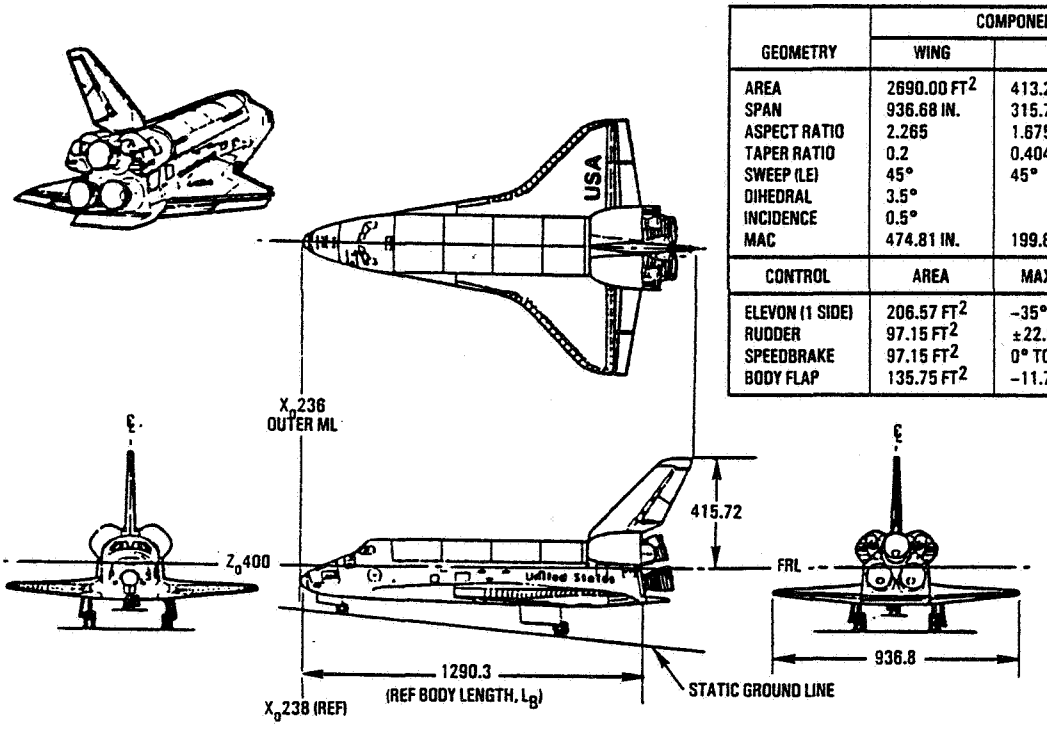

GEOMETRY	COMPONENT	
	WING	VERTICAL
AREA	2690.00 FT^2	413.25 FT^2
SPAN	936.68 IN.	315.72 IN.
ASPECT RATIO	2.265	1.675
TAPER RATIO	0.2	0.404
SWEEP (LE)	45°	45°
DIHEDRAL	3.5°	–
INCIDENCE	0.5°	–
MAC	474.81 IN.	199.81 IN.
CONTROL	**AREA**	**MAX DEFLECTION**
ELEVON (1 SIDE)	206.57 FT^2	−35° TO +20°
RUDDER	97.15 FT^2	±22.8°
SPEEDBRAKE	97.15 FT^2	0° TO 87.2°
BODY FLAP	135.75 FT^2	−11.7° TO +22.55°

2. Orbiter Geometry

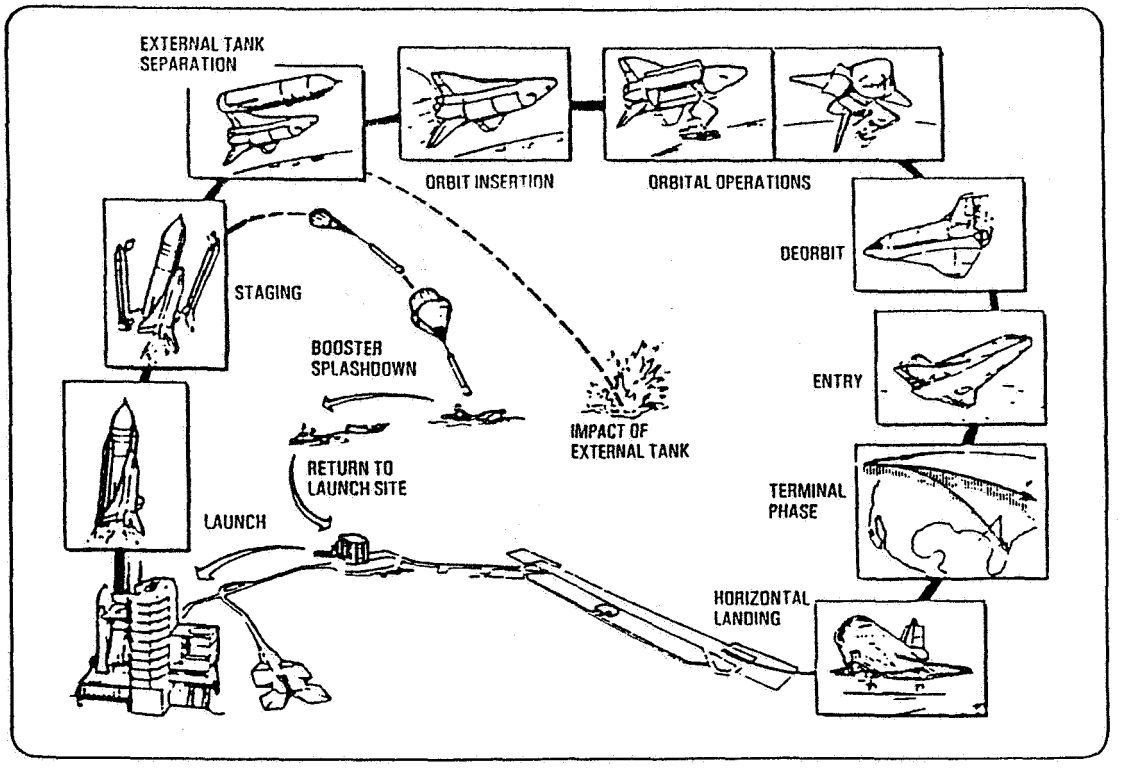

Space Shuttle Mission

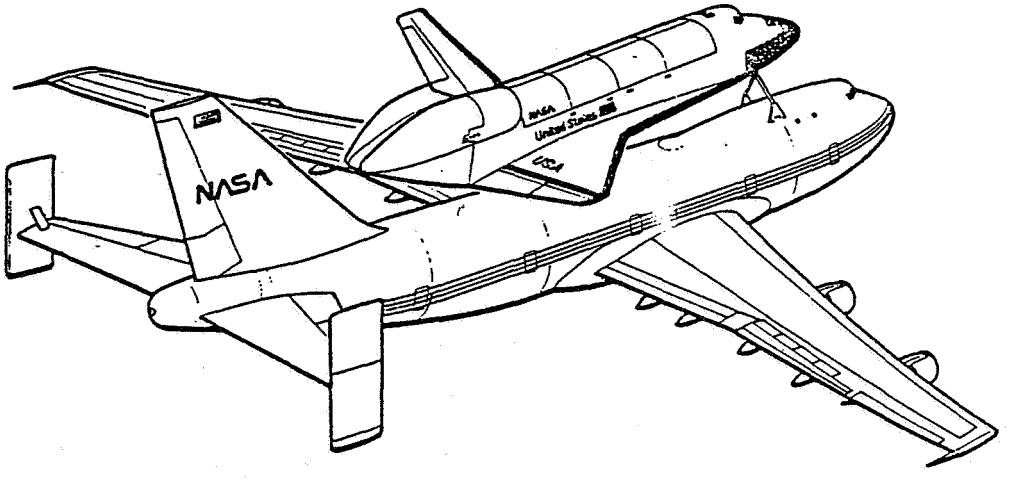

4. Mated Orbiter / 747 Configuration for Ferry Flights

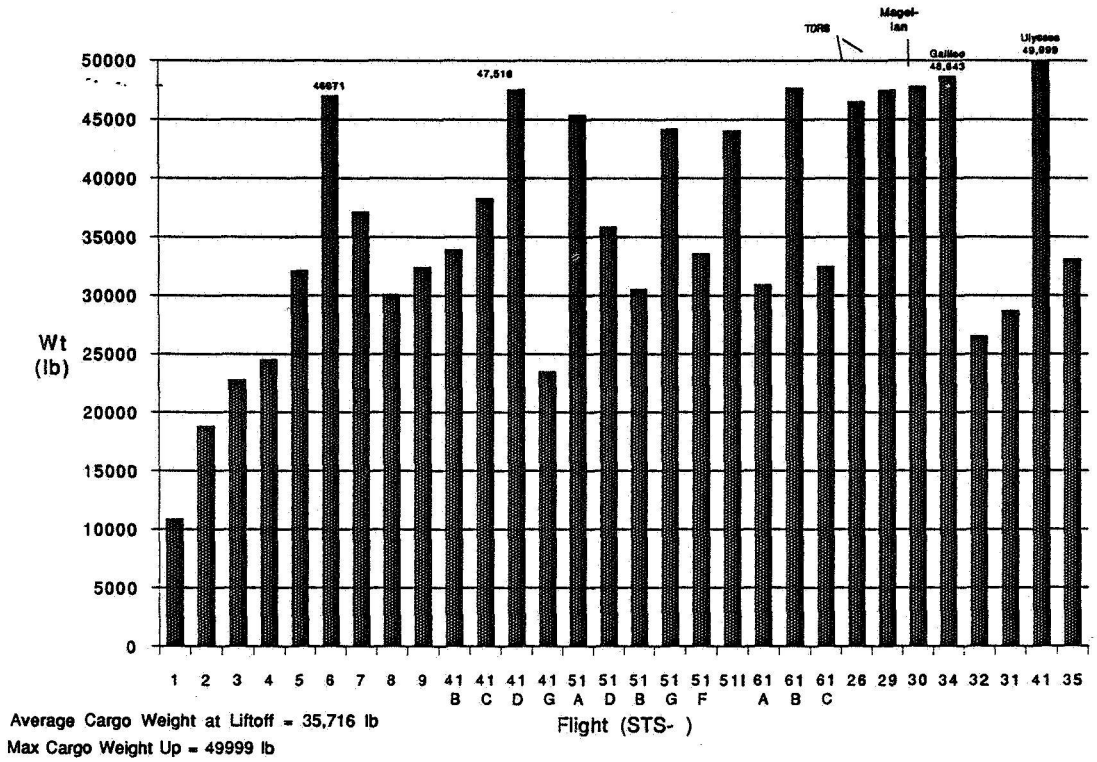

5. Cargo Weight at Liftoff

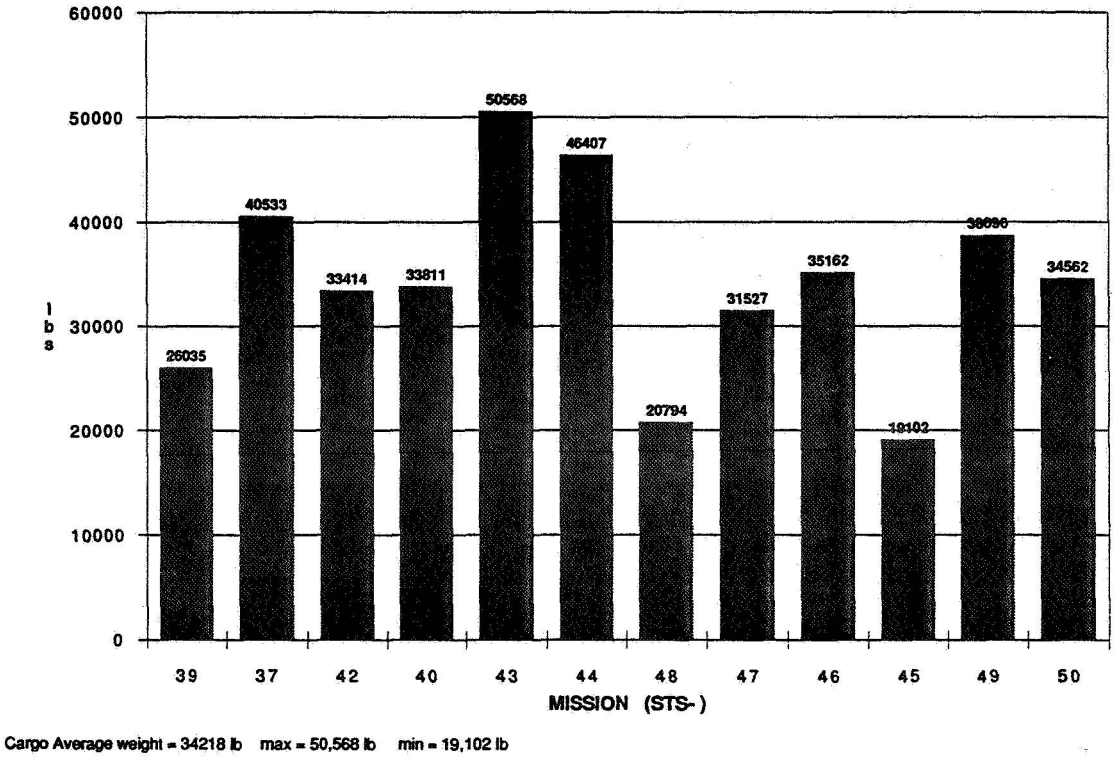

6. Cargo Weight for the Next 12 STS Flights

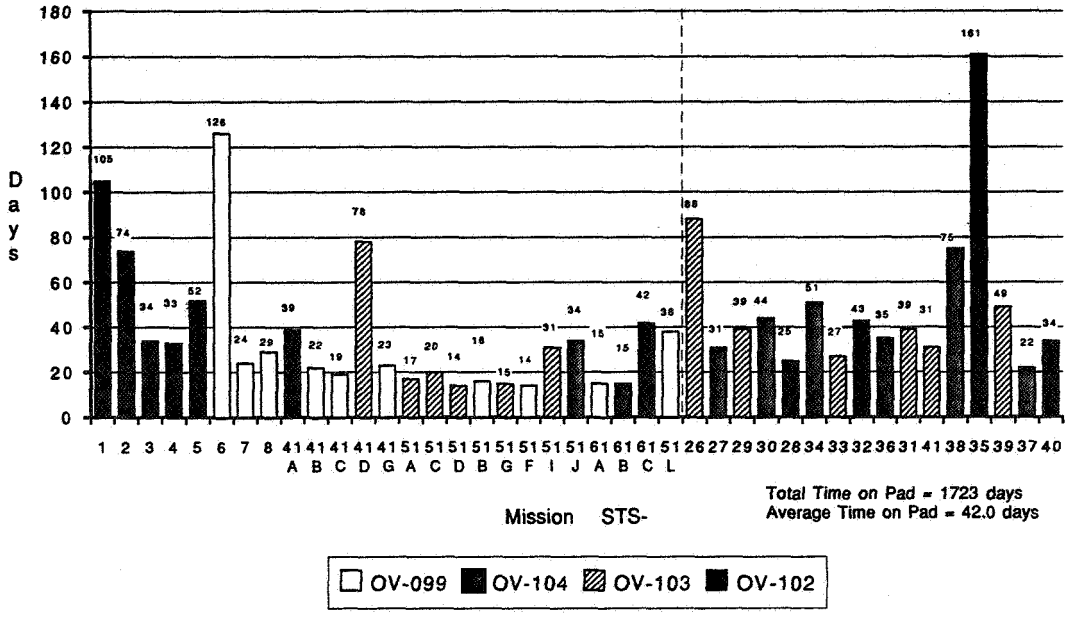

7. Time on Launch Pad for Each Mission

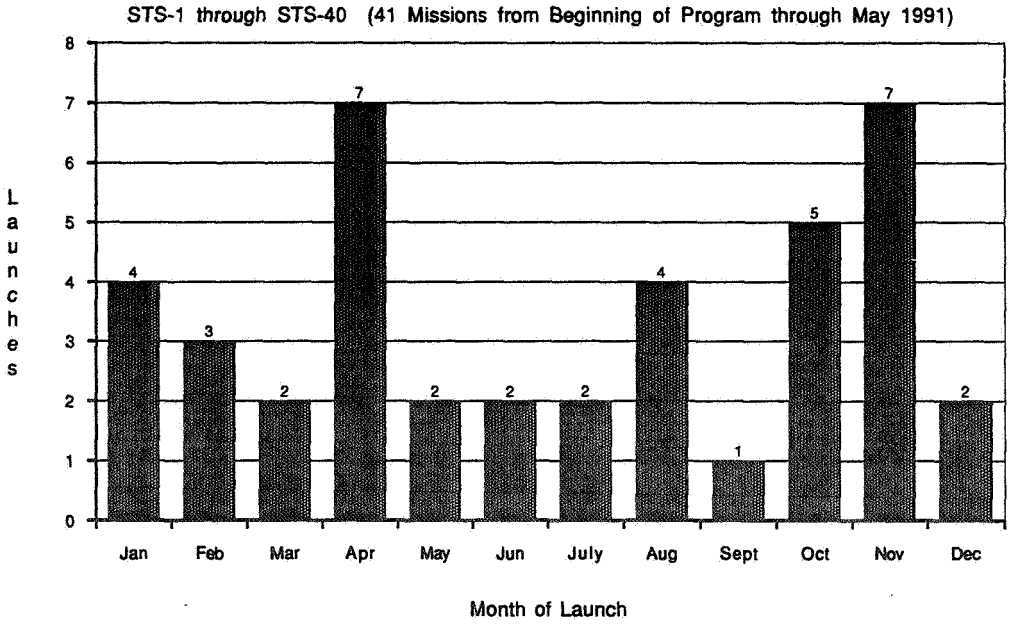

8. Number of Shuttle Launches in Each Month

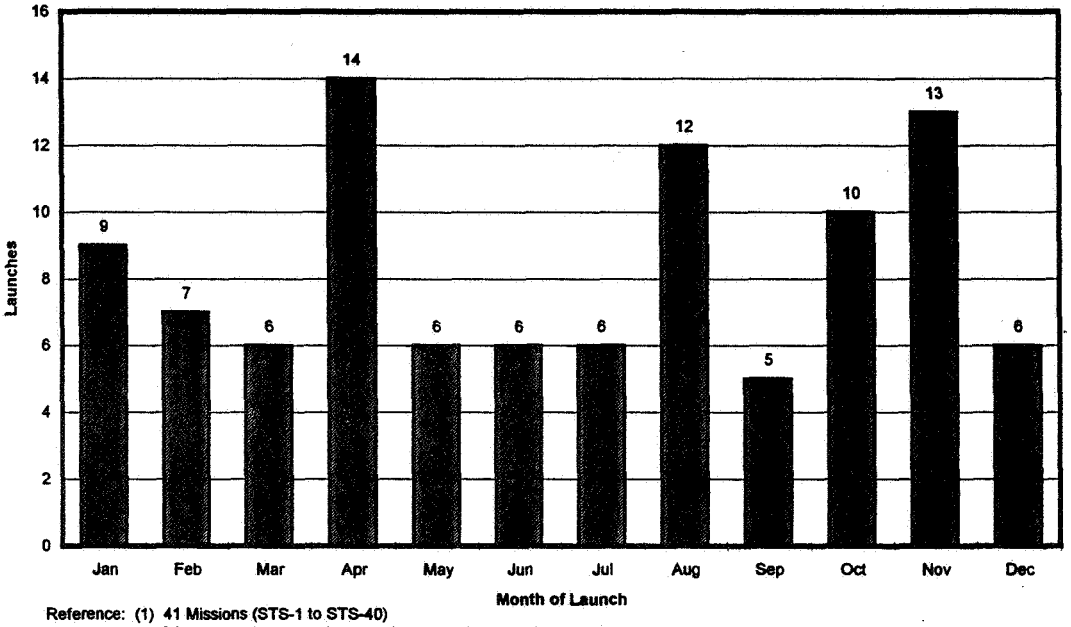

Reference: (1) 41 Missions (STS-1 to STS-40)
(2) 3 Missions after (1) and 48 missions from flight manifest (1992-1997)
(3) 8 Missions projected based on (1) and (2)

9. Distribution of 100 Missions from KSC

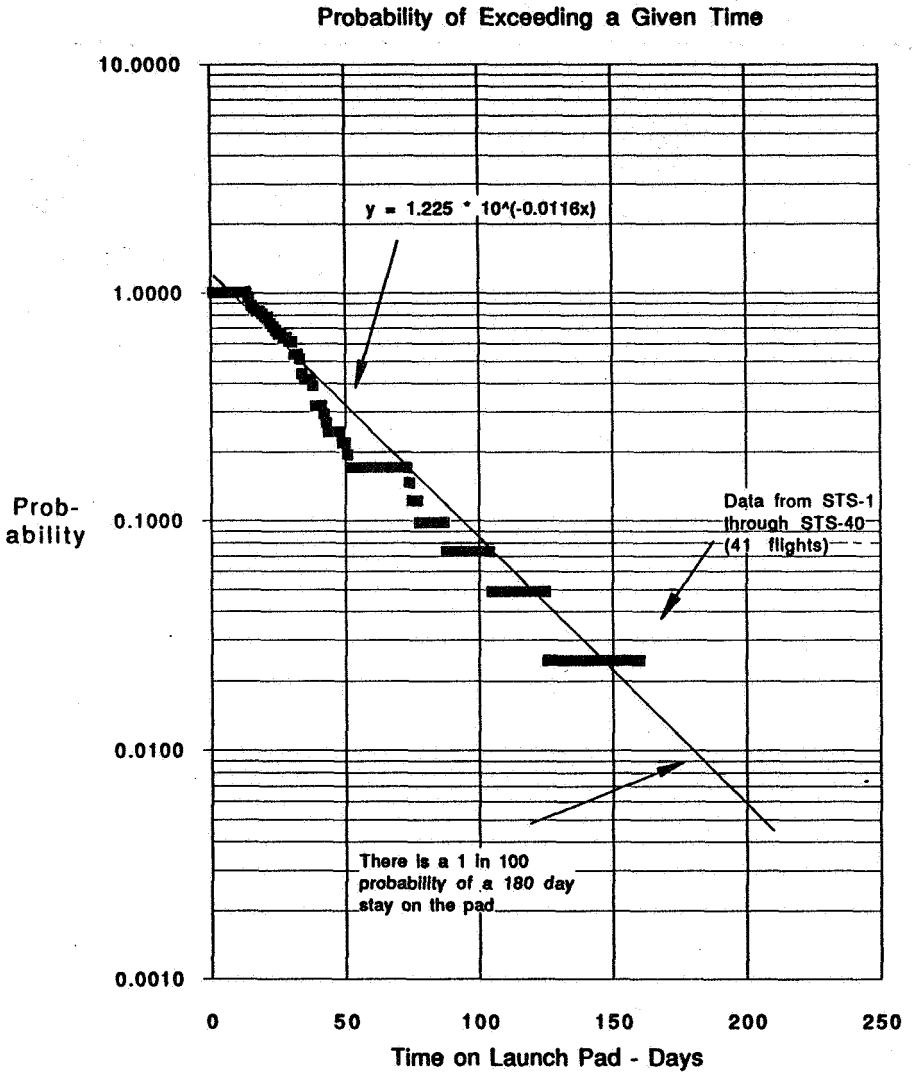

10. Time on Launch Pad

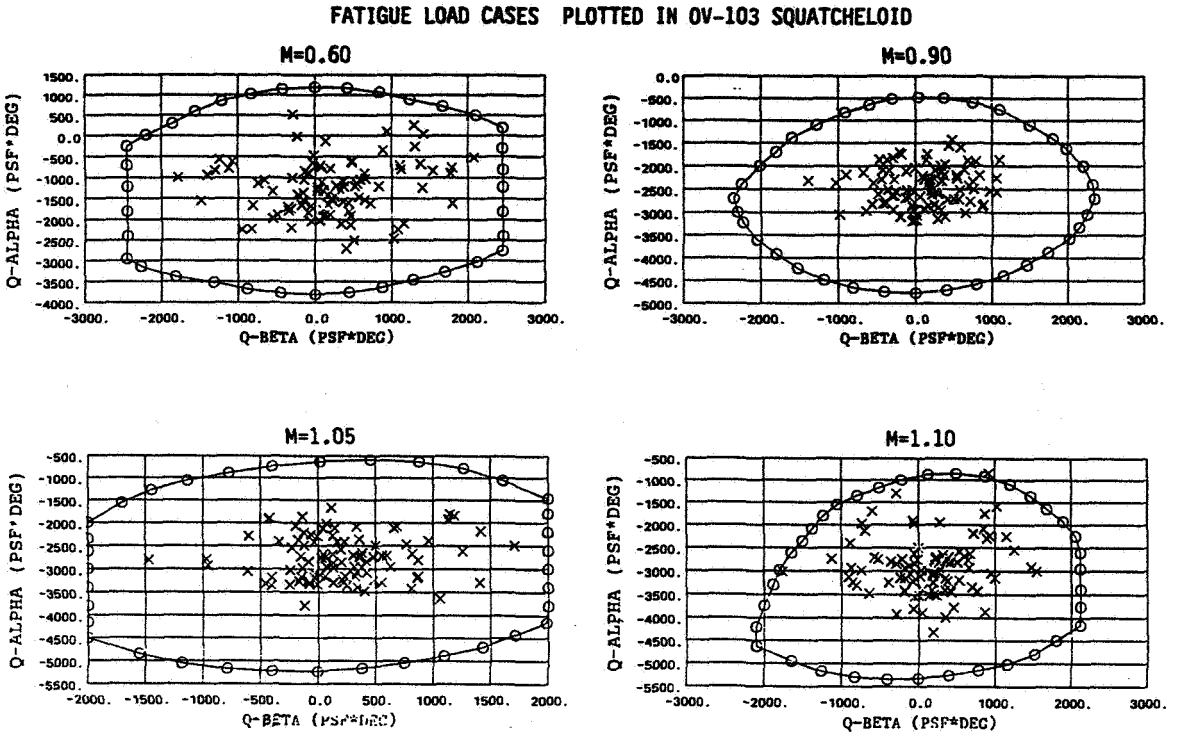

11. Q-alpha & Q-beta Products of 100 selected TRAKR Cases(M=0.6 thru M=1.10)

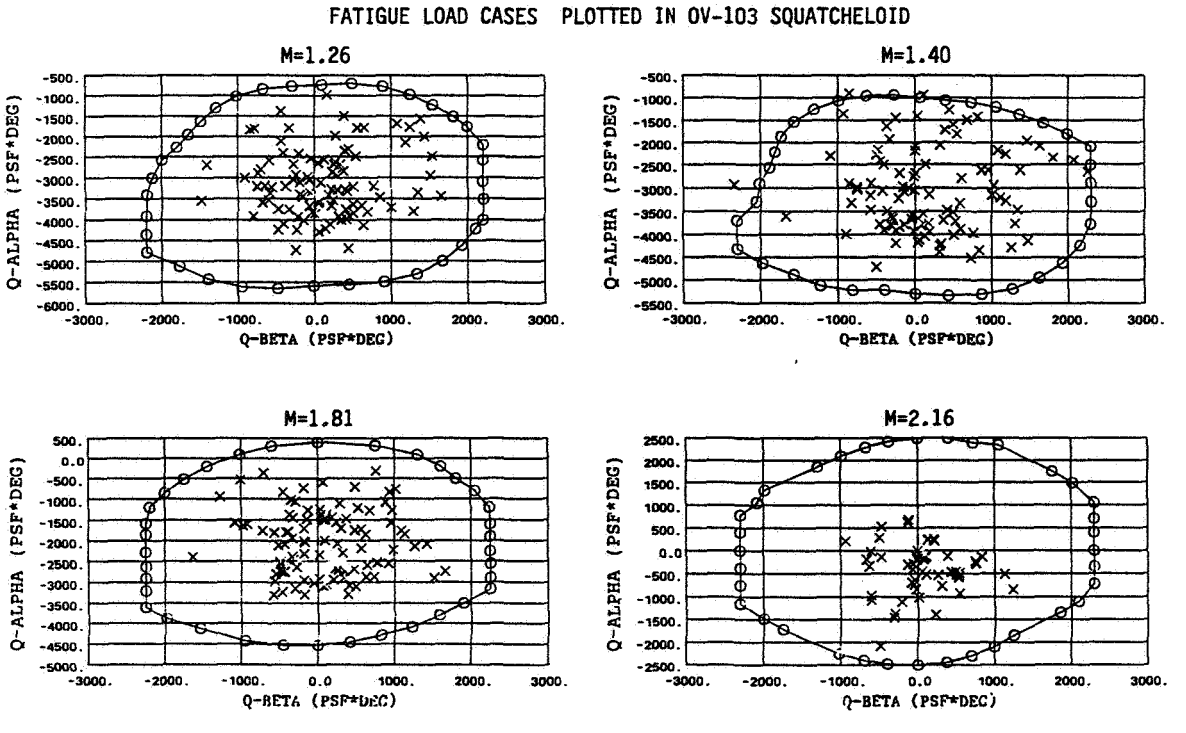

12. Q-alpha & Q-beta Products of 100 selected TRAKR Cases(M=1.26 thru M=2.16)

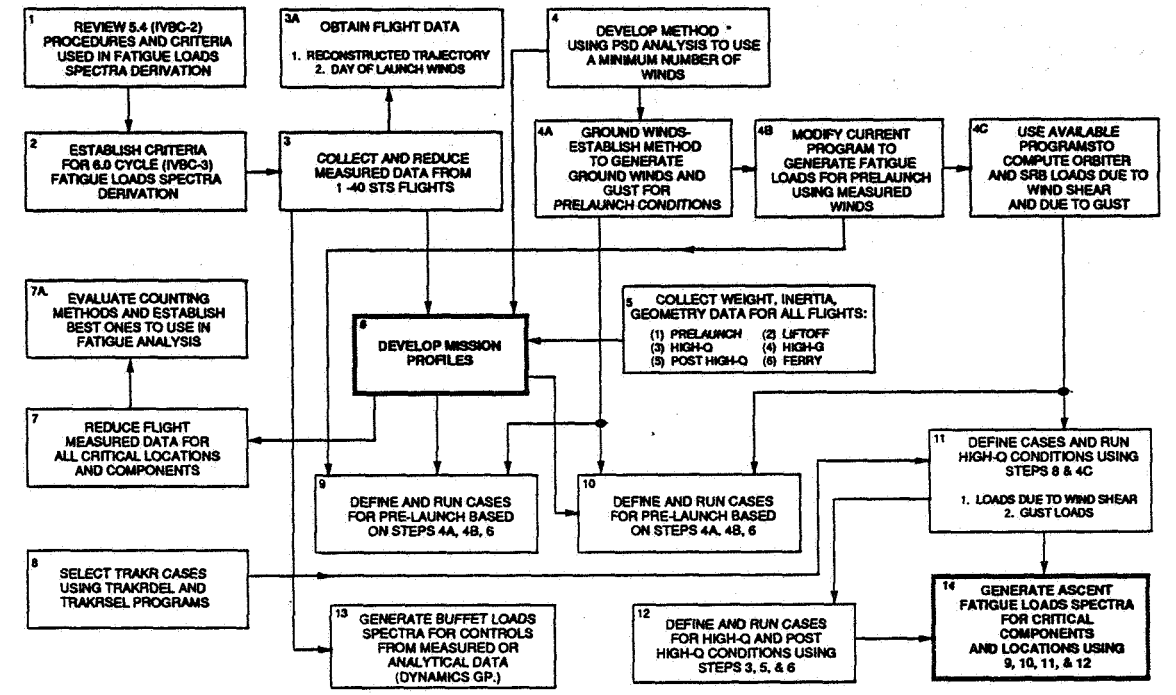

* METHOD WAS DEVELOPED BUT NOT APPLIED IN THE SELECTION OF THE WINDS HI-Q CASES. METHOD NEED TO BE FURTHER DEVELOPED TO BE APPLICABLE

13. Flow Chart of IVBC-3 Fatigue Loads Spectra Generation

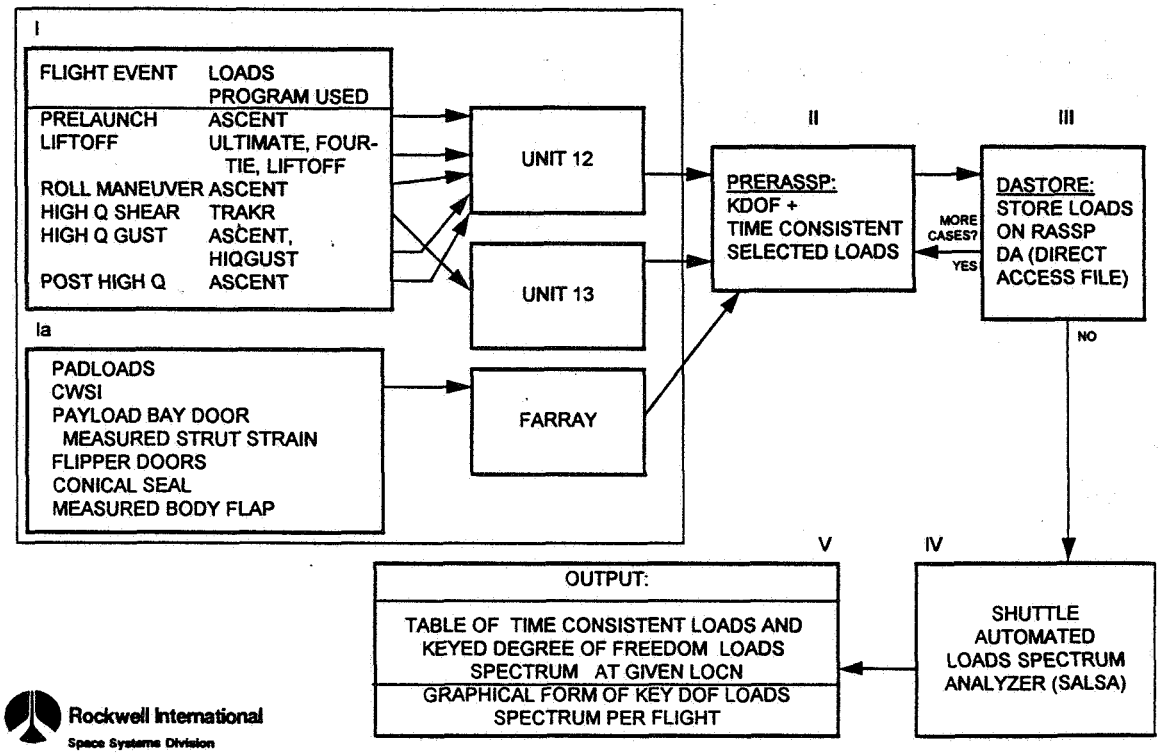

14. Generate Fatigue Loads Spectra Using Following Process

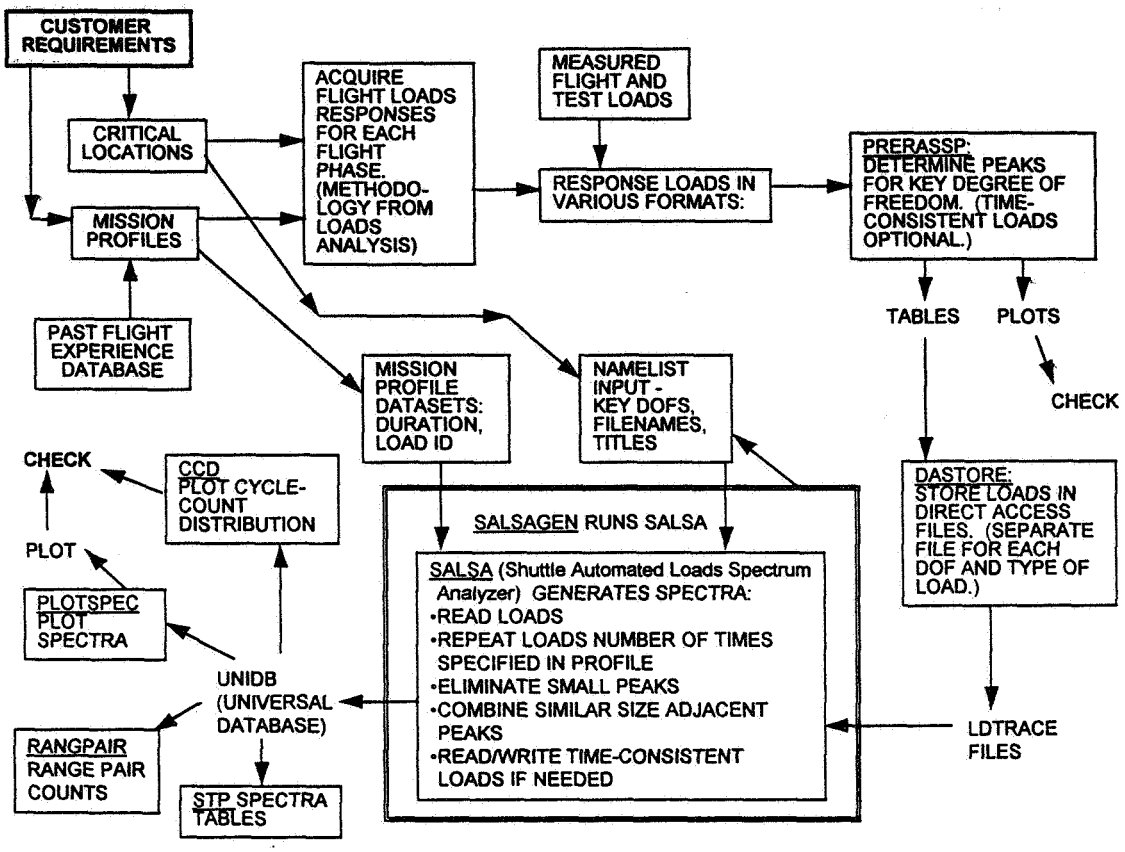

15. Fatigue Loads Process Flow

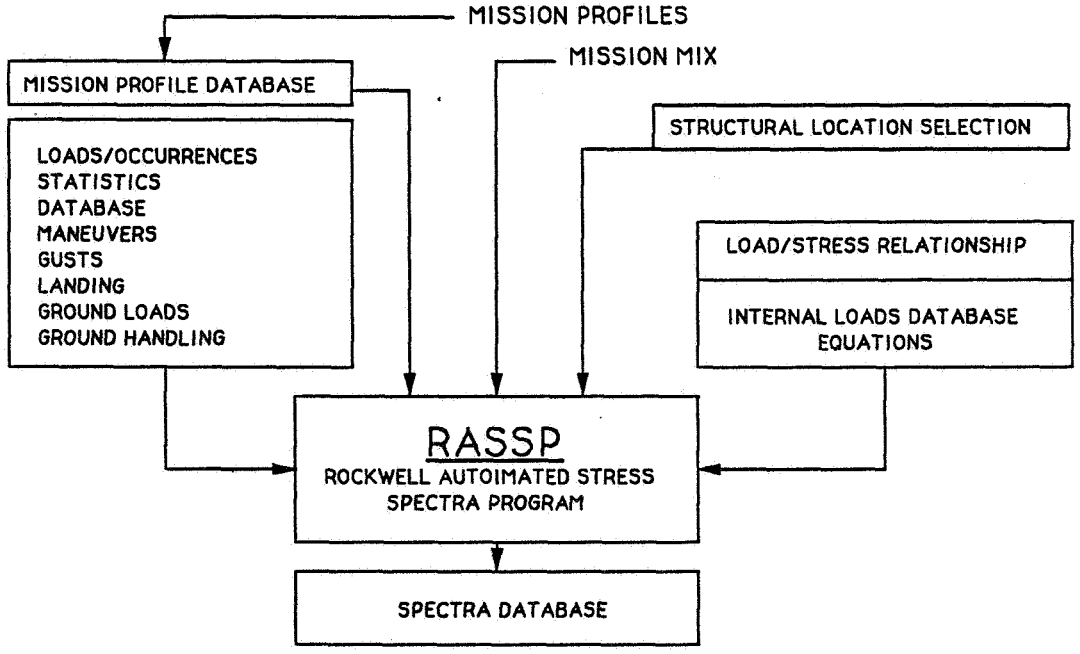

16. RASSP Fatigue Spectrum Generation Flow Diagram

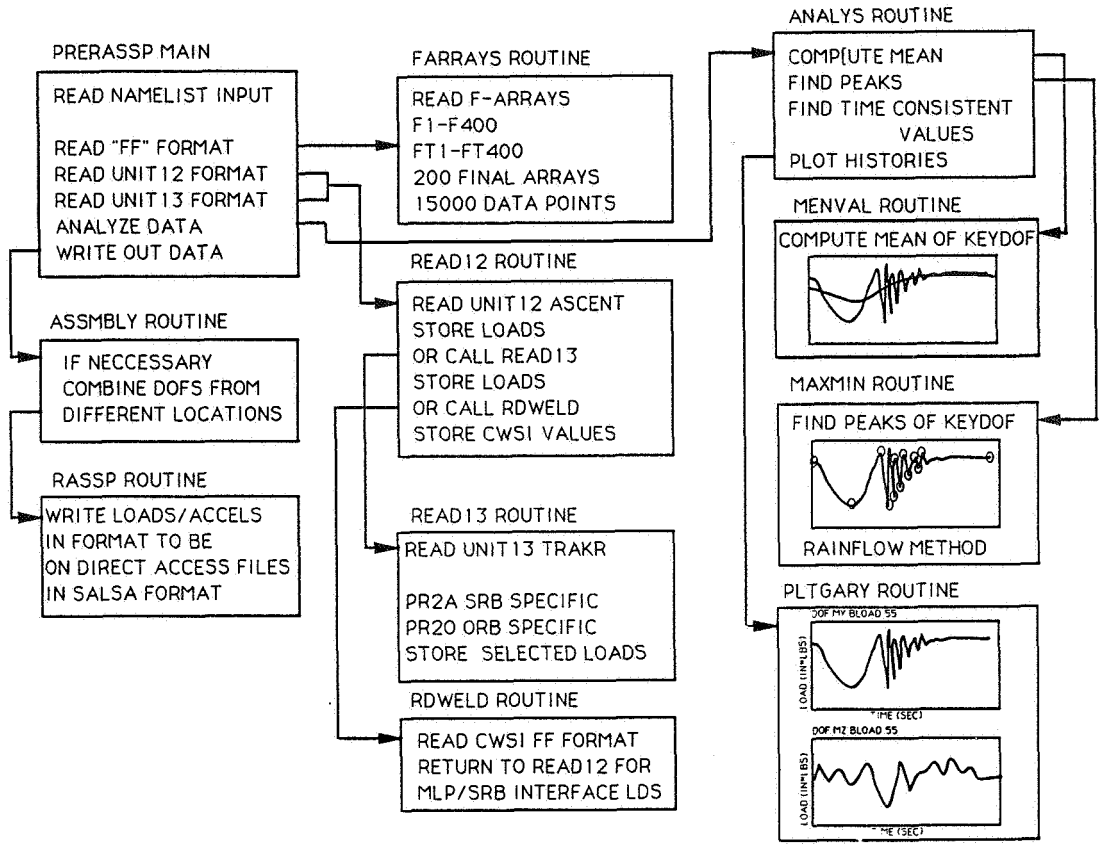

17. PRERASSP Flow Diagram

PREDICTION OF FATIGUE CRACK GROWTH UNDER FLIGHT-SIMULATION LOADING WITH THE MODIFIED CORPUS MODEL

U.H. Padmadinata
Laboratory for Strength of Materials, Components and Structures
PUSPIPTEK Serpong, Tangerang 15310, Indonesia

J.Schijve

Faculty of Aerospace Engineering, Delft University of Technology
Kluyverweg 1, 2629 HS Delft, The Netherlands

ABSTRACT

The CORPUS crack growth prediction model for variable-amplitude loading, as introduced by De Koning, was based on crack closure. It includes a multiple-overload effect and a transition from plane strain to plane stress. In the modified CORPUS model an underload affected zone (ULZ) is introduced, which is significant for flight-simulation loading in view of the once per flight compressive ground load. The ULZ is associated with reversed plastic deformation induced by the underloads after crack closure has already occurred. Predictions of the crack growth fatigue life are presented for a large variety of flight-simulation test series on 2024-T3 sheet specimens in order to reveal the effects of a number of variables: the design stress level, the gust spectrum severity, the truncation level (clipping), omission of small cycles, and the ground stress level. Tests with different load sequences are also included. The trends of the effects induced by the variables are correctly predicted. The quantitative agreement between the predictions and the test results is also satisfactory.

INTRODUCTION

Fatigue crack growth predictions are needed in the aircraft industry for design and certification purposes. Predictions can indicate the trend of the effects of design variables, but it is meaningful only if the predictions are quantitatively reasonably accurate.

Fatigue loads in service, especially for wing structures, are generally a random variable-amplitude loading, rather than constant-amplitude loading. Different types of load sequences are known to induce load interaction effects, which can result in significant accelerations and retardations of fatigue crack propagation. Interaction effects imply that the crack

extension in a load cycle depends on what occurred in the preceding cycles, i.e. on the previous load history. There are so-called history effects.

The modified CORPUS model [1] is a modification of the CORPUS model (Computation Of Retarded Propagation Under Spectrum loading), which was proposed by De Koning [2] in 1981. However, the CORPUS model gives a rather conservative prediction for cases, where the most severe negative gust is more compressive than the ground load of the flight simulation load history. The conservative prediction is caused by the rarely occurring most severe compressive gust, which governs the crack opening level in the plastic zone region created by the rarely occurring maximum overload. This underload effect of the severe negative gust is lasting very long, because it is coupled to a relatively large plastic zone region. In most cases it implies that it will last almost during the full flight-simulation history. The modified CORPUS model is "uncoupling" underload effects from plastic zone regions created by the maximum overload. In addition to the overload affected zone, which is used in the CORPUS model, an underload affected zone (ULZ) is introduced in the model.The ULZ is associated with compressive loads and reversed plastic deformation induced by those underloads, also by the frequently occurring ground load (once per flight).

The CORPUS model basically is associated with plastic deformation left in the wake of the crack (Elber's mechanism). Elber [3] observed that permanent plastic deformation ahead of the crack tip, generated by high load excursions, is still present on the crack surface after subsequent crack growth has occurred. These deformations can cause the crack surfaces to remain in partial contact even under tensile loading. Elber introduced the notion of the crack closure and crack opening load, defined as the load required for the entire crack surface to be free of contact. Loads exceeding this level will lead to crack extension.

The modified CORPUS model is, to a large extent, similar to the CORPUS model. The model includes consideration of plane stress and plane strain condition for the plastic zone size and a correction for the effect of high loads on the crack opening stress. The multiple overload interaction is maintained as an important feature, which leads to an increasing S_{op} .

The model is briefly described and prediction results for a large variety of flight-simulation test series are compared to test results. The comparison between predictions and test results is restricted to sheet material of the 2024-T3 alloy. Results on 7075-T6 sheet material are also covered in [1]. However, 2024-T3 is a more interesting material to check the validity of predictions of a crack growth model. First, 2024-T3 is usually adopted for fatigue critical components. Secondly, 2024-T3, in view of its larger ductility, gives larger plastic zones than 7075-T6. As a consequence, larger interaction effects occur, which implies that it is a more difficult material to arrive at accurate predictions.

FATIGUE CRACK GROWTH MODELLING

The model will not be described in full detail. The main features will be indicated. For a complete description the reader is referred to [1] and [2]. The process of crack growth modelling is illustrated in the flow diagram in Fig.1. As a consequence of crack closure, crack extension in every cycle is determined by the effective stress range. In cycle (i) Δa_i is:

$$\Delta a_i = f(\Delta K_{eff,i})$$

where: $$\Delta K_{eff,i} = C\, \Delta S_{eff,i} \sqrt{\pi a}$$

The cycle (i) is defined by a maximum $S_{max,i}$ followed by a minimum $S_{min,i}$. The effective stress range is determined as,

$$\Delta S_{eff,i} = S_{max,i} - S_{min,i} \text{ if } \sigma_{op} \leq S_{min,i}$$

$$\Delta S_{eff,i} = S_{max,i} - \sigma_{op} \quad \text{if } S_{min,i} < \sigma_{op} < S_{max,i}$$

where σ_{op} is the maximum crack opening stress level left from the load history.

Underload Affected Zone

The underload affected zone should be associated with compressive loads and reversed plastic deformation induced by underloads after the crack has been closed. The K range to be considered is $K_{op} - K_{min}$. It may be expected that severe downward loads will be able to induce reversed plasticity. It is assumed that this reversed plasticity in the underload affected zone occurs under plane strain conditions. The size of the reversed plastic zone is then approximated by the Irwin type equation:

$$D_u = \frac{1}{9\pi}\left[\frac{K_{op} - K_{min}}{2\sigma_y}\right]^2$$

As long as the crack tip is between a and ARP = a + D_u the underload will be effective. Here a is the crack length at the moment that the underload was applied.
An underload affected zone can overlap with another underload affected zone. The zones should be stored in the memory of the computer. However, the most severe underload is considered to be the dominant one. It is used to determine the S_{op} level.

Overload affected zone

The effect of an overload is effective as long as the crack tip is in its plastic zone. The plastic zone size depends on the state of stress at the crack tip, plane strain, plane stress or a transition

between those two conditions. De Koning [2] derived a special equation for the plastic zone. It was based on the Irwin type equation, but it was modified to account for large zones if the stress level approaches the net section yield limit. The plastic zone size is:

$$\frac{D}{a} = \frac{1-\gamma\left(\frac{S_{max}}{\sigma_y}\right)^2+\left(\frac{a}{b}\right)^2}{2\left(\frac{a}{b}\right)^2} - \frac{\sqrt{\left[1-\gamma\left(\frac{S_{max}}{\sigma_y}\right)^2+\left(\frac{a}{b}\right)^2\right]^2-4\left(\frac{a}{b}\right)^2}}{2\left(\frac{a}{b}\right)^2} - 1$$

where b is the semi-width of the specimen and γ depends on the state of stress. For plane stress $\gamma = 1/1.32$ and for plane strain $\gamma = 1/9$.

In the model, the crack tip state of stress depends on the size of the plastic zone relative to the thickness. First, the plastic zone size is calculated under plane stress conditions (D_{ss}). If $D_{ss} \geq 0.5t$ (t=sheet thickness) then the plastic zone is supposed to be in plane stress. If $D_{ss} \leq 0.35t$, the plastic zone is supposed to be in plane strain, size D_{sn}. During the transition from plane strain to plane stress ($0.35t < D_{ss} < 0.5t$), the plastic zone size is given by:

$$D = D_{sn} + 2D_{ss}[(D_{ss}/t - 0.35)/0.15]^4 (D_{ss} - D_{sn})/t$$

The overload will be effective as long as the crack tip is between a and ADP = a+D. Also here a is the crack length at which the overload occurred.

During crack growth under variable amplitude loading various plastic zones will be created. If they can affect the crack opening stress in later cycles they must be stored in the material memory (plastic zone history, ADP-values labelled as ADPH with H from history). For example, consider a crack length a_1 with a plastic zone size dp_1. A second plastic zone dp_2 will be memorized if (a_2+dp_2) is longer than (a_1+dp_2). In this case, a new plastic zone penetrates the elastic material ($ADP_2 > ADPH_1$).
Fortunately, not all plastic zones can affect S_{op}, because their effect on S_{op} is overruled by other plastic zones with a higher S_{max} ($S_{max} > SH_{max}$). A higher overload overrules the previous lower overload. The series of overload affected zones is characterized by a decreasing series of S_{max}-values (SH_{max}-values). As a consequence only a limited number of plastic zones must be stored in the material memory.

Selection of Crack Opening Stress in Every Cycle

Two different crack opening occurrences are defined in the modified CORPUS model, i.e. (1) crack opening related to the history stress levels (SH_{max} and SH_{min}, associated with plastic zones

created previously) and (2) crack opening related to the current stress cycle ($S_{max,i}$, $S_{min,i}$). The history values are related to overloads (SH_{max}), which produced primary plastic zones, and to dominant underloads (SH_{min}) of the underload affected zones. As a consequence of the concept of the underload affected zone, the dominant (i.e. the highest one) SH_{max} must be combined with the dominant SH_{min}, i.e. the lowest SH_{min} in order to calculate the relevant S_{op} (=SH_{op}) for the current cycle.

The crack opening level induced by the current cycle is determined from $S_{max,i}$ and the successive $S_{min,i}$. This S_{op} is applied in the next cycle only, and only if it exceeds the above SH_{op}.

Interaction of Overloads

As already mentioned in the introduction, overload interaction effects play an important role in the CORPUS model. De Koning recognized that overloads with overlapping primary plastic zones will cause an extra increase of the crack opening level, which will give more crack growth retardation (multiple overload effect). The crack opening stress level for single overload and underload is:

$$S_{op} = S_{max} (-0.4R^4 + 0.9R^3 - 0.15R^2 + 0.2R + 0.45) \qquad \text{if } R > 0, \text{ and}$$

$$S_{op} = S_{max} (0.1R^2 + 0.2R + 0.45) \qquad \text{if } -0.5 < R < 0$$

where R is the stress ratio (S_{min}/S_{max}). Newman [4] demonstrated that the opening stress level does not only depend on S_{min} and S_{max}, but also on the maximum stress in relation to the yield stress, i.e. S_{max}/σ_y. In Newman's analysis elastic-perfectly-plastic material behaviour was assumed with a kind of an average yield stress: $\sigma_y = (\sigma_{o.2}+\sigma_u)/2$. De Koning [2] defined a correction function h which is a good fit to Newman's results. The correction function h is:

$$h = 1 - 0.2(1 - R)^3 \left(\frac{S_{max}}{1.15\sigma_y} \right)^3$$

The corrected stress opening level then is SH_{op}. If interaction between overloads occur, this opening stress level will increase due to the multiple overload effect. The opening is increased after each overload until it has reached a certain upperbound. The equations proposed by De Koning will not be reproduced here, since they need a fairly extensive explanation. It includes one material constant δ, which was obtained by analyzing empirical data. A full description is given in [1] and [2].

PREDICTION RESULTS

Flight-simulation test results used in this chapter are adopted from different references. It includes results obtained with six spectra, i.e. CN-235 spectrum [5], F-27 spectrum [6], TWIST [7], miniTWIST [8,9], FALSTAFF and MiniFALSTAFF[10], and a simplified flight-simulation loading [11]. Most of the spectra are related to civil transport aircraft, except FALSTAFF and miniFALSTAFF, which are standardized flight simulations for fighter wing structures. The material was 2024-T3 Alclad sheet material, except for the tests with FALSTAFF and miniFALSTAFF, where 2024-T3 bare material was used.

Variables of the test programs were:

- CN-235 : design stress level and truncation level
- F-27 : 12 combinations with different
  - gust spectrum severity
  - ground stress severity
  - design stress level
- TWIST : truncation level
- miniTWIST : ground stress level
- FALSTAFF : design stress level
- miniFALSTAFF : design stress level

The variations of the gust spectrum severity of the F-27 were obtained by increasing or decreasing the ratio between gust amplitudes and the mean stress in flight (S_g/S_{mf}). There are three gust spectrum severities, viz. severe, normal and light. Also three ground load levels were adopted with S_{gr}/S_{mf} vary from -0.5 (severe), -0.234 (normal) to +0.125 (light).

In the miniTWIST and CN-235 tests, the crack increments in the most severe flight (type A) were recorded.

The load sequences used in the simplified flight-simulation loading tests [11] are shown in Fig.2. During one test all flights were equal. There are three types of flights. The mean stress in flight was 80 MPa and the stress amplitude was 40 MPa. Two values of numbers of cycles per flight were used, m=5 and m=100 cycles. The purpose of the tests was to study the effect of periodic overloads and underloads. Furthermore, a load sequence effect might occur in view of the low-high and high-low sequence of the flight profiles II and III respectively.

Prediction results compared to test results are presented in Figures 3 to 9.

DISCUSSION

For most flight-simulation tests the modified CORPUS model and the CORPUS model gave approximately similar predictions, with some noteworthy exceptions. The predictions compared

to test results discussed below are those obtained with the modified CORPUS model. Predictions of both models are given if significant differences were found.

Effect of spectrum severity

The effect of the severity of the spectrum is illustrated by the results in Fig.3. It clearly shows an increasing crack growth life if the spectrum becomes less severe. This applies to each of the three ground stress levels. The trend is a logical one, and as shown by Fig.3, the trend is accurately indicated by the prediction model.

Effect of design stress level

The systematic effect of the design stress level is illustrated by Figs 4 and 6 for three different load spectra. The design stress level is represented by either S_{max} of the load spectrum or the mean stress in flight, S_{mf}. It should be understood that all stress levels of the load spectrum are proportional to S_{max} or S_{mf}. As shown by the results, the trend of the effect of changing the stress level was correctly predicted, although an accurate life prediction was not always obtained.

Effect of the truncation level

The effect of truncation of the rarely occurring very high loads of a load spectrum (clipping) has been well known for a long time (survey in [12]). Predictions in Fig.5 confirm this trend, shorter crack growth lives for lower truncation levels. This is the reason why high truncation levels should be avoided in full-scale flight-simulation tests in order to obtain conservative results.

Effect of omitting small cycles

In a gust load spectrum cycles with a small amplitude are quite numerous. If such cycles can be omitted from a test, saving of testing time is considerable. MiniTWIST was derived from TWIST by a drastic reduction of the small cycles. The average number of cycles per flight is 100 for TWIST and 15 for miniTWIST. It leads indeed to a shorter testing time, but the crack growth life in flights is increased about 2 times. The small cycles of TWIST were still damaging. This trend agrees with predictions (results not presented here).

In Fig.6 a comparison is made between FALSTAFF and miniFALSTAFF. In miniFALSTAFF about 50% of the smaller load excursions are removed by a rain-flow procedure. The predictions indicate a negligible effect on the crack growth life in agreement with the test results.

Effect of the ground stress level

The ground stress level (S_{gr}) in a wing, as compared to the mean stress in flight (S_{mf}), is dependent on the aircraft configuration (engines, landing gear, fuel tanks) and the rib station. As shown by Figs 3 and 7, a more severe ground stress level can imply a significant reduction of the crack growth life. This trend is predicted by the modified CORPUS model, but not always by the CORPUS model; see next paragraph.

Comparison between predictions of CORPUS and the modified CORPUS model

As pointed out before, the CORPUS model and the modified CORPUS model gave similar results in most cases. However, this is not true if a rarely occurring negative gust load is a more severe down load than the frequently occurring ground load. This condition occurred in the F-27 tests with a "mild" ground stress (S_{gr}/S_{mf} = +0.125); see Fig.3c, and in the miniTWIST tests with S_{gr}/S_{mf} = 0 (Fig.7). The predictions of the CORPUS model are indicated by a black dot. The CORPUS model gives a significant underestimation, contrary to the modified CORPUS model. Actually, this kind of comparative result was the argument for developing the modified CORPUS model as discussed before.

Effect of load sequence

Load sequences variations were applied in the simplified flight-simulation tests (Fig.2). The modified CORPUS model predicts a negligible difference between load sequences II and III. That is in agreement with the test results, see Fig.8. However, the CORPUS model predicts a systematic effect if there are 100 cycles in a flight. The life is significantly shorter for sequence III with the OL at the end of the flight. The different predictions of the two models are caused by different S_{op} developments due to the underload affected zone in the modified CORPUS model.

Crack increment in the most severe flight

In some tests the crack increment Δa in the most severe flight (type A) could be determined by measuring the crack length at the beginning and the end of the flight. Results for miniTWIST and CN-235 shown in Fig.9 indicate that the measured increments were significantly larger than predicted for those severe flights. The underestimation of the prediction does not have a significant influence on the predicted crack growth life, because the more severe flight is a rare occurrence. However, it shows a weakness of the prediction model. This is discussed in more detail by De Koning et al.[13] (see also [14]).

Quantitative accuracy of the predictions

The quantitative accuracy of the individual predictions was quite good for a fatigue prediction as illustrated in Figs 3 to 8. The average ratio of predicted crack growth life and test life was 0.87 for the modified CORPUS model (85 test results, including results for 7075-T6) with a standard deviation of 0.182. For CORPUS the average ratio was 0.89, practically the same value as for modified CORPUS, with standard deviation of 0.275, which is significantly higher than for modified CORPUS.

Non-interaction predictions (Miner approach)

The non-interaction prediction model is by far the most simple model, because it ignores any effect of previous load cycles. There is no material memory. In each cycle Δa is calculated with $\Delta K = C\Delta S\sqrt{\pi a}$ and ΔS following from S_{min} and the directly following S_{max}. It is a kind of a Miner approach, because the Minter rule also ignores effects of previous load cycles. For the flight simulation tests with a gust spectrum the average prediction to test result was 0.21 for 2024-T3 specimens (29 test results). It illustrates that large interaction effects did occur. For 7075-T6 (20 test results) this ratio was 0.45, a higher value associated with smaller interaction effects in the lower ductility alloy. For the manoeuvre spectra the average ratio was 0.45 (2024-T3 results only), which also indicate less effective interaction effects. It is associated with the effect that manoeuvre spectra have relatively more high amplitude cycles and less low amplitude cycles.

One trend is extremely poorly predicted by the non-interaction procedure, i.e. the effect of the truncation level. According to the non-interaction concept a lower truncation level leads to a negligible increase of the crack growth life, whereas in reality it implies a significant life reduction as shown by test results and is in agreement with the model predictions.

CONCLUSIONS

Test results on fatigue crack growth in 2024-T3 sheet material under flight-simulation loading were compared to predictions with the modified CORPUS model in the previous chapter. The main conclusions are summarized below:

1. Empirical trends of the effects of test variables are correctly predicted. It includes the effects of the gust severity of the spectrum, the design stress level, the truncation of rarely occurring high loads (clipping), the omission of small cycles, and the ground stress level.
2. Although the CORPUS model also predicts most trends in a similar way, the effect of rarely occurring severe negative gusts combined with a not severe, but frequently

occurring ground load is not correctly predicted by the CORPUS model. Modified CORPUS gives correct predictions also for this case.

3. A load sequence effect in simplified flight-simulation tests was predicted by CORPUS, whereas modified CORPUS predicts this sequence effect to be absent. The latter prediction is in agreement with the test results.
4. The crack extension in the rarely occurring most severe flight was poorly predicted by both the modified CORPUS and the CORPUS model.
5. The quantitative accuracy of the modified CORPUS model was generally good. Non-interaction predictions gave insignificant underpredictions and misleading indications on the effects of test variables.

REFERENCES

[1] Padmadinata,U.H.,"Investigation of crack-closure prediction models for fatigue in aluminum sheet under flight-simulation loading", Doctor Thesis, Delft Un. of Technology, 1990.

[2] De Koning, A.U. and Van der Linden,H.H., "Prediction of fatigue crack growth rates under variable loading using a simple crack closure model", Proc. 11th ICAF Symp., Noordwijkerhout. May, 1981, paper 2.6. Nat.Aerospace Lab. NLR, Amsterdam.

[3] Elber,W.,"The Significance of Fatigue Crack Closure". Damage Tolerance in Aircraft Structures, ASTM STP 486, 1971 ,p.230-242.

[4] Newman Jr.,J.C.,"A crack closure model for predicting fatigue crack growth under aircraft spectrum loading". ASTM, STP 748, 1981, pp.53-84.

[5] Padmadinata,U.,"CN-235 load spectrum study in fatigue crack propagation", Delft Un. of Tech., Fac. of Aerospace Eng., Report LR-510, 1987.

[6] Van der Linden,H.H.,"NLR test results as a data base to be used in a check of crack propagation prediction model. A GARTEUR activity", Nat. Aerospace Lab. NLR TR 79121, 1979.

[7] ProvoKluit,J.C.,"Significance of crack closure for crack growth in 7075-T6 and 2024-T3 Al-alloy under flight simulation loading with different truncation levels", (in Dutch), Master thesis, Delft Un. of Tech., Fac. Aerospace Engineering 1978.

[8] Padmadinata,U.H.,"Sequence effects of high-amplitude loads in the most severe flights of mini-TWIST on fatigue crack growth in Al-alloy sheet material", Delft Un. of Tech., Fac. Aerospace Eng., Report LR-493, 1986.

[9] Padmadinata,U.H.,"Sequence effects of high-amplitude loads in the most severe flights of miniTWIST with a light ground stress level", to be published.

[10] Vlutters,A.M.,"Crack growth flight simulation tests with FALSTAFF and shortened version, miniFALSTAFF, at two design stress levels", Master thesis, Delft Un. of Technology, Fac. Aerospace Eng.,1982.

[11] Misawa,H. and J.Schijve,"Fatigue crack growth in aluminium alloy sheet material under constant-amplitude and simplified flight-simulation loading". Delft Un. of Tech., Fac. Aerospace Eng., Report LR-381, 1983.

[12] Schijve,J.,"The significance of flight simulation fatigue tests", Proc. 13th ICAF Symp., Pisa 1985. EMAS, Warley 1985, pp.71-170.

[13] Koning,A.U.de and Dougherty,D.J.,"Prediction of low and high crack growth rates under constant and variable amplitude loading", Fatigue crack growth under variable amplitude loading. Elsevier, 1988, pp.208-217.

[14] Schijve,J.,"Fundamental aspects of predictions on fatigue crack growth under variable-amplitude loading. Theoretical concepts and numerical analysis of fatigue. Proc. Conf. Birmingham, May 1992, EMAS 1992, pp.111-130.

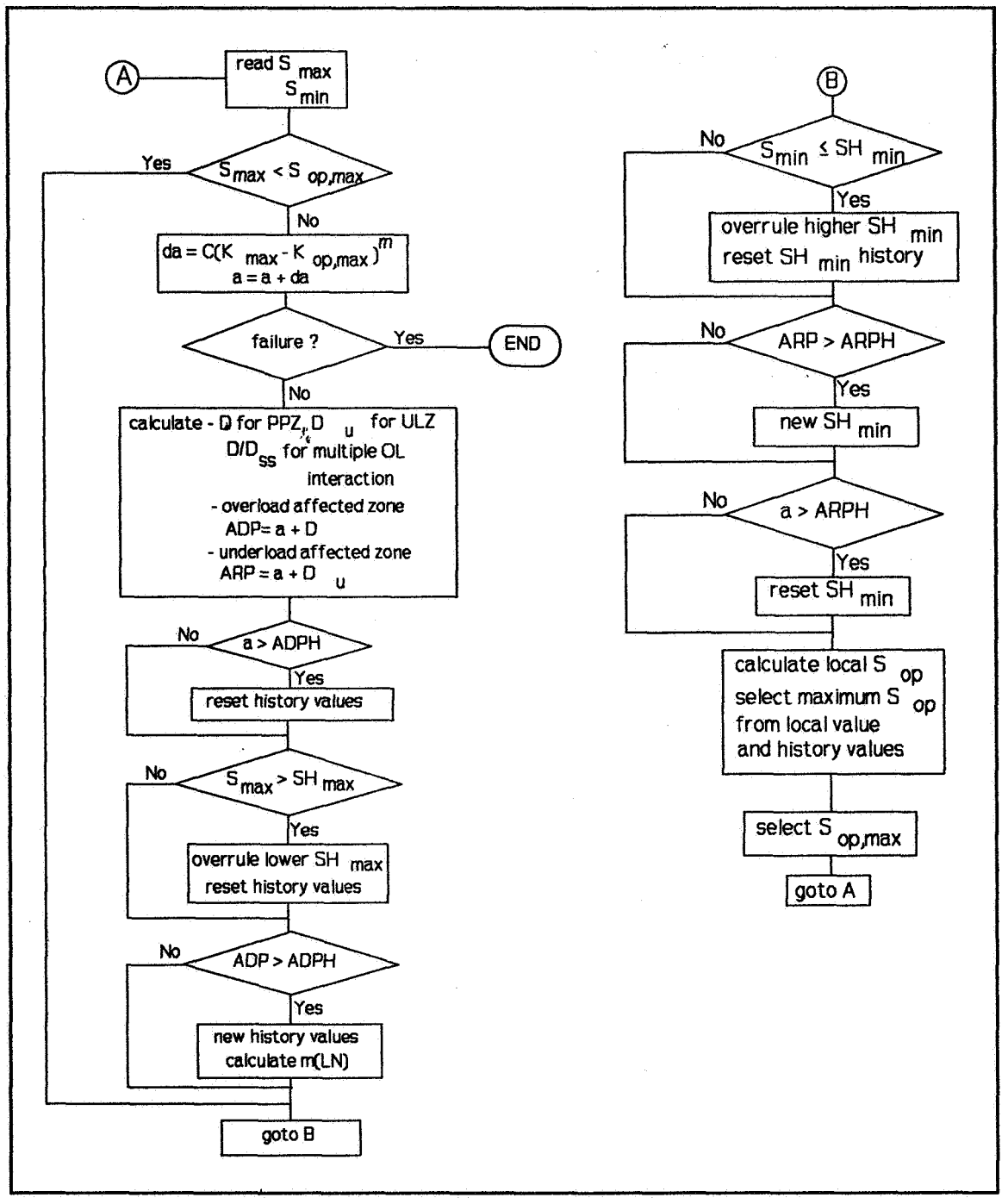

Fig.1 Flow diagram of the Modified CORPUS Model.

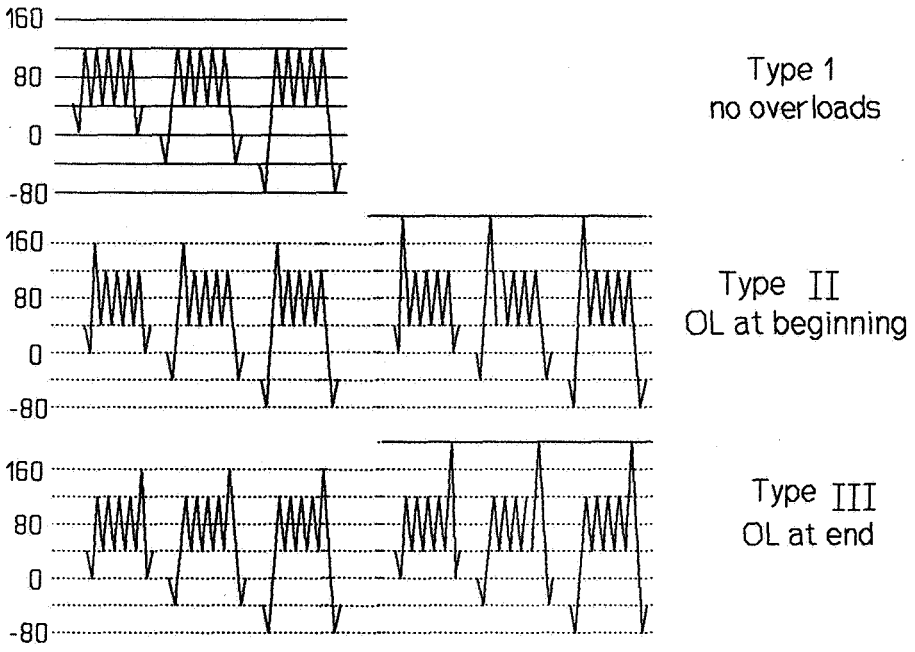

Fig.2 **Load sequences of simplified flight-simulation tests with 5 cycles per flight (m = 5). Also tests with m = 100.**

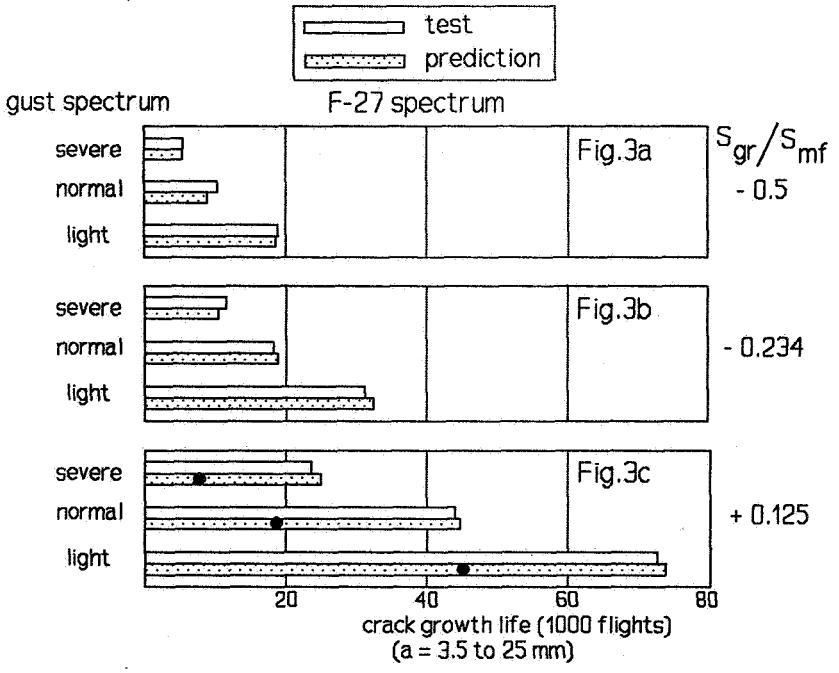

Fig.3 **The effect of the gust spectrum severity and the ground stress on the crack growth fatigue life. Comparison to modified CORPUS predictions (Some predictions for CORPUS ●).**

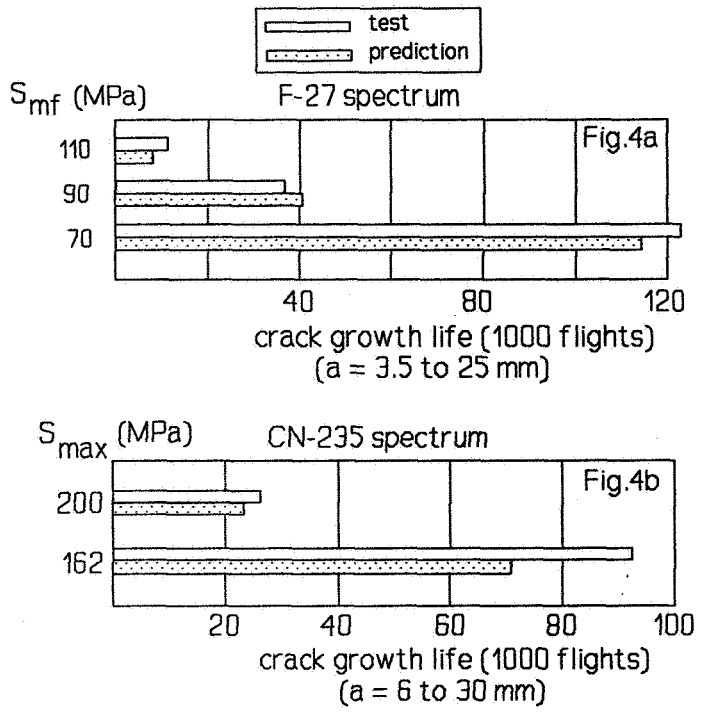

Fig.4 **Effect of the design stress level on the crack growth fatigue life, compared to predictions.**

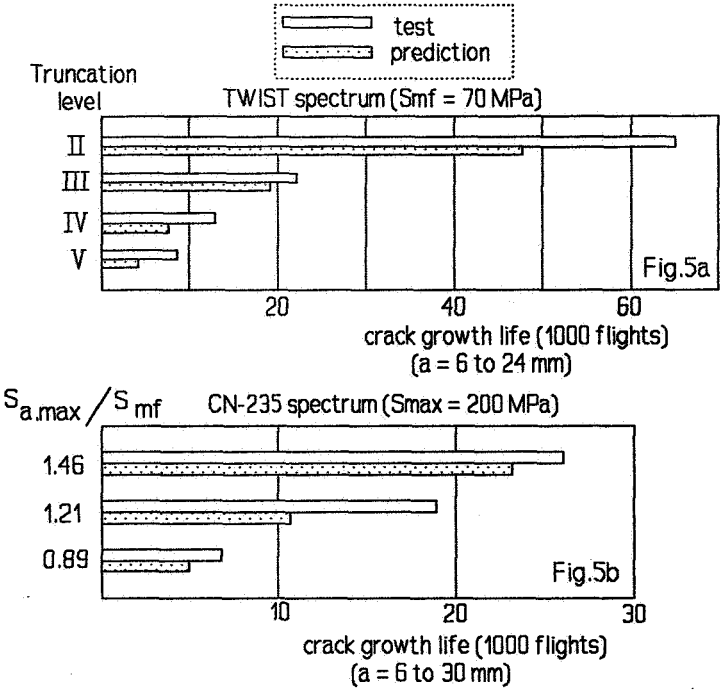

Fig.5 **Effect of truncating high gust loads (clipping) on the crack growth fatigue life. Comparison to predictions.**

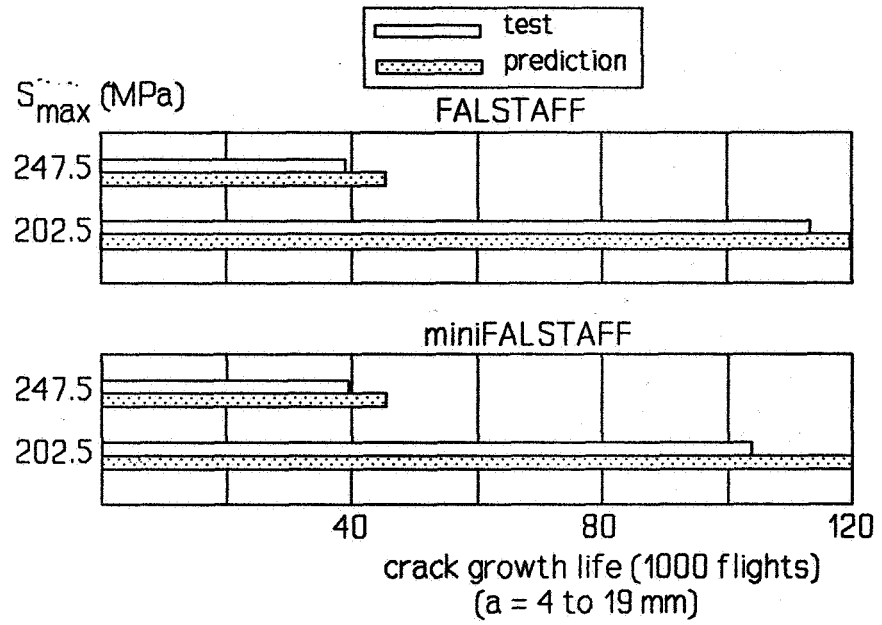

Fig.6 **Effects of the design stress level and omitting small cycles on the crack growth fatigue life. Comparison to predictions.**

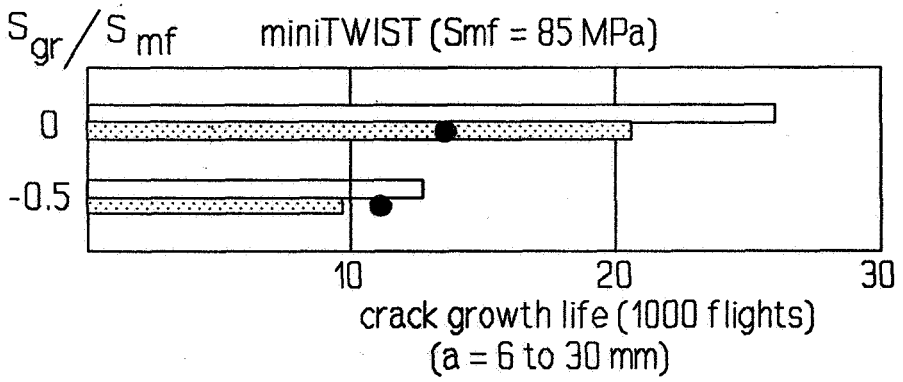

Fig.7 **Effect of ground stress level on the crack growth fatigue life. Comparison to the modified CORPUS and the CORPUS predictions (●).**

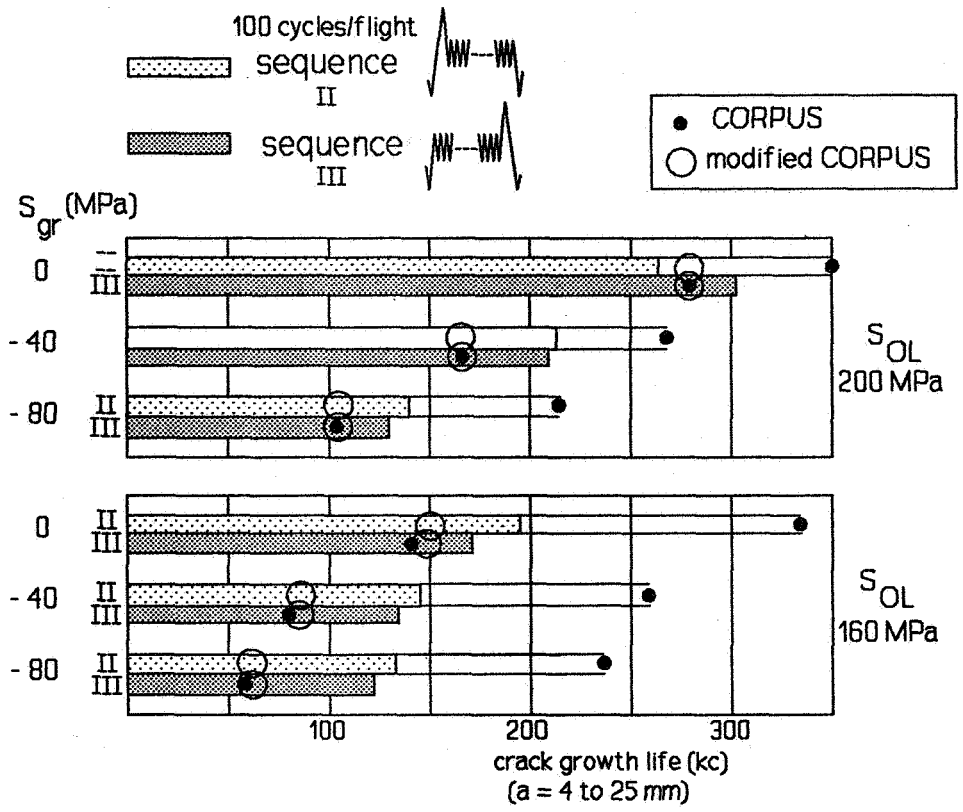

Fig.8 **Effects of overload stress level, S_{gr} and the load sequence on the crack growth fatigue life. Comparisons to predictions with the modified CORPUS and the CORPUS model (●).**

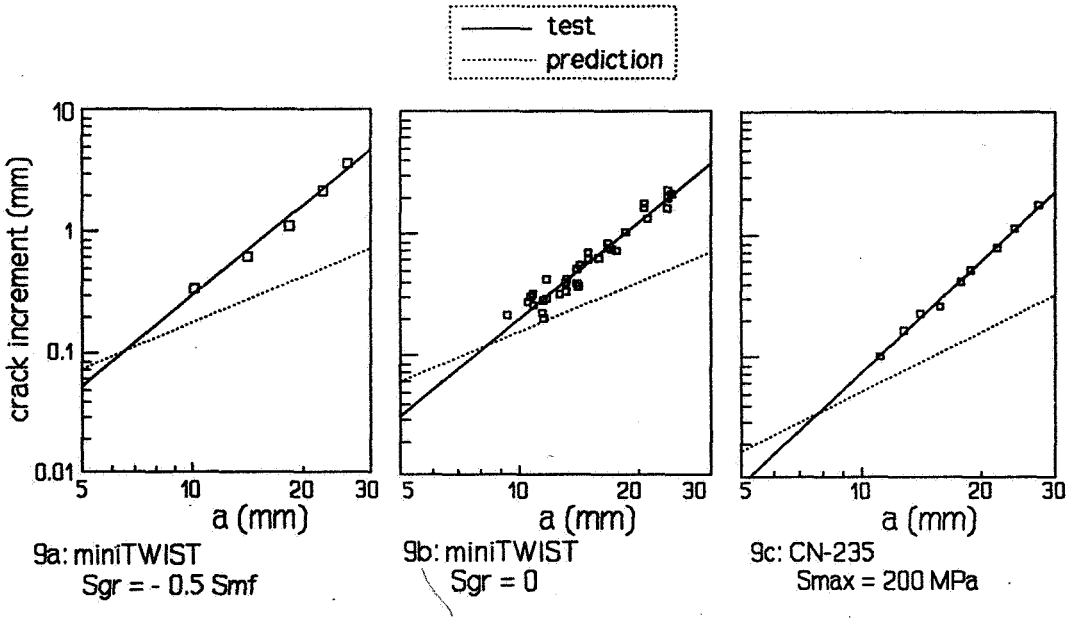

Fig.9 **Crack growth increments in the most severe flight A. Test results and predictions.**

THE CHARACTERIZATION OF WIDESPREAD FATIGUE DAMAGE IN FUSELAGE STRUCTURE

Robert S. Piascik
NASA Langley Research Center
Hampton, VA

Scott A. Willard
Lockheed Engineering and Science Company
Hampton, VA

Matthew Miller
Boeing Commercial Airplane Group
Seattle, WA

ABSTRACT

The characteristics of widespread fatigue damage (WSFD) in fuselage riveted structure were established by detailed nondestructive and destructive examinations of fatigue damage contained in a full size fuselage test article. The objectives of this work were to establish an experimental data base for validating emerging WSFD analytical prediction methodology and to identify first order effects that contribute to fatigue crack initiation and growth.

Detailed examinations were performed on a test panel containing four bays of a riveted lap splice joint. The panel was removed from a full scale fuselage test article after receiving 60,000 full pressurization cycles. The results of *in situ* examinations document the progression of fuselage skin fatigue crack growth through crack linkup. Detailed tear down examinations and fractography of the lap splice joint region revealed fatigue crack initiation sites, crack morphology and crack linkup geometry. From this large data base, distributions of crack size and locations are presented and discussions of operative damage mechanisms are offered.

INTRODUCTION

The incidence of airframe fatigue damage increases as airplanes are operated past their economic design objective, typically 20,000 flights. Because of reduced durability and related safety concerns, the commercial aircraft industry has instituted elaborate inspection and maintenance requirements to ensure continued airworthiness of aging airplanes. As part of industry's initiative to ensure safe operation of aging commercial aircraft, pressure testing of full scale fuselage structure is conducted to simulate flight loads [1-4]. Detailed structural examinations performed during the full pressurization tests often lead to design improvements and practical inspection programs. The airframe industry has entered into a cooperative aging aircraft program with NASA Langley Research Center (LaRC) to resolve durability issues associated with the aging commercial airplane fleet. As part of this cooperative effort, LaRC has performed detailed examinations of commercial aircraft structure that has been subjected to long term pressure tests. The objectives of these examinations are two fold: (1) Develop an understanding of widespread fatigue damage (WSFD) in fuselage lap splice joint structure, characterize crack initiation, growth and link-up, and (2) Use the knowledge gained here to benchmark critical laboratory simulations, analytical predictions and advanced nondestructive inspection techniques. Described herein are the results of detailed teardown examinations performed on a fuselage skin lap splice joint containing widespread fatigue damage.

BACKGROUND

Full scale testing of a fuselage structure was conducted to demonstrate structural airworthiness to 60,000 full pressure (0 to 9.0 psi) cycles, i.e., three times the minimum economic design objective [1]. Details of the fuselage structure and test conditions are described in reference 1. During pressure testing, *in situ* inspections were performed to develop a detailed understanding of fuselage durability. Cracks in the fuselage skin lap splice joint were observed in a few localized regions of the structure. The lap splice joint is formed by overlapping and joining two sections of fuselage skin (Alclad 2024-T3) using a four row riveted (Briles design) construction. Each bay is separated by a bonded and riveted

tear strap identified by the vertical dashed lines in Figure 1. The function of the tear strap is to act as a fail safe load path and a crack arrest feature. A horizontal frame (stiffener), not shown in Figure 1, is riveted (third row from the top) along the length of the lap splice joint inner surface. A sealant is applied to the lap splice mating surfaces to prevent internal pressure loss during flight and to inhibit joint corrosion.

Figure 1 is a schematic of bay #1 summarizing the results of *in situ* visual examinations conducted during fuselage pressure testing. After 20,000 pressure cycles, inspections were conducted at intervals of approximately 1700 cycles. The small arrows in Figure 1 mark the upper row rivet locations that contained visible cracks. The first evidence of cracking was observed near the mid-bay after 38,333 cycles. No further cracking was observed in bay #1 until 50,250 pressurizations, when three mid-bay cracks were noted. At 55,500 cycles, ten rivet locations contained cracks. ' The first evidence of crack link-up was observed after 58,200 cycles. An additional 1800 pressurizations were performed, totaling 60,000 cycles, before cracks at all upper row rivet locations had linked-up. A single long crack, 47.9 cm (18.85 inch) in length, had formed along the upper row of rivets, terminating at the adjacent tear straps. After completing the three lifetime test, the four bay region containing wide spread fatigue damage was removed for detailed teardown inspection at LaRC. Upon completion of pressure testing and in situ inspections, a four bay panel of lap splice joint containing WSFD was removed from the fuselage test article for a detailed teardown inspection at LaRC. Reported herein are the results of examinations conducted on one (bay #1) of the bays from that four-bay panel.

LaRC INSPECTION RESULTS

Non-destructive Examinations (NDE)

Prior to destructive examination, bay #1 was examined visually (10X) and by eddy current techniques. These laboratory inspections yielded results similar to that obtained by *in situ* examination. With one exception, all outer skin fatigue cracks were observed in the upper row rivet locations shown in Figure 1. The single exception was observed in the most

forward rivet of the second row. The location and description of this outer skin crack was confirmed later by the destructive examination. Subsurface or inner skin fatigue cracking was not detected by NDE. Figure 2 is a photograph showing the long outer skin crack located along the upper row of rivets in bay #1. Figure 2b details the link-up crack path for fatigue cracks propagating from rivets 5, 6, and 7. Interacting "curved" cracks shown in Figure 2b have been observed in the laboratory and modeled by Ingraffea et al. [5].

The following is a summary of observations from the bay #1 lap splice joint nondestructive examinations.

1. Through-thickness outer skin cracking is primarily contained along the upper row of rivets.
2. All upper row fatigue cracks initiated at the rivet hole horizontal centerline or in the upper half of the hole. The crack propagated nearly normal to the fuselage hoop stress. A curved crack path in middle bay regions, noted in Figure 2, occurred as a result of crack interactions during link-up. Crack link-up of long to short cracks at the outer extremities of the bay exhibited less curvature. The long upper row crack was somewhat deflected by both tear straps; a slight upward crack path was noted at each end of the bay.
3. The upper surface of the long crack was displaced outward, "pillowed". Here, the outer skin was no longer captured by the rivet head. This observation and destructive examination results, discussed later, suggest Mode III displacements had occurred after crack link-up between many rivets, possibly 8 to 10 rivet lengths. Presumably, at long crack lengths, the outer skin can no longer be restrained by the rivet heads and forces due to internal pressure resulted in pronounced out-of-plane displacements. This Mode III effect has been studied by Hui and Zehnder [6].
4. Examination of bay #1 inner surfaces revealed no evidence of cracking.

Destructive Examinations

Destructive examinations were performed to characterize wide spread fatigue cracking in lap splice fuselage structure. Special care was taken when dismantling the bay #1 lap splice joint to maintain traceability and to eliminate possible extraneous damage and/or contamination. The entire upper row of rivets containing the long crack was removed intact by making a horizontal cut slightly below the upper row. This allowed the removal and subsequent examination of the long crack fracture surface without disturbing the remainder of the bay. Each of the remaining 52 rivet locations contained in the lower three rows were individually removed from the panel as illustrated in Figure 3. After each rivet location was removed, the rivet was sectioned from top to bottom, using a slow speed diamond saw, exposing the aft and forward sections of the rivet hole. Each rivet half was removed with little or no force, thus exposing the hole inside diameter without disturbing the surface. To open small incipient fatigue cracks located on the rivet hole surface, each specimen (a total of 102 specimens) was strained in a three point bend fixture depicted in Figure 3. All rivet hole surfaces were examined in detail using both optical and scanning electron microscopy (SEM). Typically, each specimen was examined three times. The hole surface was examined twice after partial straining operation; the location of small partially opened incipient cracks were charted after each straining operations. A third detailed fractographic examination was performed after final fracture of the specimen which typically exposed the major fatigue crack.

Fatigue Crack Location

Figure 4 summarizes the results of the destructive examination. Figure 4a is a schematic of bay #1 identifying the four rows of rivets (rows G, H, I and J), the location of the long crack along row J and the location of smaller cracks found in rows G, H and I during the destructive examination. Figures 4b, 4c and 4d are schematics (not drawn to scale) of each rivet row detailing the location, initiation site (arrow) and length of each fatigue crack. Crack depth was computed from the point of initiation to the point of greatest crack depth (length) or, for through-thickness cracks, from the rivet hole surface to the point

of greatest crack depth. In rows G, H and I, 17 holes of the 52 examined were found to contain fatigue cracks. A total of 23 fatigue cracks were found in rows G, H and I. Row I contained six outer skin cracks; the crack located at hole position "0" was detected by eddy current inspection. All other fatigue cracks in row I were small and located under the rivet head. Row H contained four inner skin fatigue cracks, two through-thickness cracks located at positions 17 and 18 and small cracks at positions 4 and 15. Row G exhibited cracking in eight rivet holes. Hole locations 13 and 14 contained through-thickness fatigue cracks. The remaining six holes contained smaller surface and corner cracks. The site of crack initiation varied; Row I contained outer skin cracking that primarily initiated along the mating surface between the outer and inner skin, Row H contained inner skin cracks that initiated at rivet hole corners, rivet hole surface and outer/inner skin surface, and Row G contained cracks that initiated at rivet hole corners, rivet hole surfaces and outer/inner skin surface.

Fatigue Crack Morphology

The SEM micrographs shown in Figure 5 illustrate the typical transgranular morphology and location of fatigue cracks observed in the outer and inner skin of bay #1. Outer skin countersink cracking, located in region b in Figure 5a, is shown in Figure 5b. Typically, countersink cracks initiate at the inboard corner of the rivet hole marked by the arrow in Figure 5b. Here, the inboard corner of the countersink exhibits disturbed metal and possible evidence of local clad thinning. The outer skin surface cracks, shown in Figure 5c, initiate at surface clad discontinuities marked by the arrow. These surface cracks are located at the outer/inner skin interface near the rivet hole countersink, identified by region c in Figure 5a. Evidence of surface clad abrasion (fretting) was observed at the point of crack initiation, i.e., clad surface disturbed metal, black oxide debris at the outer/inner skin interface and secondary microcracks at the clad metal interface in some cases. Rivet hole surface cracks, region d in Figure 5a, typically initiate at surface discontinuities identified by the arrow (fig. 5d). Inner skin corner cracks, located at region e in Figure 5a, initiate at corner discontinuities identified by the arrow in Figure 5e.

Detailed examination of the fracture surface from the long crack contained in upper row J (Figure 4a) revealed that outer-skin fatigue cracks initiated along the lap splice joint interface, identical to that shown in Figure 5c. Further examination of the fatigue fracture surfaces from each rivet hole revealed a thin region (ligament) exhibiting evidence of ductile tearing located along the outboard surface of the outer skin. Figure 6 shows the fracture morphology of upper row fatigue cracks at different stages of propagation from rivet holes located in adjacent bay #2. From Figures 6b, 6c and 6d, a pattern of fatigue crack propagation has been derived for the upper row locations and illustrated in Figure 6a. Figure 6d shows a third outer skin crack of approximately 3.8 mm (0.150 in) in length. Here, the subsurface crack had formed an outboard surface ligament similar to that observed in the upper row on bay #1. These results show that outer skin cracks initiate at the inner/outer skin interface (arrows in Figures 6b, 6c and 6d) and propagate in a subsurface manner depicted in Figure 6a.

Laboratory fatigue tests conducted at LaRC have confirmed that the fatigue crack morphology shown in Figure 6 is indicative of out-of-plane bending loads. Tension-bending (T/B) constant amplitude fatigue tests were conducted using 2.1 mm thick center-cracked alloy 2024T3 sheet specimens. The fatigue crack fracture morphology from a specimen tested at a T/B ratio of 1.5 is shown in Figure 7. Figure 7a is a SEM micrograph showing the fatigue crack front (dashed line) at region A in Figure 7b. The remaining ligament, shown in Figure 7a, exhibits a ductile tearing morphology produced when breaking the specimen by overload after fatigue testing. The fatigue crack/ligament morphology was formed on the compressively-loaded surface while substantial fatigue crack growth continued on the tension surface, thus forming a crack geometry similar to that observed along the lap splice upper row rivet holes.

Complex loading during fatigue cracking of the upper rivet row was also noted by scratches on the fracture surface oriented transverse to the direction of through-crack propagation. Presumably, out-of-plane motion of the upper portion of the fracture surface occurred at relatively long crack lengths, i.e., multiple fatigue crack link-up. This motion rubbed the mating fracture surfaces, forming the transverse scratches similar to that observed

by Zehnder and coworkers during Mode III testing of 2024-T3 sheet [7]. Based on fractographic analysis, significant out-of-plane (Mode III) motion is likely only when cracks are long and no longer captured by the rivet heads.

Lap Splice Joint Fretting

Upper rivet row fatigue cracking at the inner/outer skin interface shown in Figures 5c and 6 suggests that crack initiation is associated with localized damage due to fretting [8]. Evidence of fretting fatigue was noted by a black oxide deposit on the mating surface between the inner/outer skin around each rivet hole. Depicted in Figure 8 is the extent (area drawn to scale) of fretting debris (black oxide) observed on the inboard surface of bay #1 lap splice joint outer skin by estimating the area of fretting debris at each hole location. The amount of fretting was estimated by determining an arithmetic average of fretted surface area per the procedure shown in Figure 9. Here, a scaling factor was assigned to estimate the amount of fretting in each quadrant shown in Figure 9. The value 0 was assigned when no fretting was observed and 5 represented the highest degree of fretting. A "fretting Average" (FA) was calculated for each rivet position. A direct correlation of "fretting average" with rivet hole cracking was not conclusive, i.e., all fretting initiated cracks were observed in holes that exhibited a relatively high FA $>$ 3.00, but, all holes that exhibited a FA $>$ 3.00 did not contain fretting initiated cracks. Figure 10 is a plot of FA versus rivet hole location for the rows G, H, I and J. Here, a distinct correlation is observed for FA and rivet row, i.e., upper row J which contains the greatest number of fretting fatigue cracks, also exhibits the greatest evidence of fretting damage (highest FA level).

SUMMARY

The detailed destructive examination of bay #1 has shown that localized regions of fuselage lap splice joints do contain WSFD after 60,000 full cycle pressurizations. A summary of fatigue cracking contained in bay #1 is shown in Figure 11. Illustrated is the crack length distribution for the 53 fatigue cracks found in bay #1. The majority of cracks having lengths greater than 1.2 mm (30 of the 36 fatigue cracks) were contained in upper

row J. The majority of fatigue cracks observed in the remaining lower three rivet rows exhibited crack depths of less than 1.2 mm. Rows I and J, the two upper rivet rows, exhibited outer skin cracking. Only inner skin cracking was observed in lower rows G and H. Fatigue crack initiation occurs in regions of high K_T located at or near rivet holes. Typically, cracks were found to initiate at rivet hole corners, surface discontinuities (burrs, dents, etc.) and abraded (fretted) surfaces.

Results from fractographic analyses of upper row cracking suggested complex loading. Evidence of out-of-plane loading was suggested by subsurface fatigue crack propagation. In addition, increased Mode III displacement was evidenced by transverse rubbing of fatigue crack surfaces in regions where the outer skin bulging was no longer contained by the rivet head.

Evidence of fretting fatigue damage, black oxide debris, was noted at every rivet hole / lap splice interface in bay #1. Most fretting initiated fatigue cracks were contained in the upper row; here, all fatigue cracks initiated in the outer skin at the inner/outer skin interface in regions that exhibited increased surface abrasion (fretting damage).

ACKNOWLEDGEMENT

The contribution of Mr. E.P. Phillips is gratefully acknowledged. Mr. Phillips provided fatigue fracture surfaces from laboratory tension/bending tests.

REFERENCES

1. Gopinath K.V., Structural Airworthiness of Aging Boeing Jet Transports - 747 Fuselage Test Program, AIAA 92-1128, Feb. 1992.

2. Goranson, Ulf, G., and Miller, Matthew, Aging Jet Transport Structural Evaluation Programs, *Structural Integrity of Aging Airplanes*, Atlanta, GA, March 1990, Atluri, S.N., Sampath, S.N., and Tong, P., eds., Spinger-Verlag Berlin, 1991, pp. 131-140.

3. Hoggard, Amos, W., Fuselage Longitudinal Splice Design, *Structural Integrity of Aging Airplanes*, Atlanta, GA, March 1990, Atluri, S.N., Sampath, S.N., and Tong, P., eds., Spinger-Verlag Berlin, 1991, pp. 167-181.

4. Roll, R., van Dalan, A, and Jongebreur, A.A., Results of Review of Fokker F28

"Fellowship" Maintenance Program, *Structural Integrity of Aging Airplanes*, Atlanta, GA, March 1990, Atluri, S.N., Sampath, S.N., and Tong, P., eds., Spinger-Verlag Berlin, 1991, pp. 309-320.

5. Ingraffea, A.R., Grigoriu, M.D. and Swenson, D.V., Representation and Probability Issues in the Simulation of Multi-Site Damage, *Structural Integrity of Aging Airplanes*, Atlanta, GA, March 1990, Atluri, S.N., Sampath, S.N., and Tong, P., eds., Spinger-Verlag Berlin, 1991, pp. 183-197.

6. Hui, C.Y. and Zehnder, A.T., A Theory For The Fracture of Thin Plates Subjected to Bending and Twisting Moments, *Int. J. Fracture*, 61, 1993, pp. 211-229.

7. Zehnder, A.T., Communication, Dept. of Theoretical and Applied Mechanics, Cornell University, NY (1994).

8. Schijve, J., Multiple-Site-Damage Fatigue of Riveted Joints, *Durability of Metal Aircraft Structures*, Atluri, S.N., Harris, C.E., Hoggard, A., Miller, N., and Sampath, S.N., eds., Atlanta Tech. Pub., Atlanta, GA, 1992, pp. 2-27.

9. Hartman, A., Some Tests on the Effect of Fatigue Loading on the Friction in Riveted Light Alloy Specimens, Nat. Aerospace Lab., Amsterdam, The Netherlands, TN M.2088, 1961.

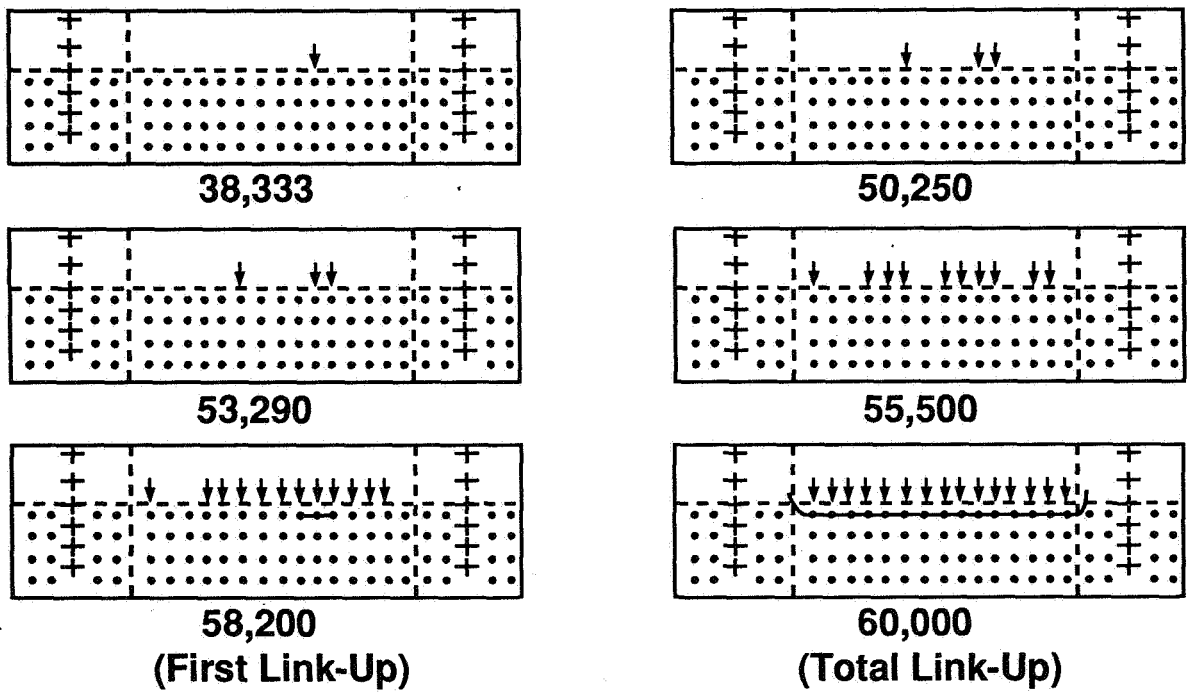

Figure 1. A schematic of bay #1 summarizing the location of outer skin fatigue cracks identified during visual in situ examinations.

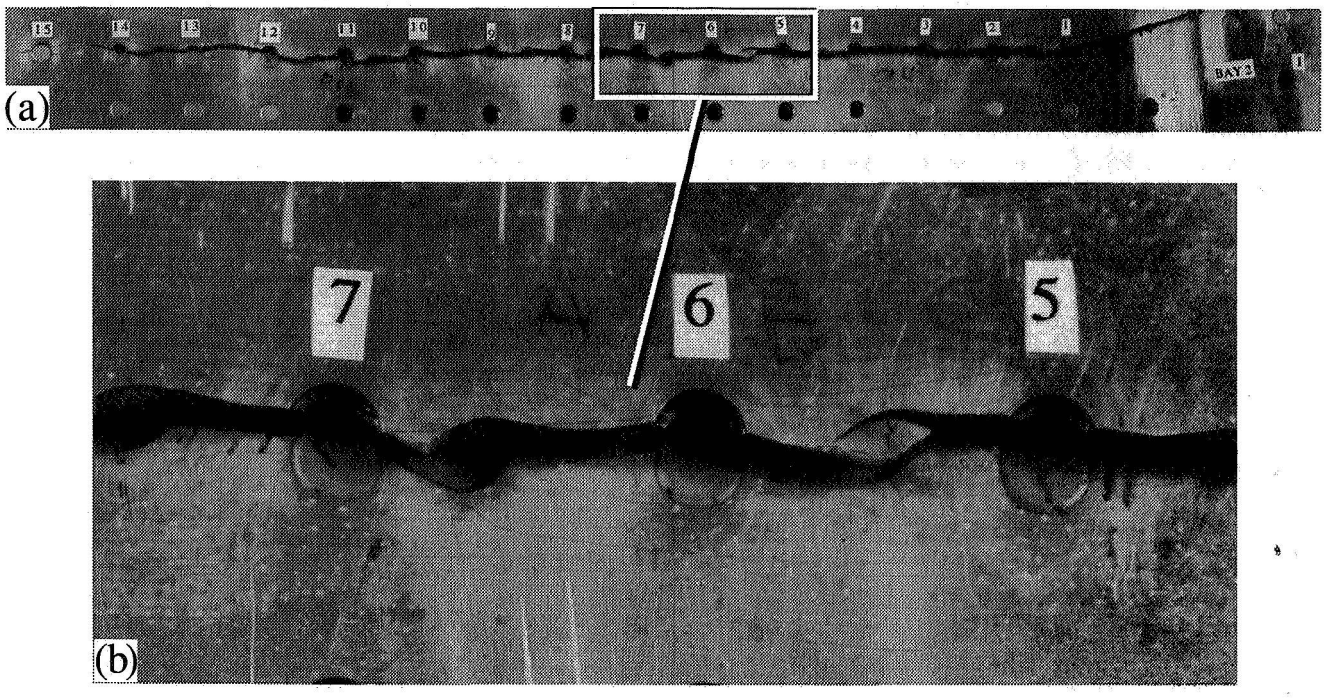

Figure 2. Photographs showing the fatigue cracking after link-up in bay #1 lap splice joint.

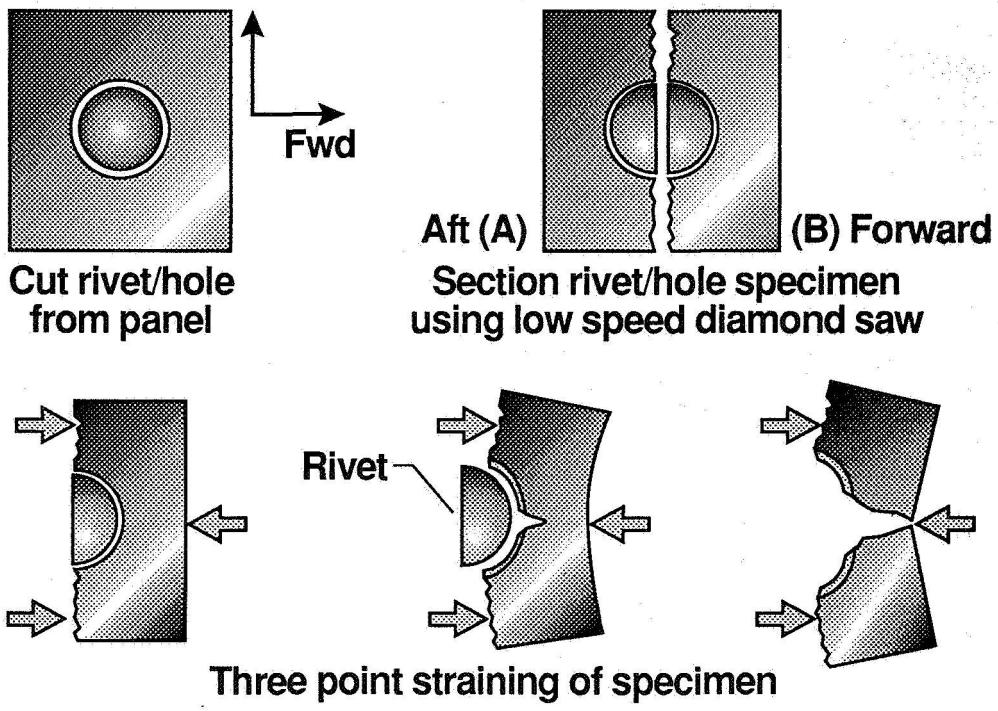

Figure 3. Schematic illustrating rivet hole destructive examination procedure.

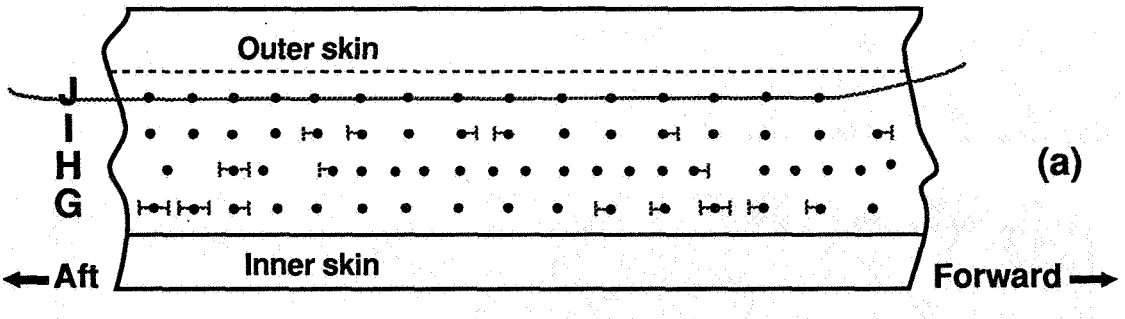

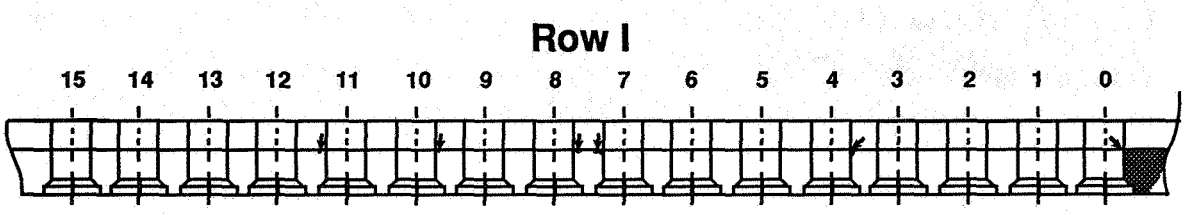

Hole #	Location	Length mm(in)	Hole #	Location	Length mm(in)
0 (FWD)	Outer skin	2.33 (.092)	8 (FWD)	Outer skin	0.073 (.003)
4 (FWD)	Outer skin	0.102 (.004)	10 (FWD)	Outer skin	0.140 (.006)
7 (Aft)	Outer skin	0.112 (.004)	11 (Aft)	Outer skin	0.058 (.002)

(b)

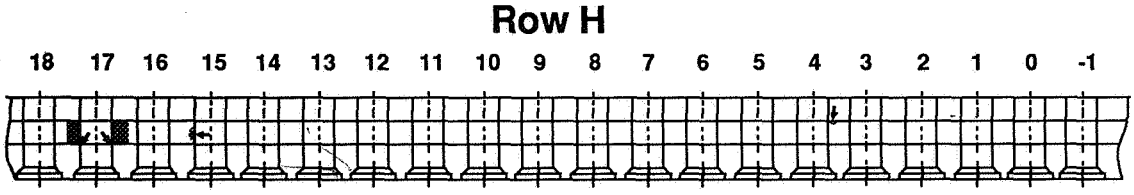

Hole #	Location	Length mm(in)	Hole #	Location	Length mm(in)
4 (FWD)	Inner skin	0.110 (.004)	17 (FWD)	Inner skin	3.51 (.138)
15 (Aft)	Inner skin	ND	17 (Aft)	Inner skin	4.00 (.157)

(c)

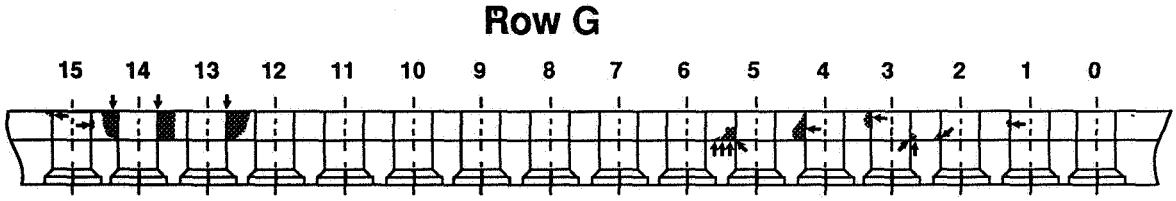

Hole #	Location	Length mm(in.)	Hole #	Location	Length mm(in.)
1 (Aft)	Inner skin	0.250 (.010)	13 (FWD)	Inner skin	2.750 (.108)
2 (Aft)	Inner skin	0.100 (.004)	14 (Aft)	Inner skin	2.720 (.107)
3 (1FWD)	Inner skin	0.170 (.007)	14 (FWD)	Inner skin	5.00 (.197)
3 (2FWD)	Inner skin	0.335 (.013)	15 (FWD)	Inner skin	0.163 (.006)
3 (Aft)	Inner skin	0.360 (.014)	15 (1-Aft)	Inner skin	0.115 (.004)
4 (Aft)	Inner skin	0.615 (.024)	15 (2-Aft)	Inner skin	0.128 (.005)
5 (Aft)	Inner skin	0.680 (.027)			

(d)

Figure 4. Illustrations showing the location of fatigue cracks in bay #1.

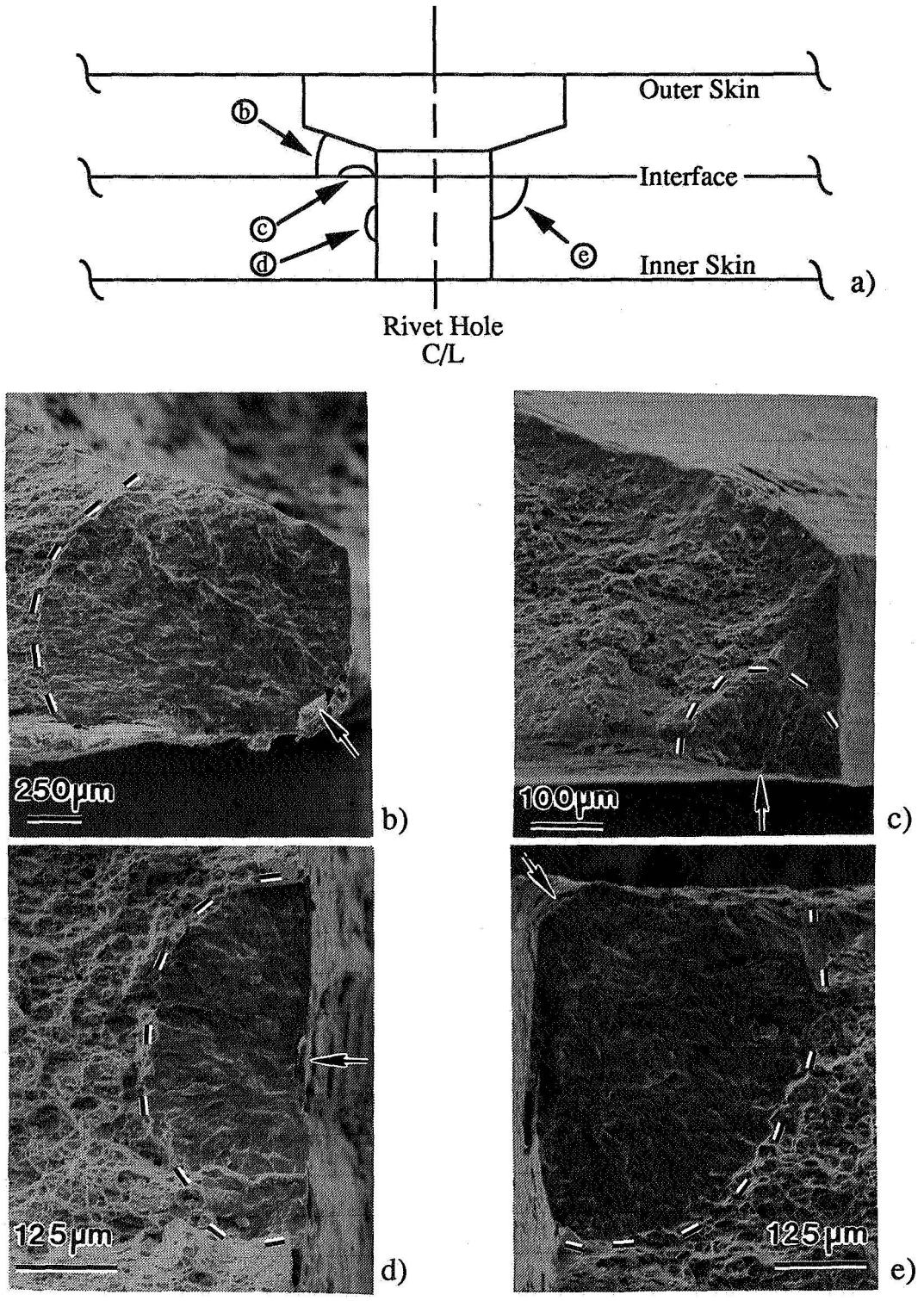

Figure 5. Schematic and SEM micrographs showing the location of fatigue cracking, crack initiation site (arrows) and fracture morphology of fatigue cracks in bay #1.

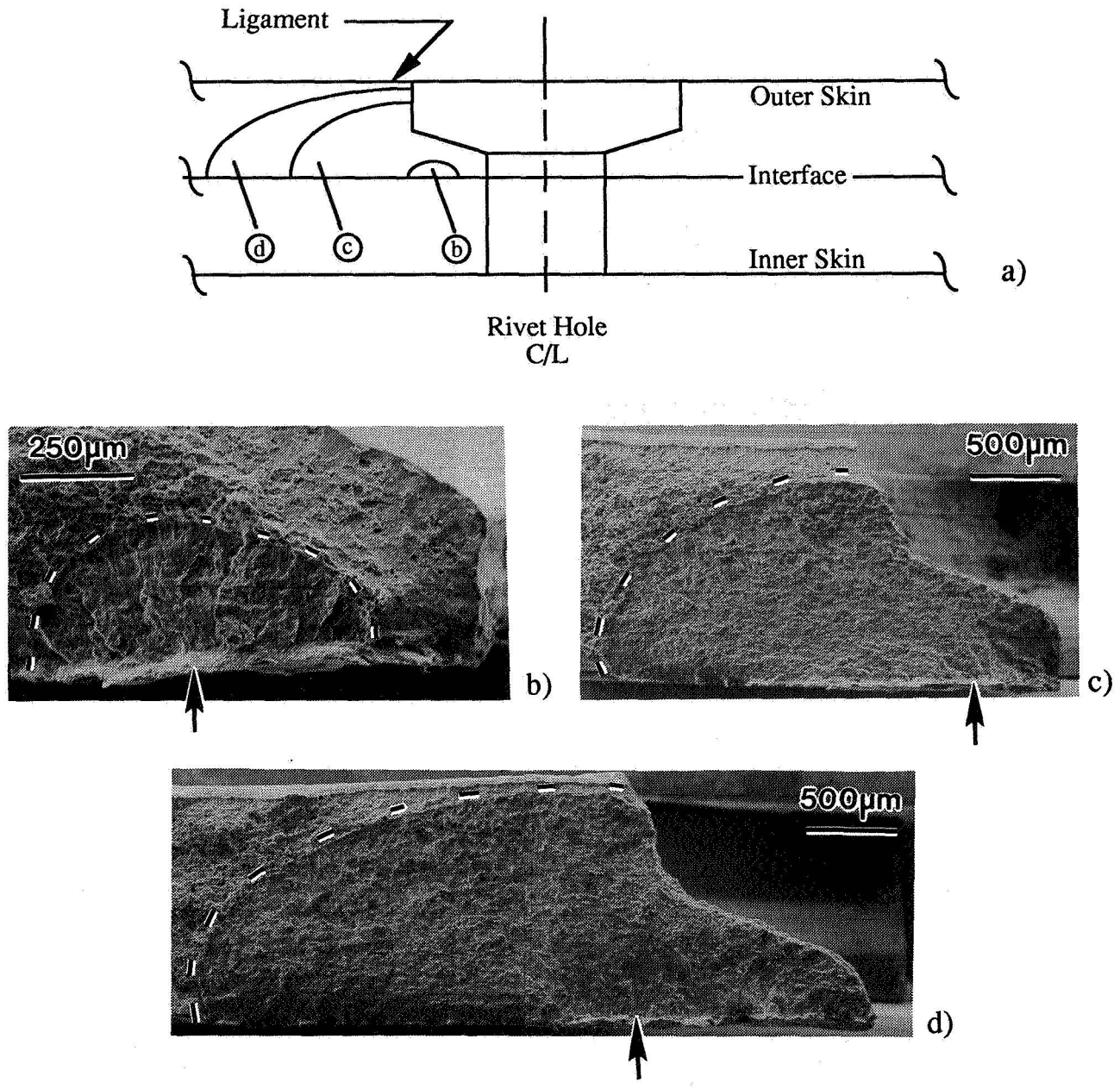

Figure 6. Schematic and SEM micrographs illustrating the location of fatigue crack initiation (arrows) and sequence of crack propagation in the lap splice upper rivet row.

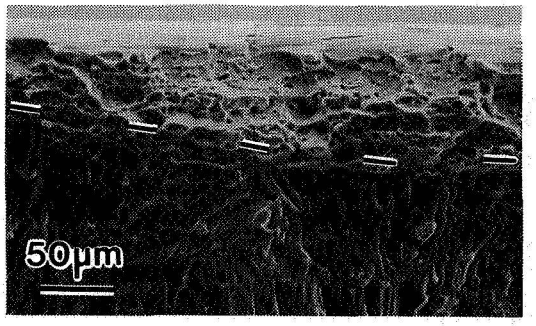

a)

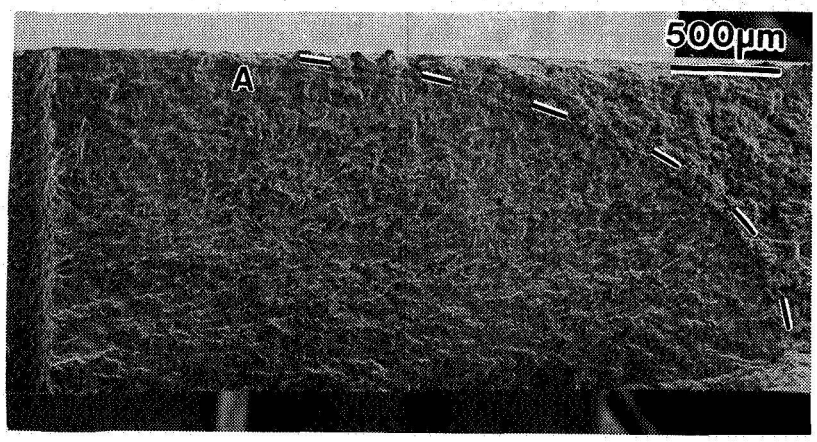

b)

Figure 7. SEM micrograph illustrating the fatigue crack path produced as a result of tension/bend constant amplitude testing.

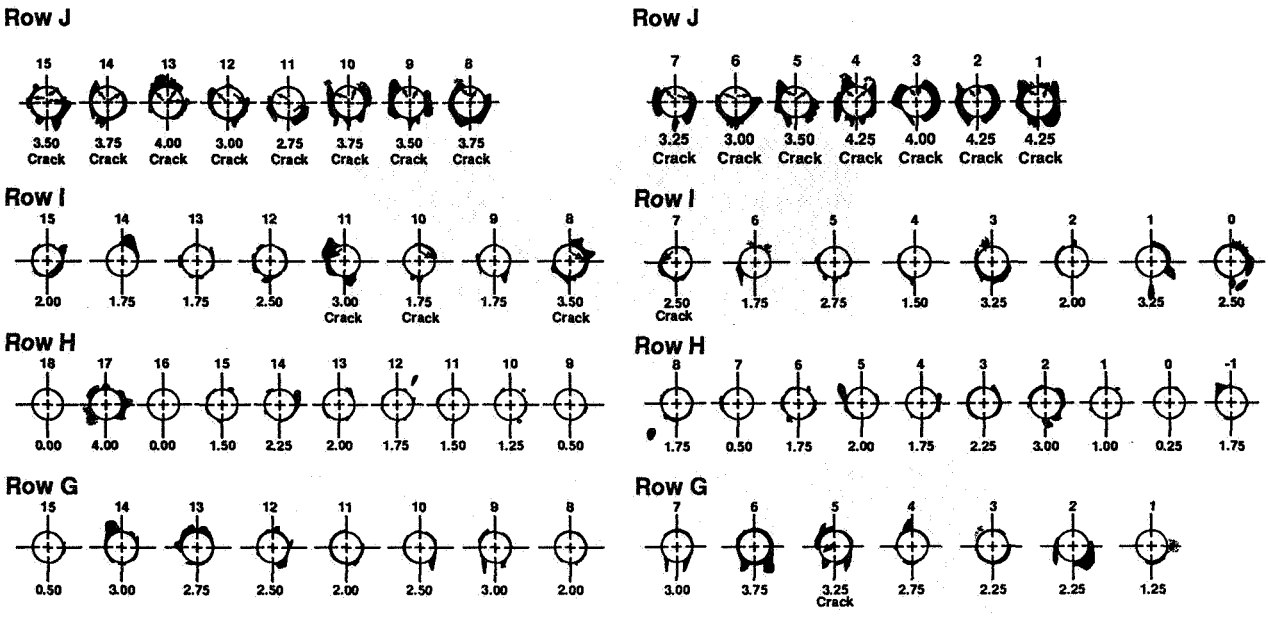

Figure 8. A schematic showing the interior surface of bay #1 lap splice outer skin. Illustrated is the location of black oxide film, the location of fretting intiated fatigue cracks and noted is the fretting average value determined by the procedure shown in Figure 9.

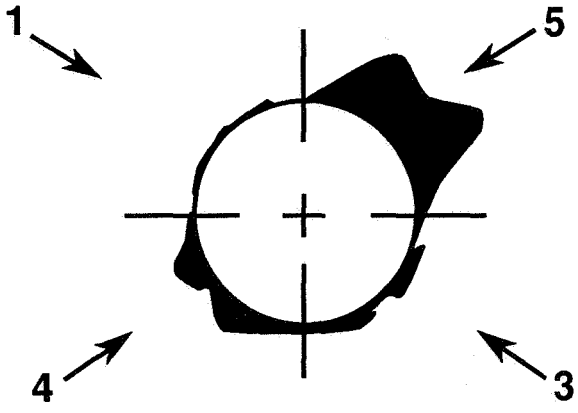

Fretting Average = (1+5+4+3)/4=3.25
Top Fretting Average = (1+5)/2=3.00
Bottom Fretting Average = (4+3)/2=3.50
LHS Fretting Average = (1+4)2=2.50
RHS Fretting Average = (5+3)/2 =4.00

Figure 9. A schematic showing the procedure used for estimating the extent of fretting fatigue by averaging the amount (area) of visual black oxide observed on the inside surface of the lap splice outer skin.

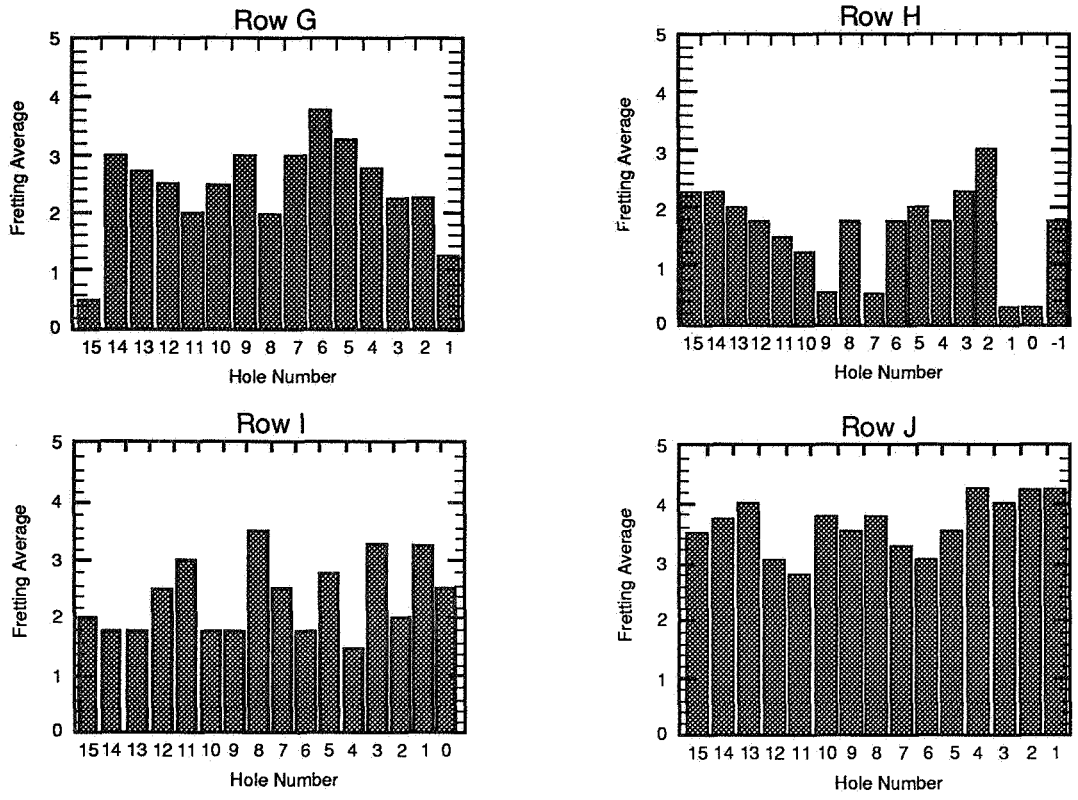

Figure 10. A plot of fretting average value versus rivet hole number is given for each rivet row (G, H, I and J) contained in bay #1.

Crack Length mm (x10^{-3}in.)	Number of Cracks Bay #1
0 to 1.19 (0 to 47)	17
1.2 to 2.39 (>47 to 94)	2
2.4 to 3.59 (> 94 to 141)	5
3.6 to 4.79 (>141 to 189)	6
4.8 to 5.99 (>189 to 236)	5
6.0 to 7.19 (>236 to 283)	5
7.2 to 8.39 (>283 to 330)	2
8.4 to 9.59 (>330 to 378)	0
9.6 to 10.79 (>378 to 424)	3
10.8 to 11.99 (>424 to 472)	2
12.0 to 13.19 (>472 to 519)	4
13.2 to 14.39 (>519 to 566)	1
14.4 to 15.59 (>566 to 614)	1
20.4 to 25.00 (>803 to 985)	0

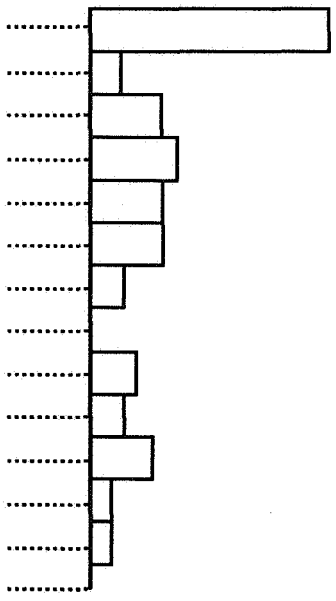

Figure 11. A plot showing the fatigue crack length distribution in bay # 1.

DISCRETE CRACK GROWTH ANALYSIS METHODOLOGY FOR THROUGH CRACKS IN PRESSURIZED FUSELAGE STRUCTURES

David O. Potyondy
Georgia Institute of Technology
Computational Modeling Center
Atlanta, GA

Paul A. Wawrzynek and Anthony R. Ingraffea
Cornell University Fracture Group
Ithaca, NY

SUMMARY

A methodology for simulating the growth of long through cracks in the skin of pressurized aircraft fuselage structures is described. Crack trajectories are allowed to be arbitrary and are computed as part of the simulation. The interaction between the mechanical loads acting on the superstructure and the local structural response near the crack tips is accounted for by employing a hierarchical modeling strategy. The structural response for each cracked configuration is obtained using a geometrically nonlinear shell finite element analysis procedure. Four stress intensity factors, two for membrane behavior and two for bending using Kirchhoff plate theory, are computed using an extension of the modified crack closure integral method. Crack trajectories are determined by applying the maximum tangential stress criterion. Crack growth results in localized mesh deletion, and the deletion regions are remeshed automatically using a newly developed all-quadrilateral meshing algorithm. The effectiveness of the methodology and its applicability to performing practical analyses of realistic structures is demonstrated by simulating curvilinear crack growth in a fuselage panel that is representative of a typical narrow-body aircraft. The predicted crack trajectory and fatigue life compare well with measurements of these same quantities from a full-scale pressurized panel test.

INTRODUCTION

Concern for the safety of aging airliners motivates the development of a methodology for simulating the behavior of long through cracks in the skin of pressurized fuselages wherein crack trajectory is not known *a priori*. Long cracks in the fuselage skin can arise from accidental damage during flight, e.g., the failure of an engine component resulting in a puncture of the skin, or from fatigue crack growth whereby several smaller cracks along a row of rivets might have linked up. The cabin of a passenger aircraft is pressurized. Since the loading from pressurization is cyclic, with one pressure cycle for each flight, older aircraft can accumulate significant numbers of cycles and substantial fatigue crack growth. Regardless of the cause of crack formation, simulation, along with experimental testing, can help one arrive at a better understanding of the behavior of such cracks. Also, an experimentally verified simulation methodology could help quantify the effect of major design parameter changes on aircraft damage tolerance.

Crack growth simulations, in general, are difficult to perform using existing codes for computational solid mechanics alone. The difficulty lies in the need for a continual updating of the geometry, as well as the discretization of the structure, as a result of crack initiation and propagation. Most available codes will not allow the geometry of the structure to evolve automatically during the course of a simulation, thereby forcing the analyst to perform tedious and time-consuming manual updates to the model for each step of crack growth. These difficulties can be overcome by use of a single fracture simulation program containing a representational model of the problem that separates the problem description from the problem discretization. Such a program provides the necessary framework for the entire simulation process, employing an existing computational solid mechanics module simply as an analysis engine whenever the structural response of a particular cracked configuration is necessary. The representational model consists of a geometrical model to which simulation attributes, such as loads and boundary conditions, can be attached once at the start of the simulation. In this way, information is inherited automatically by each computational mesh that is generated during crack growth. The primary components of this discrete crack growth analysis methodology are shown in Figure 1. It has been implemented within the FRANC3D fracture simulation program [Wawrzynek, *et al.* (1988); Martha (1989); Wawrzynek (1991)], a general software framework that supports simulation of curvilinear discrete crack propagation in stiffened, thin shell structures [Potyondy (1993)] and non-planar discrete crack propagation in solid structures [Potyondy, *et al.* (1992); Martha, *et al.* (1993); Gray, *et al.* (1994)].

The discrete crack growth analysis methodology described here utilizes the FRANC3D software framework. It accounts for the dominant influence factors affecting crack growth behavior and integrates these with a set of fracture parameters that characterize the fracture process. The mechanics considerations underlying the methodology are summarized in the next section. This is followed by a description of the modeling approach that supports simulating crack growth in realistic fuselage panels. Then, two example simulations are presented in which computed stress intensity factor histories are used to predict crack trajectory and fatigue life and a comparison is made with measurements from a full-scale pressurized panel test. A more thorough description of this work can be found in Potyondy (1993) and Potyondy, *et al.* (1994b).

MECHANICS CONSIDERATIONS

The behavior of long through cracks in the skin of pressurized fuselages is dominated by the following four factors [Rankin, *et al.* (1993)]: 1) a geometrically nonlinear stiffening effect (hereafter referred to as the bulge-out effect), caused by tensile membrane stresses in the direction parallel to the crack that restricts the crack edge bulging; 2) the mechanical loads, in addition to the internal pressure, acting on the superstructure that alter the stress distribution in the skin; 3) the presence of stiffening elements (frames and stringers) that alter locally the stress distribution in the skin; and, 4) plasticity effects around the crack tip. The first three factors can be modeled using a geometrically nonlinear shell finite element analysis procedure in which cracks are represented discretely in the mesh. In the present work, the nonlinear shell finite element code STAGS [Almroth, *et al.* (1986)], is used along with a hierarchical modeling strategy to account for the second factor. The effect of plasticity at the crack tips is ignored. (This effect is accounted for in the work of Shenoy, *et al.* (1994), who compute T^*, a relevant nonlinear fracture parameter, for typical fuselage structures. Refer to that paper for further details.)

The use of a geometrically nonlinear finite element shell model captures the global structural response by idealizing the fuselage as a cracked, stiffened, thin shell structure; however, additional modeling idealizations are required to predict crack trajectory and fatigue life. For cases in which the linear thin shell equations are applicable, stress intensity factors can be defined [Potyondy, *et al.*

(1994b)]. However, in the present case, wherein geometrically nonlinear effects play a significant role in the shell behavior, there is no clear consensus about the proper definition of stress intensity factors.

Many workers in the field have adopted an engineering approach that restricts the generality of the solution procedure. First, only straight cracks, oriented and loaded symmetrically with respect to the stiffeners, are considered; thus, a single similitude parameter, the mode-I stress intensity factor K_I, can be used to correlate crack growth rate with experimentally obtained fatigue crack growth data. Also, crack trajectory is not considered, since the crack growth is assumed to be self-similar. The bulge-out effect is modeled by using a geometrically nonlinear solution procedure, and the energy release rate G, is computed. K_I is obtained from the linear elastic, plane stress relation $K_I = \sqrt{EG}$ where E is Young's Modulus.

In contrast, the present methodology addresses the more general problem in which the cracks may be curved and need not be oriented or loaded symmetrically. Such cracks experience a combination of in-plane membrane loading and out-of-plane bending loading. The computed deformation pattern for such a case is shown in Figure 8. The unsymmetric out-of-plane bending could be called a nominal mode-III deformation. Hui and Zehnder (1993) propose a set of four stress intensity factors, (k_1, k_2, K_I, K_{II}), to account for this general loading. The mechanical behavior of the region near the crack tips is idealized using Kirchhoff plate theory to account for the bending loads and two-dimensional plane stress elasticity to account for the membrane loads. The stress intensity factors based on Kirchhoff plate theory are denoted by k_1 and k_2 while those based on two-dimensional elasticity theory are denoted by K_I and K_{II}. All four stress intensity factors have the units of force/length$^{3/2}$. The four modes of loading are depicted in Figure 2. Note that the unsymmetric out-of-plane bending in Figure 8 is characterized by k_2.

The stress intensity factors described above arise from the assumptions of small deflection plate theory; however, a geometrically nonlinear shell finite element procedure is required to account for the bulge-out effect experienced by a long crack in a pressurized fuselage structure. In the present work, the engineering assumption is made that these stress intensity factors can also be used to characterize the fracture process for such structures. Thus, the stress intensity factors correspond to the equilibrium state obtained from the geometrically nonlinear shell computation. They are computed using an extension of the modified crack closure integral method [Potyondy (1993); Potyondy, *et al.* (1993)] that is implemented as a post-processing step to the shell finite element analysis. The individual components of the energy release rate G_i, are obtained from the nodal forces and displacements in the shell finite element mesh near the crack tip. These components are, in turn, related to the stress intensity factors via the expressions:

$$
\begin{aligned}
G &= \sum_{j=1}^{5} G_j \\
G_1 &= \frac{K_I^{\,2}}{E} \\
G_2 &= \frac{K_{II}^{\,2}}{E} \\
G_4 &= \frac{k_1^{\,2}\,\pi}{3E}\left(\frac{1+\nu}{3+\nu}\right)
\end{aligned}
\qquad (1)
$$

$$G_3 + G_5 = \frac{k_2^{\,2}\,\pi}{3E}\left(\frac{1+\nu}{3+\nu}\right)$$

The stress intensity factors so obtained correspond to an equivalent model of a cracked Kirchhoff plate with the same energy release rate as that computed for the geometrically nonlinear problem.

No generally accepted criterion exists for predicting trajectories of cracks in pressurized thin shells. Existing criteria strictly apply for pure membrane stress conditions only. The stress state about a crack in a pressurized thin shell will always contain out-of-plane bending components, and additionally, these bending components will become large as the crack approaches stiffening elements. It is not yet apparent in what way these bending components are to be incorporated into an appropriate criterion. Rankin, *et al.* (1993) comment on this problem and refer to the summary of Zaal (1992); however, no suggestions are made for incorporating the bending components.

In this work, the crack front fields are described by (k_1, k_2, K_I, K_{II}). These fields apply to a crack in a plate wherein the crack front is assumed to be straight and aligned with the plate normal direction. (If the crack front were to deviate from this shape and orientation, a three-dimensional model of the crack front stress field involving $(K_I(s), K_{II}(s), K_{III}(s))$ would be required where s parameterizes the crack front through the thickness.) Therefore, crack trajectory can be described fully by the path of a single point on the crack front at the shell midsurface. The path is described in terms of the instantaneous angle of crack propagation ϕ, with which the crack will deviate from its current self-similar direction. ϕ will lie in the tangent plane to the midsurface at the crack tip. The maximum tangential stress theory [Erdogan and Sih (1963)] is used to predict ϕ via the relation

$$K_I \sin\phi + K_{II}(3\cos\phi - 1) = 0 \qquad (2)$$

Since ϕ is determined only at the shell midsurface, the two bending stress intensity factors do not enter into the relation.

MODELING APPROACH

Hierarchical Modeling Strategy

A hierarchical modeling strategy [Starnes and Britt (1991)] consisting of a series of models at differing scales provides a general mechanism for modeling pressurized fuselage structures by representing the important global and local features of a shell structure subjected to combined internal pressure and mechanical loads. The hierarchical modeling levels range from a relatively coarse global shell model for determining the internal load distribution and global response of the shell, to a highly refined local shell model for determining crack growth behavior.

The three hierarchical modeling levels employed in both of the simulations are depicted in Figure 3 and include a global shell model, a 6x6 bay stiffened panel model, and a 2x2 bay stiffened panel model. The global shell model can be subjected to internal pressure and mechanical loads that represent

a bending moment, a vertical shear load, and a torsional load applied to the shell. A geometrically nonlinear analysis of the global shell model provides the internal load distribution for the shell as well as the kinematic boundary conditions (displacements and rotations) along the boundaries of the 6x6 bay stiffened panel model. In addition to these kinematic constraints, the 6x6 bay stiffened panel model is also subjected to internal pressure. A geometrically nonlinear analysis of the 6x6 bay stiffened panel model provides a more accurate determination of the interaction between skin, frames, and stiffeners as well as the kinematic boundary conditions along the boundaries of the 2x2 bay stiffened panel model. In addition to these kinematic constraints, the 2x2 bay stiffened panel model is also subjected to internal pressure. A geometrically nonlinear analysis of the 2x2 bay stiffened panel model provides the detailed force and deformation field near the crack tips used to compute (k_1, k_2, K_I, K_{II}) for successive crack lengths. An initial crack is present in all three of the hierarchical models, but the crack is grown only in the 2x2 bay stiffened panel model; thus, its kinematic boundary conditions are not recomputed during crack growth. All of the analyses are conducted using the STAGS shell finite element analysis code.

Modeling Crack Growth

All crack growth takes place in the 2x2 bay stiffened panel model that is constructed within FRANC3D and shown in Figure 4. The general steps of the process are illustrated in Figure 1. (In this case, the simulation attributes include the generalized displacements obtained from the 6x6 bay stiffened panel model and are attached to the corresponding edges along the boundary of the FRANC3D geometrical model.) During all stages of the simulation, the analyst can manipulate a perspective view of this model and its discretization interactively.

Once all of the simulation attributes have been attached to the geometrical model, the simulation process consists of iterating through the following steps: 1) A STAGS finite element model is generated from FRANC3D for the current cracked configuration. 2) After obtaining the equilibrium state by executing the STAGS code, the values of (k_1, k_2, K_I, K_{II}) are computed and are used to estimate crack growth direction. 3) The analyst determines the amount of crack extension at each crack tip. 4) The crack growth alters the topology of the FRANC3D geometrical model and leads to localized mesh deletion. 5) The deletion region is remeshed automatically using a newly developed all-quadrilateral element meshing algorithm [Potyondy, *et al.* (1994a)] which generates a graded mesh that is fine near the crack tips and coarser away from the crack tips. A four-noded, six degree-of-freedom per node, shell element [Rankin and Brogan (1991)] is used within the entire deletion region, including the area immediately adjacent to the crack tips. (The errors introduced in the stress intensity factor computation from element distortion are examined in Potyondy (1993). For the meshes used in the example simulations, the errors in K_I and K_{II} are believed to be below 2 percent while the errors in k_1 and k_2 may reach 15 percent.) The process repeats with step 1. Proceeding in this fashion, both the trajectory and the stress intensity factor history are determined.

Generic Narrow-Body Panel

A fuselage panel that is representative of a typical narrow-body aircraft has been modeled. The dimensions and description are from Miller, *et al.* (1992). The panel consists of 2024-T3 clad skin of thickness 0.036 inches, reinforced by stringers at 9.25 inch spacing, and frames, without shear-ties, at 20 inch spacing. Tear straps of thickness 0.036 inches run circumferentially at 10 inch spacing, centered on

the frame and midway between frames, and longitudinally under the stringers.

The panel is comprised of the following structural components: skin, frames, stringers, tear straps, and stringer clips. These are shown in Figure 4. Typically, the tear straps are bonded directly to the skin whereas the other components are connected with rivets. In the work of Miller, *et al.* (1992) fastener flexibility was modeled using rigid body elements for rotational and axial displacements, and spring elements for transverse displacements. In the present work, fastener flexibility has not been modeled; it is assumed that there is a perfect bond between all structural components along their entire area of overlap.

Different modeling idealizations have been employed in the three models of the analysis hierarchy. In the global shell model, the skin is modeled with shell elements; the frames are modeled with shell elements to which beam elements are attached along some of the shell element edges; and, the stringers, tear straps, and stringer clips are modeled with beam elements. In the 6x6 bay stiffened panel model, all structural components are modeled with shell elements and beam elements are also included along the tops of the stringers. In the 2x2 bay stiffened panel model, these beam elements are replaced by shell elements that approximate the hooked shape. In both the 6x6 and 2x2 bay stiffened panel models, each layer in the overlap areas is modeled with its own separate shell elements by providing the eccentricity from a reference wall surface. The material properties used in the three models of the analysis hierarchy were a Poisson's ratio of 0.33 for all structural components; and, a Young's modulus of 10,500 ksi for the skin and tear straps, and 10,700 ksi for the frames, stringers, and stringer clips.

EXAMPLE SIMULATIONS

Simulation 1: Trial Problem

The initial crack is located in a panel near the crown of the fuselage. It is a straight 6.0 inch crack oriented parallel to the stringer and centered on the midbay tear strap 2.31 inches from the stringer centerline. The crack cuts completely through both the tear strap and the skin. The boundary conditions for the global shell model are a uniform internal pressure of 8.0 psi and a mechanical load consisting of a bending moment applied to the fuselage barrel. A plane of symmetry is assumed at one end of the barrel. The other end is restrained to remain in a plane and two equal but opposite point forces are applied at the top and bottom of the barrel. The point forces produce a moment of 5.65×10^6 inch-pounds, directed so as to compress the fuselage crown. The applied moment is slightly less than the value that just causes buckling of the skin between frames in the fuselage crown. The crack is grown in one inch increments at each crack tip up to a total piecewise crack length of 16 inches. Both the global shell and the 6x6 bay stiffened panel models contain approximately 100,000 degrees of freedom. The FRANC3D models contain from 11,000 to 14,000 degrees of freedom.

The deformed structure for various crack lengths is shown in Figure 5. The computed crack trajectory, shown in Figure 6, appears reasonable. The crack is curving away from the nearest stringer. This is the observed behavior in pressurized panel tests of narrow-body fuselage structures wherein the crack is located closer to the stringer. (See the description of the test results in a subsequent section and Figure 9).

The stress intensity factor history for the right crack tip is plotted in Figure 7 in terms of relative crack length L/B where L is the horizontal distance between crack tips and B is the distance between frames. The stress intensity factor history for the left crack tip is similar. The following trends in the stress intensity factor history can be identified:

- K_I is the dominant stress intensity factor and increases as the crack grows.
- The ratio K_{II}/K_I becomes small after the crack is allowed to curve and remains small throughout crack growth. This behavior is known to occur for isotropic materials subjected to in-plane loading only [Wawrzynek (1991)].
- The ratio k_2/K_I is small for the initial straight crack, but as the crack begins to curve, the value of k_2 increases such that the ratio of k_2/K_I becomes large.
- The ratio k_1/K_I remains small throughout crack growth.

The value of k_2 is affected by the resistance of opposing crack edges to out-of-plane deformation. Two trends are expected to occur: 1) as a longitudinal crack is moved closer to a stringer, the stiffness of the crack edge nearest to the stringer should increase relative to that of the opposing crack edge; and, 2) as the crack begins to curve, the stiffness of the crack edge on the concave side should diminish relative to that of the crack edge on the convex side. (The tensile membrane stresses in the longitudinal direction that restrict the bulging cannot develop in the peninsula of material on the concave side.) The initial crack in the trial problem is not near enough to the stringer for the first trend to be observed; however, it is observed in the validation problem (see Figure 8). The second trend is observed in both the deformed shapes of Figure 5 and the stress intensity factor history of Figure 7, i.e., as the crack curves, both the unsymmetric out-of-plane deformation and the value of k_2 increase. In the trial problem, the ratio of k_2/K_I reaches 0.36 for the 14 inch crack.

There is little symmetric bending occurring for the crack in the trial problem as indicated by the low value of k_1. The significant amount of membrane stretching occurring in the fuselage skin keeps this value low. The predominant crack tip loading consists of membrane stretching, characterized by K_I, and unsymmetric out-of-plane bending, characterized by k_2.

Simulation 2: Validation Problem

Description of Experiment

Two generic pressure test fixtures have been fabricated by the Boeing Commercial Airplane Group. The fixtures can be used for fatigue, fatigue crack growth, or residual strength tests. One fixture has a radius of curvature of 74 inches to match narrow-body airplanes, while the other has a radius of curvature of 127 inches to match wide-body airplanes. One end of each fixture is mounted in a rigid framework and the other on rollers to allow longitudinal displacement. Removable test sections are inserted in cutouts in the barrel-shaped fixtures. Tests are conducted under pressure loading only, using air as the pressurizing medium. More information about the fixtures and the Boeing test program can be found in the papers of Miller, *et al.* (1992) and Maclin (1991).

Experimental data generated using the test fixtures was made available to the authors by Boeing [Worden (1993)]. The data is from a typical narrow-body test panel with bonded tear straps. The panel had initial damage consisting of a 5.0 inch saw cut centered on the midbay tear strap and just above the stringer tear strap. The saw cut went completely through both the skin and the midbay tear strap. The panel was inserted into the test fixture and pressure cycled at 7.8 psi. The pressure cycles fluctuated between maximum pressure and zero pressure. During the test, the position of each crack tip was monitored and recorded along with the number of pressure cycles. The experimental data can be found in Potyondy (1993) and Potyondy, *et al.* (1994b).

Description of Simulation

The test fixture approximates the behavior of an actual pressurized fuselage. Thus, a cracked pressurized fuselage is modeled using the analysis methodology described above. The validation problem differs from the trial problem only in the following details: 1) initial crack size and location; and, 2) boundary conditions applied to the global shell model. The initial straight 5.0 inch crack is located in a panel that is representative of the fuselage crown. In both the global shell model and the 6x6 bay stiffened panel model, the initial crack is located in the same location as the saw cut. In the FRANC3D model, the initial crack has been translated a distance of 0.45 inches (half the stringer width) away from the stringer, because the current version of FRANC3D cannot model cracks at the interface of the stringer and skin.

The boundary conditions applied to the global shell model are a uniform internal pressure of 7.8 psi and no mechanical loading. A plane of symmetry is assumed at one end of the barrel while the other end is constrained to remain in a plane. Note that this model corresponds with an open cylinder, and thus the longitudinal stress in the model is less than the longitudinal stress in the test fixture, since the test fixture is a closed cylinder. The crack is grown in one inch increments at each crack tip up to a total piecewise crack length of 19 inches.

The deformed structure for various crack lengths is shown in Figure 8. The computed crack trajectory is plotted in Figure 9 along with the measured trajectory from the panel test. The computed stress intensity factor history for the right crack tip is plotted in Figure 10. The stress intensity factor history at the left crack tip is similar.

There is no analytical solution with which the computed stress intensity factors can be compared. However, the computed values of K_I can be compared to those obtained from the finite element analysis of Miller, *et al.* (1992) of a similar panel test. The comparison is described in Potyondy (1993) and Potyondy, *et al.* (1994b) where it is shown that the trends and values from both analyses are similar.

Fatigue Life Prediction. A life prediction has been made using the computed stress intensity factor history and a Paris fatigue crack growth model. Fatigue crack growth data from a flat 2024-T3 panel tested at stress intensity factors in the range of 50-80 ksi-sqrt (in) was made available to the authors by Boeing [Worden (1993)]. The crack growth equation is of the form

$$(10{,}000)\frac{da}{dN} = \left(\frac{K_{max}}{C}\right)^n \tag{3}$$

and for 2024-T3 aluminum T-L crack growth ($R = 0$ and ambient lab environment)

$$\begin{matrix} C = 28 \\ n = 4.9 \end{matrix} \quad ; \quad \text{for } K_{\max} \left(\text{ksi}\sqrt{\text{inch}}\right) \tag{4}$$

By using the computed values of K_I, and assuming that K_I varies linearly between the data points in Figure 10, life predictions were made and are compared with measured life in Figure 11 (K_{eff} is defined below by Eq. (6); for $\alpha = 0$, $K_{eff} = K_I$).

The total predicted life is obtained by integrating the crack growth model until K_I reaches K_{app}, the apparent toughness of the material. K_{app} is a function of thickness and crack orientation relative to material rolling direction. The values of K_{app} for this material and thickness are

$$\begin{aligned} K_{app} &= 100 \text{ ksi}\sqrt{\text{inch}} \qquad \text{(T-L crack growth)} \\ K_{app} &\approx 105 - 120 \text{ ksi}\sqrt{\text{inch}} \quad \text{(L-T crack growth)} \end{aligned} \tag{5}$$

T-L crack growth refers to the crack aligned with the rolling direction, while L-T crack growth refers to the crack perpendicular to the rolling direction. For the panel tested, the rolling direction is the longitudinal direction; thus, cracks growing from the initial saw cut are experiencing T-L crack growth. The computed value of K_I for $L/B = 0.77$ is 112 ksi-sqrt (in). At this point, the crack has curved considerably and is oriented at nearly 45 degrees with respect to the two orthogonal rolling directions; thus, the value of K_{app} will lie within the range of T-L and L-T crack growth. For the purposes of making a total life prediction, it is assumed that $K_I = K_{app}$ for $L/B = 0.77$.

Discussion of Fatigue Life Prediction. The life prediction for the validation problem compares well with the measured life. For all crack lengths considered in the simulation, the predicted life is never more than 25 percent greater than the measured life. In addition, the total life prediction is 628 cycles. In the panel test, crack growth ceased after 626 cycles because of the large flap that had formed in the skin making further pressurization impossible. Thus, the total predicted life is in excellent agreement with the measured life; however, such an *extremely* close comparison is surely serendipitous.

Life predictions within a factor of two are considered good for this test for the following reasons:

- The crack growth rates throughout the test are high; thus, the predicted life is sensitive to small changes in the computed values of K_I because of the large coefficient of 4.9 in the Paris crack growth model.
- During the final stages of crack growth, the computed values of K_I are approaching K_{app}; thus, the crack growth is about to become unstable. It is likely that large plastic zones were present at the crack tips, thereby casting doubt on applicability of the LEFM assumptions. However, this effect is offset by the use of Paris model coefficients that were obtained for stress intensity factors above 50 ksi-sqrt (in).

A final observation is that the prediction of slower crack growth than observed supports the hypothesis that the presence of k_2 will increase the crack growth rates from those obtained by

considering only K_I. It is expected that the experimental work of Zehnder, *et al.* (1992) and Viz and Zehnder (1994) will shed more light on this issue and may result in a modified procedure for determining life. In lieu of such a procedure, a simple empirical procedure for incorporating and bounding the effect of the additional stress intensity factors on the crack growth rate is proposed here. It assumes that a fraction of the energy from the additional stress intensity factors contributes to fatigue crack growth. Replace the value of K_I in the fatigue crack growth model with an effective stress intensity factor K_{eff}, that is related to an effective energy release rate G_{eff}, via

$$\begin{aligned} K_{eff} &= \sqrt{E\,G_{eff}} \\ G_{eff} &= G_1 + \alpha\left(G_2 + G_3 + G_4 + G_5\right) \quad ; \quad 0 \le \alpha \le 1.0 \end{aligned} \tag{6}$$

where E is Young's modulus, G_i are the separate components of the energy release rate that are related to the four stress intensity factors by Eq. (1), and α is an empirical coefficient that scales the contribution from the additional stress intensity factors.

The empirical procedure is applied to the validation problem, and the resulting life predictions for α equal to 0.0 and 1.0 (expected lower and upper bounds) are compared with measured life in Figure 11. The α coefficient shifts each computed data point to the left by a fixed amount, e.g., the last computed data point will coincide with the measured value by setting $\alpha = 0.4$. Also, total life is decreased as α is increased. During crack growth, although the ratio of k_2/K_I increases by almost 40 percent, the contribution of K_I to the total energy release rate decreases by less than 4 percent suggesting that k_2 may have a minor effect on crack growth for this class of problems.

Discussion

The present analysis methodology allows the cracks to curve and accounts for the nonlinear bulge-out effect and the presence of stiffening elements by using a geometrically nonlinear solution procedure. Also, the interaction between the mechanical loads acting on the superstructure and the local structural response near the crack tips is accounted for by employing a hierarchical modeling strategy. The computed stress intensity factors exhibit the expected trends and their values are reasonable. The computed crack trajectory and predicted life agree well with the measured quantities from a full-scale pressurized panel test. The effect of the additional stress intensity factors, in addition to K_I, on crack growth rate can be incorporated into a life prediction using an effective stress intensity factor.

The unsymmetric, out-of-plane deformation experienced by a crack in a pressurized fuselage structure can be seen clearly in the geometrically nonlinear finite element models (see Figures 5 and 8) and can be accounted for by the computation of k_2. However, the effect of k_2 on crack growth rate is still uncertain. It is expected that further testing by Zehnder, *et al.* (1992) and Viz and Zehnder (1994) will determine this effect. The slight underprediction of crack growth rate for the validation problem may indicate that the presence of k_2 increases the crack growth rate beyond that obtained by only considering K_I; however, this result is preliminary. Other factors, such as the lack of applying a longitudinal loading to the global shell model, may also account for the slight underprediction of crack growth rates. Further comparisons between predicted and measured lives must be made before more definitive conclusions can be drawn.

The maximum tangential stress crack growth directional criterion used here predicts a crack trajectory in good agreement with the measured trajectory from a full-scale pressurized panel test (see Figure 9). Depending upon the accuracy required in the trajectory determination, this simple criterion may be sufficient for most practical situations.

The fact that the boundary conditions on the 2x2 bay stiffened panel model were not altered during crack growth; i.e., the crack was only grown in the 2x2 bay model, and did not seriously affect the accuracy of the trajectory and life predictions. The kinematic boundary conditions are affected minimally by crack growth near the center of the panel and must only be updated when the crack begins to approach the panel boundary. The crack behavior is affected to a much greater extent by the live pressure loading, and the effect of this loading is being recomputed after each step of crack growth.

Restarting the geometrically nonlinear finite element computation from zero load after each crack growth increment requires a significant computational effort. The computational efficiency could be improved by using the previously computed equilibrium state as an initial condition for the succeeding computation after the crack has grown. The procedure is described in the paper of Potyondy and Ingraffea (1992). Its implementation would reduce the total computation time to perform a crack growth simulation significantly.

It is known that fastener flexibility alters the stress distribution locally in the fuselage skin which influences the behavior of cracks in these regions. The effect of neglecting fastener flexibility in the current analysis methodology should be examined. Also, the repeatability of the panel test experiments should be determined along with the effect of small variabilities, such as fit-up stresses and rivet forces, on crack growth behavior.

CONCLUSIONS

The present methodology provides an effective engineering approach to simulate crack growth in pressurized aircraft fuselages where crack trajectory is not know *a priori*. It accounts for the dominant influence factors affecting crack growth behavior (the bulge-out effect; presence of stiffening elements; and, mechanical loads, in addition to the internal pressure, acting on the superstructure) and integrates them with a set of LEFM fracture parameters to support trajectory and life predictions. The predicted crack trajectory and life agree well with the measured quantities from a full-scale pressurized panel test indicating the effectiveness of the methodology. A logical extension of the present methodology would be to account for plasticity effects at the crack tips, as these effects may become significant for long cracks encountered during residual strength computations.

ACKNOWLEDGEMENTS

This work was performed with support from the NASA Langley Aircraft Structural Integrity Program under contract NAG-1-1184. Ms. Vicki Britt of the NASA Langley Aircraft Structures Branch performed the global shell analyses to provide the boundary conditions for the FRANC3D models of the

example simulations. Dr. Charles Rankin, Dr. Frank Brogan, and Mr. Harold Cabiness of the Lockheed Palo Alto Research Laboratory provided the STAGS shell finite element code. Dr. Matthew Miller and Dr. R. Elaine Worden of the Boeing Commercial Airplane Group provided the structural details and dimensions of the typical narrow-body fuselage panel and the experimental data of the full-scale pressurized panel test. And finally, the authors would like to thank Prof. Alan Zehnder, Mr. Mark Viz, and Dr. Bruce Carter for many helpful discussions.

REFERENCES

Almroth, B.O., Brogan, F.A., and Stanley, G.M., 1986, "Structural Analysis of General Shells," User's Instructions for STAGSC-1, Vol. 2, Lockheed Missiles and Space Company, LMSC D633873.

Erdogan, F., and Sih, G.C., 1963, "On the Crack Extension of Plates under Plane Loading and Transverse Shear," *Journal of Basic Engineering*, 85, No. 4, pp. 519-527.

Gray, L.J., Potyondy, D.O., Lutz, E.D., Wawrzynek, P.A., Martha, L.F., and Ingraffea, A.R., 1994, "Crack Propagation Modeling," to appear in *Mathematical Models and Methods in Applied Sciences*.

Hui, C.Y., and Zehnder, A.T., 1993, "A Theory for the Fracture of Thin Plates Subjected to Bending and Twisting Moments," *International Journal of Fracture*, Vol. 61, pp. 211-229.

Maclin, J.R., 1991, "Performance of Fuselage Pressure Structure," *Proc. of 1991 International Conference on Aging Aircraft and Structural Airworthiness*, Washington, D.C. (November 19-21, 1991), C.E. Harris, ed., NASA Conference Publication 3160, pp. 67-74.

Martha, L.F., 1989, "Topological and Geometrical Modelling Approach to Numerical Discretization and Arbitrary Fracture Simulation in Three-Dimensions," Ph.D. Thesis, Cornell University, Ithaca, NY.

Martha, L.F., Wawrzynek, P.A., and Ingraffea, A.R., 1993, "Arbitrary Crack Representation Using Solid Modeling," *Engineering with Computers*, Vol. 9, pp. 63-82.

Miller, M., Kaelber, K.N., and Worden, R.E., 1992, "Finite Element Analysis of Pressure Vessel Panels," *Durability of Metal Aircraft Structures* : Proc. of International Workshop on Structural Integrity of Aging Airplanes, S.N. Atluri, C.E. Harris, A. Hoggard, N. Miller, and S.G. Sampath, eds., Atlanta Technology Publications, Atlanta, GA, pp. 337-348.

Potyondy, D.O., and Ingraffea, A.R., 1992, "A Methodology for Simulation of Curvilinear Crack Growth in Pressurized Fuselages," *Durability of Metal Aircraft Structures* : Proc. of International Workshop on Structural Integrity of Aging Airplanes, S.N. Atluri, C.E. Harris, A. Hoggard, N. Miller, and S.G. Sampath, eds., Atlanta Technology Publications, Atlanta, GA, pp. 217-230.

Potyondy, D.O., Gray, L.J., and Ingraffea, A.R., 1992, "Simulation of 3D Non-planar Fatigue Crack Growth in a Turbine Blade Root," *Computer Technology: Advances and Applications* : Proc. of ASME Pressure Vessels and Piping Conference, R.S. Gallagher and G.M. Hulbert, eds., PVP-Vol. 234, ASME, New York, pp. 31-42.

Potyondy, D.O., 1993, "A Software Framework for Simulating Curvilinear Crack Growth in Pressurized Thin Shells," Ph.D. Thesis, Cornell University, Ithaca, NY.

Potyondy, D.O., Rankin, C.C., Riks, E., Viz, M.J., and Zehnder, A.T., 1993, "Computation of Membrane and Bending Stress Intensity Factors for Thin, Cracked Plates," submitted to *Journal of Applied Mechanics.*

Potyondy, D.O., Wawrzynek, P.A., and Ingraffea, A.R., 1994a, "An Algorithm to Generate Quadrilateral or Triangular Element Surface Meshes in Arbitrary Domains With Applications to Crack Propagation," submitted to *International Journal of Numerical Methods in Engineering.*

Potyondy, D.O., Wawrzynek, P.A., and Ingraffea, A.R., 1994b, "Discrete Crack Growth Analysis Methodology for Through Cracks in Pressurized Fuselage Structures," submitted to *International Journal of Numerical Methods in Engineering.*

Rankin, C.C., and Brogan, F.A., 1991, "The Computational Structural Mechanics Testbed Structural Element Processor ES5: STAGS Shell Element," NASA Contractor Report 4358, Lockheed Missiles and Space Company, LMSC-D878511.

Rankin, C.C., Brogan, F.A., and Riks, E., 1993, "Some Computational Tools for the Analysis of Through Cracks in Stiffened Fuselage Shells," *Journal of Computational Mechanics*, Vol. 13, pp. 143-156.

Shenoy, V.B., Potyondy, D.O., and Atluri, S.N., 1994, "A Methodology for Computing Nonlinear Fracture Parameters for a Bulging Crack in a Pressurised Aircraft Fuselage," to appear in *Journal of Computational Mechanics.*

Starnes, J.H., and Britt, V.O., 1991, "Damaged Stiffened Shell Research at NASA Langley Research Center," *Proc. of 1991 International Conference on Aging Aircraft and Structural Airworthiness*, Washington, D.C. (November 19-21, 1991), C.E. Harris, ed., NASA Conference Publication 3160, pp. 203-220.

Viz, M.J. and Zehnder, A.T., 1994, "Fatigue Crack Growth in 2024-T3 Aluminum Under Tensile and Tearing Loads," FAA/NASA Intnl. Symposium: *Advanced Structural Integrity Methods for Airframe Durability and Damage Tolerance*, NASA CP-3274, 1994.

Wawrzynek, P.A., Martha, L.F., and Ingraffea, A.R., 1988, "A Computational Environment for the Simulation of Fracture Processes in Three Dimensions," *Analytical, Numerical, and Experimental Aspects of Three Dimensional Fracture Processes*, A.J. Rosakis, *et al.*, eds., ASME, New York, ASME AMD-Vol. 91, pp. 321-327.

Wawrzynek, P.A., 1991, "Discrete Modelling of Crack Propagation: Theoretical Aspects and Implementation Issues in Two and Three Dimensions," Ph.D. Thesis, Cornell University, Ithaca, NY.

Worden, R.E., 1993, private communication from Boeing Commercial Airplane Group.

Zaal, K.J.J.M., 1992, "A Survey of Crack Path Stability Theories with an Eye to an Application to Crack Flapping Phenomena in Pressurized Fuselages," Faculty of Aerospace Engineering, Delft University, Delft, The Netherlands, Report LR-681.

Zehnder, A.T., Viz, M.J., and Ingraffea, A.R., 1992, "Fatigue Fracture in Thin Plates Subjected to Tensile and Shearing Loads: Crack Tip Fields, J Integral and Preliminary Experimental Results," Proc. of the *VII Society for Experimental Mechanics International Congress on Experimental Mechanics*, Las Vegas, Nevada, June 8-11, 1992.

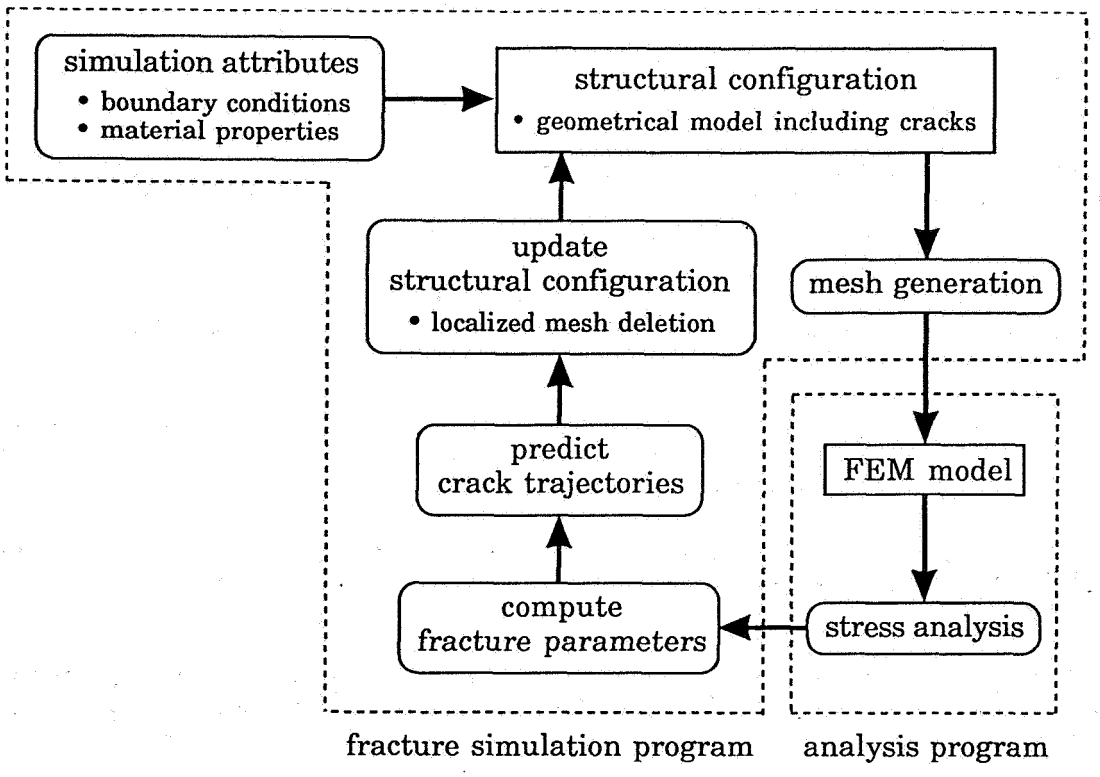

Figure 1: Discrete crack growth analysis methodology.

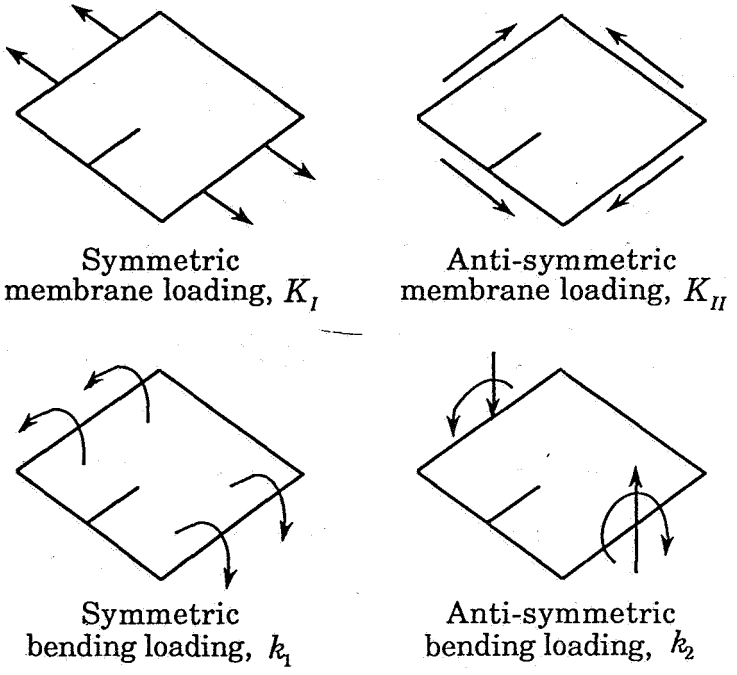

Figure 2: The four loading modes and their corresponding stress intensity factors for a through crack in a thin plate idealized using plane stress elasticity to account for the membrane loads and Kirchhoff plate theory to account for the bending loads.

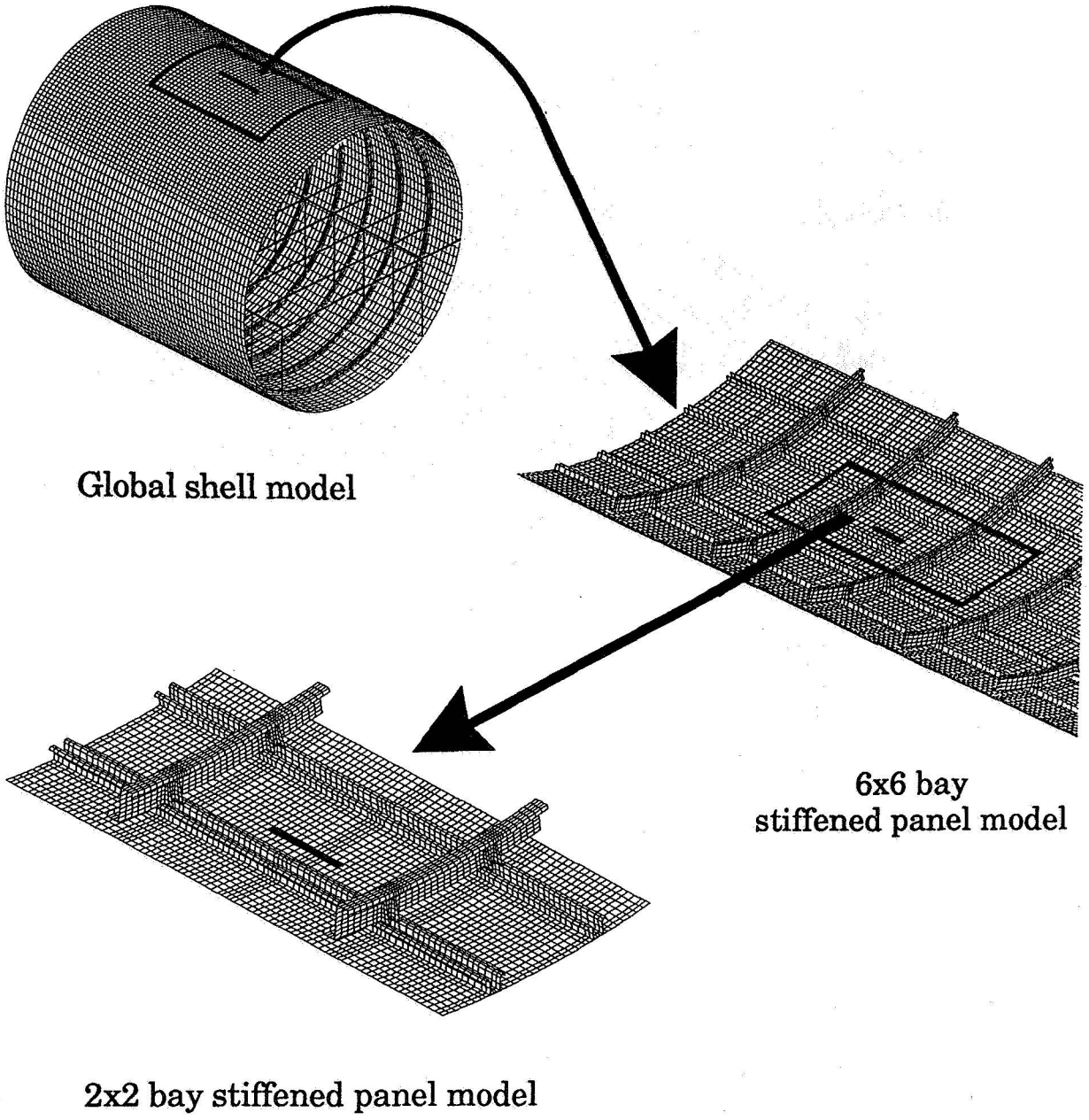

Figure 3: The three hierarchical modeling levels. Each model obtains its kinematic boundary conditions from the preceeding model in the hierarchy.

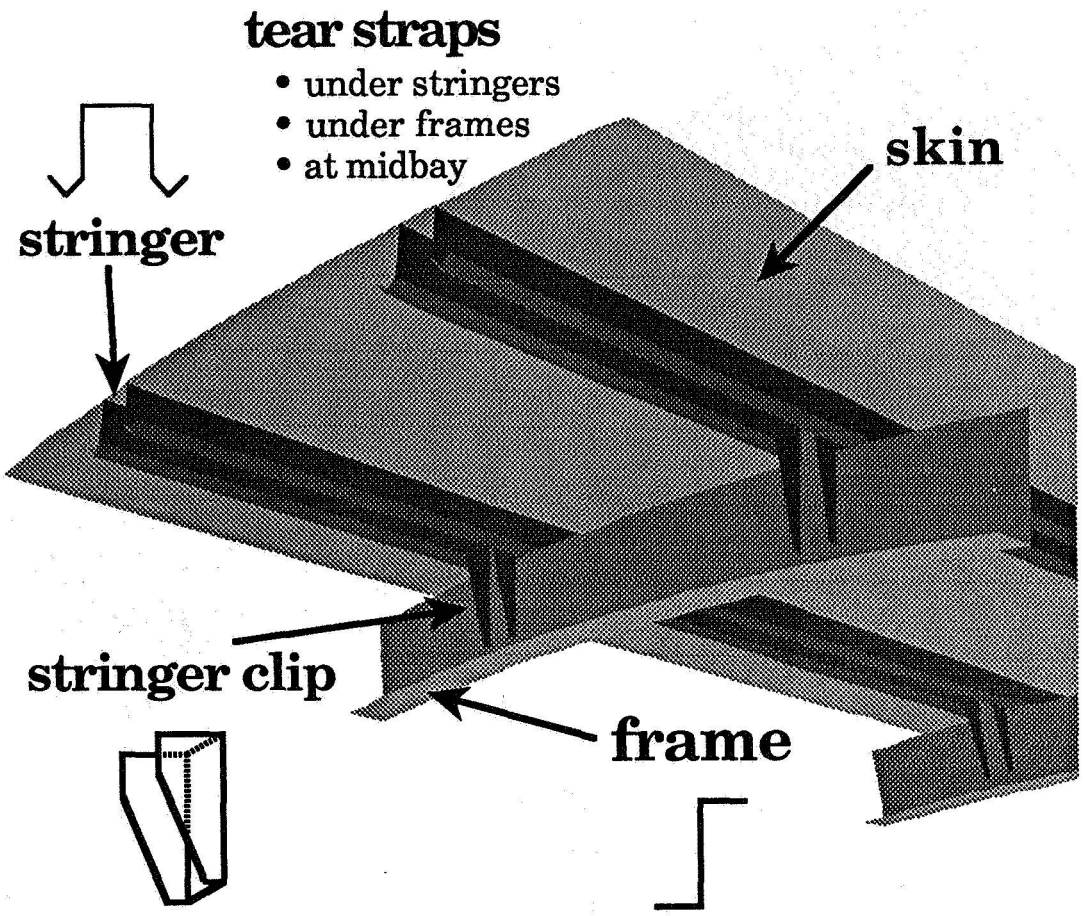

Figure 4: The 2x2 bay stiffened panel model as represented within FRANC3D as a geometrical model. The structural components and their cross sections are labelled.

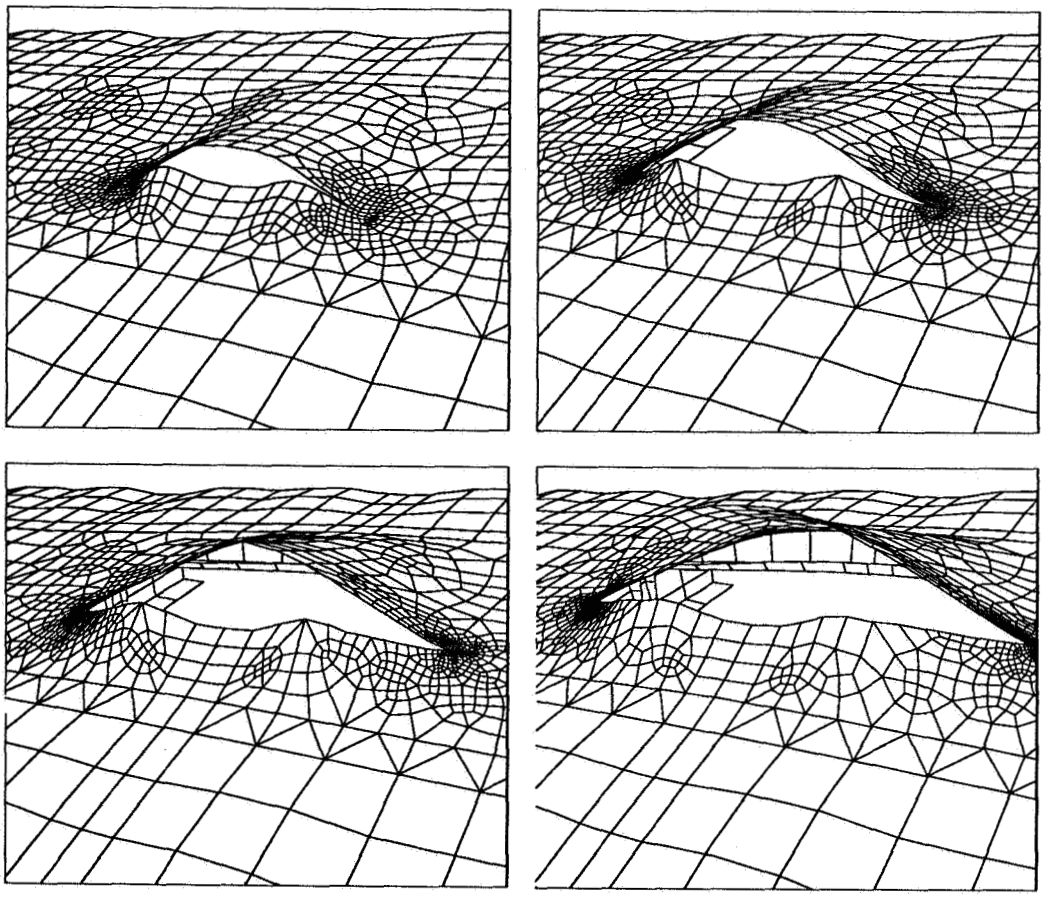

Figure 5: Deformed structure during crack growth for total crack lengths of 6, 8, 10, and 12 inches for the trial problem. Magnification factor for all images is five.

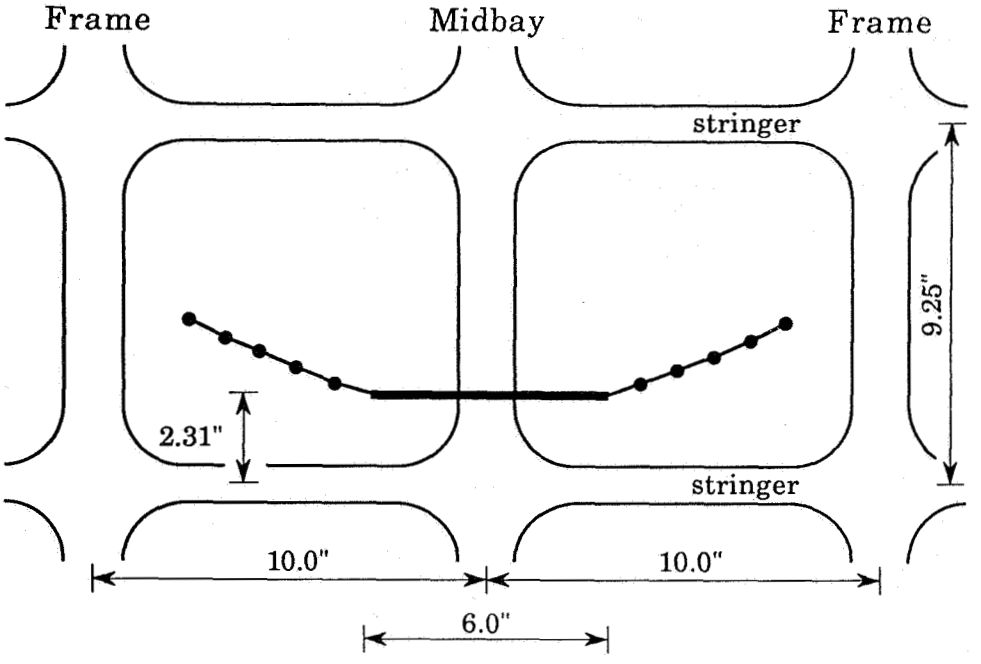

Figure 6: Computed crack growth trajectory for the trial problem. The black circles denote computed crack tip locations.

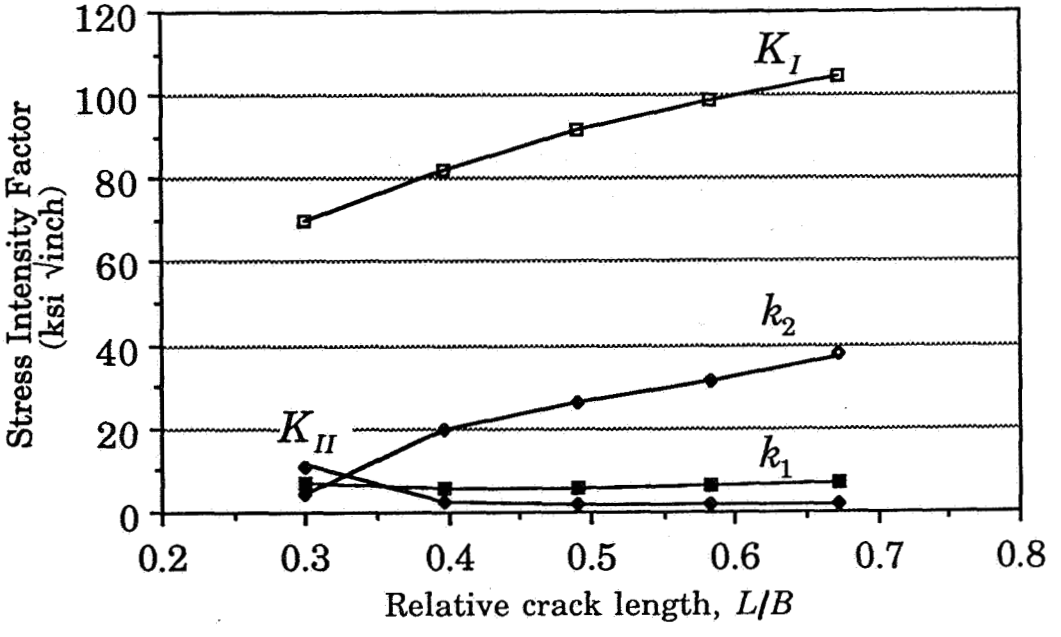

Figure 7: Computed stress intensity factors at right crack tip for the trial problem.

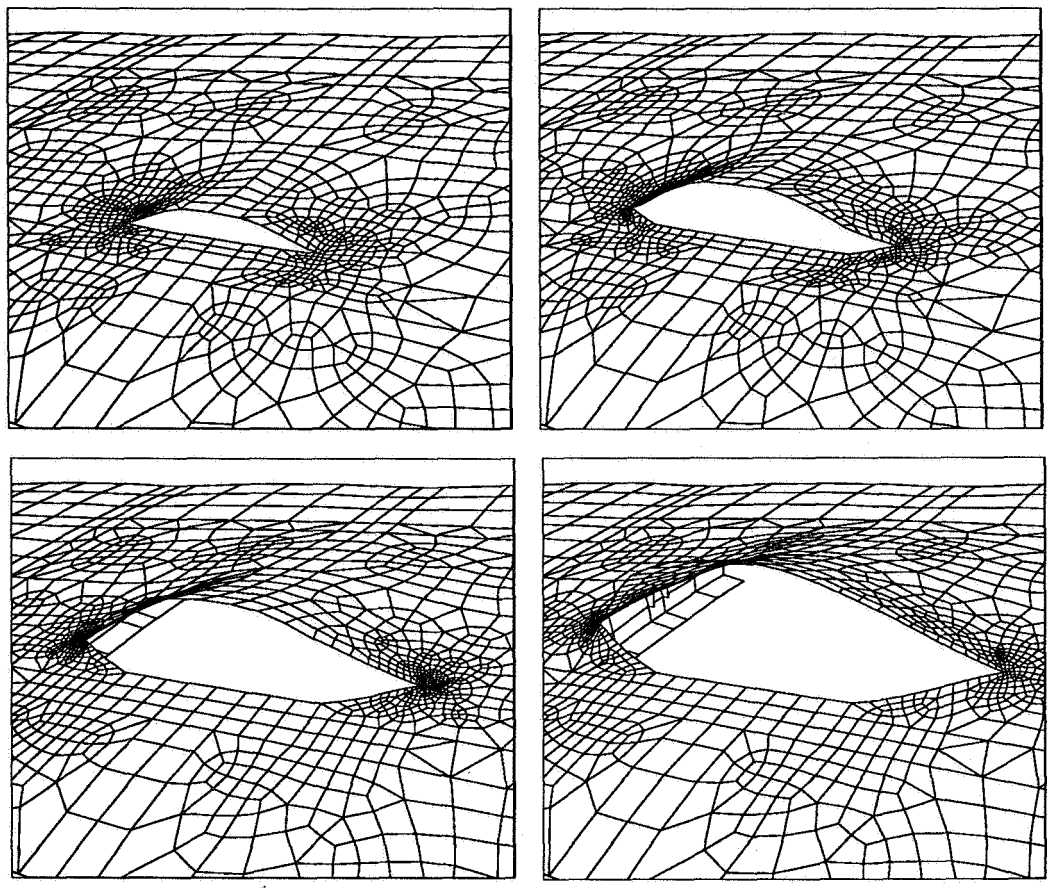

Figure 8: Deformed structure during crack growth for total crack lengths of 5, 7, 9, and 11 inches for the validation problem. Magnification factor for all images is five.

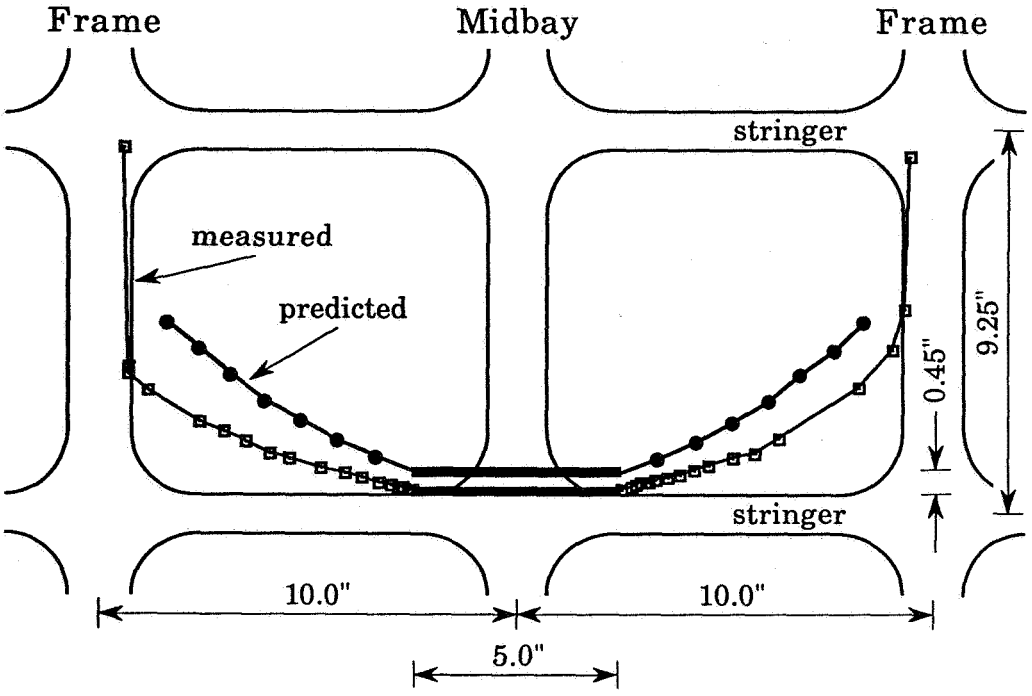

Figure 9: Comparison between computed and measured crack growth trajectories for the validation problem. The black circles and open boxes denote computed and measured crack tip locations, respectively.

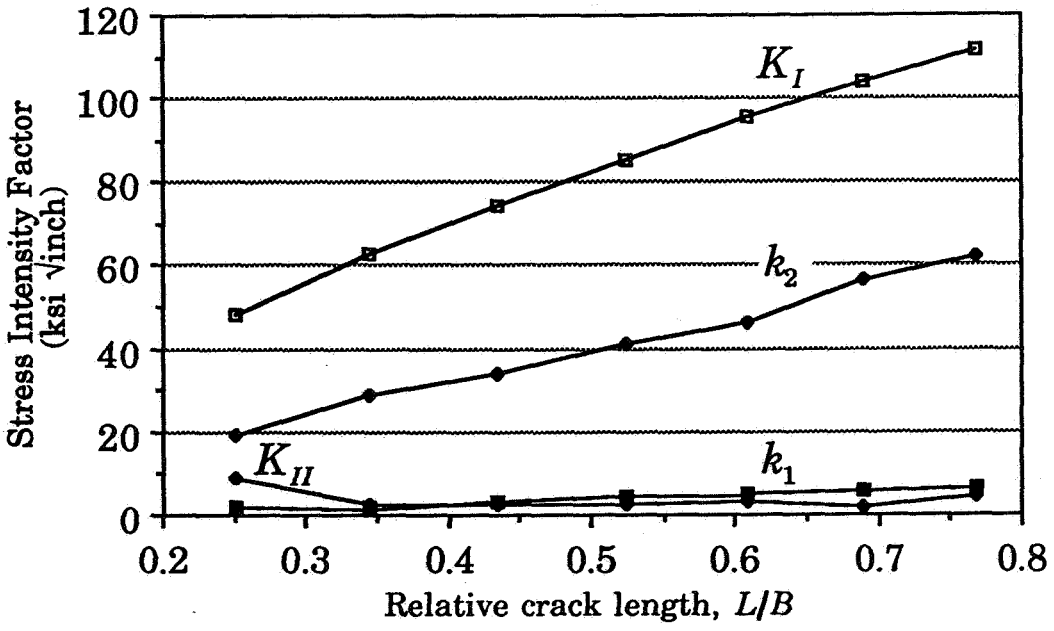

Figure 10: Computed stress intensity factors at right crack tip for the validation problem.

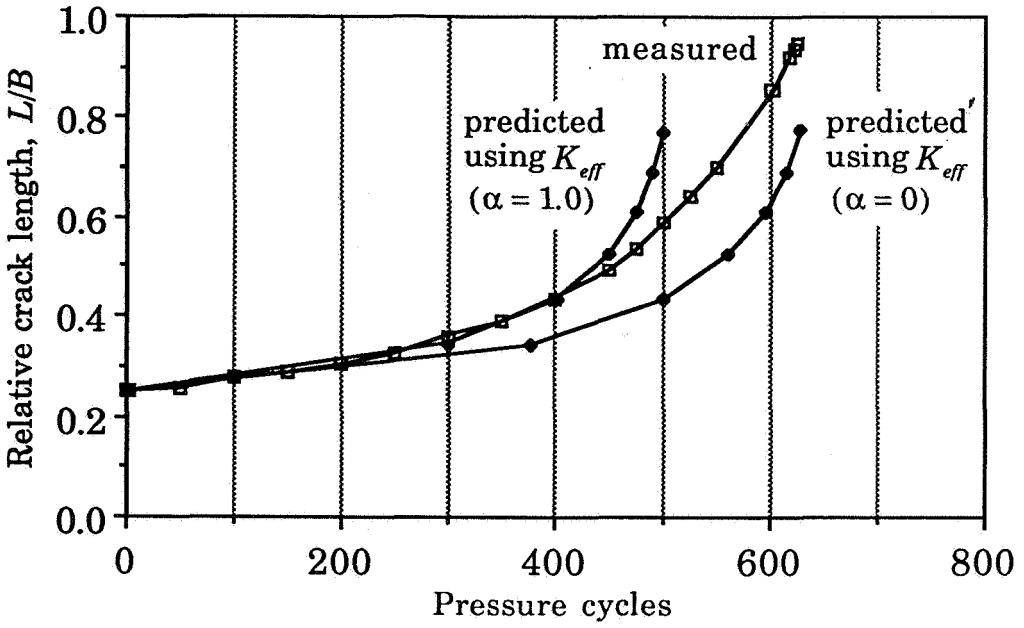

Figure 11: Comparison between predicted and measured fatigue life. The life prediction is made using the effective stress intensity factor of Eq. (6).

A NEW STOCHASTIC SYSTEMS APPROACH TO STRUCTURAL INTEGRITY

James W. Provan
University of Victoria
Victoria, BC, Canada

Khalil Farhangdoost
McGill University
Montreal, Quebec, Canada

SUMMARY

This paper develops improved stochastic models for the description of a large variety of fatigue crack growth phenomena that occur in components of considerable importance to the functionality and reliability of complex engineering structures. In essence, the models are based on the McGill-Markov and Closure-Lognormal stochastic processes. Not only do these models have the capability of predicting the statistical dispersion of crack growth rates, they also, by incorporating the concept of crack closure, have the capability of transferring stochastic crack growth properties measured under ideal laboratory conditions to situations of industrial significance, such as those occurring under adverse loading and/or environmental conditions. The primary data required in order to be in a position to estimate the pertinent parameters of these stochastic models are obtained from a statistically significant number of replicate tests. In this paper, both the theory and the experimental technique are illustrated using a Ti-6Al-4V alloy. Finally, important structural integrity, reliability, availability and maintainability concepts are developed and illustrated.

INTRODUCTION

While most industrial failures involve fatigue, the assessment of the fatigue reliability of structural components being subjected to a variety of dynamic loading situations is still one of the most difficult engineering problems that remains to be solved. This is because material property degradation processes due to fatigue are extremely sensitive to material, component geometry, loading, and environmental conditions. To control the failure of components and systems, within specified performance limits and for a specified length of time, the concepts of Reliability, Availability and Maintainability (RAM) have been brought into play.

The study of structural reliability and the scatter in mechanical failure data was placed on a sound footing by Freudenthal (ref. 1) and Weibull (ref. 2). Lately, however, more research has been devoted to the derivation of reliability models based on probabilistic interpretations of the fatigue process. Thus, Birnbaum and Saunders (ref. 3) proposed a life distribution to characterize fatigue crack extension failures and Freudenthal and Shinozuka (ref. 4) presented a similar law substantiated by several sets of fatigue data. Subsequently, Payne (ref. 5) introduced a statistical reliability model for assessing the fatigue strength of aircraft structures by evaluating the random variability in crack propagation rates and residual strengths of crack structures at any stage during their evolution. Provan *et al.* (refs. 6, 7, 8) have derived and experimentally investigated new reliability distributions based on probabilistic micromechanic concepts applied to the fatigue failure of polycrystalline metals. Bogdanoff and Kozin (ref. 9) and Yang *et al.* (ref. 10) have investigated the stochastic fatigue crack growth process based on Markov and lognormal processes, respectively, a view that is shared in the current investigation.

Turning attention to the fatigue process itself, Elber (ref. 11) observed that fatigue-crack surfaces contact each other even during tension-tension cyclic loading. This simple observation of the crack-closure phenomenon immediately explained many crack growth characteristics that had been troubling researchers during the '60s. Since then, several closure mechanisms have been identified, among them, "plasticity" induced closure. These new closure mechanisms and the influence of the plastic wake on the local crack-tip strain field have greatly advanced an understanding of the fatigue-crack growth and fracture behaviour of metallic materials, under, for example, variable amplitude loading. Furthermore, the occurrence of crack-closure significantly affects the local crack driving force stress-intensity factor and plays a crucial role in quantifying the fatigue crack growth or arrest characteristics of the material in question. Thus, while the qualitative interpretation of the closure phenomena justifies a large number of fatigue crack anomalies, a quantitative knowledge of the crack closure stress intensity level is required to correlate fatigue crack growth data.

Most fatigue design requirements based on damage tolerance concepts assume the existence of flaws in the component either from the initial delivery or from some later stage during the service life. To assure a high level of reliability and before these flaws grow to critical lengths, it is necessary to either repair or replace the component. Thus, in-service inspections are required to detect various sizes and shapes of cracks and other defects. For a reliability analysis of an in-service airframe, for example, fatigue, environment and accidental events are three sources of damage that must be taken into consideration.

Hence, the importance of fatigue; the unifying nature attributed to closure; the need for a stochastic process interpretation of the whole fatigue process, and the need for reliability analyses are clear. While crack closure and stochastic processes are briefly detailed, this paper primarily concerns an investigation of new methods of assessing the fatigue reliability of structures based upon probabilistic approaches. It summarizes: i) the experimental determination of a statistically significant number of crack growth rates for a Ti-6Al-4V titanium alloy; ii) the determination of the Closure-Lognormal, c, m, $\tilde{\sigma}^2$, ξ parameters for Ti-6Al-4V; iii) the simulation of the crack propagation based upon these Closure-Lognormal parameters; iv) the determination of the McGill-Markov λ and κ parameters for the Ti-6Al-4V alloy in question; and v) the RAM assessment of Ti-4Al-6V.

Fatigue Crack Closure

An understanding of crack closure under cyclic tension was developed by Elber (ref. 11) who showed that the occurrence of premature contact between the opposing crack faces during unloading was due to the residual plastic stretch in the crack wake. During the loading portion of a cycle, the elastic constraints acting on the residual material in the wake of an advancing crack, keep the crack tip closed until these constraints are overcome by the externally applied load. The stress intensity factor associated with a fully opened crack, K_{op}, based upon the crack opening load, P_{op}, is necessary for the quantitative knowledge of the effective stress intensity range factor, ΔK_{eff}, which is used in life prediction through $K_{eff} = K_{\max} - K_{op}$ and the well known Paris-Erdogan relation $da / dN = c\Delta K_{eff}{}^{m}$.

ΔK_{eff} is an appropriate field parameter for correlating crack growth under constant-amplitude loading conditions to the influence of a large number of variables, such as an actual load spectrum, load ratio and/or a specific environment, that are known to affect the rate at which cracks grow in any practical situation. As an example, fatigue crack closure effects at different load ratios have been extensively investigated by Ritchie *et al.* (ref. 12), who initially showed a significant difference in the $da / dN - \Delta K$ behaviour due to different load ratios over a wide range of ΔKs, but, when plotted as a function of ΔK_{eff}, were able to eliminate this discrepancy and consolidate the curves into a narrow band.

Stochastic Processes

Stochastic processes deal with statements that can be made concerning a random phenomenon, and a random phenomenon has the property that under a particular set of conditions its observation leads to a multitude of possible outcomes in such a way that statistical regularity can be observed.

The Lognormal Process. The aim of the present study of lognormal process is to consider fatigue crack growth rates as random phenomena. A random variable x has a lognormal distribution if its probability density function is given by:

$$f(x) = \frac{1}{\tilde{\sigma}\sqrt{2\pi}x} \exp\{-\frac{(\ln x - \mu)^2}{2\tilde{\sigma}^2}\} \tag{1}$$

where μ and $\tilde{\sigma}^2$ and the mean and variance of the associated normal distribution.

The validity of lognormal crack growth rate models, including the lognormal random process, white noise, and random variable models along with the general lognormal random process model, have been investigated using extensive fatigue crack growth data gathered from fastener hole specimens by Yang *et al.* (ref. 10, 13, 14, 15). In order to account for the random nature of crack growth rate, use was made of the following model for constant amplitude loading situations:

$$\frac{da}{dN} = X(t)F(\Delta K, K_{max}, R, S, a), \tag{2}$$

where a(t) is the random crack size, and X(t) is a non-negative random process. Based on extensive experimental data, Yang proposed X(t) as a non-negative, stationary lognormal random process. The lognormal random process, X(t), is defined by the it's logarithm being a normal random process, i.e., Z(t) is a normal random process, where Z(t) = log X(t). The stationary normal random process Z(t) is defined by the mean value μ_z and the autocorrelation function $R_{zz}(\tau)$ given by:

$$R_{zz}(\tau) = E[Z(t)Z(t+\tau)], \tag{3}$$

where E[ ] indicates the expected value.

The mean value, μ_z, of Z(t) is equal to the logarithm of the median value of X(t). Since the median value of X(t) is equal to unity, the mean value μ_z is equal to zero. Hence Z(t) is a stationary normal random process with zero mean, and is completely defined by the autocorrelation function given in eqn(3).

Yang, *et al.* (ref. 10) chose the autocorrelation function to be an exponentially decaying function of time difference τ, as follows:

$$R_{zz}(\tau) = \tilde{\sigma}^2 \exp\{-\xi|\tau|\}, \tag{4}$$

where ξ is the correlation parameter determined from a comparison with experimental test results. This correlation parameter plays a significant role in describing the statistical fatigue crack growth rate and propagation behaviour of materials.

The McGill-Markov Process. In order to further evaluate the stochastic characteristics of fatigue crack propagation processes, it is necessary to consider the concepts behind the McGill-Markov process. Any Markov process is based upon the assumption that the prediction of the process that is going to occur is influenced only by the properties of the current state which the process is in and not by the history that led to its present state. According to Provan and Rodriguez (ref. 16) and the nature of fatigue crack growth, the crack propagation process is a discrete-state continuous-parameter and nonhomogeneous Markov process since the transition probability density is a variable which depends only on the time difference τ. Furthermore, the crack size variable, a(t), can only be measured to within equipment and operator limitations. By considering the observable zones, i, the crack size may be written as:

$$a_i < a(t) < a_i + \Delta a_i, \tag{5}$$

where i is the state number and Δa_i is the width of a state. A discrete-state and continuous-parameter stochastic process, $\{a(t), t \in \tau\}$, may be described by a one step transition probability of the form:

$$P\{a(t) = j | a(\tau) = i\} = p_{ij}(\tau, t), \qquad 0 \le \tau \le t, \tag{6}$$

where i and j are integer states and τ and t are times. This probability is called the transition probability and is defined as the probability of a transition from state i to state j during the time interval τ to t.

In order to solve the Kolmogorov differential equations which govern p_{ij}, an infinitesimal transition scheme must be specified. After a review of the existing intensity functions, Provan and Rodriquez (ref. 16) developed a new intensity which gives a good description of the time evolution of material property degradation processes. The intensity functions of the McGill-Markov process are:

$$q_j(t) = \lambda_j = \frac{\lambda j(1+\lambda t)}{1+\lambda t^{\kappa}} \qquad for \qquad j = 1,2,..., \tag{7}$$

$$q_{ij}(t) = \begin{cases} \lambda_{j-i} = \dfrac{\lambda(j-1)(1+\lambda t)}{1+\lambda t^{\kappa}} & for \quad i = j-1, \\ 0 & otherwise. \end{cases} \tag{8}$$

λ and κ are empirical system parameters which are determined by a fit to experimental data. They are positive empirical system parameters that describe all of the various effects that influence the process, such as, temperature, material properties, experimental error, etc. When these parameters are found, the system may be modeled. If the system is changed, new system parameters must be found. These intensity functions are then used in the Kolmogorov forward differential equation, which becomes:

$$\frac{\partial p_{ij}(\tau,t)}{\partial t} = -\lambda_j p_{ij}(\tau,t) + \lambda_{j-1} p_{i,j-1}(\tau,t). \tag{9}$$

Hence, by solving this Kolmogorov equation governing a linear nonhomogeneous birth process, the transition probabilities $p_{ij}(\tau,t)$ are determined.

Finally, in order to determine the entire history of the crack propagation distribution, the total probability may be continuously monitored via the fundamental absolute probability relation:

$$P_j(t) = \sum_{i=1}^{j} p_{ij}(\tau,t) P_i(\tau), \tag{10}$$

where $P_j(t)$ is the probability of being in the j-th (later) state at time t; $P_i(\tau)$ is the probability of being in the i-th (earlier) state at time τ; and $p_{ij}(\tau,t)$ are the transition probabilities of a Markov process. Hence, for any McGill-Markov process, it is necessary to specify the initial state and the transition probabilities in terms of λ and κ in order to describe the evolution of the entire process.

Reliability Analyses

One of the main objectives of this paper is to introduce reliability maintenance and inspection/correction procedures via the McGill-Markov interpretation of material property degradation. Inspection/correction failure control systems play a significant role in a reliable repair policy which adheres to well scheduled inspection programs. Reliability is defined as the probability of satisfactory performance of a component for a specified period in a specified environment. Hence, the reliability can be found if the critical crack size is known; it is the probability that the crack does not exceed this critical size. This quantity can be obtained by summing up the probability of a crack being any sub-critical size, i.e.:

$$R(t) = \sum_{j=0}^{j=N_f} P_j(t), \tag{11}$$

where N_f is the identity of the state corresponding to the critical crack size.

Two specific uses of McGill-Markov model are as follows: the first use is for the prediction of repair times in order to maintain a certain level of reliability, and the second is the determination of the optimum time for an inspection/correction procedure.

Reliability Maintenance - Inspection/Correction Process. The operator of a structure will often decide upon a desired level of reliability. Once this level has been determined, perhaps by company policy, standard industry practices or other means, it becomes necessary to determine when to schedule the maintenance procedures that correspond to the desired level of reliability. This may be accomplished by employing the McGill-Markov model to predict when the probability of failure will reach the desired limit and then calling for an inspection/correction procedure. Briefly, inspection/correction processes are summarized as: stopping the degradation process; locating components that pose a risk to structural integrity; and carrying out the necessary maintenance procedure.

Analytically, as a result of the removal and replacement of some components, there are two distinct populations referred to as Population I, which consists of the remaining components from the initial group, and Population II, which is the group of replacement components. For an inspection/correction at time $T_{inspect}$, the fatigue process continues for Population I while for Population II it starts at time T=0 and ends at time $T = T_{final} - T_{inspect}$. As long as the fatigue loading situation remains the same, the system parameters λ and κ can be used for populations, I, II,... Following the development of Rodriguez and Provan (ref. 17), this total probability of failure is a combination of the probabilities of failure of Populations I and II. This process can easily be extended to include as many inspection/correction procedures as desired.

Reliability Maintenance - Inspection Optimization. Another useful form of reliability analysis which can be carried out with the McGill-Markov model is the optimization of the inspection time. As an example, suppose that it is desired to minimize the total probability of failure at a future time, and

furthermore there will be only one inspection/correction process in a given interval time. Hence, the question: "what is the optimum time for this procedure ?" is an appropriate one. In order to decrease the probability of failure an inspection/correction procedure will be carried out at some time. An inspection too early in the service life will, on the one hand, remove few components that may subsequently fail while a later inspection may be too late to remove components that will have failed. The optimum time for inspection will depend on several variables such as: critical crack size, repair size, inspection process, and the quality of replacement components. Hence, the McGill-Markov model, used in conjunction with a failure control methodology, can be a useful tool for obtaining valuable reliability information.

EXPERIMENTAL PROCEDURE AND BASIC RESULTS

Exerimental Procedure. A computer controlled, increasing stress intensity factor ΔK test method, according to the American Standard Test Method ASTM E647 (ref. 18), was applied to eighteen standard C(T) specimens manufactured from a forged Ti-6Al-4V jet engine, fan disk grade, titanium alloy. The main objectives of carrying out these experiments were to examine the stochastic properties of crack growth for Ti-6Al-4V, and then to analyze the results in an effort to establish the parameters associated with the Closure-Lognormal and McGill-Markov stochastic processes and in the reliability assessment of components manufactured from this titanium alloy.

The fatigue tests were carried out under the control of the in-house "FATIG" computer program based on a crack closure compliance method. For the compliance calculations, the CMOD measurement was determined using a mechanical clip gage with a maximum resolution of 0.00025 mm, while that of the load cell was 0.005 kN. The FATIG program utilizes three main loops and determines: i) the crack length based on load vs. CMOD data (compliance); ii) the ΔK based upon the ASTM E647 standard; and iii) the ΔK_{eff} based upon ΔK and the closure load. During each "data acquisition" block, the load vs. CMOD curve for 200 individual data points was obtained. The lower limit was a variable such that the nonlinearity was distinguished by FATIG as the closure load. A linear curve fit was made through the remaining points to obtain the normalized compliance, and the relationship between the compliance and crack length was determined by that proposed by Mirzaei and Provan (ref. 19), namely:

$$\frac{EBv}{P} = \frac{3(\alpha+1)(\alpha+2.3)}{\alpha^2-2\alpha+1} + 8(1+v)\alpha; \qquad \alpha = \frac{a}{W}. \tag{12}$$

In eqn(12), α is the normalized crack length, E = 117,000 MPa is the elastic modulus of Ti-Al-4V, v is the CMOD, B the specimen thickness, P the load and W the specimen width. From this information the ΔK_{eff} was determined from the expression given in the ASTM E674 standard, except that $\Delta P = P_{max} - P_{op}$, P_{op} being the closure load.

When a specific test was completed, the stored data was analyzed with the second in-house "FADA" program to obtain a da/dN vs. ΔK_{eff} curve using the incremental polynomial method with n=3 , i.e., 7 successive data points. The FADA program plotted the crack length, a, vs. the number of cycles, N, and the crack growth rate, da/dN vs. ΔK_{eff}.

Experimental Test Results For Ti-6Al-4V. Results were obtained from eighteen standard C(T), Ti-6Al-4V specimens prepared according to conventional procedures. The fatigue crack propagation for all eighteen specimens are shown in fig. 1(a), while the associated da/dN vs. ΔK_{eff} curves are presented in fig. 1(b). Examination of the data revealed a few surprising observations. The most unexpected observation was the change in the growth rate which occurred in almost every test, indicating that fatigue crack propagation is not a stable, smooth, well ordered process. A close observation of the fatigue crack growth rates show two transition points, namely, at $\Delta K_{eff} \cong 8-9 MPa$ and at $\Delta K_{eff} \cong 13-14 MPa$.

Hence, the fatigue crack growth process is highly complex, especially in the Paris-Ergodan regime and it is reasonable to have different Paris-Erdogan regimes correlated to these experimental results. However, from the viewpoint of reliability analyses the first part of the fatigue crack growth rate curve, i.e., prior to the first transition point, is more important than the second.

THE CLOSURE-LOGNORMAL CHARACTERISTICS OF Ti-6Al-4V.

As introduced above, a lognormal process is defined by the fact that its logarithm is a normal random process. Also, the general form of fatigue crack propagation laws indicates that the crack growth rate is a function of the stress intensity factor, maximum stress intensity factor, stress amplitude, load ratio, and so on. Some commonly used crack growth rate functions, such as the Paris-Erdogan model (ref. 20) are such that c and m are functions of the load condition and environment.

A comprehensive assessment of the closure phenomena necessitates the evaluation of the state of residual stress and strain in the neighbourhood of the crack tip and the extent of crack closure. Crack closure effects are most pronounced at low ΔK levels. This can be seen in fig. 2 which shows the results obtained from the eighteen specimens of Ti-6Al-4V tested as described above. Hence, P_{op} for Ti-6Al-4V as a function of crack length, a, is found by a polynomial curve fit to be as follows:

$$P_{op} = 2.90203 - 0140572a + 0.0021723a^2; \quad (kN;mm). \tag{13}$$

As detailed previously, the crack closure concept may be used to describe the influence of the actual load spectrum, load ratio and/or environmental parameters and, therefore, the quantitative knowledge of the crack closure stress intensity level is required to correlate fatigue crack growth rate data. Using the sense of "closure", in the form of the effective stress intensity range factor for fatigue crack propagation, the following equation, eqn(14), is adopted in such a manner that it is independent of component geometry, loading spectrum or load ratio, environment, etc. In this way, the entire description of the statistical scatter in fatigue crack growth data may be incorporated into the assessment of the reliability of any prospective component prior to its manufacture.

Hence, in order to account for the random nature of the crack growth rate, the following model is suggested:

$$\frac{da}{dt} = X(t)c(\Delta K_{eff})^m, \tag{14}$$

where a(t) is now the random crack size and X(t) is a non-negative random process. In this case, ΔK_{eff} is a function of crack length and closure effects, and X(t) is a lognormal random process. By taking the logarithm of both side of eqn(14), it follows that:

$$\log(\frac{da}{dt}) = \log X(t) + \log c + m\log(\Delta K_{eff}). \tag{15}$$

By substitution $\Psi = \log(\frac{da}{dt})$, $Z(t) = \log X(t)$, $C = \log c$, $\Gamma = \log(\Delta K_{eff})$, eqn(15) may be rearranged into the form:

$$\Psi = m\Gamma + C + Z(t). \tag{16}$$

Z(t) describes the inherent scatter of a specific material. These parameters, as well as the variance $\tilde{\sigma}^2$ and the autocorrelation parameter, ξ, are obtained from the Ti-6Al-4V test results of the crack growth rate vs. the effective stress intensity range in the logarithmic scale.

According to the stochastic model, eqn(14), and the sense of closure for fatigue crack propagation, four important Closure-Lognormal parameters, namely m, c $\tilde{\sigma}^2$ and ξ, may be interpreted as material properties. Table 1 shows these Closure-Lognormal parameters for Ti-6Al-4V. Hence, a complete specification of a material's stochastic fatigue crack growth characteristics are found from the Closure-Lognormal model. These parameters may be interpreted as material properties that are independent of component geometry, loading spectrum or load ratio, environment, etc. In this way, the entire description of the statistical scatter in actual test results or simulated fatigue crack growth data (see the next section), may be incorporated into the assessment of component reliability. Since, by using these parameters and the simulation procedure, a definitive reliability, availability and maintainability procedure may then be carried out using the associated McGill-Markov parameters, a complete specification of a material's stochastic crack growth characteristics based upon the Closure-Lognormal interpretation of scatter is of paramount importance to the assessment of crack growth rates in any practical situation.

SIMULATION OF CRACK PROPAGATION -- Ti-6Al-4V

In order to remove the limitation of a specific crack geometry, loading, or environment, etc., and to be in a position to use both the previous Closure-Lognormal and the following McGill-Markov procedures of describing the statistics associated with the fatigue crack growth process, a simulation procedure plays a crucial role in transferring information from data generated by a standardized Closure-Lognormal procedure to real crack propagation processes as they occur in actual components and under any of a large number of specified situations. The stationary Gaussian random process Z(t), may be simulated using the well-known Fast Fourier Transform (FFT) technique to simulate the two parameters, ξ, and $\tilde{\sigma}^2$.

As an example, the C(T) specimen geometry along with a knowledge of the P_{op} for the Ti-6Al-4V was used to generate the simulated fatigue crack growth characteristics of this material. The results of these analyses are shown in fig. 3, which clearly shows that the two sets of data, one experimentally obtained and the other simulated, superimpose on each other.

ΔK_{eff}, incorporating a quantitative knowledge of the crack opening stress level, now appears as an appropriate field parameter for correlating knowledge of the constant-amplitude crack rates to practical growth rate situations. Specifically, knowing in terms of m, c $\tilde{\sigma}^2$ and ξ, the crack growth rate as a function of ΔK_{eff} for a specific material, such as Ti-6Al-4V, then the influence of an actual load spectrum, load ratio and/or environment may be incorporated during the design stage into an estimate of the fatigue reliability of a specific component. In this way, the simulation process plays an important role in removing the dependency on actual experimental results obtained under specific loading and environmental conditions. Hence, the closure behaviour, either experimentally determined or predicted by a model, expressed in terms of the effective stress intensity factor range expressions found in handbooks and the Closure-Lognormal parameters, constitute the only information required for analysing any particular situation.

THE MCGILL-MARKOV PARAMETERS FOR Ti-6Al-4V

The major objective of this section is the determination of the McGill-Markov stochastic fatigue crack growth properties of Ti-6Al-4V. As was described in the introduction, the two constant parameters λ and κ in the intensity functions q_i and q_{ij}, defined in eqns(7) and (8), are related to the stochastic properties of the material system being investigated. Accordingly, the probability of the crack tip being in

state i is increased, state by state, as the process progresses. Essentially, failure means a situation that, in a finite time interval, there is a probability that the state goes past a prescribed limit, which causes a failure of the structure. Hence, the McGill-Markov system parameters control the system failure and play a significant role in both reliability assessment and in inspection/correction procedures. Applying the McGill-Markov model to the Ti-6Al-4V data is an appropriate way to illustrate the capabilities of this approach.

These parameters are determined by a fit to the experimental or simulated data. Several steps, however, must be taken before this iterative process is undertaken. The first step is the normalization of data to an initial crack length of a_0 at time t=0. This is done to eliminate the crack initiation stage. In the next step, the data is discritized into states of width Δa. Using the resulting λ and κ, the probability histograms at future times are generated and the mean and variance. The system parameters, are thus determined by an iterative process of fitting the model predictions to the simulated Ti-6Al-4V data. For this case, a state size of 0.4mm along with a failure state of $N_f = 40$ were chosen this was judged to be a sufficient number for the interval of time t=0 through t=2E+06 cycles. The values of λ and κ which give a good fit to the simulated (or, in this case the experimental) data are:

$$\lambda = 0.14 \quad , \quad \kappa = 0.98. \tag{17}$$

A comparison between the experimental, simulated and McGill-Markov model predictions, shown in fig. 4, shows that the whole concept of treating fatigue crack growth as stochastic processes is a flexible method of predicting crack propagation for industrially significant materials and situations. The fact that the λ and κ parameters are applicable in reliability prediction and inspection/correction procedure development, as detailed in the following section, again allude to the benefits of this approach.

RELIABILITY ANALYSIS OF Ti-6Al-4V

The combination of a failure control procedure with the McGill-Markov technique can be a very powerful tool for practical engineering reliability calculations. Two specific uses of the McGill-Markov approach are detailed. The first application is for the prediction of repair times in order to maintain a certain level of reliability, while the second is the determination of the optimum time for a single inspection/correction procedure. Before these are examined, however, a method that is central to both, the method of predicting reliability at a future time, is presented.

Reliability of Ti-6Al-4V. Reliability, as was discussed earlier, has been defined as the probability a component will perform satisfactorily for a specified period of time. For determining reliability, the first step is to use another in-house program, SOLVE, to generate probability histograms for crack sizes at given future times. The reliability can then be found if the critical crack size is known; it is the probability that the crack does not exceed this critical length. This is illustrated in fig. 5 as a function of time.

RAM for Ti-6Al-4V. By defining the replacement size (state), N_r, to be 25 and the desired reliability to be 0.9999, the total probability of failure for times 0.8E+06to 2.0E+06 cycles were obtained as illustrated in fig. 6(a). The optimum times for the inspection/correction procedures are thus: i) the first inspection time will be at 1.500E+06 cycles, ii) the second time at1.700E+06 and the third at 1.88E+06.

Furthermore, the results for a change in acceptable reliability level from 0.9999 to 0.9995 are presented in fig. 6(b). From a comparison with fig. 6(a), it is apparent that not only will the first maintenance procedure be carried out at a later time but that one fewer procedure will be necessary.

The effect of varying the repair size while maintaining the desired level of reliability at 0.9995 is illustrated in fig. 7. This figure shows how the inspection interval is affected by a change in repair size (state) from $N_r = 20$, through $N_r = 25$, to $N_r = 30$ prior to 2.0E+06 cycles. There are a total of two

inspection/corrections for $N_r = 20$, three for $N_r = 25$ and four for $N_r = 30$. These figures illustrate the type of information that can be obtained from this approach.

Inspection Optimization. Finally, in order to carry out an inspection optimization analysis, the design engineer must control such variables as failure state, N_f, repair size (state), N_r, and the desired level of reliability. By using $N_f = 40$ and $N_r = 30$, the solid line in fig. 8 is obtained. From this figure it is apparent that the optimum time for inspection/correction is at 1.700E+06 cycles and that the total probability of failure is decrease by 88% over the no inspection case. By changing repair policy, such that N_r is varied from 30 to 20, different curves, also shown in fig. 8, are obtained. In this way, it is shown that while the optimum inspection time is increased by increasing the repair crack size from 20 to 30, the overall reliability of system is reduced.

CONCLUDING REMARKS

The conversion of ΔK into ΔK_{eff} through the inclusion of closure effects plays a significant role in reliability analysis. By using ΔK_{eff}, it now becomes possible to transfer the stochastic properties of crack growth rates, measured under ideal laboratory conditions, to practical situations. Incorporating the sense of closure into both the fatigue crack growth rate description and the lognormal interpretation of the scatter has led to the development of the Closure-Lognormal model which describes the statistical nature of crack growth rates.

On the other hand, the McGill-Markov process, employing data generated by simulations of the information contained in the Closure-Lognormal interpretation of the basic material's fatigue crack growth characteristics, vary with respect to closure effects that describe the influence of variations in the loading, environment, crack geometry, etc. With the crack propagation characteristics being predictable, the reliability and inspection processes may then be evaluated.

REFERENCES

[1] Freudenthal. A. M.: Safety of Structures, *Trans. ASCE*, vol. 112, pp. 125 - 180, (1947).

[2] Weibull, W.: A Statistical Distribution of Wide Applicability, *Journal of Applied Mechanics*, vol. 18, pp. 293 - 297,(1951).

[3] Birnbaum, Z. W. and Saunders, S. C.: A New family of Life Distributions, and Estimation for a Family of Life Distributions with Applications to Fatigue, *Journal of Applied Probability*, vol. 6, pp. 319 - 347, (1969).

[4] Freudenthal, A. M. and Shinozuka, M.: Structural Safety under Conditions of Ultimate Load-Failure and Fatigue, *WADD Technical Report*, pp. 61 - 77, (1961).

[5] Payne, A. O.: A Reliability Approach to Fatigue for Structures, *Probabilistic Aspects of Fatigue*, ASTM STP 511, pp. 106 - 155, (1972).

[6] Provan, J. W.: Probabilistic Approaches to the Material-Related Reliability of Fracture-Sensitive Structures, *Probabilistic Fracture Mechanics and Reliability*, J.W. Provan (ed), Martinus Nijhoff, pp. 1 - 45, (1987).

[7] Provan, J. W. and Theriault, Y.: An Experimental Investigation of Fatigue Reliability Laws, *Defects, Fracture and Fatigue*, G. C. Sih and J. W. Provan (eds.), Martinus Nijhoff, (1983).

[8] Provan, J. W. and Bohn, S. R.: Stochastic Fatigue Crack Growth and the Reliability of Deteriorating Structures, *Fatigue 90*, H. Kitagawa, and T. Tanaka, Eds., vol. IV, pp. 2259 - 2264 (1990).

[9] Bogdanoff, J. L. and Kozin, F.: *Probabilistic Models of Cumulative Damage*, John Wiley & Sons, (1985).

[10] Yang, J. N., Hsi, W. H. and Manning, S. D.: Stochastic crack growth models for application to aircraft structures, *Probabilistic Fracture Mechanics and Reliability*, J. W. Provan (ed), Martinus Nijhoff, The Hague, pp. 171 - 212, (1987).

[11] Elber, W.: Fatigue Crack Closure Under Cyclic Tension, *Engineering Fracture Mechanics*, vol. 2, pp. 37 - 45, (1970).

[12] Ritchie, R. O., Yu, W., Holm, D. K., and Blom, A. F.: *Mechanics of Fatigue Crack Closure*, ASTM STP 982, J. C. Newman, Jr. and W. Elber, (eds), American Society for Testing and Materials, Philadelphia, pp. 300 - 316, (1988).

[13] Yang, J. N. and Manning, S. D.: Stochastic crack growth analysis methodologies for metallic structures, *Engineering Fracture Mechanics*, vol. 37, No. 5, pp. 1105 - 1124, (1990)

[14] Yang, J. N.: Simulation of Random Envelope Processes, *Journal of Sound and Vibration*, vol. 21, no. 1, pp. 73-85, (1972).

[15] Yang, J. N.: Statistical modeling of fatigue-crack growth in a nickel-base superalloy, *Engineering Fracture Mechanics*, vol. 18, no. 2, pp. 257-270, (1983).

[16] Provan, J. W. and Rodriguez III, E. S.: Part I: Development of a Markov Description of Pitting Corrosion, *Corrosion Science*, vol. 45, no. 3, pp 178 - 192, (1989).

[17] Rodriguez III, E. S. and Provan, J. W.: Part II: Development of a General Failure System for Estimating the Reliability of Deteriorating Structures, *Corrosion Science*, vol. 45, no. 3, pp 193 - 206, (1989).

[18] *Annual Book of ASTM Standards*, Section 3, Vol. 3.01, (1993).

[19] Mirzaei, M. and Provan, J.W.: A New Method for the Analysis and Assessment of fatigue Crack Closure. I: Modeling and II: Experimental Study, *Theoretical and Applied Fracture Mechanics*, vol 18, pp. 47 - 63, (1992).

[20] Paris, P. C., and Erdogan, F.: A Critical Analysis of Crack Propagation Laws, *J. Basic Engng., Trans. ASME, Series D*, vol 85, pp. 528 - 534, (1963).

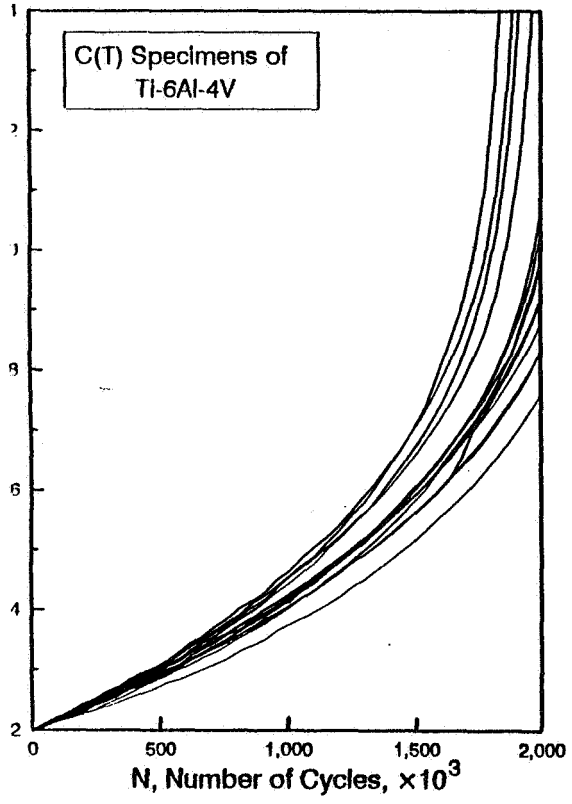

Figure 1(a): a vs N for Ti-6Al-4V

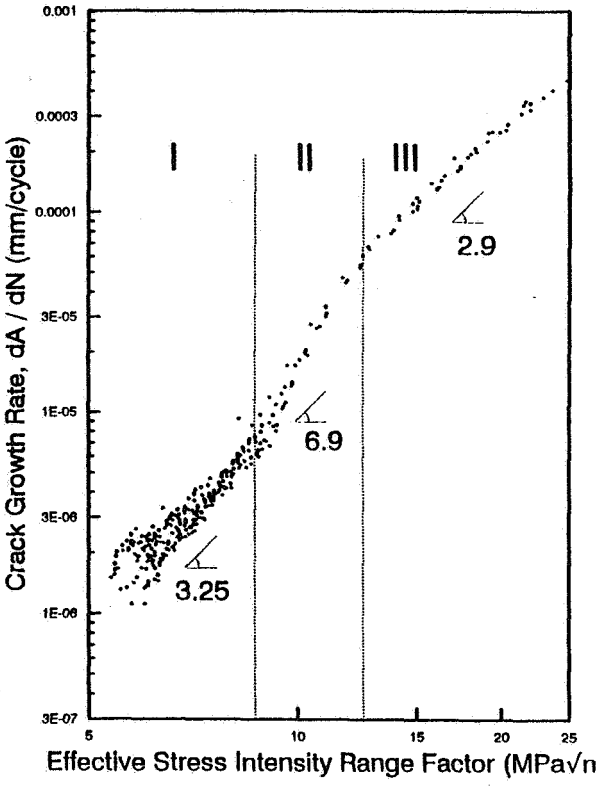

Figure 1(b): da/dN vs ΔK_{eff} for Ti-6Al-4V

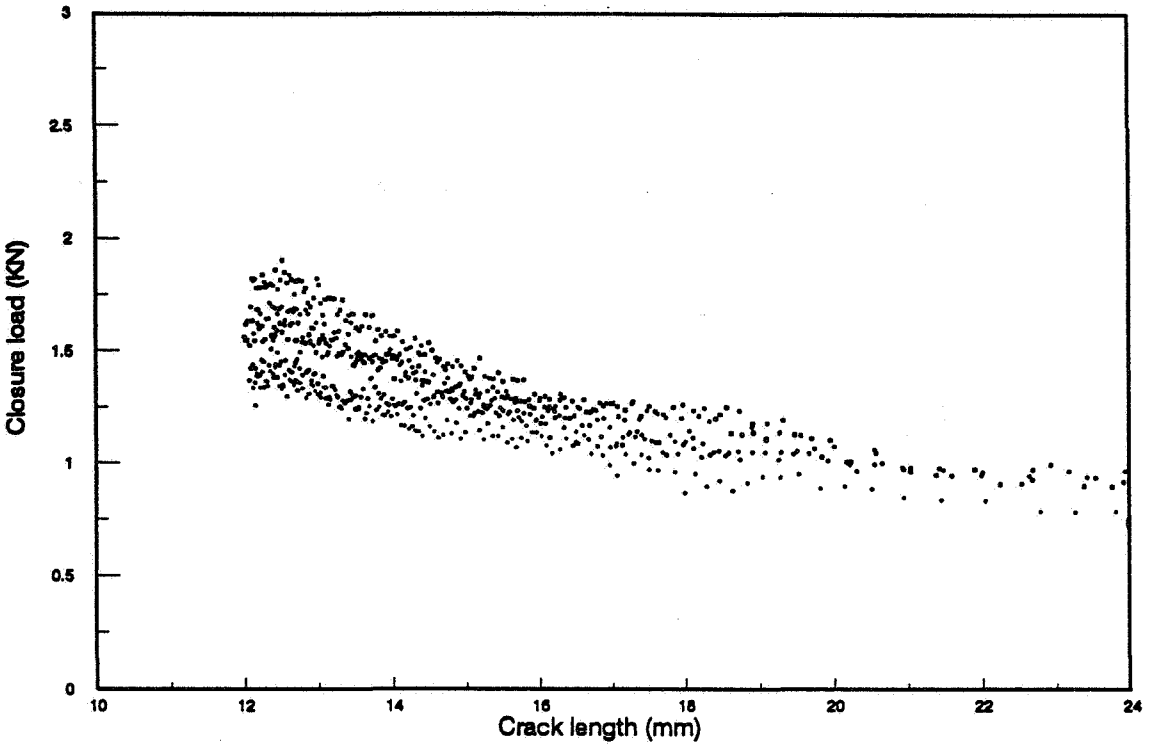

Figure 2: Closure Load vs Crack Length for Ti-6Al-4V

Table 1: Closure-Lognormal Parameters for Ti-6Al-4V

Closure-Lognormal parameters	σ^2 10^{-4}	ξ 10^{-4}	m	c 10^{-9}
Ti-6Al-4V	47	1.4	3.25	5.4

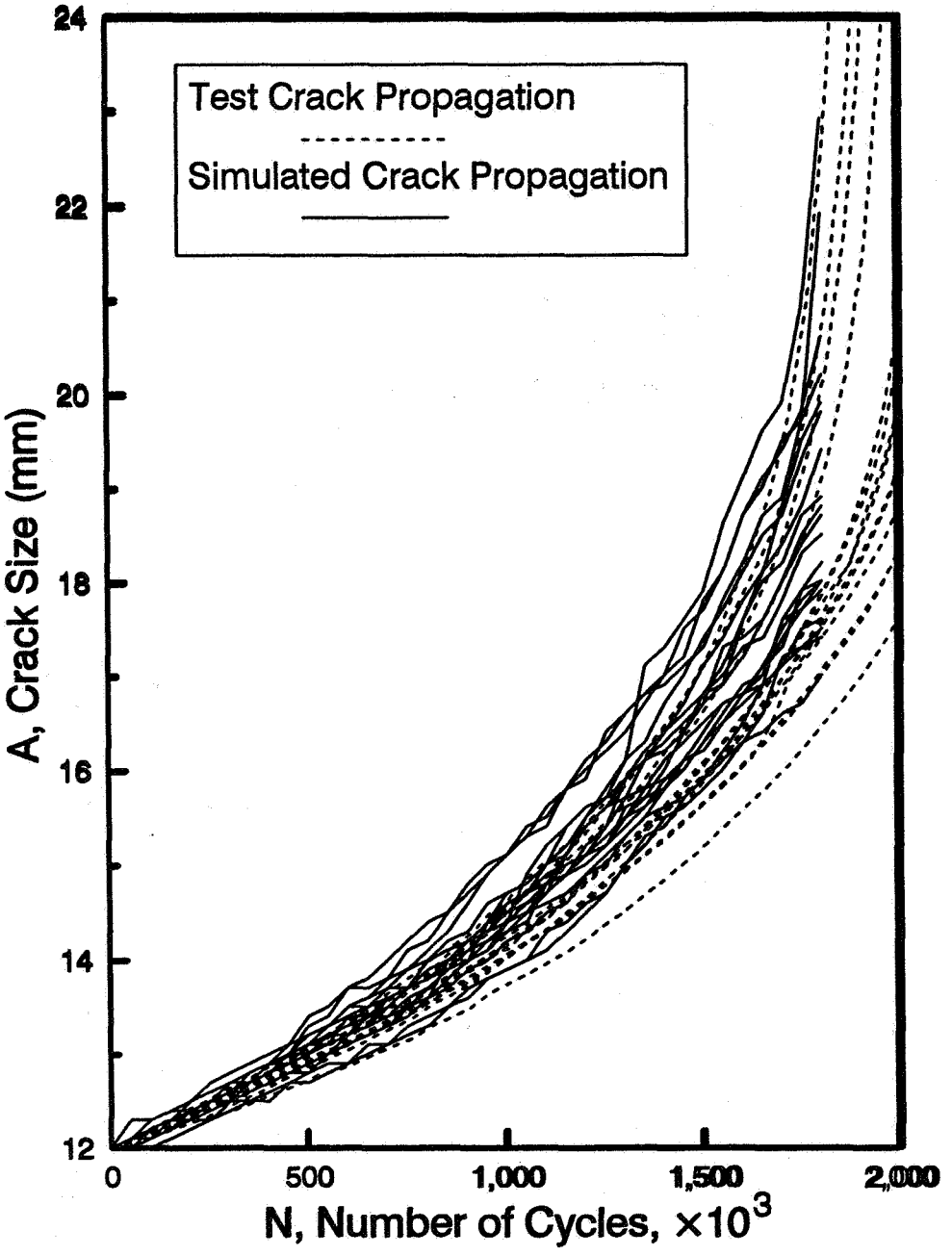

Figure 3: The Simulated and Experimental Crack Propagation of Ti-6Al-4V

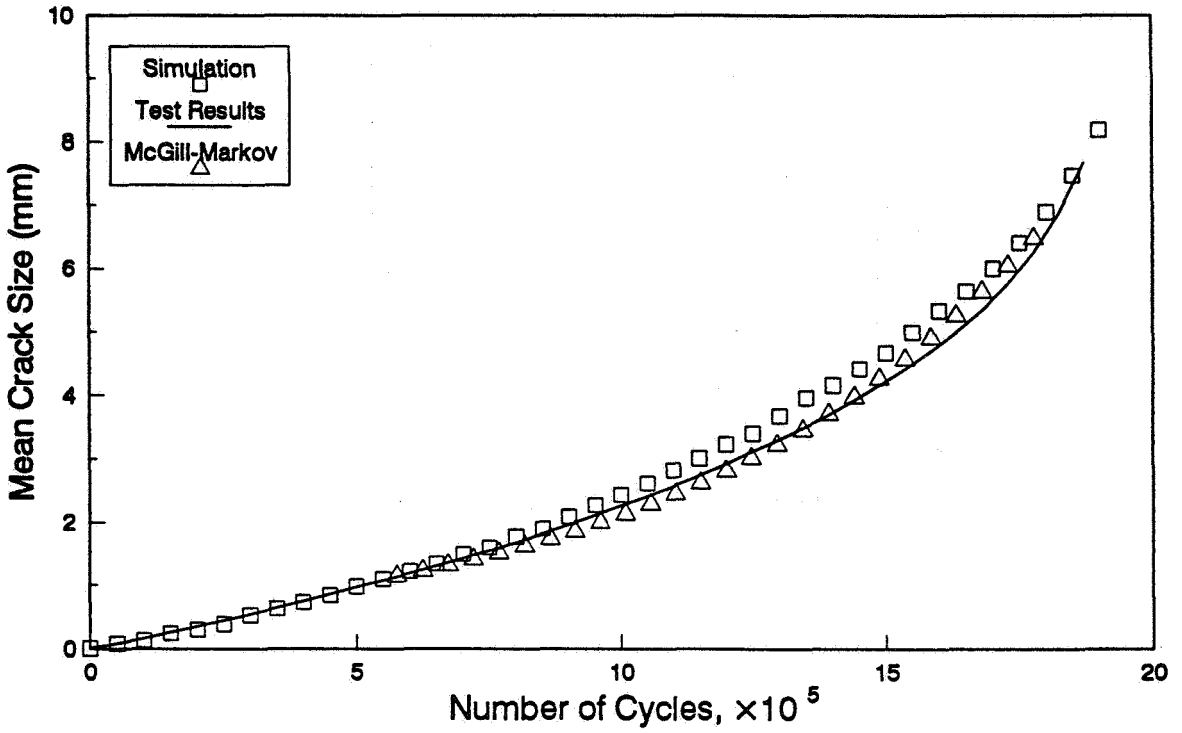

Figure 4(a): Ti-6Al-4V mean crack size, from McGill-Markov, simulated sample, and experimental test crack propagation.

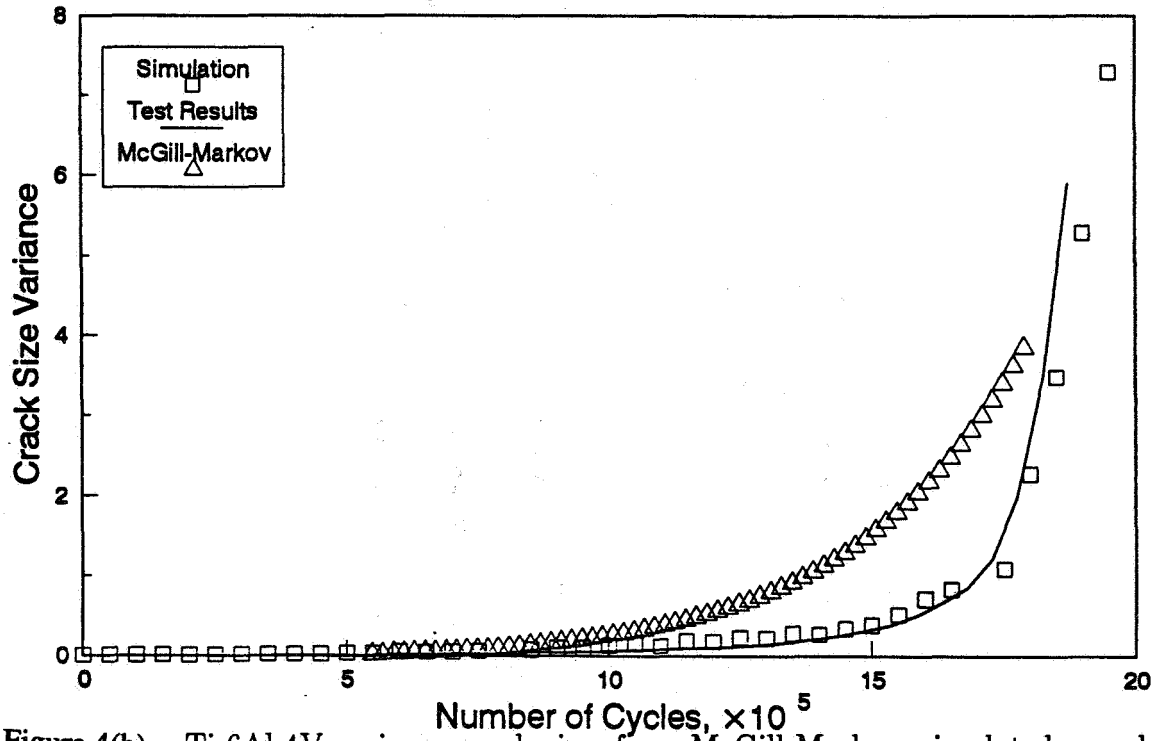

Figure 4(b): Ti-6Al-4V variance crack size, from McGill-Markov, simulated sample, and experimental test crack propagation.

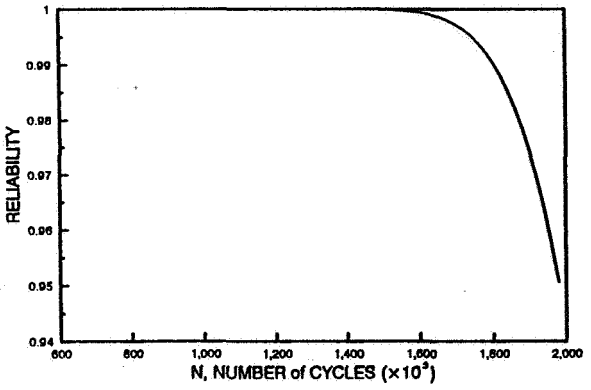

Figure 5: Reliability as a Function of Fatigue Cycles

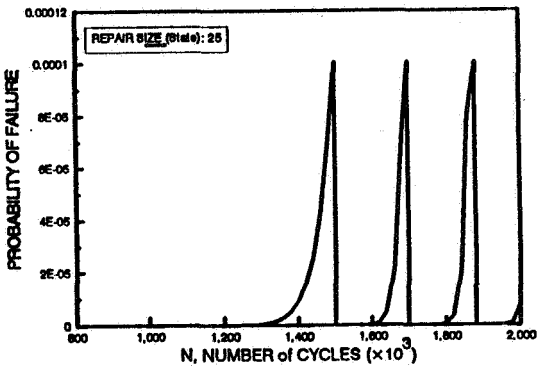

a) At 0.9999 maintenance reliability

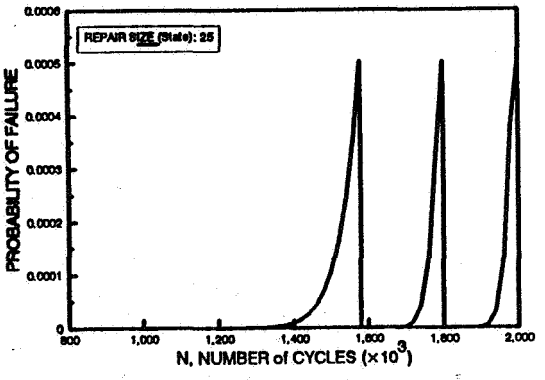

b) At 0.9995 maintenance reliability

Figure 6: Inspection/Correction Procedure for Ti-6Al-4V

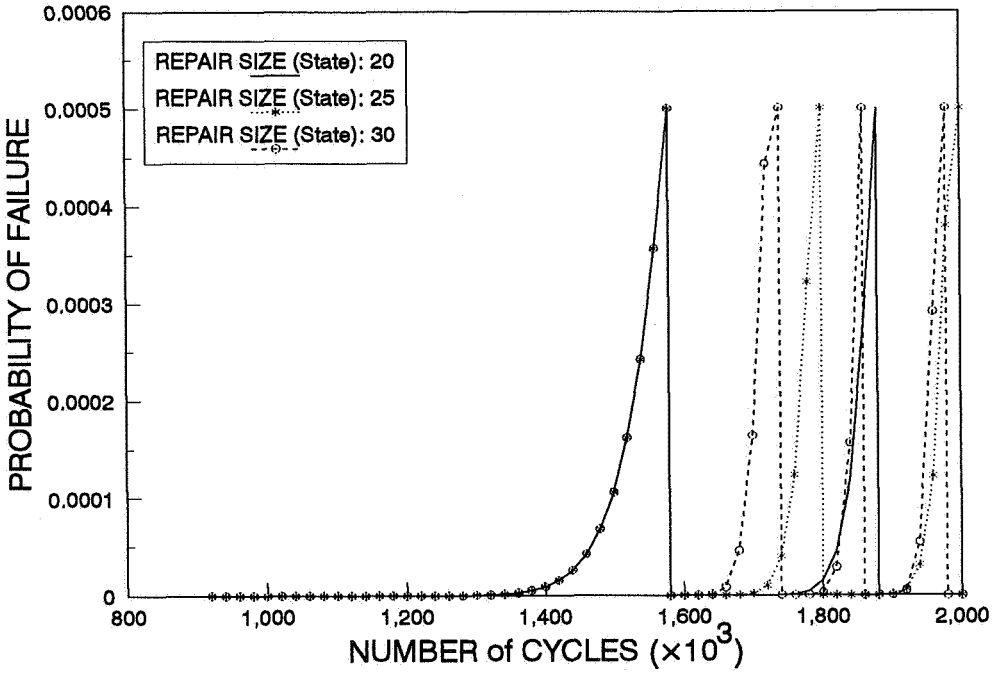

Figure 7: Inspection/Correction under different Repair Sizes

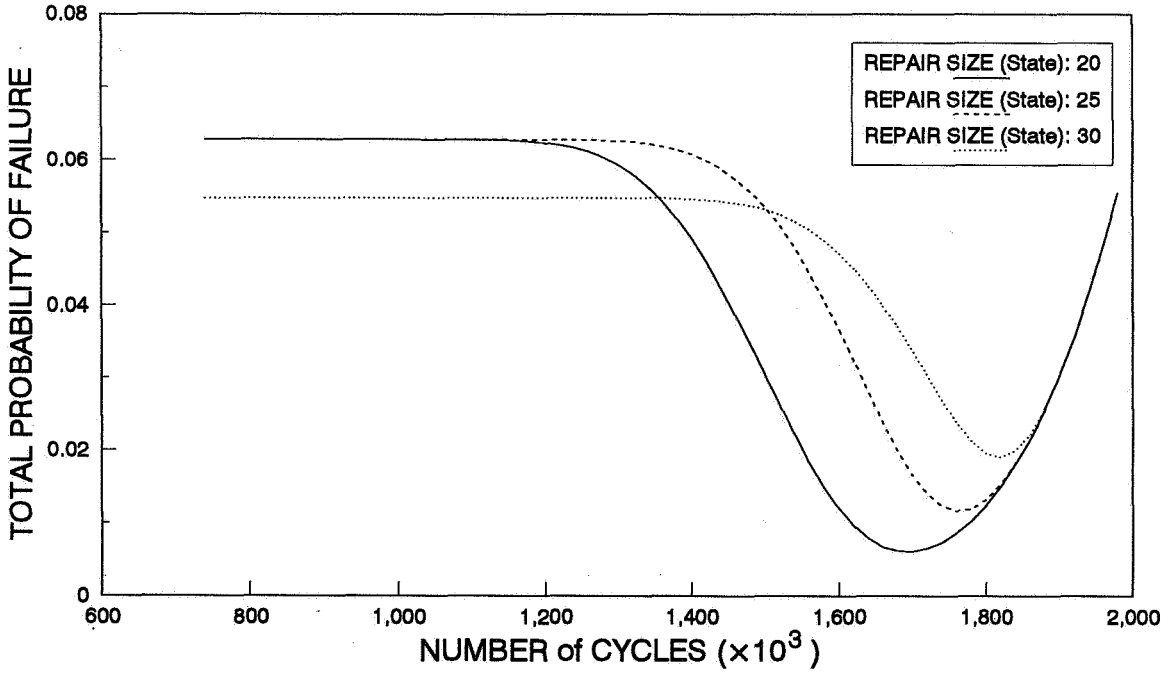

Figure 8: Inspection Optimization for Ti-Al-4V

FATIGUE AND DAMAGE TOLERANCE SCATTER MODELS

Veniamin L. Raikher
Central Aerohydrodynamics Institute (TsAGI)
Zhukovsky, Moscow region, Russia

SUMMARY

Effective Total Fatigue Life and Crack Growth Scatter Models are proposed. The first of them is based on the power form of the Wöhler curve, fatigue scatter dependence on mean life value, cycle stress ratio influence on fatigue scatter, and validated description of the mean stress influence on the mean fatigue life. The second uses in addition are fracture mechanics approach, assumption of initial damage existence, and Paris equation.

Simple formulae are derived for configurations of models. A preliminary identification of the parameters of the models is fulfilled on the basis of experimental data. Some new and important results for fatigue and crack growth scatter characteristics are obtained.

INTRODUCTION

The total fatigue life (from the initial condition to the failure) or the life between any two conditions of element damage (for example, from the moment when the damage is detectable to the moment when the damage becomes a critical one) are random values, and therefore they should not be described by mean values only and should be characterized by a complete probability distribution or, at least, by both mean values and standard deviations.

The scatter is usually so big that it cannot and should not be considered as an annoying thing that hinders the investigator to reveal the "pure" fatigue life characteristics (FLC). On the countrary, the scatter must be considered as a very important feature of the fatigue life which demands special and careful attention.

These considerations are especially referred to the structures of "high criticality" whose failure may lead to serious results. Indeed, the procedures of ensuring service safety should be based in this case on the "worst copy" characteristics which are much more or less (about 3 - 5 times or more) than the mean value. Such a large "scatter penalty" may turn the very hard activity for a 10-20 percent saving in mean fatigue life to an "absurd" work.

The conclusion is clear: a deep scientific study of scatter characteristics as a research target is needed. The reasons for scatter, the values of scatter, the influences on scatter; in other words, the mechanism of scatter forming should be known. On the basis of the

abovementioned knowledge the phenomenological models of high probability should be created.

THE FORMING OF FATIGUE LIFE MODELS.

Let us name as Life Parameters (LP) such factors "included" into the relations of accepted form which simply give the necessary FLCs (the crack growth included). As an example of LPs one can consider the factors of analytical presentations of endurance curves in power or any other form, the factors of Paris equation, etc.

Let us formulate assumptions which form the basis of models to be proposed:

(i)Between the LPs and FLCs "quasi-deterministic" relations exist

(ii)The forms of the relations are similar for any copy of the airframe structure. The scatter of FLCs is connected therefore only with LPs scatter.

Using these assumptions we can obtain the solution to a complicated problem through answers on two more simple questions:

-what are the forms of equations;

-what kind of "satisfaction" of these equations by random factors is suitable.

The assumptions are naturally not exact. Indeed, the same "input" should not give the same "output" because "parasitic scatter" connected with many influences has not been taken into account. But if the LPs totality is chosen sufficiently this additional scatter can be considered as a negligible one.

THE SCATTER MODEL OF TOTAL FATIGUE LIFE (TFL) FOR PULSING LOADING.

The TFL means the number of cycles up to failure (or to the fatigue damage condition close to failure).

A simple and effective model is proposed based on the vast amount of experimental data. The collection of data of that kind began in the late 40s. Many investigations of test results developed in the USSR during 1948-1969 were fulfilled in TsAGI (ref.1 and 2). The test amount is illustrated in table 1. The example of test results interpretation is shown on figure 1; mean values of the fatigue life logarithm are plotted on the X-axis, its standard deviation values - on the Y-axis. The generalized data (figure 2) emphasize a common rule: the minimum scatter takes place in the vicinity of 10^4 cycles mean life; the scatter increases both by increasing and by decreasing the life from this value.

The same conclusions are made by A.M.Stagg as a result of his detailed investigations. Let us cite some words from his paper (ref.3):

"(1)The coefficient of variation increases with an increase in the

life of a specimen above a value of $logN$ of about 4.

(2)The coefficient of variation increases with a decrease in the value of $logN$ below a value of 4. This trend is by no means as well supported as (1) above".

A significant experimental result was obtained in ref.4: a "quasi-interaction point" of fatigue curves exists (see figure 3 where both scales, X and Y, are logarithmic) for several aluminium alloy semi-finished products. This observation in addition to other experimental data mentioned above gives an important argument to the following scatter model formulation (ref. 5 and 6):

> Every copy of an airframe element has an individual fatigue curve. The form of the relation between fatigue life and the maximum stress value σ_o in case of the pulsing loading is kept similar to the form of the mean curve. For example, it can be a curve of power form
>
> $$N(\sigma_o/\sigma_o^*)^m=A^*, \qquad (1a)$$
>
> or be logarithmed as
>
> $$logN+mlog(\sigma_o/\sigma_o^*)=logA^*=C^*. \qquad (1b)$$
>
> The parameters m and A^* (or C^*) are random and are altered from one copy of an airframe to another.

The stress value σ_o^* which corresponds to the "neck" of the "fan" formed by individual curves is apparently the material feature (figure 4). It can be shown (ref.5) that the C^* value which is equal to the fatigue life logarithm at the σ_o^* level does not correlate with the parameter m; this parameter evidently characterized the slope angle of fatigue curves as straight lines in double logarithmic scale. As the correlation factor r_{mC^*} is equal to zero the main equations for the mean life logarithm value $\overline{logN}$ and for the standard deviation S_{logN} would be written as

$$\overline{logN} = \overline{C^*} - \bar{m}log(\sigma_o/\sigma_o^*) \qquad (2)$$

$$S_{logN} = \sqrt{d^2 + a^2(\overline{logN} - b)^2}, \qquad (3)$$

where $a^2=D_m/\bar{m}^2$, $b=\overline{C^*}$, $d^2=D_{C^*}$. A standard notation D for a dispersion is used.

Equation (3) describes (figure 5) the relation of the figure 2 type quite sufficiently. For example, the values $a\simeq0.2$, $b\simeq4.5$ and $d\simeq0.1$ are valid for D16 aluminium alloy sheets.

GENERALIZATION OF THE TFL SCATTER MODEL IN THE CASE OF THE POSITIVE MEAN VALUE OF THE LOAD CYCLE (MVLC).

The form of the type (1) equation for this case may be accepted on the basis of a well confirmed approach to the evaluation of MVLC influence on

mean TFL. The proposals of ref.7 and 8 known for many years and based on energetic considerations turned out to be valid.

There is a simple equation

$$\sigma_o^{eq} = \sigma_{max}(1 - R)^{\theta}, \qquad (4)$$

which one can use to obtain a maximum value of a pulsing cycle load that corresponds to the same mean fatigue life but for the loading with an any positive MVLC. The parameters of this equation have the following sense: σ_{max} and σ_{min} are the maximum and the minimum values of the cycle load; $R = \sigma_{min}/\sigma_{max}$ is the stress ratio which may alter (for arbitrary positive MVLC) within $-1 \le R \le +1$ range. The parameter $0 \le \theta \le 1$ is a new fatigue life parameter.

The generalized equations similar to (1a) and (1b) would be written as

$$N(\sigma_{max}/\sigma_o^*)^m(1-R)^{m\theta} = A^* \qquad (5a)$$

or, be logarithmed and inserted with a notation $\beta = m\theta$, as

$$\log N + m\log(\sigma_o/\sigma_o^*) + \beta\log(1-R) = \log A^* = C^*. \qquad (5b)$$

These equations are sufficiently valid (ref.9 and 10). An example of a straight regression line is given on figure 6 for coupon test data (aluminium alloy D16, sheet). The tests are fulfilled in a wide range of stress ratios. Each experimental point corresponds to mean life for the sample of at least five specimens (the total scope is 233 specimens). The mean values of the abovementioned parameters are: $m=4.66$; $\theta=0.575$; $\beta=2.68$.

The analysis shows that in the presence of a new fatigue life parameter β the form of equation (3) and the value of the parameter a must not be changed but the formulae for parameters b and d which are included in the equation (3) become more complicated and should be written as follows:

$$b = \bar{C}^* - \bar{\beta}(1 - r_{m\beta}(\gamma_\beta/\gamma_m))\log(1-R), \qquad (6)$$

$$d^2 = D_c^* + D_\beta(1 - r_{m\beta}^2)\log^2(1-R) - 2r_{\beta c}^* \sqrt{D_\beta D_c^*}\,\log(1-R). \qquad (7)$$

The equation (7) includes a dispersion D_β and paired correlation factors $r_{m\beta}$ and $r_{\beta c}^*$; about the values of these factors some reasonable assumptions should be proposed.

Indeed, if the parameter θ is not random and its value is the same for any copy of the airframe structure; i.e $\theta = \bar{\theta} = \text{const}$, the correlation factor $r_{\beta c}^* = 0$ and (it can be simply shown) $r_{m\beta} = 1$. In other words the parameters β and C^* are practically independent, but parameters m and β are statistically "tied".

If the parameter β is random, i.e. it has an individual value for any copy of the airframe structure, one may suppose that the situation inverses, i.e. $r_{\beta c}^* \to 1$, but $r_{m\beta} \to 0$. An additional argument for that assumption is the result of its application in the equations (6) and (7); the formulae become graceful and symmetric as

$$b=\bar{C}^* - \bar{\beta}\log(1-R), \tag{6a}$$

$$d=S_{C^*} - S_{\beta}\log(1-R); \tag{7a}$$

here S_{C^*} and S_{β} are corresponding standard deviations.

Thus the generalized TFL scatter model is characterized by three fatigue life parameters: m, $\bar{C}^*$ and β; any of them should be defined by two values - mean and standard deviation.

As an example the identification of this model was done (figure 7) on the basis of aluminium alloy 2024 coupon test results (ref.11). One should take into account that the fatigue life experimental standard deviations are only estimates. The characteristics of fatigue life parameters are the following: $\bar{m}=4$; $\bar{C}^*=4.5$, $\bar{\beta}=2$; $S_m=0.22$, $S_{C^*}=0.046$ and $S_{\beta}=0.07$.

It is interesting to note that mean values of the parameters are practically the same as the analogic values for the aluminium alloy D16, but the standard deviation of the parameter m (it may be considered as a material parameter) is bigger ($S_m=0.8$) for the D16 alloy. As for approximately two times difference in C^* scatter ($S_{C^*}=0.046$ for the 2024 alloy coupons instead of $S_{C^*}=0.1$ for D16 alloy generalized data) the explanation is very simple: the coupons for laboratory tests are made, as usual, more carefully to avoid the "annoying scatter".

THE FATIGUE CRACK GROWTH SCATTER MODEL

The present-day methods of service safety insurance for structures of "high criticality" use the Damage Tolerance Principle; therefore the problem of fatigue crack growth scatter should attract extreme attention.

For the case of cyclic pulsing loading one may use (in the course of a preliminary approach) a suitable linear fracture mechanics model (ref.12) taking into account that for large cracks (which can be detected by simple visual methods) the distortion effect of the stress intensity coefficient due to the stress concentrator existence will be negligible.

An additional assumption is adopted that the total fatigue life is exhausted by the crack growth only. The growth begins from a conditionally existent "initial crack" (considered as a quantitative symbol of generic initial state); the value of its length l_{ini} may be obtained by an extrapolation procedure from real crack length's range.

Using the Paris equation one may obtain a very simple formula for the relation "crack length l - fatigue life N" as

$$l = l_{ini} / (1 - N / N_{asy})^{1/q} \tag{8}$$

where N_{asy} is the abscissa of the vertical asymptote (figure 8); n is the

power factor of the Paris equation; $q=(n-2)/2$.

An important formula may be derived as

$$N_{asy}(\sigma_o/\sigma_o^*)^n = \tilde{N}^*_{asy}\left[l_{ini}/\bar{l}_{ini}\right]^{1/q}, \qquad (9)$$

which expresses a random value N_{asy} through the individual (random and statistically independent) fatigue life parameters n, l_{ini} and the parameter $\tilde{N}^*_{asy}$ defined as a parameter N_{asy} for $l_{ini}=\bar{l}_{ini}$ and for stress σ_o which is equal to σ_o^* stress in the individual fatigue curves "fan neck". The value $\bar{l}_{ini}$ is the mean value of the "initial flaw".

If the value N_{asy} may be approximately considered as the total fatigue life, the similarity of (9) and (1a) equations is evident; the conclusion is that the fatigue curve parameter m and the Paris equation parameter n should be close to one another.

It is followed from equations (8) and (9) that the logarithm of the fatigue life up to any state which is characterized by a crack length $l>l_{ini}$ is defined as

$$\log N(l)=a^*-qb_{ini}-n\log(\sigma_o/\sigma_o^*)+\log[1-10^{qb_{ini}}(\bar{l}_{ini}/l)^q], \qquad (10)$$

where

$$a^*=\log\tilde{N}^*_{asy}; \qquad b_{ini}=\log(l_{ini}/\bar{l}_{ini}). \qquad (11)$$

The crack growth duration ΔN in the crack detectable range may be derived by the eqauation (10) as $\Delta N = N_{asy} - N(l_{det})$ where l_{det} is the crack length which can be reliably detected by using check methods.

On the basis of the proposed model an important result is obtained: the correlation factor between ΔN and N_{asy} is not a constant value but it depends on loading conditions and other essential parameters. It can vary throughout the whole interval of its existence ($-1\le r\le 1$). In particular, if

-load level is high;

-the scatter characteristics of the initial "flaws" dimensions are low (i.e. the manufacturing process is highly stable);

-the mean value of the ratio $\Delta N / N_{asy}$ is large (i.e. the inspection methods allow technicians to detect the fatigue cracks of short lengths),

then ΔN and N_{asy} can correlate positively and strongly. These conditions usually take place in the laboratory sample tests.

However, the practical use of the Damage Tolerance Principle on full size airframes shows an opposite situation: the typical load levels in service are low, the manufacturing processes are ordinary, and the most often used flaw detection method is the visual inspection that allows inspectors to detect large cracks only. Under these conditions, the correlation coefficient can reduce to zero, and even turn out to be notably negative.

The analysis shows that a close connection exists between the relation of the crack growth duration scatter to the fatigue life scatter, on the one hand, and the relation of corresponding mean values, on the other hand, i.e. between $S_{log\Delta N} / S_{logN_{asy}}$ and $\overline{N}_{asy} / \overline{\Delta N}$.

It is very important from a practical point of view that the connection is approximately the same independently to the "initial flaw" scatter. An example is given (see figure 9) for two typical values [d=0.1 and d=0.15; see equation (3)] of minimum fatigue life scatter in the "fan neck" and for typical probabilistic characteristics of fatigue life parameters.

CONCLUSIONS

Simple and effective models of total fatigue life and crack growth scatter are proposed. Preliminary results are obtained which permit consideration of the proposals as acceptable. The identification of these models on the basis of experimental data will give much possibility for

- -revealing, investigating and explaning the causes of scatter;
- -predicting the scatter characteristics for materials and structures;
- -obtaining generalized scatter characteristics for reliable standardization;
- -forming effective approaches to the scatter "bearing process" control in order to minimize its value.

REFERENCES

1.Selikhov A.F.; and Senik V.Ya.: Scatter of fatigue life characteristics of materials and structures. "Structural integrity of airframes", Kiev Institute of Engineers of Civil Aviation, Kiev, 1971, (in Russian).

2.Selikhov A.F.; and Chizhov V.M.: Probability Methods in Airframe Strength Calculations, Moscow, 1987, (in Russian).

3.Stagg A.M.: An Investigation of the Scatter in Constant Amplitude Fatigue Test Results of Aluminium Alloys 2024 and 7075, ARC CP 1093, 1970.

4.Selikhov A.F.; and Ushakov I.E.: About one special feature in fatigue characteristics of aluminium alloys, TsAGI Scientific Notes (Uchenyye Zapiski TsAGI), v.XI, No.1, Moscow, 1980, (in Russian).

5.Raikher V.L.: About some consequences from two-parametric fatigue scatter model, TsAGI Scientific Notes (Uchenyye Zapiski TsAGI), v.XIII, N1, Moscow, 1982, (in Russian).

6.Raikher V.L.; and Selikhov A.F.: Stochastic models for analyzing fatigue strength on the basis of individual S-N curves. "Mechanics and the scientific and technical progress", v.4, Nauka, Moscow, 1988, (in Russian).

7.Oding I.A.: Allowable stresses for machine building and cyclic strength of metals, Moscow, 1947, (in Russian).

8.Shiratory E.; and Obataya I.: Effect of Mean Stress on the Low-mean Fatigue Strength. Stress Amplitude-Mean Stress Relation for a Given Life. Bull. ISME, 12, N54, 1969.

9.Raikher V.L.; Bogdanov B.F.; and Ushakov I.E.: To the methodics of endurance diagrams plotting, Factory Laboratorium (Zavodskaya laboratoriya) No.4, 1978, (in Russian).

10.Ushakov I.E.: Some generalizations of endurance plots, TsAGI Papers No.2033, 1980, (in Russian).

11.Jacoby G.H.; and Nowack H.: Comparison of Scatter under Program and Random Loading and Influencing Factors, ASTM STP 511, 1971.

12.Raikher V.L.; and Luchinskaya E.L.: Principles of applied theory of safety margins in the structure fatigue life problem, Collections of abstracts to ICF-8, Part II. Lviv, Ukraine, 1993.

Table 1.

Material	Number of samples		Total number of test objects	
	Coupons	Panels, structure elements	Coupons	Panels, structure elements
Aluminium alloy D16 (2024 analogy)	1063	364	9500	1200
Aluminium alloy B95 (7075 analogy)	535	81	4173	250
Steel 30ХГСА	652	360	4000	1100

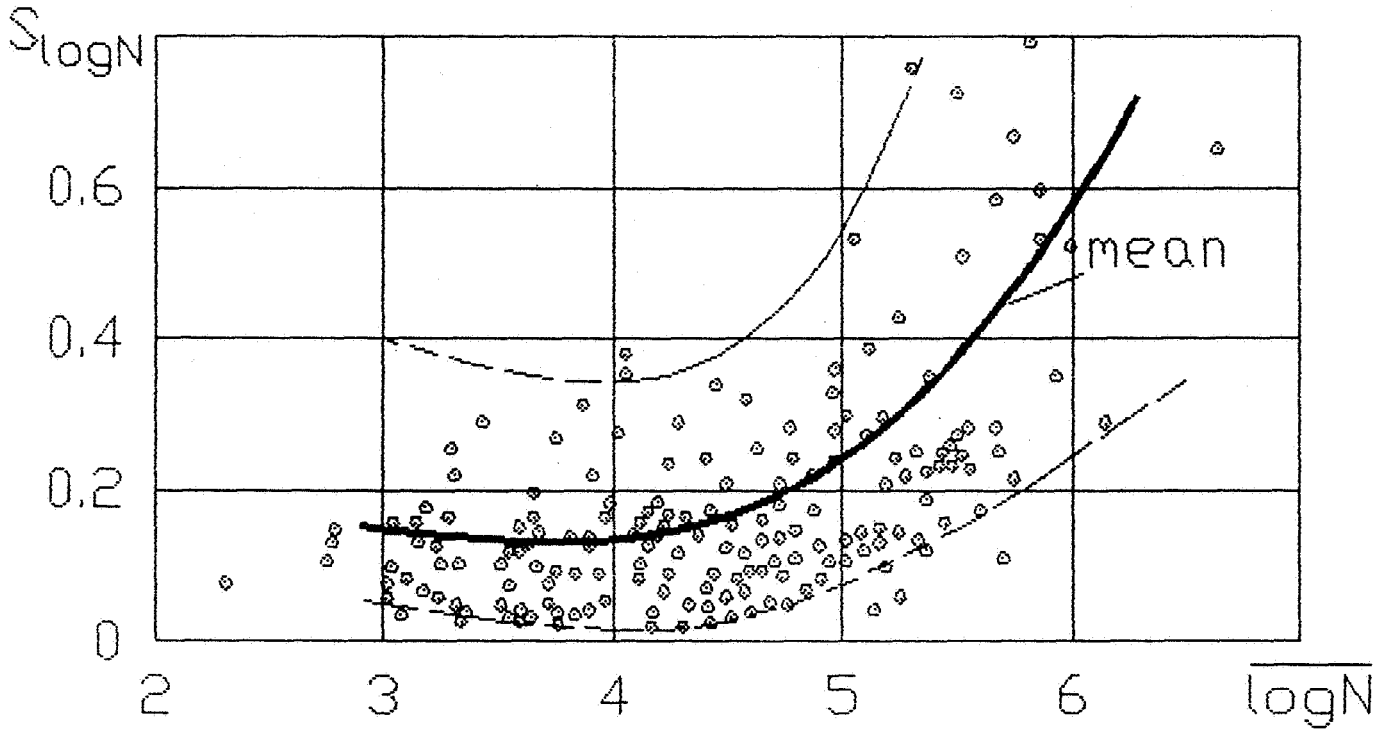

Figure 1. The example of scatter - mean life test results interpretation (ref.2).

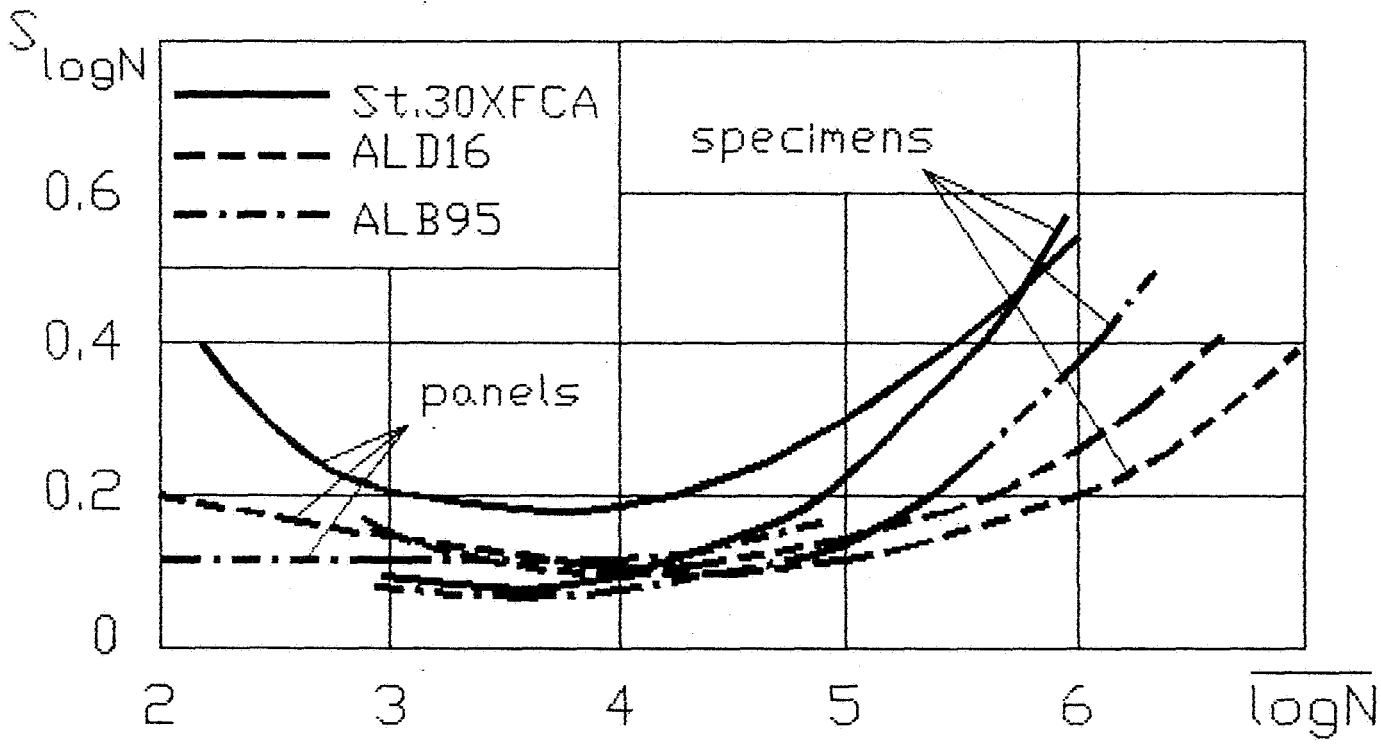

Figure 2. The generalized scatter - mean life plot (ref.1). Mean curves for different materials and test objects.

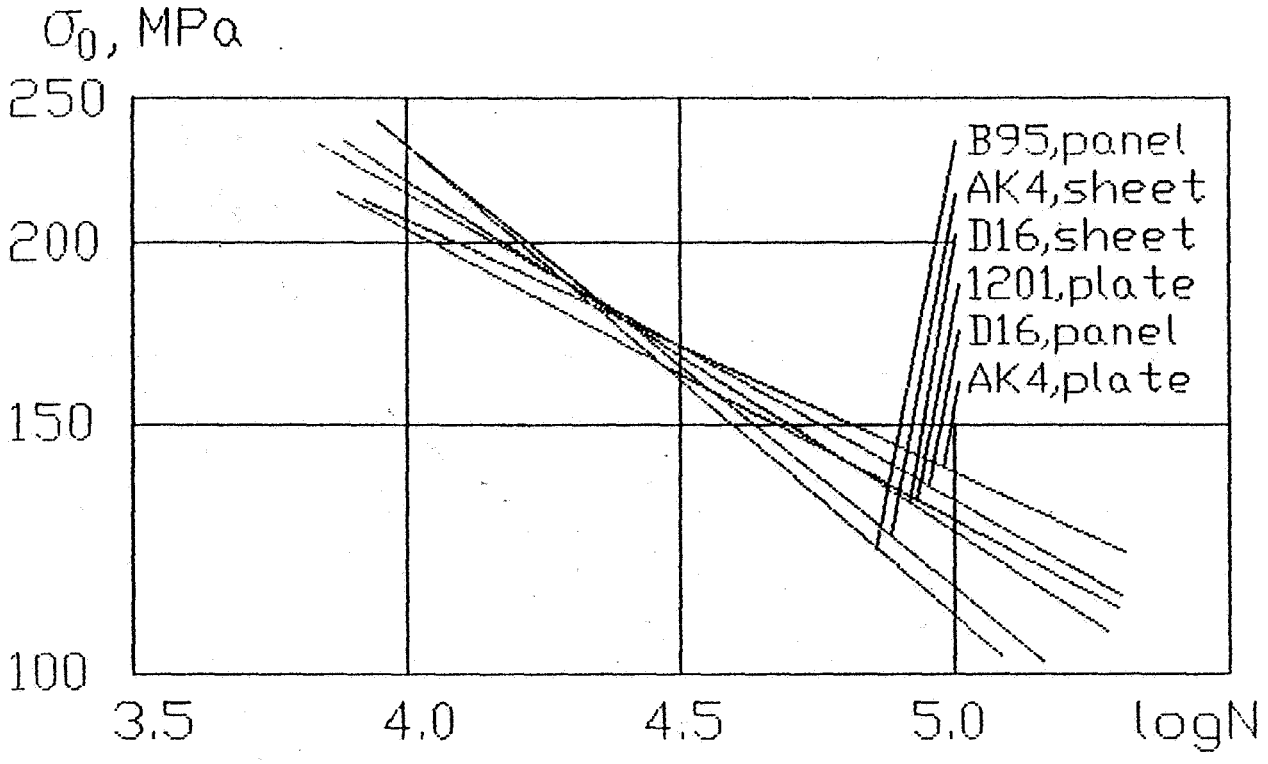

Figure 3. Fatigue curves for several aluminium alloys semi-finished products (ref.4).

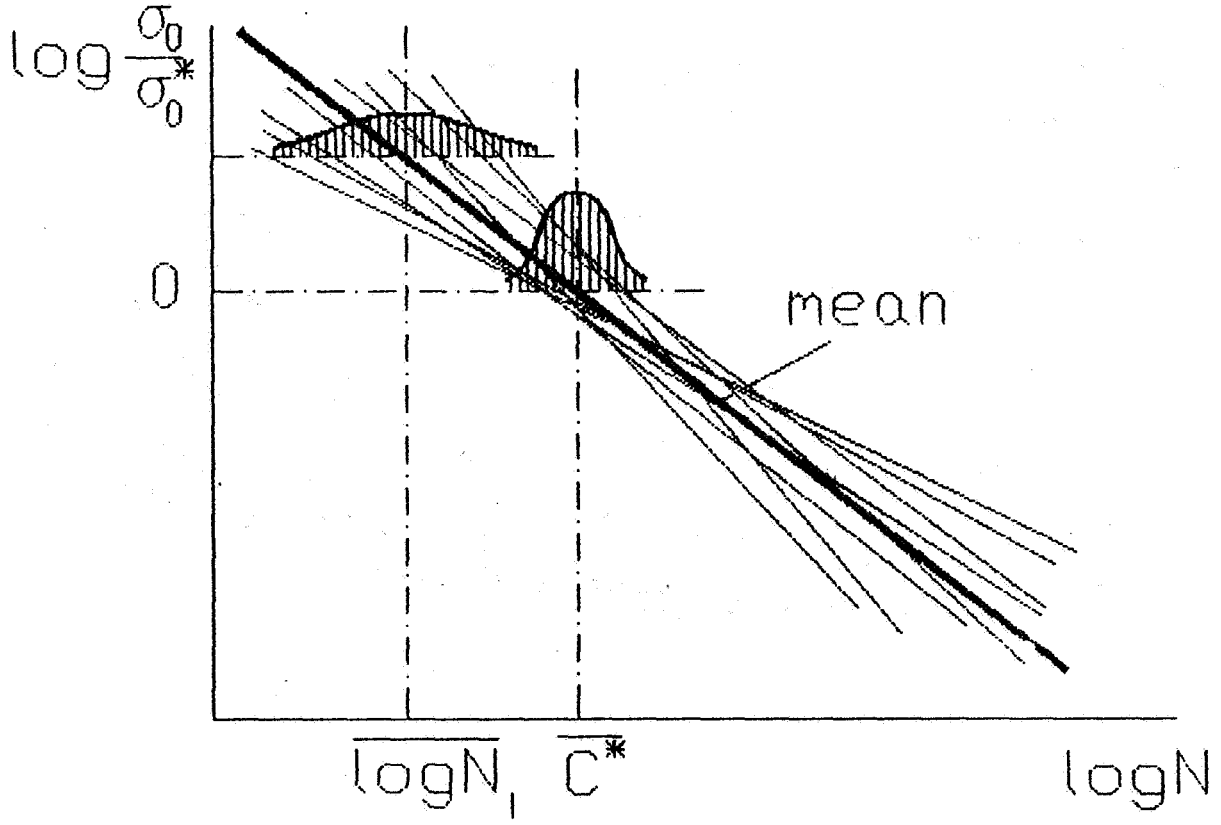

Figure 4. The "fan" of individual fatigue curves.

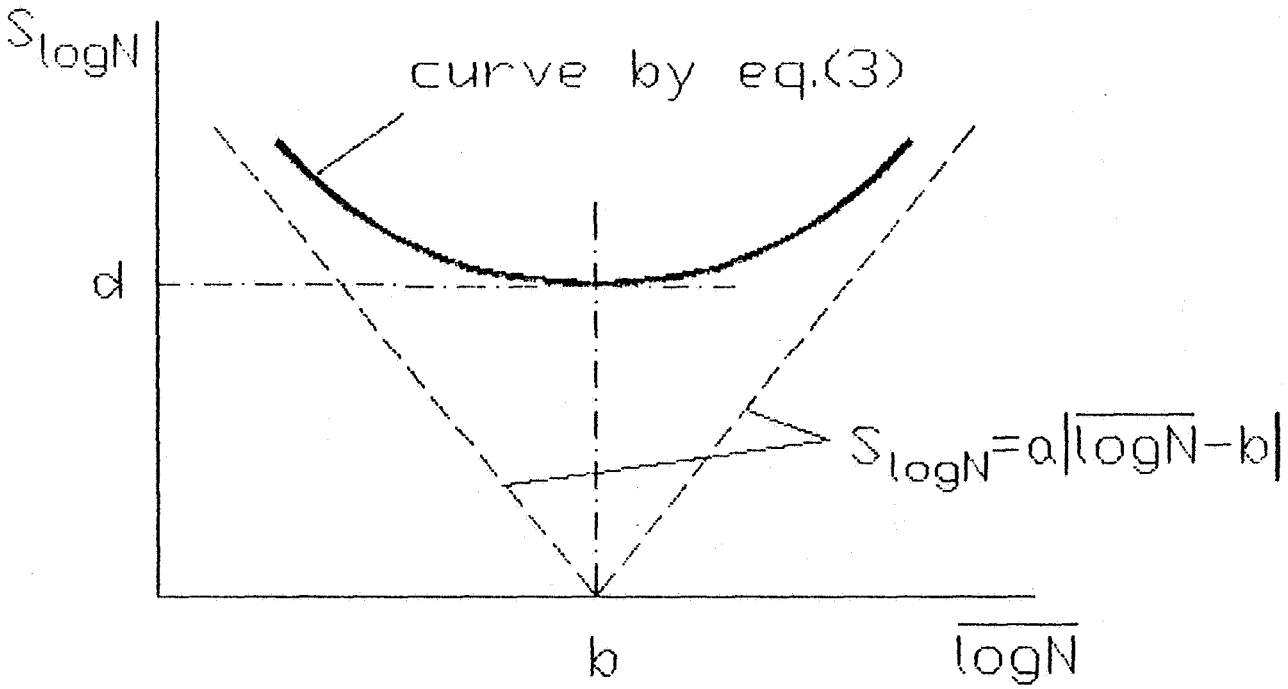

Figure 5. The theoretical "scatter - mean life" equation.

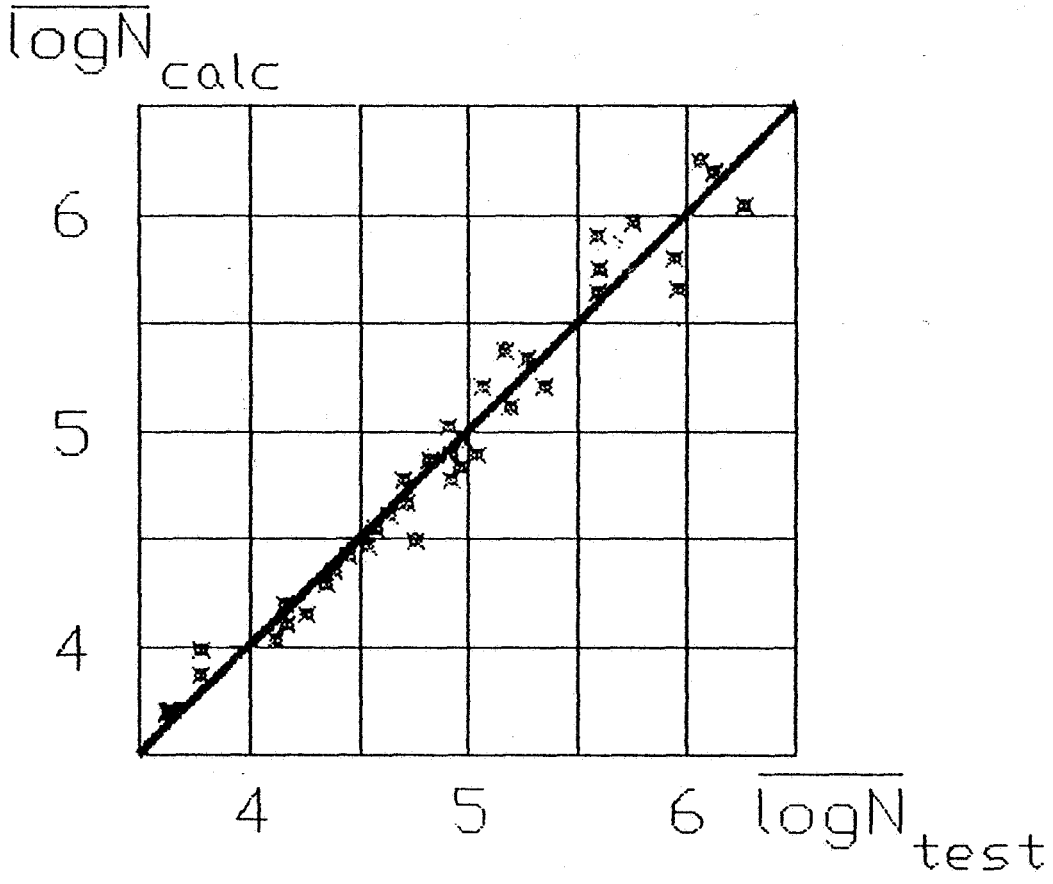

Figure 6. An example of equation (4) validation (ref.10).

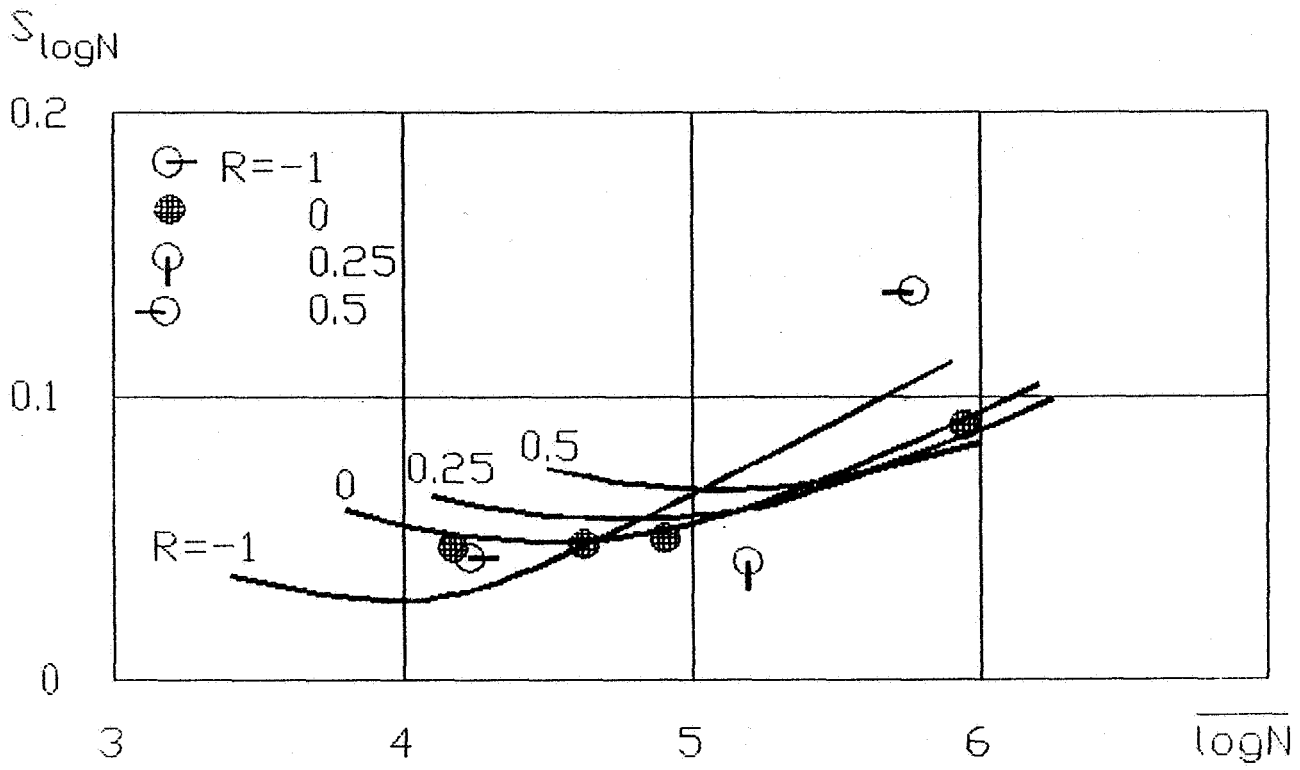

Figure 7. The influence of stress ratio on scatter characteristics. The experimental points (ref.11) and identified theoretical curves.

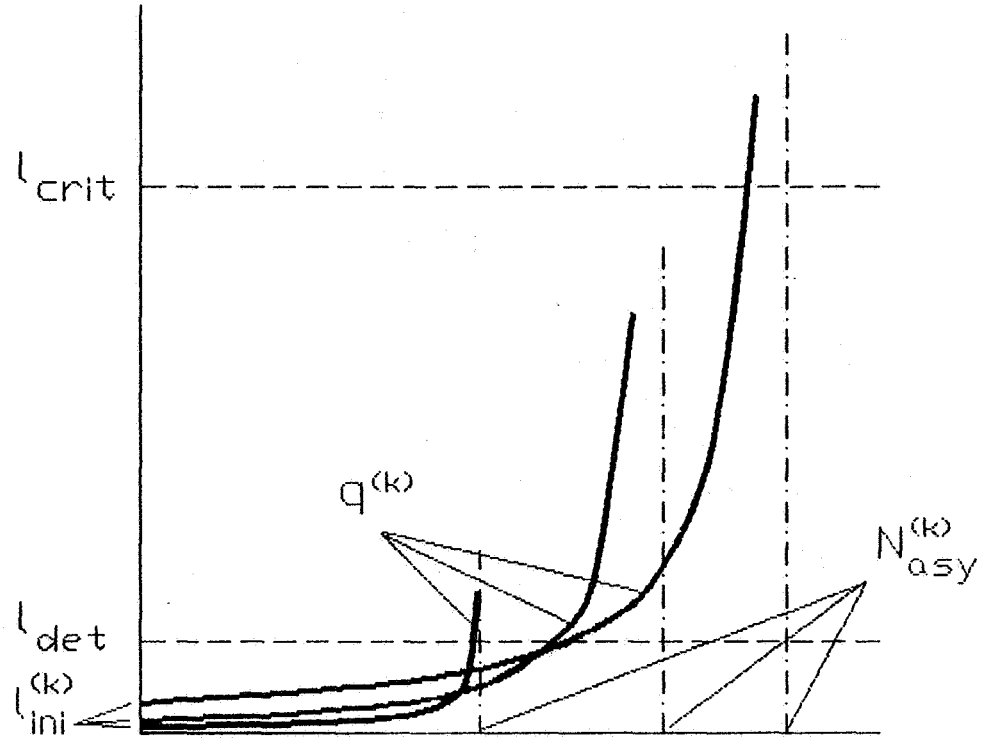

Figure 8. A crack growth scatter illustration.

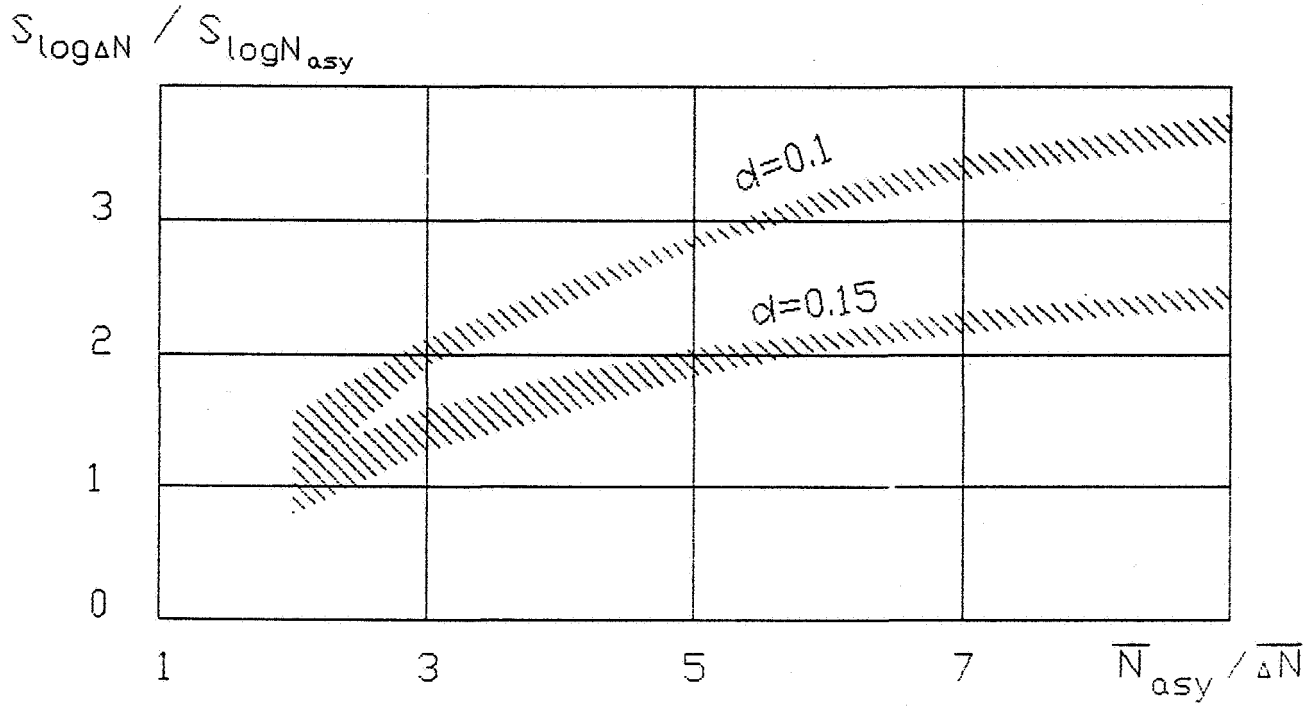

Figure 9. Relations between fatigue life and crack growth scatter values.

A PROBABILISTIC FATIGUE ANALYSIS OF MULTIPLE SITE DAMAGE

S.M. Rohrbaugh[1], D. Ruff[2], B.M. Hillberry[3], G. McCabe[4] and A.F. Grandt, Jr.[5]
Purdue University
West Lafayette, IN 47907 USA

ABSTRACT

The variability in initial crack size and fatigue crack growth is incorporated in a probabilistic model that is used to predict the fatigue lives for unstiffened aluminum alloy panels containing multiple site damage (MSD). The uncertainty of the damage in the MSD panel is represented by a distribution of fatigue crack lengths that are analytically derived from equivalent initial flaw sizes. The variability in fatigue crack growth rate is characterized by stochastic descriptions of crack growth parameters for a modified Paris crack growth law. A Monte-Carlo simulation explicitly describes the MSD panel by randomly selecting values from the stochastic variables and then grows the MSD cracks with a deterministic fatigue model until the panel fails. Different simulations investigate the influences of the fatigue variability on the distributions of remaining fatigue lives. Six cases that consider fixed and variable conditions of initial crack size and fatigue crack growth rate are examined. The crack size distribution exhibited a dominant effect on the remaining fatigue life distribution, and the variable crack growth rate exhibited a lesser effect on the distribution. In addition, the probabilistic model predicted that only a small percentage of the life remains after a lead crack develops in the MSD panel.

INTRODUCTION

Multiple site damage (MSD) refers to the accumulation of widespread fatigue cracking in aircraft structural details. MSD can be especially damaging when cracks initiate at several adjacent fastener holes in a mechanically fastened joint. Over time, the effects of the fatigue damage will reduce the residual strength of an aircraft joint and may result in a loss of damage tolerance capability. To reliably predict the capability of an MSD joint, the influences of widespread fatigue cracking and the associated crack growth mechanisms are needed.

The development of a method that incorporates the randomness in widespread fatigue cracking lends itself to a probabilistic approach. The initial crack sizes in the MSD joint can be

---

[1] Graduate Research Assistant, School of Mechanical Engineering
[2] Graduate Research Assistant, Department of Statistics
[3] Professor, School of Mechanical Engineering
[4] Professor, Department of Statistics
[5] Professor, School of Aeronautics and Astronautics

represented by randomly selecting crack lengths from an analytically or experimentally derived distribution. The distribution of fatigue crack sizes can be estimated using an equivalent initial flaw size (EIFS) method proposed by Manning and Yang [1-5]. In addition to different MSD crack lengths, each crack is expected to grow at a different rate as observed by Virkler et al. [6]. Ostergaard and Hillberry [7] derived the distributions for the fatigue crack growth parameters that described the variability observed by Virkler. From the development of accurate descriptions of the crack sizes and crack growth rate as described above, a probabilistic model can be implemented to determine the influence of these random variables on fatigue life predictions. This approach can then be applied to an unstiffened panel containing MSD cracks to provide a better understanding of the effects of widespread fatigue cracking. A model of an unstiffened MSD panel was developed by Moukawsher et al. [8-11]. Moukawsher's model deterministically calculates fatigue crack growth, incorporates crack interaction effects, and predicts panel failure. This MSD fatigue model is integrated into a probabilistic model to determine a distribution of fatigue lives for a panel containing MSD cracks.

The objectives of this study are: (1) to characterize the variables associated with widespread fatigue cracking, (2) to develop a probabilistic method that incorporates the randomness for these variables, and (3) to evaluate the influence of fatigue variability on life predictions for an aluminum alloy panel containing MSD cracks. The present goal is to observe trends in fatigue lives of panels that contain both multiple site damage on the scale observed in aging aircraft and realistic crack growth properties of the material that was used to build these aircraft.

MATERIALS AND METHODS

Multiple Site Damage Model

The multiple site damage model considered here is a panel 787 mm wide by 2.3 mm thick containing 30 holes 4.76 mm in diameter (Figure 1). The holes are equally spaced and aligned perpendicular to the applied loading. This geometry was also considered by Buhler et al. [11] in a parametric study which employed the deterministic MSD analysis developed by Moukawsher et al. [8-10]. For this study the panel material considered was 2024-T3 aluminum alloy. The initial damage state was through-the-thickness cracks emanating from each side of the 30 holes. The panel was subjected to a constant amplitude remote tension of 68.9 MPa and a stress ratio of 0.1. Failure of the panel was considered to be fracture. A residual strength criterion based on Swift's ligament yield model [12] was used to predict failure. Moukawsher et al. [9,10] experimentally tested 2024-T3 aluminum alloy panels with MSD and observed good agreement with the residual strength criterion.

Variability in Initial Crack Size

The initial fatigue cracks at the holes in the panel were represented by an analytically derived distribution of crack sizes. The Manning and Yang approach for predicting fatigue cracking in aircraft from equivalent initial flaw size distributions was followed [1-5]. An EIFS distribution represents a population of artificial cracks, which when grown forward will be similar to

observed fatigue cracking in aircraft. An EIFS is a derived quantity and not necessarily equivalent to the actual flaw sizes at the time of manufacture. EIFS values are determined by back extrapolating fractographic data to a service time t=0 by integrating the analytical crack growth rate model given by equation 1,

$$\frac{da(t)}{dt} = Q \cdot a(t) \tag{1}$$

where da(t)/dt is the crack growth rate, a is the crack size in millimeters, Q is the crack growth rate coefficient per hour, and t is the service time. The EIFS values are then fit to a Weibull compatible distribution function

$$F(a) = \exp\left\{ -\left[\frac{\ln(x_u/a)}{\phi} \right]^{\alpha} \right\} \tag{2}$$

where x_u is an upper-bound, α is the scale parameter, and ϕ is the shape parameter.

Widespread fatigue cracking in aircraft is predicted by growing the EIFS distribution (equation 2) forward to some service time t=T. To simplify the analysis, the service crack growth curve (SCGC) for a given stress region of an aircraft is estimated with the analytical crack growth rate equation (equation 1). A reasonable approximation is achieved by fitting the analytical equation in two-segments to the SCGC according to a reference crack size (a_o) as shown below:

$$\frac{da}{dt} = Q_1 \cdot a^{b1} \qquad a(t) < a_o \tag{3}$$

$$\frac{da}{dt} = Q_2 \cdot a^{b2} \qquad a(t) >= a_o \tag{4}$$

The crack growth coefficients Q_1 and Q_2 for a given SCGC are estimated from equations 5 and 6,

$$Q_1 = \xi_1 \cdot \sigma^{\psi_1} \tag{5}$$

$$Q_2 = \xi_2 \cdot \sigma^{\psi_2} \tag{6}$$

where σ is the maximum stress level of the SCGC in MPa, and ξ_1, ξ_2, ψ_1, ψ_2 are empirical constants based on crack size data observed fractographically. The crack growth exponents b_1 and b_2 were equal to one in this study as suggested by Manning and Yang [1,2]. Once the crack growth coefficients have been estimated for a given SCGC, the EIFS distribution can be analytically grown forward to determine the distribution of crack sizes at some service time t=T.

The EIFS approach was used by Yang and Manning in the durability analysis of a fighter lower wing skin [1]. The EIFS distribution parameters and empirical constants were determined from fractographic data sets for laboratory specimens under spectrum loading. The resulting EIFS distribution parameters for equation 2 were x_u=0.762 mm, α=1.716, ϕ=6.308, and the constants for equations 5 and 6 were ξ_1=2.227E-19, ξ_2=6.288E-8, ψ_1=6.374, and ψ_2=1.546. The crack growth coefficients (Q_1 and Q_2) were then estimated for ten different stress regions in the wing skin from equations 5 and 6. The analytically derived EIFS distribution can then be grown

forward by integrating equations 3 and 4 for each wing skin region to determine a distribution of crack sizes at any service time t=T.

Data reported by Yang and Manning [1] for the fighter lower wing skin were used in this study to generate the prediction for the extent of widespread fatigue cracking. The EIFS distribution was grown forward to 10,000 flight hours for stress region VI. The resulting fatigue crack sizes were then fit to a Weibull compatible distribution function (equation 2) with parameters x_u=4.27 mm, α=1.995, and ϕ=6.921. This analytically derived distribution is used to represent the initial crack sizes in the MSD panel.

Variability in Fatigue Crack Propagation

The variability in fatigue crack growth behavior was observed by Virkler et al. [6] for 68 replicate, constant amplitude tests of 2024-T3 aluminum alloy panels (Figure 2). Virkler measured the fatigue crack growth (*a vs. N*) in center cracked panels cut from the same material lot. The data were readily described by a modified Paris law [7]

$$\frac{da}{dN} = C \cdot (\Delta K - \Delta K_{th})^m \tag{7}$$

where the crack growth rate parameters C and m are material constants, da/dN is the crack growth rate in inches/cycle, ΔK is the stress intensity range in ksi$\sqrt{in}$, and ΔK_{th} is the threshold stress intensity. The threshold stress intensity value used by Ostergaard and Hillberry [7] and in this study was 2.75 ksi$\sqrt{in}$. Ostergaard and Hillberry [7] used a finite integral optimization (FIO) method to determine the fatigue crack growth rate parameters such that upon integration of equation 7 the original *a vs. N* data were accurately reproduced. The FIO method optimizes each parameter set by determining the C_i and m_i that give the best-fit to the *a vs. N* data according to a prescribed minimum error function.

From the 68 sets of optimized values for the crack growth parameters C_i and m_i, Ostergaard used a least-squares regression analysis of the *log m vs. log C* data to show that the mean crack growth behavior could be described by equation 8,

$$\log \hat{C}_i = b_0 + b_1 \cdot \log m_i \tag{8}$$

with mean crack growth parameter $\hat{C}_i$. The least-squares estimates were b_0 = -5.7792 and b_1 = -4.6150. The deviations of the fitted value log $\hat{C}_i$ (from equation 8) compared to log C were used to describe the variability in crack growth rate. This variability was characterized by the parameter F defined below

$$F_i = \frac{\hat{C}_i}{C_i} \tag{9}$$

$$\log F_i = -(\log C_i - \log \hat{C}_i) \tag{10}$$

where the logarithm of F_i represents the least-squares residuals from the regression analysis. The results are two independent crack growth parameters m_i and F_i that describe the variability in the fatigue crack growth rate.

The derived m_i and F_i values from the *a vs. N* data showed a best-fit of the F parameter to the 3-parameter log-normal distribution function,

$$f(F) = \frac{1}{(F-\tau)\sqrt{2\pi\beta}} \cdot \exp\left(-\frac{1}{2\beta}\{\log(F-\tau) - \alpha\}^2\right) \tag{11}$$

where the scale, shape and threshold parameters were estimated to be $\alpha = -0.737$, $\beta = 0.025$, and $\tau = 0.807$ respectively. The m parameter showed a best-fit to the 2-parameter log-normal distribution function,

$$f(m) = \frac{1}{m\sqrt{2\pi\beta}} \cdot \exp\left(-\frac{1}{2\beta}\{\log m - \alpha\}^2\right) \tag{12}$$

where the scale and shape parameters are $\alpha = 0.35508$, and $\beta = 7.1162E\text{-}4$ respectively. The stochastic descriptions in equations 8-12 are used in the probabilistic model to represent the variability in fatigue crack growth rate.

Probabilistic Modeling

An important aspect in probabilistic modeling is to use a mechanistic approach that describes the fatigue process. The MSD fatigue model developed by Moukawsher et al. [8-11] provides a fracture mechanics approach to predict the fatigue life of a remotely loaded panel containing MSD cracks. The model incorporates the location, length, type of crack, and crack interaction effects in the calculation of the stress intensity factor (ΔK) solution for each crack. The corresponding crack growth rate is calculated from the da/dN vs. ΔK relationship, in this case a modified Paris law. The remaining fatigue life of the MSD panel is predicted by deterministically growing the cracks until the panel fails according to a residual strength criterion.

A Monte-Carlo simulation incorporates the fatigue variability with the MSD fatigue model described above to determine a distribution of remaining fatigue lives for the MSD panel. This probabilistic approach is used to investigate the influences of the variability in fatigue behavior and fatigue crack sizes by comparing different simulation conditions. The crack conditions considered were: 1) mean size cracks emanating from both sides of each fastener hole, 2) a random symmetric crack size emanating from both sides of each fastener hole, and 3) a random unsymmetric crack size emanating from both sides of each fastener hole. The crack growth rate conditions considered were: 1) mean crack growth parameters, 2) random crack growth parameters for each panel (homogeneous panel), and 3) random crack growth parameters at every ligament for each panel (heterogeneous panel).

Six Monte-Carlo simulations of 1000 trials each were investigated for the three crack size conditions and the three fatigue crack growth rate conditions. The influence of the fatigue variability was considered by evaluating simulations with different conditions of one fatigue

variability, while holding the other variability the same. The different simulation cases are described below, and are identified in Table 1.

- Case 1: mean crack sizes emanating from both sides of each hole and a randomly selected crack growth rate for each panel.
- Case 2: randomly selected symmetric crack sizes and a mean crack growth rate for each panel.
- Case 3: randomly selected unsymmetric crack sizes and a mean crack growth rate for each panel.
- Case 4: randomly selected symmetric crack sizes and a randomly selected crack growth rate for each panel.
- Case 5: randomly selected unsymmetric crack sizes and a randomly selected crack growth rate for each panel.
- Case 6: randomly selected symmetric crack sizes and a randomly selected crack growth rate at every ligament for each panel.

By direct comparison of the fatigue life distributions for these cases, the fatigue life variability can be quantified to provide a better understanding of the uncertainties in the MSD panel.

Table 1. Monte-Carlo Combinations of the MSD Panel

Case	Crack size parameter	Material parameter
1	mean crack size every hole	variable crack growth rate each panel
2	variable symmetric crack size every hole	mean crack growth rate each panel
3	variable unsymmetric crack size every hole	mean crack growth rate each panel
4	variable symmetric crack size every hole	variable crack growth rate each panel
5	variable unsymmetric crack size every hole	variable crack growth rate each panel
6	variable symmetric crack size every hole	variable crack growth rate every hole

RESULTS AND DISCUSSION

The six Monte-Carlo simulations predicted stochastically tight distributions for the remaining fatigue lives of the MSD panels (Figures 3-8). To directly compare the different cases, the means and standard deviations are plotted in a bar chart for each case (Figure 9). *Case 1 vs. 4* compares the mean crack sizes and the randomly selected crack sizes for the same crack growth rate condition. In this comparison, the mean fatigue life decreased significantly for the randomly selected cracks due to cracks larger than the mean value interacting with the adjoining cracked holes. As a result, a dominant crack would link-up to form a lead crack, whereby the panel would fail soon thereafter as a result of the loss in residual strength. *Case 2 vs. 4* compares the mean crack growth rate with the randomly selected crack growth rate for the same initial crack size condition. No significant difference in the mean fatigue lives occurred; however, the standard deviation increased with the addition of the variable crack growth. This suggests that the mean fatigue life is not sensitive to the variability in fatigue crack growth rate, but the shape of the distribution is affected. *Case 4 vs. 6* compares the variable crack growth rate for each panel and the variable crack growth rate for each ligament in the panel. Both cases exhibited similar distributions which support the previous observations. *Case 2 vs. 3* and *Case 4 vs. 5* compares the symmetric crack sizes and the unsymmetric crack sizes. These comparisons show an increase in the mean fatigue lives and a decrease in the standard deviation for the unsymmetric crack conditions. The increase in mean life is expected since a large crack that is symmetric is more damaging than a large/small unsymmetric crack condition. Overall, the crack size distribution exhibited a dominant effect on the fatigue life predictions, and the variable crack growth rate exhibited a lesser effect on the fatigue life predictions. Due to the panel containing a large number of consecutive holes, the probability increased that each panel would contain a large flaw. This combined influence of the number of holes and the fatigue variability on the life distribution warrants further investigation.

Panel failure occurred in *Cases 2-6* as a result of the formation of a lead crack reducing the residual strength of the panel. This behavior was investigated by calculating the percent remaining life after the first link-up. Histogram plots of the percentages are shown in Figures 10 through 14. Comparing the means and standard deviations for each case in the bar chart (Figure 15) shows that approximately 5% of the life remains after the development of a lead crack. This suggests that the majority of the life is spent propagating the initial cracks; therefore, a reliable analysis must include a good representation of the input variables. The uniform cracking in *Case 1* never developed a lead crack and the panel failed from net section yielding.

The utility in analyzing trends between different cases depends on appropriately representing the fatigue variabilities in the MSD panel. It was determined that for the analytically derived crack size distribution that approximately 33% of the cracks would propagate. This is a result of the modified Paris crack growth equation (equation 7) preventing cracks from growing at stress intensities below the threshold value. The derived crack size distribution in the MSD panel at 10,000 flight hours was compared to observed crack size data reported by Lincoln [13] for 19 trainer aircraft. Lincoln reported the destructive tear down and inspection of trainer wings revealing 25-50% of the fastener holes had detectable cracks. Additionally, the initial crack size distribution for this study compares favorably with the fitted distribution to the observed cracks found in the trainer aircraft (Figure 16). The distributions of fatigue crack growth parameters were developed from a 2024-T3 aluminum alloy produced in 1976 which is of the same vintage as the material used in the aging aircraft fleet.

Although the current paper has expressed the results of the probabilistic MSD analysis in terms of remaining fatigue life distributions, the approach could also be used to determine the variation in residual strength as a function of elapsed cycles. In that case, Monte-Carlo

simulations would be performed as before to predict distributions in MSD crack patterns at various predetermined life intervals. The various crack patterns would then be combined with a failure criterion to compute the distribution in residual strength for a given point in life. Determining the distributions in residual strength as a function of elapsed cycles would, then, give an indication of how the safe load carrying capability of the structure decays with service usage.

SUMMARY

A probabilistic model that includes the variability in crack size and fatigue crack growth rate has been developed for investigating the fatigue lives of MSD panels. These variables were defined from examples that represent MSD in aging aircraft and represent the properties of the materials that was used to build these aircraft. Six Monte-Carlo simulations were run with variations of fixed and variable conditions for different random variable combinations. The MSD crack size distribution had a dominant effect on the fatigue lives, and the variability in crack growth rate had a lesser effect. The model predicted that the majority of life was spent propagating the MSD cracks until adjacent crack-tips link-up, and then approximately 5% of the panel life remains. The probabilistic model provides an improved understanding of the influences of widespread fatigue cracking on remaining fatigue lives.

ACKNOWLEDGEMENTS

This research was sponsored by the Air Force Office of Scientific Research under grant F49620-93-1-0377.

REFERENCES

1. Yang, J. N.; and Manning, S. D.: Demonstration of Probabilistic-Based Durability Analysis Method for Metallic Airframes. *J. Aircraft*, vol. 27, no. 2, February 1990, pp. 169-175.

2. Manning, S. D.; and Yang, J. N.: USAF Durability Design Handbook: Guidelines for the Analysis and Design of Durable Aircraft Structures. AFWAL-TR-83-3027, Air Force Flight Dynamics Laboratory, WPAFB, OH, January 1984.

3. Manning, S. D.; and Yang, J. N.: Advanced Durability Analysis, Volume I - Analytical Methods. AFWAL-TR-86-3017, Air Force Wright Aeronautical Laboratories, WPAFB, OH, July 1987.

4. Manning, S. D.; and Yang, J. N.: Advanced Durability Analysis, Volume II - Analytical Predictions, Test Results and Analytical Correlations, AFWAL-TR-86-3017, Air Force Wright Aeronautical Laboratories, WPAFB OH, February 1989.

5. Yang, J. N.; and Manning, S. D.: Distribution of Equivalent Initial Flaw Size. *1980 Proceedings of Annual Reliability and Maintainability Symposium*, January 1980, pp. 112-120.

6. Virkler, D. A.; Hillberry, B. M.; and Goel, P. K.: The Statistical Nature of Fatigue Crack Propagation. AFFDL-TR-78-43, Air Force Flight Dynamics Laboratory, WPAFB, OH, April 1978.

7. Ostergaard, D. F.; and Hillberry, B. M.: Characterization of the Variability in Fatigue Crack Propagation Data. *Probabilistic Fracture Mechanics and Fatigue Methods: Applications for Structural Design and Maintenance, ASTM STP 798*, American Society for Testing and Materials, 1983, pp. 97-115.

8. Moukawsher, E. J.; Neussl, M. A.; and Grandt, A. F., Jr.: A Fatigue Analysis of Panels with Multiple Site Damage. Proceedings of the 1992 USAF Structural Integrity Program Conference, Technical Report Wl-TR-4080, Wright Patterson Laboratory, WPAFB, September 1993, pp. 257-273.

9. Moukawsher, E. J.; Neussl, M. A.; and Grandt, A. F., Jr.: Analysis of Panels with Multiple Site Damage. AIAA-94-1459, April 1994.

10. Moukawsher, E. J.: Fatigue Life and Residual Strength of Panels with Multiple Site Damage. M.S. Thesis, School of Aeronautics and Astronautics, Purdue University, West Lafayette, IN, May 1993.

11. Buhler, K.; Grandt, A. F., Jr.; and Moukawsher, E. J.: Fatigue Analysis of Multiple Site Damage at a Row of Holes in a Wide Panel. Advanced Structural Integrity methods for Airframe Durability and Damage Tolerance, NASA CP-3274, 1994.

12. Swift, T.: Damage Tolerance Capability. *Fatigue of Aircraft Materials*, Proceedings of the Specialists Conferences dedicated to the 65th birthday of J. Schijve, 1992, Delft University Editors, Delft University Press, 1992, pp. 351-387.

13. Lincoln, J. W.: Risk Assessment of an Aging Military Aircraft. *J. Aircraft*, vol. 22, no. 8, August 1985, pp. 687-691.

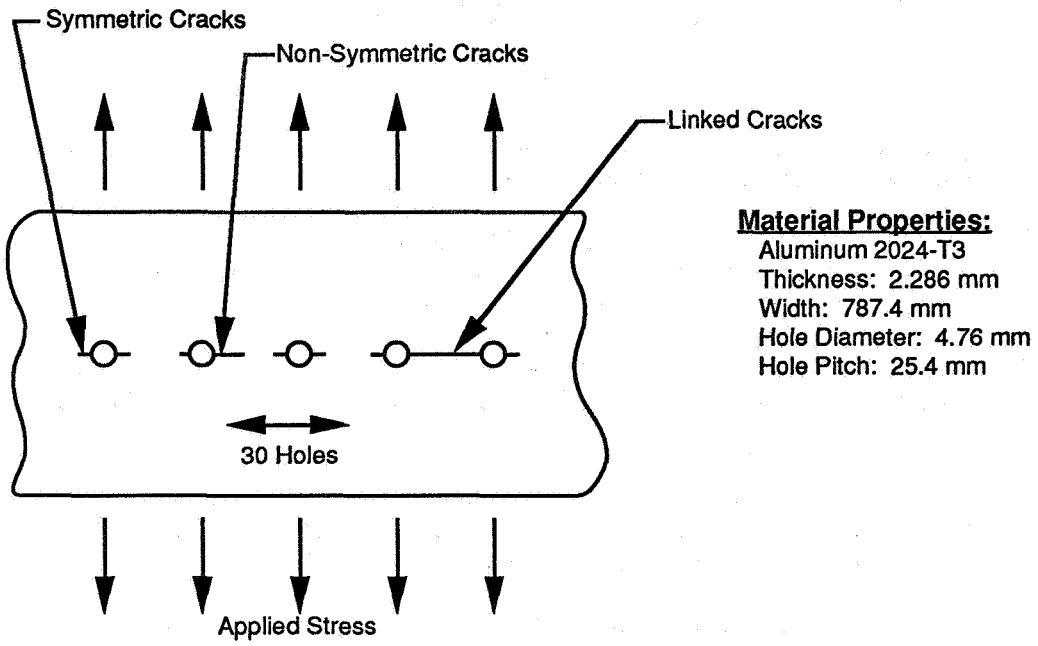

Figure 1: MSD panel.

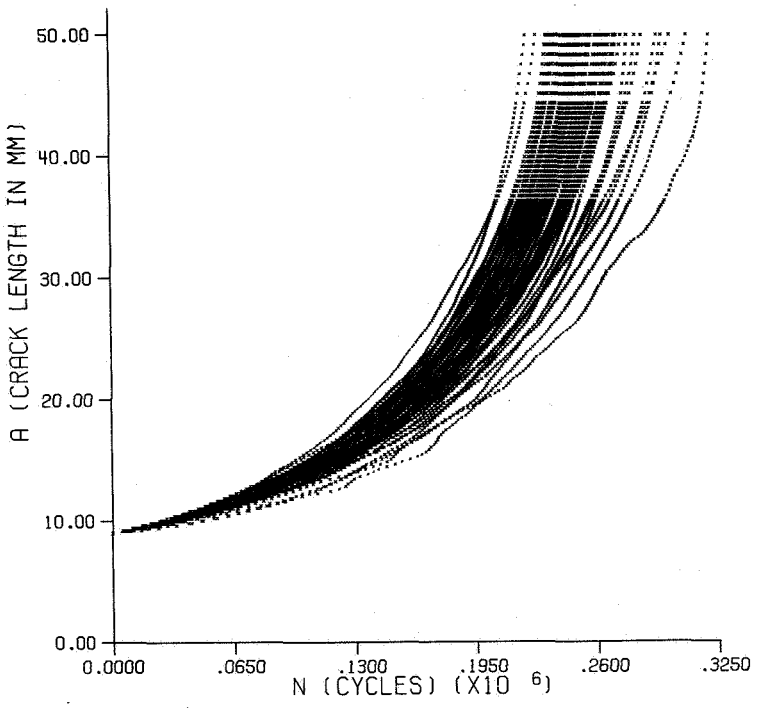

Figure 2: Virkler's data from 68 replicate fatigue crack growth tests in 2024-T3 aluminum alloy specimens.

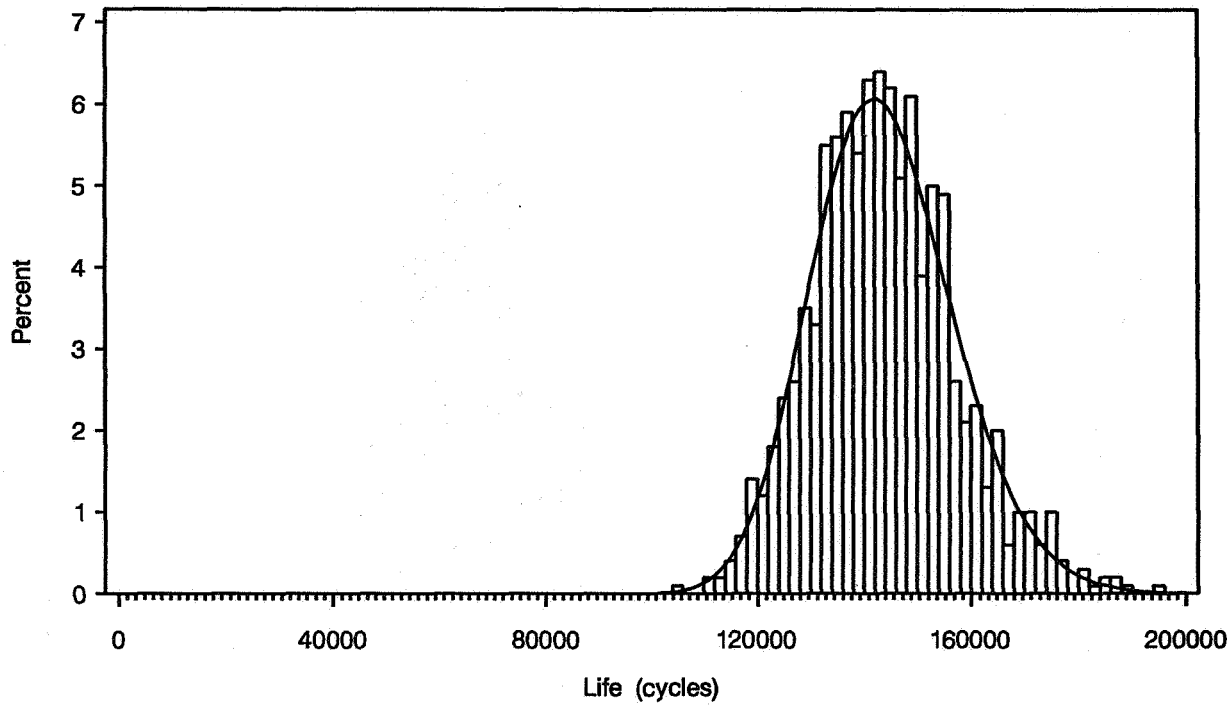

Figure 3: Remaining fatigue life histogram, Case 1: mean size cracks; variable growth parameters for each panel.

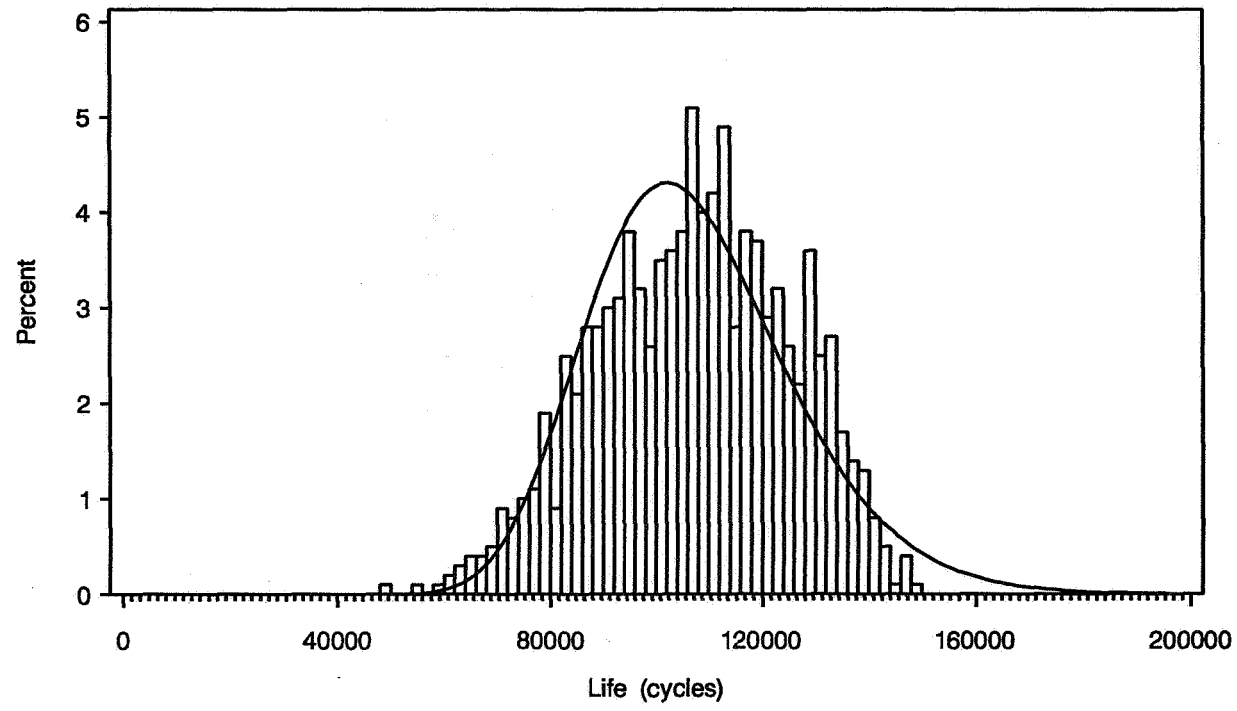

Figure 4: Remaining fatigue life histogram, Case 2: variable symmetric crack-sizes; mean crack growth parameters.

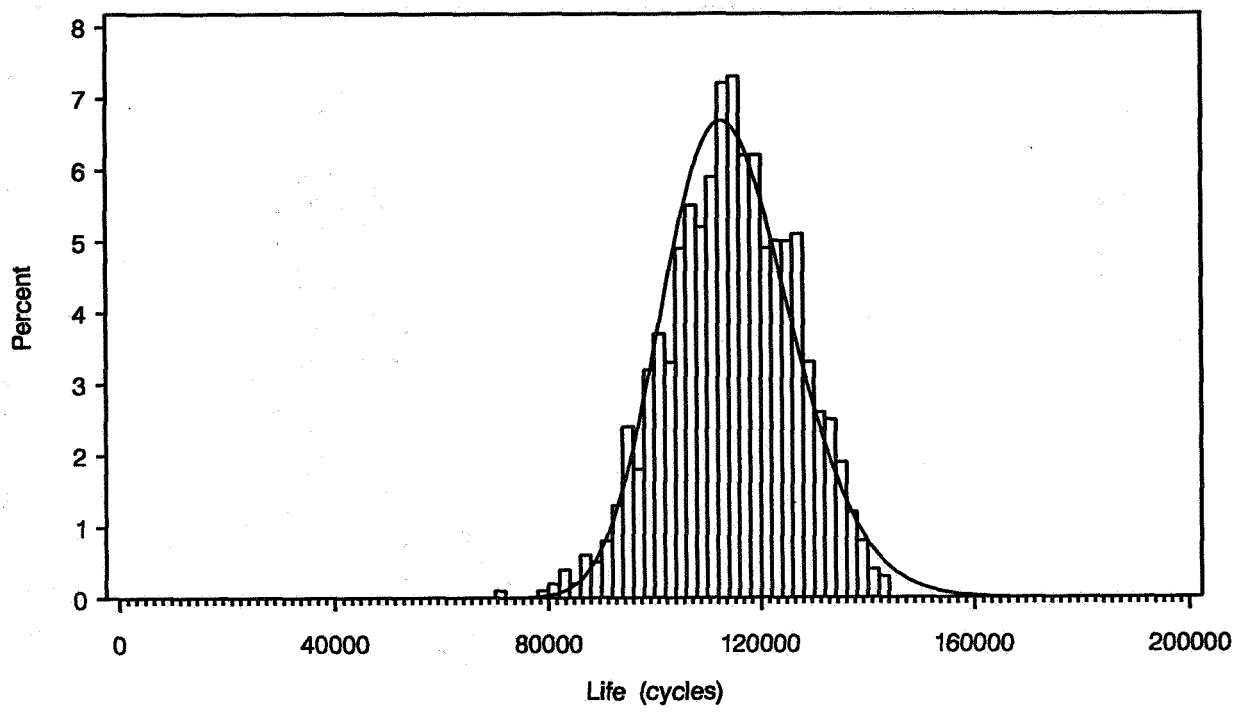

Figure 5: Remaining fatigue life histogram, Case 3: variable unsymmetric crack sizes; mean crack growth parameters for each panel.

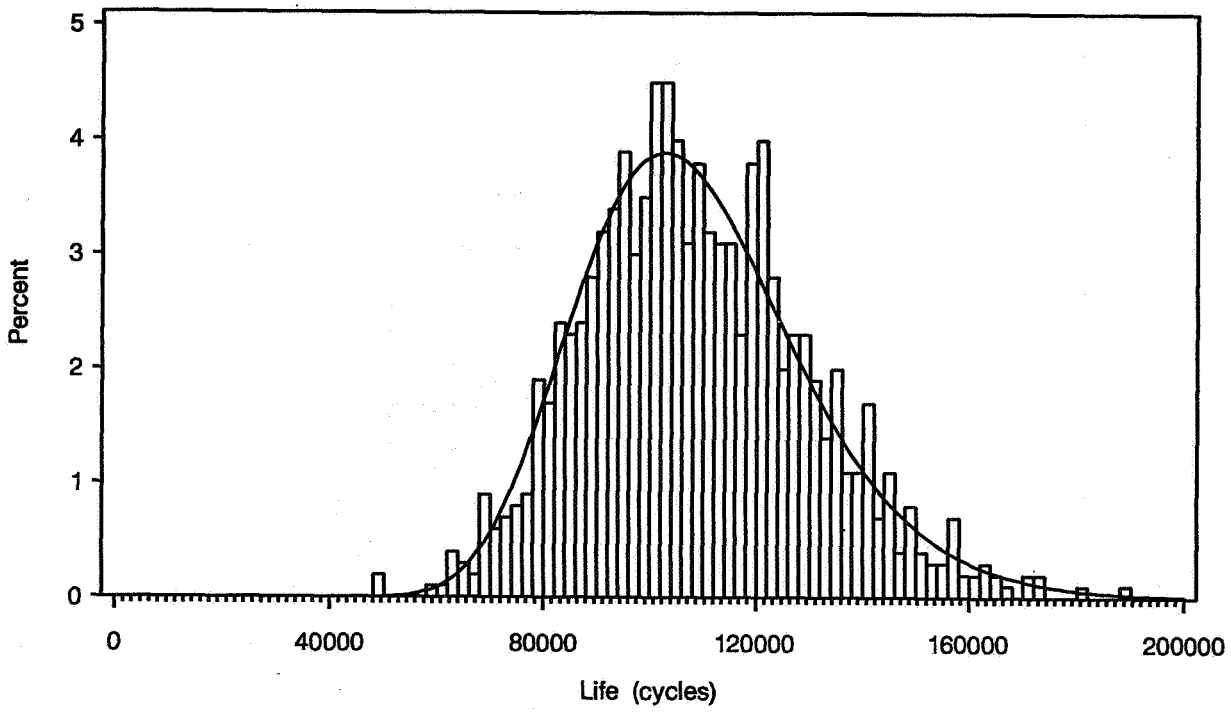

Figure 6: Remaining fatigue life histogram, Case 4: variable symmetric crack sizes; variable crack growth parameters for each panel.

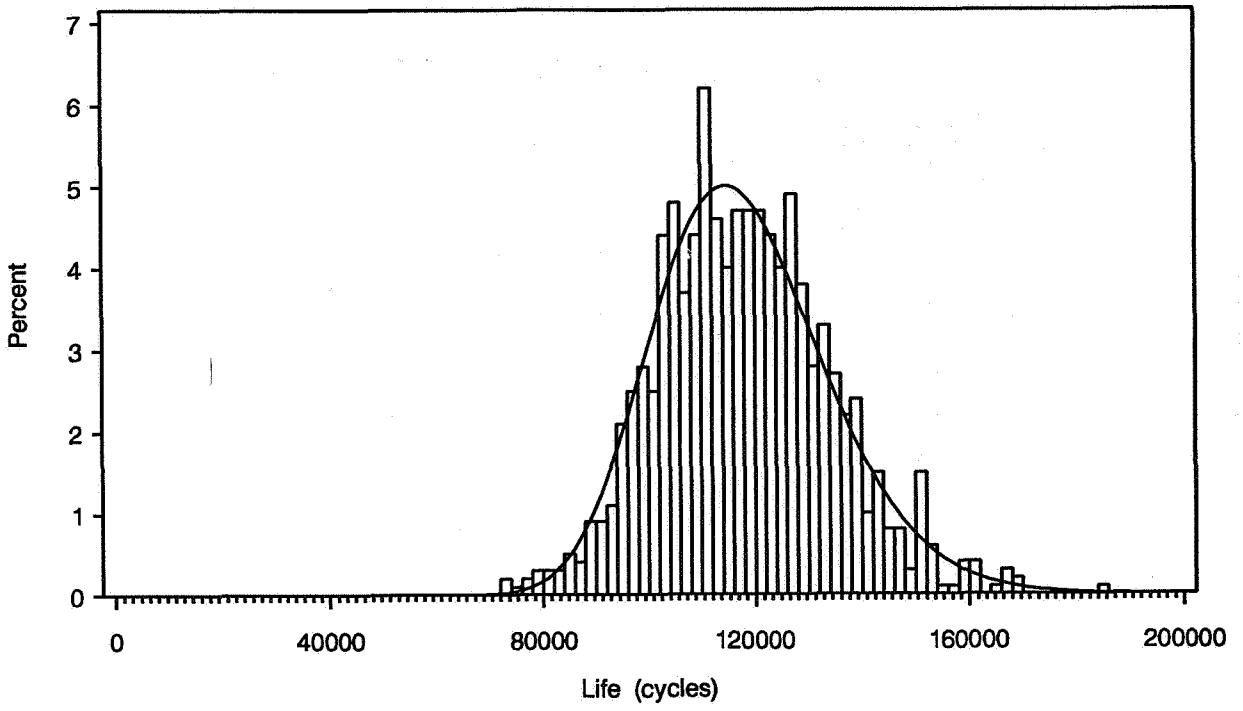

Figure 7: Remaining fatigue life histogram, Case 5: variable unsymmetric crack sizes; variable crack growth parameters for each panel.

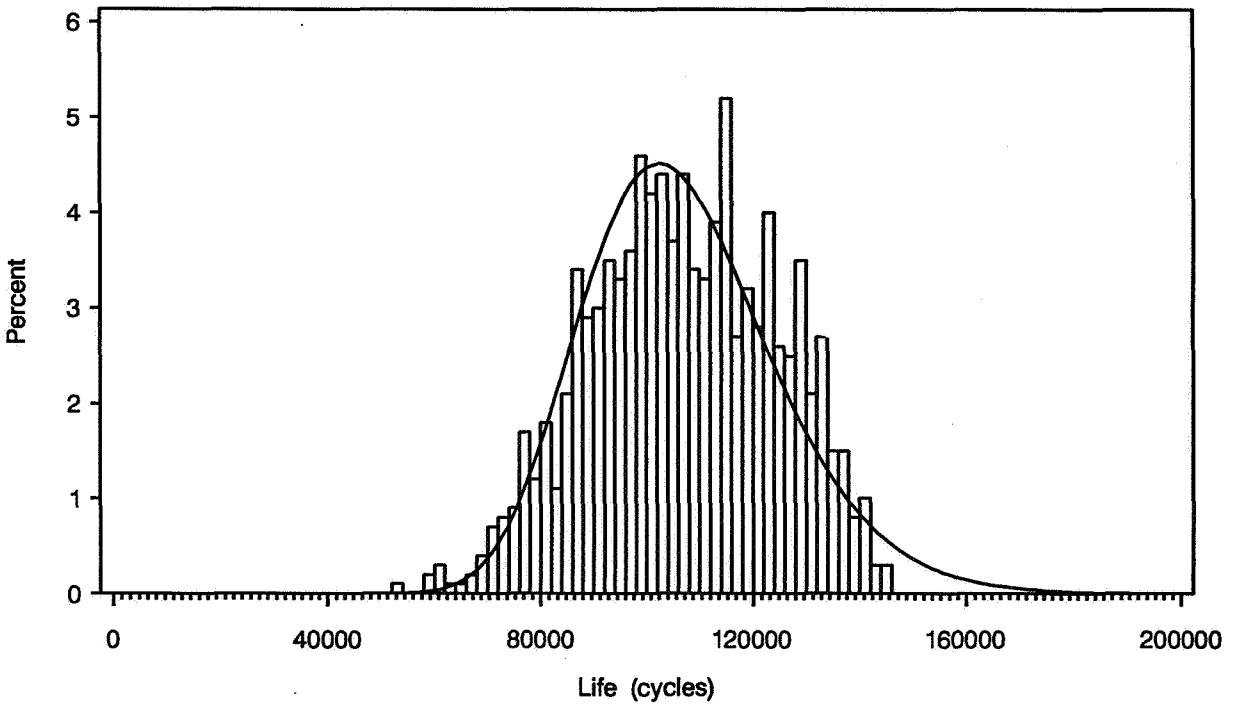

Figure 8: Remaining fatigue life histogram, Case 6: variable symmetric crack sizes; variable crack growth parameters at each hole for each panel (heterogeneous panel).

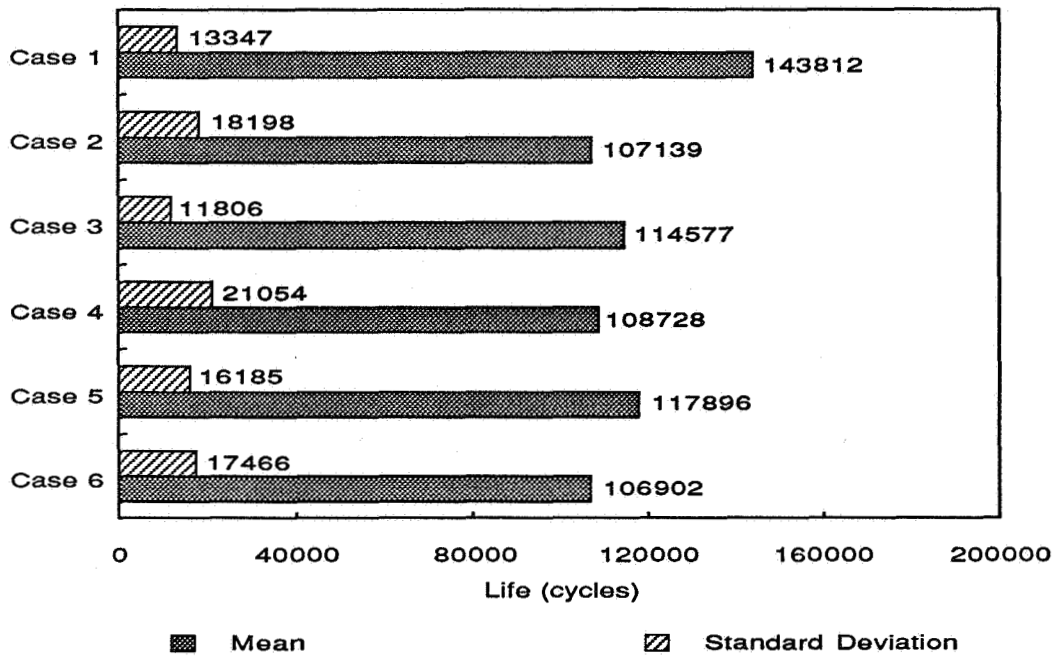

Figure 9: Remaining fatigue life bar chart of mean and standard deviation for Cases 1-6.

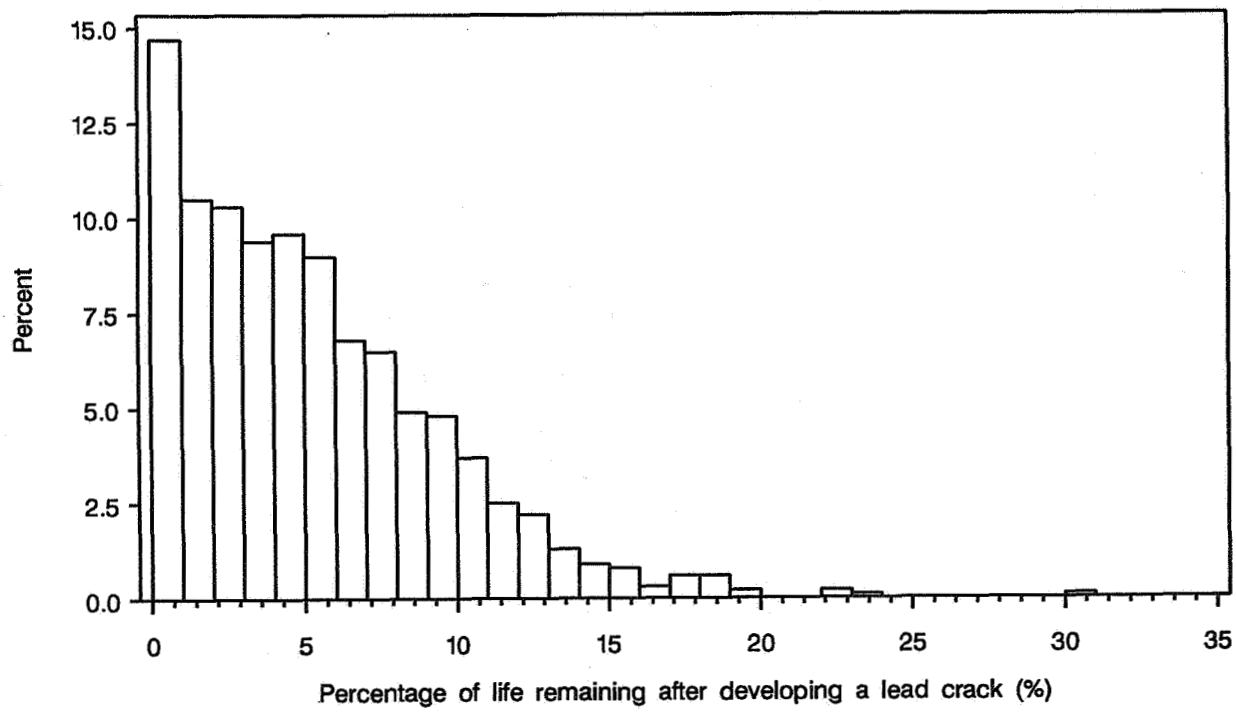

Figure 10: Percent remaining fatigue life histogram after developing a lead crack, Case 2: variable symmetric crack sizes; mean crack growth parameters.

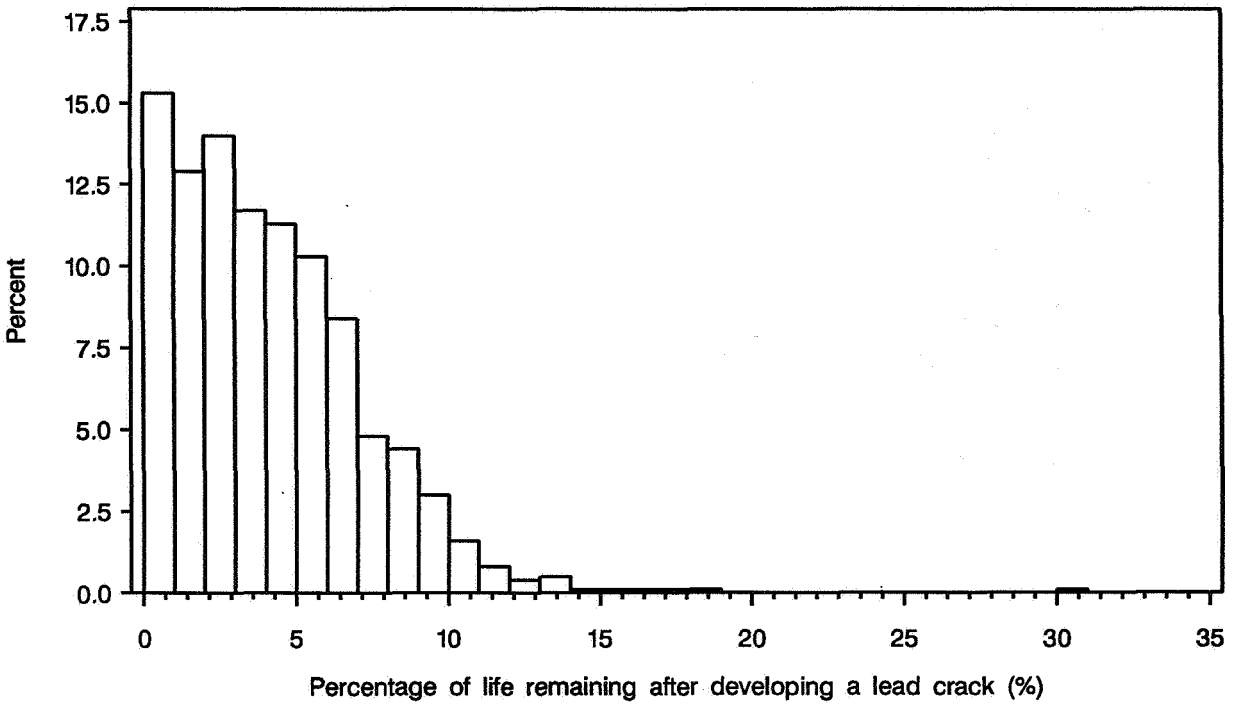

Figure 11: Percent remaining fatigue life histogram after developing a lead crack, Case 3: variable unsymmetric crack sizes; mean crack growth parameters for each panel.

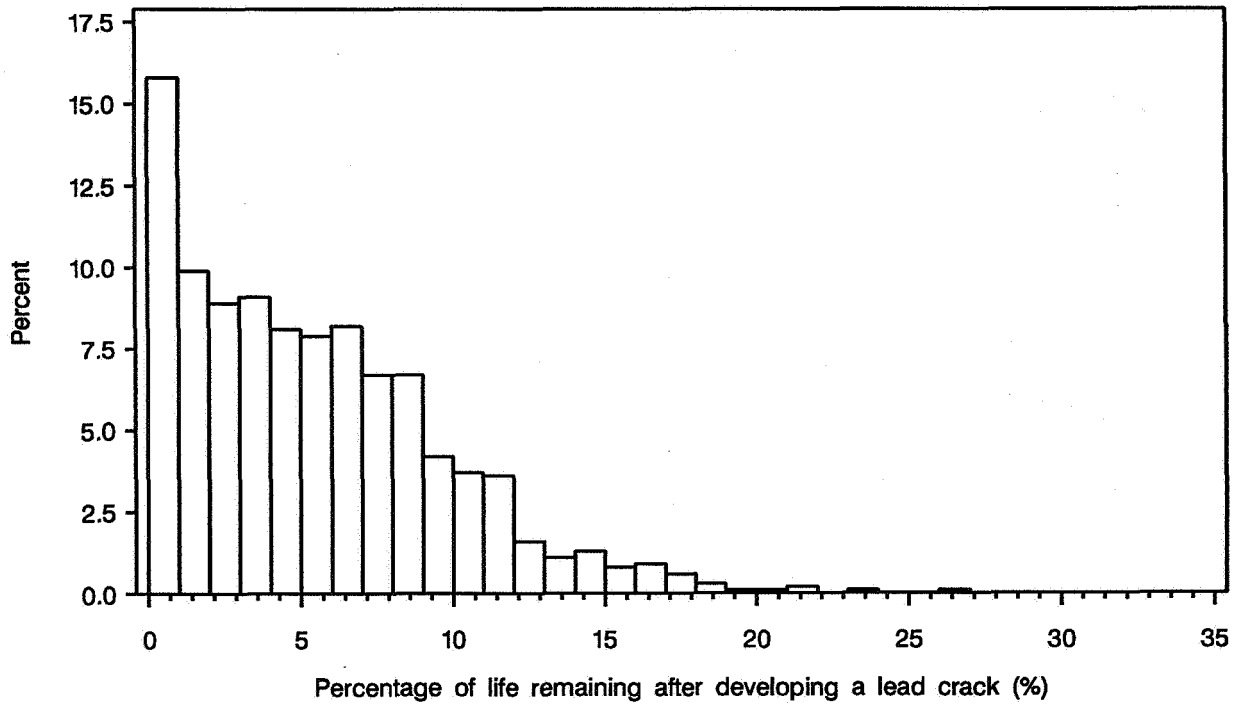

Figure 12: Percent remaining fatigue life histogram after developing a lead crack, Case 4: variable symmetric crack sizes; variable crack growth parameters for each panel.

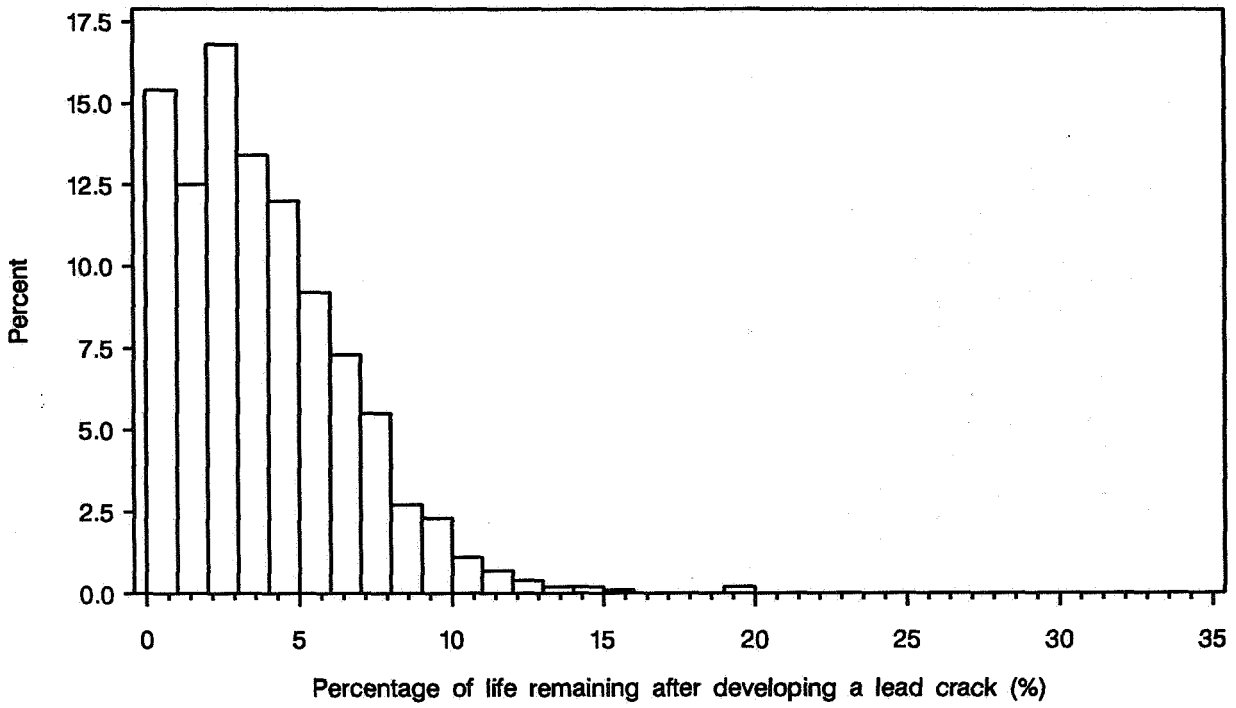

Figure 13: Percent remaining fatigue life histogram after developing a lead crack, Case 5: variable unsymmetric crack sizes; variable crack growth parameters for each panel.

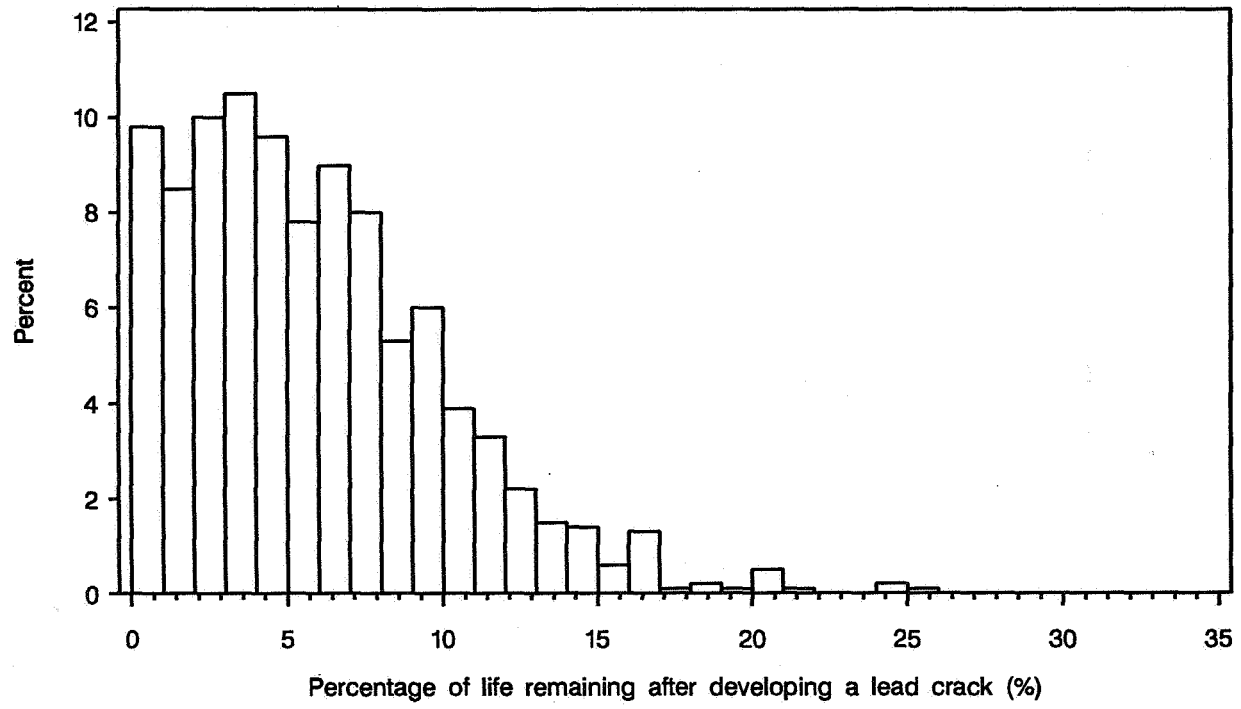

Figure 14: Percent remaining fatigue life histogram, Case 6: variable symmetric crack sizes; variable crack growth parameters at each hole for each panel (heterogeneous panel).

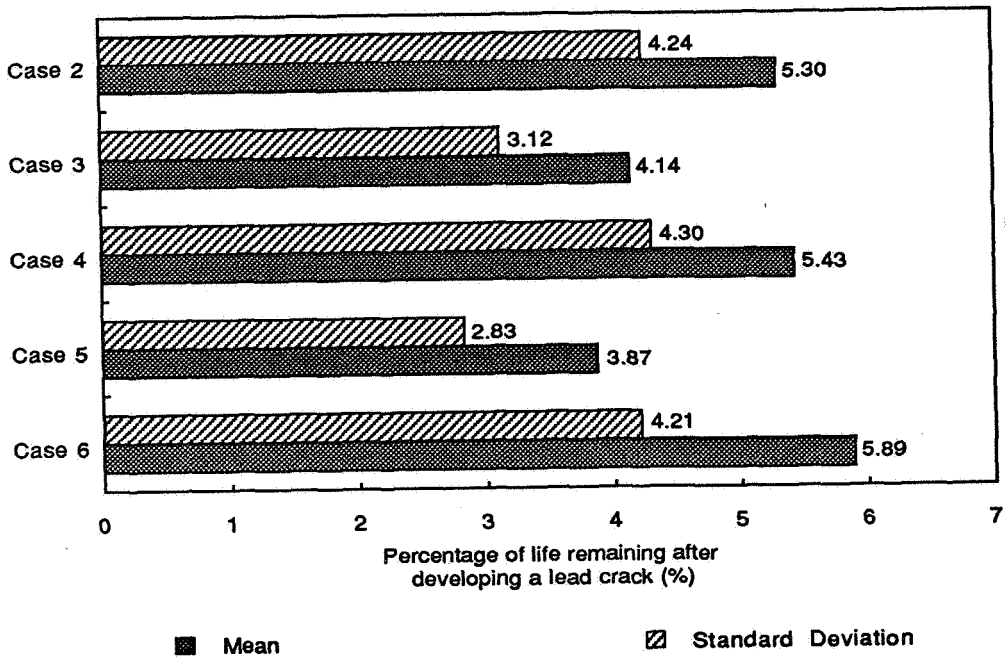

Figure 15: Percent remaining fatigue life bar chart of mean and standard deviation after developing a lead crack (cases 2-6).

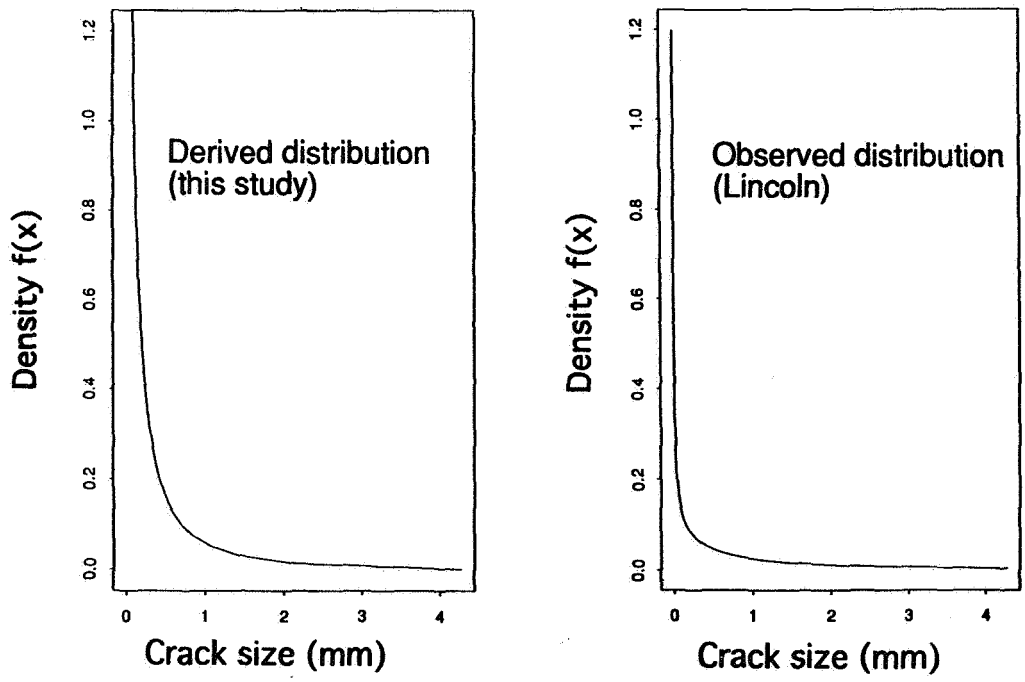

Figure 16: Analytically derived initial crack size distribution compared with observed cracks reported by Lincoln.

EVALUATION OF THE FUSELAGE LAP JOINT FATIGUE AND TERMINATING ACTION REPAIR

N95-19477

Gopal Samavedam*, Douglas Thomson*, and David Y. Jeong**

113061

SUMMARY

P. 12

359232

Terminating action is a remedial repair which entails the replacement of shear head countersunk rivets with universal head rivets which have a larger shank diameter. The procedure was developed to eliminate the risk of widespread fatigue damage (WFD) in the upper rivet row of a fuselage lap joint.

A test and evaluation program has been conducted by Foster-Miller, Inc. (FMI) to evaluate the terminating action repair of the upper rivet row of a commercial aircraft fuselage lap splice. Two full scale fatigue tests were conducted on fuselage panels using the aircraft panel test facility at FMI. The first was conducted to characterize initiation and growth of fatigue cracks in the lap joint. The second test was performed to evaluate the effectiveness of the terminating action repair. In both tests, cyclic pressurization loading was applied to the panels while crack propagation was recorded at all rivet locations at regular intervals to generate detailed data on conditions of fatigue crack initiation, ligament link-up, and fuselage fracture.

This program demonstrated that the terminating action repair substantially increases the fatigue life of a fuselage panel structure and effectively eliminates the occurrence of cracking in the upper rivet row of the lap joint. While high cycle crack growth was recorded in the *middle* rivet row during the second test, failure was not imminent when the test was terminated after cycling to well beyond the service life. The program also demonstrated that the initiation, propagation, and linkup of WFD in full-scale fuselage structures can be simulated and quantitatively studied in the laboratory.

This paper presents an overview of the testing program and provides a detailed discussion of the data analysis and results. Crack distribution and propagation rates and direction as well as frequency of cracking are presented for both tests. The progression of damage to linkup of adjacent cracks and, to eventually, overall panel failure is discussed. In addition, an assessment of the effectiveness of the terminating action repair and the occurrence of cracking in the middle rivet row is provided, and conclusions of practical interest are drawn.

---

* Foster-Miller, Inc., Waltham, MA 02154-1196 USA.

** U.S. Department of Transportation, Research and Special Programs Administration, Volpe National Transportation Systems Center, Cambridge, MA 02142-1093 USA.

BACKGROUND

The problems associated with fatigue were brought to the forefront of research by the explosive decompression and structural failure of the Aloha Airlines Flight 243 in 1988. The structural failure of this airplane has been attributed to debonding and multiple cracking along the longitudinal lap slice in the fuselage [1].

The Federal Aviation Administration Technical Center (FAATC) has initiated several research programs to investigate the structural integrity of aging airplanes. Particular attention has been given to understanding the phenomenon of multiple cracking. The term "Widespread Fatigue Damage" (WFD) is commonly used to refer to a type of multiple cracking that degrades the damage tolerance capability of an aircraft structure. One of the issues regarding WFD is to determine its onset, or the point in time when the presence of multiple cracks are of sufficient size and density whereby the structure will no longer meet its damage tolerance requirement. Foster-Miller, Inc., under contract with the John A. Volpe National Transportation Systems Center, has conducted several test programs to support these investigations [2,3,4].

This paper summarizes the results from fatigue tests performed on two full-scale fuselage panels. A unique test facility, specially designed and built by Foster-Miller, Inc., was used to conduct these tests. A description of this test facility can be found in References [2] and [3]. The objectives of these fatigue tests are:

(1) to characterize lap joint fatigue of an aircraft fuselage.

(2) to study the initiation, growth, and linkup of multiple cracks.

(3) to evaluate the effectiveness of the terminating action repair.

The first fatigue test addresses the first two objectives, and is regarded as a baseline test. In this paper, it is also referred to as the fatigue characterization test. A second test on a second full-scale panel was performed to address the last objective. Specific details of these full-scale fatigue tests can be found in Reference [4].

PANEL DESIGN

The basic panel configuration was developed under previous test programs conducted by Foster-Miller [2,3]. The panel was designed to be representative of older commercial aircraft with skin lap construction. Figure 1 shows a photograph of the underside of the test panel.

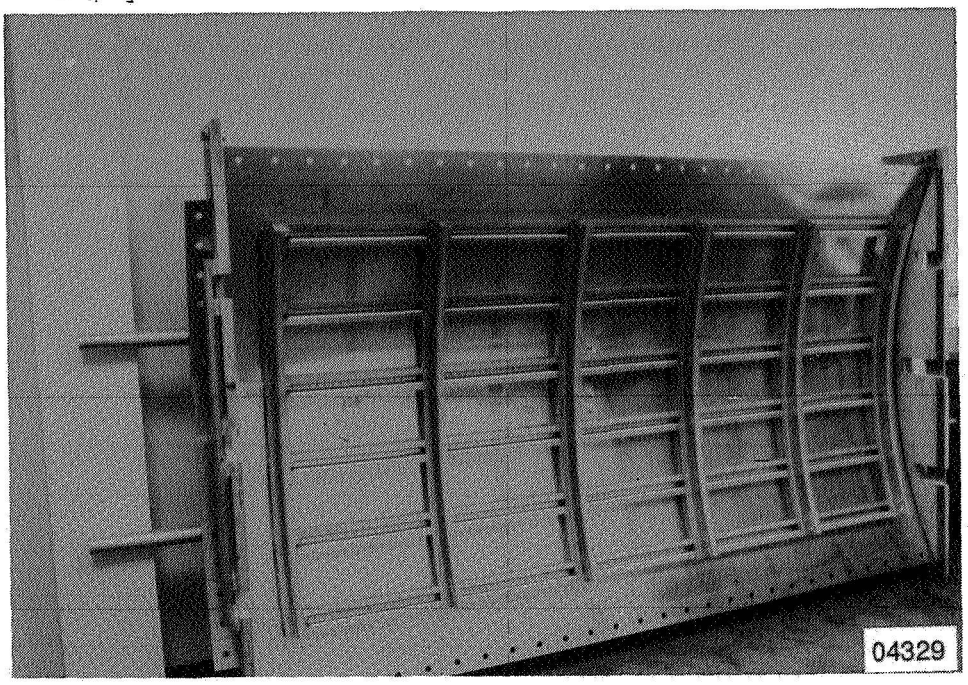

Figure 1. Photograph of test panel underside.

Specific key features of this panel include the following:

(1) The panel material is 2024-T3 alclad aluminum alloy. The thickness of each skin is 0.036 inch.

(2) Stringer ties were employed to join the stringers to the frames.

Additional panel features and dimensions are listed in Table 1.

Due to manufacturing and cost limitations, the test panel deviates in some design features from an actual commercial aircraft. While the fabrication process is simplified, these modifications do not impact structural performance of the fuselage panels. The most significant modifications include the following:

(1) A tear strap and filler strip arrangement was used in place of the waffle doubler design found in actual aircraft. Typical aircraft construction consists of bonding two pieces of skin together and then chemically removing all the material which is not a tear strap or does not lie over a stringer. Thus, a continuous waffle pattern doubler is produced beneath the skin. In the test panels, continuous tear straps were bonded to the skin and longitudinal filler strips were used over the stringers.

(2) The countersunk rivets were replaced with larger universal head rivets to prevent any unrepresentative cracking at the non-lap joint locations of stringers. In actual aircraft, the waffle pattern doublers over the stringers are hot bonded, eliminating the knife edge crack initiation site.

Table 1. Fatigue Panel Characteristics

Panel length (inches)	120
Panel width (inches)	68
Panel radius (inches)	75
Number of frames	6
Number of tear straps	11
Number of stringers	6
Frame spacing (inches)	20
Tear strap spacing (inches)	10
Stringer spacing (inches)	9.6
Skin thickness (inch)	0.036
Tear strap thickness (inches)	0.036
Skin and tear strap material	2024-T3 Aluminum alloy (clad)

FATIGUE CHARACTERIZATION TEST

The pressure range for both test panels was between 1.0 and 9.5 psi. The pressure differential of 8.5 psi was used to account for the effects of aerodynamic suction and transverse shear due to body bending in addition to nominal cabin pressure. The rate of loading was 0.2 Hertz or 720 cycles per hour.

Cracking in the upper row of rivets was first observed after 37,000 cycles. Figure 2 shows the distribution of cracks along the upper rivet row at different points in time as the panel was cycled. The abscissa represents the rivet location where rivets have been numbered sequentially from the left to right on the test panel.

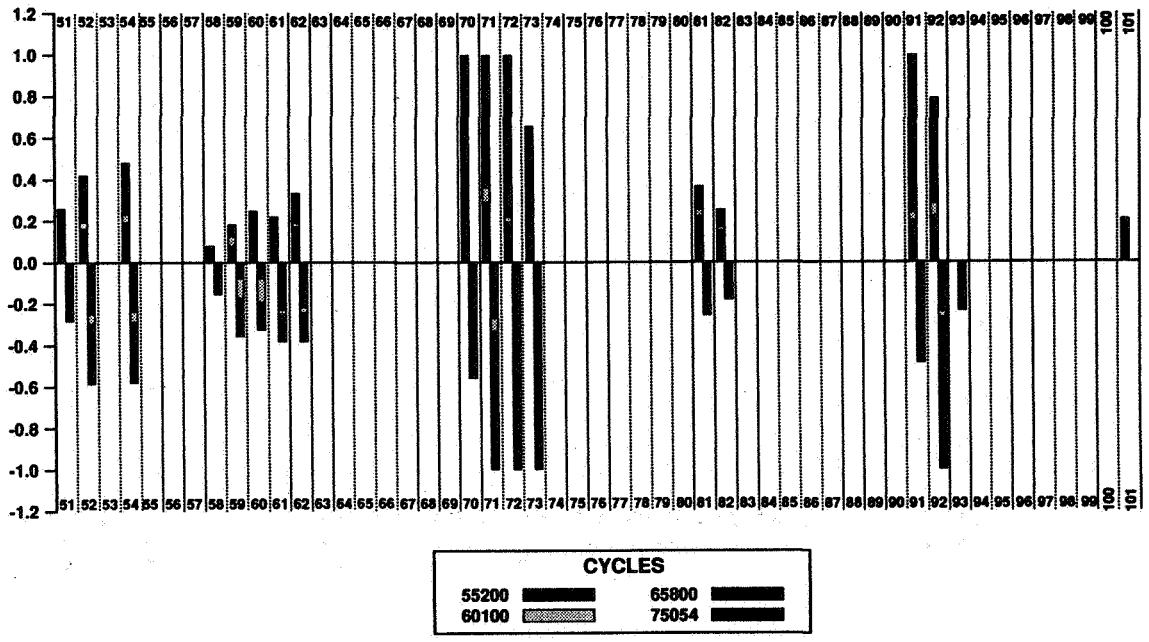

Figure 2. Distribution of cracks in the upper rivet row.

Figure 3 shows the sequence of multiple crack linkup events which led to failure of the panel. The first linkup of multiple cracks was observed after 69,400 cycles in the ligament between rivets 71-72. Similar linkups occurred in ligaments 91-92 after 73,325 cycles later, and in ligaments 46-47 and 47-48 after 74,493 cycles. Panel failure occurred after 75,263 cycles when several multiple cracks linked together to form a single crack over 50 inches in length.

The cumulative frequency of cracking along the upper rivet row can be plotted as a function of minimum crack length and of total cycles. Figure 4 shows this type of plot for 3 different points in time during the life of the panel. Thus, after 50,000 cycles, 9% of the rivets in the upper row had cracks greater than 0.2 inch. Further, after 70,000 cycles (or when 93% of the panel fatigue life had been consumed), 13% of the rivets in the upper row had cracks greater than 0.4 inch, while 3% of these rivets were greater than 0.8 inch. The cumulative frequency of cracking is simply a function of cycles and load levels.

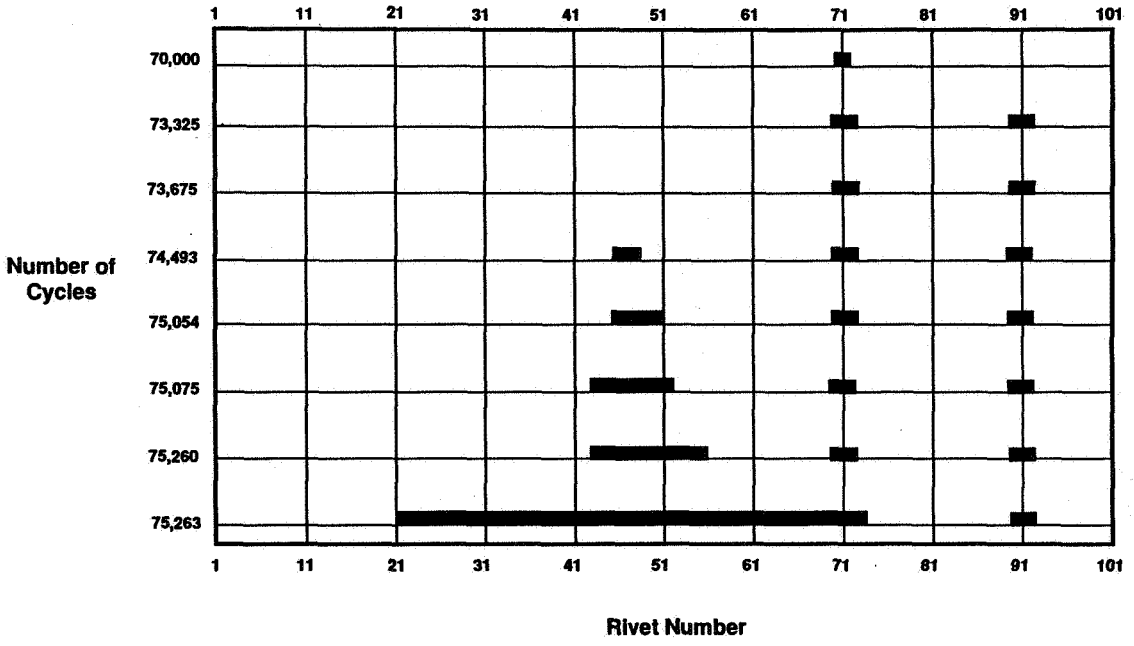

Figure 3. Sequence of multiple crack linkup events.

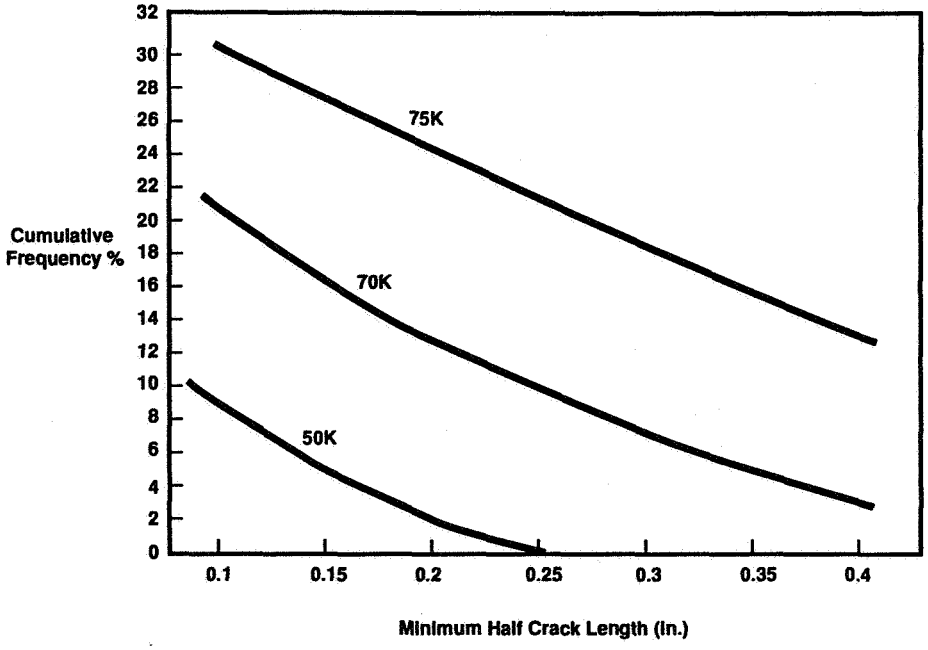

Figure 4. Cumulative frequency of cracking in baseline test.

TERMINATING ACTION EFFECTIVENESS TEST

Boeing Service Bulletin 737-53A 1039 Revision 3 [5] describes a remedial repair for fuselage lap splices. This repair has become widely known as the "terminating action" because its application terminates fatigue damage inspection. In 1987, the Federal Aviation Administration (FAA) issued Airworthiness Directive (AD) 87-21-08, mandating certain transport category aircraft to comply with this service bulletin. Basically, the repair entails replacement of shear head countersunk rivets in the upper row of the lap joint with universal head rivets which have a larger shank diameter.

The terminating action was applied to an initially undamaged test panel after 30,000 cycles, which is within specifications of the AD. Thus, all of the countersunk rivets in the upper row along the lap joint were drilled out and replaced with universal head rivets. Although three small cracks (all of which were less than 0.020 inch in length) were found at the time of the repair, they were completely drilled out when the holes were enlarged to accommodate the universal head rivets.

Some of the debonded tear straps were also repaired in this second panel, as further required by the Boeing Service Bulletin. All debonded tear straps in the regions two stringer bays above and one stringer bay below the lap joint were re-attached using universal head rivets. Specific details of the debonded tear strap repair are described in the Boeing Service Bulletin [5].

Cracking was observed in the *middle* row of rivets in the lap joint 37,800 cycles *after* the terminating action had been applied. Figure 5 shows a photograph of cracks in the middle rivet row of the panel with the terminating action repair. Middle rivet row cracking was also observed during fatigue tests conducted on flat lap splice coupons [4]. In Reference [4], the effect of different lap joint design parameters on the formation of multiple cracking was investigated in the laboratory. Middle row cracking was not observed, however, until after substantial cracking had occurred in the upper row. In addition, middle row cracking in a fuselage lap splice was observed in the Aloha airplane, as reported in Reference [1].

The application of the terminating action appears to retard the rate of crack growth. Crack growth curves for the baseline panel are compared to those for the terminating action repair panel in Figure 6. The rate of middle row crack growth *after* the terminating action is about one-third of upper row crack growth rate without the terminating action. Table 2 compares crack growth rates from other sources of data as well.

Figure 7 shows the distribution of cracks observed in the middle rivet row during cycling of the panel. (For purposes of comparison, the scale for crack length in Figure 7 is different than Figure 2.) Cracking appears to be concentrated in the midbay areas with relatively few cracks over the tear straps. This distribution is in contrast to the fairly random distribution observed in the baseline test.

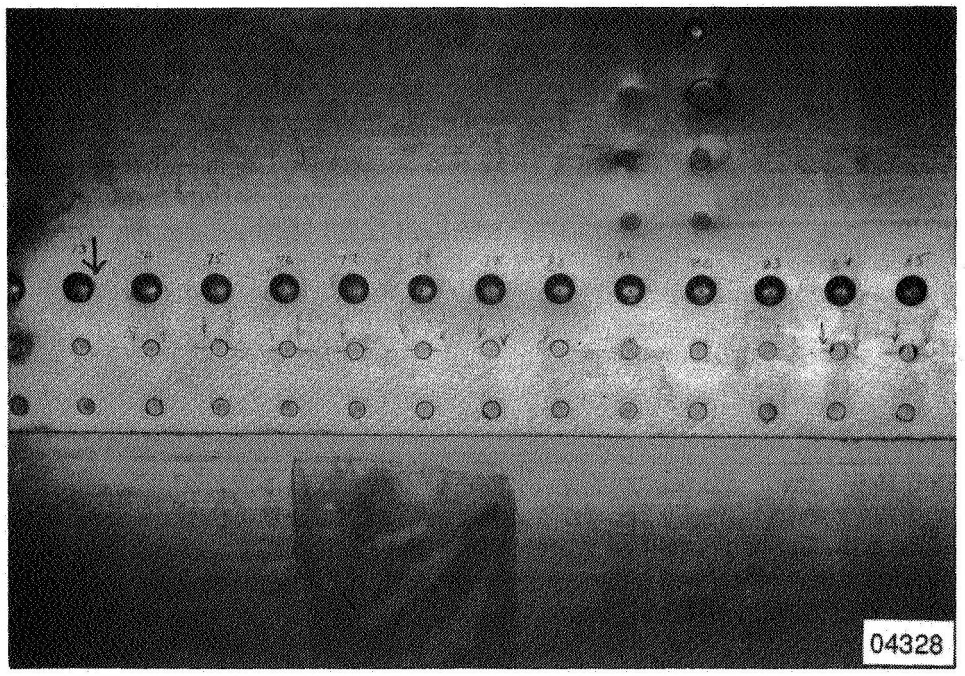

Figure 5. Middle rivet row cracking in terminating action repair test.

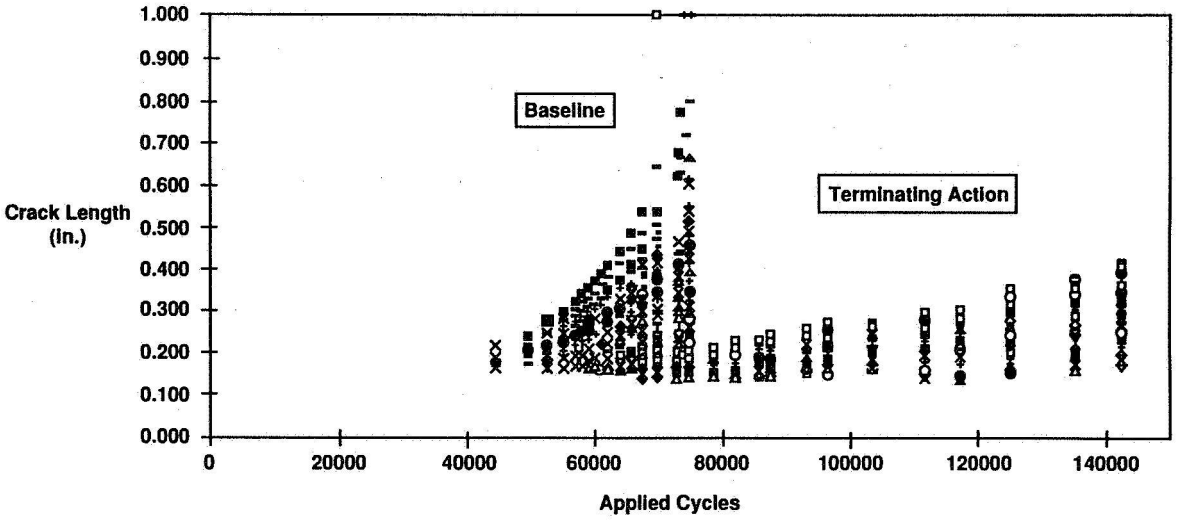

Figure 6. Crack growth rates observed during full-scale fatigue tests.

Table 2. Crack Propagation Rates from Different Sources

Data Source	Skin Thickness (in.)	Hoop Stress (ksi)	Range of Crack Propagation Rate (μin./cycle) 1	2	3	4	5	6	7	8	9
Baseline Test	0.036	17.7					▼				
Aloha 243	0.036	-					▼				
FAA POD Panel 1	0.040	15.9							▼		
FAA POD Panel 2	0.040	15.9						▼			
Terminating Action Test	0.036	17.7			▼						

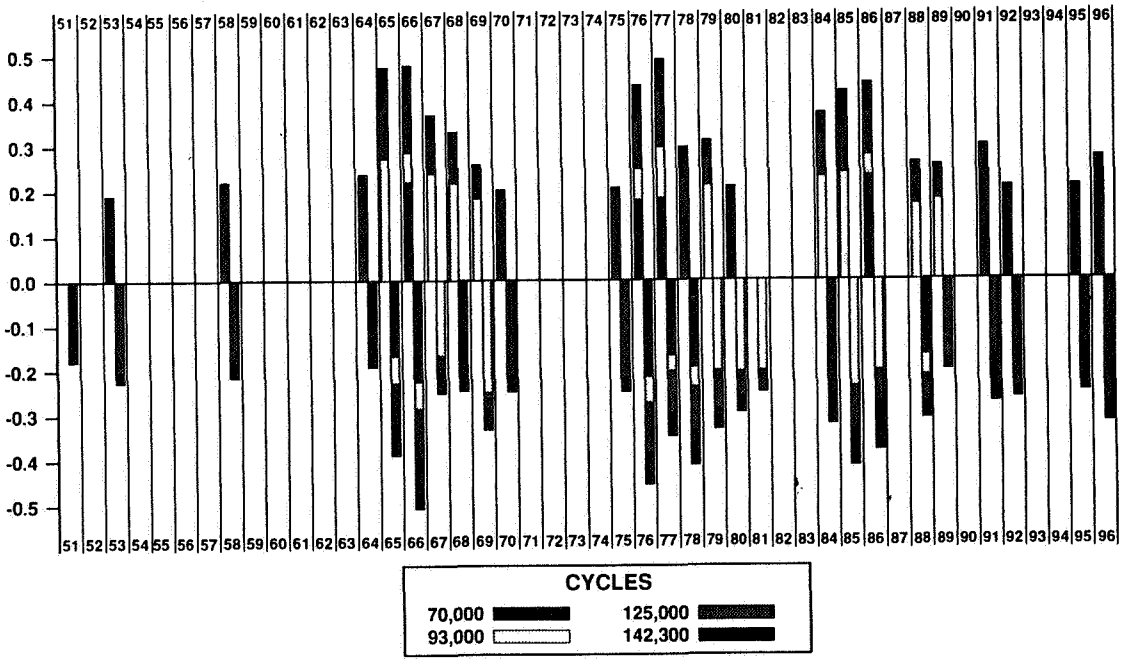

Figure 7. Distribution of cracks in middle rivet row in terminating action repair test.

Figure 8 shows the cumulative frequency of cracking in middle rivet row as a function of minimum crack length at 3 instances of time during the progression of the test. After 70,000 cycles, 17% of the rivets in the middle row had cracks greater than 0.2 inch in total length. At the termination of the test, 50% of the cracks had cracks greater than 0.30 inch.

The panel was fatigued for a total of 142,883 cycles. At that point, eighty-nine (89) cracks were found along the middle rivet row of the lap joint, but no linkup of cracks occurred. The longest of these cracks was measured to be 0.41 inch. The underside of the panel was inspected and no damage was found. Moreover, no cracks were detected in the upper row of rivets.

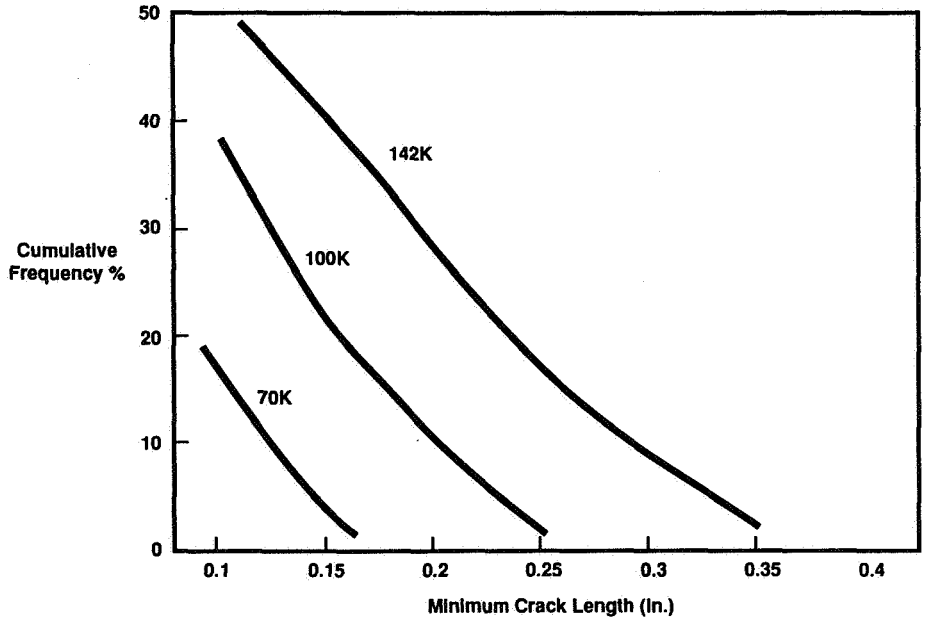

Figure 8. Cumulative frequency of cracking in terminating action repair test.

CONCLUSIONS

The results from two full-scale fatigue tests were reported in this paper. Based on the results from these tests, the following conclusions have been made.

(1) Field representative WFD can be generated and quantitatively studied in the laboratory. The fatigue life of a lap splice panel loaded to a pressure differential of 8.5 psi is approximately 75,000 cycles. The first linkup of multiple cracks occurs at about 92% of this life.

(2) The terminating action repair effectively eliminates cracking in the upper rivet row, and extends life by some margin.

(3) Middle rivet row cracking could be expected at about 37,800 cycles *after* the terminating action had been applied to an initially undamaged panel. Although this middle row cracking in the fuselage panels with terminating action would not result in a catastrophic structural failure, it will draw the attention of maintenance staff and call for repair action which can be expensive.

Acknowledgement - The research described in this paper was performed in support of the Federal Aviation Administration Technical Center's Aging Aircraft Research Program. The support and interest from Dr. Michael L. Basehore at FAATC is gratefully appreciated by the authors.

REFERENCES

[1] National Transportation Safety Board: Aircraft Accident Report - Aloha Airlines Flight 243, Boeing 737-200, N73711, Near Maui, Hawaii, April 28, 1988, NTSB/AAR-89/03, PB89-910404, June 1989.

[2] Samavedam, G.; and Hoadley, D.: Fracture and Fatigue Strength of Multiple Site Damaged Aircraft Fuselages - Curved Panel Testing and Analysis, Final Report, DOT/FAA/CT-94/10, DOT-VNTSC-FAA-93-8, January 1994.

[3] Samavedam, G.; Hoadley, D.; and Thomson, D.: Full-Scale Testing and Analysis of Curved Fuselage Panels, Final Report, DOT/FAA/CT-93/76, DOT-VNTSC-FAA-93-10, December 1993.

[4] Thomson, D.; Samavedam, G.; Hoadley, D.; and Jeong, D.Y.: Aircraft Fuselage Lap Joint Fatigue and Terminating Action Repair, Draft Final Report, August 1993.

[5] Boeing Service Bulletin No. 737-53A1039: Body Skin Lap Joint Inspection and Repair, Revision 3, August 20, 1987.

[6] Mayville, R.A.; and Sigelmann, M.: A Laboratory Study of Multiple Site Damage in Fuselage Lap Splices, Final Report, DOT/FAA/CT-93/74, DOT-VNTSC-FAA-93-12, December 1993.

FATIGUE LIFE UNTIL SMALL CRACKS IN AIRCRAFT STRUCTURES. DURABILITY AND DAMAGE TOLERANCE

J.Schijve
Delft University of Technology
Faculty of Aerospace Engineering
Kluyverweg 1, 2629 HS Delft, The Netherlands

SUMMARY

Crack initiation in notched elements occurs very early in the fatigue life. This is also true for riveted lap joints, an important fatigue critical element of a pressurized fuselage structure. Crack nucleation in a riveted lap joint can occur at different locations, depending on the riveting operation. It can occur at the edge of the rivet hole, at a small distance away from the hole, but still with subsequent crack growth through the hole, and ahead of the hole with a crack no longer passing through the hole. Moreover, crack nucleation can occur in the top row at the countersunk holes (outer sheet) or in the bottom row at the non-countersunk holes. Fractographic evidence is shown. The initial growth of the small cracks occurs as an (invisible) part through crack. As a consequence, predictions on the crack initiation life are problematic. After a through crack is present, the major part of the fatigue life has been consumed. There is still an apparent lack of empirical data on crack growth and residual strength of riveted lap joints, five years after the Aloha accident. Such data are very much necessary for further developments of prediction models. Some test results are presented.

INTRODUCTION

Small fatigue cracks are of considerable interest for aircraft structures in view of a number of practical reasons:

- In general aircraft structures are not designed for an infinite life but for a finite life in view of weight considerations. It implies that small cracks will be initiated in service, hopefully after a sufficiently long service life.
- A practical definition of the fatigue life in service is not the life until failure, but the life until a small fatigue crack can be detected. This life should be called the *crack initiation life*. Obviously, the crack initiation life will depend on possibilities for crack detection and inspection procedures.
- Predictions on the crack initiation life should be most useful as a design tool in view of a sufficient durability of the aircraft structure.

With the last argument we enter a controversial problem setting. In the literature on fatigue prediction problems, one approach is based on the prediction of the stress-strain history at the root of a notch. It is supposed to include such a difficulty as variable-amplitude loading. Since no theory can be

accepted without a proof by experimental evidence, a definition of the fatigue life is essential for the comparison between experiment and prediction. Usually this aspect is dealt with in a somewhat loose manner by assuming that predictions indicate some crack initiation life. It is tacitly assumed that the remaining crack growth life of a specimen will be rather short and can be ignored. In other words, the life until specimen failure is supposed to be approximately the crack initiation life. A weakness of several prediction models is that the large effect of material surface conditions on the crack initiation life is disregarded.

A second approach, which appears to be a more practical and safe conception, is based on assuming some small initial defect. The problem is then reduced to crack growth predictions for small cracks, starting from some very small initial defect. Fracture mechanics is supposed to be applicable. Two obvious questions are, what is the size of the initial defect, and what is the present state of the art of fracture mechanics, is it capable to predict the growth of very small cracks? The practical implication of these questions is not always realized. Small changes in the assumptions to be made can have a large quantitative effect on the predicted life. It is well known by now that small cracks can grow at ΔK levels significantly below the $\Delta K_{threshold}$ of large cracks. This observation can even be understood from a physical point of view, but it is of little help to arrive at accurate prediction methods for such small cracks.

In spite of the above observations, the aircraft industry is under pressure to give due attention to the crack initiation life. In the discussions between the industry, the airlines and the airworthiness authorities new life definitions have entered our jargon:

- operational life
- economical life
- crack free life
- threshold inspection

The arguments of the operators are evident. In view of reducing the operational costs, they want to spend very limited efforts on inspections for fatigue cracks. As a consequence, they highly prefer visible inspections, rather than more sophisticated inspection techniques. The aircraft industry can improve the fatigue quality of the aircraft structure. However, it will lead to a more expensive structure or to an increased weight. On the other hand, the aircraft industry wants to simplify the production of the structure to reduce the manufacturing costs, which can imply that stress allowables must be increased, or that more inspections in service are necessary.

In addition to conflicting economic arguments, safety aspects can also lead to controversial design options. In the arena of "durability" (economical aspect) and "damage tolerance" (safety aspect

with economical consequences), the airworthiness authorities should take care of safety aspects by developing suitable requirements to be met by both the aircraft industry and the airlines. In the past, safety requirements were changed and extended, when experience and improved understanding showed it to be necessary. It should be admitted that some milestone accidents have highly influenced our philosophy with respect to safety, durability and damage tolerance, see the table below.

	Accidents	Lessons learned
1954	Two Comet aircraft exploded at cruising altitude, due to fatigue cracks and insufficient life.	Full-scale tests are essential to reveal fatigue critical locations and to show sufficient life. Such tests should not be done on a structure used for static tests before.
1969	F-111 wing failure due to a material flaw, slightly extended by fatigue in a material with low fracture toughness	Damage tolerance design is essential. Fracture toughness is important.
1977	Lusaka accident. A 707 lost a stabilizer, due to an unknown fatigue crack.	"Geriatric" aircraft require additional inspection procedures.
1988	Aloha accident. A 737 lost a large part of the fuselage skin due to many fatigue cracks in lap joints.	Multiple-Site-Damage (MSD) in "aging" aircraft can lead to extensive aircraft damage.

Over the past decades our understanding of the fatigue phenomenon in materials and structures has considerably increased. Qualitatively, our knowledge seems to be quite good, but unfortunately that knowledge has also made it clear that quantitative predictions should be expected to have a limited accuracy. That is an important argument for requiring full-scale fatigue testing, which now is part of a recently proposed revision of FAR AC 25.571-1A (Oct. 19, 1993).

With respect to predicting the durability and damage tolerance properties of an aircraft structure, there are three different problems:

1. Prediction of fatigue life until a small crack is present, i.e. the crack initiation life.
2. Prediction of fatigue crack growth following the crack initiation life.
3. Prediction of the reduced strength by a growing fatigue crack in order to know when a critical failure situation can arise.

The problems involved are essentially different for these three categories. For the second and the third one, fatigue crack growth resistance and fracture toughness are essential material properties respectively. They are supposed to depend on the "bulk" behaviour of the material (and the thickness as well). However, crack initiation life is highly depending on the material surface conditions at the potential crack initiation location. The crack initiation resistance is not a bulk property, but rather a surface property. Although the local stress level is a function of the geometry of the structure, there are several most relevant surface conditions, such as: material roughness, fretting corrosion (in joints),

surface damage, residual stress in a surface layer, material quality and material defects in the surface layer. Those circumstances do not have such a significant effect on crack growth and residual strength. As a consequence, accurate predictions of the crack initiation life are still subjected to several uncertainties. This is especially true for joints, which unfortunately represent a major fatigue critical location in aging aircraft structures.

With the above general introduction in mind some more detailed attention will now be given to crack initiation and small cracks. More in particular, small cracks in riveted joints and related aspects of fatigue of lap joints in pressurized fuselages will be discussed.

CRACK INITIATION AND SMALL CRACKS

In the early sixties we made observations with binocular microscopes (30x) on small fatigue cracks in unnotched specimens and specimens with a central hole [1]. Tests were carried out under constant-amplitude loading (R≈0) at various S_{max}-values. The smallest crack that could be detected had a length in the order of 0.1 mm (0.004") (a length corresponding to 300 000 interatomic distances!). All cracks in the 2024-T3 specimens (bare sheet, t = 2 mm) were corner cracks. Results of central-hole specimens are shown in Fig.1. Instead of plotting the crack size ℓ as a function of cycles, ℓ is plotted as a function of the percentage of life until failure. A few observations can be made:

- After some 50% of the life small cracks were found. The results suggest that minute fatigue cracks must have been initiated early in the fatigue life.
- At low stress levels it takes a relatively larger period for cracks to be initiated. It indicates that there is a kind of a threshold stress level for crack initiation. This agrees with the definition of the fatigue limit as being the minimum cyclic stress level required to initiate a crack that will grow to failure.

In 1979 at an ICAF Symposium, Stone and Swift [2] reported on fractographic results of D.Y.Wang [3]. Flight-simulation tests with a severe cargo transport spectrum were carried out on 2024-T3 and 7075-T6 specimens (thickness 6.35 mm) with many open holes (diameter 6.35 mm). In the electron microscope (SEM) the most severe flights could be traced backwards. The crack growth curves clearly suggested immediate microcrack growth at the beginning of the fatigue life, starting with some initial flaw. The flaw was associated with either some kind of a tool marking or an intermetallic inclusion. The size of the flaws (EIFS = Equivalent Initial Flaw Size) was presented as a statistical distribution, see Fig.2. The average size was in the order of 20 μm. It was suggested by Stone and Swift, that the

prediction of the complete fatigue life may well be considered as a prediction of crack growth only.

A similar fractographic investigation (optical microscope) was reported in 1983 by Potter and Yee [4], for 7475-T7651 specimens with two 6.35 mm holes with a fastener installed. The specimens were loaded by some kind of a programmed fighter manoeuvre spectrum. Crack growth curves of 37 similarly loaded specimens are shown in fig.3. Microcracks started from inclusions, tool marks and other damage. The initial flaw for the results in Fig.3 corresponds to an average EIFS of about 8 μm.

The present problem of aging aircraft is associated with fatigue of riveted lap joints in pressurized fuselage structures. In view of predictions of crack initiation life and crack growth, it is of great interest to have similar evidence on crack nucleation in riveted lap joints. Unfortunately, at the time of the Aloha accident, the available evidence was rather limited. In an older report (1963) by Walter Schütz [5], three crack growth curves were presented obtained in a large test program on riveted lap joints. They are reproduced in Fig.4.[a] In spite of the limited evidence, the crack growth curves illustrate two important aspects for fatigue of riveted lap joints:

- The crack initiation life is by far the major part of the fatigue life.
- After a crack became visible, the remaining life until specimen failure was relatively short. It implies that visible crack growth to cause ligament failure between the rivets covered a relatively small part of the life.

At the time of the Aloha accident, information on crack initiation in riveted joints was not collected systematically for the purpose of safety considerations. The effect of fatigue cracks on the residual strength of a lap joint was unknown. Actually empirical evidence on these issues is still rather scant more than 5 years after the Aloha accident.

SMALL CRACKS IN RIVETED LAP JOINTS

In my paper at the International Workshop on Structural Integrity of Aging Aircraft I have collected information on the failure modes of riveted joints [6]. Some useful descriptions were available from older reports. Moreover, riveted lap joint specimens tested in our laboratory by students were still available for examination. Pictures of characteristic fracture surfaces are shown in Fig.5.

Fig.5a shows the characteristic appearance of fatigue crack nuclei at both sides of a countersunk rivet. Crack initiation started at the edge of the rivet hole because of the local stress concentration. However, fretting corrosion will have contributed, due to fretting between either the two

---

[a] For a long time Schütz's data were the only results which I could find in the literature. Most probably, there is more in test reports of the aircraft industry, but unfortunately those are not published.

sheets or between the rivet shank and the wall of the rivet hole. Moreover, secondary bending, which can be quite high at the first rivet row, will also contribute to crack initiation.

Fig.5b shows crack nucleation in the sheet material away from the rivet hole. This is a consequence of improved clamping, obtained by a more intensive squeezing of the rivets (higher squeeze force). It was recently shown by Slagter [7] that plastic deformation of the rivet and the sheet material, during the riveting operation, can leave residual tensile stress in the circumferential direction around the hole at a short distance of the edge of the hole. This residual stress, the improved filling of the rivet hole and the increased clamping, will remove the critical location from the edge of the hole.

Fig.5c shows a fatigue crack, which does no longer grow through the hole, but instead propagates around the hole This is the result of a still further increased clamping of the rivet. Apparently, the material around the rivet hole, together with the rivet itself, is now acting as a single continuous piece of material. The maximum stress concentration then occurs ahead of the rivet head, where secondary bending and fretting corrosion will cooperate to initiate fatigue crack nuclei. If this type of cracking occurs, more adjacent crack nuclei are created, which usually leads to a rough crack surface when the nuclei overlap, see Fig.5c. Crack growth around the rivet hole was found by Hartman [8] for huckbolt fasteners, which are known for a high clamping force.

Another typical and important feature of fatigue crack nuclei in riveted lap joints is that the cracks start as part-through cracks at the mating surfaces. It takes some time before the cracks have penetrated through the full sheet thickness. It is exactly for that reason that small cracks in riveted joints are invisible for a large part of the fatigue life. After breakthrough of the crack to the outer surface of the sheet, it rapidly becomes a crack with a length that is no longer small as compared to the rivet pitch. That explains why the visible crack growth period in Fig.4 was relatively short.

The significance of part-through cracks has recently been emphasized in test series carried out by Soetikno [9,10]. He interrupted fatigue tests after $nx10^5$ cycles for a static test until failure (n = 1,2,3,etc.). The purpose of the tests was to measure the decrease of the residual strength as a function of the previous fatigue loading. At the same time, the size and the shape of the fatigue cracks could be determined after the static tests. The fracture surfaces in Fig.6 clearly confirm the original part through character of the crack nuclei. Small crack nuclei could already be observed after 100 kc, which is about 20% of the fatigue life until failure. The initial reduction of the static strength is limited, but when linking up of cracks is imminent, the strength is rapidly decreasing. The same figure

also shows residual strength results for a GLARE 3 riveted joint, based on 2024-T3 (3/2 lay-up)[a]. In this fiber-metal laminate (thickness 1.4 mm as compared to 1.6 mm for the 2024-T3 specimens; the GLARE specimens were 21% lighter) fatigue cracks for a long time occurred in one of the three layers only, which explains the superior residual strength behaviour.

Another complication of riveted lap joints should be mentioned here. In a lap joint with two or more rows of rivets, there are two fatigue critical rows, the outer rows, see sketch. The upper sheet is fatigue critical in the top row with the countersunk holes. In several tests on riveted lap joints failure occurred in this row. The lower sheet is critical in the bottom row at the non-countersunk holes. Fatigue cracks have been found in the bottom row, both in service and in specimens. Fig.7 shows some small fatigue cracks in the bottom row of a specimen that failed in the top row. Apparently, the bottom row was less critical, but not non-critical. Müller recently observed a tendency for cracking at the bottom row with the non-countersunk holes [13], if riveting is done more intensively (e.g. by a higher squeeze force, which increases the fatigue life considerably).

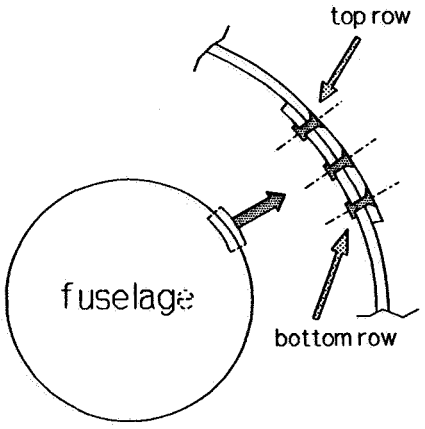

FATIGUE OF RIVETED LAP JOINTS IN PRESSURIZED FUSELAGES

Fatigue cracks in riveted lap joints of pressurized fuselages have occurred in service, but also in full-scale fatigue tests, including extensive cracking with significant decompression failures. The classical case is the Aloha accident. In view of monitoring crack growth, it is extremely important whether such cracks occur in the top row or in the bottom row. If it occurs in the top row, visual inspections can be sufficient. If it occurs in the bottom row, a visual inspection can only be made during a major overhaul (D-check). Improved riveting can increase the fatigue life, and thus alleviate the MSD problem, but instead of the top row being fatigue critical, it is possible that the bottom row becomes fatigue critical. *The paradoxical question is whether we prefer the longer fatigue life at the cost of an inferior detectability?*

---

[a] GLARE 3 is one type of the new fiber-metal laminates developed for high fatigue resistance [11,12]. The fiber-metal laminates are built up of thin Al-alloy layers with intermediate unidirectional fiber layers in an adhesive as a matrix. GLARE 3 has fiber layers in two perpendicular directions for application as fuselage skin material.

As pointed out in [6], the analysis of fracture surfaces of riveted lap joint specimens very often shows fatigue cracks at many rivets. Examples were already shown in Fig.6. Several other examples are documented in [13,14]. In other words, multiple-site damage (MSD) seems to be a normal pattern for riveted lap joints, if loaded under constant-amplitude fatigue loading (R=0). Actually, this is not a surprising behaviour. If the life is finite, crack initiation at a rivet hole is not a problem, it will occur. A conclusion postulated in [26] is: *If the fatigue life of a riveted lap joint is limited, cracks will occur at many rivets in the same row, and a potential MSD problem is present.* A practical problem is that cracks can remain small and hidden for quite a long time. As a consequence, there will be several small cracks in one row. In our laboratory Müller [13] carried out cyclic pressurization tests in a small barrel test set up (diameter 1200 mm). He also found MSD in a longitudinal lap joint of the biaxially loaded cylindrical specimen. At the ends of the cylinder (length 420 mm) the hoop stress was lower, due to the steel pressure bulkheads. As a result, cracks did not occur at the last few rivets close to the ends of the specimen, but they were found at all other rivet holes.

A similar phenomenon occurs in a pressurized fuselage. Due to pillowing of the skin (Fig.8), the hoop stress distribution in a fuselage is inhomogeneous with a lower hoop stress at the frames and a higher hoop stress between the frames. The inhomogeneity is caused by the restraint on radial expansion of the skin at the connections to the frame. The variation depends on the stiffness of the skin/frame connection. Differences of about 25% are mentioned in [15], but for a low stiffness skin/frame connection it may be lower. Mayville and Warren [16] refer to MSD found in an aging 727 aircraft with multiple cracks in three bays between the frames, but no cracks at rivet holes at the frame location, see the results in Fig.9. Similar crack patterns were predicted by a computer model developed by Broek [17].

Interesting results were published by Goranson and Miller [18,19], Gopinath [20] and Maclin [21] obtained in fatigue tests on two old fuselages of Boeing aircraft, purchased by Boeing from the airlines; viz., a 737 fuselage (59,000 pressure cycles in service) and a 747-100 fuselage (20,000 pressure cycles in service). A new 747-400 forward fuselage (new) was also tested to check redesigned parts of the structure. Small cracks in the lap joints were found in the 737 fuselage after 79,000 flights ($\approx$ 24 years). Linking up of cracks occurred at a later stage, with a decompression failure (flapping, total crack length $\approx$ 0.8 m) at 100,600 flights ($\approx$ 30 years). In the 747-100 cracks in some lap joints occurred after $\approx$ 30,000 flights onwards, with linking up at only one location before the test was stopped at 40,000 flights. In the new 747-400 forward fuselage cracks were detected from 33,500 pressure cycles onwards, with some linking up after an additional 10,000 to 20,000 cycles. By the end

of the test (60,000 flights) the largest crack was about 0.48 m with some cracking in an adjacent bay, but without any unstable crack extension. The tests confirmed that the cracks started predominantly at rivets midway between the frames, due to a higher hoop stress (fuselage pillowing). However, the most important finding was that the damage development was rather slow in terms of crack growth per year. It thus should be possible to detect the cracks during scheduled inspections. Probably not everybody will be prepared to generalize this conclusion. There is at least one good reason for some concern. In the Boeing tests the crack occurred in the top row, where crack detection is relatively easy. However, if cracks initiate in the bottom row, the inner sheet is critical. As said before, visual inspection then is rather problematic.

A second matter of concern has been indicated by Swift [22] and Broek [23,24], and it was emphasized again by Swift [25] in the aging aircraft meeting in Hamburg last year. It is the problem that MSD can lead to a significantly reduced crack arrest capability of the structure. Crack arrest is necessary if large incidental damage occurs (rotor burst) or if inspection is extremely poor.

The above references were discussed in some detail in [26]. It appears that some remarkable inconsistencies are entering our philosophy on durability and damage tolerance of pressurized fuselages. In general inhomogeneous stress distributions are considered to be uneconomical, and also in this case it was not the aim of the designer. It was simply unavoidable. However, thanks to the inhomogeneity, fatigue cracks in the lap joints start between the frames, and not all together along the entire longitudinal lap splices. *The paradox is that an inhomogeneous hoop stress distribution will be favourable for safe crack detection, i.e. for damage tolerance.*

Another controversial aspect is offered by the tear straps. High strength and stiff crack stoppers should prevent extensive multi-bay crack extension. However, it is a kind of an "emergency" solution, which should not make us happy. Moreover, effective crack stopper straps will amplify the inhomogeneity of the hoop stress distribution[a]. The production shop anyhow dislikes tear straps because it implies a more complex and costly production. *The paradox is that a structure without tear straps, and with a more homogeneous hoop stress distribution, can lead to an increased durability at the cost of less damage tolerance.* Or the complementary paradox: *The crack stopper bands as a medicine can make the MSD-illness acceptable, if not stimulate it.*

---

[a] It is noteworthy that the tear strap designs of several aircraft industries are all different with respect to material (2024-T3, Ti-6Al-4V), the connection to the skin (riveted, bonded), location of the straps (at the frames, between the frames), and the extent of the straps (full circumferential straps, local patches at the longitudinal lap joints, and no straps at all).

SUMMARY AND CONCLUSIONS

In the previous chapters observations on crack initiation and initial crack growth in riveted lap joints were discussed. It has led to the following conclusions:

Observations

1 Crack nucleation can occur at several locations around the rivet hole, at the edge of the hole, and away from the hole. In the latter case the crack initiation life is usually superior. Crack nucleation quite often occurs in the critical row with countersunk holes (top row), but it can also occur in the bottom row at the non-countersunk holes.

2 The occurrence of MSD in riveted lap joints under constant-amplitude loading is a normal cracking pattern, that should be expected, also under biaxial load conditions.

3 Small cracks initially grow as part through cracks, either in some quarter-elliptical shape from the edge of the hole, or in a semi-elliptical shape away from the hole. These cracks are still invisible. Only after penetrating the sheet thickness the cracks can be detected visibly.

4 In a lap joint the top row with countersunk rivets may be more fatigue critical than the bottom row, but the bottom row can also be critical. Even if the top row is critical, the bottom row is not necessarily non-critical.

Predictions

5 Predictions of the crack initiation life on the basis of material properties are not realistic. Fatigue data of riveted joints have to be used.

6 Prediction models for the propagation of through cracks in a riveted lap joint are now developed. Unfortunately, the empirical verification is still very limited due to the lack of crack growth data from riveted lap joints.

7 Prediction on the residual strength of riveted lap joints with MSD is another problem of current interest. Also in this case available evidence is quite limited. Curves as shown in Fig.6 (strength reduction during the fatigue life) are extremely scarce, although such a curve is frequently used in papers on Damage Tolerance Principles, however, without having test results available.

Design aspects

8 An inhomogeneous hoop stress distribution with a maximum between the frames is favourable for damage tolerance (more time for crack detection), but unfavourable for durability (shorter crack initiation life).

9 The nature of tear straps is an emergency design for the case that large cracks occur. The straps can indeed be favourable for the damage tolerance behaviour, while they can also be

favourable to achieve flapping as a final failure mode. They are undesirable from a production point of view.

10 The escape from the controversial issues mentioned in 8 and 9 is to design for fully avoiding the occurrence of MSD, i.e. to design for a sufficiently long crack initiation life, in other words lap joints, which will not become fatigue critical during the operational life of the aircraft.

Recommendations

11 The lack of experimental data on crack growth and residual strength, more than 5 years after the Aloha accident, is surprising. There is indeed a great need for systematic experimental investigations on these issues. For the growth of small cracks some kind of marker loads should be used.

REFERENCES

[1] Schijve,J. and Jacobs,F.A., Fatigue Crack Propagation in Unnotched and Notched Aluminium Specimens. National Aerospace Laboratory, TR-2128, Amsterdam, May 1964.

[2] Stone,M. and Swift,T., Future damage tolerance approach to airworthiness certification. 10th ICAF Symposium, Brussels, 1979, paper 2.9.

[3] Wang,D.Y., A study of small crack growth under transport spectrum loading. AGARD-CP-328, paper 14, 1983. Shorter version in ASTM STP 761, 1982, pp.191-211.

[4] Potter,J.M. and Yee,B.G.W., Use of small crack data to bring about and quantify improvements to aircraft structural integrity. AGARD-CP-328, Paper 4, 1983.

[5] Schütz,W., Zeitfestigkeit einschnittiger Leichtmetall-Nietverbindungen. LBF, Bericht Nr.F-47, 1963.

[6] Schijve,J., Multiple-Site-Damage fatigue of riveted joints. Durability of Metal Aircraft Structures. Proc. of the Int. Workshop Structural Integrity of Aging Airplanes. Atlanta, 31 Mar.-2 April, 1992, pp.2-27. Also: Fac.Aerospace Eng.,Report LR-679, Delft 1992.

[7] Slagter,W.J., Static strength of riveted joints in fibre metal laminates. Doctor thesis, Delft University of Technology, 25 April 1994.

[8] Hartman,A., Jacobs,F.A. and van der Vet,W.J., Constant load amplitude and programme fatigue tests on single lap joints in Clad 2024-T3 and 7075-T6 aluminium alloy with two rows of rivets or huckbolts. Nat.Aerospace Lab. NLR, TN M.2147, 1965.

[9] Soetikno,T.P., Residual strength of the fatigued 3 rows riveted GLARE3 longitudinal joint. Master thesis, Faculty of Aerospace Eng., Delft, May 1992.

[10] Schijve,J., Fatigue of riveted lap joints of GLARE 3. Fac.Aerospace Eng., LR-Doc. b2-93-6, Delft, 6 Dec.1993.

[11] Gunnink,J.W., Vogelesang,L.B. and Schijve,J., Application of a new hybrid material (ARALL) in aircraft structures. Proc. 13th I.C.A.S. Congress, August 1982.

[12] Gunnink,J.W.and Vogelesang,L.B., Metal Laminates - The Advancements in Aircraft Materials. Conf. Advanced Materials, 35th Int. SAMPE Symposium, Anaheim, April 1990

[13] Müller,R., Fatigue crack initiation in riveted lap joints and in pressurized fuselages. SAMPE European Conference, Birmingham, 19-21 October 1993. Report LR-725, Delft Un. of Tech.,

Fac. of Aerospace Eng., 1993.

[14] Wit,G., MSD in fuselage lap joints. Report LR-697, Delft Un. of Tech., Fac. of Aerospace Eng., July 1992.

[15] Molent,L. and Jones,R.: Crack growth and repair of multi-site damage of fuselage lap joints. Eng.Fracture Mech., Vol.44, 1993, pp.627-637.

[16] Mayville,R.A. and Warren,T.J.: A laboratory study of fracture in the presence of lap splice multiple site damage. Structural Integrity of Aging Airplanes, Springer Verlag, Berlin 1990, pp.263-273.

[17] Sampath,S. and Broek,D.: Estimation of requirements of inspection intervals for panels susceptible to multiple site damage. Structural Integrity of Aging Aircraft. Springer Verlag, Berlin, 1991, pp.339-389.

[18] Goranson,U.G. and Miller,M., Aging jet transport structural evaluation programs. Proc. 15th ICAF Symp.,Jerusalem, 1989, EMAS Warley, 1989, pp.319-351.

[19] Goranson,U.G., Continuous airworthiness of aging jet transports. Proc.2nd Int.Conf. Aging Aircraft, Baltimore, Oct.1989. FAA, U.S. Dept. of Transportation, 1990, pp.61-89.1990.

[20] Gopinath,K.V., Structural Airworthiness of Aging Boeing Jet Transports - 747 Fuselage Fatigue Test Program. 1992 Aerospace Design Conference, Feb.3-6, Irvine, 1992. AIAA 92-1128.

[21] Maclin,J.R., Performance of fuselage pressure structure. Paper 3rd Int.Conf. on Aging Aircraft and Structural Airworthiness. Washington,D.C., 19-21 Nov.,1991.

[22] Swift,T.: Damage tolerance capability. Fatigue of Aircraft Materials. Proc. Specialists Conference, Delft, 14-15 Oct.1992. Delft University Press 1992, pp.351-387.

[23] Broek,D.: Fatigue and damage tolerance, the Schijve era and beyond. Fatigue of Aircraft Materials. Proc. Specialists Conference, Delft, 14-15 Oct.1992. Delft University Press 1992, pp.19-41.

[24] Broek,D.: The effects of multiple-site-damage on the arrest capability of aircraft fuselage structures. FractuREsearch TR 9302, June 1993

[25] Swift,T.: Widespread fatigue damage monitoring issues and concerns. Paper 5th Int. Conf. on Structural Airworthiness of New and Aging Aircraft. Hamburg, 16-18 June, 1993

[26] Schijve,J., Multiple-site damage in aircraft fuselage structures. Faculty of Aerospace Engineering, Report LR-729, Delft, July 1993.

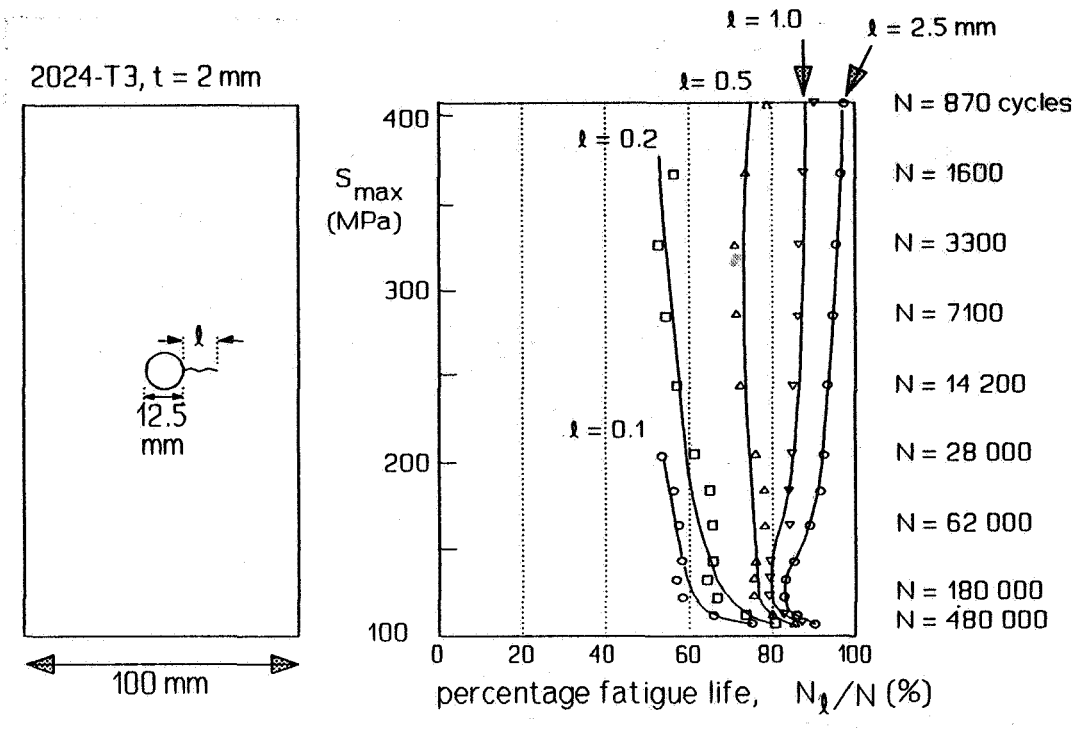

Fig.1 Small cracks in an open hole specimen [1]. Microscopical surface observations.

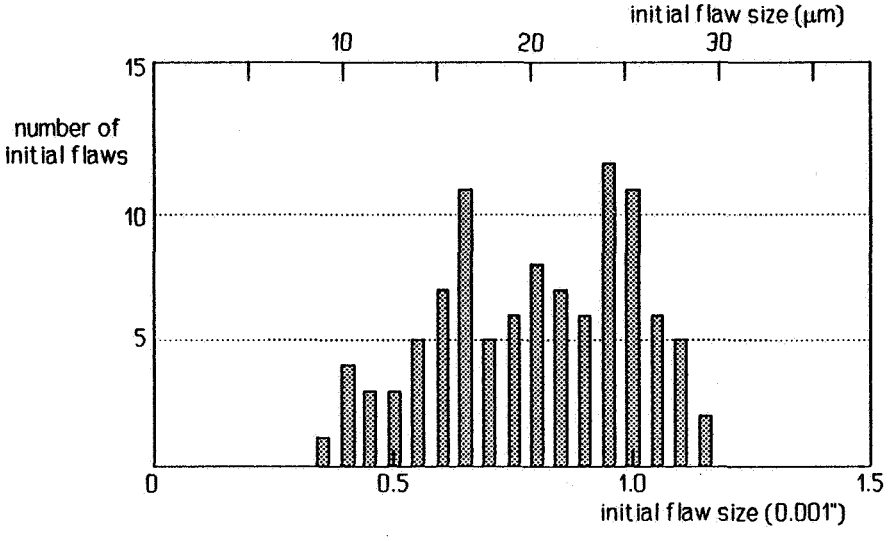

Fig.2 Equivalent initial flaw sizes observed in flight-simulation tested 2024-T3 specimens [2].

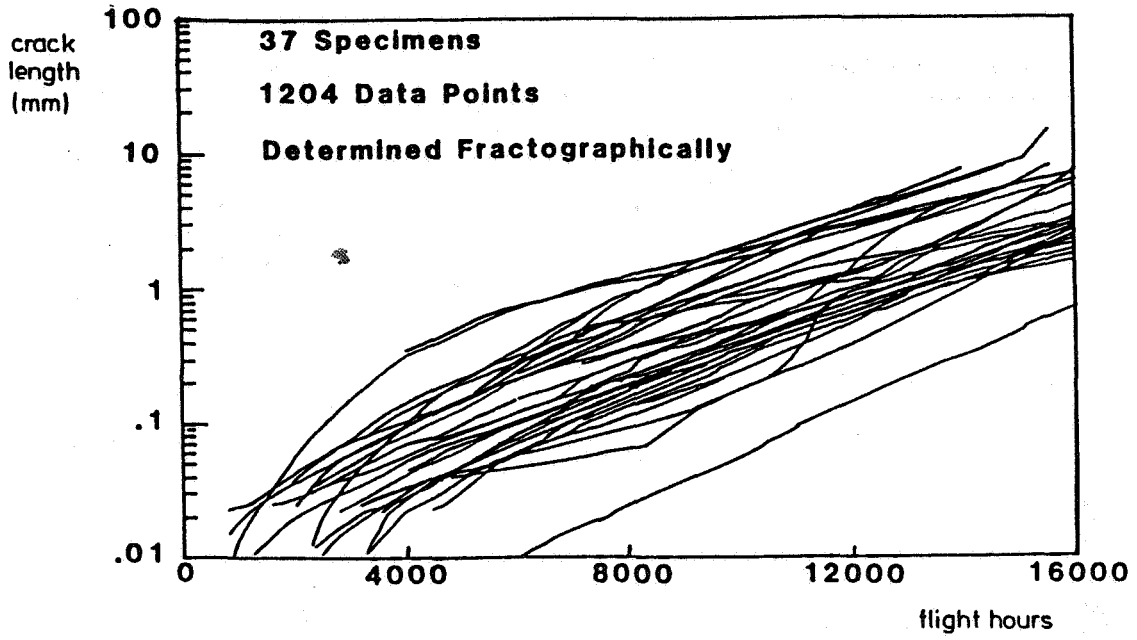

Fig.3 Crack growth curves of small cracks in service simulation test (manouevre spectrum) as derived from fractographic observations [4].

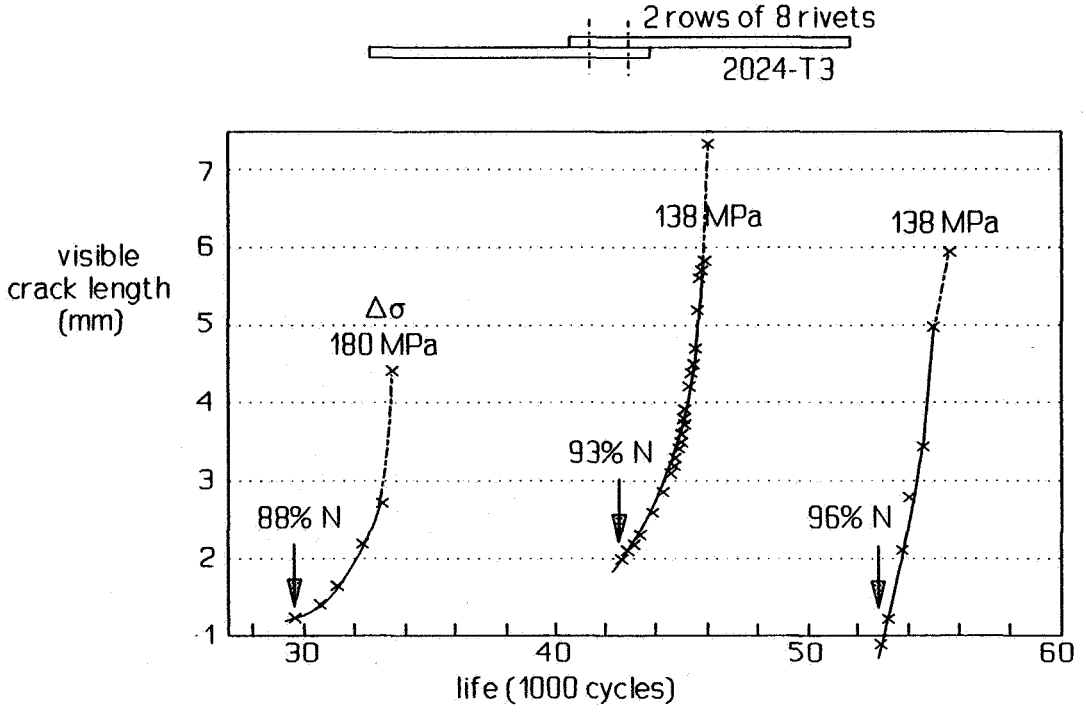

Fig.4 Crack growth curves for riveted lap joints obtained by Schütz [5].

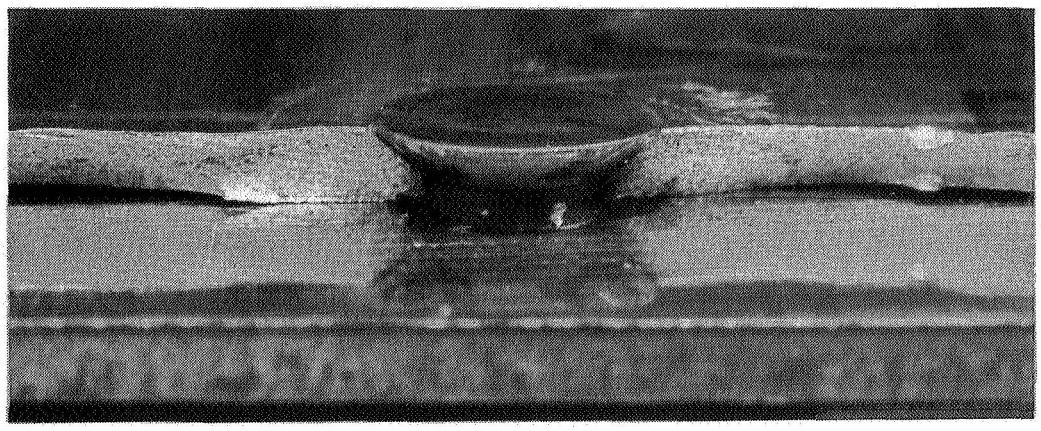

Fig. 5a Cracks at both sides of a countersunk hole.

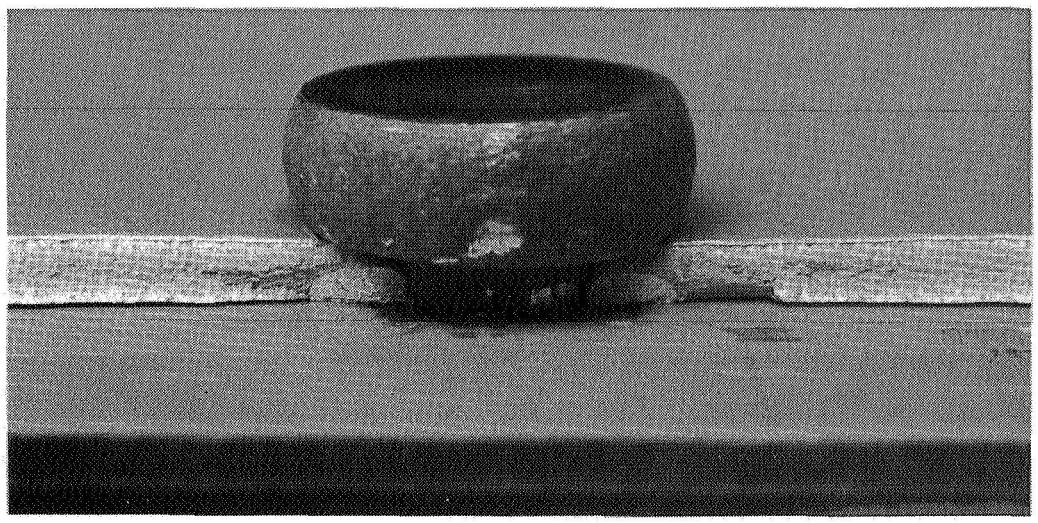

Fig. 5b Semi-elliptical crack nuclei, initiated away from the rivet.

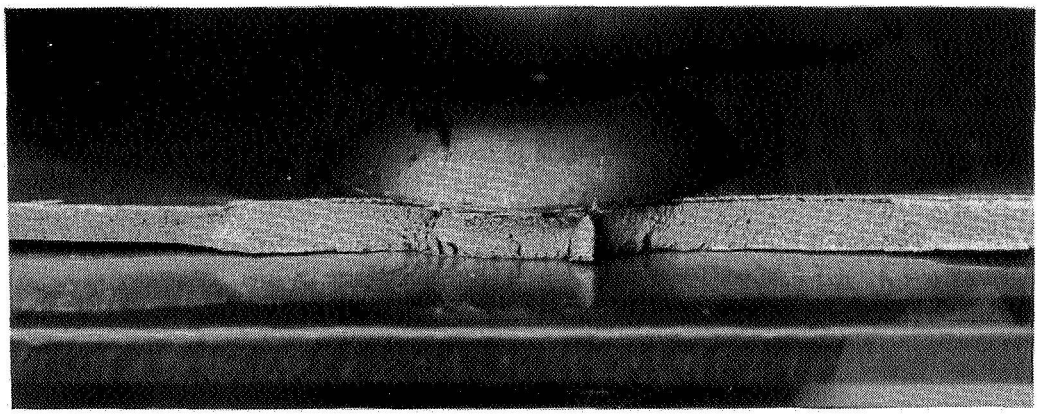

Fig. 5c Cracks started ahead of the rivet. Crack path no longer through the hole (good clamping).

Fig.5 Different types of fatigue crack nuclei in riveted joints [6].

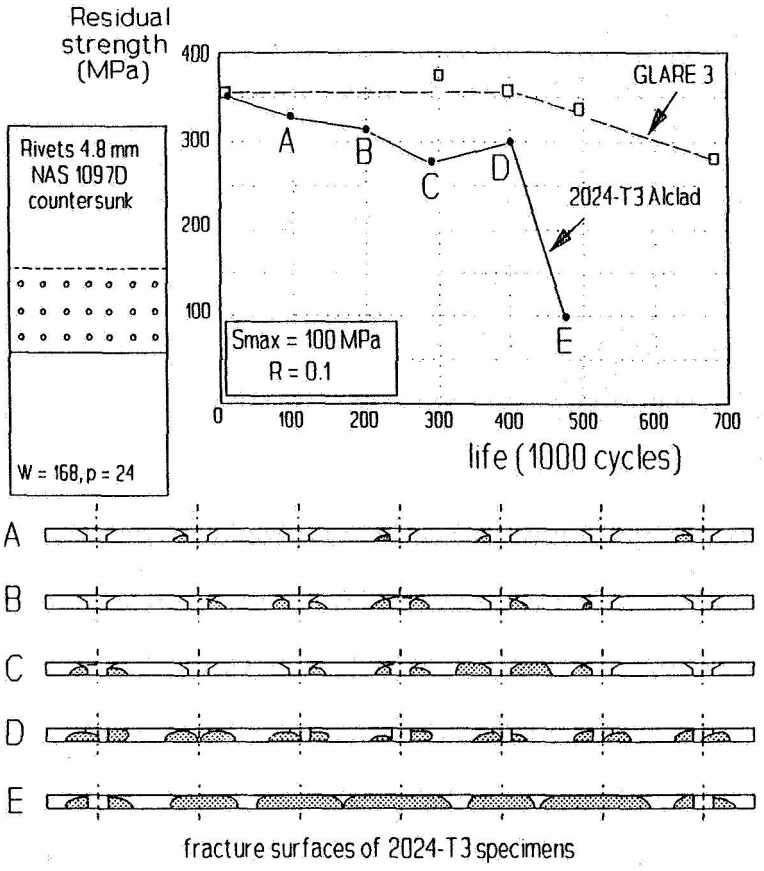

Fig.6 Reduction of static strength of a riveted lap joint due to fatigue. Results for 2024-T3 Alclad (t = 1.6 mm) and GLARE 3 (t = 1.4 mm) based on 2024-T3 [9,10].

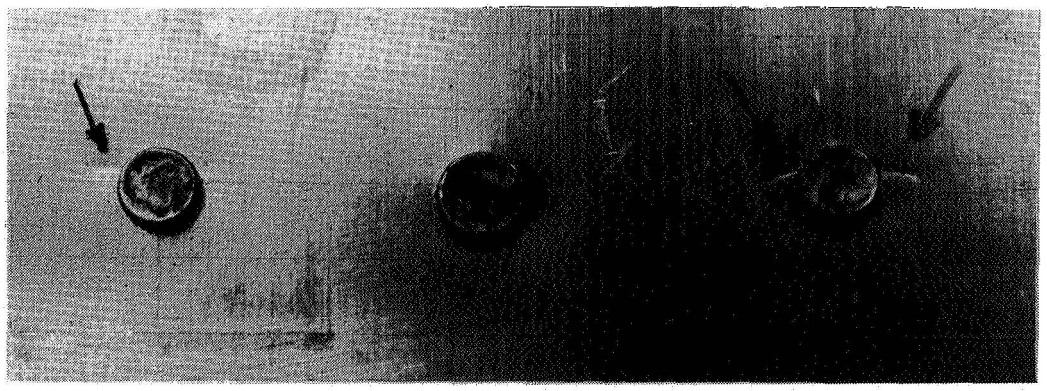

Fig.7 Small cracks at non-countersunk rivet row. These cracks were present after failure occurred at the other critical row with countersunk rivets. (2024-T3 Alclad, t = 1 mm, 3 rows of 7 rivets, d = 3.2 mm, S_{max} = 106 MPa, R = 0, N = 182000 cycles).

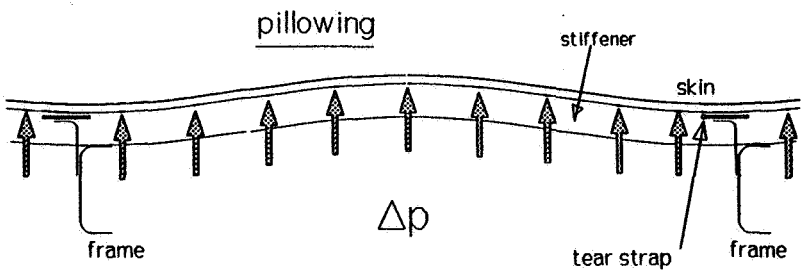

Fig. 8 Pillowing of an aircraft fuselage.

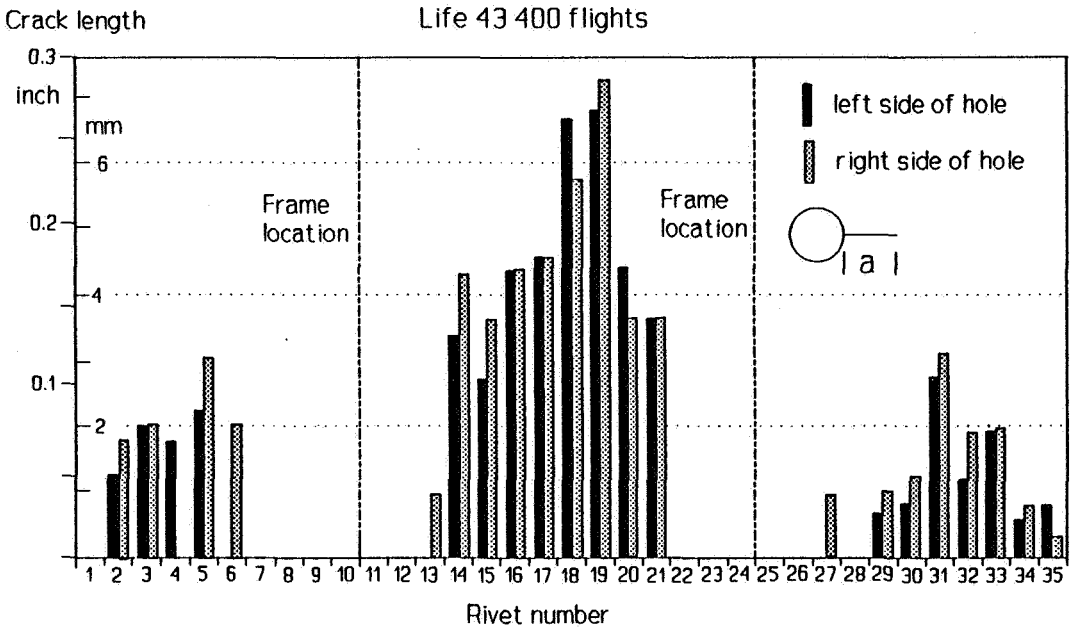

Fig.9 Fatigue cracks in a riveted lap joint of an aging 727 fuselage [14]

Development of Load Spectra for Airbus A330/A340 Full Scale Fatigue Tests

N95-19479

H.–J. Schmidt and Th. Nielsen
Fatigue and Fracture Mechanics Department

Deutsche Aerospace Airbus GmbH, Hamburg, Germany

113063

359243

P. 15

Summary

For substantiation of the recently certified medium range Airbus A330 and long range A340 the full scale fatigue tests are in progress. The airframe structures of both aircraft types are tested by one set of A340 specimens.

The development of the fatigue test spectra for the two major test specimens which are the center fuselage and wing test and the rear fuselage test is described. The applied test load spectra allow a realistic simulation of flight, ground and pressurization loads and the finalization of the tests within the pre–defined test period.

The paper contains details about the 1g and incremental flight and ground loads and the establishment of the flight–by–flight test program, i.e. the definition of flight types, distribution of loads within the flights and randomization of flight types in repeated blocks. Special attention is given to procedures applied for acceleration of the tests, e.g. omission of lower spectrum loads and a general increase of all loads by ten percent.

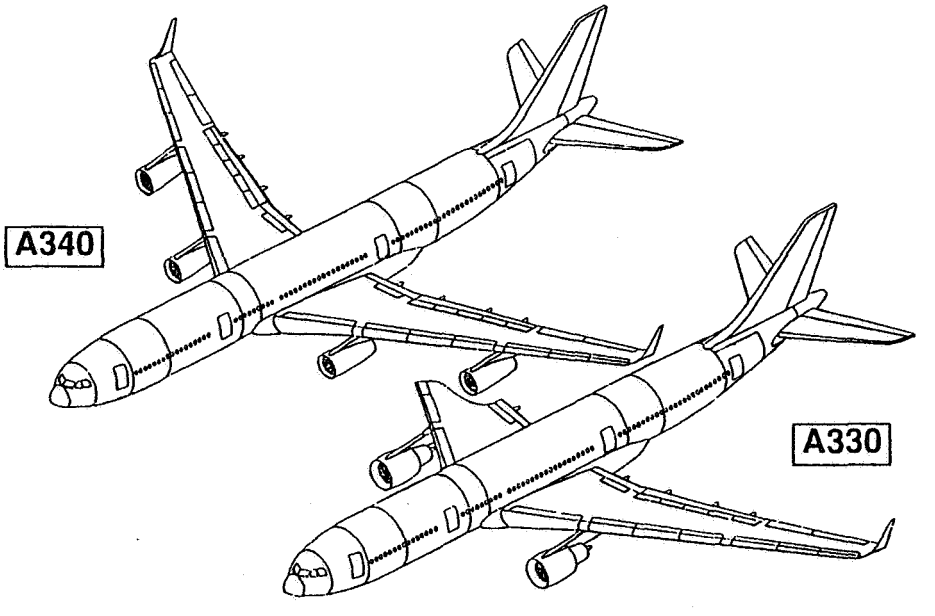

Fig. 1 Airbus aircraft.

1. Introduction

The newest Airbus products, the medium range A330 and the long range A340 have been certified in 1992 and 1993, respectively. The structure of both aircraft types is very similar (Fig. 1). However, the A340 is equipped with 4 engines with a maximum thrust of 130.000 lbs and the A330 with 2 engines with a maximum thrust of 136.000 lbs. Furthermore the A340 contains a center undercarriage in addition. With respect to this similarity both aircraft types are justified by one set of specimens using the A340–300 structure for the multi–section full scale fatigue test. Four major specimens are tested which are the forward fuselage, the center fuselage and wing, the rear fuselage and the horizontal tailplane.

The development of the load spectra for the two major tests, i.e. center fuselage and wing test and rear fuselage test, is described. These load spectra allow a realistic simulation of all flight, ground and pressurization loads to achieve the most accurate prediction of the fatigue and damage tolerance behavior. The major differences between A330 and A340 regarding design service goals, mission profiles and resulting external loads are considered.

2. Operational Conditions and Representation

All Airbus aircraft are designed for an in–service life of more than 20 years. With respect to earlier Airbus experience and the customers' requirements typical A330 and A340 mission profiles have been defined which were the basis for type certification and have been used for test load spectra definition, see Fig. 2. The typical A330 mission contains an average block time of 90 min. and an operation altitude of 35.000 ft. For A340 two typical mission profiles are defined, i.e. a short range mission with 75 min./35.000 ft and a medium range mission with 405 min./39.000 ft. With respect to the planned service time of more than 20 years the design service goals are 40 000 flights for the A330 and 20 000 flights for the A340; the latter figure consists of 10 000 short range plus 10 000 medium range flights.
Since the real operation may deviate from the typical mission profiles the fatigue and damage tolerance behavior of additional mission profiles will be evaluated to allow an adaptation of the structural inspection program.

65 percent payload fatigue mission			
units	A330 SR	A340 SR	A340 MR
flight time [min]	90	75	405
distance [nm]	500	380	2960
max. alt. [ft]	35000	35000	39000

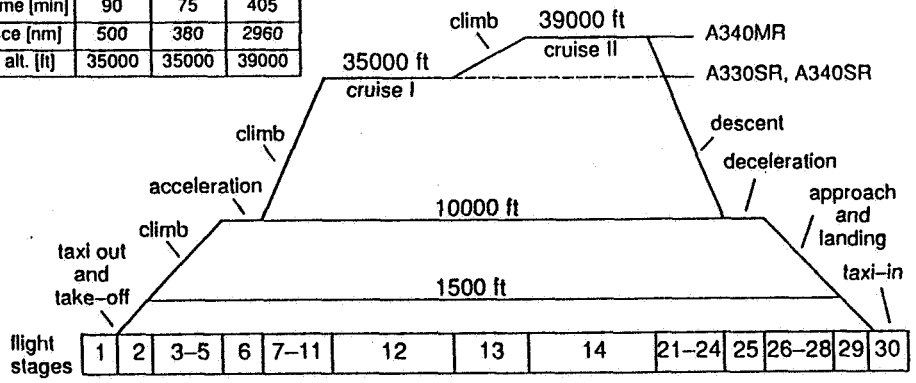

Fig. 2 Mission profiles.

The mission profiles have been divided in more than 30 flight stages for which all relevant flight and ground loads and the corresponding internal pressure have been determined, see. Fig. 3. The splitting of the structure in more than one test specimen allows an optimized representation of the operational loads by consideration of their effect on the fatigue and damage tolerance behavior. Insignificant load cases are deleted for one or the other test specimen which saves test time for the exact representation of the significant load cases.

The major differences between the center fuselage and wing test compared with the rear fuselage test are the representation of the lateral gusts and lateral and vertical manoeuvre which are only applied to the rear fuselage specimen. On the other side the ground loads for the rear fuselage specimen are limited to taxi–in and taxi–out, take off, landing run and touch down.

This approach has been used for all previous Airbus full scale fatigue tests and the correctness is confirmed by the in–service experience.

operational basic condition	loading component	centre fuselage / wing	rear fuselage	representation
standing		X	X	steady case
taxi–out		X	X	two cycles per flight
preflight braking		X	–	one cycle per flight
ground turning		X	–	two cycles per flight
take–off run		X	X	two cycles per flight
rotation		X	X	steady case
initial climb	vertical gust	X	X	stepped spectra
climb	vertical manoeuvre	–	X	stepped spectra
cruise I	lateral gust	–	X	stepped spectra
cruise II	lateral manoeuvre	–	X	stepped spectra
initial descent	Δp	X	X	stepped spectra
descent	temperature loads	–	X	stepped spectra
approach				
touch down		X	X	one cycle per flight
landing roll		X	X	two cycles per flight
braking		X	–	one cycle per flight
ground turning		X	–	two cycles per flight
taxi–in		X	X	two cycles per flight

Fig. 3 Application and representation of operational condition.

3. Development of Load Spectra for Center Fuselage and Wing Test

The center fuselage and wing specimen EF2 is identical to the A340–300 and contains 31 m of the fuselage structure as well as the center and outer wings without movable surfaces; see Fig. 4. All attachments to movable surfaces, undercarriages, pylons and winglets are original structures. Pylons, undercarriages and winglets are dummies for load introduction purposes. The specimen is supported by 6 links at the forward and rear dummy steel bulkheads and is loaded by 92 hydraulic jacks and internal pressure.

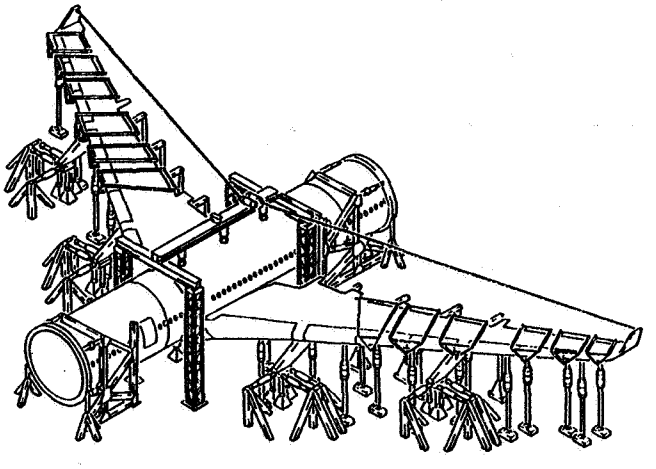

Fig. 4 Full scale fatigue test EF2 "center fuselage and wing".

C-3.

The goal of the EF2 test is the simulation of 80 000 test flights considering the increase of all test loads by 10 percent and the simulation of A340 loads in phase I and A330 loads in phase II; see Fig. 5. The design service goal of the A340 is verified after reaching 40 000 test flights, whereby the A330 service goal needs a demonstration of 80 000 test flights. The insertion of artificial damages is scheduled latest at 1.5 times of the design service goals.

The reason for increasing all test loads by 10 percent is to save test time which is mainly influenced by the high deflection of the outer wings. An increase of test loads leads to a decrease of the number of flights to be simulated.

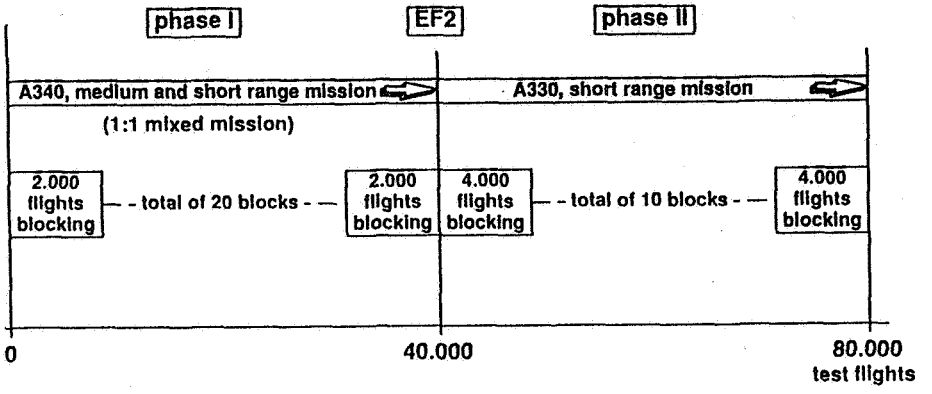

Fig. 5 Test phases and sequence of blocks.

3.1 Flight Load Spectra Representation

Each typical mission profile includes more than 30 flight stages; see Fig. 6. For representative fuselage and wing sections the 1g load time histories are plotted and up to nine representative test flight segments are selected for simplification of the load spectra. The selection considers four criteria:

- maintaining maximum original 1g variation
- maintaining maximum original 1g wing and fuselage bending moments
- representing original flap and slat conditions
- representing the cruise flight stage in a separate segment

The simplification described above leads to an adequate representation of the 1g variation which is important for the correct fatigue damage in test.

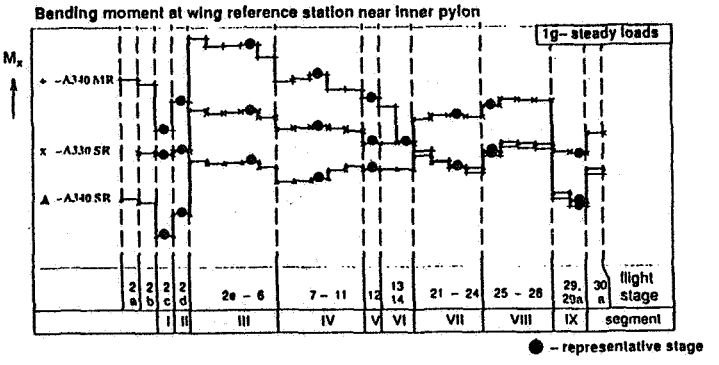

Fig. 6 Representation of 1g- condition.

For each of the segments vertical gust load spectra are calculated. Instead of using ESDU 69023 as done for previous tests the vertical gust load spectra are based on the data presented in the AGARD report No. 605. A new interpretation of this data was focussed on the high levels of gust velocity and presented in the CAA report NPA25C–205. Since the equation leads to a single slope curve which gives an insufficient agreement with the measured data for low gust velocities, a second slope has been introduced by Airbus Industrie in the gust statistical data. The gust modeling used for A330/A340 gust spectra is described by the following equation:

$$n_{\mu_0} = A \times e^{\frac{-B\mu_0}{K_0}} \times K_1$$

where:

n_{μ_0}	:	number of exceedences of gust velocity μ_0 (ft/s) per nautical mile
μ_0	:	gust velocity in ft/s EAS
A,B	:	function of altitude different for $\mu_0 < 10$ ft/s EAS and $\mu_0 > 10$ ft/s EAS
K_0	:	factor 1.00 for vertical gust 1.15 for lateral gust
K_1	:	*ratio of upgust or downgust to total gusts (function of altitude) where* K_1 up + K_1 down = 1.0.

The application of the equation given above leads to the vertical gust spectra for the wing rib 10 shown in Fig. 7 LH side. The spectra include the 1g loads which are defined for the segments. The RH side of Fig. 7 shows the ground–air–ground spectra (GAG) which were developed using the method of ESDU 79024.

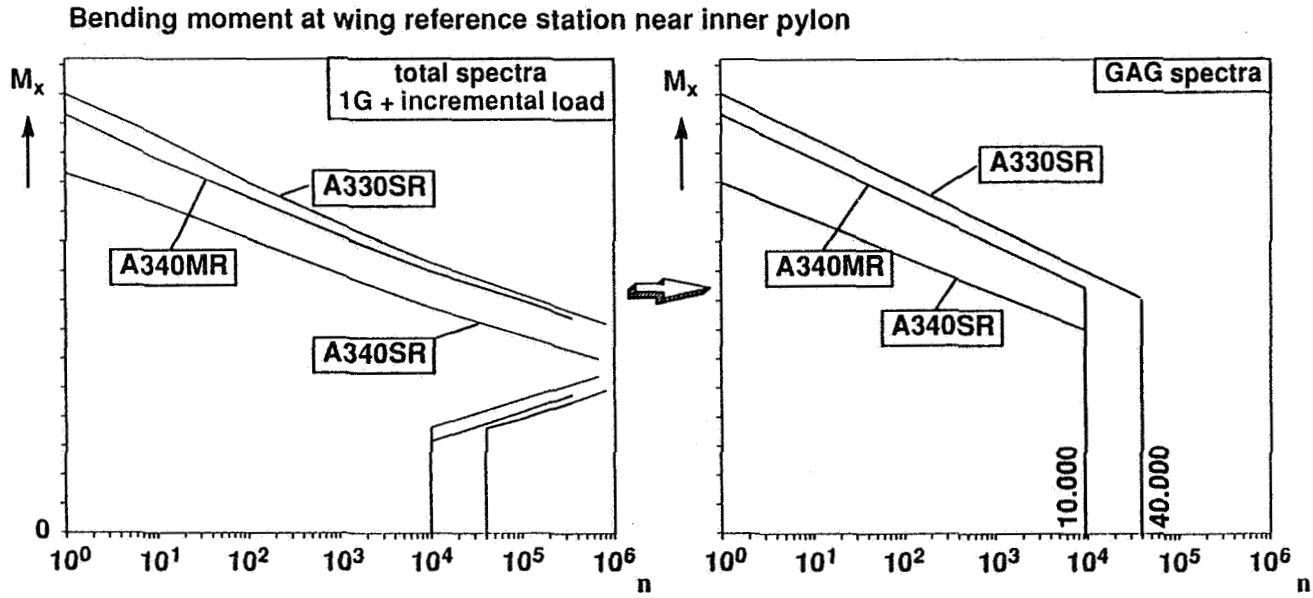

Fig. 7 Total vertical gust spectra and ground air ground spectra (GAG).

The simulation of the GAG spectrum is applied during the cruise stage, since the gust loads with the highest load levels occur during the cruise stage. However, this type of application is conservative for the pressurized fuselage. The simulation of the GAG spectrum during cruise has to be considered by a reduction of the segment spectra as described in Fig. 8.

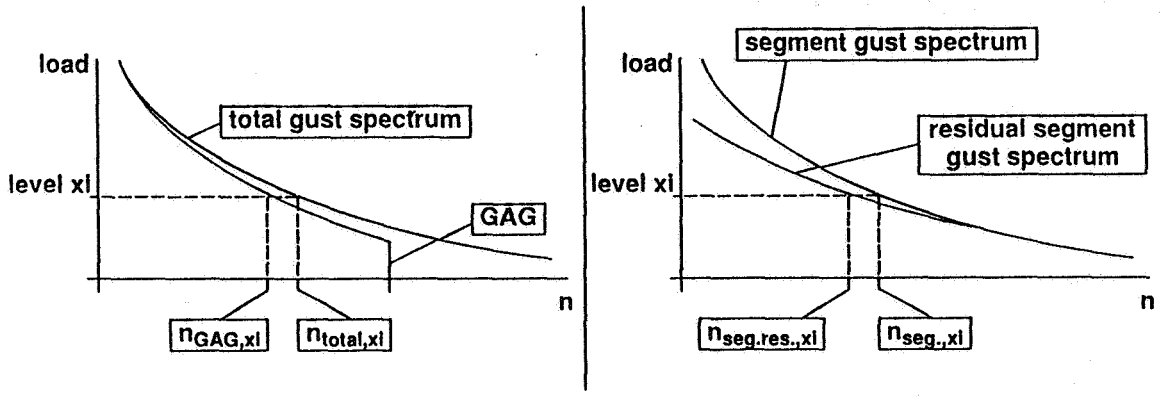

For the different load levels x_i the number of cycles for the residual gust spectrum $n_{seg.res.,xi}$ has to be calculated as follows:

$$n_{seg.res.,xi} = n_{seg.,xi} - \frac{n_{seg.,xi}}{n_{total,xi}} \times n_{GAG,xi}$$

Fig. 8 Determination of residual gust spectra.

The load spectra for the individual segments and for the GAG spectrum are stepped into six to nine load levels and distributed to eight basic flight types, i.e. A to H. These flight types occur with different frequencies in repeated blocks of 2.000 flights (A340 SR and MR) and 4.000 flights (A330 SR), and are supposed to represent different weather conditions.

An example for the described procedure is shown in Fig. 9 which represents the total gust spectrum, the resulting GAG, the original gust spectrum for cruise and the residual gust spectrum for cruise.

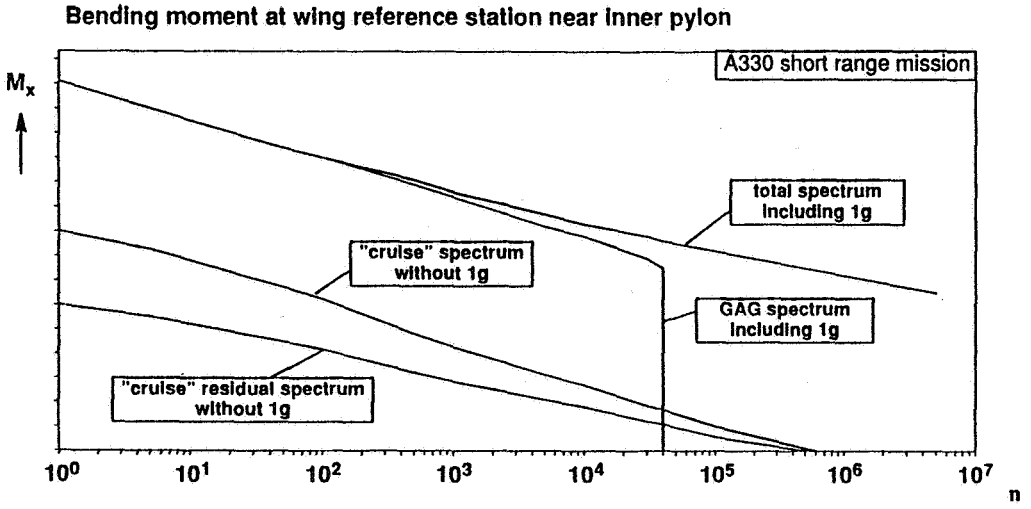

Fig. 9 "Cruise" residual spectrum.

The matrix of Fig. 10 shows the simulation of the GAG spectrum and the load cycles for the residual spectrum. This procedure of stepping and representation has been applied to all segments for the three mission profiles.

Summary of load step frequencies A330 (short range): "cruise"													
flight type	frequency of flight type per block	step I	step II	step III	step IV	step V	step VI	step VII	step VIII	step IX	load cycles per flight	load cycles per block	load cycles per life
A	5	+1			1	2	4	5	7	22	41	205 +5	2 050 +50
B	7		+1			1	2	4	6	21	34	238 +7	2.380 +70
C	22			+1			1	3	5	15	24	528 +22	5.280 +220
D	56				+1			2	4	10	16	896 +56	8 960 +560
E	130					+1			3	8	11	1.430 +130	14.300 +1.300
F	380						+1		2	6	8	3 040 +380	30.400 +3.800
G	1.000							+1		3	3	3 000 +1 000	30 000 +10.000
H	2.400								+1	1	1	2.400 +2.400	24.000 +24.000
gust load cycles per block		+5	+7	+22	5 +56	17 +130	56 +380	231 +1 000	1561 +2.400	9 867		Σ	117.370 +40 000
gust load cycles per life		+50	+70	+220	50 +560	170 +1.300	560 +3 800	2 310 +10.000	15 610 +24 000	98.670			
cumulative no. of cycles per life		+50	+120	+340	50 +900	220 +2.200	780 +6 000	3.090 +16.000	18 700 +40 000	117.370			

Fig. 10 Loads matrix, ground air ground spectrum (GAG) (example for A330 short range mission).

3.2 Definition of Truncation and Omission

The test spectrum definition includes the consideration of truncation (high load clipping) and omission (low load clipping), see Fig. 11. The truncation level has a significant impact on fatigue crack initiation and on crack growth. Different methods exist for definition of the truncation level which lead to different test results especially for wing structure. The method applied to the EF2 spectra is a statistical approach. The defined truncation level will be reached or exceeded by 99 percent of the in–service aircraft within an inspection interval, i.e. from a statistical point of view only one percent of the in–service aircraft may crack earlier than the test specimen and show a faster crack growth. According to this procedure the maximum test load is 79 percent of the load occurring once per inspection interval.

- level is set to 79 percent of the incremental loads level, which occurs once per an inspection interval:
  –> A330: 8.000 flights,
  –> A340: 4.500 flights,
- value represents the 99 percent confidence level that this load will be exceeded by the aircraft fleet within the interval.

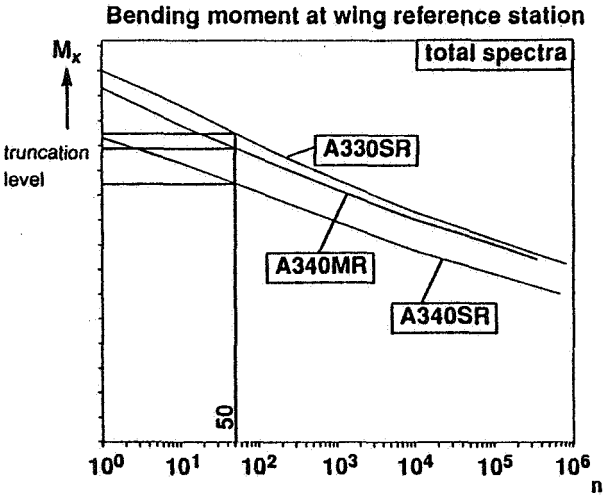

Fig. 11 Truncation level.

The determination of the omission level is described in Fig. 12. Many investigations have shown the importance of a low omission level to achieve representative crack growth results. Since this is important for both, natural and artificial damages, this aspect has been considered from the beginning of the test. Based on the comparative coupon tests for the A320 (Ref. /1/) the omission was set to 11 to 12 MPa for a representative bottom wing station which results in 26 to 33 gust cycles per flight depending on the aircraft type and mission.

- determination of the omission level to realize gust distribution by steps but with a minimum error in fatigue life and crack propagation:
  - test phase I with A340 loads and in average 26 gust cycles + 1 GAG cycle per flight,
  - test phase II with A330 loads and in average 25 gust cycles + 1 GAG cycle per flight,
- stress level of about 11 MPa in wing panels.

A340MR:

32+1 gust cycles/flight: (32+1) x 10.000 = 330.000 cycles

A340SR:

20+1 gust cycles/flight: (20+1) x 10.000 = 210.000 cycles

A330SR:

25+1 gust cycles/flight: (25+1) x 40.000 = 1.040.000 cycles

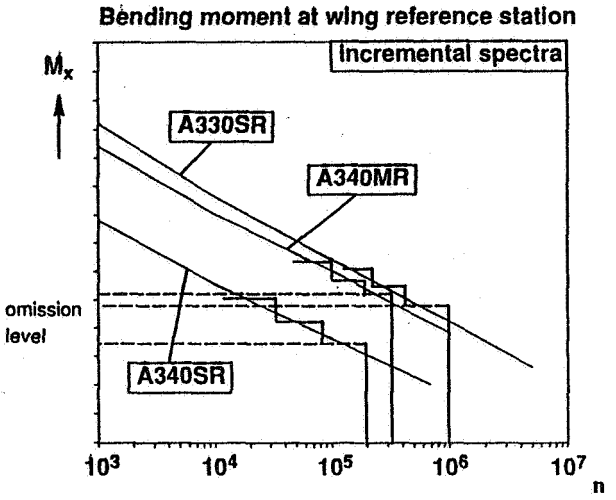

Fig. 12 Omission level.

3.3 Ground Load Spectra Representation

The full scale fatigue test considers a total of seven different 1g conditions on ground, i.e. four before and three after the airborne time. The basic 1g loads are superimposed by incremental loads due to taxi, turning, rotation, braking and touch down, where the load distribution for taxi and turning are based on the ESDU data sheets 75008.

Fig. 13 contains the load spectrum for touch down which was already used for all previous Airbus full scale fatigue tests. The touch down loads are simulated by three loading steps representing sinking speeds of 2.0, 3.5 and 6.0 ft/s. The three step spectrum is based on an equivalent damage approach. Fig. 13 also shows the braking spectrum which is based on earlier Airbus A300 measurements and simulated by a two step spectrum with decelerations of 0.2 g and 0.3 g.

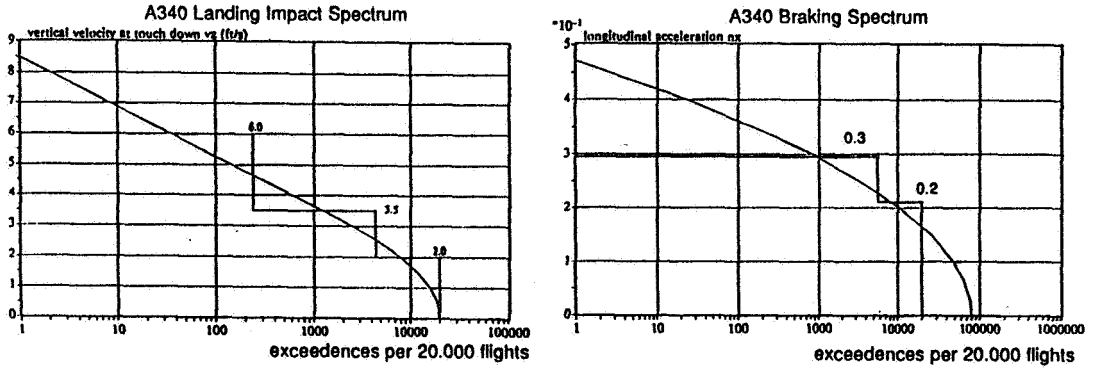

Fig. 13 Landing and braking spectrum.

The combination of the basic flight types A to H with the ground loads which are different in the flight types, i.e. touch down, taxi and braking, is given in Fig. 14. As a result of this combination 21 flight types are defined for each mission profile, i.e. in test phase I (two missions) 42 different flight types are simulated and 21 flight types in test phase II (one mission).

- simulation of rough and smooth flights by 8 basic flight types A to H to represent severity of weather and landing conditions,
  - severity: rough <——————> smooth
  - flight type: A—B—C—D—E—F—G—H
- combination with additional three ground cases to consider typical runway configurations (X, Y and Z),
- in total 21 flight types

aircraft mission	flight type	total number of flights	number of taxi cases			number of landing cases			number of braking cases	
			step X	step Y	step Z	6.0 ft/s	3.5 ft/s	2.0 ft/s	–0.3g (x,y)	–0.2g (z)
A330 SR	A – H	4.000	160	960	2.880	50	830	3.120	1.120	2.880
A340 SR	A – H	1.000	40	240	720	12	208	780	280	720
A340 MR	A – H	1.000	40	240	720	12	208	780	280	720

Fig. 14 Combination of ground and flight load cases.

3.4 Definition of Loading Sequence

Besides the ground and flight loads described above, the cabin differential pressure is simulated during application of flight loads. The cabin differential pressure distribution is in accordance with the mission profile and simplified by a linear variation between defined fix–points and a maximum of 574 hPa at cruise; see Fig.15.

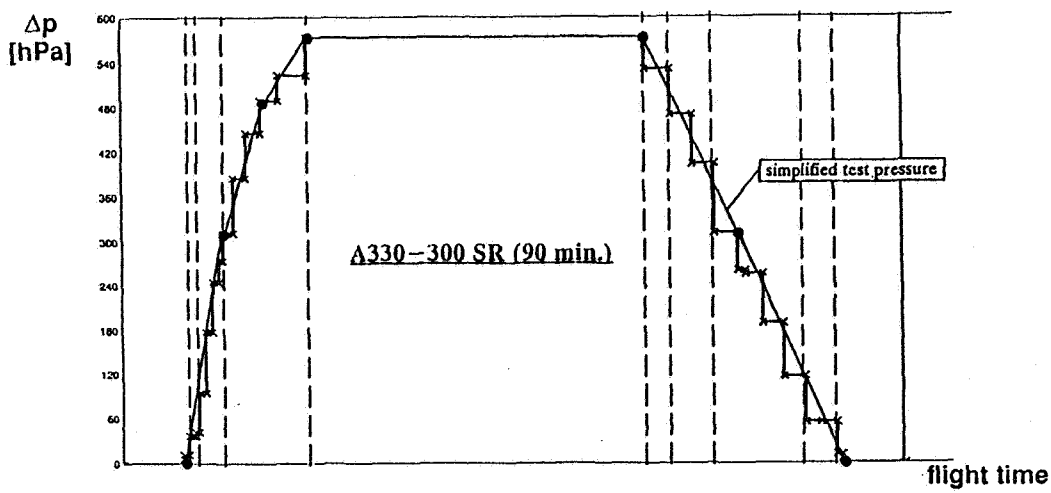

Fig. 15 Cabin pressure differential.

The definition of the loading sequence contains three aspects, i.e. definition of flight types, definition of the sequence of the flight types in a given block and the sequence of the blocks.

Fig. 16 contains the load time histories for the most severe flight type AZ and the smoothest flight type HZ for the A340 medium range. The main distribution of loads is pre–defined by the load spectra for the representative segments and the described combination between flight and ground loads. The load distribution within the segments is randomized with some limitations as no half cycle representation; an upgust is followed by a downgust, an upward taxi bump is followed by a downward taxi bump.

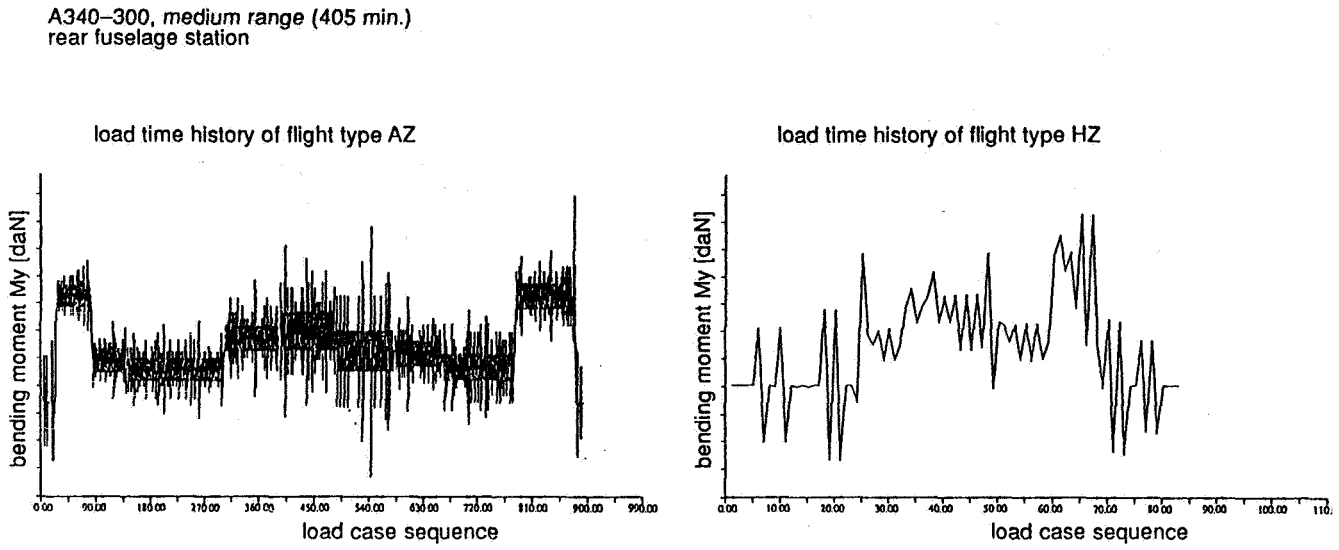

Fig. 16 Load sequence in test flights.

Fig. 17 contains the distribution of the A330 short range flight types within a block of 4.000 flights which is repeated 10 times within test phase II. The more severe flight types AZ to DZ are positioned by an equal space distribution whereby the other flight types are randomly distributed. During test phase I 20 blocks will be applied containing A340 loads and afterwards during test phase II 10 blocks of A330 loads.

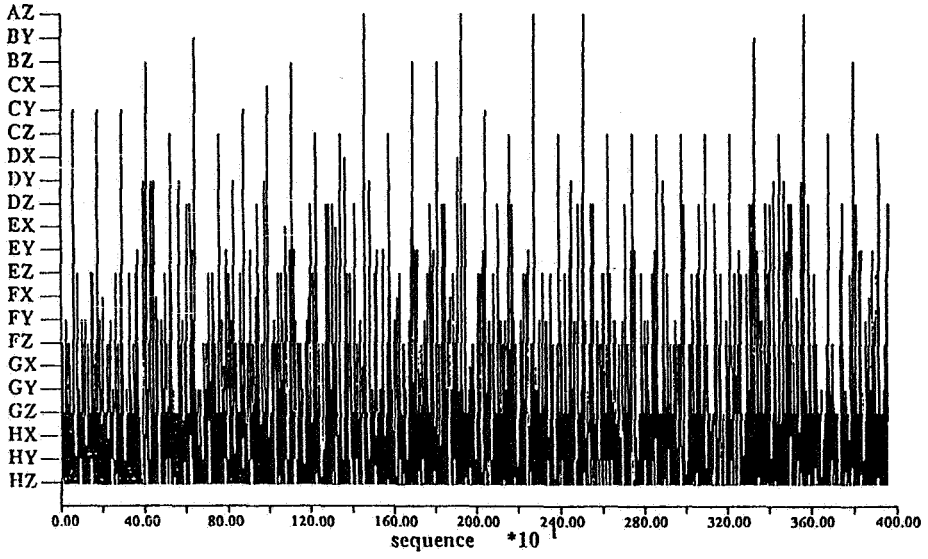

Fig. 17 Block sequence.

3.5 Interpretation of Test Results

Due to the fact that one specimen is used to justify the A340 and A330 and all test loads are increased by 10 percent, all test results have to be evaluated carefully. The test results have to be recalculated to define the relevant fatigue crack initiation and the crack growth periods for the three aircraft types certified up to now, i.e. A340–200, A340–300 and A330–300. The re–evaluation of the fatigue crack initiation is normally carried out by a Miner calculation and the periods between damage detection and repair by crack growth calculations or Miner calculation (risk analysis for parts not inspectable for less than load path failure).

The effect of the load increase can be determined by using the relevant SN curve for the structural detail. The slope of the SN curve $\varkappa$ is dependent on the loading environment (load level, spectrum shape etc.) and geometry (stress concentration, eccentricity, pre–stresses etc.). In general $\varkappa$ for constant amplitude tests and TWIST spectra is greater than 3; therefore a load increase of 10 percent results in a justified fatigue life of at least 1.25 times of the test life. For most of the structural details $\varkappa$ or the exponent n of the Forman equation is significantly greater than 3, so that an individual re–evaluation leads to more than 1.25 times of the test life. The accuracy of the relevant $\varkappa$ or the n to be applied needs not to be very high, since a variation of the exponent of ± 0.5 results in approximately ± 5 percent on life for a 10 percent load increase.

4. Development of Load Spectra for Rear Fuselage Test

The rear fuselage specimen EF3 contains 21 m of the rear fuselage structure up to the attachment of the rear spar of the horizontal tailplane; see Fig. 18. The horizontal tailplane and the APU compartment are replaced by steel constructions for load introduction purposes. The vertical tailplane loads are applied to the fuselage attach fittings by hydraulic jacks, because the CFRP vertical tailplane is tested separately. The specimen is supported by a steel construction at the forward end.

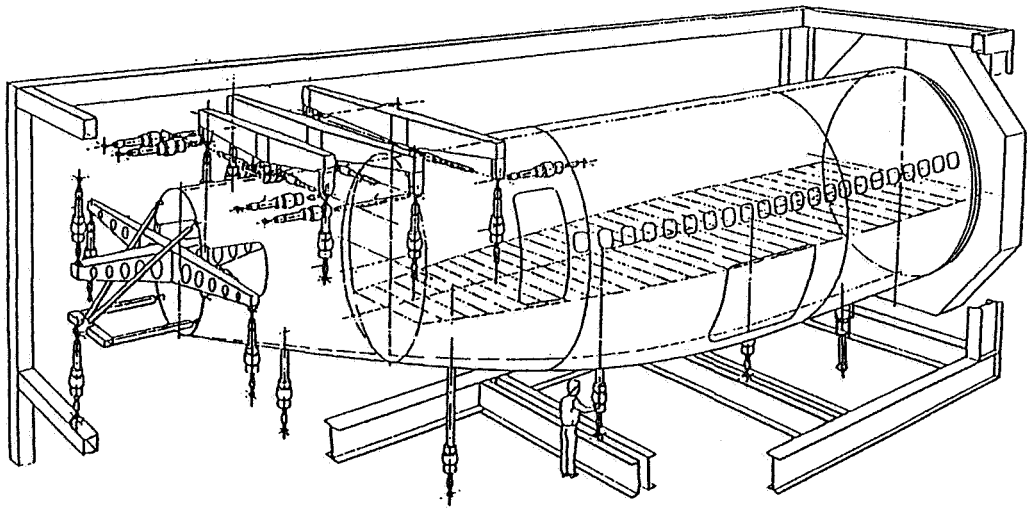

Fig. 18 Full scale fatigue test EF3 "rear fuselage".

In contrast to the EF2 specimen the goal of the EF3 test is > 100 000 flights, since no load increase factor of 10 percent is applied and at least 2.5 lifetimes should be justified. The application of a load increase was considered not to be necessary, since the test speed is similar to previous Airbus tests.

In general the test execution is very common to the EF2 test; i.e. A340 loads will be applied during phase I (50 000 flights) and A330 loads during phase II (> 50 000 flights). The following sub–chapters contain the major differences between EF2 and EF3 tests. Similar details are not addressed again.

4.1 Test Loading

Fig. 19 includes an overview about the EF3 test loading. This table shows that the EF3 is loaded additionally by lateral gusts and lateral and vertical manoeuvre as well as by temperature loads at the fuselage pick–up points to the CFRP vertical tailplane.

	basic loads (1G)	incremental loads	internal pressure	temperature effects
ground	standing on ground, taxi–out, take off run, rotation	taxi bumps (low speed) rolling bumps (high speed)		
flight	climb . cruise . approach (up to eleven different flight cases)	vertical gust lateral gust vertical manoeuvre lateral manoeuvre	according to altitude given in mission profile	according to altitude and defined temperature profile
ground	touch down, landing roll–out, taxi in	landing (2.0–6.0ft/s) rolling bumps (high speed) taxi bumps (low speed)		

Fig. 19 Test loading.

The lateral gust spectra which are important for the fuselage attachment area to vertical tailplane are based on the same statistics as the vertical gusts as described in chapter 3.1. The difference between vertical and lateral frequencies is considered by the factor K_0. Fig. 20 shows an example of a lateral gust spectrum for cruise.
The GAG spectrum is included due to the definition of the different flight types. The application of the definition according to ESDU 79024 is not considered, since this information is mainly valid for the wing.

The vertical and lateral manoeuvres are important for the unpressurized fuselage and the fuselage attachment areas to horizontal and vertical tailplanes. The manoeuvre spectra are calculated using the following equation:

$$\log N_{(y)} = \log P_L / L \times Y + \log (M_F \times D_F \times N_F)$$

where $N_{(Y)}$: load frequency exceeding load Y, sum of load cycles with a loading higher than value Y

P_L: probability of occurrence of limit load per load cycle

	normal flights	crew training flights
vertical manoeuvre	1.0×10^{-12}	7.0×10^{-6}
lateral manoeuvre	1.0×10^{-5}	7.0×10^{-3}

L : limit load
Y : loading
M_F : manoeuvre frequency in relation to flight distance (for normal and crew training flights)
D_F : flight distance
N_F : number of normal of crew training flights in one aircraft design goal.

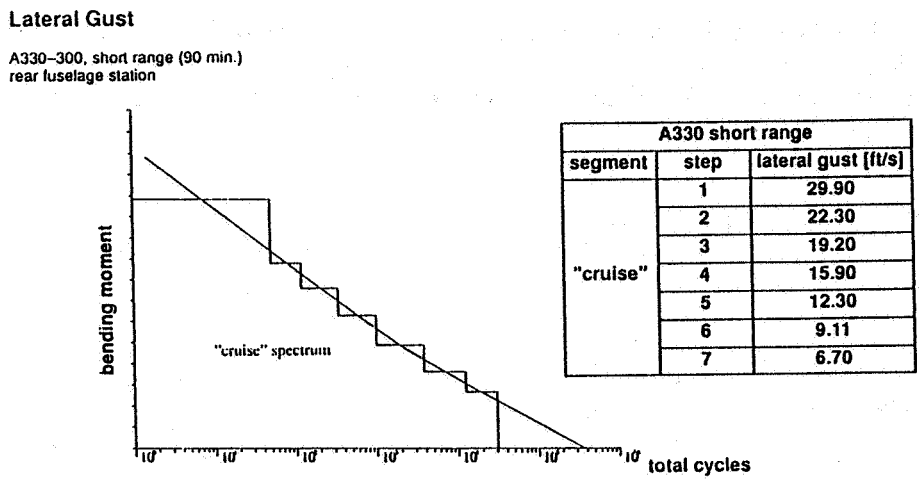

A330 short range		
segment	step	lateral gust [ft/s]
"cruise"	1	29.90
	2	22.30
	3	19.20
	4	15.90
	5	12.30
	6	9.11
	7	6.70

Fig. 20 Lateral gust.

The ratio between crew training and normal flights is set to 1:50. Fig. 21 shows examples of the lateral and vertical manoeuvre spectra.

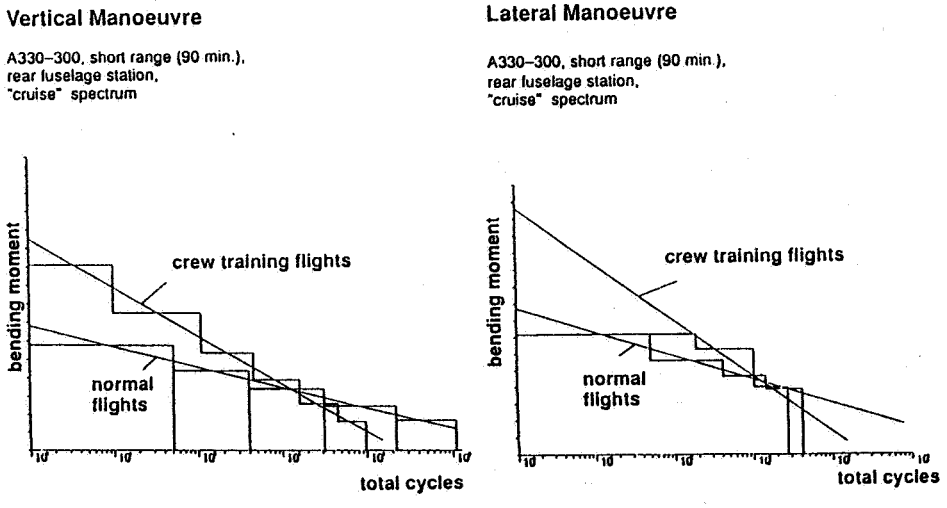

Fig. 21 Vertical and lateral manoeuvre.

The application of the ground loads at the EF3 is similar to the EF2 except turning and braking which are deleted due to their insignificance for the rear fuselage.

Due to the existence of a CFRP vertical tailplane temperature x–loads result from the different thermal expansions of the Al–fuselage and the CFRP tailplane. Therefore it is not possible to test the fuselage and the vertical tailplane structure in one specimen. Seven different temperature profiles are defined to consider the various missions as shown in Fig. 22.

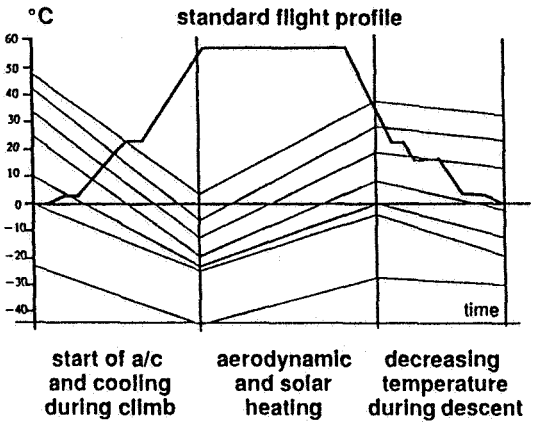

number of flights		
	A330	A340
T7	1.500	540
T6	9.400	4.680
T5	8.340	4.160
T4	15.220	7.700
T3	4.800	2.400
T2	360	180
T1	300	140
Σ	40.000	20.000

Fig. 22 Temperature loads.

4.2 Definition of Flight Types and Loading Sequence

For each of the three mission profiles 12 different basic flight types are defined, i.e. eight for normal operation and four for crew training flights. These basic flight types are combined with the different ground load types similar to EF2 and temperature load profiles. In addition the airbrakes extension is simulated in 50 percent of the flights with 50 percent full and 50 percent half angle airbrake extension. Fig. 23 shows the combination of basic flight types with taxi and touch down loading types resulting in 29 flight types for A330 and 27 flight types for A340 which are combined further with the seven temperature profiles and the different airbrakes conditions.

The methods for definition of the loading sequence within the flights and the sequence of the flight types within a block are similar to the EF2 test program.

flight type	number of taxi steps per block							
	A330 SR				A340 MR / SR each			
	X	Y	Z	Σ	X	Y	Z	Σ
A	–	–	5	5	–	–	5	5
B	–	2	5	7	–	2	4	6
C	1	5	16	22	1	3	7	11
D	2	14	40	56	1	6	18	25
E	5	31	94	130	2	13	38	53
F	16	92	272	380	4	26	80	110
G	39	234	707	980	9	57	169	235
H	92	552	1.696	2.340	21	130	384	535
I	–	–	1	1	–	–	1	1
J	–	–	4	4	–	–	4	4
K	1	5	13	19	–	1	4	5
L	3	23	30	56	–	2	8	10
total	159	958	2.883	4.000	38	240	722	1.000

Fig. 23 Definition of flight types

5. Conclusion

The tests and test programs described are examples of the test philosophy and load spectra development for large transport aircraft investigated by multi–section testing.

Two aircraft types with mostly similar structure can be covered by one set of specimens as demonstrated. This is an important economical benefit which is reached without unacceptable technical constraints. The envisaged changes of regulations and advisory circulars should allow similar procedures in the future.

The applied increase of spectrum loading by 10 percent leads to a significant economical benefit regarding test execution and earlier information about necessary actions for in–service and production aircraft. However, the implications of this procedure regarding technical and economical advantages and disadvantages should be carefully assessed before application, especially for other aircraft types. The increased engineering effort for re–evaluation and interpretation of test results necessary to cover the above mentioned aspects is small compared with the advantages.

6. References

/1/ Fatigue Crack Propagation Programme for the A320 Wing
British Aerospace Civil Aircraft Division
by: I. G. Gray

AIRCRAFT STRESS SEQUENCE DEVELOPMENT
A COMPLEX ENGINEERING PROCESS MADE SIMPLE

K.H. Schrader, D.G. Butts, W.A. Sparks
Structural Engineering Department
Southwest Research Institute
San Antonio, Texas

Development of stress sequences for critical aircraft structure requires flight measured usage data, known aircraft loads, and established relationships between aircraft flight loads and structural stresses. Resulting cycle-by-cycle stress sequences can be directly usable for crack growth analysis and coupon spectra tests. Often, an expert in loads and spectra development manipulates the usage data into a typical sequence of representative flight conditions for which loads and stresses are calculated. For a fighter/trainer type aircraft, this effort is repeated many times for each of the fatigue critical locations (FCL) resulting in expenditure of numerous engineering hours.

The Aircraft Stress Sequence Computer Program (ACSTRSEQ), developed by Southwest Research Institute under contract to San Antonio Air Logistics Center, presents a unique approach for making complex technical computations in a simple, easy to use method. The program is written in Microsoft Visual Basic for the Microsoft Windows environment. This environment has become common among users of personal computers and offers a consistent user interface. The benefit of a common user interface is to reduce the time required for an individual to learn the operation of a program written for that environment.

The program was originally developed for the T-38 aircraft. Subsequently, capabilities for T-37, F-5A, F-5B, F-5E, and F-5F aircraft were added. Although, ACSTRSEQ performs many complex engineering computations, these complexities are not apparent to the user. The user is exposed to a number of choices such as aircraft type, FCL of interest, and type of stress sequence desired. To further simplify the process for the user, choices are made by a pointing device such as a mouse on either menu items or screen images of the aircraft structure of interest. Screen images are either photographic or schematic depending on the information or detail that is required at that point in the decision process. Various levels of information detail are available to the user depending on knowledge or experience level. Less experienced users can choose structural areas of interest from screen pictures of the wing, fuselage, and empennage. However, users experienced in aircraft structural considerations and program usage may select program options from textural menus. In addition, schematics are provided for each FCL which show the general orientation of the FCL as well as details such as fastener hole diameters and material thicknesses and other crack parameters. These structural details are required for the crack growth analysis procedures for which the stress sequences are produced.

Printed user and programmer documentation is provided with ACSTRSEQ and is also available as part of the program "help" facility. The on-line "help" capability, which includes the full text of the user/programmer logic manual, allows the user full access to information regarding all program aspects through the use of index, search, and hyper-text linking functions. Included

in this documentation are engineering considerations, equations, and brief tutorials on data sources and results applications. As such, the on-line documentation provides a basic level of training for the determination of aircraft loads, stresses, and stress sequences required for crack growth analyses and laboratory testing.

The Aircraft Stress Sequence Computer Program integrates large, cumbersome reference information with the complex techniques of stress sequence development in a graphical user interface (GUI) that is suitable for both novice users as well as engineers experienced in spectra development. The result is a tool which provides accurate and repeatable results in a timely fashion to meet the demands of continuous damage tolerance analyses and testing programs. The concepts exhibited by this computer program only begin to explore the possibilities of productivity gains which can be obtained with properly designed state-of-the-art software.

A reduced copy of the poster is shown in the following figure.

Aircraft Stress Sequence Development (ACSTRSEQ)

Kurt H. Schrader, Devin G. Butts, William A. Sparks; Southwest Research Institute, San Antonio, Texas

Introduction

State-of-the-art computer program which produces stress sequences for fighter/trainer aircraft. Program requires flight measured usage data as input and utilizes known aircraft loads and their relationships between structural stresses at fatigue critical locations. The program produces flight-by-flight, cycle-by-cycle stress sequences in a variety of formats for use in analytical crack growth analysis and laboratory testing. The ease of use and speed of the program allow for the development of critical stress sequences using minimum engineering time.

Benefits

- Rapid Stress Sequence Development
- Minimum Time Required to Learn Program
- Produce Repeatable and Consistent Results
- Easily Modify Mission Mix to Evaluate New Usage
- Productivity Increase

Features

- Graphical User Interface
- Multiple Output Formats
- Adaptable for Other A/C Types
- Multi-Tasking in Windows Environment
- Can Be Used by Experienced and Novice Users
- Combines Published Loads Data in One Source
- Embedded Engineering Tasks
  - Randomization of Usage Data
  - Conversion of Maneuver Data to Stresses

FCL Selection / Review

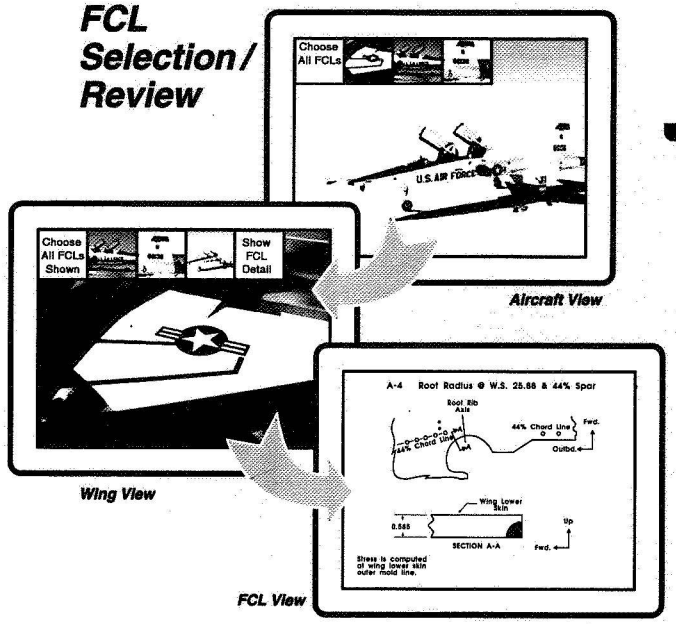

Run Parameters

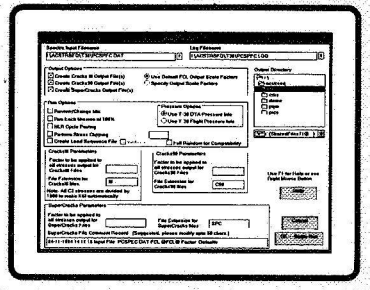

- Input/Output
- Mission Mix
- Documentary Information
- Crack Growth Formats
  - Cracks III
  - Cracks 90
  - SuperCracks

Stress Calculator

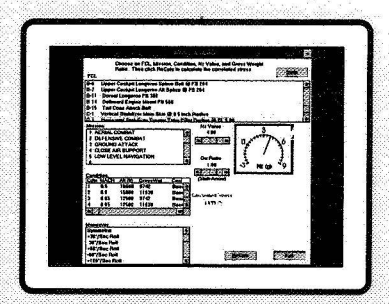

- Compute Stress Due to a Single Maneuver
  - Determine maximum spectrum stress
  - Verify flight measured strains
- Parameter Sensitivity Studies
  - Flight condition
  - Maneuver type
  - Mission type
  - Vertical acceleration
  - Gross weight

THE LOAD SEPARATION TECHNIQUE IN THE ELASTIC-PLASTIC FRACTURE ANALYSIS OF TWO- AND THREE-DIMENSIONAL GEOMETRIES

Monir H. Sharobeam
Richard Stockton College of New Jersey
Pomona, NJ

SUMMARY

Load separation is the representation of the load in the test records of geometries containing cracks as a multiplication of two separate functions; a crack geometry function and a material deformation function. In this paper, load separation is demonstrated in the test records of several two-dimensional geometries such as: compact tension geometry, single edge notched bend geometry, and center cracked tension geometry and three-dimensional geometries such as semi-elliptical surface crack. The role of load separation in the evaluation of the fracture parameter *J*-Integral and the associated factor η for two-dimensional geometries is discussed. The paper also discusses the theoretical basis and the procedure for using load separation as a simplified, yet accurate approach for plastic *J* evaluation in semi-elliptical surface crack which is a three-dimensional geometry. The experimental evaluation of *J*, and particularly J_{pl}, for three-dimensional geometries is very challenging. A few approaches have been developed in this regard and they are either complex or very approximate. The paper also presents the load separation as a mean to identify the blunting and crack growth regions in the experimental test records of precracked specimens. Finally, load separation as a methodology in Elastic-Plastic Fracture Mechanics is presented.

INTRODUCTION

The path independent *J*-integral was first introduced by Rice (1) as a crack tip parameter for two-dimensional geometries made of linear or non-linear elastic materials. This line integral form can be written as:

$$\int_{\Gamma} \left(W dy - T \frac{\partial u}{\partial x} ds \right) \qquad [1]$$

where Γ is a contour around the crack as shown in figure 1, W is the strain energy per unit volume, T is the tension vector perpendicular to Γ, u is the displacement in the x-direction and ds is an element of the contour. The experimental evaluation of J using the line integral can be done by placing strain gauges on the outside surface of the specimen along a contour in a plane perpendicular to the crack front. By defining the strain, external traction, and displacement in the x-direction along this contour, J can be evaluated. However, this technique is usually inaccurate

and impractical. An equivalent, yet more practical J expression was introduced by Rice (1) as:

$$J = -\frac{1}{B}\left[\frac{\partial U}{\partial a}\right]_v \qquad [2]$$

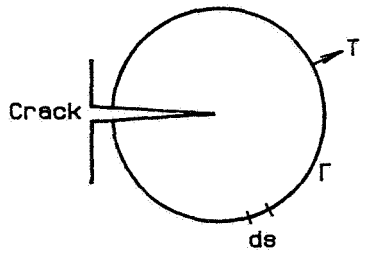

Figure 1 The J-integral contour.

where U is the potential energy and can be measured as the area under the load-line displacement record, a is the crack length, B is the specimen thickness and v is the load-line displacement. This J expression allowed Landes and Begley (2) to develop their multispecimen technique to evaluate J. Their approach requires the testing of many identical blunt notched specimens with different crack lengths in order to develop the U versus a relationship, from which J can be evaluated. Despite the accuracy and reliability of this technique, the high cost of specimens preparation and testing made it impractical. A single specimen technique was later developed for special geometries and crack ranges where the load can be represented in a particular form as will be discussed next.

Rice reduced the energy rate interpretation J form given in eq [2], for deeply cracked bend specimens (3), into:

$$J = \frac{2}{B}\frac{U}{b} \qquad [3]$$

where b is the uncracked ligament. This J expression was based on representing the applied bending moment M versus the angle of rotation due to the crack presence θ as:

$$\theta = f(M/b^2) \qquad [4]$$

The J expression in eq [3] can be obtained from the test record of a single bend specimen. Merkle and Corten (4) also developed a single specimen J expression for compact specimen. They represented the load using limit load analysis as:

$$P = [\sigma_y B(b/2)(2\alpha)]\, g(\theta_p) \qquad [5]$$

where σ_y is the yield strength, θ_p is the plastic rotation due to the crack and α is a function of a and b. Using this form, they developed J as:

$$J = \frac{2(1+\alpha)}{1+\alpha^2}\frac{U}{Bb} \qquad [6]$$

This J expression can be also evaluated by testing a single compact tension specimen.

The load expressions in eqs [4] and [5] can be described as separable forms. This means that the load is represented as a multiplication of two separate functions: a crack geometry

function and a material deformation function and can be written as:

$$P \text{ or } M = G(b \text{ or } a) \cdot H(\theta \text{ or } v) \quad [7]$$

Also, the single specimen J form can be generally written as:

$$J = \eta \frac{U}{Bb} \quad [8]$$

where the modification factor η is a function of the crack length and the geometry. Ernst and Paris (5) proved that the single specimen J form and η-factor only exist if the load can be represented by a separable form.

Further studies suggested representing J as the sum of two parts; J_{el} and J_{pl}. The elastic part, J_{el}, can be evaluated using Linear Elastic Fracture Mechanics as $[K^2/E']$ where K is the stress intensity factor and E' is the effective Young's Modulus. The plastic part, J_{pl}, can be written, according to the ASTM standard test method (6), as:

$$J_{pl} = \eta_{pl} \frac{A_{pl}}{Bb} \quad [9]$$

where A_{pl} is the area under the load versus plastic displacement test record and the η_{pl}-factor is considered as:

$$\eta_{pl} = 2 \qquad \textit{for bend specimen and}$$
$$\eta_{pl} = 2 + 0.522 \frac{b}{W} \quad \textit{for compact specimen} \quad [10]$$

The latter was the linear approximation of Merkle-Corten expression as shown in eq [6]. The single specimen J_{pl} form in eq [9] is based on the load separable form given as:

$$P = G(b/W)\, H(v_{pl}/W) \quad [11]$$

where W is the specimen width and $G\,(b/W)$ and $H(v_{pl}/W)$ are the geometry and deformation functions.

J-integral was first considered as a stationary crack parameter because it is based on the deformation theory of plasticity. However, it was later applied to extended cracks (7) if the crack growth is of the order of the non-proportional plastic region at the crack tip. This allowed Ernst et al (8) to develop a technique to evaluate a J-R curve for precracked specimen with J updated for the crack growth. This technique is also based on the single specimen J form. Thus, load separation must also exist during crack growth.

The available load separation expressions which are based on limit load analysis have been mainly developed for two-dimensional bending geometries such as bend and compact

tension specimens. This limited the single specimen J form to this geometry only. In this paper, load separation will be demonstrated in bending as well as tension geometries, in stationary as well as growing crack test records, and in two- as well as three-dimensional geometries. It will be also presented as a mean to define crack blunting and growth regions. It will be also used in a new η_{pl} method and to develop a key curve that can provide predicted load-displacement records. By extending load separation to three-dimensional geometries, an equivalent single specimen J form can be developed. Very few techniques are currently available for the experimental evaluation of J for these complex geometries and they are either impractical or inaccurate. Finally, the load separation as a methodology in Elastic-Plastic Fracture Mechanics will be presented.

LOAD SEPARATION IN TWO-DIMENSIONAL GEOMETRIES

Stationary Cracks

In order to study load separation in stationary crack test records, a separation parameter S_{ij} is introduced. This separation parameter represents the ratio of the loads $P(a_i)$ and $P(a_j)$ in the test records of two identical blunt notched specimens with crack lengths a_i and a_j at the same plastic displacement v_{pl}. Thus S_{ij} can be written as:

$$S_{ij} = \left[\frac{P(a_i)}{P(a_j)}\right]_{v_{pl}} \qquad [12]$$

If the load is separable, eq [12] can be rewritten as:

$$S_{ij} = \left[\frac{G(b_i/W)\,H(v_{pl}/W)}{G(b_j/W)\,H(v_{pl}/W)}\right]_{v_{pl}} = \frac{G(b_i/W)}{G(b_j/W)} \qquad [13]$$

For stationary cracks, S_{ij} should maintain a constant value over all of the plastic region. Figure 2 shows the test records of ten identical bend specimen made of HY130 steel with different crack lengths. The specimens are 0.9 inch thick and 2.0 inch wide and have span to width ratio of 4.0. They were originally reported in Ref. (9). When the loads in the different test records were divided by that of the specimen with $a_j/W=0.75$ at the same plastic displacement, the load ratios maintained constant values over all of the plastic region except for a small part at the early plastic behavior, see figure 3. Figure 4 shows the test records of ten HY130 center cracked tension specimens with different crack lengths and figure 5 shows the separation parameter for this set of test records. These specimens (9) were also 0.9 inch thick and 2.0 inch wide. It is clear that load separation exists in tension geometry such as the center cracked tension as well as

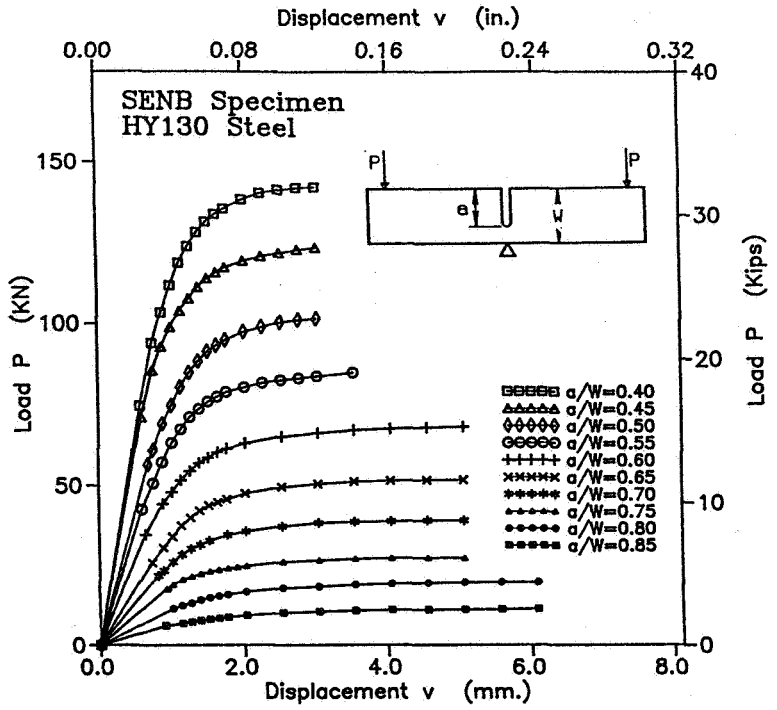

Figure 2. The test records of ten single edge notched bend specimens.

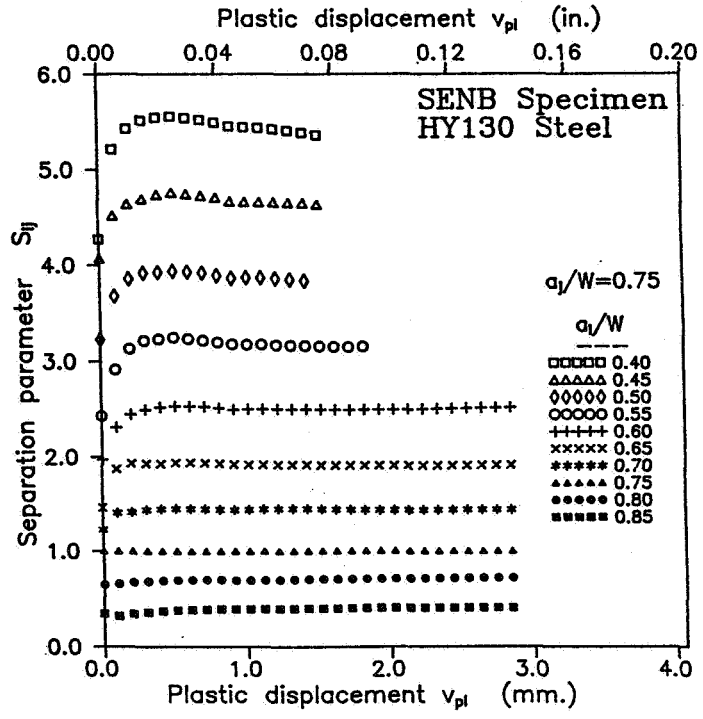

Figure 3. Load separation in the experimental test records of bend specimens.

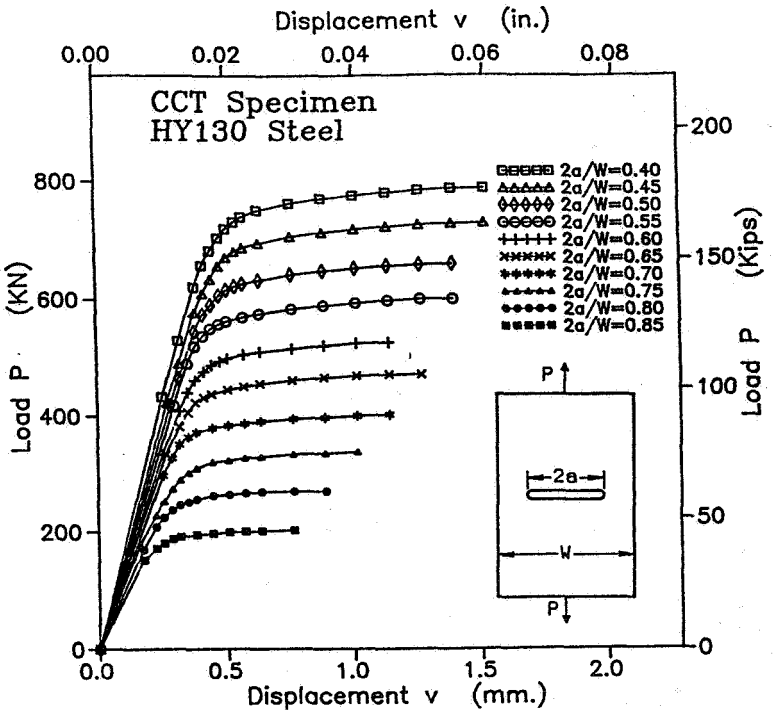

Figure 4. The test records of ten center cracked tension specimens.

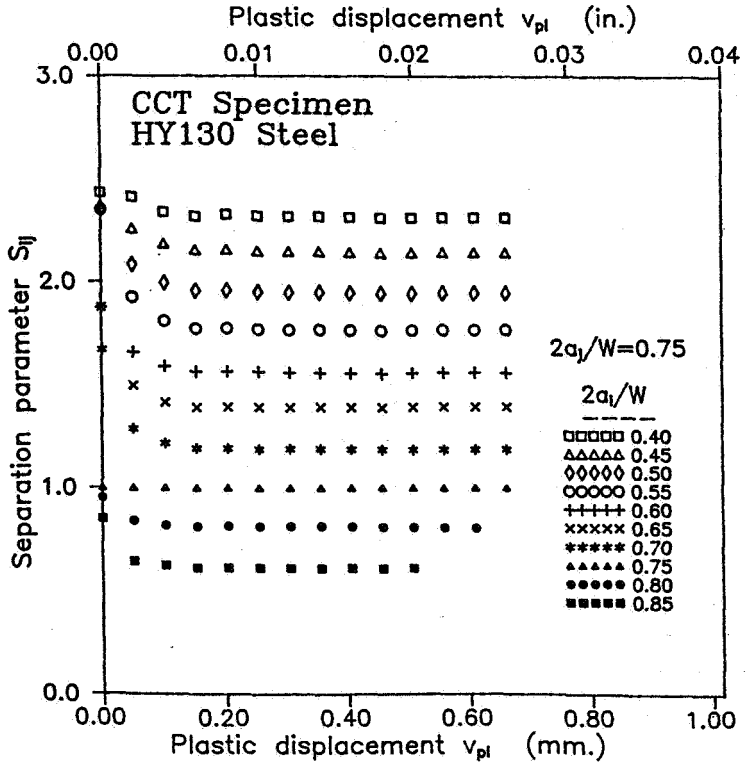

Figure 5. Load separation in the experimental test records of center cracked tension specimens.

bending geometry such as the bend specimen. Sharobeam and Landes (10,11) studied load separation in 12 sets of test records and found that load separation is dominant in all of the studied cases. Their study included different work hardening materials, different bending and tension geometries and wide range of crack length and geometrical proportions.

Precracked Specimens

Initially, we will assume that load separation also exists in the precracked test records but with different geometry and deformation functions than those for stationary cracks test records. Thus, the load in precracked specimen and blunt notched specimen test records can be written as:

$$P_p = G_p(b_p/W)\, H_p(v_{pl}/W) \qquad \textit{for precracked specimen and} \qquad [14]$$

$$P_b = G_b(b_b/W)\, H_b(v_{pl}/W) \qquad \textit{for blunt notched specimen} \qquad [15]$$

where the subscript p denotes precracked specimen while b denotes blunt notched specimen. The separation parameter can be then written as:

$$S_{pb} = \left[\frac{P_p}{P_b}\right]_{v_{pl}} = \left[\frac{G_p(b_p/W)\, H_p(v_{pl}/W)}{G_b(b_b/W)\, H_b(v_{pl}/W)}\right]_{v_{pl}} \qquad [16]$$

S_{pb} represents the ratio of the load in precracked specimen test record to the load in the test record of an identical specimen but with a stationary crack. Since $G_b(b_b/W)$ is constant because the crack is stationary, S_{pb} can be rewritten as:

$$S_{pb} = A\, G_p(b_p/W)\, h_{pb}(v_{pl}/W) \qquad [17]$$

where A is a constant and $h_{pb}(v_{pl}/W)$ is the ratio between the two deformation functions at the same plastic displacement. If several precracked test records are used with the same blunt notched record, one gets S_{pb} for each precracked specimen test record as:

$$S^i_{pb} = A\, G^i_p(b_p/W)\, h^i_{pb}(v_{pl}/W) \qquad [18]$$

where i denotes the different precracked specimen test records. If the different S_{pb}'s were plotted together versus b_p/W and collapsed into one record, then S_{pb} would be independent of v_{pl} and all the records would have the same geometry function $G_p(b_p/W)$. Thus, S_{pb} can be written as:

$$S_{pb} = A\, G_p(b_p/W) \qquad [19]$$

This would also indicate that the load is separable for precracked test records and can be represented as a multiplication of geometry and deformation functions. Figure 6 shows the test

records of three precracked specimens (E71, E75, E76) and a blunt notched specimen (E73). The specimens are compact tension and made of A533B steel with 1.0 inch thickness, 2.0 inch width and 20% side grooving. They were originally used in Ref. (12). The initial crack to width ratios for the precracked specimens are 0.608, 0.607 and 0.607 and the final crack to width ratios are 0.656, 0.7115, and 0.794 respectively. Figure 7 shows S_{pb} versus b_p/W for the different precracked specimen test records on a log-log graph. All of the records collapsed together into one which proves the assumption of load separation. Sharobeam and Landes (13) studied load separation in four sets of precracked specimen test records of different materials and with large crack growth. They indicated that load separation existed in all of the studied cases.

In precracked test records, load separation can be also used to define both the blunting and growing crack regions. Figure 8 shows both b_p/W and S_{pb} versus v_{pl} for one of the A533B precracked specimens. There are three regions for S_{pb} versus v_{pl}. The first region is very small at the early plastic behavior and is usually called the non-separable region. Then there is a second region where both S_{pb} and b_p/W almost maintain constant values. This is the blunting region. In the third region, both S_{pb} and b_p/W decrease indicating crack growth. The blunting and crack growth regions can be also identified in figure 7. The blunting region looks like a vertical line while the crack growth region looks like an inclined line.

Plastic η Development

Based on eqs [2] and [11], η_{pl} can be written as:

$$\eta_{pl} = \frac{b/W}{G(b/W)} \frac{\partial G(b/W)}{\partial (b/W)} \qquad [20]$$

The geometry function $G(b/W)$ can be obtained using the separation parameter S_{ij} or S_{pb}. The stationary crack separation parameter S_{ij} maintains constant value over all of the plastic region for specific a_i and a_j values. If S_{ij} is developed for different a_i values with respect to a single a_j value, one can construct the relationship S_{ij} versus a_i/W (or b_i/W) as:

$$S_{ij} = \left[\frac{G(b_i/W)}{G(b_j/W)}\right]_{vary\ b_i} = A\, G(b_i/W) \qquad [21]$$

where A is a constant equal to the inverse of $G(b_j/W)$. The S_{ij} expression in eq [21] can be then used directly in eq [20] instead of $G(b/W)$ to evaluate η_{pl}. Figures 9 and 10 show the variations of S_{ij} versus b/W on log-log graphs for both the bend and center cracked tension sets of test records shown before in figures 2 and 4. The power law function fits well the S_{ij}-b_i/W relationship in both cases. Thus, S_{ij} can be written as:

$$S_{ij} = A_1 (b/W)^m \qquad [22]$$

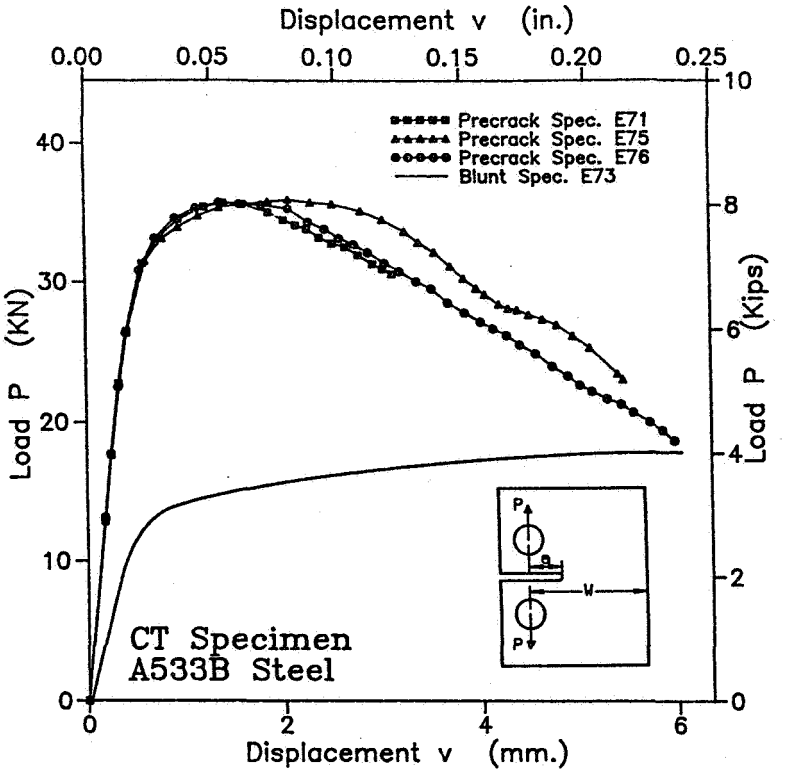

Figure 6. The test records of three precracked and one blunt notched compact tension specimens.

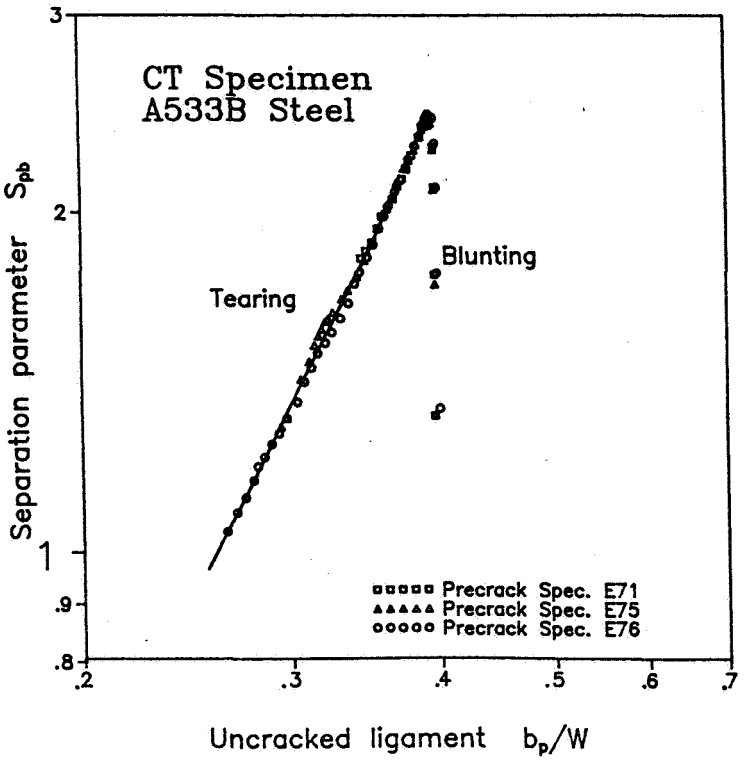

Figure 7. Load separation in the precracked compact tension specimens test records.

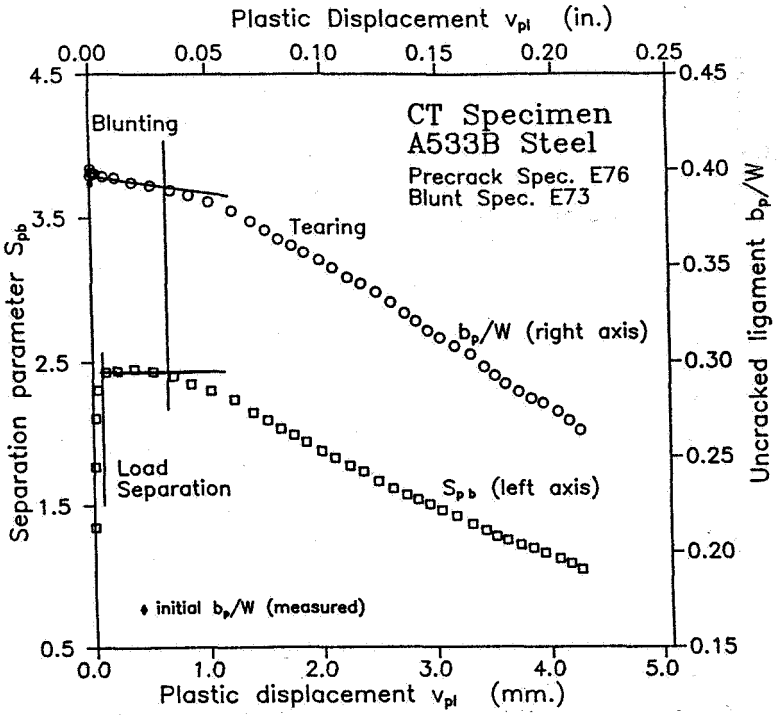

Figure 8. The blunting and tearing regions in the precracked specimen test record.

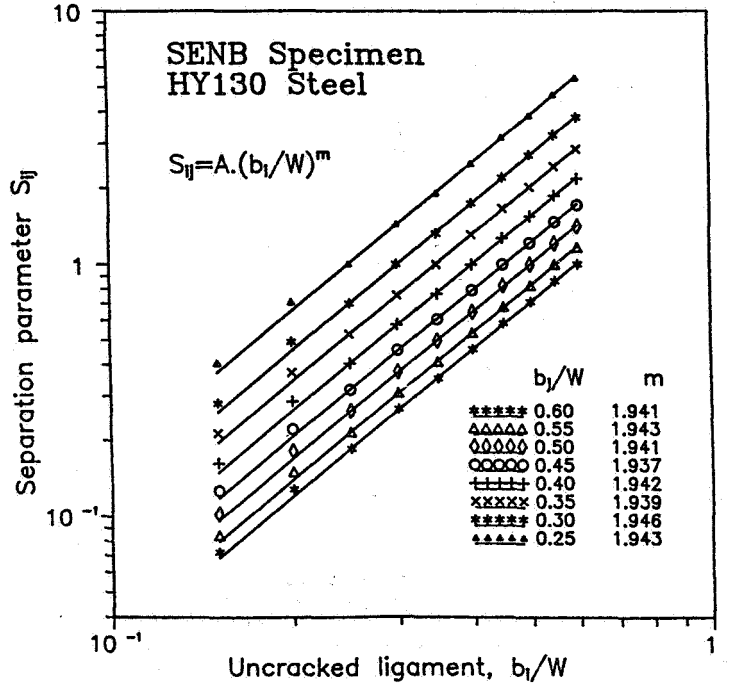

Figure 9. The separation parameter S_{ij} versus b_l/W in the bend specimen test records.

where A_1 is a constant and m is the power law exponent. From eqs [20], [21] and [22], η_{pl} is equal to the power law exponent m. For the given set of bend specimens, η_{pl} has an average value of 1.96 and for the center cracked specimens, it is equal to 0.96. The evaluation of η_{pl} using the load separation technique is discussed in detail in Ref. (13).

For the precracked specimens, the separation parameter S_{pb} is equal to the geometry function times a constant as shown in eq [19]. Thus by constructing the relationship S_{pb} versus b_p/W, the geometry function can be developed. Figure 7 shows the variation of S_{pb} with respect to b_p/W on a log-log graph for the A533B compact tension set. The relationship can be well fitted by a power law function with a power law exponent of 2.12 which is also the value of η_{pl} for this set as discussed early. When identical A533B compact tension specimens but with stationary cracks used to evaluate η_{pl} using the stationary crack separation parameter S_{ij}, a value of 2.17 was obtained which is very consistent with the precracked specimens results.

Thus, η_{pl} can be obtained using either test records of a set of identical blunt notched specimens with different crack sizes or a precracked specimen test record together with a test record of an identical blunt notched specimen.

The Key Curve

As the geometry function is developed, an expression for the normalized load, P_N, can be written as:

$$P_N = \frac{P}{G(b/W)} = H(v_{pl}/W) \qquad [23]$$

The normalized load is a function of the plastic displacement only and is independent of the crack length. The P_N versus v_{pl} relationship is commonly called the key curve. Figures 11 and 12 show the key curves for both the bend and center cracked tension sets. Figure 13 shows the key curve for the A533B precracked specimen test records together with three test records of identical blunt notched specimens. Our studies showed that the geometry and deformation functions are the same for both stationary and growing crack test records of same material and geometry. The key curve can be used to construct the load-displacement test record of any specimen of same material and geometry with any crack length within the range of the key curve.

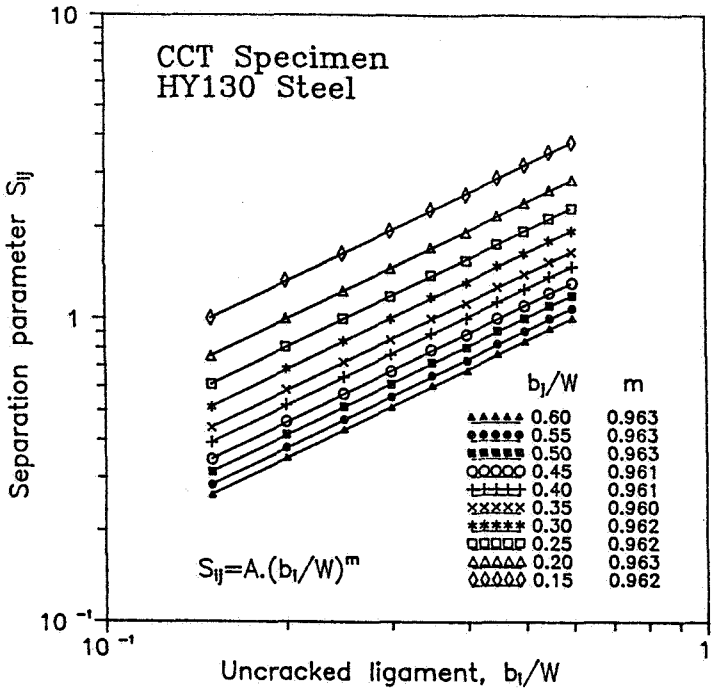

Figure 10. The separation parameter S_{ij} versus b_l/W in the center cracked tension specimen test records.

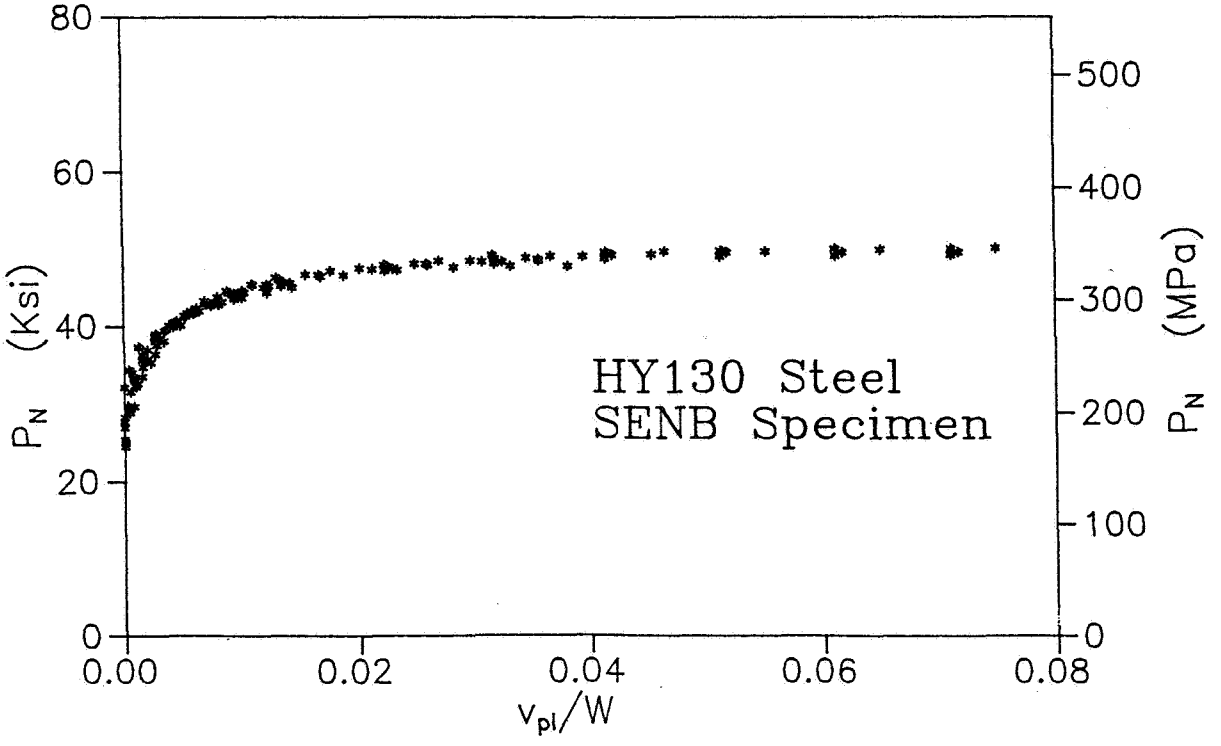

Figure 11. The key curve for the HY130 bend specimens.

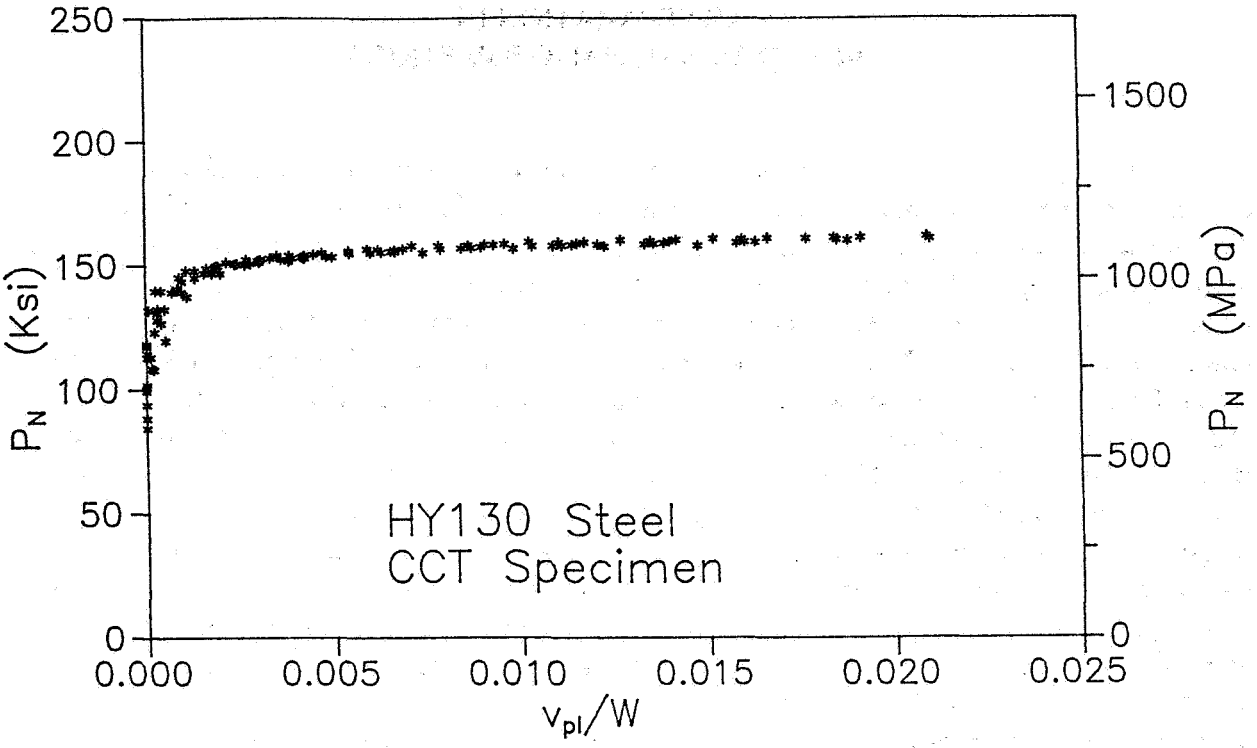

Figure 12. The key curve for the HY130 center cracked tension specimens.

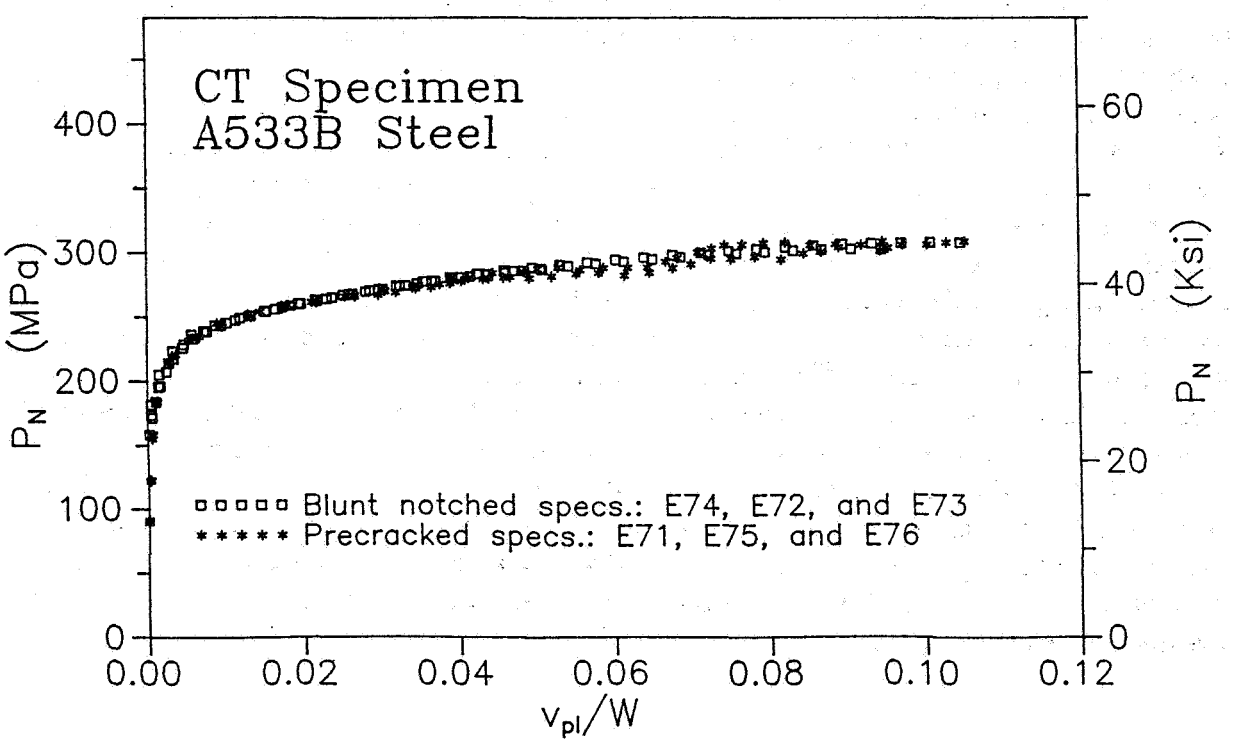

Figure 13. The key curve for the A533 precracked and blunt notched compact tension specimens.

LOAD SEPARATION IN THREE-DIMENSIONAL GEOMETRIES

The experimental evaluation of J in three-dimensional geometries is usually very challenging. The single specimen J form given in eqs [8] and [9] is not directly applicable to three-dimensional geometries because of different reasons. The single specimen J form can be used only for single valued J as in two-dimensional geometries. J in three-dimensional geometries is not single valued but it varies along the crack front. The single specimen J form requires load separation which is not fully studied yet in three-dimensional geometries. The area under the test record in the single specimen J form is based on the Load-Line Displacement (LLD). In some three-dimensional geometries such as surface cracks, the LLD is insensitive to the crack size and the Crack Mouth Opening Displacement (CMOD) is the displacement that is commonly measured. The crack in the single specimen J form is defined by one parameter, its length, while in three-dimensional geometries, it is defined by two parameters, its depth and width. Thus, in order to simplify J evaluation in three-dimensional geometries and develop a form equivalent to the single specimen J form in two-dimensional geometries, these issues need to be addressed. Load separation in three-dimensional geometries need to be studied. The variable J needs to be replaced by an equivalent single-valued J. The two-parameter crack may need to be represented by an equivalent single parameter crack. A factor equivalent to η_{pl} in the two-dimensional analysis needs to be developed. Finally, the relationship between the LLD and CMOD needs to be studied.

We will focus our discussion here on semi-elliptical surface crack as an example of three-dimensional geometries, see figure 14a. Both experimental and numerical data will be analyzed. The experimental data are for panels made of 2219-T87 aluminum as a base metal with tungsten arc-weld seam that is blunt notched with semi-elliptical surface crack. The panels are 1.0 inch thick and 4.0 inch wide. These data were originally used by McCabe et al (15) in a study on developing J-integral for surface cracks using the equivalent energy approach. The numerical data were developed using a finite element model with 2927 nodes and 387 20-nodes hybrid brick elements. The mesh in the crack vicinity includes several rings of focused elements as shown in figure 14b. The crack tip sides of the first ring elements were collapsed to capture the $1/r$ singularity and the mid-side nodes in the first three rings elements were moved to the quarter point to capture the $1/r^{1/2}$ singularity. The adequacy of the mesh and accuracy of the model results were verified by comparing the results with Newman-Raju elastic solutions and also some experimental test records, see Ref. (16). The model is used to provide load-LLD records, load-CMOD records, and J-integral at different locations on the crack front for different combinations of material, crack depth, crack width, and panel size. These numerical data together with the experimental data will be used here to address the conditions listed above to develop a single specimen J form for surface cracks equivalent to the single specimen J form in two-dimensional geometries.

Load Separation

Figure 15 shows three experimental test records for different crack sizes and figure 16 shows the separation results for this set of records. Also, figure 17 shows several numerical records for several combinations of crack depth and width and figure 18 shows the separation results for this set. σ in the numerical test records represents the remote tensile stress and is equal to the load per unit area. It is clear that load separation also exists in the test records of semi-elliptical surface cracks and the load can be then written as:

$$\sigma = G(a,c)\,H(v_{pl}) \qquad [24]$$

where a is the crack depth, c is the crack width and v_{pl} here is the plastic CMOD.

Effective Crack Length

Sharobeam and Landes (16,17) studied several expressions for effective crack length and concluded that the expression suggested by the R6 method works well for short surface cracks. This expression can be written as:

$$a_e = \frac{\pi a}{2\left[2 + \dfrac{a/c}{a/t}\right]} \qquad [25]$$

where a_e is the effective crack length and t is the specimen thickness. For deeper cracks, this expression may need to be modified.

The Single Specimen Form

They also developed an energy rate interpretation form for surface crack as:

$$J_{pl,av} = -\frac{1}{S}\left[\frac{\partial U_{pl}}{\partial a_e}\right]_{v_{pl}} \qquad [26]$$

where S is the crack front length and $J_{pl,av}$ is the average J_{pl} over the crack front and can be written as:

$$J_{pl,av} = \frac{1}{S}\int_S J_{pl}(s)\,dS \qquad [27]$$

where s is any point along the crack front. From load separation, eq [24], and the energy rate interpretation form, eq [26], a single specimen J form can be written as:

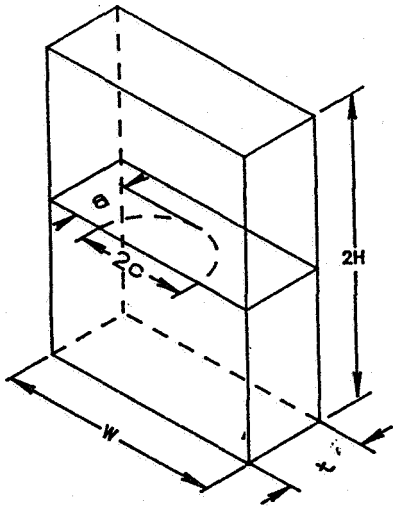

Figure 14a. The semi-elliptical surface crack.

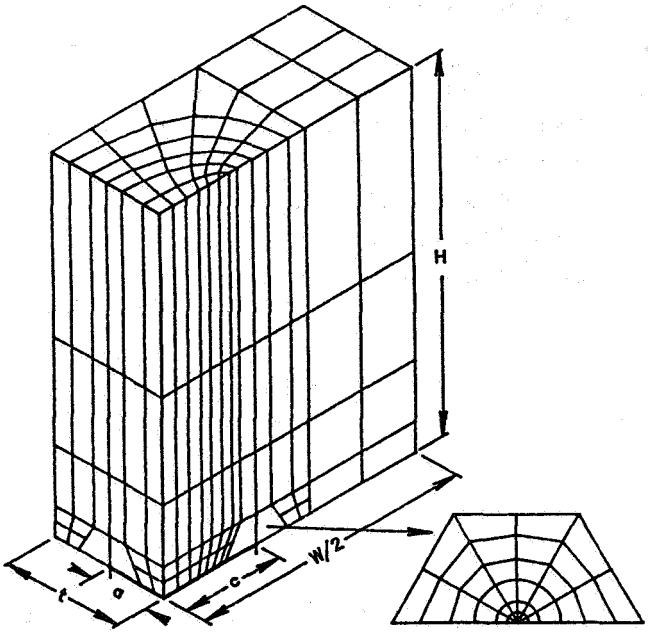

Figure 14b. The finite element model.

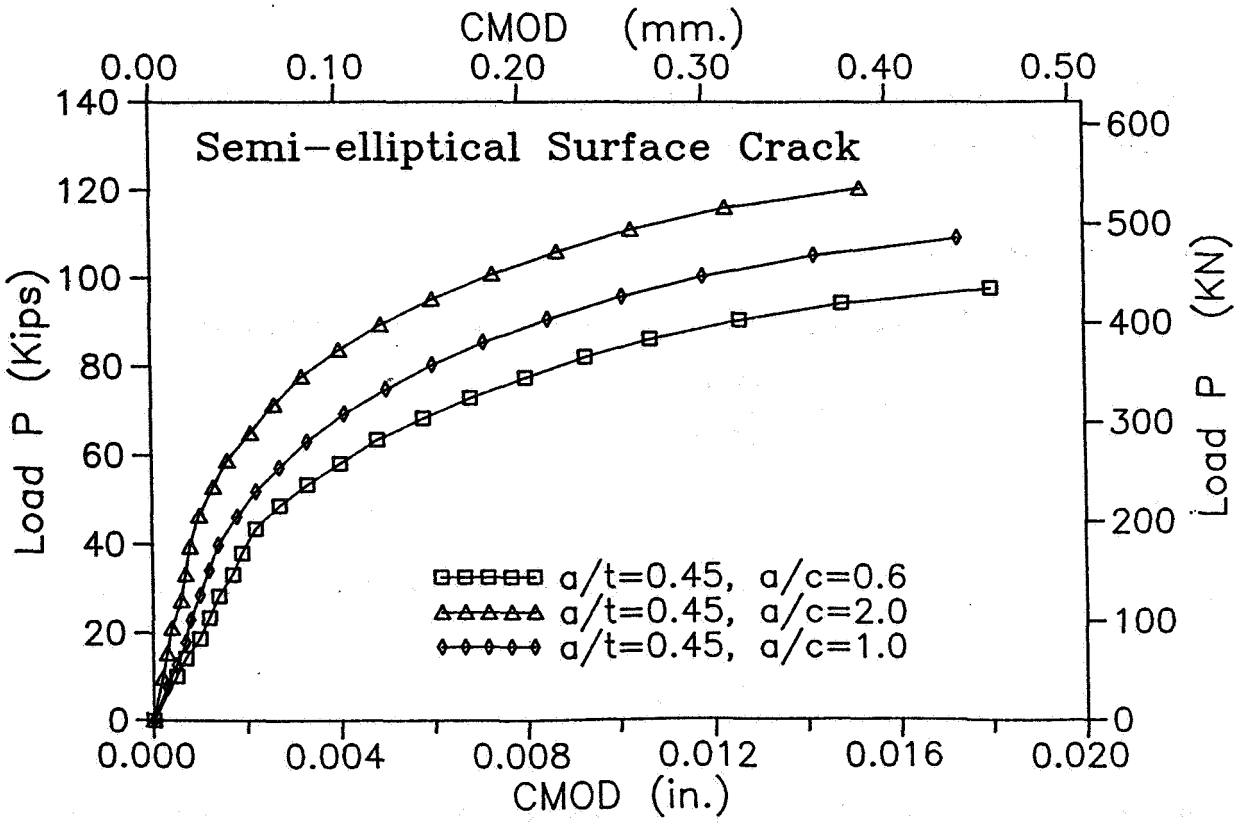

Figure 15. Experimental test records of three surface cracks.

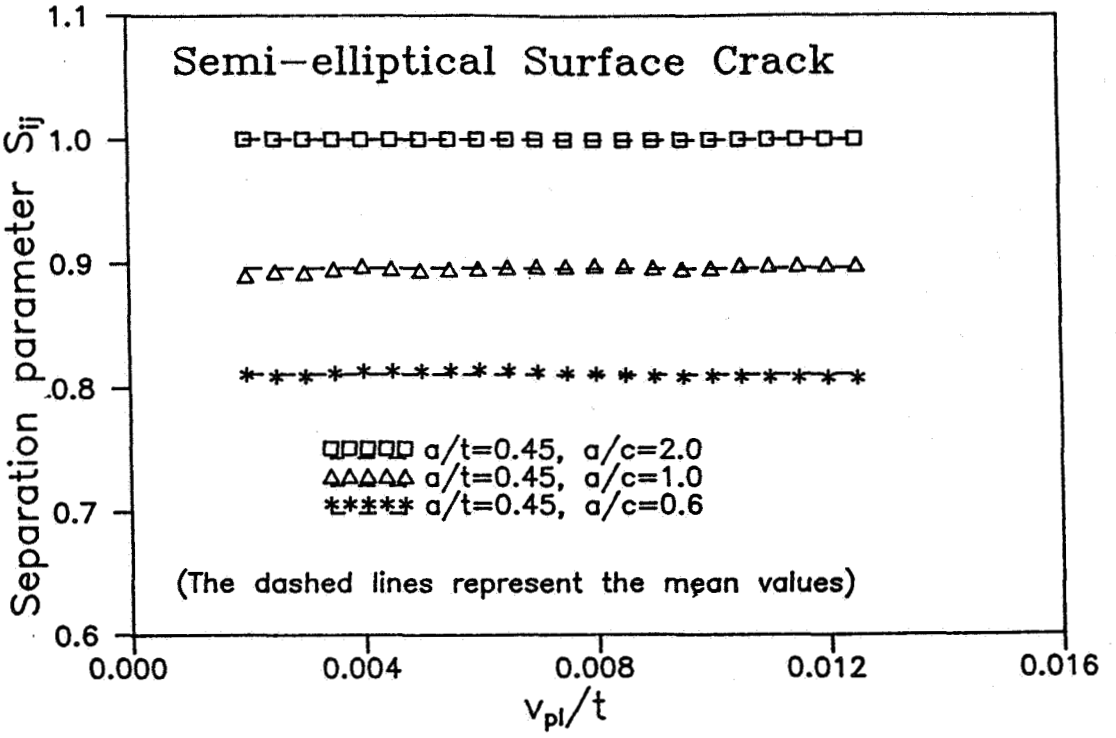

Figure 16. Load separation in the experimental test records of surface cracks.

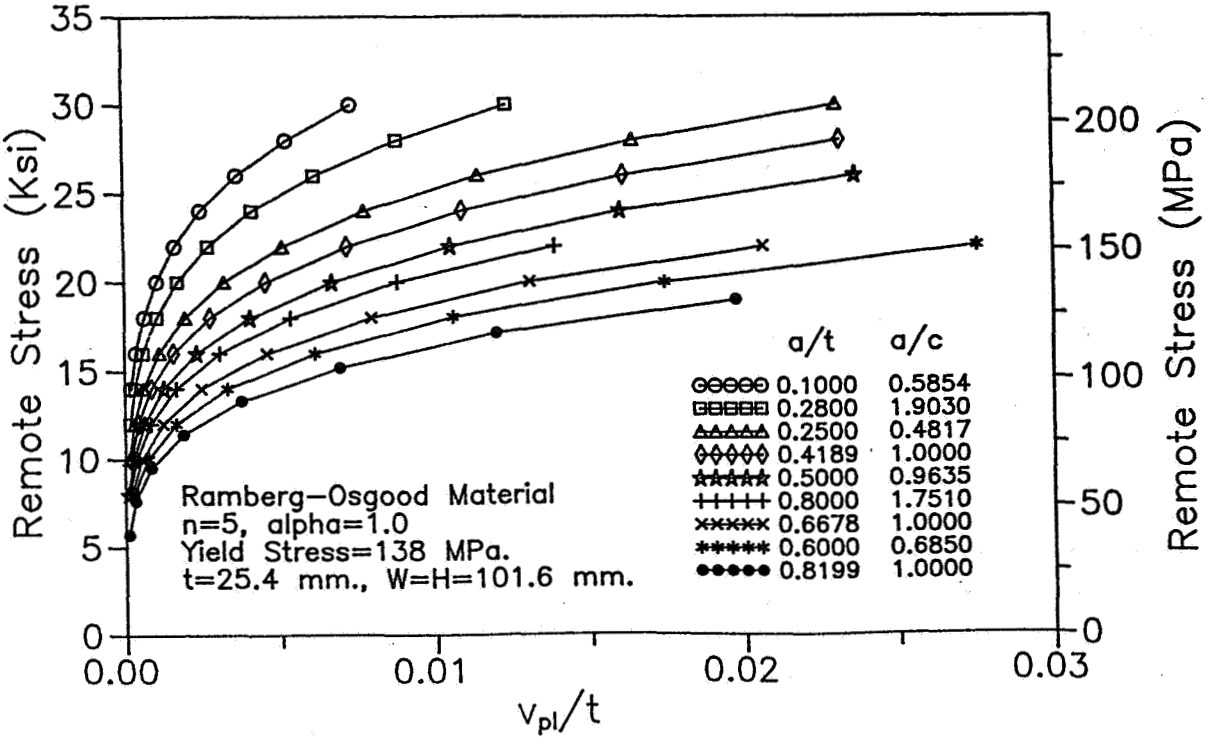

Figure 17. Numerical test records of semi-elliptical surface cracks.

$$J_{pl,av} = -\frac{1}{SG}\frac{\partial G}{\partial a_e}\int \sigma\, dv_{pl} \qquad [28]$$

where G is the geometry function expressed as a function in a_e. The plastic displacement, v_{pl}, in eq [28] could be either plastic LLD or plastic CMOD. It can be shown that the ratio between both plastic displacements is independent of the amount of plasticity for the same crack size and material. Figure 19 shows the ratio between plastic CMOD and plastic LLD at different stages of loading represented by amount of plastic displacement, for different crack sizes. The ratios maintained constant values over most of the plastic region. Thus, each type of plastic displacement can be considered as a constant times the other. Equation [28] can be written in a form similar to the single specimen J form in two-dimensional geometries as:

$$J_{pl,av} = \zeta_{pl}\int \sigma\, dv_{pl} \qquad [29]$$

where:

$$\zeta_{pl} = f\left[\left(\frac{a}{c},\frac{a}{t}\right), geometry, material\right] \qquad [30]$$

The factor ζ_{pl} is equivalent to the η_{pl} factor in two-dimensional geometries. Full description of ζ_{pl} is given in ref. (16). $J_{pl,av}$ in eq [29] can be obtained from the test record of a single specimen. In some cases, the maximum value of J on the crack front and not the average value is required. Sharobeam and Landes (16) developed a relationship between the maximum J and $J_{pl,av}$. They found that this relation is almost independent of the material and specimen size and it can be represented as a function of a/t and a/c only.

THE LOAD SEPARATION METHODOLOGY IN ELASTIC-PLASTIC FRACTURE MECHANICS

Figure 20 shows a schematic flow chart of the load separation methodology in Elastic-Plastic Fracture Mechanics. By testing a set of blunt notched specimens or at least a single blunt notched specimen together with one or more precracked specimens, η_{pl} and the key curve can be developed using load separation. Thus the calibration curves $J(a,P)$ can be obtained. The J-R curve can be developed using a precracked specimen test record and the value of η_{pl} obtained using load separation. The calibration curves $J(a,P)$ together with the J-R curve provide the full elastic-plastic behavior of any structure of same geometry and material as the tested specimen even if it has a different crack size.

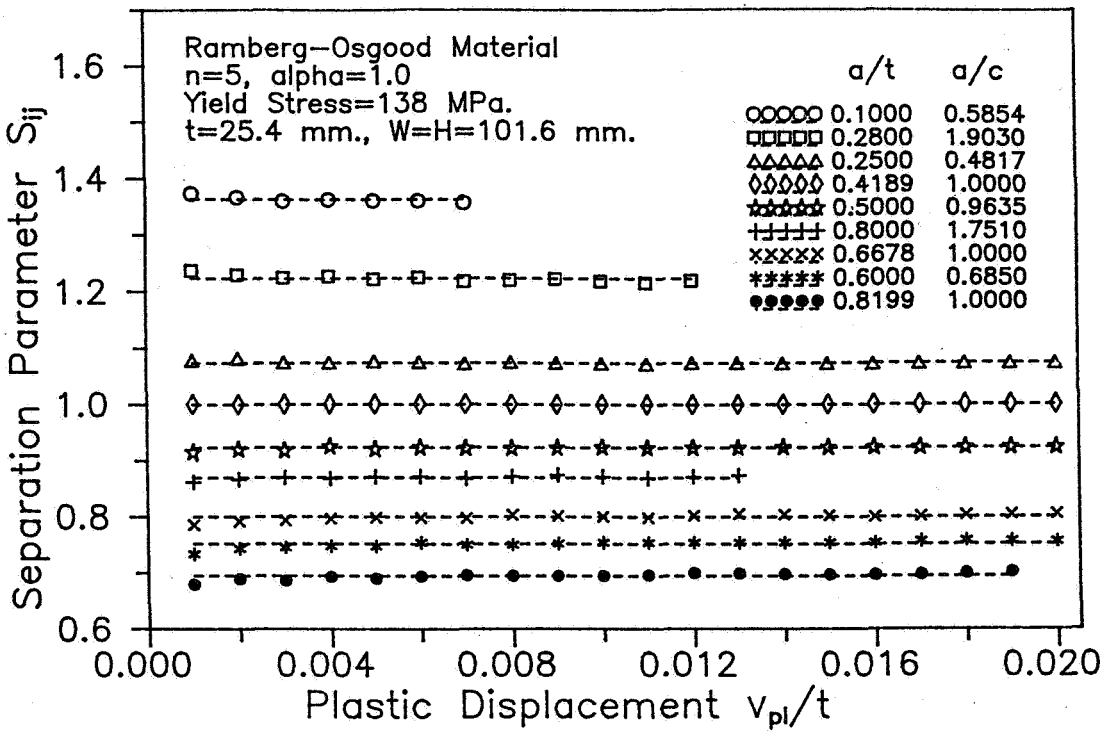

Figure 18. Load separation in the numerical test records of surface cracks.

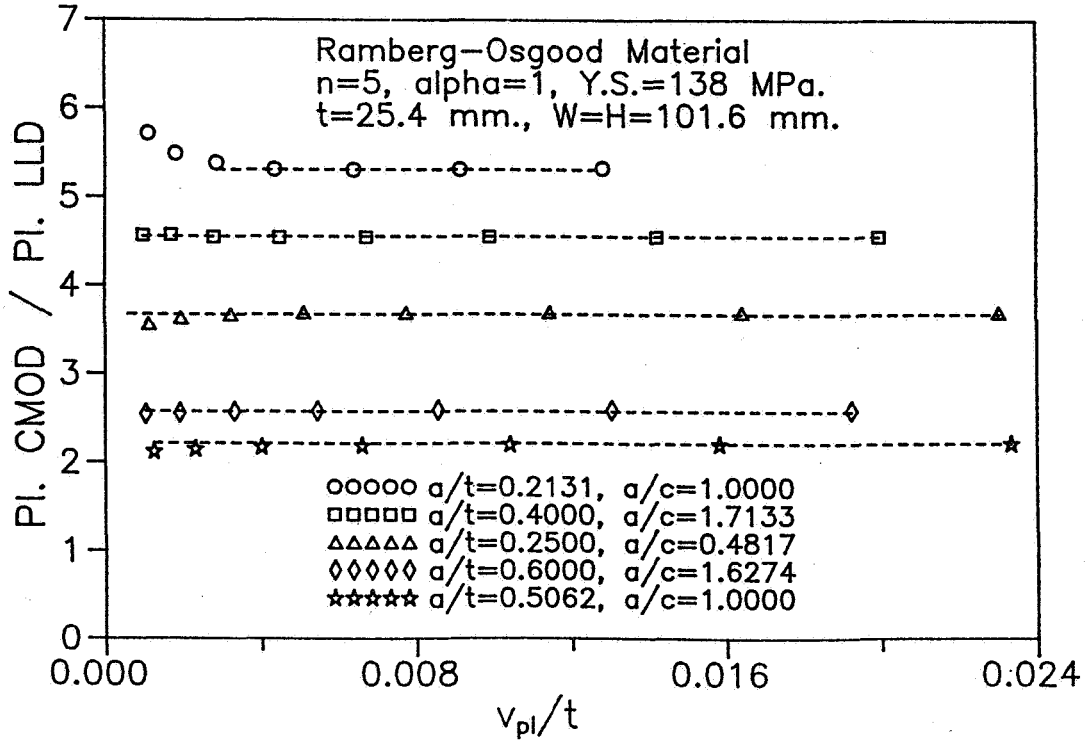

Figure 19. The ratio [plastic CMOD/plastic LLD] versus [plastic CMOD/thickness].

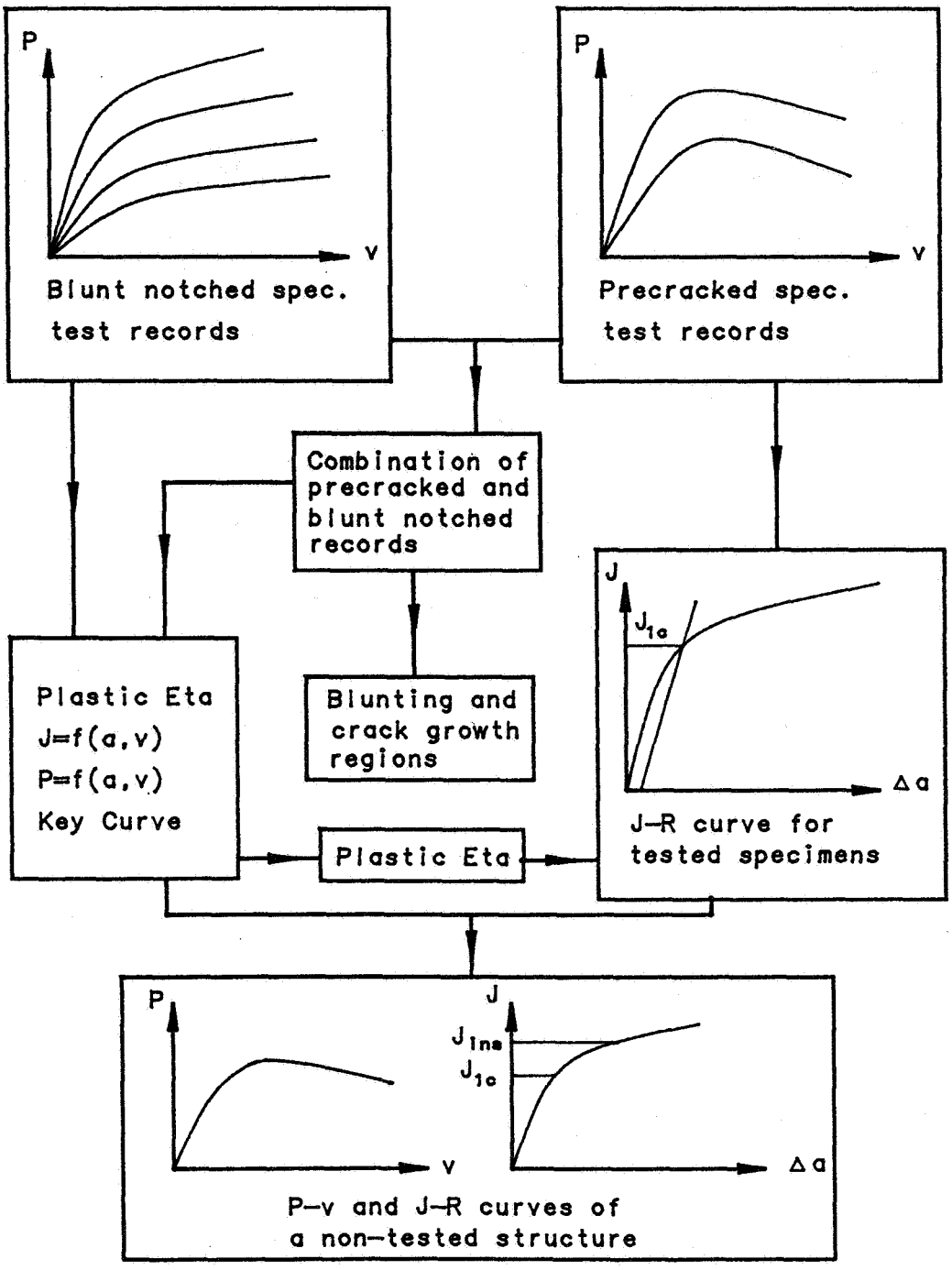

Figure 20. The load separation methodology in Elastic-Plastic Fracture Mechanics.

CONCLUSIONS

Load separation is dominant in both tension and bending two-dimensional geometries. It can be also extended to three-dimensional geometries such as surface cracks. This allows the development of an equivalent single specimen J expression for surface cracks. Load separation exists in both stationary and growing crack test records. It can be used to identify both the blunting and growing crack regions. The η_{pl} factor can be developed using the separation parameters obtained from load separation. Generally, load separation yielded a new simplified approach in Elastic-Plastic Fracture. This approach can be applied to any geometry as long as its test records are showing load separation.

REFERENCES

(1) Rice, J. R.: A Path Independent J-Integral and the Approximate Analysis of Strain Concentration by Notches and Cracks. *J. of Applied Mechanics*, 1968, pp. 379-386.

(2) Begley, J. A. and Landes, J. D.: The J-Integral as a Fracture Criterion. *Fracture Toughness*, ASTM STP 514, 1972, pp. 1-23.

(3) Rice, J. R., Paris, P. C., and Merkle, J. G.: Some Further Results of J-Integral Analysis and Estimates. *Progress in Flow Growth and Fracture Toughness Testing*, ASTM STP 536, 1973, pp. 231-245.

(4) Merkle, J. G. and Corten, H. T.: A J-Integral Analysis for the Compact Specimen, Considering Axial Force as Well as Bending Effects. 74-PVP-33, ASME, 1974.

(5) Ernst, H. A. and Paris, P. C.: Techniques of Analysis of Load-Displacement Records by J-Integral Methods. NUREG/CR-1222, Nuclear Regulatory Commission, Jan. 1980.

(6) 1991 Annual Book of ASTM Standards, Vol. 03.01.

(7) Hutchinson, J. W. and Paris, P. C.: Stability Analysis of J-Controlled Crack Growth. *Elastic-Plastic Fracture*, ASTM STP 668, pp. 37-64.

(8) Ernst, H. A., Paris, P. C. and Landes, J. D.: Estimation on J-Integral and Tearing Modulus T From a Single Specimen Test Record. ASTM STP 743, pp. 476-50.

(9) Landes,J. D., Walker, H. and Clarke, G. A.: Evaluation of Estimation Procedures Used in J-integral Testing. *Elastic-Plastic Fracture*, ASTM STP 668, 1979, pp. 266-287.

(10) Sharobeam, M. H. and Landes, J. D.: The Load Separation Criterion and Methodology in Ductile Fracture Mechanics. *International J. of Fracture*, Vol 47, 1991, pp. 81-104.

(11) Sharobeam, M. H.: The Geometry and Deformation functions in Ductile Fracture Mechanics and Methodologies. Ph.D. dissertation, University of Tennessee, 1990.

(12) Joyce, J. A., Davis, D. A., Hackett, E. M. and Hayes, R. A.: Application of the J-integral and Modified J-integral to Cases of Large Crack Extension. NUREG CR-5143, Feb. 1989.

(13) Sharobeam, M. H.: The Load Separation and η_{pl} Development in Precracked Specimen Test Records. *International J. of Fracture*, Vol 59, 1993, pp. 213-226.

(14) Sharobeam, M. H., Landes, J. D. and Herrera, Ruben: Development of ETA Factors in Elastic-Plastic Fracture Testing Using a Load Separation Technique. *Elastic-Plastic Fracture Test Methods*, ASTM STP 1114, 1991, pp. 114-132.

(15) McCabe, D. E., Ernst, H. A. and Newman, J. C.: Application of Elastic and Elastic-Plastic Methods to Surface Flaws. *Fracture Mechanics: 22nd symp.*, ASTM STP 1131, Vol. 1, 1992, pp. 495-518.

(16) Sharobeam, M. H. and Landes J. D.: A single Specimen Approach for J-integral Evaluation for Semi-elliptical Surface Cracks. *Fracture Mechanics: 25 Symp.*, ASTM STP 1220, 1994.

(17) Sharobeam, M. H. and Landes J. D.: A Simplified Approach for Ductile Failure Analysis of Semi-elliptical Surface Cracks. *International J of Fracture*, 1993, Vol. 61, pp. 397-395.

AN ARTIFICIAL CORROSION PROTOCOL FOR LAP-SPLICES IN AIRCRAFT SKIN*

Bevil J. Shaw

Alloy Technology Division
Alcoa Technical Center
Alcoa Center, Pennsylvania 15069-0001

SUMMARY

This paper reviews the progress to date to formulate an Artificial Corrosion Protocol for the Tinker AFB C/KC-135 Corrosion Fatigue Round Robin Test Program. The project has provided new test methods to faithfully reproduce the corrosion damage within a lap-splice by accelerated means, the rationale for a new laboratory test environment and a means for corrosion damage quantification. The approach is pragmatic and the resulting Artificial Corrosion Protocol lays the foundation for future research in the assessment of aerospace alloys. The general means for quantification of corrosion damage has been presented in a form which can be directly applied to structural integrity calculations.

INTRODUCTION

The life extension program for the USAF C/KC-135 fleet necessitates the inclusion of corrosion damage in the life considerations: a factor which previously may have had a minor impact compared with fatigue damage incurred due to flight cycles. The reason for this is that under suitable climatic situations the corrosion damage continues to accumulate irrespective flight time. The program therefore includes, as a major component, the characterization of the effects of corrosion damage on structural integrity and the concomitant changes that may be required in the inspection periods. The damage associated with corrosion can be very important to component life. The damage factors include:

(i) dimensional changes of components which are of two primary types
- change in gauge thickness, due to general corrosion (which results in increased stress);
- localized corrosion (which can act as a microcrack with enhanced local stresses); and

(ii) changes in material mechanical response to loading via
- change in mechanical properties (due to the absorption of hydrogen) and
- change in fatigue crack propagation rates (acceleration by corrosion fatigue).

* Work performed under subcontract to The Boeing Company, Wichita Kansas, as part of U.S. Air Force Contract F34601-90-C-1336.

Since many aircraft in the fleet were fabricated over 20 years ago, and during the interim period slight modifications and improvements in both compositional range and processing parameters for alloys have been introduced, it is necessary to assess samples of the original material from tear-down aircraft of the aging fleet. These samples have varying degrees of service corrosion damage (natural damage) and can be used directly to assess the related changes in fatigue life. Inspection of the material gathered to date has shown that there may be insufficient samples with significant corrosion damage to provide a reasonable test matrix. Consequently, additional samples are being made by introducing simulated corrosion damage in the laboratory.

The current phase of the USAF C/KC-135 program contains interrelated pilot programs designed to form the framework upon which the new structural integrity issues may be assessed. These include:

(#1) Laboratory Certification for Fracture Mechanics testing,
(#2) Artificial Corrosion Protocol, and
(#3) Test/Evaluation Protocols.

A report on the Test/Evaluation Protocols for Corrosion Damage Assessment (Pilot Program #3) (Ref. 1) was recently issued and it describes the means for optimizing information from a limited matrix of specimens, using a fracture mechanics residual strength model. Pilot Program #2 (Ref. 2), the subject of this paper, is devoted to defining the Artificial Corrosion Protocol, i.e., the means for simulating service corrosion damage in the laboratory. This has to be consistent with the production, within a limited time frame, of a significant number of test specimens to be used in the main component of the fracture mechanics test matrix.

This paper first describes the "natural" damage found in fuselage skin within lap-splices of C/KC-135 aircraft in terms of both the morphology of the damage and the important role of the clad in Alclad skin. The results of corrosion damage produced in C/KC-135 lap-splice samples by three candidate "artificial" laboratory environments are compared with the "natural" corrosion damage and found to be close in appearance. The reasons for long term (up to 60 days) laboratory exposure required to replicate the more severe natural corrosion condition are discussed. Lastly, a general means for quantification of corrosion damage is presented in a form which can be applied parametrically to the structural integrity calculations described in Ref. 1. It should be emphasized that the damage quantification is a most important pivotal issue since it provides the (only) link between NDE (non-destructive evaluation) responses and the damage metrics required for structural integrity calculations and residual life predictions.

NATURAL CORROSION DAMAGE

The term natural corrosion damage is introduced to differentiate the effect of service environments from laboratory environments. The latter is termed "artificial" corrosion damage or "simulated" corrosion damage. This section describes the natural corrosion damage found in samples from fuselage skin lap-splices of C/KC-135 aircraft. It does not include corrosion damage from galley spills (coffee, etc.) or from toilet areas (blue flush, etc.). The general appearance of the damaged skin material and the appearance of corrosion damage in metallographic cross sections are documented. In order to provide a better understanding of the damage process, the results of an experiment which gives a direct observation of the corrosion process in the faying area of a lap-splice are discussed. This information about the evolution and distribution of the corrosion damage is needed to clarify how it should be sampled to provide a meaningful quantification. The natural damage found in fuselage skin of a C/KC-135 aircraft is also analyzed in terms

of depth of attack. The terms "Light", "Moderate" and "Severe" corrosion damage are discussed in terms of both the morphology of the damage and the important role of the clad.

General Appearance of Natural Corrosion Damage

The type of corrosion damage found at a lap-splice is exemplified by a "pillowing" or tufting of the outer skin, similar to the tufted appearance of stuffed upholstery. Figure 1 shows a schematic of a lap-splice and how metallographic sections are oriented. Cross sections of the fasteners from lap-splices showed that the tufting effect is caused by corrosion product forcing the skin sheets apart in the presence of fasteners or rivets. It was found that this effect can cause cracking in the rivets. Extreme corrosion damage was also found in the vicinity of spot welds. Damage to the rivets and to welded metal (including the heat-affected zone, HAZ, of the weld) is important but not the primary consideration of this paper.

The corrosion process cannot initiate unless moisture has access to a bare aluminum surface in the faying area. Since the C/KC-135 surfaces are painted and sealed prior to service, the corrosion damage is initiated after the protecting surface has deteriorated. The deterioration is probably a function of paint aging combined with stresses which result from service use and thermal sources (e.g., differential expansion and contraction at a rivet). Inspection of aging aircraft skin structure has shown that crevices in paint are often formed at the fillet and also at the periphery of rivets. Corrosion damage from the crevice around the rivets of a fuselage lap splice *appears* to be somewhat less prevalent than damage from the fillet. Consequently, damage from the fillet is emphasized in this paper.

Natural Corrosion Damage – Light, Moderate and Severe

As part of the Tinker AF project, Boeing-Wichita had characterized the nature and distribution of corrosion damage on a tear-down C/KC-135 aircraft. This natural corrosion damage, which was designated "Light, Moderate and Severe" was approximately characterized by

"light"	"L"	less than 1 mil,
"moderate"	"M"	1 to 10 mils
"severe"	"S"	greater than 10 mils

They found that after stripping the paint, the "M" damage inspected under a high powered (X20) glass appeared as small black specks to the trained eye. Metallographic cross sections of the "L" and "M" conditions were made for evaluation on an IBAS (system for automatic image analysis). The maximum depth for the "L" condition fell between 10 and 25 microns (25 microns is about 1 mil) and the "M" condition had a maximum of 55 microns. It is reasonable that the "M" condition should include "L". It is important to note that the sample of "L" and "M" fuselage skin was Alclad and that the thickness of the clad was 60 ± 10 microns. An inspection of over 30 one-inch-long sections of this sample of "L" and "M" damage showed that it all was within the clad. Further evaluations of 7075-T6 and 2024-T3 lap-splice samples from a C/KC-135 had similar characteristics.

In the course of the inspection of *cross sections* of corroded specimens, it became apparent that the distribution of the corrosion damage, as a function of distance from the fillet of the lap splice, was quite irregular. For example, proceeding from a heavily corroded section adjacent to the fillet, one might find a section of no corrosion followed again by heavy corrosion. In other words, the corrosion damage, judged by depth or area in the cross section, was not a simple decreasing function of the distance from the fillet.

A number of lap-splices were taken apart and it was found that the faying surface of the inner skin was not painted. This suggests that the skin is undercoated on the inner surface prior to construction and the outer surface is painted after construction. The one residual bare aluminum surface in the faying area often appears to be chemically treated, e.g., with Alodine, but it is also the preferentially attacked surface since it is not painted.

Plexiglas Simulation Experiment

In order to observe the corrosion phenomenon in the faying area, a simulation lap splice was made in which the outer, completely painted skin surface was replaced with a sheet of Plexiglas attached to an Alclad sheet by nylon bolts. The specimens were stood upright so that the fillet was just immersed in a solution (EXCO (Ref. 3) to which hydrogen peroxide (H_2O_2) was added at the rate of 10 ml/litre/day.) which was drawn up into the faying area by capillary action. Moisture entry in service must be somewhat similar to this process. The faying areas of the simulation lap-splices had a similar appearance to that of the service specimens. Inspection on daily intervals showed that the solution was not drawn uniformly into the crevice and that the distribution of corroded surface was correspondingly irregular. The total corroded area also varied discontinuously with time, probably because the corrosion product filling the crevice gradually lifted the Plexiglas until the condition for further solution penetration into the faying area was created.

In the simulation experiment it was observed that the paint adjacent to the fillet (equivalent to the outside skin surface) was lifted from the aluminum surface. In the service situation, the degraded paint surface would be repaired by paint removal and repainting. This procedure will serve to introduce paint in the fillet (a paint wedge which can be 10 mils thick) in so far as the corrosion product has not been removed. There are important consequences to this situation since the resulting configuration, with substantial new paint included in the fillet compared with none previously, will provide *additional protection* to the faying area. The additional time required to reactivate corrosion process within the faying area will be as long as it takes either to undermine the paint wedge or to penetrate the area from the side. It is evident from this discussion that a lap-splice which *appears* to be unaffected by corrosion may and often does contain *occluded* corrosion damage if it has been repainted.

Discussion of the Role of the Clad

Alclad sheet product has been employed in aircraft construction for corrosion resistance and strength retention characteristics since 1928. The clad, typically 1 to 10% of the thickness of the sheet (i.e., usually in the range 1 to 3.5 mils or 25 to 90 microns) is metallurgically bonded to the core (Ref. 4). There are two stages to the protection. First, the clad itself is more resistant to corrosion than the core. Secondly, since the clad is also anodic to the core, it provides electrochemical protection of the core. If a corrosive solution is in contact with both the core and the clad, current from the anodic cladding flows through the electrolyte to the core which is then protected since the clad tends to dissolve. This protection depends upon conductivity in the electrolyte.

In the faying area of the lap-splice, moisture (rainwater) containing environmental pollutants (NaCl, H_2SO_4, etc.) is probably introduced by capillary action. Once a crevice has formed in the protective paint at a fillet, the clad in the faying area (not in contact via an electrolyte to the core in the initial stage) can be corroded by the moisture. When contact via the electrolyte has been made with the core, the primary

corrosive action will be the dissolution of the clad. This contact may be made by attack through the clad or from within a hole for a fastener or rivet in the skin. Normally, this stage provides protection for a very long time. Consequently, it is commonly observed that the faying surfaces of a lap-splice, which has been taken apart, are covered with (a white) corrosion product which very often does not penetrate the core. Penetration is achieved in circumstances where contact between the clad and core has been lost or the "throwing power" (Ref. 5) is limited by distance between the clad and core.

From the mechanistic point of view there are three stages of corrosion damage to the skin.

(i) Pitting of the clad, which can be loosely associated with the light, "L", condition of attack less than 1 mil.
(ii) More general dissolution of the clad, resulting from the electrochemical protection. Provided the clad is greater that 1 mil thick, which it usually is, this stage falls in the moderate attack, "M", condition.
(iii) Attack beyond the clad into the core of the skin. This stage can fall within the "M" or "S", severe, condition. Note that the attack of the core can and often does include intergranular cracks and (equivalently) exfoliation crevices.

ARTIFICIAL CORROSION DAMAGE

This section provides a review of results from corrosion in laboratory environments, termed artificial or simulated corrosion damage. The primary emphasis has been on the replication of the corrosion damage found in the skin due to natural environments. The program required the development of a protocol for the simulation of severe "S" corrosion damage in as short a time as possible. All of the C/KC-135 fuselage lap-splices samples received for the study were Alclad on both faces except for one sheet of one lap-splice which was clad on one face only. This was one of the painted surfaces in the faying area and so it was relatively free from attack. Consequently, the discussion of the role of the Alclad given in the previous section pertains to the artificial corrosion study. Procedural rules for the corrosion protocol included the requirement to make the method as close to the natural process as possible. Thus, lap-splice specimens were cut from a dismantled C/KC-135 aircraft and tested without modification except that the paint at the fillet could be broken by local impact.

Corrosion in the Faying Area of the Lap-Splice – Environments

In the service situation moisture will be retained within the faying area crevice while the outside of the aircraft can be dry. This extended moisture period should be examined, possibly by use of specimens with a Plexiglas face, in order to determine a relationship between the service experience and the laboratory test. The following example gives an idea of the order of magnitude involved. A lap-slice which had been tested in EXCO was dismantled to expose to air the moist corrosion product on the faying surfaces. Under an orthoscope it was observed that hydrogen was evolving from the corroded surface and continued to evolve for five days. The relative humidity was not high, between 40 to 50%, for the entire period. Clearly, the faying area of the lap-splice would have retained moisture for a longer period.

In a series of experiments on a separate Alcoa project, it was demonstrated that the most degrading condition in the Alternate Immersion (AI) test (Ref. 6) is towards the end of the drying cycle. It was also shown that this condition was related to oxygen content of the solution and that it could be replicated by the addition of H_2O_2. Similarly, Ishihara et al. (Ref. 7) demonstrated that fatigue crack growth is strongly

influenced by the transport of oxygen to the solution localized at the tip of the crack. In fact, one of the ASTM standard methods, G 110- 92 (Ref. 8), for evaluating intergranular corrosion resistance of heat treatable aluminum alloys employs a NaCl + H_2O_2 solution. The blending of this method with the EXCO method therefore appears to be a logical way of accelerating the attack. Oxygen reduction on the metal outside the crevice, especially because the area of exposed metal outside the crevice is small, is a rate limiting factor for the crevice corrosion. Hence, the addition of the H_2O_2 to the solution optimizes the crevice corrosion process.

It is known that adjacent to a crack tip the pH will increase to a value of 3 to 4, due to "buffering" or the dissolution of A (Refs. 9, 10). In fact, the pH within a crack has been found to be relatively insensitive to the pH of the solution. Within the faying area crevice the conditions will be similar. In the EXCO or EXCO + H_2O_2 test, the corrosion rate is slower within the crevice than on the outer surface where the pH is maintained at .5 to 1.5. It follows that whereas the experimental condition may be similar to service conditions for the faying area, they are quite different on the outer surface. In the experimental condition part of the sample is immersed in the solution whereas in service the skin is in air. For this reason particular care has to be taken to seal the specimen outside of the crevice at the fillet.

Returning again to the requirement that the laboratory process should closely replicate the natural environment, it is evident that whereas EXCO and EXCO + H_2O_2 replicates the corrosion damage *appearance* of heat treatable aluminum alloys, the EXCO solution bears little resemblance to the rainwater which would be found around the world in service situations. It might be considered to be representative of sea-board or marine spray, but S. B. Lyon et al. (Ref. 11) state that this kind of test environment is not appropriate for atmospheric corrosion testing since there is little similarity to naturally occurring rainfall and the corrosion products could be different from those produced during natural weathering. Certainly, EXCO contains no H_2SO_4 and almost invariably sulfur is found in natural corrosion products produced by rain. The composition and pH of the "artificial acid rain" (AR) solution provided by S. B. Lyon et al., compared with EXCO is shown in Table 1.

An experiment was carried out to compare the relative attack caused by AR and EXCO, with and without H_2O_2, on the bare surface of a 7146-T6 alloy which is used as an exfoliation standard. The corrosion damage is enhanced by the H_2O_2 and the EXCO is considerably more aggressive than the artificial rain but the metallographic cross sections of the specimens all show similar exfoliation corrosion characteristics. Since the EXCO is far removed from the natural acid rainwater composition and the "artificial acid rain", even with H_2O_2, is not very aggressive, it was decided to employ a more concentrated composition of AR which approximates to a log mean between AR and EXCO. The composition and pH of the "concentrated artificial acid rain" (ARX) are given in Table 1. AR and ARX have pH values less than will be expected within the crevice but they will not lift paint from the skin surface quite as aggressively as EXCO. The relative performance of the three solutions, EXCO, AR and ARX with H_2O_2 addition is given in the next section.

Corrosion in the Faying Area of the Lap-Splice – Corrosion Rates

Lap-splice specimens from a tear down C/KC-135 aircraft of Type #1 (7075-T6) and Type #3 (2024-T3) were used for the primary experiments. All areas except the cracked paint at the fillet were sealed with Finch primer or RTV. The specimens were stood upright so that the fillet was just immersed in the solution which was drawn up into the faying area by capillary action. The specimens were tested in the three solutions listed in Table 1. It was established that 15 day intervals would be sufficient to adequately

follow the damage evolution in the faying area. In the initial experiments metallographic sections were taken perpendicular to the fillet (i.e., perpendicular to the line A-A in Figure 1) with a view to measuring the "damage" along this length to represent the effect of distance from the fillet. However, it was subsequently found that the damage is not a uniform function of distance from the fillet and hence, for the 30 and 45 day analyses sections were taken as indicated in Figure 1. After metallographic sectioning, statistics of the corrosion damage were gathered on the IBAS (system for automatic image analysis).

The IBAS stores a representation of the image on its computer and hence allows for image enhancement and rapid quantification of features depicted via pixels on the monitor screen. Figure 2 shows a typical (IBAS image enhanced) metallographic section from corrosion damaged faying area with light "L" and moderate "M" damage characteristics. The appearance of the natural corrosion damage (Ref. 2) is the same as the artificial corrosion shown in these figures. The IBAS data gathered from the damaged skin cross sections was:

(i) The maximum depth of the damage, $d_{(max)}$,within a given field of analysis (L_f)
(ii) The total area of the damage (ΣA) within a given field of analysis (L_f).
(iii) The total surface length of damage, (ΣL)within a given field of analysis (L_f).

where L_f is the length of the cross section of the skin which has been analyzed at a given location. These data are sufficient to characterize the corrosion damage for the Artificial Corrosion Protocol purposes. The acuity (or sharpness quantified in degrees) of pits or crevices can also be readily determined on the IBAS. However, important as acuity may be to the life prediction (local stress enhancement leading to reduced time for crack initiation) it was not included in the current study which is designed to introduce the damage. The data package generated for the test matrix contained four primary variables as follows:

(i) specimen type	Type #1, Type #3 (7075-T6, 2024-T3)
(ii) location (distance, Y, from fillet)	0.25 inch intervals to 2 inches Y0, Y1, Y2,...Y_n..
(iii) solution	EX, ARX and AR.
(iv) time	0, 15, 30 and 45 days

From the above data set, representations of damage distribution, both for exposure time and location, can be graphically depicted provided a metric of damage is defined. For a skin section, the "loss of area" is the change in thickness of the skin times the length of skin section under load. Consequently, thickness or change in thickness is the required metric. Non-uniform loss due to corrosion damage raises interesting questions for the definition of the term "equivalent loss of area". At one extreme there is the *local* thickness (which in fact could include acuity, for which one may attribute an equivalent flaw) and at the other extreme the *average* thickness. The two measures of the skin damage (which are estimates of the change in thickness of the skin) may be regarded as approximations to an upper bound and a lower bound to the loss of area.

For the upper bound, a (first) approximation is the "average maximum pit depth" (i.e., average of $d_{(max)}$) in each location (Y). This is proportional to the maximum depth of the corrosion damage across the faying area in each location. The actual maximum depth can be estimated from application of extreme statistics to the maximum depth distribution. For the lower bound, a (second) approximation is the "average depth of attack" of the skin in each location (Y). This is the total area of the damage divided by the total surface length of damage within the field of analysis in each location (Y) or $[\Sigma A/\Sigma L]_Y$.

The approximation for "equivalent loss of area" is not limited to these two estimates. The upper extreme bound could be represented by some change in thickness which takes into account the extreme maximum pit depth and an equivalent flaw factor associated with acuity. The lowest extreme bound would be represented by an "average thickness loss" of the skin which is the total area of damage divided by the surface length in the field of analysis in each location (Y) or $[\Sigma A/Lf]_Y$. Examples of distributions of the "loss of area" approximated by the "average maximum pit depth" - as a slightly low estimate for the upper bound - and "average depth of attack" - as a lower bound - may be represented graphically .

In this paper one example, Fig. 3, showing the effect of the test solutions and time at the fillet (Y=0) and another, Fig. 4, showing the effect of time and distance from the fillet ($Y=Y_n$) on the average maximum pit depth serve to represent the general trends found in the experiments. (See Ref. 2 for more detailed treatments.) In general, the corrosion damage rate for EX>ARX>AR, though ARX and AR are not as clearly separated as EX and ARX. Note that the zero day damage is the natural damage found in the "as-received" condition. The effect of time and distance from the fillet on the average maximum pit depth shows the expected trends that

(i) damage penetration from the fillet increases with time
(ii) the depth of corrosion damage at a given time (pitting or clad dissolution) is reduced with distance from the fillet and
(iii) damage tends to be greater in Type #1 (7075-T6) than Type #3 (2024-T3).

Figures 3 and 4 show that in the AR environment the damage barely exceeds the depth of the clad within the faying area whereas the penetration of damage beyond the clad is significant in both ARX and EXCO.

The clad alloys for 7075 and 2024 are 7072 and 1230, respectively. Typically, the 7072 is less resistant to corrosion than 1230. However, with no clad, 7075-T6 is more resistant to corrosion than 2024-T3. It follows then that the initial "damage" in terms dissolution of the clad will proceed faster in the 7075-T6 samples. Most importantly, the undercutting of the paint immediately adjacent to the fillet is lifted faster in 7075-T6 than 2024-T3 samples. Also, our observations of the rate of paint undercutting are EX>ARX>AR as expected. Since the corrosion rate in the faying area increases with the uncovered metal immediately outside the fillet (Ref. 12), the initial crevice corrosion rate within the clad should be faster in Type #1 than Type #3 for both reasons (clad resistance and undercutting rate).

Referring again to the Plexiglas experiment described above, it was found that a "Heavy" corrosion product adjacent to the Plexiglas of the simulation lap-splice experiment fillet was equivalent to "M" corrosion within the clad. The rate of growth of the "M" corrosion attack perpendicular to the fillet is approximately 0.8 to 1 mm per day (about 1-1.25 inches per month) in the 2024-T3 specimen. The average penetration of "M" corrosion in the 7075-T6 specimen was difficult to measure, because the interface with lighter corrosion was obscure, but it appeared to have a slightly faster growth rate.

The Plexiglas simulation experiment can be compared with the artificial corrosion experiment. Figure 4 shows that the moderate damage condition for the Alclad 2024-T3 in the EXCO test is found approximately 0.5 in from the fillet after 30 days and 1.25 inches after 45 days, i.e., a rate of 0.5 to 0.8 inch per month. This is in reasonable agreement with the observed Plexiglas experiment rate of about 1 inch per month, considering that the Plexiglas should be lifted more readily by the accumulated

corrosion product than aluminum. The corresponding rate for the Alclad 7075-T6 in the EXCO test, Figure 4, is about 1.25 inch per month.

DISCUSSION AND CONCLUSIONS

The experiments have shown that initially an aggressive environment (e.g. EXCO) has to be used to lift the paint and dissolve the clad adjacent to the fillet within a short time (i.e. days). In this stage, (i) corrosion damage will extend from the fillet crevice both into the faying area and under the adjacent exterior paint, and (ii) all surfaces except the paint crevice at the fillet must be carefully protected in order to limit specimen surface degradation. The artificial acid rain solution (AR) is not sufficiently aggressive for this stage. Since the solution in the faying area is "buffered", the subsequent corrosion rate within the faying area is probably similar for the three test solutions evaluated. The corrosion rate in the faying area should increase with uncovered metal immediately outside the fillet. As a result of these considerations, the damage should be introduced in two stages.

(1) Rapidly undercut the paint outside the fillet with an aggressive environment, e.g., EXCO + H_2O_2.
(2) Maintain an optimum crevice corrosion condition which limits rapid attack outside the fillet. This can be achieved by alternate immersion in AR or ARX + H_2O_2 in which the crevice retains moisture. The composition of the second stage environment is a concentrated rain which is representative of the natural environment.

Since the paint lifting from the specimen surface in stage (1) will be a function of the Alclad alloy and the quality and type of paint, the metal surface area in contact with the solution will be an (uncontrollable) function of time. This means that for a given time of exposure to the EXCO solution, the amount of damage for one sample will not necessarily be the same as for another. It follows that each batch of material should be processed independently to produce the same amount of corrosion damage.

The quantification of corrosion damage is discussed only from the point of view of geometric change and does not include important considerations such as crack growth in the presence of a corroding environment (corrosion-fatigue) or the role of absorbed hydrogen on crack initiation or propagation. The mechanistic point of view indicates three stages of corrosion damage to the skin:

(i) Pitting of the clad, which can be loosely associated with the light, "L", condition of attack less than 1 mil.
(ii) More general dissolution of the clad, resulting from the electrochemical protection. Provided the clad is greater that 1 mil thick, which it usually is, this stage falls in the moderate attack, "M", condition.
(iii) Attack beyond the clad into the core of the skin. This stage can fall within the "M" or "S", severe, condition. From this viewpoint it would be simpler to define "M" as stage (ii) i.e. greater than 1 mil and within the clad and "S" as attack extending into the core, i.e. greater than 2 to 3 mils.

Quantification of the corrosion damage is required for life analysis methodologies and structural integrity calculations. The simplest model should consist of two parameters which may be determined from metallographic cross sections:

(i) Loss in thickness of the skin which is directly related to the "loss of area" is discussed and

(ii) An "equivalent flaw" component which represents pits, intergranular cracking or exfoliation crevices in excess of the average loss in area.

ACKNOWLEDGMENTS

I am indebted to R. J. Bucci, E. L. Colvin and J. P. Moran for valuable technical discussions. B. J. Johnson carried out the IBAS analyses on metallographic sections prepared by J. C. Vilsack. The specimen preparation and corrosion tests were carried out by C. L. Kulick, P. K. Vandenburgh and P. R. Ziman with the general project supervision by J. J. Liput.

REFERENCES

1. Bucci, R. J. et al.: "Test/Evaluation Protocols for Corrosion Damage Assessment," Report for Boeing Company as part of U.S. Air Force Contract F34601-90-C-1336 (1993). Also, "A Fracture Mechanics Based Approach for Quantifying Corrosion Damage," Tri-Service Conference on Corrosion, Orlando, Florida (1994).

2. Shaw, B. J: "An Artificial Corrosion Protocol for Lap-Splices in Aircraft Skin (Pilot Program #2) C/KC135 Corrosion Fatigue Round Robin Test Program," U.S. Air Force Contract F34601-90-C-1336, Alcoa Technical Report No 56-94-OM219, (1994).

3. ASTM G 34-90 "Standard Test Method for Exfoliation Corrosion Susceptibility in 2XXX and 7XXX Series Aluminum Alloys (EXCO Test)" (1990).

4. Brown, R. H.: "Alclad and Clad Aluminum Alloy Products," ENGINEERING LAMINATES, ed. A. G. H. Dietz, pp. 227-239 (1969).

5. Metals Handbook Ninth Ed., ASM Vol. 13, "Glossary of Terms," (1987).

6. ASTM G 44-88 "Standard Practice for Evaluating Stress-Corrosion Cracking Resistance of Metals and Alloys by Alternate Immersion in 3.3% Sodium Chloride Solution" (1990).

7. Ishihara et al., "Effects of Dissolved Oxygen in Solution on the Small Corrosion Fatigue Crack Growth Behaviors in Aluminum Alloy," Bull. Fac. Eng., Toyama Univ., 38, pp. 19-33 (1987).

8. ASTM G 110-92 "Standard Practice for Evaluating Intergranular Corrosion Resistance of Heat Treatable Aluminum Alloys by Immersion in Sodium Chloride + Hydrogen Peroxide Solution," (1992).

9. Sedricks, A. J. et al.: "On the Chemistry of the Solution at the Tips of Stress Corrosion Cracks in Al Alloys," Corrosion 27, pp. 198-202 (1971).

10. Brown, B. F. et al: "Methods for Studying the Solution Chemistry Within Stress Corrosion Cracks," J.. Soc., 116, pp. 218-219 (1969).

11. Lyon, S. B. et al: "Materials Evaluation Using Wet-Dry Mixed Salt-Spray Tests," ASTM STP 1134, V. S. Agarwala and G. M. Ugiansky, Eds., pp. 20-31 (1992). (See Table 3 p. 26).

12. Kaesche, H.: "Metallic Corrosion," NACE publn. (1985).

Table 1. Compositions of EXCO, Concentrated Acid Rain and Artificial Acid Rain. Laboratory tests were carried out in these solutions with the addition of 10 ml/litre/day of H_2O_2.

Solution Concentrations [per litre]			
	(1)	(2)	(3)
	EXCO	Concentrated Acid Rain	Artificial Acid Rain*
NaCl	234 g	5 g	0.085 g
KNO_3	50 g	—	—
HNO_3	6.3 ml	0.25 ml	16 mg
H_2SO_4	—	0.5 ml	32 mg
$(HN_4)_2SO_4$	—	1500 mg	46 mg
Na_2SO_4	—	1000 mg	32 mg
$NaNO_3$	—	750 mg	21 mg
pH	~0.6	~2	~3

* Ten times average concentration in Greater Manchester [U.K.] in 1986. (Industrial Environment)

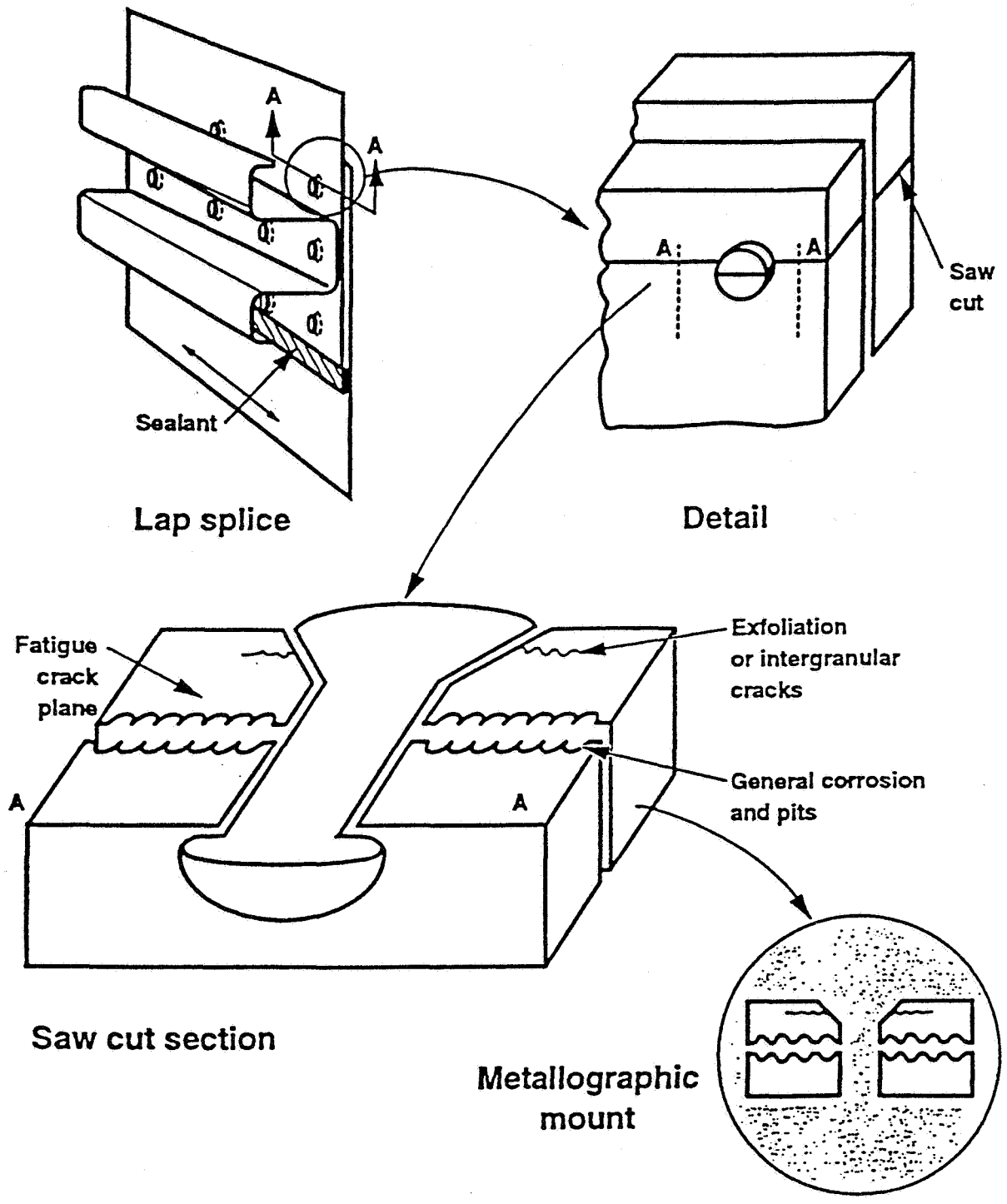

Figure 1. A schematic of a lap-splice showing how metallographic sections are oriented.

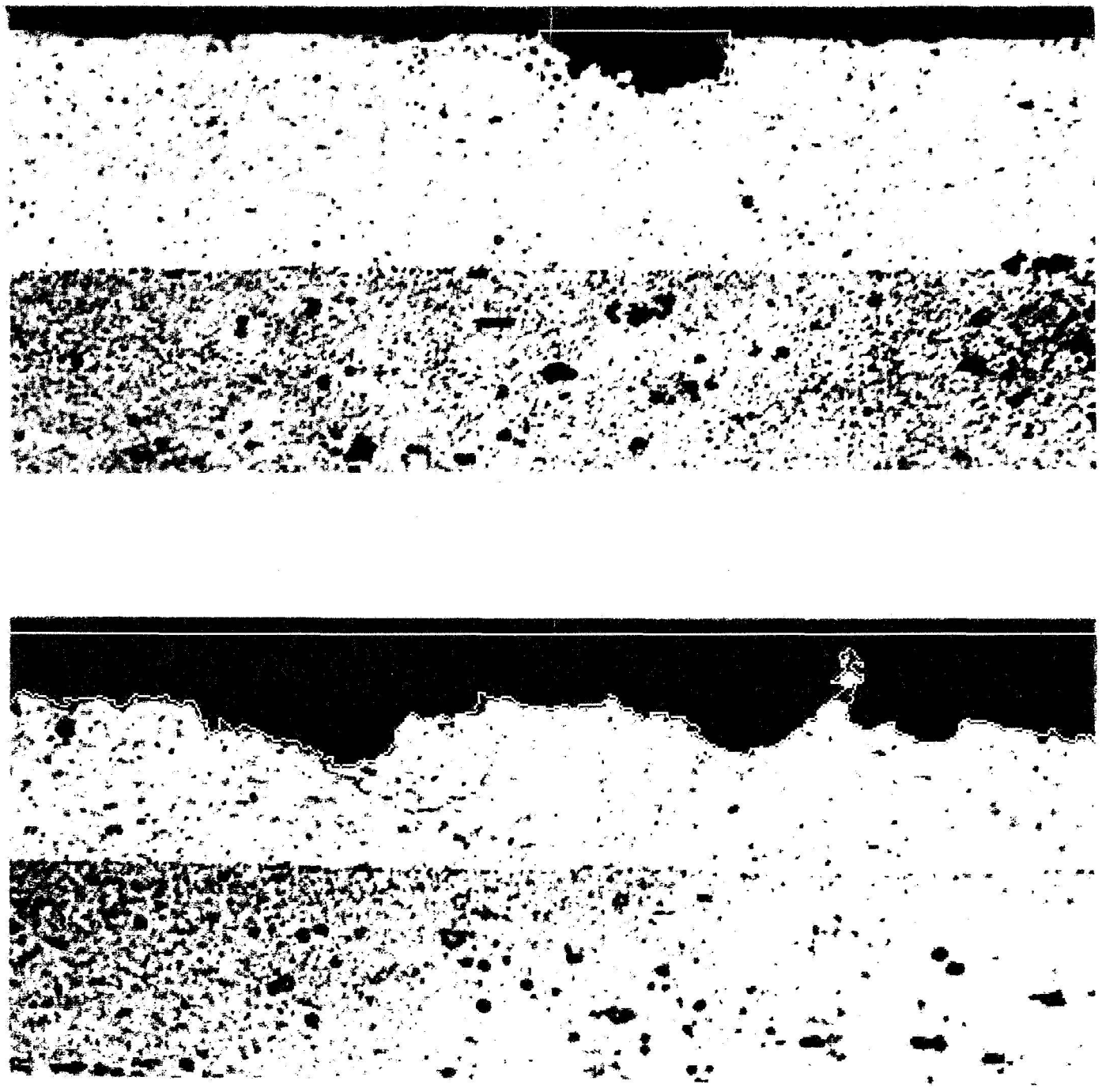

Figure 2. Image analyser micrograph showing (a) light (L) and (b) moderate attack (M) of the joint faying area made from 2024-T3 Alclad sheet. The clad layer is the lighter structure at the top of the micrograph, about three mills thick. The white line at the top of the micrograph shows the original location of the clad surface. The quantitative measurements include the area loss within the length of a cross section and the average and maximum depth of penetration. Magnification X500.

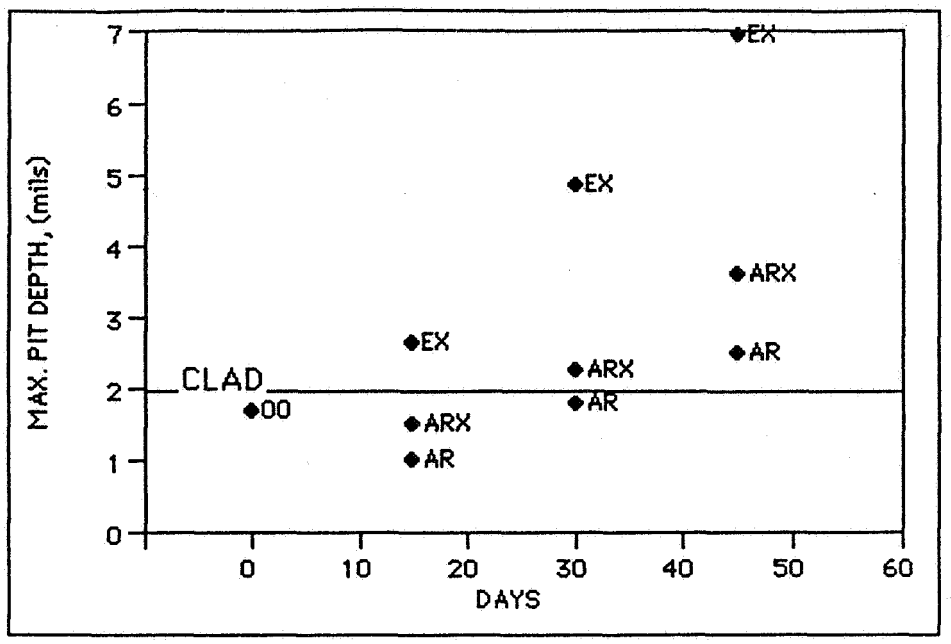

7075-T6 AT FILLET

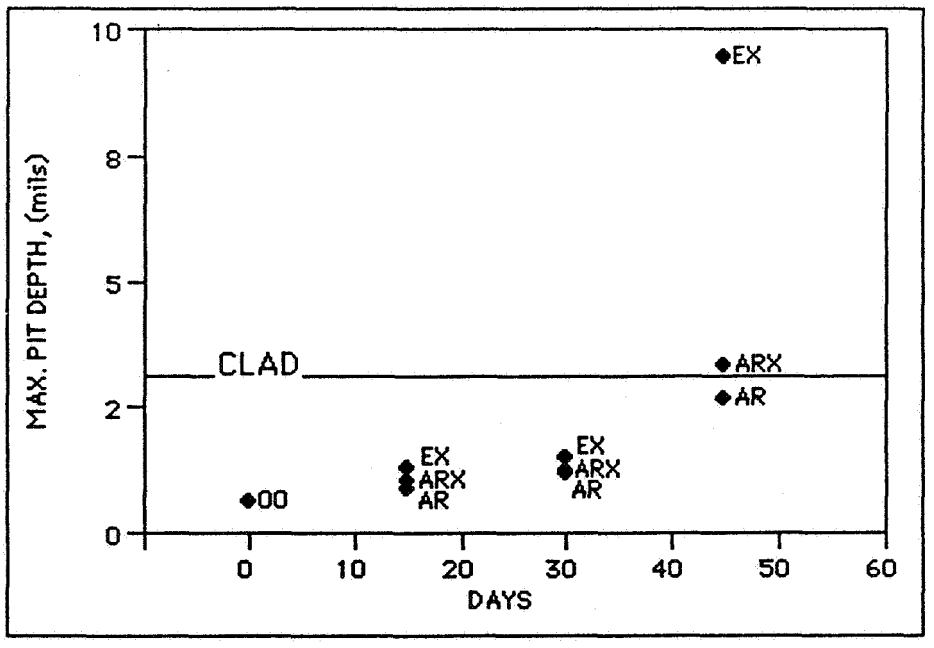

2024-T3 AT FILLET

Figure 3. The average maximum pit depth at the fillet for Type #1 (Alclad 7075-T6) and Type #3 (Alclad 2024-T3) lap-splices as a function of the number of days exposure . The test solutions are indicated by AR, artificial acid rain + H_2O_2, ARX, concentrated artificial acid rain + H_2O_2 and EX, EXCO + H_2O_2.

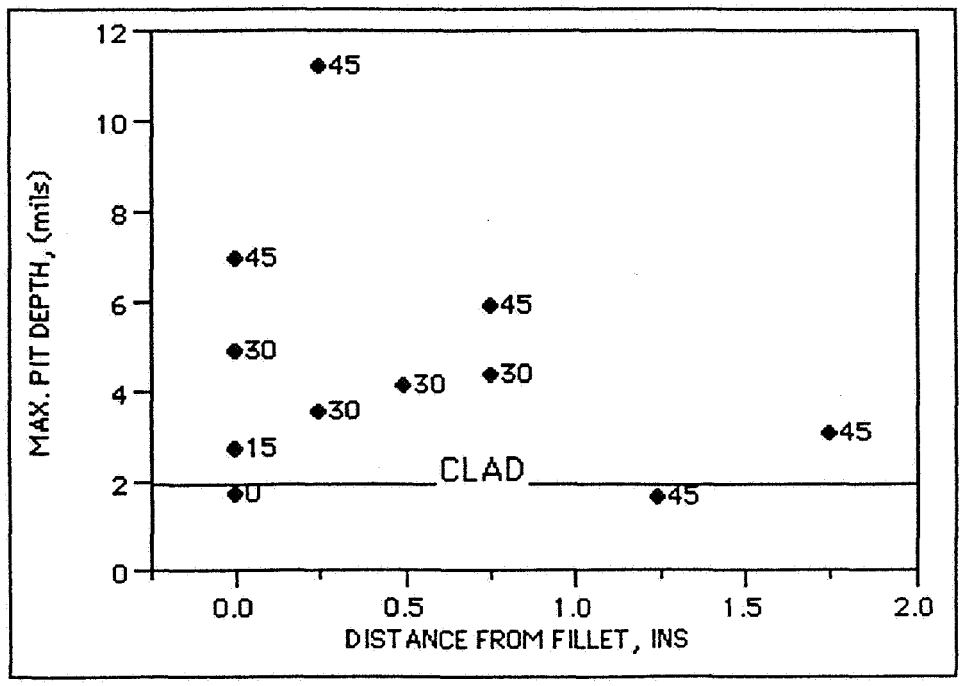

7075-T6 IN EXCO

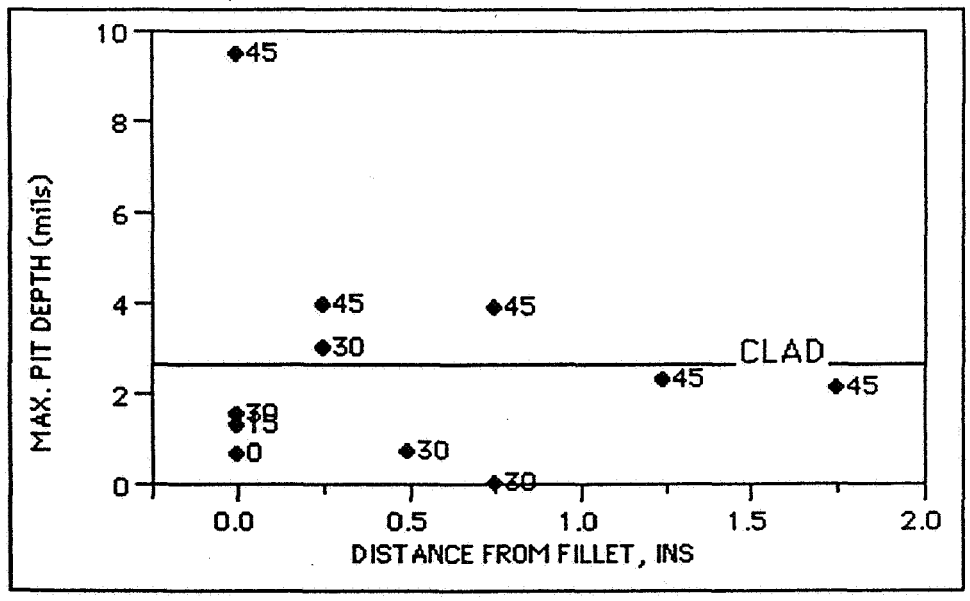

2024-T3 IN EXCO

Figure 4. The average maximum pit depth resulting from exposure to EXCO+ H_2O_2 solution as a function of the distance from the fillet for Type #1 (Alclad 7075-T6) and Type #3 (Alclad 2024-T3) lap-splices. The number of days exposure is indicated adjacent to each point.

THE APPLICATION OF NEWMAN CRACK - CLOSURE MODEL TO PREDICTING FATIGUE CRACK GROWTH

N95-19483

Erjian Si
Shanghai Aircraft Research Institute P.O.Box 232 - 003 No.72
Shanghai 200232, China

113067

359255

SUMMARY

P.13

Newman Crack - closure model and the relevant crack growth program were applied to the analysis of crack growth under constant amplitude and aircraft spectrum loading on a number of aluminum alloy materials. The analysis was performed for available test data of 2219-T851, 2024-T3, 2024-T351, 7075-T651, 2324-T39 and 7150-T651 aluminum materials.

The results showed that the constraint factor is a significant factor in the method. The determination of the constraint factor is discussed in this paper.

For constant amplitude loading, satisfactory crack growth lives could be predicted. For the above aluminum specimens, the ratio of predicted to experimental lives, Np/Nt, ranged from 0.74 to 1.36. The mean value of Np/Nt was 0.97. For a specified complex spectrum loading, predicted crack growth lives are not in very good agreement with the test data. Further effort is needed to correctly simulate the transition between plane strain and plane stress conditions, existing near the crack tip.

INTRODUCTION

Crack growth analysis is one of the distinct elements of damage tolerance design for aircraft structure.

Prediction of crack growth under aircraft spectrum loading is very difficult because of retardation due to overloads, acceleration due to underloads which are followed by an overload and reduction of retardation caused by underloads following an overload.

There are a number of crack growth models. Table 1 gives the comparison of the typical models (ref.1).

In these models, crack closure models are mathematically more complicated, they offer the potential to analytically predict many more characteristics than yield zone models and have received more and more attention. Newman's crack - closure model is one of the most recent works on this topics.

This paper summarizes the analytical results of crack growth under constant amplitude and aircraft spectrum loading on a number of aluminum alloy materials. Newman crack - closure model and the relevant crack growth program were applied to the analysis (ref. 2). The purpose of this analysis is to compare Newman's method with test and further to understand its application to aircraft structural damage tolerance design.

CRACK - CLOSURE MODEL

The crack - closure model developed by Newman was based on a modification to the Dugdale model describing the plastic-zone ahead of a crack. It is assumed that the crack could be fully or partially closed at positive minimum stresses due to residual plastic deformations left in the wake of an advancing crack. Upon reloading, the crack surfaces gradually separate until the crack is fully open at an applied stress equal to the " crack opening stress ". Figure 1 shows a schematic of the model.

The crack opening stresses (Sop) were calculated from the contact stress at minimun load. The contact stresses were calculated from displacement compatibility equations with constraints added.

A constraint factor α was introduced to account for the effect of the state of stress on the plastic-zone size. The material is assumed to yield in tension when the stress is $\alpha \sigma_o$ and in compression when the stress is $-\sigma_o$. The flow stress σ_o is taken to be the average between the yield stress and the ultimate tensile strength. Ideal plane stress or plane strain conditions are simulated with $\alpha = 1$ or 3, respectively. In general, the constraint factor will lie between the ideal limits and may additionally vary with crack length.

Newman's crack growth rate equation is as follows:

$$\frac{da}{dN} = C_1 \Delta K_{eff}^{C_2} \frac{1 - \left(\frac{\Delta K_o}{\Delta K_{eff}}\right)^2}{1 - \left(\frac{K_{max}}{C_5}\right)^2} \qquad (1)$$

Where

$$\Delta K_o = C_3 \left(1 - C_4 \frac{S_{op}}{S_{max}}\right) \qquad (2)$$

$$K_{max} = S_{max} \sqrt{\pi a}\, F \qquad (3)$$

$$\Delta K_{eff} = (S_{max} - S_{op}) \sqrt{\pi a}\, F \qquad (4)$$

The coefficients C_1 to C_5 were determined from the best fit to constant amplitude experimental data. For 2219-T851 aluminum plate, the coefficients are (ref. 2):

$$C_1 = 1.764 \times 10^{-10}$$
$$C_2 = 3.18$$
$$C_3 = 2.97 \text{ Mpa } m^{1/2} \qquad (5)$$
$$C_4 = 0.8$$
$$C_5 = 77 \text{ Mpa } m^{1/2}$$

TEST DATA

The analysis was performed for the available test data (ref. 3 and ref. 4). Crack growth tests were all for center cracked tension (CCT) specimens. For constant amplitude loading, the test data on 2219- T851 aluminum material are shown in Table 2 ; the test data on 2024- T3, 2024-T351, 7075-T651, 2324-T39 and 7150- T651 aluminum materials are shown in Table 3. For spectrum loading, the test data on 2024- T3 and 2024-T351 aluminum material are shown in Table 4.

CRACK GROWTH RATE DATA

To obtain the crack growth rate $\frac{da}{dN}$ against ΔK_{eff} relationship, the following methods can be used:

1) Newman's crack growth rate equation (see equation (1)), which was employed for 2219-T851 specimens in this paper.

2) Table look - up method, which was employed for all specimens except 2219-T851 in this paper.

The $\frac{da}{dN}$ versus K_{max} relationship was obtained from the test and further was transformed into $\frac{da}{dN}$ versus ΔK_{eff} using Newman's crack opening stress equation (ref. 5).

RESULTS AND DISCUSSION

The crack growth lives from the initial crack length to the final crack length were calculated with various constraint factors.

1) Results for constant amplitude loading

The effect of the constraint factor on the ratio of predicted to experimental lives for various materials is summarized in Figure 2.

Figure 2 shows that there is a value of α, which gives the best comparison with calculated results for a material of a given thickness and stress ratio.

For 2219-T851, Reference 2 pointed out that the equations (1) through (5) with $\alpha = 2.3$ would give a good correlation under constant amplitude loading. But in our analysis (see Table 2), it was found that at the intermediate stress level (S_{max} = 138 MPa), the crack front is in a state of stress transition. As a consequence $\alpha = 1.9$ is found to give a better correlation. At the higher or lower stress level, the prediction could not best fit the test data. It seems necessary to fit a new set of coefficients and constraint factor. The tendency is as follows: at the lower stress level (S_{max} = 55 MPa) - plane strain conditions should prevail and α should vary from 2.3 to 3. 0 as stress ratio R decreases; at the higher stress level (S_{max} = 276 MPa) - plane stress conditions should exist and α should approach 1.0 at positive R.

The calculated lives are not very sensitive to α when using the table look - up method. For all other aluminum materials except 2219-T851, with R = 0.1 (S_{max} = 124.2, 82.8 MPa), α = 1.0 (t < 3.175 mm) and 2.7 (6.35 mm $\leq$ t $\leq$ 12.7 mm) give the best results respectively.

Comparison of experimental and predited crack growth lives obtained with the optimum α for all specimens is shown in Table 3. Figures 3 through 5 show the crack growth analysis curves and test curves for three aluminum materials.

The ratio of predicted to experimental crack growth lives, Np/Nt, ranged from 0.74 to 1.36 for all 29 constant amplitude data. The mean value of Np/Nt was 0.97.

2) Results for spectrum loading

The original crack growth program only allowed input loading with a specified periodic load sequence. It has been modified to be able to analyze typical transport spectra, which have a random sequence in a block included thousands of flights.

For this spectrum loading, predicted crack growth lives are not in very good agreement with the test data. Comparison of experimental and predicted crack growth lives for 2024 aluminum alloy under transport spectrum loading is shown in Table 4.

The predictions made under spectrum loading were more sensitive to the constraint factor. Therefore, it is very important to correctly simulate the stress state, either plane stress or plane strain, existing near the crack tip.

CONCLUSION

Newman crack - closure model was applied to the analysis of crack growth under simple and complex load histories for a number of aluminum materials.

The conclusions are drawn as follows:

The key to applying the Newman crack - closure model is to determine a proper constraint factor α. There is a value of α, which gives the best calculated result for a material of a given thickness and stress ratio. It means that correct judgement and adequate assumptions in the state of stress have an important effect on the accuracy of analysis.

For constant amplitude loading, in general, satisfactory crack growth lives could be predicted once the proper constraint factor α has been determined. The ratio of predicted to experimental crack growth lives, Np/Nt, ranged from 0.74 to 1.36 for 29 constant amplitude data. The mean value of Np/Nt was 0.97.

For spectrum loading, the analytical complications increase and the information on the transition between plane strain and plane stress is needed. The constraint factor α would be a variable and a function of the plastic zone to thickness ratio. At short crack lengths and low stress levels, plastic zone size is small compared to material thickness, plane strain conditions may prevail and α may be in the range between 2 and 3. As the crack grows longer, α will drop steadily until at some longer length where plastic zone size is more likely close to the thickness, plane stress conditions may prevail and hence α nears 1.

One thing which could be pointed out is that the material input data should cover the complete relevant range of ΔK and R values when using fatigue crack growth rate table as the input to the crack growth program.

Note that crack - closure model, which performs a cycle by cycle calculation, is time - consuming. It is hopeful to do some simplification for engineering practice.

The following are some recommendations for the program:

As the calculated crack opening stress was held constant in the program while the crack growth over the length ΔC^*, the crack growth accumulation procedure may be simplified.

An " equivalent " crack opening stress might be used as early as possible in order to reduce the computer time.

REFERENCES

1. Si, E.: A Comprehensive Review of Models of Crack Growth Analysis and Life Prediction Methods under Spectrum Loading. ACTA Aeronautica ET Astronautica Sinica Vol. 8, No. 2, 1987.
2. Newman, J.C., Jr.: A Crack - Closure Model for Predicting Fatigue Crack Growth under Aircraft Spectrum Loading. ASTM STP 748, 1981.
3. Chang, J.B. and Stolpestad, J.H.: Improved Methods for Predicting Spectrum Loading Effects - Phase I Report. AFFDL-TR-79-3036, Vol. II, March 1978.
4. Miller, M., Luthra, V.K. and Goranson, U.G.,: Fatigue Crack Growth Characterization of Jet Transport Structure. 14th Symposium of the International Committee on Aeronautical Fatigue (ICAF), Ottawa, Canada, June 1987.
5. Newman, J.C., Jr.: A Crack Opening Stress Equation for Fatigue Crack Growth. International Journal of Fracture, Vol. 24, 1984.

Acknowledgements - This work was completed while the author worked at the Boeing Commercial Airplanes, Seattle, U.S.A. The author is very grateful to Dr Ulf G. Goranson, Dr Matthew Miller, Mr Vijai K. Luthra and other Boeing Structural Damage Technology specialists for their guidance and help.

Table 1. Comparison of Typical Crack Growth Models

TYPE	FEATURE PARAMETERS	CONTRIBUTORS
[1] Plastic Yield Zone Model	Effective Stress Intensity Range	Wheeler (1970) Willenborg (1971) Gallagher (1974) Chang (1981) Johnson (1981)
[2] Crack Closure Model	Crack Opening Stress	Elber (1969) Newman (Finite element 1974) (Contact stress 1981) Bell (AFFDL) (1974) Maarse (1977) Matsuoka (1976) De Koning (1980)
[3] Modified Model Based on One or Both of above Types	One or Both of [1] and [2]	Huang (1980) He (1980)

Table 2. Comparison of Experimental and Predicted Crack Growth Lives for 2219-T851 Aluminum Alloy

Smax MPa	R	a_i mm	a_f mm	Np/Nt α=1.0	α=1.9	α=2.3	α=2.7
55	-0.1	3.91	18.7			1.62	1.36
55	0.0	3.55	52.4			0.99	0.83
55	0.3	3.87	6.9			0.76	0.64
138	-0.3	4.13	45.7		1.11		
138	-0.1	3.85	43.0		0.99		
138	0.01	3.87	50.0		0.99	0.83	
138	0.01	4.00	42.0		1.04		
138	0.01	6.67	38.3		0.95		
138	0.2	4.57	48.0		1.22		
138	0.3	4.06	43.6		0.80		
138	0.7	3.94	12.1	1.12	0.87		
276	-0.1	3.94	21.4			1.15	1.09
276	0.01	3.83	14.9	0.75	0.75	0.72	
276	0.3	3.94	12.9	0.74	0.60	0.58	
276	0.7	3.94	23.5	0.86			

Note: R - Stress Ratio (Smin/Smax)
a_i - Half Length of initial crack
a_f - Half Length of final crack
Np - Number of cycles predicted from analysis
Nt - Number of cycles from test

Table 3. Comparison of Experimental and Predicted Crack Growth Lives for Various Aluminum Materials under Constant Amplitude Loading

Material	Temper	Smax (MPa)	R	t (mm)	a_i (mm)	a_f (mm)	Np/Nt	α
2024	T3	124.2	0.1	3.175	7.214	57.302	0.92	1.0
	T3	124.2	0.1	1.600	8.687	59.715	0.96	1.0
	T351	124.2	0.1	3.175	10.008	57.302	0.97	1.0
	T351	124.2	0.1	6.350	8.992	56.667	0.93	2.7
	T351	124.2	0.1	12.70	8.484	58.522	0.98	2.7
7075	T651	82.8	0.1	3.175	7.366	60.452	0.97	1.0
	T651	82.8	0.1	6.350	6.655	58.293	0.99	2.7
	T651	82.8	0.1	12.70	6.985	58.141	0.99	2.7
2324	T39	82.8	0.1	3.175	14.808	102.438	0.93	1.0
	T39	82.8	0.1	7.087	16.866	114.071	0.95	2.7
	T39	82.8	0.1	12.649	25.375	112.293	0.99	2.7
7150	T39	82.8	0.1	3.302	15.773	111.836	0.95	1.0
	T39	82.8	0.1	6.350	15.926	87.401	0.96	2.7
	T39	82.8	0.1	12.70	17.475	117.450	0.99	2.7

Table 4. Comparison of Experimental and Predicted Crack Growth Lives for 2024 Aluminum Material under Transport Spectrum Loading

Temper	t (mm)	a_i (mm)	a_f (mm)	Np/Nt
T3	3.175	6.528	25.349	1.52
T351	6.350	5.842	60.198	0.30

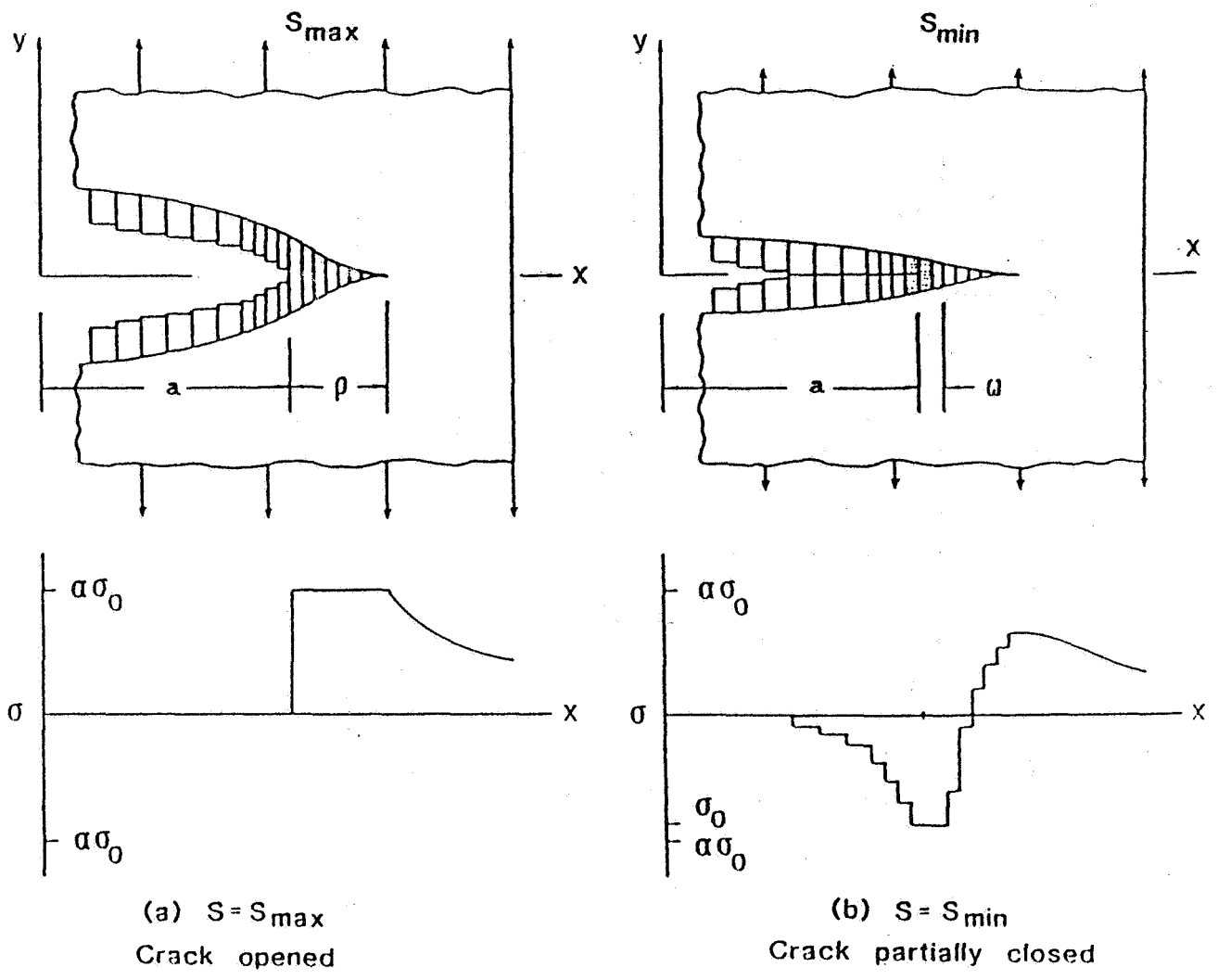

Figure 1. Schematic of crack closure model.

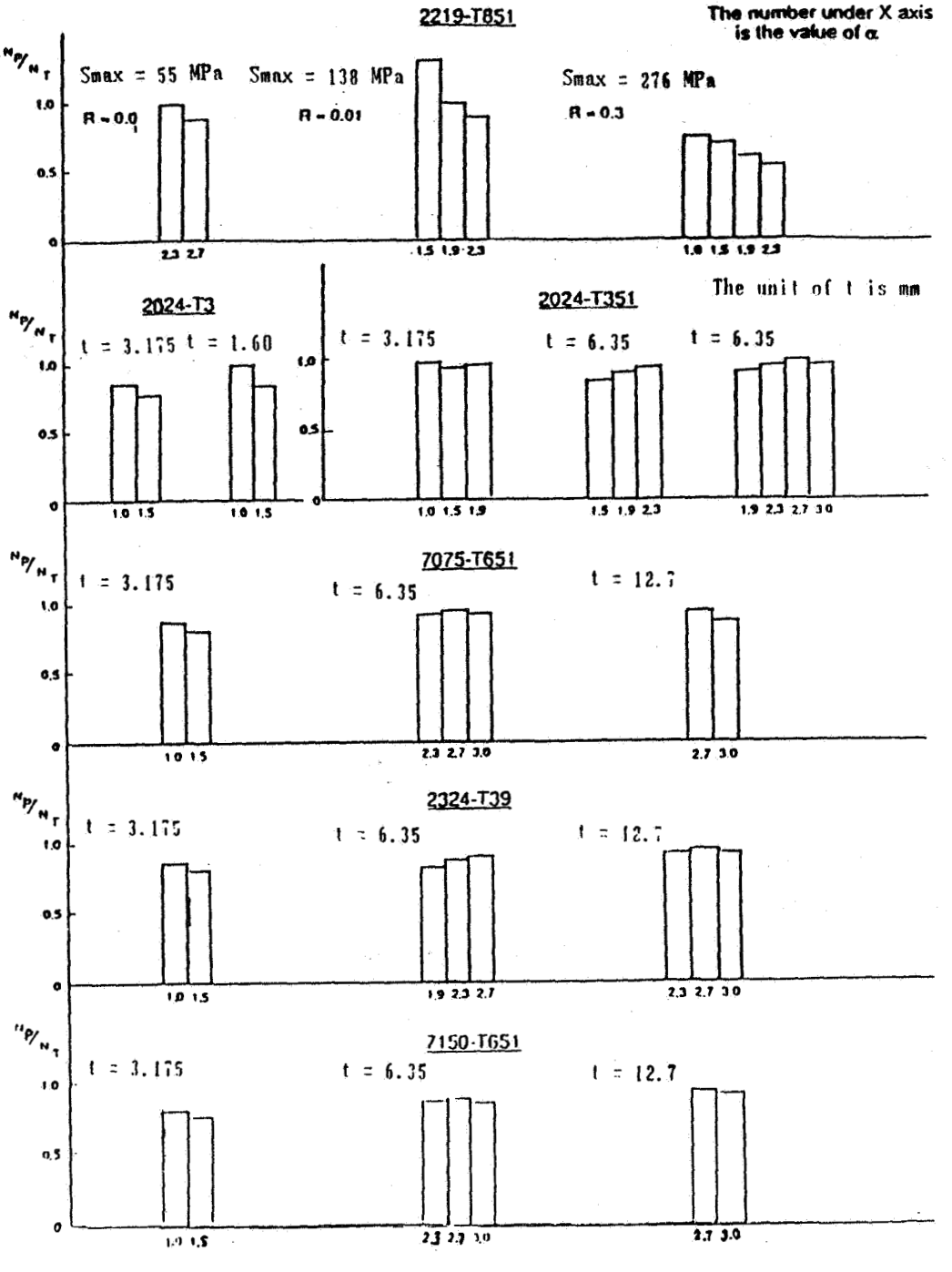

Figure 2. The effect of the constraint factor α on predicted lives.

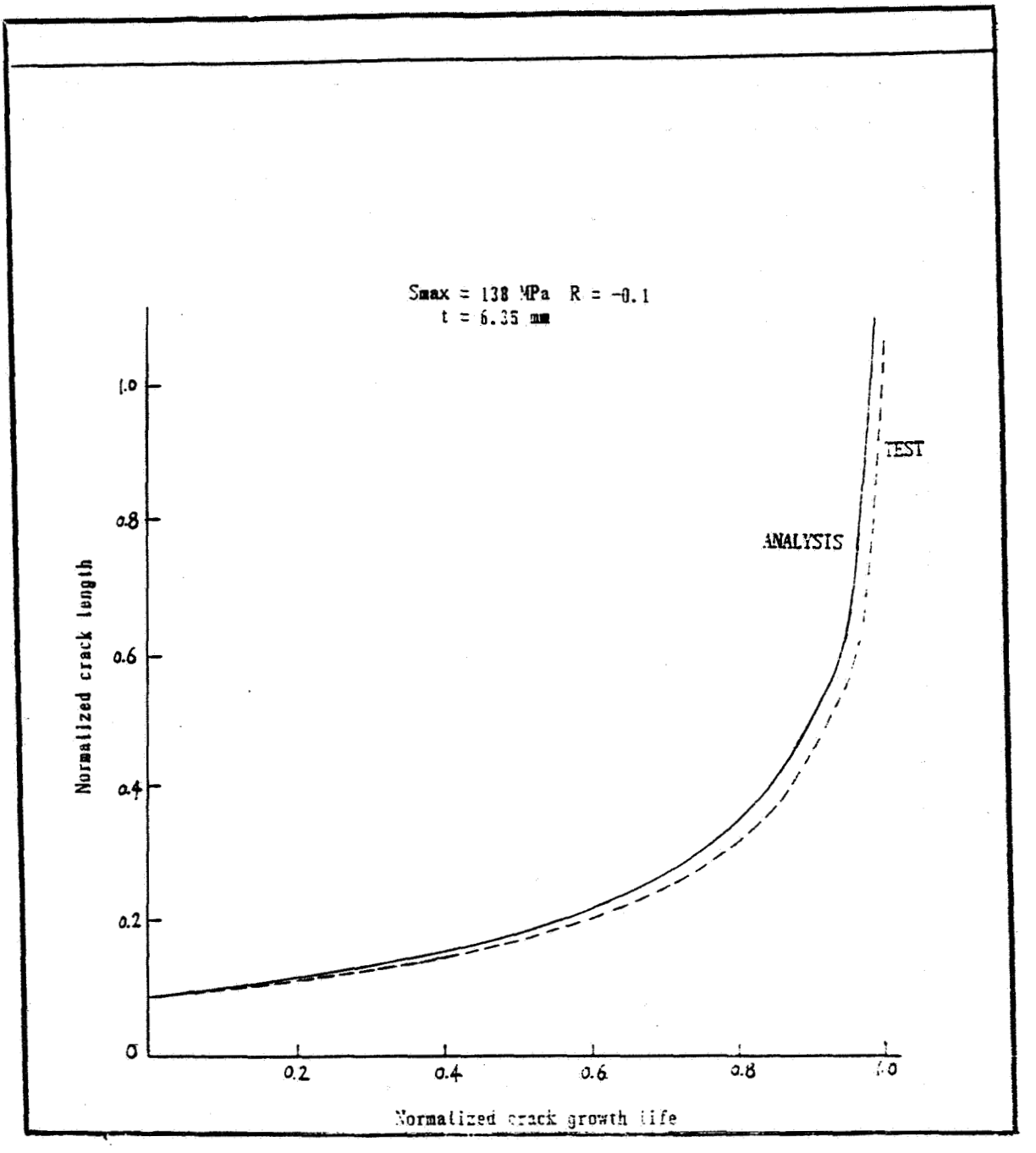

Figure 3. Crack growth comparison between prediction and test for 2219 - T851.

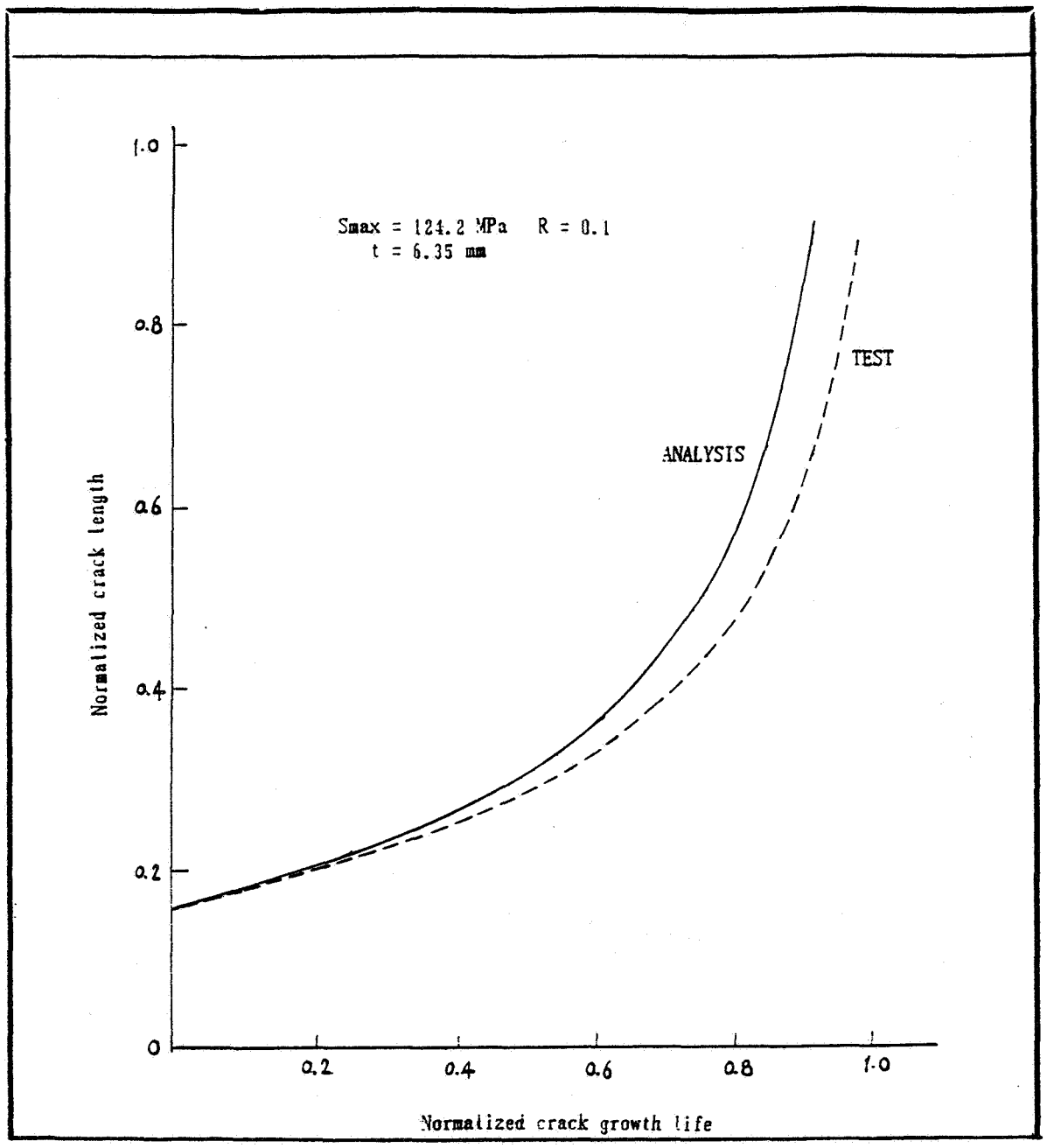

Figure 4. Crack growth comparison between prediction and test for 2024 - T351.

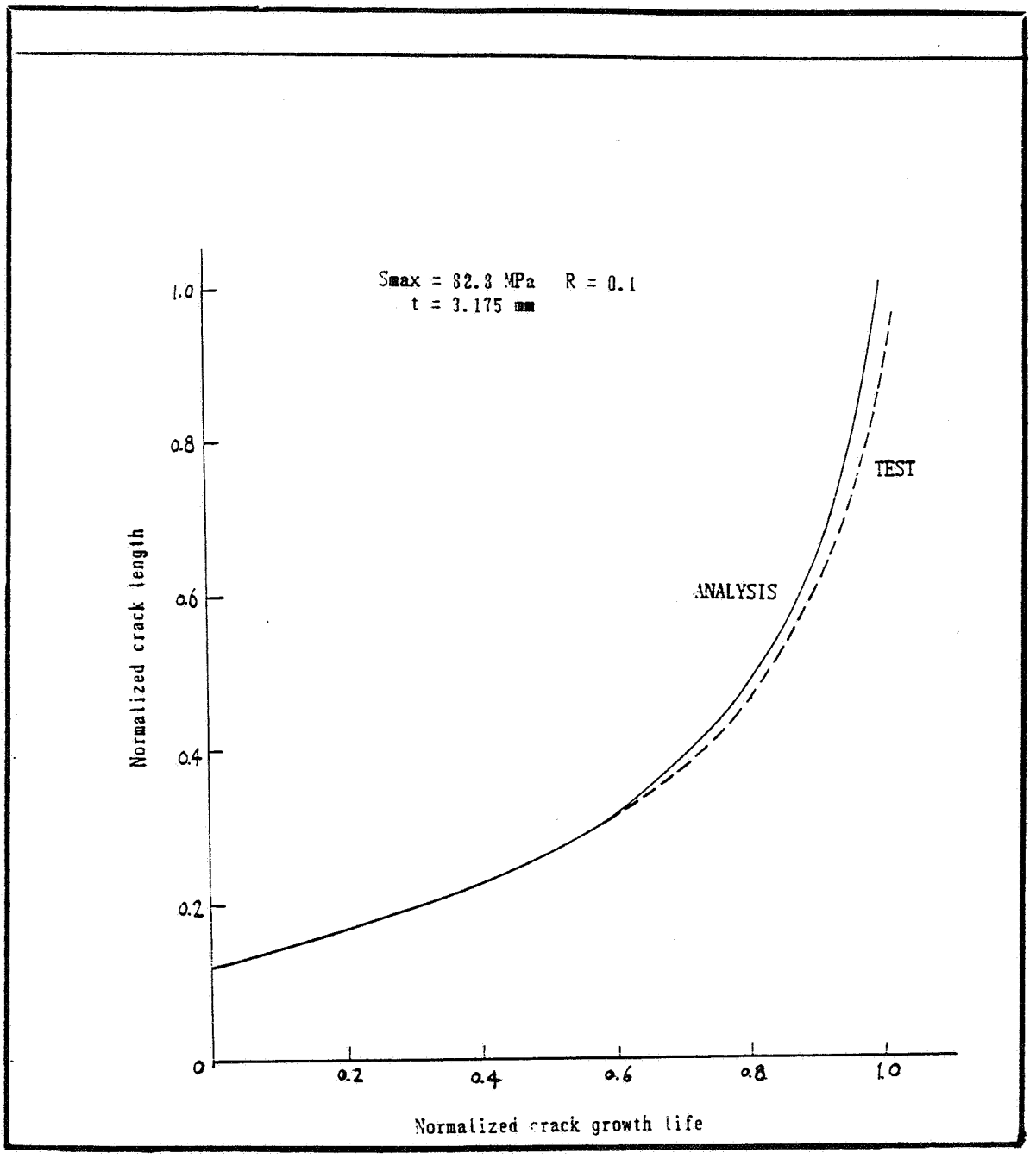

Figure 5. Crack growth comparison between prediction and test for 7075 - T651.

FATIGUE CRACK GROWTH UNDER VARIABLE AMPLITUDE LOADING

Jihad A. SIDAWI

College of Engineering, CEEP

University of Bahrain

Issa Town, BAHRAIN

SUMMARY

Fatigue crack growth tests were conducted on an Fe 510 E C-Mn steel and a submerged arc welded joint from the same material under constant, variable, and random loading amplitudes. Paris-Erdogan's crack growth rate law was tested for the evaluation of m and C using the stress intensity factor K, the J-Integral, the effective stress intensity factor Keff, and the root mean square stress intensity factor Krms fracture mechanics concepts. The effect of retardation and residual stresses resulting from welding was also considered. It was found that all concepts gave good life predictions in all cases.

INTRODUCTION

Since most structural components are subjected in service to variable amplitude loading, a study of the fatigue behavior of the material under the effect of these loadings is essential. Different models contributed to a better understanding of the retardation or acceleration caused by the influence of load sequence (ref. 1-10). Further work is needed on the influence of these effects on fatigue lives.

Several authors have shown that residual stresses resulting from welding have a major influence on the fatigue lives of welded components (ref. 11-12). Modern sources studied this influence under the action of constant amplitude loading. Limited work on welded components subjected to variable amplitude loading have been deployed (ref. 13-14). This is due to the complexity of the problem under consideration.

The mechanism of failure under cyclic loading is a very complicated process. The fatigue strength of metals as well as welded joints is affected by a number of factors which determine fatigue life. The application of fracture mechanics showed that it is a suitable tool for the evaluation of fatigue lives not only for unwelded, but also for welded components (ref. 14-15)

In welded elements and components, cracks spend most of their lives growing (ref. 16). This fact is explained by the effect of inhomogeneities which usually exist in welded joints and which accelerates the initiation of cracks.

Irrespective of the mathematical expression of fatigue crack growth used, the expression must have the most essential parameters for solving the loading conditions as well as the material properties of a specific fatigue growth process (ref. 17). This fact is to be considered for both constant and variable amplitude loadings.

An estimation of the fatigue crack growth under variable amplitude loading can be done by assuming the existence of a threshold value ($\Delta K_0 = 2$ MPa.m $^{1/2}$ for C and C-Mn steels) (ref. 18), and that the fatigue crack growth can be predicted by linear damage summation (ref. 19-20) such that the effect of load changes is ignored.

List of Symbols and Abbreviations

CCT: Center-Cracked-Tension test specimen or M(T): Middle - Tension.
CT : Compact-Tension test specimen.
ao [mm]: Initial crack length.
2a [mm]: Crack length of a CCT (MT) specimen 2a = 2x a (measured) + 2 ao.
a [mm]: Half crack length of a CT specimen a = a (measured) + ao.
N [kc]: Number of collapsed cycles.
da/dN [mm/kc]: Fatigue crack growth rate.
Fmin, Fmax, ΔF [kN]: Minimum, maximum loads and load range. (ΔF = Fmax-Fmin).
R : Load or stress ratio. Fmin/Fmax or Smin/Smax.
ΔK [MPa.m$^{1/2}$]: Stress intensity factor range.
ΔJel [N/m] : Elastic part of the cyclic J-integral range.
E [MPa] : Young's elastic modulus E= 2.06x 10^5 for C steels.
ΔJpl [N/m]: Plastic part of the cyclic J-integral range.
A [kN.mm] : Area under the force-displacement loop.
ΔJ [N/m] : Cyclic J-integral range.
ΔKeff [MPa.m$^{1/2}$]: Effective stress intensity factor range.
ΔKo [MPa.m$^{1/2}$]: Threshold value of the stress intensity factor range.
Reff : Effective load or stress ratio.
ΔS [MPa]: Stress range.
Re [MPa]: Yield strength (0.2Re).
ΔKrms [MPa.m$^{1/2}$]: Root mean square value of the stress intensity factor range.
m : Index in Paris-Erdogan's crack growth law da/dN = C $(\Delta K)^m$.
C : Coefficient in Paris-Erdogan's crack growth law.
Nt [kc]: Actual (tested) fatigue life {N(final)-N(initial)}.
Np [kc]: Predicted fatigue life: $Np = \int da / C (\Delta K)^m$

Experimental Procedures

Test Materials

The material used in all experiments was from a 20mm thick C-Mn Fe 510 E steel plate. Weld joints were prepared by the submerged arc-welding technique, so that the weld line was perpendicular to the rolling direction of the material.

Chemical analysis and mechanical properties of Fe 510 E steel and weld metal are documented in table.1 and table.2 , respectively. Figure 1 shows the microstructure of the base metal and the weld metal. No trace of defects was observed in either the weld metal or the heat affected zone (HAZ), (width 3-4mm).

Welding Parameters and Technology:

A direct current ESAB welding machine was used with the positive pole on the electrode.

- Flux: N-70
- Filler wire: A-234 (Cast No.74035) (0.079%C- 1.14%Mn- 0.22%Si- 0.15%P- 0.018%S- 2.80%Ni (2%Ni spectral))
- Root run welding parameters: 400A- 30V- 35 m/h
- Beads: 450A- 32V- 35 m/h
- Preheating at 120° C
- Interpass temperature: 100-160° C (150° C).

Test Specimens

CCT (20x 120x 600 mm) and CT (20x 100 mm) specimens were machined from the plate. The direction of the loading axis was perpendicular to the weld line. The CCT notch was prepared by drilling a hole of ϕ4mm into the center of the polished pass in the middle of the width of the weld metal. Then, a thin sawcut was made on both sides of the hole such that the direction of the loading axis was kept perpendicular to the weld line. A sharp notched crack was made. The CT fatigue crack was oriented by a notch into the center of the weld metal.

Test Equipment and Machines

The CCT specimens were tested at room temperature at 5Hz in laboratory air using a 1600 KN servohydraulic Schenck fatigue testing machine connected to a computer. A cylindrical clip gauge was inserted into the ϕ4mm hole to measure the displacement range. The clip gage was also connected to the computer. From the computer two channels transferred the loading force and the displacement ranges

into a memory, from which the memorized cycle could be traced on a plotter. Another channel transferred the displacement range before entering into the memory to another plotter, which traced the crack opening displacement by time. From the first plotter both the loading forces and displacement ranges are then transferred into another computer programmed to integrate the area of the closed loop traced by the plotter and to calculate the loading force range and the displacement range as well.

The CT specimens were also tested by the same procedure using another Schenck fatigue testing machine at 40 Hz.

Identification of Specimens and Types of Loadings

The specimens can be identified by the material and type of loadings as follows:

1) BCA: Base metal constant amplitude loading ΔF_1
2) BVA: Base metal variable amplitude step low-high loading. $\Delta F_1 = 2\ \Delta F_2$
3) BRA: Base metal random amplitude loading.

To distinguish the weld metal from the base metal, a W replaced the B.

Table 1. Chemical Analysis of Fe 510 E Steel and Welded Metal SAW
[% Weight]

ANALYSIS	C	Mn	Si	P	S	Cr	Ni	Al	Nb
Base Metal	0.16	1.2	0.35	0.036	0.0216	0.05	0.03	0.04	0.02
Weld Metal	0.06	1.48	0.29	0.026	0.0172	0.11	2.23	0.01	0.00

Table 2. Mechanical Properties of Fe 510 E Steel and Weld Metal SAW

ANALYSIS	Yield Strength Re [MPa]	Tensile Strength Rm [MPa]	Elongation A [5%]	Contraction Z [%]	Toughness (20 °C) KCV [J.cm^{-2}]
Base Metal	430	572	27	57	108
Weld Metal	574	672	22	61	122

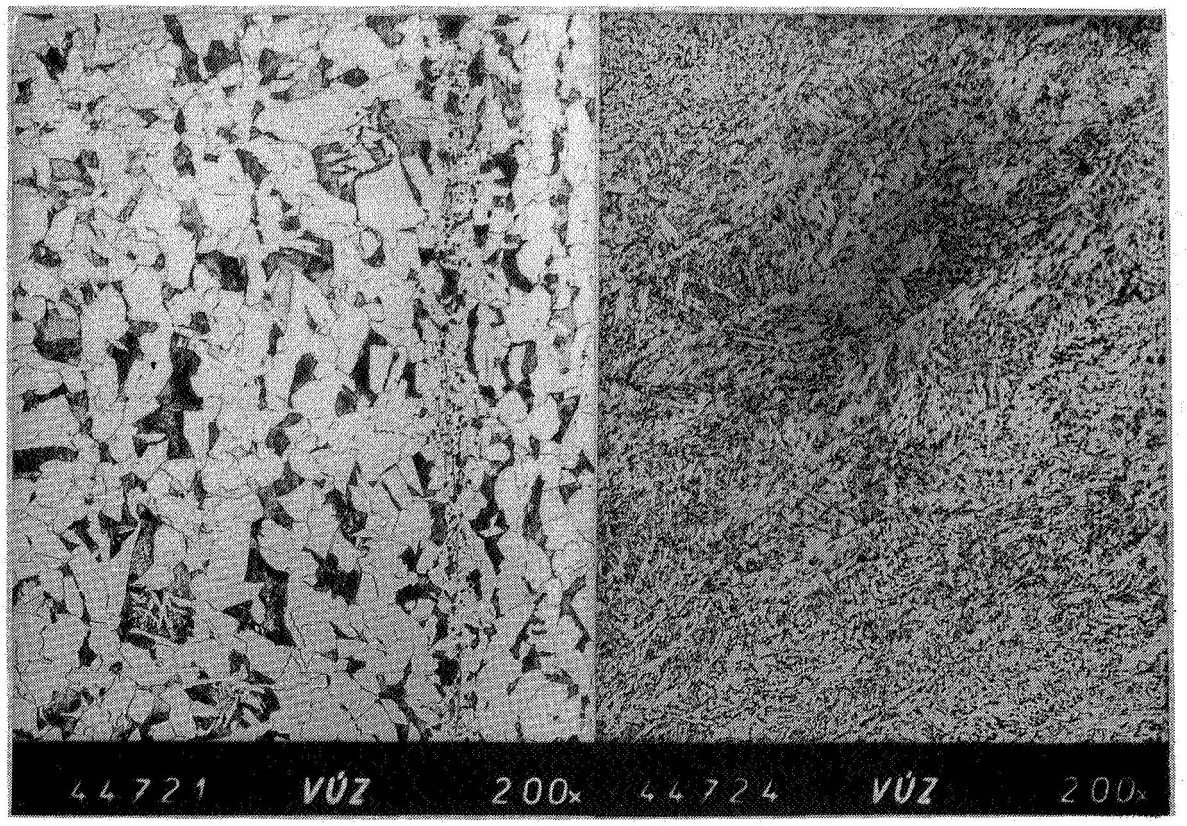

Figure 1. The microstructure of the base metal (left) and the weld metal (right) of Fe 510 E steel.

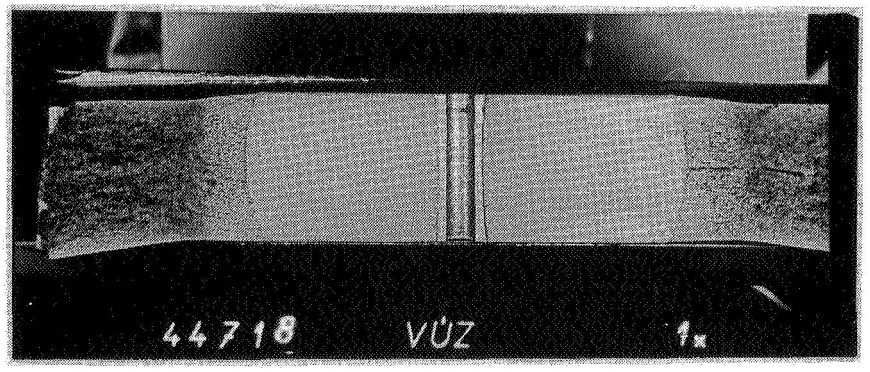

Figure 2. Fracture surface of a base metal, constant amplitude loading CCT specimen.

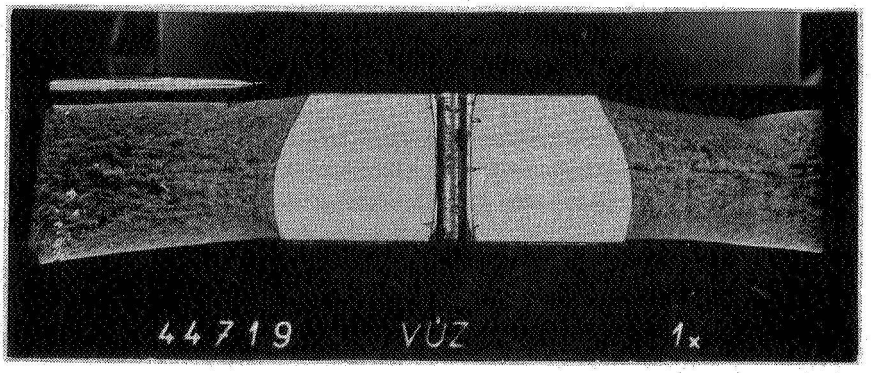

Figure 3. Fracture surface of a base metal, variable amplitude loading CCT specimen.

Fractographical Analysis

With the aid of a scanning electron microscope, fractographical analysis of the surface of the cracks was done. Four CCT specimens were analysed.

1) Base metal, constant amplitude loading. (Figure 2)
2) Base metal, variable amplitude loading. (Figure. 3)
3) Weld metal, constant amplitude loading.
4) Weld metal, variable amplitude loading.

The surface of the cracks in Figure 2 and Figure 3 can be relatively divided into a fine fracture surface and a coarse grained fracture surface, on which the rolled texture of the material is reflected.

While the specimen with a constant amplitude loading has a rubbering surface, without macroscopic traces, the one with variable amplitude loading has some narrow dark bands (striations). These are associated with the fact that the specimen was held at the mean load for some time until the replacing load was adjusted. These are sometimes called "Rest Bands". It is clear from the figures that the fatigue crack grew symmetrically around the central groove.

The only difference between the second series of specimens (Weld metal) and the first (Base metal) is that the inclusions in the weld metal are globular.

It is important to notice the fact that from the crack's micromorphological aspect, no difference between specimens subjected to constant or variable loading was observed.

Measured Data and Testing Procedure

All specimens were precycled until a clear fatigue crack was visually observed (min 2mm). The crack length was calculated from the average of two values measured visually by the aid of a scale attached to both the right and left side of the specimen. When possible four values were measured on both the front and back surfaces of the CCT specimen.

The loading forces were changed manually and checked by the computer readings. The displacement range and the area of the closed loop were also available on the computer readings. The mean displacement value was documented from the readings on the testing machine itself. It is important to note that the crack opening displacement measured is not the crack tip opening displacement.

Methods of Evaluation

Four methods were used for the prediction: the stress intensity factor, cyclic J-integral, effective stress intensity factor, and the root mean square stress intensity factor.

C and m were predicted using Paris-Erdogan's equation:

$$da/dN = C\,(\Delta K, \Delta J, \Delta Keff, \Delta Krms)^{m} \quad (1)$$

The ΔK for both the CCT and the CT types of specimens were calculated according to ASTM E 647-93 .The ΔJ values for CCT specimens were calculated using the Dowling (ref. 22) equations:

$$\Delta J = \Delta Jel + \Delta Jpl \quad (2)$$

$$\Delta Jel = \Delta K^2 / E \quad (3)$$

$$\Delta Jpl = A /[B (W-2a)] \quad (4)$$

The $\Delta Keff$ values were calculated using the recommendation of the IIW document (ref. 18), which suggested equations for $\Delta Keff$ prediction in air and sea water for 97.7% probability of survival. The Kopen was not experimentally measured.

Δ Keff :

a) Base metal (C-Mn steel):

$$\Delta K_0[N.mm^{-3/2}] = 170-214\ R \quad \text{for } 0 \le R \le 0.5 \quad (5)$$

or

$$\Delta K_0[\ MPa.m^{1/2}] = 5.375 - 6.767\ R \quad (6)$$

$$\Delta K_0 = 63\ [N.mm^{-3/2}] \text{ or } \Delta K_0 = 2\ [\ MPa.m^{1/2}] \quad \text{for } R \ge 0.5 \quad (7)$$

$$\Delta Keff = \Delta K \quad \text{for} \quad \Delta K > \Delta K_0/R \quad \text{and } R > 0 \quad (8)$$

$$\Delta Keff = (\Delta K - \Delta K_0)/(1- R) \quad \text{for } \Delta K \le \Delta K_0/R \quad (9)$$

b) Weld metal (C-Mn steel):

i) Constant amplitude loading:

$$\Delta K_0[N.mm^{-3/2}] = 214\ (\ \Delta S/Re)- 42 \quad (10)$$

or

$$\Delta K_0[\ MPa.m^{1/2}] = 6.767\ (\Delta S/Re)- 1.328 \quad (11)$$

$$\Delta K_0 = 63\ [N.mm^{-3/2}] \text{ or } \Delta K_0 = 2\ [\ MPa.m^{1/2}] \quad \text{if } \Delta S < Re/2 \quad (12)$$

$$\Delta S\ [MPa] = F/ (B.W) \quad (13)$$

Re [MPa]: 0.2% weld yield strength = 574 MPa.

$\Delta Keff = \Delta K$ for $\Delta K > \Delta K_0/Reff$ and $Reff > 0$ (14)

$\Delta Keff = (\Delta K - \Delta K_0)/(1 - Reff)$ for $\Delta K \leq \Delta K_0/Reff$ (15)

$Reff = (Re-\Delta S)/Re$ (16)

ii) Variable amplitude loading:

$\Delta K_0 = 63$ [N.mm$^{-3/2}$] or $\Delta K_0 = 2$ [MPa.m$^{1/2}$] (17)

The ΔKrms was calculated according to Barsom (ref. 23):

$$\Delta Krms = \sqrt{\sum_{i=1}^{k} (\Delta K_i)^2 / n} \quad (18)$$

where n= number of measurements.

Fatigue Crack Growth Results and Discussion

Fatigue crack growth results are presented in table 3. The most important features are discussed in what follows:

a) Addition of Small Loading Amplitudes.

The addition of small loading amplitude blocks to the constant amplitude block resulted in the decrease of the crack growth rates, thus in a significant increase in the fatigue lives as shown in table 3 (tested and predicted fatigue lives Nt and Np). This is also clearly illustrated in figures 4-6 in both cases, the base and the weld metals , and for the three types of evaluation methods K, Keff, and J-integral as well.

As half loading block amplitudes are added to the constant amplitude loading block, the fatigue lives were doubled (200%), while the growth rate showed a decrease by approximately the same amount as shown in figure 3 for specimens BVA and WVA. This has not been yet quantified by other authors, although the addition of small loads resulted in doubling the fatigue life. Figures 4-6 may indicate a family of parallel curves compared to the constant amplitude curves.

In the above shown figures 4-6, BRA and WRA specimens still show an improvement in fatigue lives of 1.5-4.0. This increase does not necessarily coincide with that of BVA and WVA. This is expected because of the randomness of the excess load applied.

Table 3. Fatigue Crack Growth Results of CCT Specimens

METHOD/ SPECIMEN		BCA	BVA	BRA	WCA	WVA	WRA
	Nt	26.8	72	110	37.9	70	55
K	m	3.586	3.149	2.847	2.496	1.969	1.947
	C	1.308^{-6}	3.589^{-6}	7.603^{-6}	3.464^{-5}	3.149^{-4}	3.903^{-4}
	Np	27.04	66.30	83.647	34.166	66.77	54.54
	Np/Nt	1.009	0.9209	0.7604	0.9789	0.9539	0.9916
J	m	1.7	1.451	1.379	1.197	0.963	0.968
	C	1.412^{-7}	6.775^{-7}	1.021^{-6}	7.124^{-6}	7.018^{-5}	8.369^{-5}
	Np	27.18	66.30	83.926	34.07	66.88	54.48
	Np/Nt	1.014	0.9209	0.7629	0.976	0.9555	0.9906
Keff	m	3.425	2.955	2.637	2.496	1.969	1.947
	C	2.524^{-6}	7.874^{-6}	1.696^{-5}	3.464^{-5}	3.149^{-4}	3.903^{-4}
	Np	27.09	66.93	84.039	34.166	66.77	54.54
	Np/Nt	1.011	0.9296	0.764	0.9789	0.9539	0.9916
Krms	m	-	3.149	1.964	-	1.969	3.182
	C	-	7.54^{-6}	3.592^{-4}	-	5.004^{-4}	4.78^{-6}
	Np	-	66.153	89.98	-	66.743	54.654
	Np/Nt	-	0.918	0.818	-	0.9534	0.9937

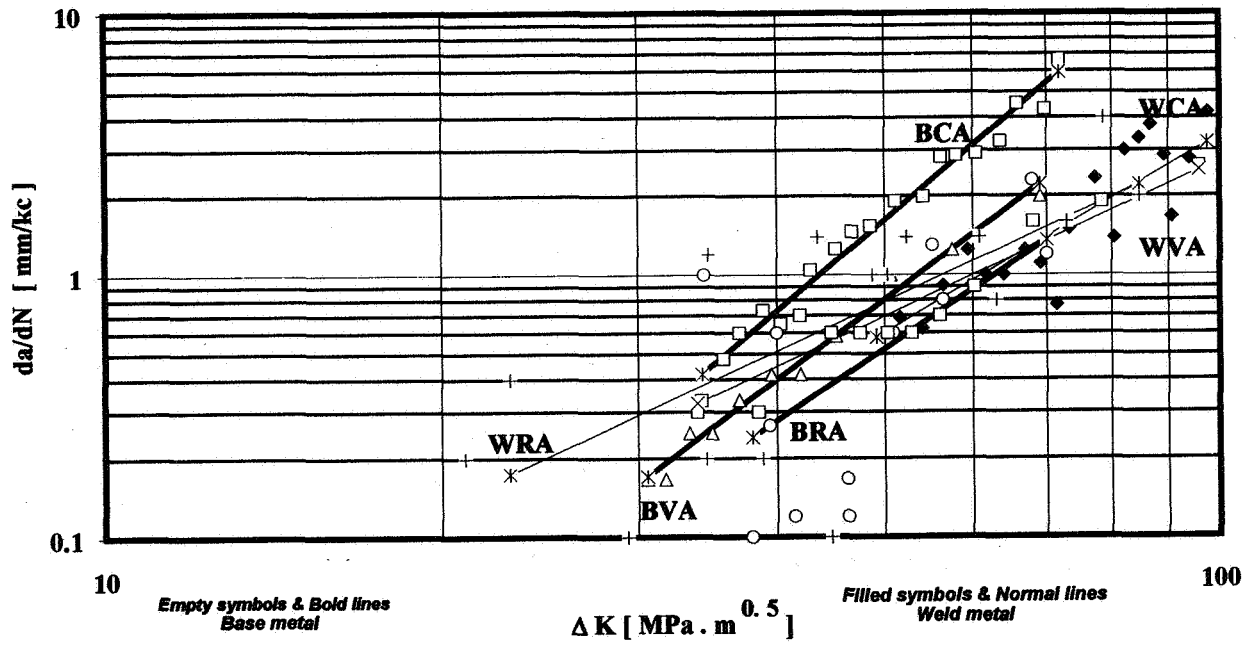

Figure 4. Fatigue crack growth rate (da/dN) vs. stress intensity factor range ΔK.

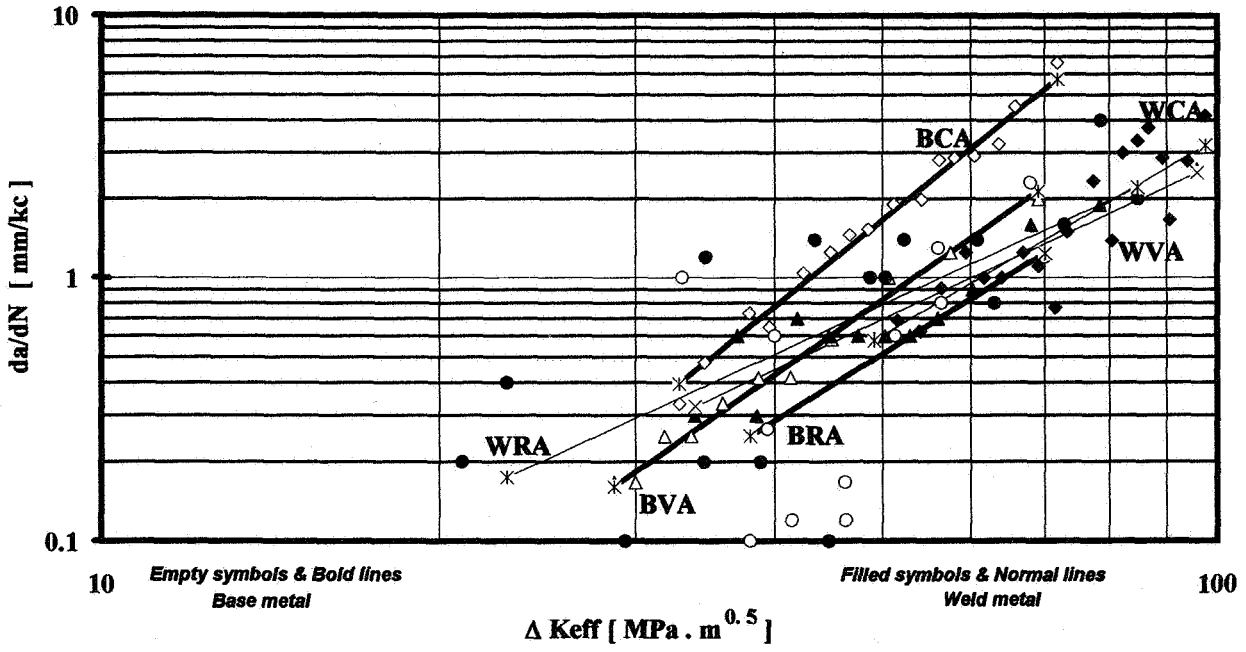

Figure 5. Fatigue crack growth rate (da/dN) vs. effective stress intensity factor range ΔKeff.

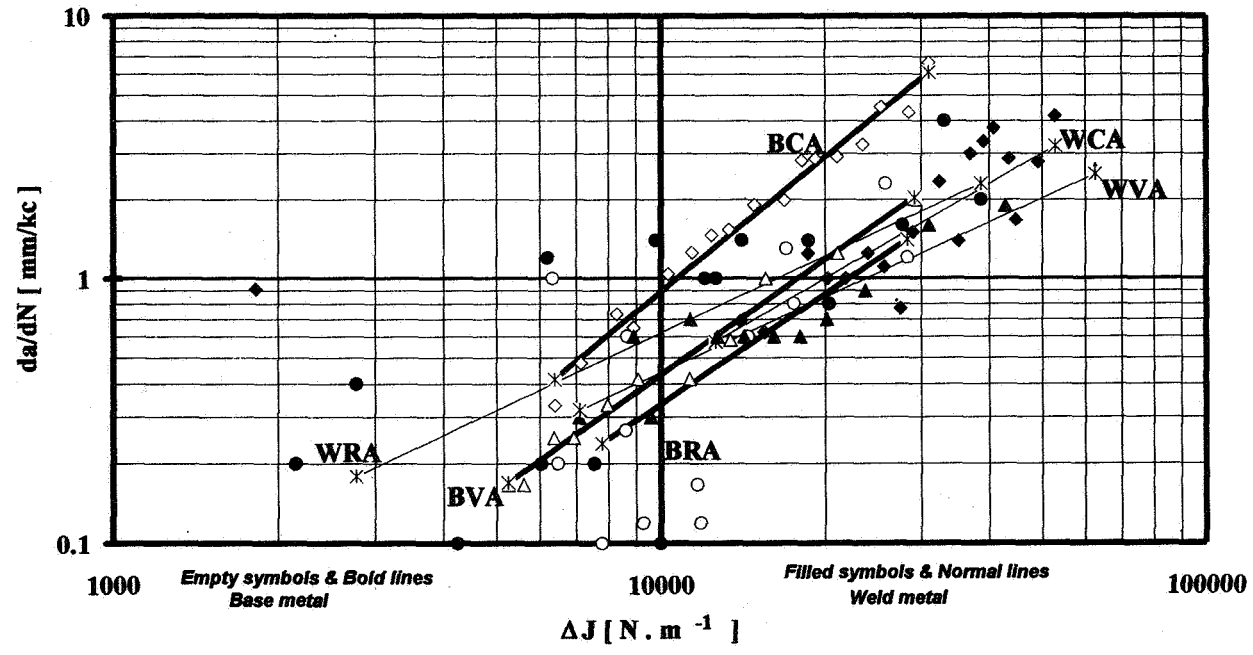

Figure 6. Fatigue crack growth rate (da/dN) vs. cyclic ΔJ-integral.

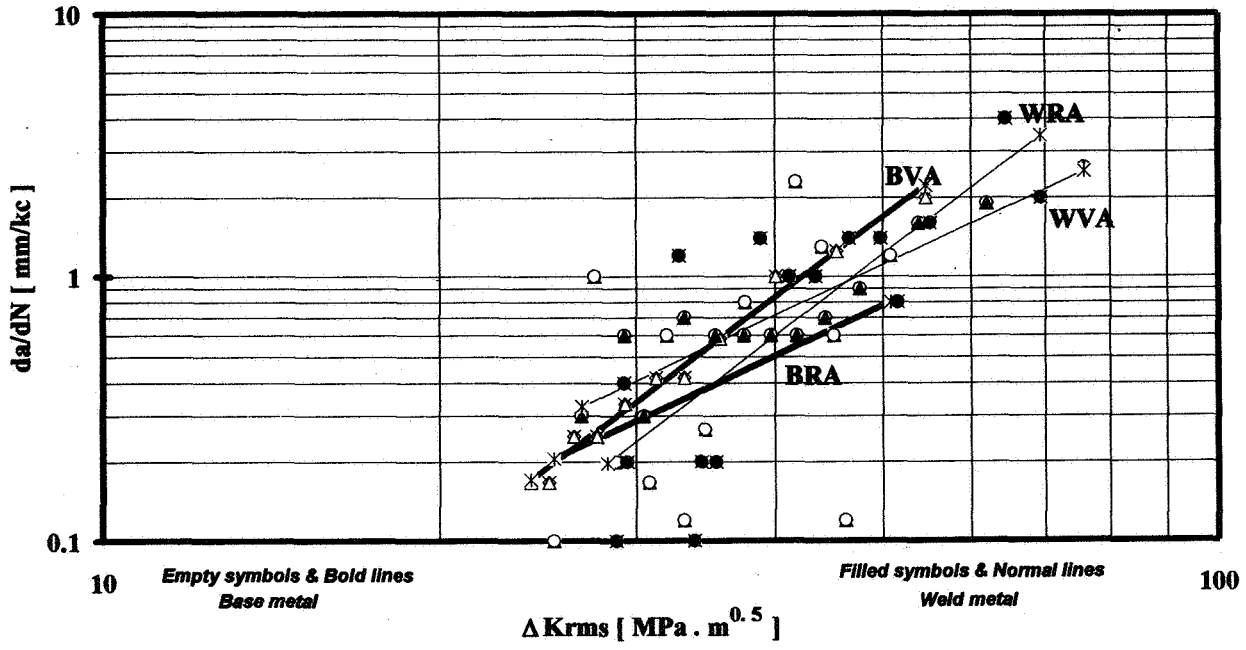

Figure 7 Fatigue crack growth rate (da/dN) vs. root mean square value of the stress intensity factor Krms.

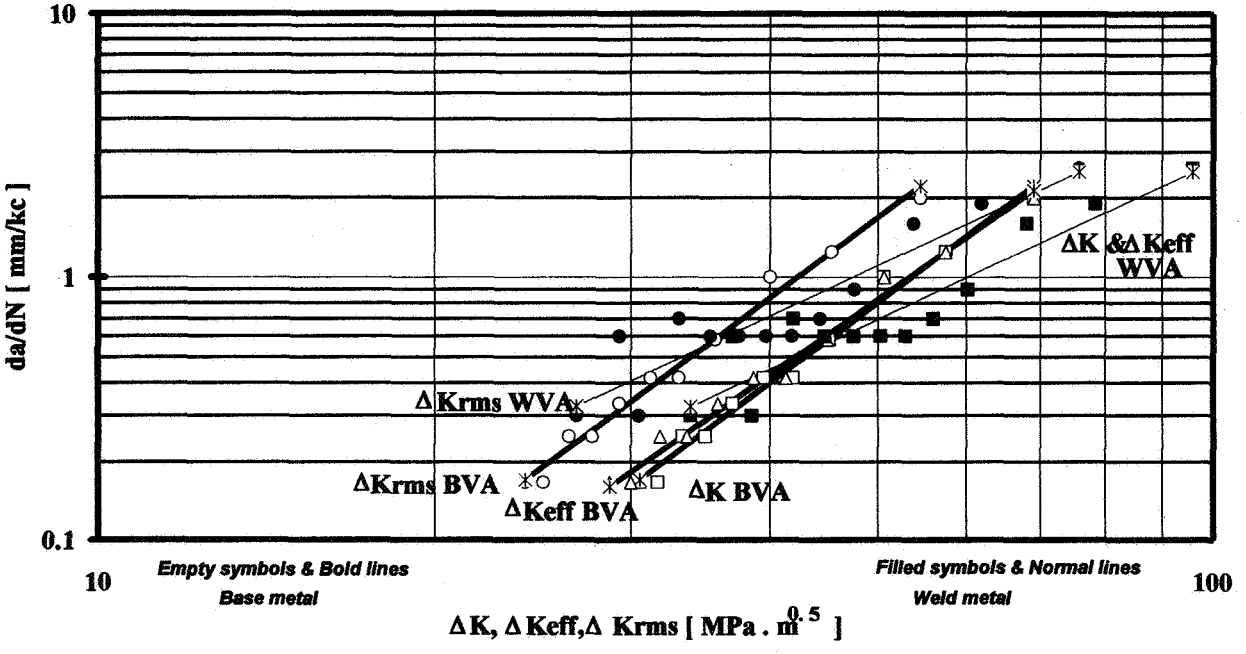

Figure 8. Fatigue crack growth rate (da/dN) vs. ΔK, ΔKeff, ΔKrms of BVA specimen.

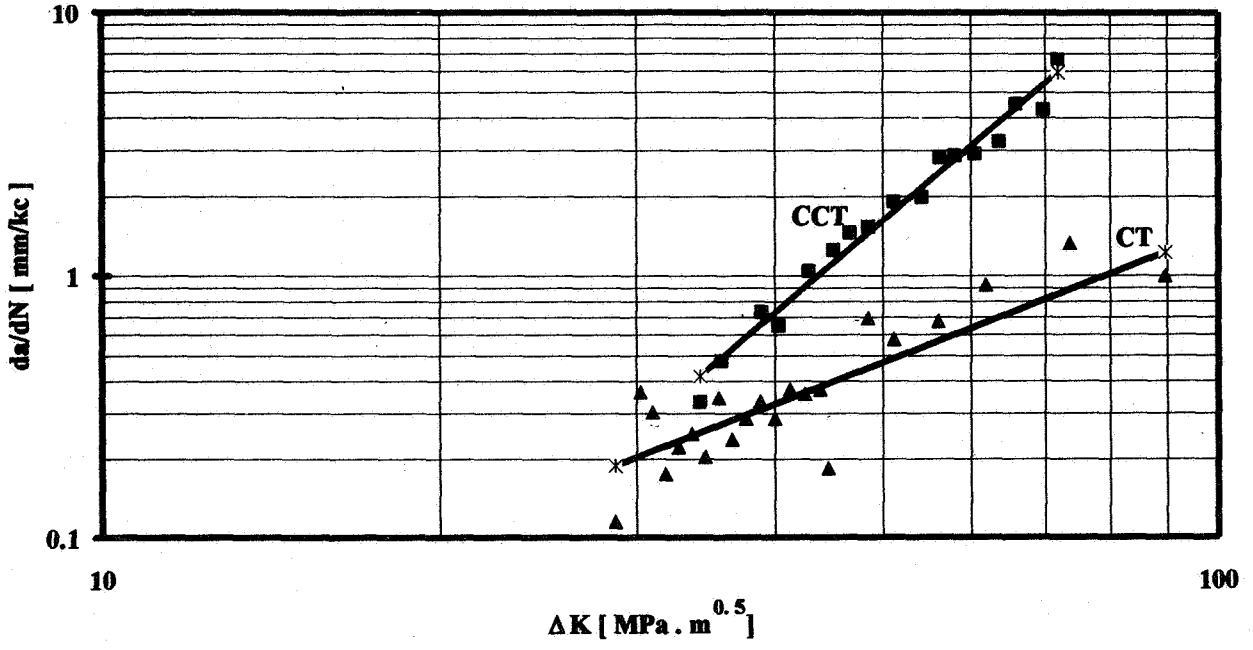

Figure 9. Fatigue crack growth rate (da/dN) vs. ΔK of a CCT and a CT specimen.

b) Residual Stresses

The effect of residual stresses resulting from welding is significant. Data are widely scattered around the lines representing the specimens as shown in figures 4-6 in the case of the weld metal. This influence is not stable, but it varies as the crack grows through the weld metal and through the heat affected zone as well. This is caused by the redistribution of the residual stresses. There is a point of intersection where the crack growth rate of both the base and weld metals coincide in either the growth rate region above or near 0.01 mm/kc.

c) The Loading Sequence

Figure 7 shows the growth rate vs the ΔKrms values of the stress intensity factor of the specimens subjected to variable and random loading amplitudes. This method of crack growth evaluation eliminates the effect of the load sequence. As it can be seen in table 3, comparing K and Krms values of the BVA and the WVA specimens, m was found to be identical in both cases, but C shifted the lines to the region of higher growth rates as also illustrated in figure 8. This is important when considering safety factor calculations in the design of steel constructions subjected to variable amplitude loading. The crack growth rates in this case are doubled related to the type of loading.

d) Fatigue Life Prediction

Table 3 contains the tested and the predicted lives of all specimens as well. Within acceptable accuracy, it was found that, after calculating the fatigue lives, all evaluation concepts fitted with the measured results. This indicates the importance of the results in safe design.

e) CCT and CT Test Specimens

According to the laws of fracture mechanics the results of the CCT and CT test specimens should coincide. By plotting the da/dN vs. ΔK as shown in figure 9, the CT specimen gave lower growth rates . Knowing that the two specimens were tested under the same laboratory conditions , and taking into consideration the reliability of the test results, the CTT specimens may be considered more suitable when testing the fatigue crack growth.

Conclusions

The following conclusions were obtained:

a) The Paris-Erdogan's fatigue crack growth law proved to be a suitable tool for life prediction and is capable of representing the phenomenon under variable amplitude loadings.

b) All the above mentioned evaluation methods provided good life predictions in most of the loading cases. Even the simple ΔK evaluation concept gave good and reliable results.

c) Addition of small loadings decreased the fatigue crack growth rate and thus extended fatigue lives. This is a significant result for both the designer and the maintenance engineer.

d) A confrontation between CT and CCT base metal constant amplitude loading specimens was designed. Results showed lower crack growth rates for CT test specimens in most cases.

e) Fractographical analysis showed no micromorphological difference between surfaces subjected to constant and variable amplitude loading.

f) The effect of the residual stresses on the fatigue crack growth has shown, once more, to be significant in comparing the base metal and welded metal of the same material.

g) Fatigue life prediction results proved to be in good correlation with the experimentally tested and in general they matched well with most of the predicted results found in many modern sources and in some cases seem to be more reliable.

Application of Results

The results of the experiments conducted in this work contribute to a wide range of theoretical and practical applications.

Within the theoretical and methodical framework, modern fracture mechanical concepts were used in the evaluation of results. The findings of the experiments of the fatigue crack growth rate under constant and variable amplitude loading showed that:

a) The CCT type of the test specimens better represent real conditions of constructions with cracks than CT test specimens.

b) The Paris-Erdogan's law is applicable to fatigue life predictions for welded and unwelded components with cracks.

c) The four life prediction methods:ΔK, Δ J, ΔK_{eff} and ΔK_{rms} can be used with good results including the simple ΔK concept .

The practical contribution of this work can be summarized as follows:

a) The designer and the maintenance engineer are provided with better information about the crack growth in the case of both the base and welded metal under constant and variable amplitude loadings.

b) Tensile overloading caused the retardation of the fatigue crack growth. This can be used not only for checking on the construction's reliability but also for increasing its fatigue life; resulting in enormous economic savings.

c) It is practically advantageous to use the ΔK parameter in the evaluation of fatigue lives of constructions subjected to variable amplitude loadings.

References

1. Ortiz, K.: Stochastic modeling of fatigue crack growth. Engineering Fracture mechanics, 29, 3, 1988, pp.317-334.

2. Ono, H.- Tsunenari, T.: A fatigue crack propagation model for application to service loads. Fatigue Fracture Engineering Materials and Structures,10, 6, 1987, pp.447-460.

3. Dolinski, K.: Fatigue crack growth with retardation under stationary stochastic loading. Engineering Fracture mechanics, 27, 3, 1987, pp.279-290.

4. Rolfe, ST.- Barsom, J.M.: Fatigue crack propagation under variable amplitude load fluctuation. Fracture and fatigue control in structures. Prentice- Hall 1977, pp.268-291.

5. Chang, J.B.- Hudson, C.M.: Methods and models for predicting fatigue crack growth under random loading. ASTM, STP 748, 1981.

6. Katcher, M.: Crack growth retardation under aircraft spectrum loads. Engineering Fracture mechanics, 5, 1973, pp.793-818.

7. Druce, S.G.- Beevers, C.J.- Walker, E.F.: Fatigue crack growth retardation following load reduction in a plain C-Mn steel. Engineering Fracture mechanics, 11, 1979, pp.385-395.

8. Fleck, N.A.: Fatigue crack growth due to periodic underloads and overloads. Acta Metall, 33, 7, 1985, pp.1339-1354.

9. Sunder, R.: A mathematical model of fatigue crack propagation under variable amplitude loading. Engineering Fracture mechanics, 12, 1979, pp.155.-165.

10. Arone, R.: Fatigue crack growth under random overloads superimposed on constant amplitude cyclic loading. Engineering Fracture mechanics, 24, 2, 1986, pp.223-232.

11. Ulrich, K.: Fatigue crack growth in welded joints. Ph.D. dissertation. Bratislava 1980.

12. Blodgett, O.W.: Designing weldments for fatigue loading. Welding Journal, 71, 7,, 1992, pp.39-44.

13. Lim, J.K.- Stephens, R.I.: Fatigue crack growth and retardation in the welded HAZ of 4140 steel. Welding Journal, 69, 8, 1990, pp. 294s- 304s.

14. Sidawi, J.A.: Fatigue crack growth under variable amplitude loading. Ph.D. dissertation. Slovak Academy of Sciences & Welding Research Institute, Bratislava, Slovakia, 1989.

15. Paris, P.C.: The fracture mechanics approach to fatigue. An interdisciplinary approach. Syracuse university press, 1964, pp.107-127.

16. Skroupa, M.: Fatigue life prediction of cruciform joints failing at the weld toe. Welding Journal, 71, 8, 1992, pp.269s- 275s.

17. Sobczyk, K.: Modeling of random fatigue crack growth. Engineering Fracture mechanics, 24, 4, 1986, pp.609-623.

18. IIW recommendation: The application of an engineering critical assessment in design, fabrication and inspection to assess the fitness for purpose welded products. Part 4, Fatigue. Com. V-878-88, X-1167-88, XIII-1283-88, XV-665-88, 03-06-1988.

19. Gregor, V.- Sidawi, J.A.: Calculation of the damage cumulation in welded beams. Welding News, Welding Research Institute, Bratislava, Slovakia, 1, 40, 1990, pp.1-8.

20. Gregor, V.- Ulrich, K.- Sidawi, J.A.: Fatigue life of welded I beams under bending loads of 15422.5 & 11523.1 steels. Welding Research Institute, Bratislava, Slovakia, 1584/3/205, 1984.

21. ASTM Standard E 647-93: Standard test method for measurement of fatigue crack growth rates. Annual Book of Standards, Vol.03.01, 1993, pp. 679-706.

22. Dowling, N.E.: J-integral estimates for cracks in infinite bodies. Engineering Fracture mechanics, 26, 3, 1987, pp.333-348.

Residual Life & Strength Estimates of Aircraft Structural Components with MSD/MED

Ripudaman Singh,* Jai H. Park† & Satya N. Atluri‡
FAA Center of Excellence for
Computational Modeling of Aircraft Structures
Georgia Institute of Technology, Atlanta, GA 30332-0356. USA

SUMMARY

Economic and safe operation of the flight vehicles flying beyond their initial design life calls for an indepth structural integrity evaluation of all components with potential for catastrophic damages. Fuselage panels with cracked skin and/or stiffening elements is one such example. A three level analytical approach is developed in this paper to analyse the pressurized fuselage stiffened shell panels with damaged skin or stiffening elements. A Global Finite Element Analysis is first carried out to obtain the load flow pattern through the damaged panel. As an intermediate step, the damaged zone is treated as a spatially 3-Dimensional structure modeled by plate and shell finite elements, with all the neighbouring elements that can alter the stress state at the crack tip. This is followed by the Schwartz-Neumann Alternating Method for local analysis to obtain the relevant crack tip parameters that govern the onset of fracture and the crack growth. The methodology developed is generic in nature and aims at handling a large fraction of problem areas identified by the Industry Committee on Wide-Spread Fatigue Damage.

INTRODUCTION

Structural integrity evaluation of airliners, which have exceeded their initial design life, but are still in operation due to economic constraints, is a major safety concern. After years of service, the micro flaws may have grown and coalesced to form detectable cracks, leading to a scenario called wide spread fatigue damage(WFD). The structural component may have a number of closely spaced small cracks, a situation called Multi-Site Damage (MSD) or a number of small cracks in neighbouring structural elements, a situation called Multi-Element Damage (MED). Although the new aircraft had the required ability to sustain a certain amount of damage, the

*Asst. Prof., Aerospace Engg., Indian Institute of Science, Bangalore 56012 India
†Visiting Scholar from Chungbuk National University, Cheongju, Korea
‡Institute Professor and Regents' Professor of Engineereing.

older aircraft with WFD may no longer have the damage tolerance capability necessary to ensure safety. At times, the situation can become catastrophic within two inspection schedules. For continued safe operation, it is desirable to understand the severity of cracks and also have an estimate of residual strength and life of the damaged structure. A reliable damage tolerance assessment requires full scale testing combined with computational analyses. A reliable computational analysis can virtually simulate a test, thus economically predicting its outcome, it can reduce the number of tests that need to be performed. A well established correlation between analyses and a test can help resolve a number of issues which were either missed or could not be extracted during testing.

The *Industry Committee on Widespread Fatigue Damage* has identified about 15 different aircraft structural details that are susceptible to widespread fatigue damage[1]. These include: (1) Longitudinal skin joints, frames, and tear straps (MSD, MED); (2) Circumferential joints and stringers (MSD, MED); (3) Stringer cutouts in frames at successive locations in the fuselage (MED); (4) Aft pressure dome outer ring and dome web splices (MSD, MED); (5) Other pressure bulkhead attachments to the skin (i.e. web attachment to stiffener and pressure decks); (6) Stringer to frame attachments (MED); (7) Window surround structure; (8) Over wing fuselage attachments (MED); (9) Latches and hinges of nonplug doors; (10) Skin at runout of large doubler (MSD) in the fuselage, wing or empennage; (11) Chordwise splices (MSD, MED); (12) Rib to skin attachments; (13) Stringer runout at tank end ribs and (14) Spar cap/web (MSD multiple cross-section). This paper presents a part of an ongoing work dedicated to the development of efficient computational tools, envisioned to involve the least amounts of engineering man power, for structural integrity evaluation of aging, repaired as well as new airplanes. We present a generic methodology developed to assess the residual strength and fatigue life of most of the above mentioned structural components with wide-spread fatigue damage. As a typical illustration of the developed generic methodology this paper presents an investigation of MSD and MED at a stringer - frame junction of a pressurized fuselage stiffened shell panel.

GENERIC METHODOLOGY

In any efficiently designed aircraft sub-structure, the stress flow pattern is fairly complex due to the presence of various stiffening elements, assembled with fasteners in a complex manner. Cracks, any where in the structure, cause further redistribution of stress and overloading of uncracked portion. A single step analytical attempt to understand the damaged substructure with all its intricacies, is not only an inefficient approach but unreliable also. The problem can be efficiently handled through a multilevel analysis, wherein we continously narrow down on the zone under investigation and increase the details in the model, and finally focus on a problem size which can be reliably dealt with well understood fracture mechanics concepts. A three level investigation is sufficient for most of the MSD/MED problems in flight vehicle structures.

Consider the case of damage in an airliner fuselage, essentially a pressurized stiffened shell structure. As a first step, a multibay fuselage panel is analysed. As a second step, a portion of the panel approximately equal to three bays in size is analysed. As a final step the cracked portion is isolated and solved using Schwartz-Neumann Finite Element Alternating Method. The crack tip parameters are then estimated and the corresponding static residual strength is

evaluated. By growing the crack and going back through the loop of analyses, residual life is estimated. The details of each of these steps and their integration to form powerful procedures are described in the following subsections.

Global Analysis

The first analysis is done at a level where only a reasonable amount of detail is modeled, the bounds are far off from the damaged zone under consideration and the boundary conditions are either known or can be easily modeled by symmetry/antisymmetry constraints. For the problem of MSD/MED in a fuselage shell structure, a multibay panel with at least two bays on each side of the damaged zone constitutes the global model.

The primary features of the global model are that the skin is modelled as a shell and the frames & stringers are modelled as beams with their neutral axis offset from the shell mid-plane, connected to the shell with a row of flexible fasteners. The shear clips are treated as integrated with the frame beam and the Tear straps are integrated with the shell. Bonded joints, if any, take into account the flexibility of the adhesive.

At this level, the types of damage that can be handled are the cracks in the skin, partially or fully failed stiffening elements such as frames or stringers, partially or fully cracked tear straps, degraded adhesive, broken fasteners and any combination thereof.

The analytical model is a 3-D spatial structure, modeled by 2-D finite elements. The shell is modeled by a 4 noded, 5 degree-of-freedom (dof) per node element, developed by Ashwell and Sabir[2]. The frames and the stringers are modeled by 2 noded, 5 dof, curved and straight beam elements, degenerated from the shell element. The fasteners are modeled by two 2 noded, 2 dof, springs placed orthogonally, with stiffnesses empirically generated using Swift's relationship[3] and 3 multipoint constraints. The damage is taken care of as geometric entities by having disconnected shell/beam elements.

The analysis is carried out by an FEM code developed inhouse, called 'SOFRAC', for damaged stiffened shell structures. The set of input files describing the model and the associated information is generated by a separate preprocessor called 'Multibay Modeler', which draws the information from the geometric and damage database. From the output of the global analysis, the displacements are extracted at the boundaries of the intermediate model.

Intermediate Analysis

At this second stage, the details in the model are refined, the bounds are relatively closer to the damaged zone and the boundary conditions in terms of prescribed displacements are known from the global analysis. For the problem of MSD/MED in a fuselage shell structure limited within about a 5″ length scale, a panel with single frame and three stringers constitutes the intermediate model.

The primary features of the intermediate model are that the skin, frames, stringers, shear clips, and tear straps are all modelled as plates and shells, connected to each other with rows of

flexible fasteners. The flanges of the stiffening elements are treated as beams to keep the problem size within limits. Bonded joints, if any, take into account the flexibility of the adhesive.

At this level, the types of damage that can be handled consist of cracks in the skin, frame, stringer, tear strap & shear clip, degraded adhesive, broken fasteners and any combination thereof.

The analytical model is a 3-D spatial structure, modeled by 2-D finite elements. All the plates & beams are modeled by 4 noded & 2 noded, 6 dof elements developed at Lockheed[4]. The fasteners are treated as beams with their section properties tailored to match the empirical behaviour of Swift's fastener. The damage is once again taken care of as geometric entities by having disconnected plate elements.

The analysis is carried out by STAGS(STructural Analysis of General Shells), a code developed at Lockheed, Palo Alto[5]. The set of input files describing the model and the associated information is generated by a separate preprocessor called 'Halfbay Modeler', which draws the information from the geometric & damage database and the displacement output of SOFRAC. From the output of STAGS and its postprocessor STAGSPP, the stresses at the boundaries of the local model and the fastener loads within the local model are extracted.

Local Analysis

At the lowest level, the model is reduced to a rectangular flat sheet with cracks and or holes along the major axis. It may or may not contain the fastener holes. The areas of local model are kept as far as possible from the cracks, with all the other structural details lying outside the rectangle or within the hole. The boundary conditions, in terms of prescribed stresses, at the edges of the rectangular sheet and the surfaces of the holes are known from the intermediate analysis.

The primary feature of the local model is that only a cracked sheet needs to be analysed, into which the influence of the rest of the structure goes as tractions at the boundaries. Concepts of fracture mechanics can now be easily applied to this simple model.

The analytical model is a 2-D spatial structure, modeled by 2-D finite elements. At this stage, we bifurcate into two paths, the inplane and the bending. For inplane analysis, 2 dof, 8 noded isoparametric elements are employed and for bending 3 dof, 4 noded quadratic elements are used.

For the inplane loading situation, the analysis is carried out by a code developed inhouse, based on Finite Element Alternating Method (FEAM) [6]. The input file describing the model is generated by an independent preprocessor called 'Local Modeler', which draws the information from the output of STAGSPP and Halfbay Modeler. For the bending part of the analysis, the FEAM code is under development. The outcome of these analyses is the crack tip parameters which can be used to determine the residual strength of the structure and crack growth rates of all the cracks. The cracks can be grown at this level, under fatigue loading, upto a stage where they either linkup or start influencing the edge tractions evaluated during intermediate analysis.

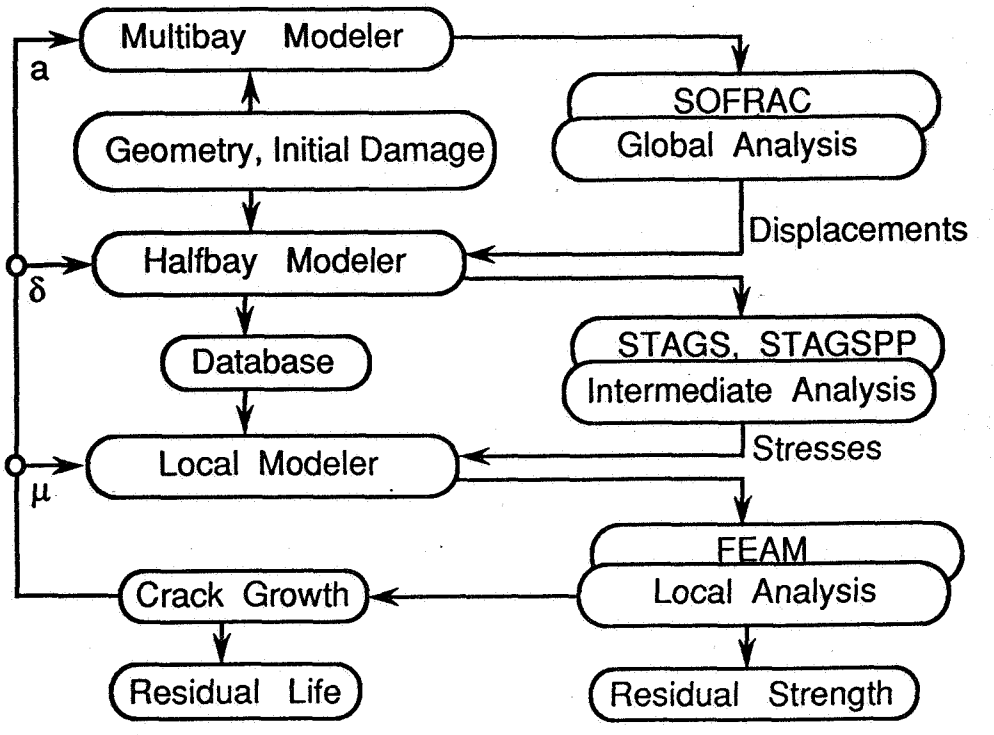

Figure 1: Computational procedure for analysis of MSD in structures.

At this stage, the damage configuration needs to be updated in the intermediate model. Net ligament yielding is considered as the linkup criterion[7].

The next three subsections describe how these modules viz., Multibay Modeler, SOFRAC, Halfbay Modeler, STAGS, Local Modeler, FEAM can be integrated in different architectures and the information can be made to flow between them so as to assess the residual strength and residual life of structural components with MSD and/or MED.

Analysis of Multi-Site Damage

For the analysis of structural components with MSD, figure 1 describes the computational procedure. Starting from the geometric and the initial damage database, the Multibay modeler generates the global model that is fed into the SOFRAC for global analysis. The Halfbay modeler generates the finite element model based on same initial geometric and damage information, with boundary conditions as prescribed displacements, extracted from the solution of SOFRAC. At this stage, another set of files is also written, containing information necessary to post process the output of STAGSPP and generate the local model. The local modeler picks up the necessary information from the output of Halfbay Modeler and STAGSPP, generates the local model and feeds into the FEAM. The FEAM code is capable of handling multiple cracks of arbitrary lengths. This local analysis gives the cracktip parameters for multiple cracks, which are now used to estimate the residual strength and crack growth rates. The cracks are grown

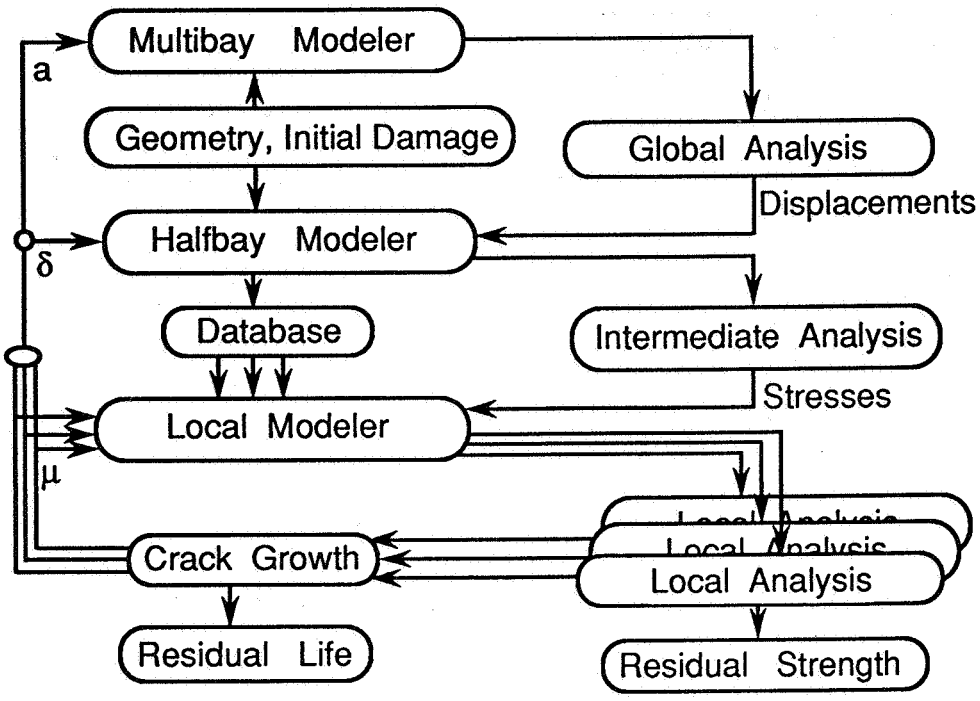

Figure 2: Computational procedure for analysis of MED in structures.

at this stage with net ligament yield as the linkup criterion(Research is now being completed to use T^* as the link-u[p criterion [8]). For very small crack growth, local analysis is performed with updated damage information. If the crack growth is large or a crack linkup occurs, the damage is updated at the intermediate analysis level. For substantial crack growths, the global analysis is redone. This procedure simulates the crack growth and provides with information about residual life. Experience has shown that for every 5 stages of local analysis, intermediate analysis needs to be done and for every 5 stages at intermediate analysis (25 local analyses), there is a requiremenet for a fresh global analysis.

Analysis of Multi-Element Damage

The modular nature of the subprocedures and their interfacing through regular ASCII files lends itself to various possibilities. One of them is the handling of structural components with MED. The Halfbay Modeler generates database for multiple local analyses, each local zone covering a damage which can be a single crack or an MSD. The Local Modeler generates multiple models and these can now be analysed independently, using FEAM. The cracks are grown in each of these analyses independently. Whenever required, the Halfbay Modeler can integrate the current damage configuration and perform fresh intermediate analysis. Figure 2 explains this procedure pictorially. The methodology at and above the level of intermediate analysis in the hierarchy remains same as before. Since the FEAM local analyses can handle multiple cracks,

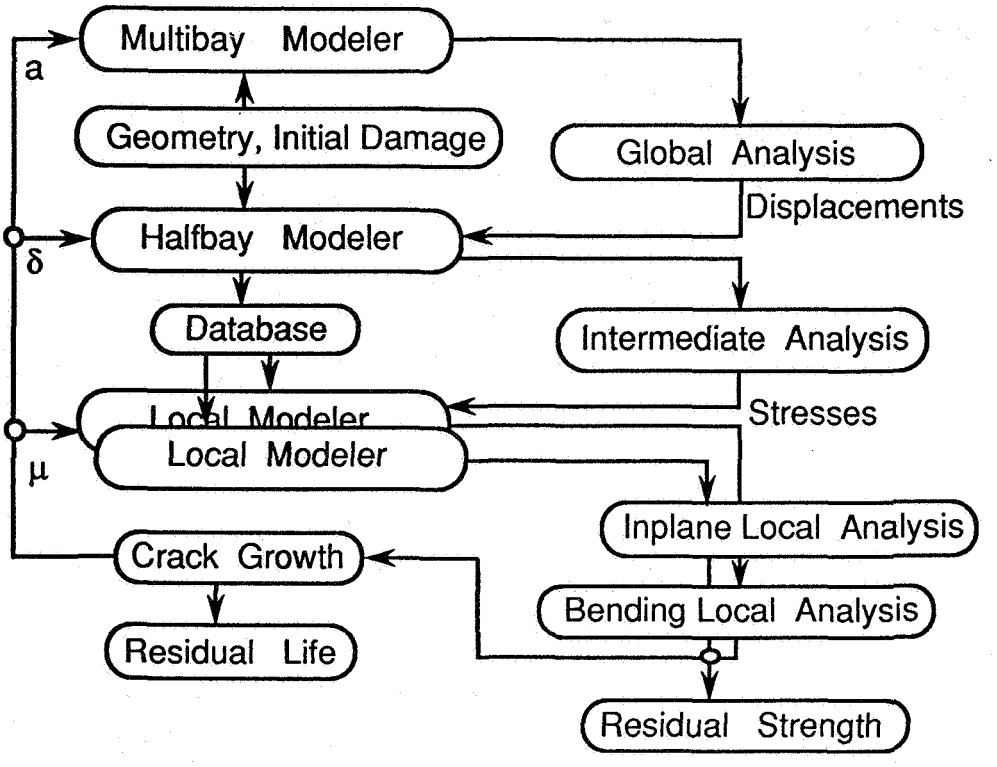

Figure 3: Computational procedure for analysis of MSD/MED with significant bending.

this procedure has the power to resolve situations where MSD exists in neighbouring elements, viz., MSD as a subset of MED.

Analysis of Problems with Bending

For the analysis at the local level, if there is a significant bending involved, the Halfbay Modeler can generate two sets of information, one for inplane and one for bending problems. The local modeler will generate two models which will go independently into two different Finite Element Alternating codes. The crack tip parameters for the two loading situations will then be integrated to evaluate the residual strength and the crack growth rates. This methodology, presented in figure 3, depends upon FEAM for cracked plate bending problems, which is under development.

The power of all these procedures emerges from the fact that a wide range of problems with widespread fatigue damage can be handled. Multiple cracks can be grown irrespective of where they are in the substructure. The efficiency has been achieved by automating the procedures to an extent where more than half a dozen modules work from a single set of initially generated input files.

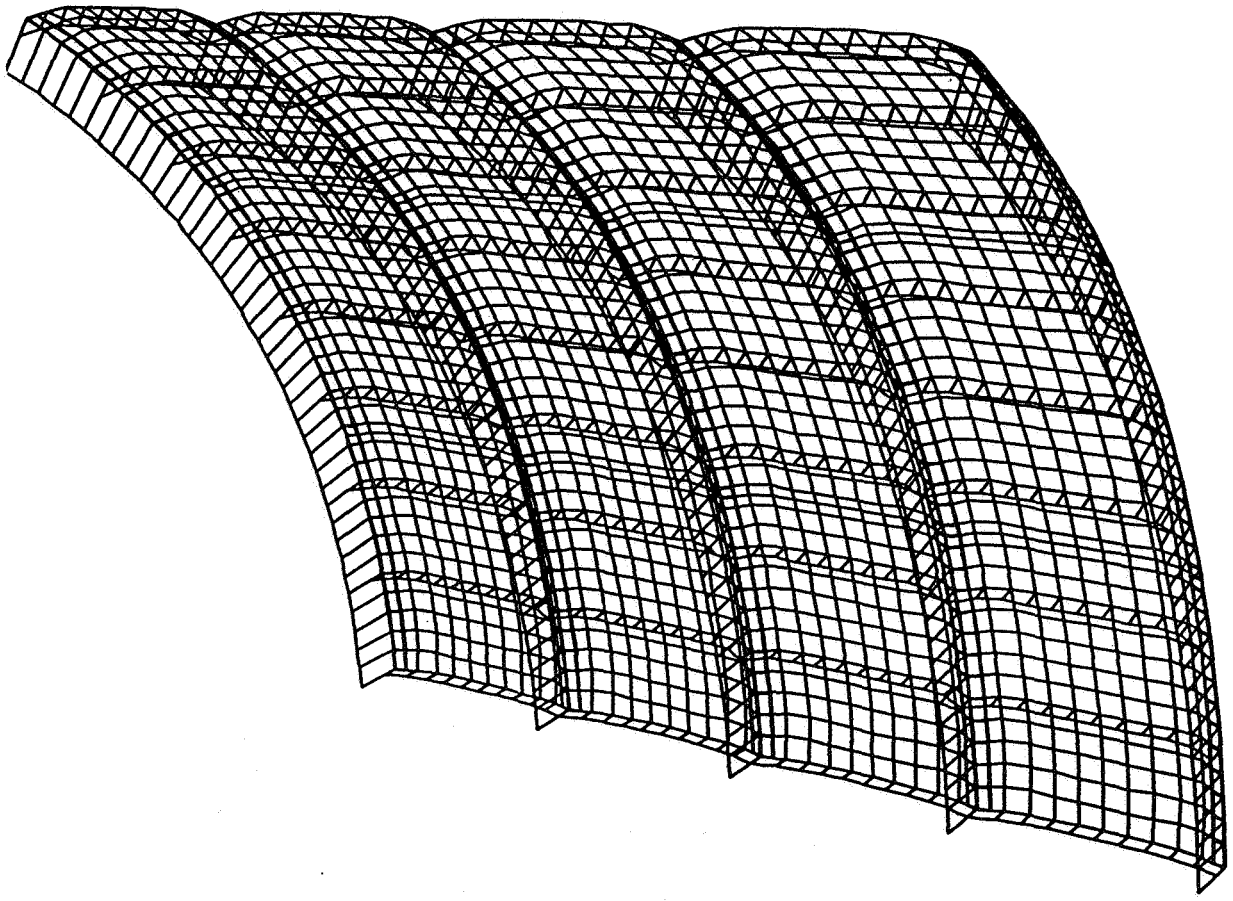

Figure 4: Deformed view of the global model of 4 × 8 bays of fuselage panel.

AN EXAMPLE PROBLEM

We now employ the above described methodologies to analyse a situation of MSD and MED at the frame stringer junction in a typical narrow body fuselage panel. This example is only intended to demonstrate the potential of the developed computational procedure.

Configuration

Consider an airliner fuselage formed by 0.036″ thick, Al 2024-T3 shell, of radius 74″ and stiffened by 'Z' section frames 20″ apart, 2″ × 0.036″ tear straps at each frame location and 'Z' section stringers 9.25″ apart, all of them attached with fasteners, 5/32″ in diameter spaced at 1″. The stringers run through the cutout in the 'L' section shear clips which attach the frames to the skin through the tear strap. The internal pressure in the fuselage is 9.0 psi.

For the purpose of global analysis, we consider a multibay panel of 5 frames and 9 stringers. A typical deformed finite element model from SOFRAC (approx 15,000 degrees of freedom, magnification = 5) is shown in figure 4. On an HP workstation 7000 900 series, the CPU time for the problem of this size is about 10 minutes.

For an intermediate analysis, a section of this consisting of a single frame, shear clip & tear strap and 3 stringers is modelled. Figure 5 shows an exploded view of a typical deformed FE model (approx 20,000 dof, magnification = 5). This problem takes about 15 minutes on an HP workstation.

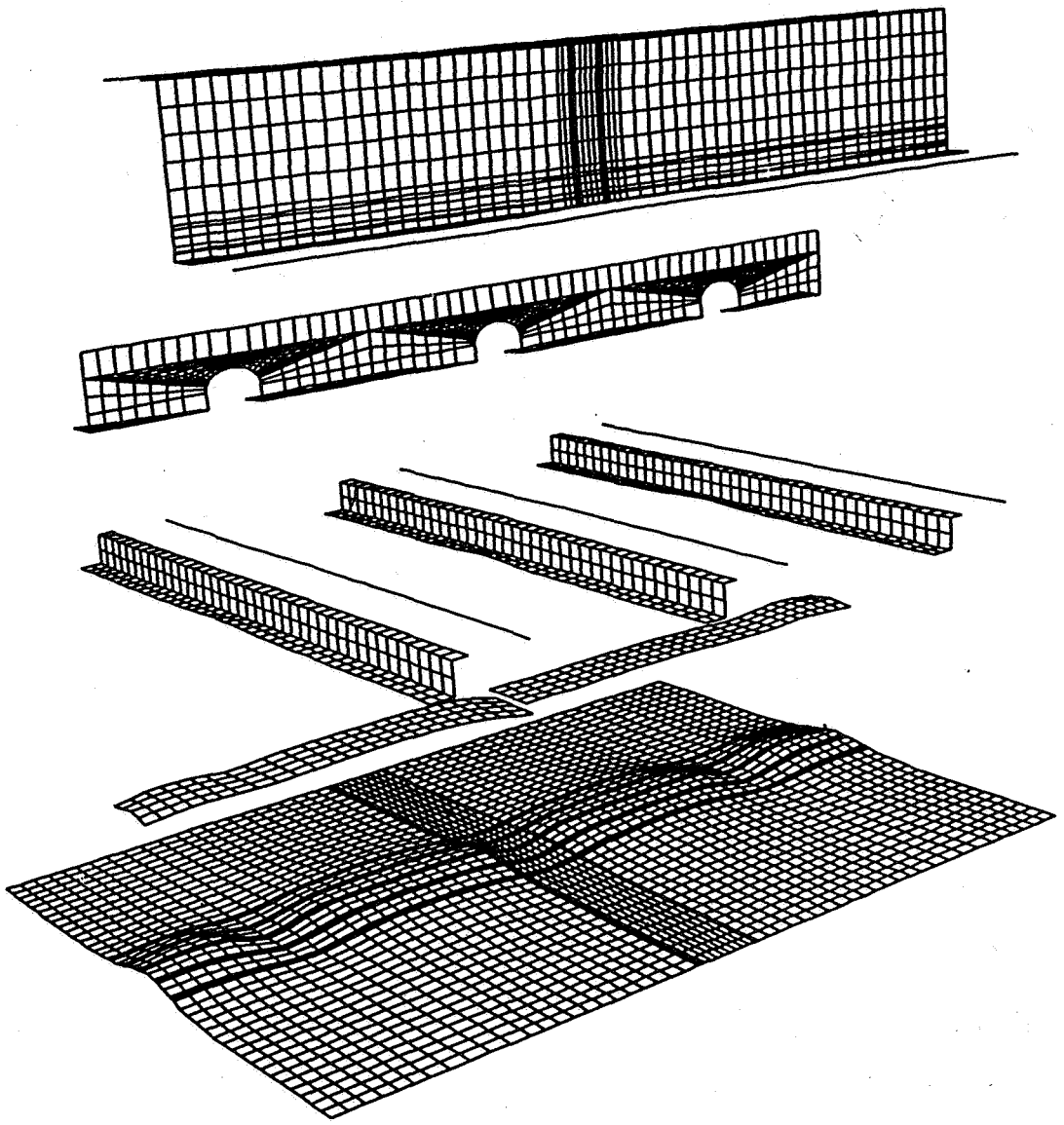

Figure 5: Exploded deformed view of the intermediate model of 1 × 3 bays of fuselage panel.

The local model consists of a flat rectangular cracked sheet and depends upon the type of damage being analysed. It takes approximately 3 minutes per crack tip for the local analysis to be complete. The damage is considered in various forms and is categorized in the following three sets.

Multi-Site Damage in the Skin

Consider the situation of an MSD cracking in the skin at the row of fasteners joining the skin and the central stringer. Let the initial crack configuration consist of 5 cracks of length 0.125″ on both sides of the fasteners, along the row of fasteners, at a location directly below the central frame. This location is marked by '*A*' in figure 5. This situation was run through the procedure of figure 1 and it was found that the first linkup of cracks occurs at 8,920 fuselage pressurization cycles. The same MSD situation was analysed with the tear strap fully cracked at the same location. The type of the damage considered in the tear strap is apparent from the figure 5. The effect of broken strap is to reduce the life to only 2,518 cycles (about 28%). This analysis is presented graphically in figure 6. The analysis is carried out only upto first linkup as it has earlier been observed [9] that the first linkup is virtually the end of the life of a panel with MSD. A lot of other damage scenarios with MSD can also be analysed in a similar manner.

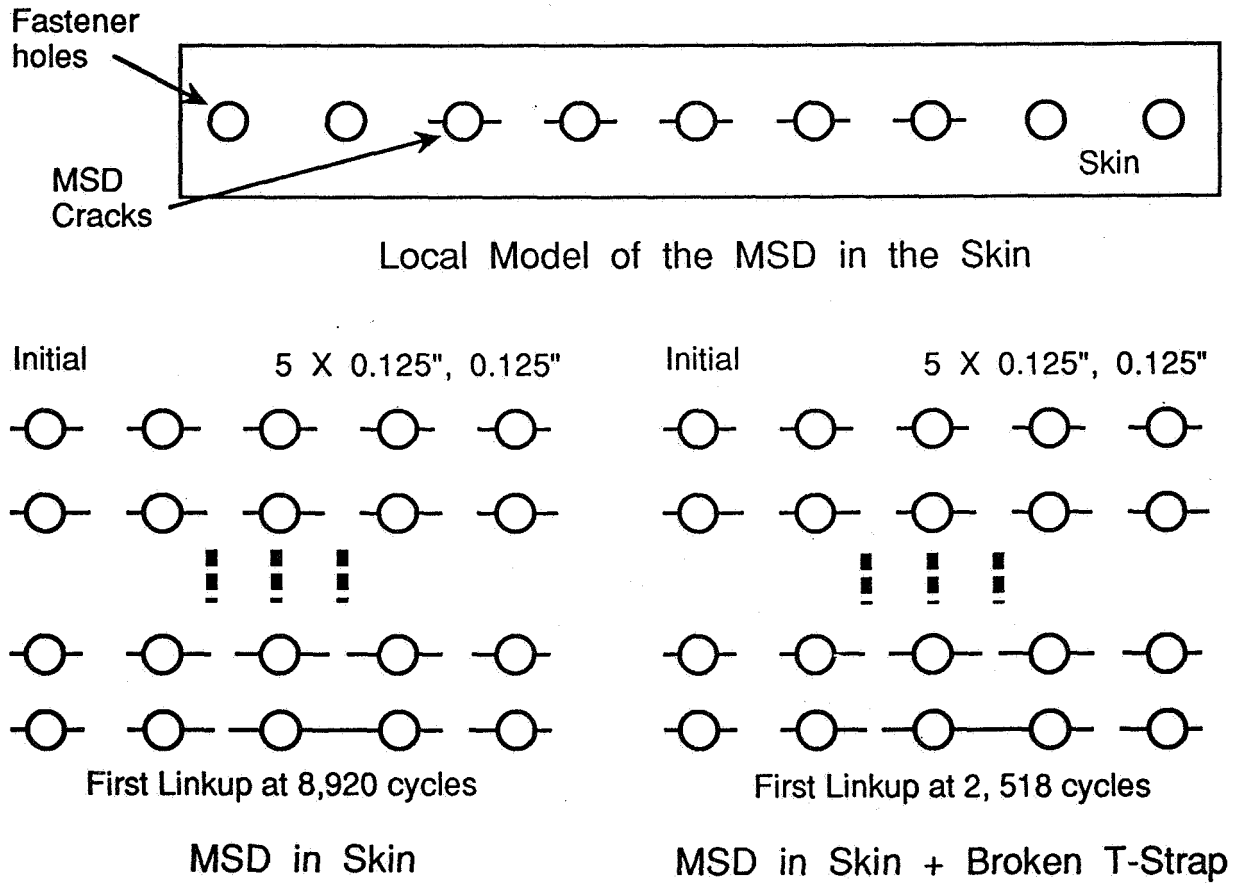

Figure 6: Analysis of MSD in the skin.

C-4.

A Crack in the Frame

Consider the situation of a single crack in the frame, emanating from a fastener, running normal to the row of fasteners joining the frame and the shear clip, located directly above the cutout in the clip through which the central stringer runs. This location is marked by '*B*' in figure 5. Initially, let the crack lengths be 0.122″ & 0.228″ respectively towards & away from the shear clip. The crack lengths are measured from the hole center to the crack tip, and have been chosen arbitrarily. The fatigue analysis is done, as per the procedure described in figure 1, upto a situation where the plastic zone size ahead of the lower crack tip (towards the shear clip) touches the flange of the frame. This corresponds to a crack length of about 0.372″. The scenario is presented in figure 7.

The above described growth of the crack is found to take 451,811 cycles of fuselage pressurization. But the situation gets suddenly worse if any of the other stiffening elements are damaged. The same crack grows about 100 times faster with a broken tear strap, about 200 times faster with a broken shear clip, about 1600 times faster with both strap and clip broken. Cracking in the skin further speeds up the crack growth. This is presented in table 1. Although, in actual case, the MSD or the lead crack in the skin will grow as the crack in the frame grows, but that is not modelled in this particular example, and is looked at in the following subsection.

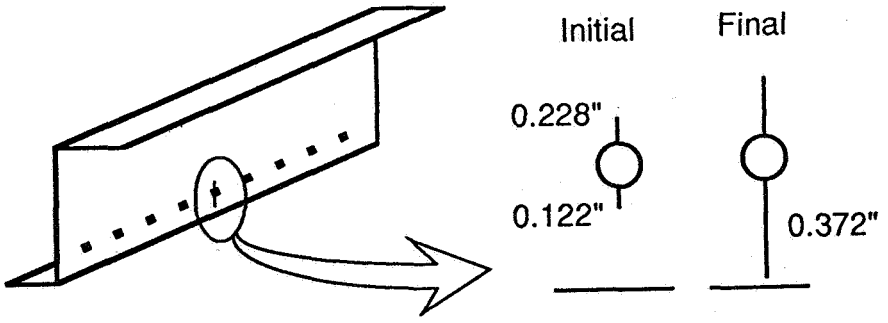

Figure 7: Analysis of a single crack in the frame.

Table 1: Effect of damaged elements on crack growth in frame

Tear strap	Shear Clip	Skin	Cycles
intact	intact	intact	451,811
broken	intact	intact	4,476
intact	broken	intact	2,172
broken	broken	intact	284
broken	broken	MSD	268
broken	broken	5″ crack	84

Multi-Site Damage in the Skin and a Crack in the Frame

Consider now a situation of Multi-Element Damage with a crack in the frame, MSD in the skin and a broken tear strap. The initial crack configuration corresponds to the combination of initial MSD situation with a fully cracked tear strap and the initial crack configuration in the frame analysed in the previous two subsections. The MSD cracking in the skin and the crack in the frame are grown by running two independent models at the local level, as described in figure 2. The first linkup of MSD in the skin occurs at 2,212 cycles. The analysis is stopped at this stage. Comparing this with results of figure 6, the crack in the frame speeds up the MSD crack growth by about 12%. In the mean time the lower crack in the frame had grown to a length of 0.354″, as shown in figure 8. For the problem in the previous subsection, the crack in the frame had grown to this length in 2,396 cycles. This implies that the MSD in the skin speeds up the crack in the frame by about 8%. Thus both MSD in the skin and the crack in the frame are found to speed up each other's growth.

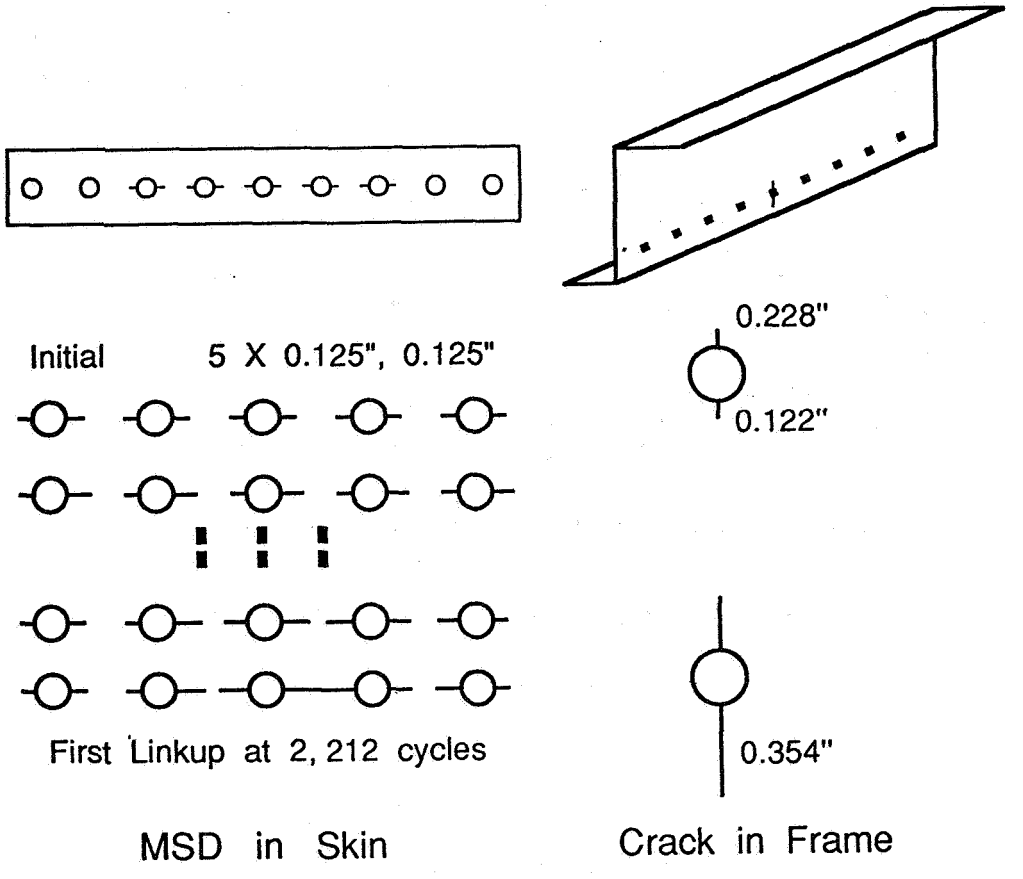

Figure 8: Analysis of MED in the skin and the frame.

The above set of examples were analysed in less than 24 computer-man hours. This shows the power and efficiency of the developed procedures.

CONCLUSION

A very powerfull and an extremely efficient computational procedure/tool has been developed, by combining the alternating technique, hierarchical finite element strategy and automatic modelling & execution. The potentials of this methodology have been demonstrated through an example of Multi-Site and Multi-Element Damage in a fuselage panel.

Acknowledgement: This work is supported by a grant from FAA to the Center of Excellence for Computational Modelling of Aircraft Structures at Georgia Institute of Technology, Atlanta. Suggestions and support from Mr Vijay Shenoy and Dr. David Potyondy are appreciated.

References

[1] Interim report of the Industry Committee on Widespread Fatigue Damage, draft, March 1993.

[2] Ashwell, D.G.; and Sabir, A.B.: A New Cylindrical Shell Finite Element based on Simple Independent Shape Functions, *International Journal of Mechanical Sciences*, Vol 14, 1972, pp. 171-183.

[3] Swift, T.: Fracture Analysis of Stiffened Structures, *ASTM STP 842*, 1984, pp 69-107.

[4] Stanley, G.M.; Park, K.C.; and Cabiness, H.: The Computational Structural Mechanics Testbed, Structural Element Processor ES 7: Revised ANS Shell Elements, NASA CR 4360, 1991.

[5] Almroth, B.O.; Brogan, F.A.; and Stanley, G.M.: Structural Analysis of General Shells, User's instructions for STAGSC-1, Lockheed Missiles and Space Company, LMSC D633873, Palo Alto, California, 1986.

[6] Park, J.H.; Ripudaman Singh; Pyo, C.R.; Atluri, S.N.; and Tan, P.W.: Residual Strength of Fuselage Panels with Wide-Spread Fatigue Damage, *Durability and Structural Reliability of Airframes*, Ed. by Blom, A.F., ICAF 1993, Stockholm.

[7] Swift, T.: Damage Tolerance in Pressurized Fuselages, 11^{th} *Plantema memorial lecture, ICAF 1987*, Canada.

[8] Pyo, C.R.; Okada. H.; and Atluri S.N.: Analysis of MSD and its Linkup in Aircraft Panels by using an Elastic Plastic FE Alternating Method, FAA/NASA International Symposium on Advanced Structural Integrity Methods for Airframe Durability and Damage Tolerance, NASA CP-3274, 1994.

[9] Park, J. H.; Ripudaman Singh; Pyo, C. R.; and Atluri, S. N.: Structural Integrity of Panels with Multi-Site Damage, AIAA-94-1457-CP, April 1994.

ULTRASONIC TECHNIQUES FOR REPAIR OF AIRCRAFT STRUCTURES WITH BONDED COMPOSITE PATCHES

S.H. Smith
N. Senapati
R.B. Francini

Battelle
505 King Avenue
Columbus, Ohio

SUMMARY

This is a paper on a research and development project to demonstrate a novel ultrasonic process for the field application of boron/epoxy (B/E_p) patches for repair of aircraft structures. The first phase of the project was on process optimization and testing to develop the most practical ultrasonic processing techniques. Accelerated testing and aging behavior of precured B/E_p patches, which were ultrasonically bonded to simulated B-52 wing panel assemblies, were performed by conducting flight-by-flight spectrum loading fatigue tests. The spectrum represented 2340 missions/flights or 30 years of service. The effects of steady-state applied temperature and prior exposure of the B/E_p composite patches were evaluated. Representative experimental results of this phase of the project are presented.

INTRODUCTION

One of the major technical thrust areas in the U.S. Air Force aging aircraft program is the development of structural repair techniques. Primary emphasis is on the development of efficient, durable, inexpensive, and easily implemented repair technology. Previous repair technology has involved the use of metallic structural repair patches and techniques using mechanical and/or bonding techniques [1]. There is an adequate structural material database and design guidelines for designing and installing these aircraft structure repairs. In the past several years, B/E_p composite patches have been used to repair several U.S. Air Force aircraft [2-9]. The thermal blanket curing process was used to install B/E_p composite precured patches. This process takes several hours to cure the adhesive at the required curing temperature not to exceed 250°F.

With U.S. Air Force support, the authors have developed an ultrasonic curing process for the field application of B/E_p composite patches to B-52 aircraft upper wing structures [10]. A summary of the results of this development project is presented in this paper. The project consisted of an initial phase for determining the desirable ultrasonic curing conditions and parameters. Double lap

shear specimens with B/E_p composite strips bonded to 7075-T6 and T651 adherents were tested to determine shear strength and preferred curing conditions. The verification testing of the composite patch design and the ultrasonic curing process consisted of conducting accelerated fatigue and prior exposure tests on repaired structural panel assemblies that simulated the B-52 wing at wing station 402, S-21. Special instrumentation was used to monitor the strain levels in the composite patches and aluminum substrates and to measure the fatigue crack growth behavior during spectrum load testing.

EXPERIMENTAL METHODS AND RESULTS

The experimental techniques and procedures used in this project are described in two parts. The first part is on approaches used in identifying the desired parameters for the ultrasonic bonding process for precured composite patches. The second part involves the experimental techniques and procedures used in the panel assembly testing.

Fabrication of Boron/Epoxy Patches and Test Specimens

The B/E_p patches were precured in an autoclave using a vacuum bag process. All plies in the patches were unidirectional and cured in accordance with the material supplier procedures at a pressure of 50 psi and a temperature of 350°F for 90 minutes. The adhesive selected for bonding the B/E_p patches to the 7075-T6 and T651 aluminum substrates was FM-73 grade 10 and had a polyester mat. The adhesive was stored at 0°F. During room temperature assembly of the specimens any adhesive left over seven days was discarded. The ultrasonic bonding of the B/E_p patches is very sensitive to the surface preparations of the aluminum substrates. Therefore, the surfaces were phosphoric acid anodize and BR127 primed according to procedures defined by the Air Force for field application to B-52 wing structures.

Identification of Process Parameters

The ultrasonic process has several advantages over the thermal blanket technique of curing adhesively bonded composite patches. The advantages are: (1) a better wetting of the substrate surface with the adhesive due to shear thinning with the high intensity ultrasonics, (2) accelerated chemical reactions, (3) less time needed to reach the required curing temperature, (4) a more consistent bond strength, and (5) lower and more uniform residual stresses after cool-down.

The laboratory scale ultrasonic bonding fixture is shown schematically in Figure 1. A series of parametric screening tests were conducted to gain insight into the primary variables and their sensitivity in ultrasonic curing of the B/E_p patches with FM-73 adhesive. It was these variables that were investigated during the parametric screening tests described below. The variables and their ranges investigated were:

Coupling Material—Its purpose was to transfer the ultrasonic energy into the patch. Without a coupling material, very little ultrasonic energy can be transferred to the adhesive via the patch. More than ten types of coupling materials were investigated under this program. The top two were a polymer compound (polyisobutadiene) and a red rubber (styrene butadiene) that was 0.060-inch thick.

Ultrasonic Power—A watt meter was used to measure the power delivered to the ultrasonic converter. The range of powers investigated was 50 to 105 watts. Power levels as high as 400 watts were investigated with the larger size validation test panels.

Duration of the Ultrasonic Energy—During the parametric screening tests the length of time the ultrasonic energy applied to the patch varied from 5 to 120 minutes.

Coupling Pressure—This is the pressure or force that was applied to the patch and test coupon during the application of ultrasonic energy. The force was applied using the hydraulic jack shown in Figure 1. The pressures investigated ranged from 5 to 15 psi.

Several screening tests were conducted to evaluate the thermal cure cycle produced by the ultrasonic bonding technique. Figure 2 shows a plot of temperature versus time for three variable combinations of power, time, and pressure. These are results for five plies of B/E_p bonded to aluminum strips. An embedded thermocouple in the FM-73 adhesive was used to measure temperature with time. As can be seen by the data, a stable temperature is reached after about 15 minutes. Several additional tests were performed with five plies and different combinations of power, time, and pressure. Some screening tests were also conducted with 15 and 40 ply samples. These data were used to select the desired conditions for ultrasonic bonding.

The results of the screening tests were used to develop a master baseline indexed sample for evaluating the degree of cure produced by the ultrasonic process. Figure 3 shows the baseline sample that was developed for undercured, cured, and overcured samples. All subsequent testing and failure mode identification of samples were correlated to this master baseline sample.

The second part of the project involved conducting mechanical tests to quantify the process. In adhesive bonding characterization testing either wedge or lap shear tests are performed to evaluate the integrity of the bondline and process. Double lap shear tests were conducted on ultrasonically cured samples that were bonded according to the desired conditions established in the screening phase. The testing procedures defined in reference 11 were followed. Table 1 shows some of the results for the lap shear strengths developed using the process.

Flight-by-Flight Spectrum Loading Fatigue Tests

Several iterations were performed on the geometry and configuration for the fatigue test specimens. The requirements for the configuration were: (1) that the panel thickness had to be 0.25-inch thick, (2) B/E_p patches were to be bonded to both sides of a single edge crack of 0.30-inch length, (3) grip ends of the specimen had to be designed such that failure would occur in the cracked

section of the panel and not in the grips, and (4) panel configuration and geometry had to be such that monitoring crack growth and load transfer during fatigue could be accommodated.

Initially a single 0.250-inch-thick 7075-T651 aluminum rectangular panel configuration with the B/E_p patches bonded to each surface of the panel with the edge crack was selected. However this configuration was not accepted because of the difficulty and unassured reliability of being able to bond two patches ultrasonically on both sides of the panel at the same time. The second idea of a configuration was to split the thickness of the panel into two 0.125-inch-thick 7075-T6 sheets and ultrasonically bond the two patches on the panels separately and then adhesively bond the two together to form the equivalent 0.250-inch thickness. This configuration had the drawback that Krak gages could not be used on the back side of the crack surface to measure and monitor fatigue crack growth rates. The final idea was to use a honeycomb core or other separator between the two skins/ sheets and cut out the core around the crack area for the Krak gages. The honeycomb core or other separator would be adhesively bonded to the aluminum face sheets/skins. This configuration had the added built-in bucking stability required for spectrum loading fatigue testing with compression loading in the spectrum. This concept was retained and the honeycomb core was replaced with Teflon sheets and not bonded to the aluminum face skins/sheets. Solid aluminum inserts were selected as spacers for the grip areas. Figure 4 shows the final specimen configuration selected for the simulated repair. The B/E_p repair patches were eight layers thick with 0.30 and 0.10 inch/ply ramp ups for the vertical and horizontal directions, respectively.

In the grip area, the two repaired sheets were separated by a 7075-T 0.190-inch-thick spacer sheet. The overall geometry of the panel was 8 x 32.5 inches and 6 x 20 inches in the test section. Three 1-inch-radii fillets were machined at the end of the test section. The panel grip ends were designed to accommodate the 50 kip machine grips and bolts with four 17/32-inch- and one 1.00-inch-diameter holes at each end. The panel grip ends and the grips were grit blasted for friction gripping in the grip area. All bolts were torqued to 110 in-lbs.

Instrumentation and Equipment

The flight-by-flight spectrum loading tests conducted on the panel assemblies consisted of four series of tests. These were room temperature, -65°F (-53.9°C), 180°F (82.2°C), and room temperature with prior exposure at 95 percent relative humidity and 180°F (82.2°C) for 60 days. Three fatigue tests were conducted per testing series. The following describes the instrumentation and equipment used for the series of tests.

Figure 5 shows a photograph of the 50 Kip INSTRON electrohydraulic system setup with gripping fixtures and load-control console equipment that was used in the fatigue and residual strength testing of the panels. In addition, this system consisted of the primary data taking equipment, which included a 486 PC computer, Labtech software, and signal conditioning equipment. This system was used to measure and monitor the output of the strain gages, Krak gages, and thermocouples. The output of the Krak gages was read by a FRACTOMAT instrument, consisting of two channels for readout. A strip chart recorder was used to continuously measure the spectrum loading applied to the panel assemblies in each test series.

The spectrum loading fatigue testing of the panels for test series 2 and 3 at -65 F(-53.9 C) and 180°F (82.2°C), respectively, required an environmental chamber around the test panel and the repaired area of the final assembled panel. Figure 5 also shows the environmental chamber and the antibuckling guides used in the fatigue testing. A Lexanl (polycarbonate) chamber was constructed and used for -65°F (-53.9°C) and 180°F (82.2°C) steady-state testing temperature environments. This chamber was designed to serve as an external out-of-plane buckling guide and used in all tests. The chamber was nominally 9 x 9 x 2 inches in volume and contained four longitudinal stiffeners, which were bonded to the Lexanl chamber walls. The stiffeners acted as buckling guides, and Teflon pads were bonded to the bottom surface to ride against the aluminum. The stiffeners were grooved to allow for environmental media circulation. The chamber was sealed with insulation material. The experimental setup for the -65°F (-53.9°C) steady-state temperature testing used liquid nitrogen as the cooling media. The temperature in the environmental chamber was controlled within ± 5°F and monitored with two probe-type thermocouples. The type of probe thermocouple that was selected was the OMEGA Type K with an exposed junction and 304SS material [12]. The temperatures were applied at a rate of 20°F per minute until the steady-state temperature was reached. The experimental setup for the 180°F (82.2°C) steady-state temperature used hot air and was circulated using a hot air blower. The temperature control and applied rates were the same as for the -65°F (-53.9°C) testing.

The series 1, 2, and 3 were preconditioned according to ASTM D 618 Procedure which was 50 percent R.H. and 73.4°F (23.0°C) for 40 hours [13]. This was performed in an ambient laboratory room. A final series of panels, series 4, were environmentally preconditioned. The composite patches which were bonded to aluminum sheets were preconditioned at 95 percent R.H. and 180°F for 60 days in an environmental preconditioning chamber. The environment was circulating hot and humid air and was monitored and controlled using thermocouples for the dry and wet bulb temperatures. The temperatures were read with a digital readout instrument.

Each of the fatigue panels in the test series was instrumented with Krak gages, strain-gage rosettes, and thermocouples as shown in Figure 4. The criteria in the selection of all of the types of instrumentation were based on the post testing environments of the spectrum loading fatigue combined with the applied steady-state environments of -65°F (-53.9°C) and 180°F (82.2°C).

Type KG-B30 with 30 mm or 1.18-inch effective crack length measurement range was selected for use with an initial edge notch of 0.30 inch or 7.62 mm. [14]. This Krak gage is a foil made of constantan alloy (5 micron or 0.0002-inch thickness) with an epoxy-phenolic glass-fiber-reinforced backing (50 microns or 0.002-inch thickness). The gages were mounted with the crack gage backing exactly flush with the longitudinal edge of the aluminum sheet. The apex of the V-groove of the gage was coincident with the tip of the machined notch. The gages were adhesively bonded to the aluminum surface using TTI 353-ND single-part epoxy adhesive. The procedures of reference 18 were followed. Figure 4 shows the edge view of the mounted Krak gages. The installation of the gages was performed in the laboratory under ambient conditions.

Strain-gage rosettes were used to measure the strain levels in the B/E_p patches and the aluminum sheets. The strain gage data taken from these rosettes was used in monitoring the load transfer behavior from the cracked skin of the aluminum to the B/E_p repair patch. This data was

used as a measure of the effectiveness of the patch in retarding or stopping fatigue crack growth. Figure 4 shows the locations of the strain gage rosettes on the B/E_p patches and the aluminum sheets.

The type of strain-gage rosette selected for the B/E_p composite patches was based on (a) thermally activated coefficient of thermal-expansion compatibility of the gage with the substrate, (b) the post-temperature steady-state temperature environments of -65°F (-53.9°C) to 180°F (82.2°C), and (c) the spectrum loading cyclic fatigue life requirement. Micromeasurements WK-06-062RB-350 (unstacked/uniplanar) 45-degree delta strain-gage rosette and bonded with M Bond 610 adhesive satisfied these criteria. All strain gages were self-temperature-compensating gages and were mounted according to the recommended guidelines of strain-gage applications to composites [15 and 16].

Each of the aluminum skins of the repaired panels was precracked under constant amplitude tension-tension loading with P_{max} = 22.5 kips (S_{max} = 15.0 ksi), P_{min} = 0.0 kips (S_{min} = 0.0 ksi), and R = 0.0. The cyclic frequency of the loading was 5 Hz. The constant amplitude fatigue loading was applied until the cracks were detected by each of the Krak gages of the panel. The results showed that all of the skin panels were precracked in 1260 to 1272 cycles.

The spectrum loading block was made up of Missions A, B, C, D, E, and F for blocks 1 and 2 and the repeat mix as shown in Table 2 test spectrum. Additional missions as defined for the 10th application of a given mission were incorporated into the building blocks of the total spectrum. The total application of the spectrum simulated 2340 missions of taxi, take-off, gust, maneuver, and ground-air-ground cycles. The loading frequency was 5 Hz. The total cyclic content of the spectrum consisted of 65,932 cycles.

Data Reduction and Analysis

The data taken included Krak gage output, strain gage rosette output, temperature and humidity, fatigue-crack-growth behavior, and residual strength. Various computer algorithms were used for data analysis. The outputs of the Krak gages, strain-gage rosettes, and thermocouples were analog, and continuous recordings were taken with the computer and data-storage software. Data plots of the Krak gages and thermocouples were generated every 10 seconds and correlated with applied cycles. The output of the load cells for applied loadings were continuously recorded on a strip chart recorder to show the cyclic loading as applied to each specimen. The fatigue-crack-growth behavior is presented as crack length, a, versus cycles. The strain-gage data was taken as continuous recordings of each of the legs of the strain gage rosettes. All data were stored for analysis. The axial/longitudinal strains of each rosette were used to monitor the behavior of the panel assembly during spectrum loading fatigue crack growth testing. The strain gage data plots were generated by sampling the output every 2 seconds at 50 Hz every 10 minutes. Further reduction of the strain gage data involved determining the transverse sensitivity of the strains in the composite patches and calculation of the maximum and minimum principal strains and stresses and the maximum shear strains and stresses.

Fatigue Results and Discussion

Room Temperature Results—Series 1: The spectrum loading fatigue crack growth results of one of the panel assemblies tested at room temperature and laboratory humidity is shown in Figure 6. The fatigue cracks in all of these skins (panels) of the panel assemblies were contained under the repair patches. That is, the total fatigue loading spectrum was applied without these panels failing during fatigue cycling (see Table 3). In addition, these results showed that the fatigue crack growth rate of the cracks in these panels were slow and almost constant. This indicated that the ultrasonically bonded composite patches were effective in slowing down the fatigue crack growth rate. Load transfer from the cracked skin into the composite patches was also effective as shown in the axial or longitudinal strain gage data and the reduced maximum principal stresses and maximum shear stresses. The axial strains, reduced maximum principal stresses, and maximum shear stresses in the patches show that some patches on one side of the panel assemblies were loaded higher than others (see Figures 7 and 8). In addition, the results showed that as the fatigue cracks propagated the strain and stress levels in the patches increased. This was the expected behavior since at longer crack lengths more load is transferred from the cracked skins into the patches.

180°F Steady-State Temperature Results—Series 2: The fatigue crack growth results for one of the panel assemblies tested at a steady-state temperature of 180°F (82.2°C) and laboratory humidity is shown in Figure 9. All of these panel assemblies failed during the spectrum loading fatigue cycling. Table 3 shows the summary of the fatigue results and the longest fatigue life was series panel 3-2B which survived the entire application of the spectrum, but the cracks in the skin sheets were 1.15 and 5.40 inches, respectively. The fatigue crack growth rates of the cracks in the skins of these panels showed that the rates were steadily increasing with applied cycles. At this high applied steady-state temperature of 180°F, ultrasonically bonded repair patches were effective in picking up load transferred from the cracked skins. The axial strains, the reduced maximum principal stresses, and maximum shear stresses in the patches show that some of the patches on one side of the panel assemblies were loaded higher than others.

-65°F Steady-State Temperature Results—Series 3: The spectrum loading fatigue crack growth results of one of the panel assemblies tested at -65°F and laboratory humidity is shown in Figure 10. The fatigue cracks in the skins of these panel assemblies showed a steadily increasing fatigue crack growth rate with the exception of skin sheet no. 31 which did not show much growth. The spectrum loading cyclic fatigue lives of these panel assemblies are also summarized in Table 3 and show much lower fatigue lives than the panel assemblies tested at room temperature or 180°F. The general trend of the effects of lower temperatures on structural adhesives is that the adhesive becomes more brittle at the reduced temperature of -65 F. Likewise at elevated temperatures the adhesive becomes more ductile. In both temperature cases, the ability of the composite patches to pick up load transferred from the cracked skins will be different due to the temperature effects on shear strength of the adhesive.

Prior Exposure and Room Temperature Results—Series 4: The spectrum loading fatigue crack growth results of one of the panel assemblies that were exposed for 60 days at 180°F and 95 percent RH and then room temperature tested is shown in Figure 11. The fatigue cracks in all of these skins (panels) showed a steadily increasing rate of crack growth. The fatigue cracks in skins 4,

9, and 10 were contained more than the others. The results of these panel tests summarized in Table 3 show that the spectrum loading fatigue lives were about the same as the -65°F fatigue lives, but not nearly as long as the 180°F fatigue lives. The 60-day exposure of the panels to the high temperature and humidity produced some degradation of the ultrasonically bonded patches. The mechanism is believed to be moisture diffusion into the bond lines between the patches and the aluminum skins. Degradation of the patches also occurred, since the color on some of the patches changed from black to light brown during exposure.

CONCLUSIONS

Based on the results of this experimental investigation, the following conclusions are made:

(1) It has been successfully demonstrated that ultrasonic energy can be used to cure FM-73 structural adhesive to bond a B/E_p patch to 7075-T and T651 aluminum. The bonding time is about an hour to achieve optimum cure of the adhesive.

(2) The ultrasonic intensity (i.e., energy per unit time per unit area) required to fully cure FM-73 in one hour is only 25 watts/square inch, and the bond strength is comparable to and often better than thermally cured specimens.

(3) At room temperature, none of the test panels with pre-cracks failed when subjected to ground-air-ground flight spectrum loading simulating 2340 missions. At extreme conditions of temperature (-65°F and 180°F) and humidity (95 percent RH), the adhesive appears to be adversely affected and some of the test panels failed before completing 2340 missions.

(4) Other structural adhesive systems under slightly different ultrasonic cure conditions may have the potential to be an effective adhesive for extreme conditions.

ACKNOWLEDGEMENTS

The authors would like to acknowledge Mr. Leonard Wright and his staff at The Boeing Company, Defense and Space Group, Wichita, Kansas, and Mr. Al Clark of Oklahoma Air Logistics Center, Tinker Air Force Base, Oklahoma, for supporting this project.

REFERENCES

1. Rice, R., Smith, S., Rahman, S., Broek, D., et al, "Effects of Repair on Structural Integrity", Final Report to FAA Tech Center, DOT/FAA/AM-DOT-VNTSC-FAA-93-11, July 1993.

2. Baker, A.A., and Jones, R., (Editors), Bonded Repair of Aircraft Structures, Martinus Nijhoff Publishers, 1988.

3. Jones, R., Molent, L., Baker, A.A., and Davis, M.J., Bonded Repair of Metallic Components: Thick Sections", Aeronautical Research Laboratories (ARL), Melbourne, Australia, Elsevier Science Publishers, 1988.

4. Sandow, F.A., and Cannon, R.K., "Composite Repair of Cracked Aluminum Alloy Aircraft Structure", Report Number AFWAL-TR-87-3072, AFWAL/FIB, 1987.

5. Kelly, L.G., "Composite Repair of Cracked Aluminum Structure", U. S. Air Force/Wright Aeronautical Laboratories, AGARD Conference, 1986.

6. Lincoln, J.D., 1987 ASIP/ENSIP Proceedings, AFWAL-TR88-4128, Cochran, J.B., (Lockheed/Georgia), Christian, T., and Hammond, D.O., "C-141 Repair of Metal Structures by Use of Composites", 1988.

7. U. S. Air Force Logistics Command, "Composite Patches for Metallic Structures", TT-89034, August 1989.

8. Baker, A.A., "Fibre Composite Repair of Cracked Metallic Aircraft Components -- Practical and Basic Aspects", Aeronautical Research Laboratories; Butterworth & Company, Composites, Volume 18, No. 4, 1987.

9. Caruso, R.P., "Boron/Epoxy Composites for Aircraft Structural Repair", Textron Specialty Materials Report, 1991.

10. Senapati, N., Smith, S.H., and Moulder, R., "Ultrasonic Technique for Repair of Aircraft Structures with Bonded Composite Patches - Phase I - Proof of Concept", Final Report to Boeing Defense and Space Group, October 1993.

11. ASTM Standard D3164, Determining Strength of Adhesively Bonded Plastic Lap-Shear Sandwich Joints in Shear by Tension Loading, 1993.

12. "OMEGA Complete Temperature Measurement Handbook and Encyclopedia," Volume 26, 1988.

13. ASTM D-618, "Method for Conditioning Plastics and Electrical Insulating Materials for Testing," ASTM Vol.8.01, 1993.

14. Instruction Manual, "Fractomat and Krak-Gage," Technical Bulletin KG-581 R, TTI Division, Hartrun Corporation, Chaska, Minnesota, 1982.

16. General Structural Testing of Composites, Applications Note, "Strain Gage Applications on Composites," Measurements Group, Inc., January 1988.

17. "Manual on Experimental Methods for Mechanical Testing of Composites," Edited by R. L. Pendelton and M. E. Tuttle, Society for Experimental Mechanics Inc., 1989

Table 1. The Lap Shear Strength of Ultrasonically Cured Specimens with 0.25-Inch-Thick 7075-T651 Aluminum Substrate

Cure Condition			Shear Strength
Power, watts	Time, minutes	B/E, plies	psi
75	60	5	257
85	60	5	1,304
95	60	5	1,275
85	60	15	808
95	60	15	1,168
105	60	15	1,439

Table 2. Flight-by-Flight and Mission Mix Spectrum

MISSION A

f_{MAX} (KSI)	f_{MIN} (KSI)	CYCLES
22.55	19.05	23
12.078	-17.83	1
12.078	9.58	4

1/10 FLTS f_{MAX} = 22.99

MISSION B

f_{MAX} (KSI)	f_{MIN} (KSI)	CYCLES
22.55	19.05	23
17.88	-17.86	1
17.88	13.38	9

1/10 FLTS f_{MAX} = 22.99

MISSION C

f_{MAX} (KSI)	f_{MIN} (KSI)	CYCLES
18.90	16.47	9
9.15	-15.25	1
9.15	6.65	1

1/10 FLTS f_{MAX} = 19.29

MISSION D

f_{MAX} (KSI)	f_{MIN} (KSI)	CYCLES
18.97	16.47	10
9.15	-11.47	1
9.15	6.65	1

1/10 FLTS f_{MAX} = 19.29

MISSION E

f_{MAX} (KSI)	f_{MIN} (KSI)	CYCLES
22.55	19.05	23
10.14	-18.59	1
10.14	7.64	1

1/10 FLTS f_{MAX} = 22.99

MISSION F*

f_{MAX} (KSI)	f_{MIN} (KSI)	CYCLES
23.80	14.30	50

TEST MISSION MIX

BLOCK 1 = ABCABDEFABCAB
BLOCK 2 = BEFBECBEFBECA

REPEAT MIX = 5(BLOCK 1) + (BLOCK 2)

NOTE: SPECTRA FOR B-52G/H WING UPPER SURFACE AT W.S. 402, S-21
MISSION MIX FOR B-52G/H BASELINE II
AIR CREW CONTINUATION TRAINING USAGE

Table 3. Summary of Fatigue Life Results for All Panel Assemblies Tested

Panel Assembly Test Series	Testing Environment	Total Applied Fatigue Cycles of Spectrum	Comments
3-1A	Room temperature	65,932	Did not fail
3-1B	Room temperature	63,373	Did not fail
3-1C	Room temperature	65,932	Did not fail
3-2A	180°F	40,937	Failure
3-2B	180°F	65,931	Failure
3-2C	180°F	47,778	Failure
3-3A	-65°F	17,463	Failure
3-3B	-65°F	20,747	Failure
3-3C	-65°F	24,024	Failure
3-4A	Room temperature	19,231	Failure
3-4B	following exposure at	25,563	Failure
3-4C	180°F and 96% RH	20,313	Failure

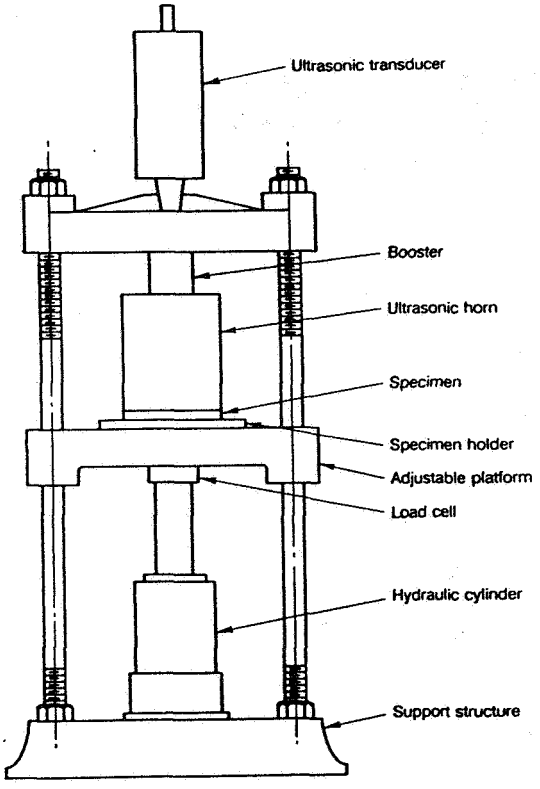

Figure 1. Schematic experimental setup for ultrasonic activation of adhesives.

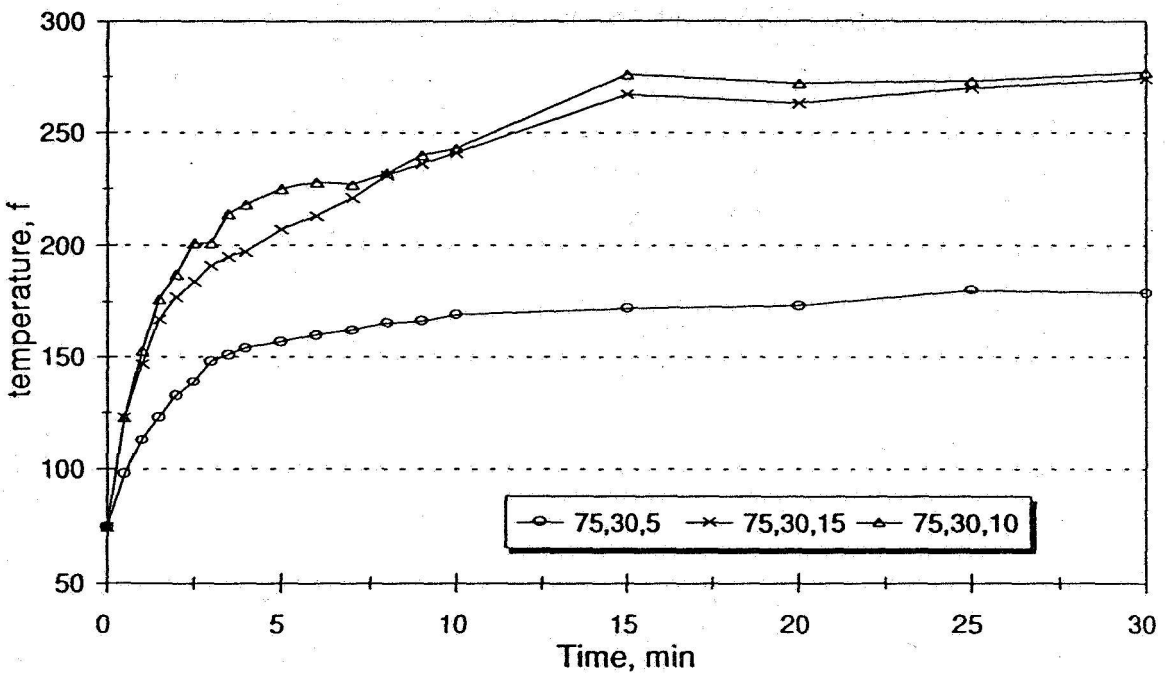

Figure 2. Plot of temperature versus time for three variable combinations.

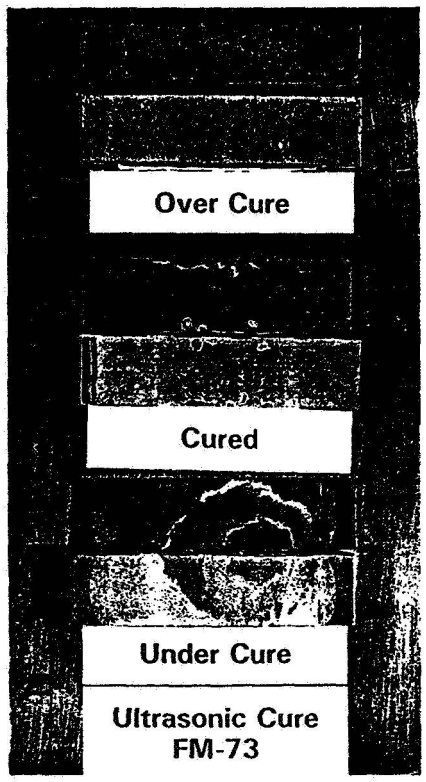

Figure 3. Baseline specimens for degree of cure evaluation.

Some original figures were unavailable at publication.)

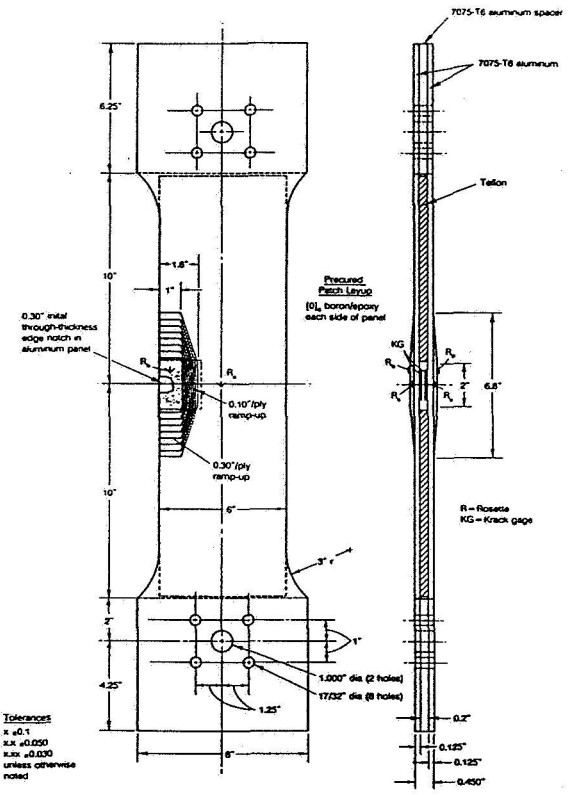

Figure 4. Simulated repair specimen with edge crack - instrumentation. (R = Rosette, KG = KRAK-GAGE).

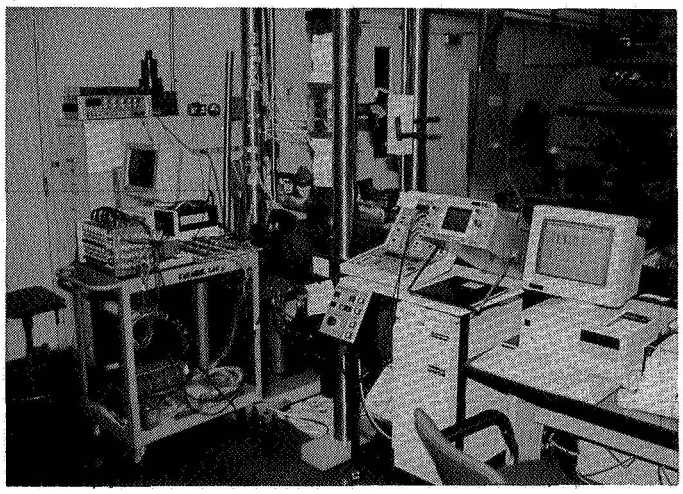

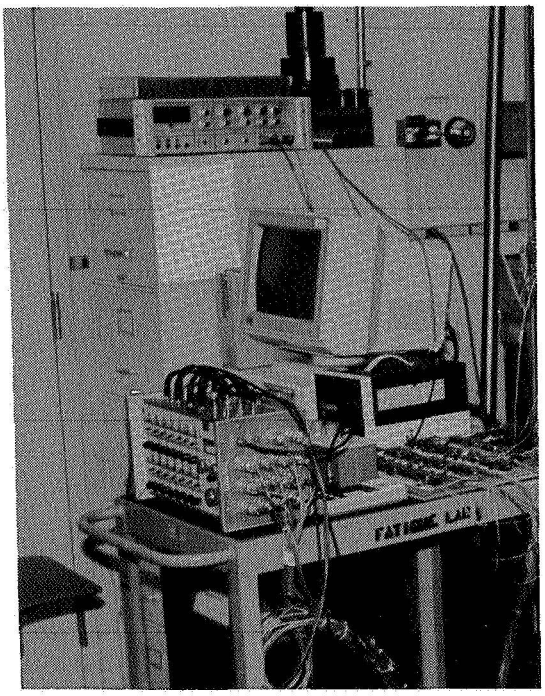

(a) Testing setup and instrumentation.

(b) Strain and Krak gage instrumentation.

Figure 5. Instron 50 Kip electrohydraulic testing machine for fatigue and residual strength testing of repaired panels.

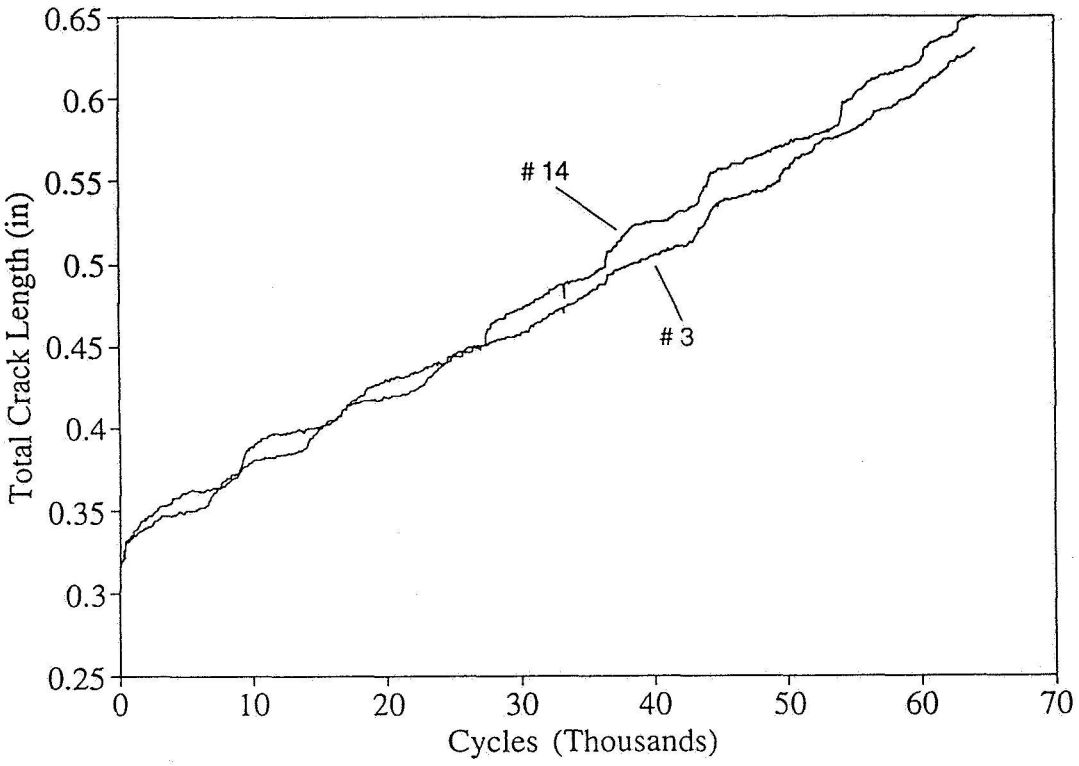

Figure 6. Spectrum loading fatigue crack growth results for skins (panels) 3 and 14, panel assembly 3-1A, room temperature.

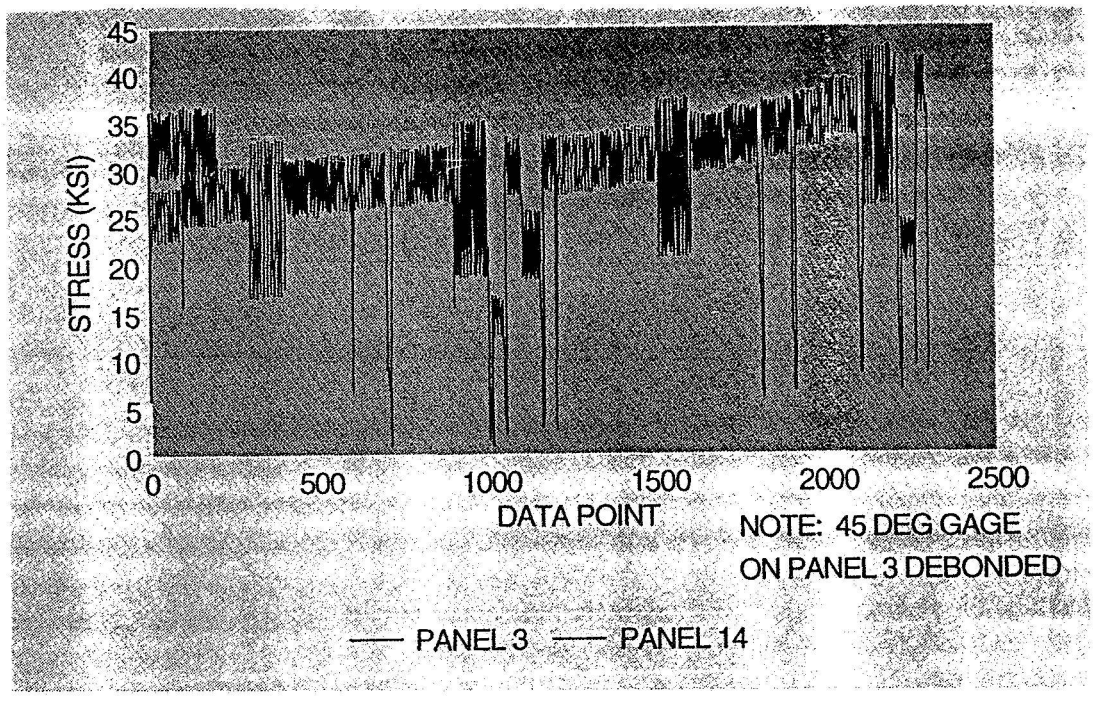

Figure 7. Maximum principal stresses in aluminum skins (panels) 3 and 14, panel assembly 3-1A, room temperature.

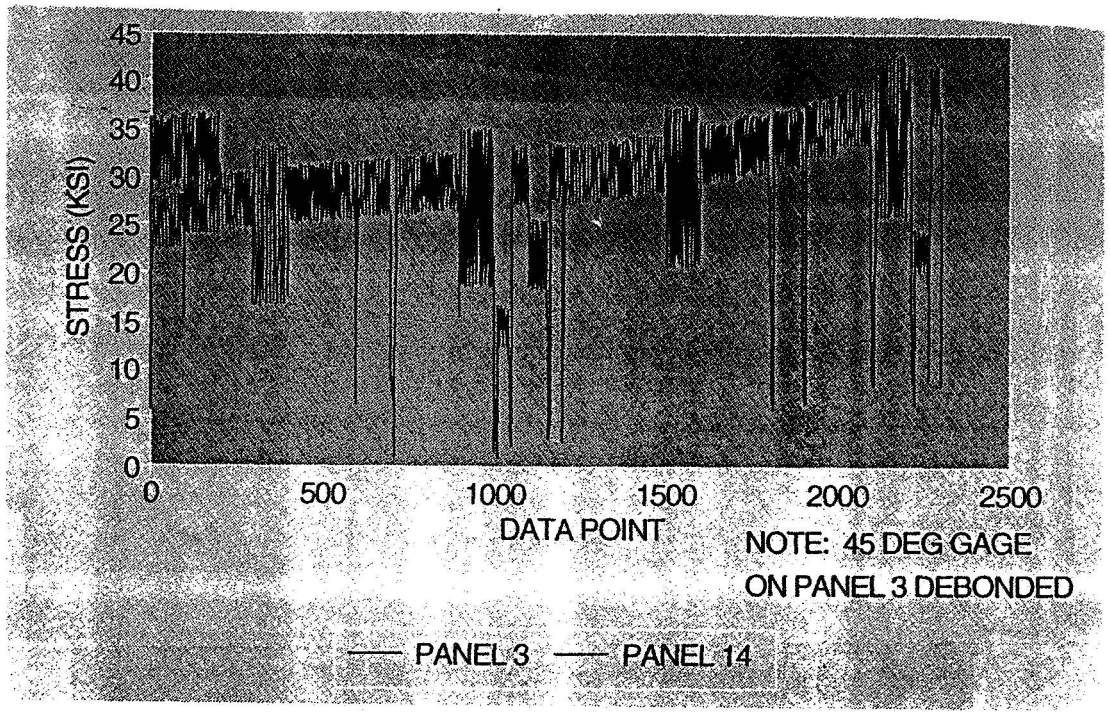

Figure 8. Maximum principal stresses in boron/epoxy patches on skins (panels) 3 and 14, panel assembly 3-1A, room temperature.

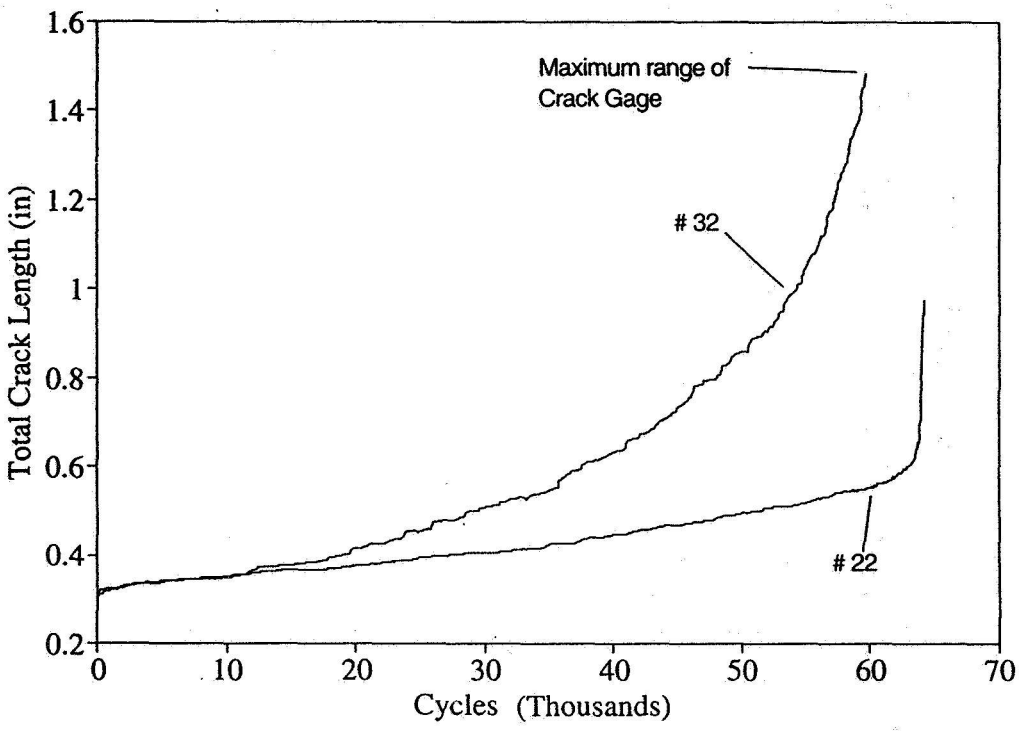

Figure 9. Spectrum loading fatigue crack growth results for skins (panels) 22 and 32, panel assembly 3-2B, 180°F temperature.

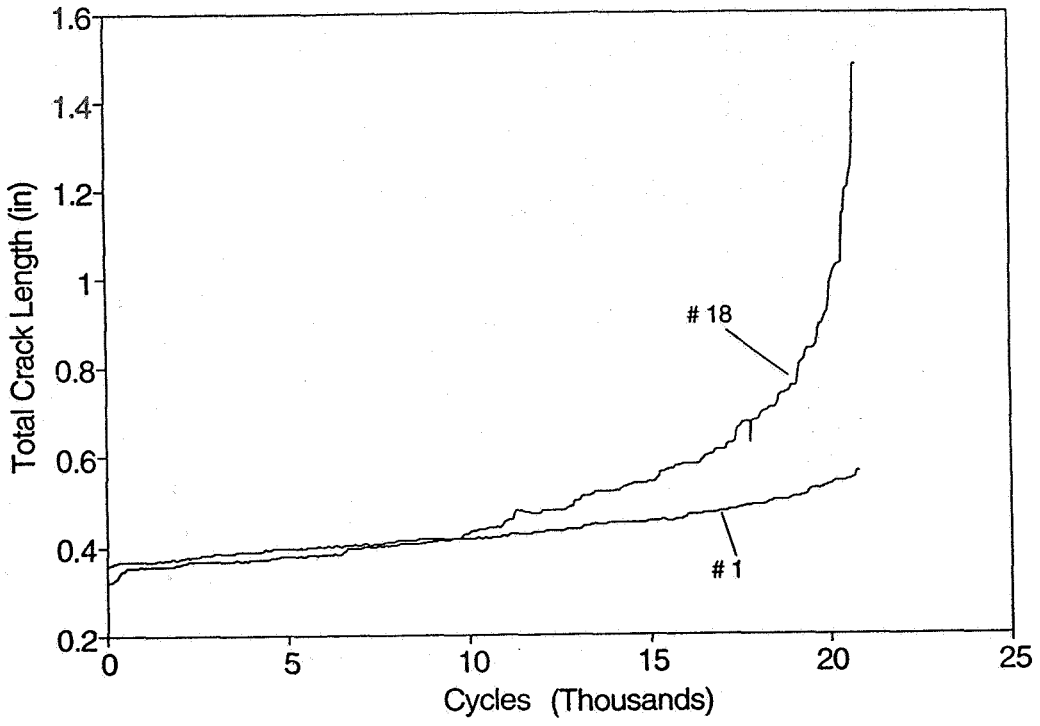

Figure 10. Spectrum loading fatigue crack growth results for skins (panels) 1 and 18, panel assembly 3-3B, -65°F temperature.

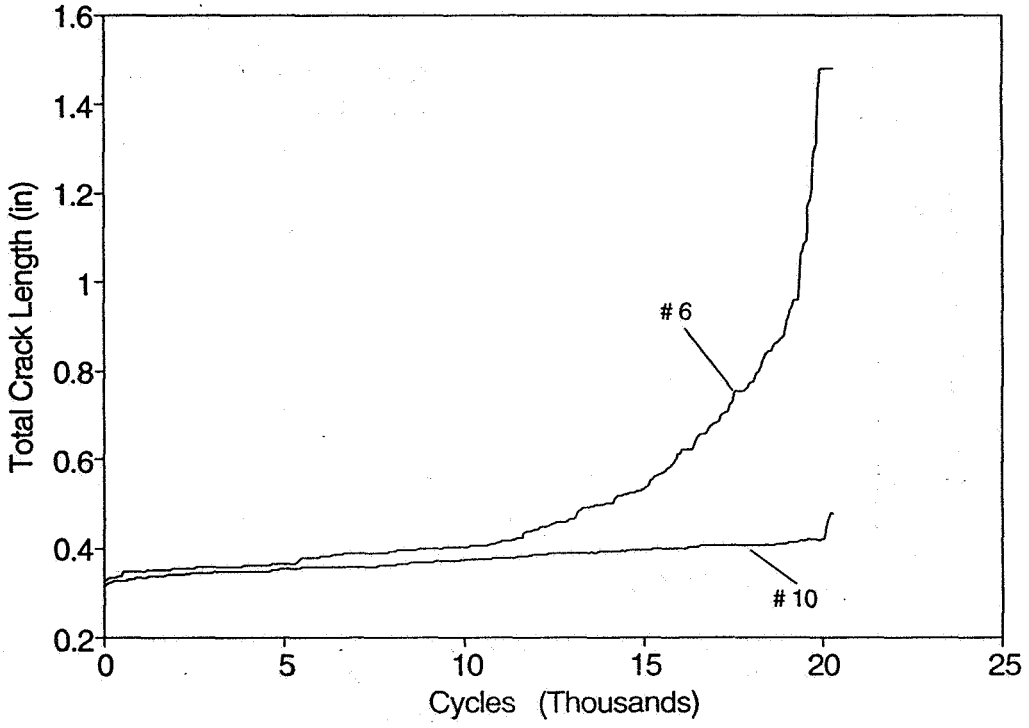

Figure 11. Spectrum loading fatigue crack growth results for skins (panels) 6 and 10, panel assembly 3-4C, prior exposure and room temperature.

Near Tip Stress and Strain Fields for Short Elastic Cracks

by

A.H. Soediono*, G.A. Kardomateas** and R.L. Carlson***

Abstract

Recent experimental fatigue crack growth studies have concluded an apparent anomalous behavior of short cracks. To investigate the reasons for this unexpected behavior, the present paper focuses on identifying the crack length circumstances under which the requirements for a single parameter (K_I or ΔK_I if cyclic loading is considered) characterization are violated. Furthermore, an additional quantity, the T stress, as introduced by Rice, and the related biaxiality ratio, B, are calculated for several crack lengths and two configurations, the single-edge-cracked and the centrally-cracked specimen. It is postulated that a two-parameter characterization by K and T (or B) is needed for the adequate description of the stress and strain field around a short crack. To further verify the validity of this postulate, the influence of the third term of the Williams series on the stress, strain and displacement fields around the crack tip and in particular on the B parameter is also examined. It is found that the biaxiality ratio would be more negative if the third term effects are included in both geometries. The study is conducted using the finite element method with linearly elastic material and isoparametric elements and axial (mode I) loading. Moreover, it is clearly shown that it is not proper to postulate the crack size limits for "short crack" behavior as a normalized ratio with the specimen width, a/w; it should instead be stated as an absolute, or normalized with respect to a small characteristic dimension such as the grain size. Finally, implications regarding the prediction of cyclic (fatigue) growth of short cracks are discussed.

Introduction

The short fatigue crack problem consists essentially of defining an alternative formulation that accounts for the observation that small cracks can propagate at rates different from the corresponding ones for long cracks at the same nominal stress intensity factors. In general, short cracks under cyclic load are observed to grow at stress intensities below threshold; some extend with decaying growth rate until arrest, while others propagate

* Research Engineer, Agency for The Assessment and Application of Technology, Indonesia.

** Associate Professor, School of Aerospace Engineering, Georgia Tech.

*** Professor Emeritus, School of Aerospace Engineering, Georgia Tech.

quite rapidly to merge with long crack behavior as shown in Figure 1. A resolution of the problem therefore has practical significance. First, it could enhance the present damage tolerance procedures. Furthermore, as overall life is mostly taken up by short crack growth, predicting the accelerated and sub-threshold extension of small flaws can lead to alternative, more accurate methods for assessing fatigue life.

Linear Elastic Fracture Mechanics (LEFM) theory is applied when the radius of the plastic zone is small compared to the critical dimensions of the body, as codified in both British and American Standards. If σ_Y is the yield stress, a is the crack length, w is the width, $w-a$ is the ligament and t is the thickness, these standards require:

$$w\ ,\quad w-a,\quad t\ \geq 2.5\left(\frac{K}{\sigma_Y}\right)^2\ , \tag{1}$$

where K is the stress intensity factor.

To describe the basis for the above premise, let r, θ be polar coordinates centered at the tip of a crack in a body under plane strain deformation. The small strain linear elastic solution results in stresses of the form

$$\sigma_{ij} = Kr^{-1/2}f_{ij}(\theta) + \text{non} - \text{singular terms} \tag{2}$$

near the crack tip, where the set of functions f_{ij} is normalized so that the singular part of the stress acting ahead of the tip, normal to the plane of the crack, is $K(2\pi r)^{-1/2}$. The small scale yielding approximation then incorporates the notion that, even though Equation (2) is inaccurate within and near a small crack tip yield zone, its dominant singular term should still govern the deformation state within that zone. Hence, the actual elastic-plastic problem is replaced by a problem formulated in boundary layer style. As is often said, the small yield zone is "surrounded" by the dominant elastic singularity, and the applied loadings and geometric dimensions and shape of the body influence conditions within the plastic region only insofar as they enter the formula for K, as computed elastically.

A consequence of this formulation is that the plastic zone dimension, r_p and the crack

tip opening displacement δ_t, are given by formulae of the type

$$r_p = \alpha K^2/\sigma_0^2 \ , \quad \delta_t = \beta K^2/E\sigma_0 \ , \tag{3}$$

where E is the elastic tensile modulus, σ_0 is the yield strength, and α, β are dimensionless factors which may, for example, depend on Poisson's ratio, strain-hardening exponent, etc., but are independent of the applied load and specimen geometry.

The plastic zone size from Equation (3) establishes a geometric dimension indicating the region over which deviations from elastic behavior occur. Rice [1] was the first to recognize that, since the crack length is a characteristic geometric dimension associated with the elastic stress field, a correction to Equation (3) is required when the length predicted by Equation (3) is comparable to or greater than the crack length, i.e. the stress intensity factor may no longer be expected to control the plasticity.

When the size of the plastic zone becomes large compared to the crack length, which is one of the characteristic dimensions, the requirements of LEFM may be invalidated. A similar question obviously exists for J-dominance. In other words, there are conditions under which a single parameter characterization of the crack tip field cannot be claimed. Indeed, it is known that for full plasticity the asymptotic plastic field is not unique but is instead a function of the geometry, loading mode and strain hardening rate and single-parameter characterization models cannot account for the differences in propagation rates from fully plastic crack growth tests (Kardomateas and McClintock,,[2]).

To further examine this notion, consider keeping the 'non-singular' terms of Equation (2). Recently, Carlson and Saxena [3] have calculated the stresses due to the second term. In another work, using the analyses of Williams [4], Rice [5] defined the T-stress from the second term of the expansion of Equation (2) as follows:

$$\begin{bmatrix} \sigma_{xx} & \tau_{xy} \\ \tau_{yx} & \sigma_{yy} \end{bmatrix} = \frac{K}{\sqrt{r}} \begin{bmatrix} f_{xx}(\theta) & f_{xy}(\theta) \\ f_{yx}(\theta) & f_{yy}(\theta) \end{bmatrix} + \begin{bmatrix} T & 0 \\ 0 & 0 \end{bmatrix} + \begin{matrix} \text{terms which vanish} \\ \text{at crack tip} \end{matrix} \tag{4}$$

Here (x, y) is the plane of straining and the crack coincides with the $x-$ axis, so it is seen

that the portion of the non-singular stress field which does not vanish at the tip amounts to a uniform stress $\sigma_{xx} = T$ acting parallel to the crack plane.

The above representation raises the issue of a two-parameter boundary layer formulation for short cracks, in which Equation (2) is replaced by the requirement of an asymptotic approach to the field given by the two leading terms of Equation (4).

In the same context, Leevers and Radon [6] introduced a biaxiality parameter B that relates the magnitude of the T-stress:

$$B = \frac{T\sqrt{\pi a}}{K} \,. \tag{5}$$

In terms of B, the displacement field can be written in the form:

$$u_{xx} = \frac{K}{E}(1+\nu)\sqrt{\frac{r}{2\pi}} f_{xx}(\theta) + (1-\nu^2)\frac{B}{E\sqrt{\pi a}} Kr\cos\theta \,, \tag{6a}$$

$$u_{yy} = \frac{K}{E}(1+\nu)\sqrt{\frac{r}{2\pi}} f_{yy}(\theta) - \nu(1+\nu)\frac{B}{E\sqrt{\pi a}} Kr\sin\theta \,. \tag{6b}$$

The biaxiality parameter B must be calculated for each particular specimen geometries to correlate the full field solutions with the two term representations. The displacements given above or the stress field expressions (4) can serve in that purpose. Concerning the displacements, it should be noted that on the crack flanks $\phi = \pi$, the angular functions $f_i(\phi)$ are zero, allowing the biaxiality parameter to be calculated by direct inspection of the asymptotic displacements given by Equation (6) and stress fields given by Equation (4). Such methods have already been used by Betegon and Hancock [7].

The above discussion summarizes the work-to-date on extending the applicability of LEFM to include cases that necessitate the inclusion of correction terms such as the present case of short cracks.

Elastic-plastic fracture mechanics, on the other hand, is based on the HRR singularity, named after Hutchinson[8], Rice and Rosengren [9], which describes the asymptotic stress and strain fields in terms of the strain hardening exponent n within the plastic zone under

small-scale yielding conditions as follows:

$$\sigma_{ij} = Y\left[\frac{J}{\epsilon_0 Y \alpha I_n r}\right]^{1/(n+1)} \tilde{\sigma}_{ij}(\phi, n) \ , \tag{7a}$$

$$\epsilon_{ij} = \frac{Ya}{E}\left[\frac{J}{\epsilon_0 Y \alpha I_n r}\right]^{n/(n+1)} \tilde{\epsilon}_{ij}(\phi, n) \ , \tag{7b}$$

where $\tilde{\sigma}_{ij}(\phi, n)$ and $\tilde{\epsilon}_{ij}(\phi, n)$ and I_n are tabulated functions. In this context the stresses and strains are uniquely characterized by the J quantity. Elastic-plastic asymptotic crack tip fields, being single parameter characterizations, would naturally have to be investigated regarding their extent of validity in the same context as the LEFM, i.e. the question of J-dominance or, in other words, that of a single parameter characterization of crack tip fields for short cracks.

Achieving crack growth prediction capabilities for short cracks can lead to formulations for predicting fatigue crack growth. Indeed, fatigue, crack nucleation and growth pass through distinct regimes which can be characterized by crack length. The relation of the fatigue failure loading boundary to crack length can be very nicely illustrated by use of the Kitagawa diagram [10] shown in Figure 1. In the plot of stress range versus crack length, the boundary is divided into three regimes which are depicted as two straight lines in regimes I and III and a curve in regime II. Stress range values below the boundary correspond to cases in which cracks are arrested. Above the boundary, crack growth occurs.

The ordinate value of the boundary in regime I corresponds to the endurance limit. The line in regime III represents the value of stress range, $\Delta\sigma$, corresponding to the threshold value of the stress intensity range, $\Delta\sigma$, in the relation

$$\Delta K = Y\Delta\sigma\sqrt{\pi a} \ . \tag{8}$$

Y is constant for the given crack configuation and a is the crack length.

If the dashed lines were extended and used as the boundary in regime II, predictions would be nonconservative because cracks are observed to grow below these lines. The

boundary in regime II is, therefore, represented by the solid curve connecting the two straight lines. Short crack behavior is characterized in Figure 1 in regime II; hence the primary emphasis here will be on regime II.

The main objective of this work is to (a) determine the crack lengths at which the K singularity cannot predict the asymptotic behavior, (b) determine the T or B parameter for these short cracks and (c) examine the influence of the third term of the asymptotic expansion of the stress field on the calculated B values. The Center-Cracked (CC) and Single Edge-Cracked (SEC) specimens are used for this purpose. They are subjected to monotonic tension stress. The finite element program, MSC/Nastran, is used for this computation.

Formulation of Non-Singular Parameters

Prediction methodologies in fracture mechanics are mainly based on the proper characterization of the crack-tip stress and strain field. Expanding the stress field in cylindrical coordinates (r, θ) about the crack tip, following the work of Williams [4],

$$\sigma_{ij} = \frac{A_1}{\sqrt{r}} f_{ij}^1(\theta) + A_2 f_{ij}^2 + A_3 \sqrt{r} f_{ij}^3 + \dots \ , \tag{9}$$

gives the first term singular at the crack tip and the remaining terms being finite and bounded. In classical linear elastic fracture mechanics, the characterization is centered around the stress intensity factor K, i.e. the first term. Elastic fracture mechanics is thus based on the premise that fracture processes which occur close to the crack tip are only determined by the first term in the expansion, allowing the asymptotic elastic stress field of a symmetrically loaded mode I crack to be expressed in the form

$$\sigma_{ij} = \frac{K_I}{\sqrt{2\pi r}} f_{ij}(\theta) \ . \tag{10}$$

Proposals have been made to provide a correction to plastic zone size estimates by extending elastic solutions to include non-singular terms of the Williams series [4]. In Equations (4), Rice [5] defined the T stress for the second term of the series; this equation

raises the issue of a two parameter boundary layer formulation for short cracks in which stresses are determined by an asymptotic approach to the field given by the two leading terms of K and T.

In the same context, Leevers and Radon [6] introduced a biaxiality parameter B that relates the magnitude of the T stress as in Equation (5). In terms of B the stress and displacement field can be written in the form:

$$\sigma_{rr} = \frac{K_I}{\sqrt{2\pi r}}\left(\frac{5}{4}\cos\frac{\theta}{2} - \frac{1}{4}\cos\frac{3\theta}{2}\right) + \frac{K_I}{\sqrt{\pi a}}B\cos^2\theta\ , \tag{11a}$$

$$\sigma_{\theta\theta} = \frac{K_I}{\sqrt{2\pi r}}\left(\frac{3}{4}\cos\frac{\theta}{2} + \frac{1}{4}\cos\frac{3\theta}{2}\right) + \frac{K_I}{\sqrt{\pi a}}B\sin^2\theta\ , \tag{11b}$$

$$\sigma_{r\theta} = \frac{K_I}{\sqrt{2\pi r}}\left(\frac{1}{4}\sin\frac{\theta}{2} + \frac{1}{4}\sin\frac{3\theta}{2}\right) - \frac{K_I}{\sqrt{\pi a}}B\sin\theta\cos\theta\ , \tag{11c}$$

$$u_{rr} = \frac{K_I\sqrt{2\pi r}}{8\pi\mu}\left[(2\kappa-1)\cos\frac{\theta}{2} - \cos\frac{3\theta}{2}\right] - \frac{K_I(r-a)}{2\mu\sqrt{\pi a}}B(cos^2\theta - \nu)\ , \tag{12a}$$

$$u_{\theta\theta} = -\frac{K_I\sqrt{2\pi r}}{8\pi\mu}\left[-(2\kappa+1)\sin\frac{\theta}{2} + \sin\frac{3\theta}{2}\right] - \frac{K_I\ r}{2\mu\sqrt{\pi a}}B\left(\frac{1}{2}\sin 2\theta\right)\ , \tag{12b}$$

where μ is the shear modulus and $\kappa = 3 - 4\nu$ for plane strain and $\kappa = (3-\nu)/(1+\nu)$ for plane stress. Furthermore, a model for plane strain yielding by Rice [5] results in the following expressions for plastic zone size and crack opening displacement:

$$r_p = \frac{\pi}{18}\left(\frac{K_I}{\sqrt{3}\tau_Y}\right)^2\left[1 - \frac{4}{3}\sqrt{\frac{2}{3}}\left(\frac{T}{\sqrt{3}\tau_Y}\right) + \ldots\right]\ , \tag{13a}$$

$$\delta_t = \frac{16}{27}\sqrt{\frac{2}{3}}\frac{(1-\nu^2)K_I^2}{E(\sqrt{3}\tau_Y)}\left[1 - \frac{2}{3}\sqrt{\frac{2}{3}}\left(\frac{T}{\sqrt{3}\tau_Y}\right) + \ldots\right]\ , \tag{13b}$$

where τ_Y is the shear yield stress. The second terms inside the brackets represent the deviation from the small scale yielding approximation. Note that K and T are directly proportional to the applied loading.

The stress intensity factor, K, which was introduced in Equation (2), defines the magnitude of the local stresses near the crack tip. This factor depends on loading, crack

size, crack shape, and geometric boundaries. Closed-form solutions for K have been derived for a number of simple configurations. For more complex situations, the stress intensity factor can be estimated by experiment or numerical analysis. The Stress Intensity Factor solutions for a single edge-cracked (SEC) and a center-cracked (CC) configuration under mode I loading, which are the object of our investigation, are [11]:

$$K_{I_{SEC}} = \left[1.12 - 0.23a/w + 10.6(a/w)^2 - 21.7(a/w)^3 + 30.4(a/w)^4\right] \sigma_\infty \sqrt{\pi a} \ , \tag{14a}$$

and

$$K_{I_{CC}} = \left[\frac{1 - 0.5a/w + 0.326(a/w)^2}{\sqrt{1 - a/w}}\right] \sigma_\infty \sqrt{\pi a} \ , \tag{14b}$$

where w is the specimen width.

Numerical Analysis and Finite Element Models. Single-edge-cracked (SEC) and center-cracked (CC) bars with (a/w) ratios of 0.02 through 0.1, where a is the crack length or half crack length, respectively, and w the width of the specimen, were considered. Concerning the other geometric dimensions, the specimens had a thickness, t and height, h, characterized by the dimensionless parameters t/w= 0.08, and h/w= 2.0 for the CC specimen and 4.0 for the SEC specimen, respectively.

The models were meshed with eight-noded quadrilateral and six-noded triangular plane strain elements provided by the finite element code MSC-Nastran [12]. These 2-D finite element grids are indicated in Figure 2. The models were force loaded on the remote boundary by a uniform tensile stress in the y-direction . The crack tip was modeled by a focused mesh with initially coincident but independent crack tip nodes. Angular spacings of 15 degrees and minimum radial spacings of 0.05 mm for every sector were used. Linear elastic material with Young's modulus E = 72 GPa and Poisson's ratio, ν= 0.3 was assumed; the yield stress, σ_Y, is taken to be such that E/σ_Y= 176.0. The mesh configuration for each specimen consists of a total of 235 elements. Furthermore,

force balance studies were also conducted to check the applied and reaction forces on each specimen in order to ensure that the mesh is performing in a satisfactory manner.

Results and Discussion

In order to correlate with the results of Leever and Radon [6] we shall give both the ratio a/ρ and a/w in presenting the results. Denote by ρ the typical grain size, ρ= 0.05 mm. The stress fields ahead of the crack are shown in Figures 3 and 4 for a/ρ ratios of 10, 20, 50 and 200 (a/w= 0.02, 0.04, 0.1, 0.4, respectively) where they are compared with the theoretical LEFM field, calculated from Equation (10). The stresses are non-dimensionalized with the remote stress σ_∞, while the original distance, r of a point ahead of the crack is non-dimensionalized with the grain size ρ. It is seen that for these crack lengths the stresses are above the LEFM values, the discrepancy increasing with the smaller crack lengths. Beyond a/ρ= 50 (a/w = 0.1), the stresses begin to converge to the LEFM predictions. Notice that Leever and Radon [6] results were for a/w values above 0.2; therefore, the present work, among others, complements the latter one.

In order to elucidate the size issue, three center-cracked specimens which have the same a/w ratio of 0.02 but different absolute sizes have been examined; they consist of a short crack (a/ρ= 6) and long cracks (a/ρ= 60 and 300) in respectively smaller and larger specimens that preserve the ratios of crack length to other dimensions. From Figure 5 it is clearly seen that the stresses follow the LEFM prediction for the long cracks, but there is a distinct discrepancy for the short crack, i.e. the LEFM prediction is no longer valid. This example shows that a/w is not the proper quantity to express the size requirements for "short crack" behavior.

Let us require that the stress ahead the crack tip must be within 10% of the LEFM field at a chosen distance from the tip for LEFM dominance criteria. It can be seen that at a distance of $r/\rho = 2$ ahead the crack tip, Figures 3a,b show that the crack tip stress field $\sigma_{\theta\theta}$ for the center-cracked specimens differs significant from the results of Equation (10) for short crack lengths; but for a longer crack, the stresses from FEM and Equation

(10) have a tendency to match, as shown in these same Figures. A similar situation also occurs in the SEC specimens, but the distance ahead the crack tip is shorter ($r/\rho = 1.5$); they are presented in Figure 4.

The biaxiality parameter B (or alternatively, the T-stress) was calculated for each of the geometries studied. The simplest and most direct method of calculating the T-stress involves inspection of the stress or displacement fields associated with the crack. Leevers and Radon [6] have introduced a more refined method for calculating B for the center-cracked specimens; they essentially adjusted the centerline traction individually according to the deviation of the calculated displacement. In this work the stress field of Equation (4) was used to calculate B from σ_{xx}.

Figures 6a,b show that the center-cracked specimens consistently have higher negative B values than the single-edge-cracked ones. The implied compressive T stresses are induced by the constraint against in-plane bending on the centerline; they are responsible for the excellent directional stability of internal cracks [6]. By using a linear aprroximation, for values of crack length less than $0.1w$ or 50ρ, B can be expressed by:

$$B = -[1 + 0.082(a/w)] \ , \tag{15a}$$

or

$$B = -[1 + 1.65\ 10^{-4}(a/\rho)] \ . \tag{15b}$$

The finite-width effect does not drastically modify B values, which remain about -1 as $2a/w$ goes to zero. Equation (15a) is slightly different than the one in Reference [6] (where there was a factor of 0.085 instead of the 0.082 here). In Ref. 6 a linear approximation was used to determine B values for crack-lengths a/w greater than 0.2, but in this research we have considered crack-lengths less than 0.2 ($a/\rho < 100$).

B values for the single-edge-cracked specimens are quite different than those of the center-cracked specimens. By using a curve fitting of polynomial third order, the B values

for the SEC specimens can be expressed by:

$$B = -0.52 - 1.50(a/w) + 12.70(a/w)^2 - 20.70(a/w)^3 \ , \qquad (16a)$$

or in term of a/ρ, it also can be written as

$$B = -0.52 - 4.17\ 10^{-3}(a/\rho) + 8.91\ 10^{-5}(a/\rho)^2 - 6.25\ 10^{-7}(a/\rho)^3 \ . \qquad (16b)$$

Figure 6b shows that the B values for the single-edge-cracked case are almost one-half those of the center-cracked specimen (as the crack length goes to zero).

Figure 7 shows the sensitivity with respect to number of elements of the stress biaxiality ratio, B, for both specimens. It can be seen that B has a stable value when the number of elements is above 225. Also Reference [6] has indicated that small values of the height, h/w can have an influence on determining B; an example for the center-cracked specimen showed that B has the tendency to be constant for values of h/w= 1.2 to 2.0 for $2a/w$= 0.5.

Figure 8 shows that the crack tip displacement field in the θ-direction for the single-edge-cracked specimens does not fit with the displacement field given by the K-singularity at the distance between 0 and 20 grains size behind the crack tip when the crack is short, but for longer cracks the displacement field gradually fits. Similar situations also occur in the center-cracked specimens, as shown in Figure 9. This confirms again the breakdown of the LEFM singularity for short cracks.

The Effect of the Third Term. An evaluation of including the effect of the third term on the biaxiality ratio, B, can be conducted by examining the stress distribution, $\sigma_{\theta\theta}(r, 0)$ on the plane in front of the crack tip. Specifically, the Williams series can be written up to the third term:

$$\sigma_{\theta\theta}(r, 0) = \frac{K_I}{\sqrt{2\pi r}} + 3C_3 r^{1/2} \ , \qquad (17)$$

i.e. $\sigma_{\theta\theta}$ includes the third term, C_3, but not the second, (or B) term.

On the other hand, up to the third term,

$$\sigma_{rr}(r,0) = K_I \left(\frac{1}{\sqrt{2\pi r}} + \frac{B}{\sqrt{\pi a}} \right) + 3C_3 r^{1/2} \ , \tag{18}$$

i.e. σ_{rr} includes the second, (or B) term as well as the third (C_3) term.

Therefore, eq (17) can be used to calculate C_3 (from the finite element data on $\sigma_{\theta\theta}$) and then the calculated value of C_3 can be used in eq (18) to find the biaxiality ratio B with the third term effects now included.

Fig. 10 shows the effect of the third term on the biaxiality ratio for the center-cracked geometry and Fig. 11 for the single-edge-cracked geometry. It seems that the third term requires a larger correction to the biaxiality ratio for short crack length and has a relatively small effect for long crack length. The biaxiality ratio would be more negative (higher in absolute value) if the third term effects are included in both geometries. Fig. 12 shows the percentage increase, $\Delta B = (B_{incl} - B_{not\ incl})/B_{not\ incl}$, which is seen to increase rapidly as $a/\rho \rightarrow 0$ (for a typical short crack $a/\rho = 10$ in the center-cracked case this is moderate, about 15%). However, it should be noted that what constitutes a significant contribution of a neglected term to the fracture behavior may depend on factors other than the percentage error. For example, although the percentage error due to the third term may appear to be moderate for typical short crack sizes, the fatigue crack growth rate in the near threshold region is drastically affected by very small changes in the value of ΔK.

By using curve fittings from the results of Figs. 10 and 11, the stress biaxiality ratio equations with the third term effects included can be presented as

$$B = -[1 + 1.65\ 10^{-4}(a/\rho) + 0.49(a/\rho)^{-0.5}] \ , \tag{19a}$$

for CC specimens and

$$B = -0.72 - 1.85\ 10^{-3}(a/\rho) + 1.05\ 10^{-6}(a/\rho)^2 - 8.96\ 10^{-9}(a/\rho)^3 \ . \tag{19b}$$

for SEC specimens. These can be compared with the equations (15b) and (16b), respectively, where the third term effects are not included.

Implications for Short Fatigue Crack Growth. As has been already stated, an extended representation of fatigue crack growth behavior may be developed by considering the Kitagawa diagram (Fig. 1) for the case in which the minimum stress is zero. Then the stress range is equal to the maximum stress, and an upper bound boundary corresponding to the fracture toughness can be included as depicted by the upper, dashed curve. The map between the boundaries may, in turn, be divided into two regions corresponding to a linear elastic fracture mechanics [LEFM] response and a nonlinear inelastic fracture mechanics response [NIFM].

Short crack behavior is characterized in Figure 1 in regime II. Serious consideration of the behavior of short fatigue cracks began with results published in 1975 by Pearson [13]. It should, however, be noted that Rice [1] had predicted earlier that the stress intensity factor may no longer be expected to control the local field for crack lengths comparable to the plastic zone size.

The behavior observed has been described as "anomalous", because crack growth for short cracks was observed to occur at values of stress intensity factor range below the threshold value.

The results of this paper indicate that the anomalous designation may be inappropriate, and it may indeed be a consequence of the use of correlation procedures which are not valid. In fact, a clarification of short fatigue crack growth behavior appears to require that two mechanisms must be considered. The first one, which was considered in this paper, involves the fact that the requirement of small scale yielding for the use of stress intensity factor range as a correlation parameter is not satisfied for short cracks (i.e. LEFM is not valid). The other, which needs to be considered in the future, concerns the role of obstruction to closure upon unloading. For a given range of stress intensity factor, obstruction to closure is generally less for short cracks than for long cracks.

Although most attention has been directed toward consideration of these two mechanisms, a third potentially important mechanism should be mentioned. It has been found

that short fatigue cracks in steels subjected to chemically active environments grow faster than long cracks for the same ΔK [14,15]. Since corrosion fatigue failures are often observed in service, this behavior should not be ignored.

A review of the literature on the growth of short fatigue cracks indicates that the research studies that have been reported have usually been motivated by one of two distinct goals. The primary goal of material scientists has been to use the results of their studies to contribute to an understanding of the fundamental mechanisms of short crack growth. Mechanics specialists have been motivated primarily by the need to develop design codes. There is a need for more collaboration between researchers from these two groups. The paper by Blom, et al [16] examines both mechanics and metallurgical issues and it provides valuable insight into the interacting aspects of the short crack growth problem.

Acknowledgement

The authors acknowledge that the studies which led to the preparation of this paper were initiated during the support of the Warner Robins Air Logistics Center, Robins AFB under Contract No: F09603-85-G-3104-0034. They are also grateful for the interest and encouragement provided by Gary Chamberlain.

References

1. J.R. Rice, in *Fatigue Crack Propagation* ASTM STP 415 (1967) 247-309.
2. G.A. Kardomateas and F.A. McClintock, *International Journal of Fracture* 35 (1987) 103-124.
3. R.L. Carlson and A. Saxena, *International Journal of Fracture* 33 (1987) 37-39.
4. M.L. Williams, *Journal of Applied Mechanics* 24 (1957) 109-114.
5. J.R. Rice, *Journal of the Mechanics and Physics of Solids* 22 (1974) 17-26.
6. P.S. Leevers and J.C. Radon, *International Journal of Fracture* (1983) 311-324.
7. C. Betegon and J.W. Hancock, *Journal of Applied Mechanics* 58 (1991) 104-110.
8. J.W. Hutchinson, *Journal of the Mechanics and Physics of Solids* 16 (1968) 13-31.

9. J.R. Rice and G.F. Rosengren, *Journal of the Mechanics and Physics of Solids* 16 (1968) 1-12.

10. H. Kitagawa and S. Takahashi, *Proceedings ICM-2* ASM (1976) 627-631

11. Kåre Hellan, *Introduction to Fracture Mechanics* McGraw-Hill Book Co., New York (1984).

12. MSC/NASTRAN User's Manual, Version 67, *McNeal-Schwindler Corporation* Vol. 1 and 2 (1991).

13. S. Pearson, *Engineering Fracture Mechanics* 7 (1975) 235-247.

14. Y. Nakai and J. Ohji, *Proceedings Fourth International Conference on Fatigue and Fatigue Thresholds* (1990) 1605-1610.

15. M. Nakajima Y. Kato and Y. Kitaoka, *ibid* 1611-1616.

16. A.F. Blom, A. Hedlund, W. Zhao, A. Fathulla, B. Weiss, and R. Stickler, *The Behavior of Short Fatigue Cracks* (K.J. Miller and E.R. delosRios editors) Mechanical Eng. Public. (1986) 37-66.

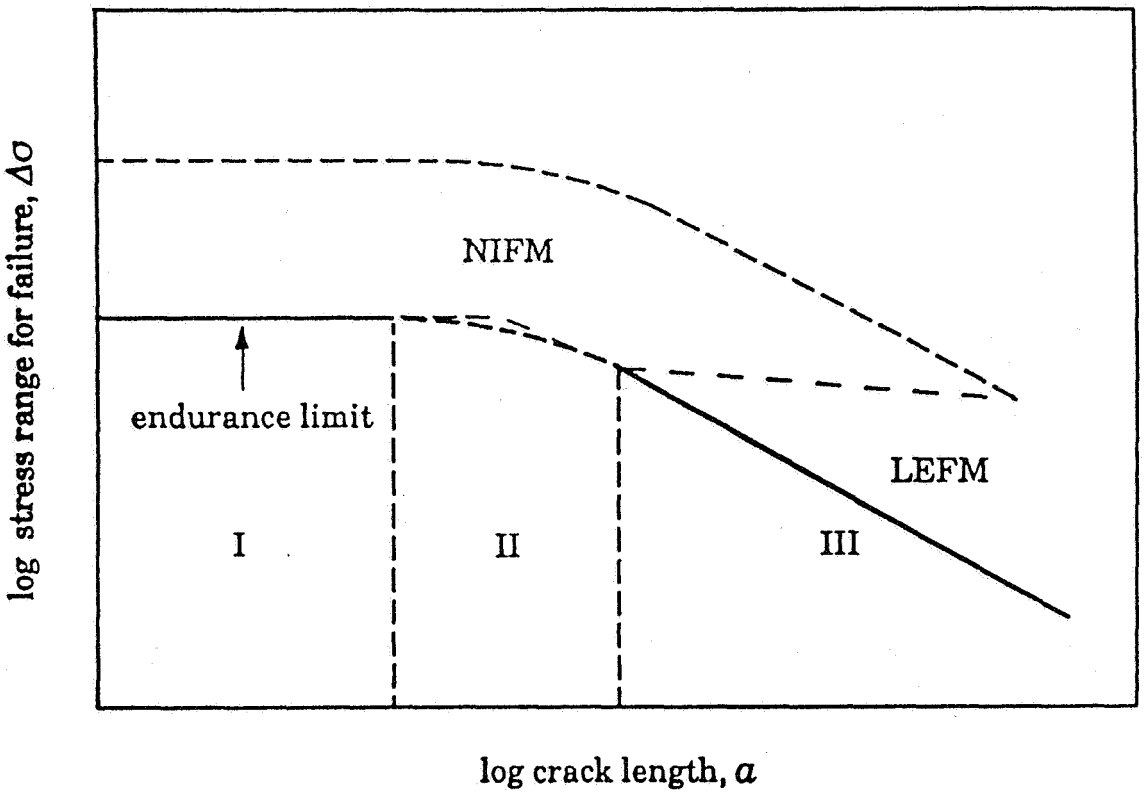

Fig. 1. The Kitagawa diagram.

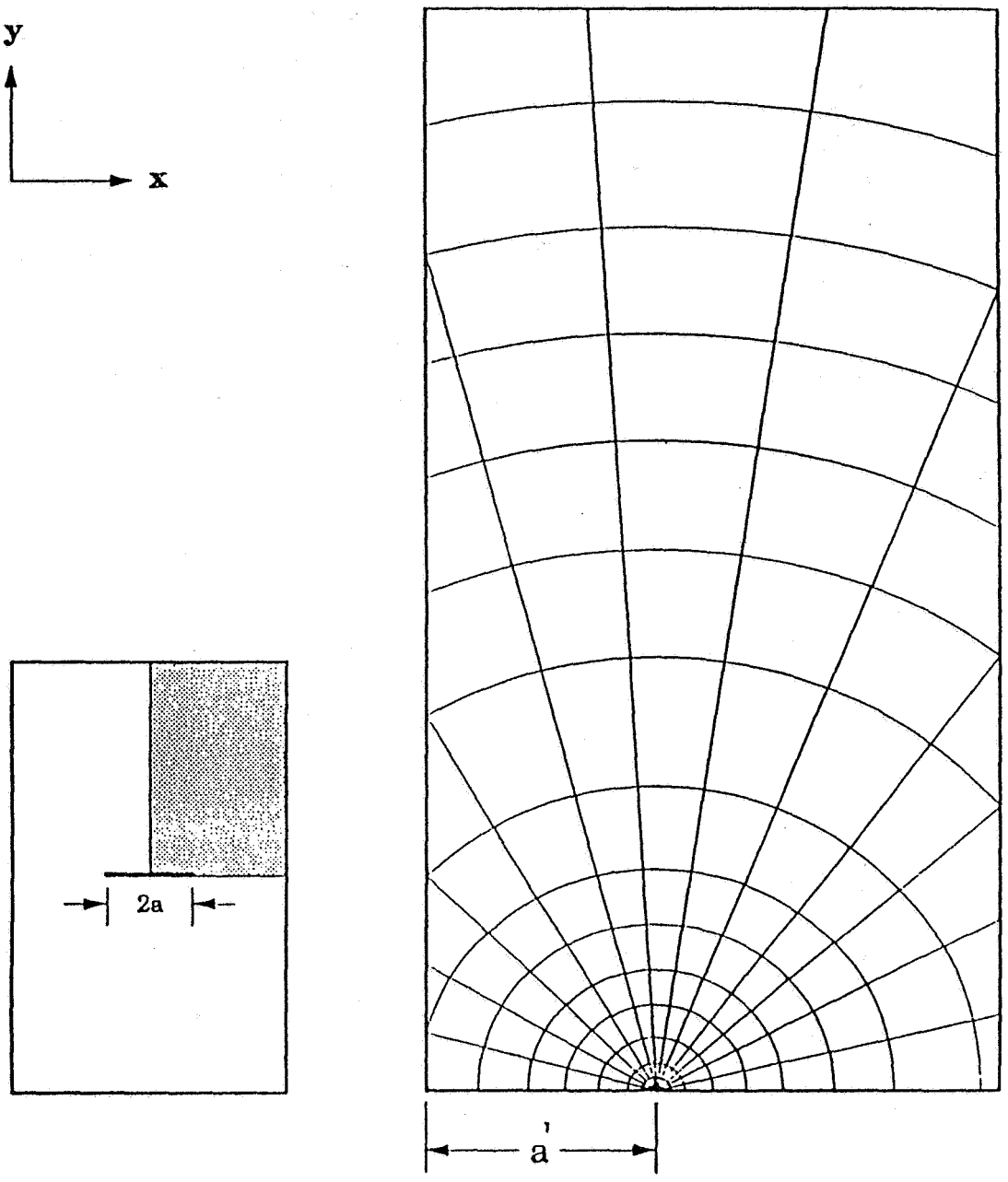

Fig. 2. The finite element mesh. For the single-edge-cracked case, a is the crack length, whereas for the center-cracked case, a is the half-length.

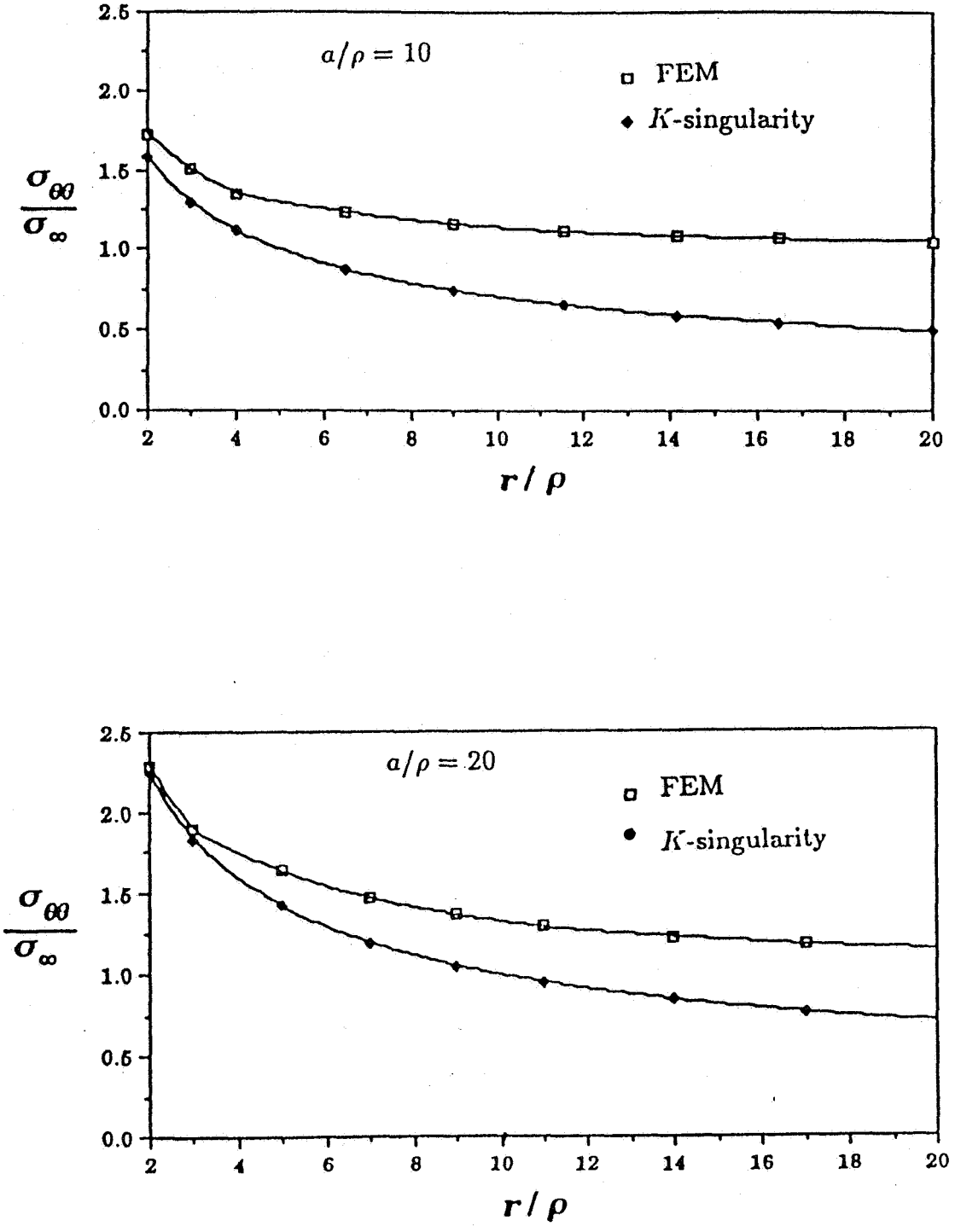

Fig. 3a. The stress field $\sigma_{\theta\theta}$ directly ahead of the crack tip for $a/\rho = 10, 20$ in the center-cracked specimen.

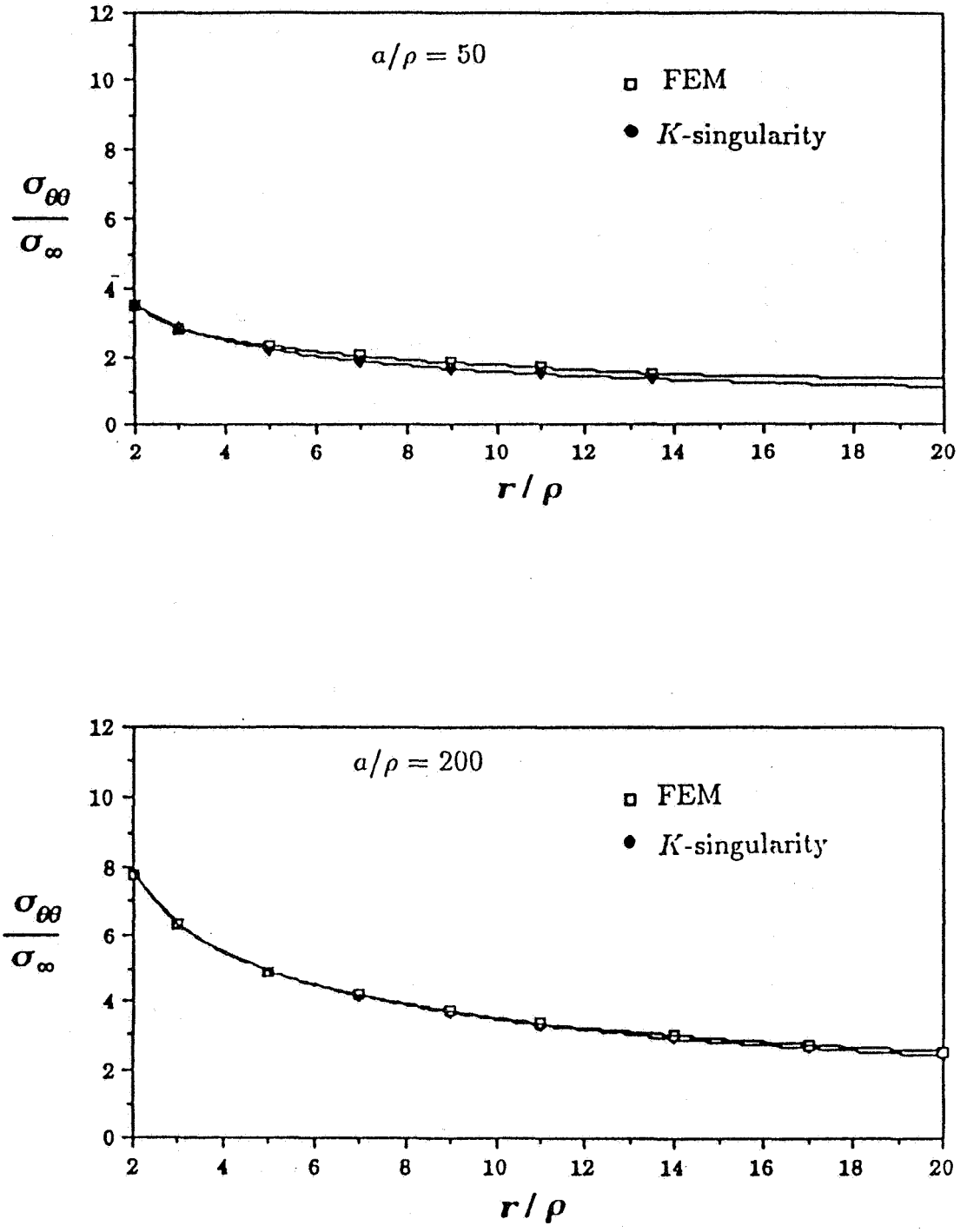

Fig. 3b. The stress field $\sigma_{\theta\theta}$ directly ahead of the crack tip for $a/\rho = 50$, 200 in the center-cracked specimen.

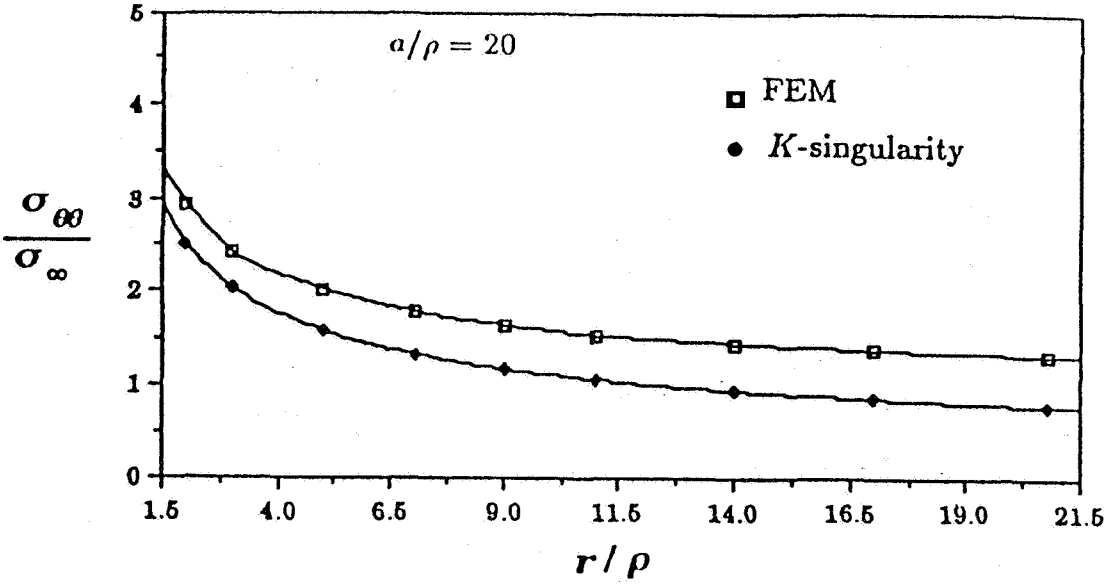

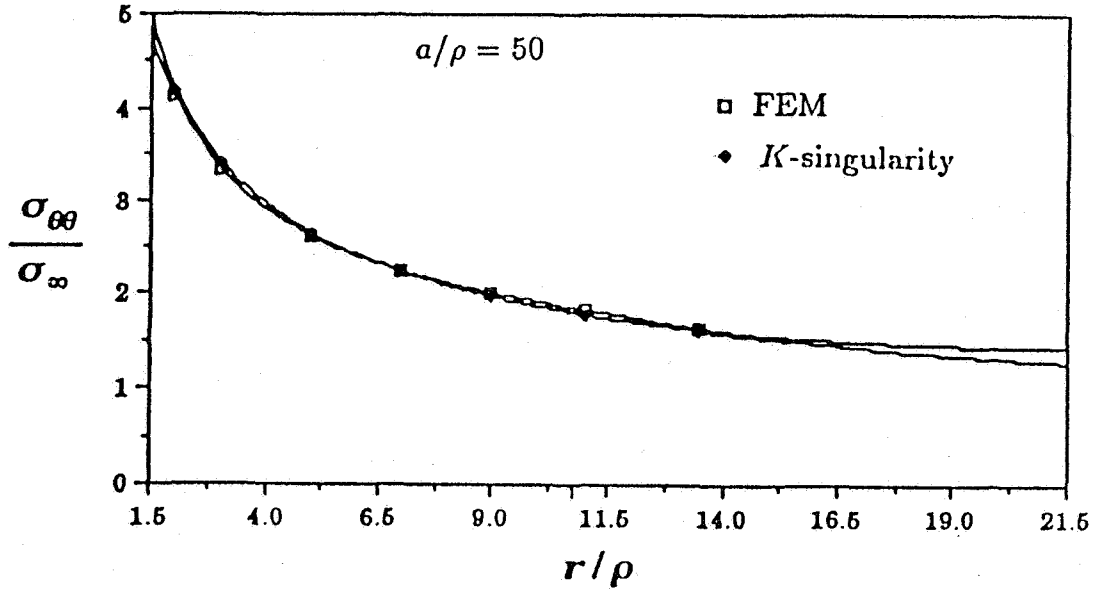

Fig. 4. The stress field $\sigma_{\theta\theta}$ directly ahead of the crack tip for $a/\rho = 20$, 50 in the single-edge-cracked specimen.

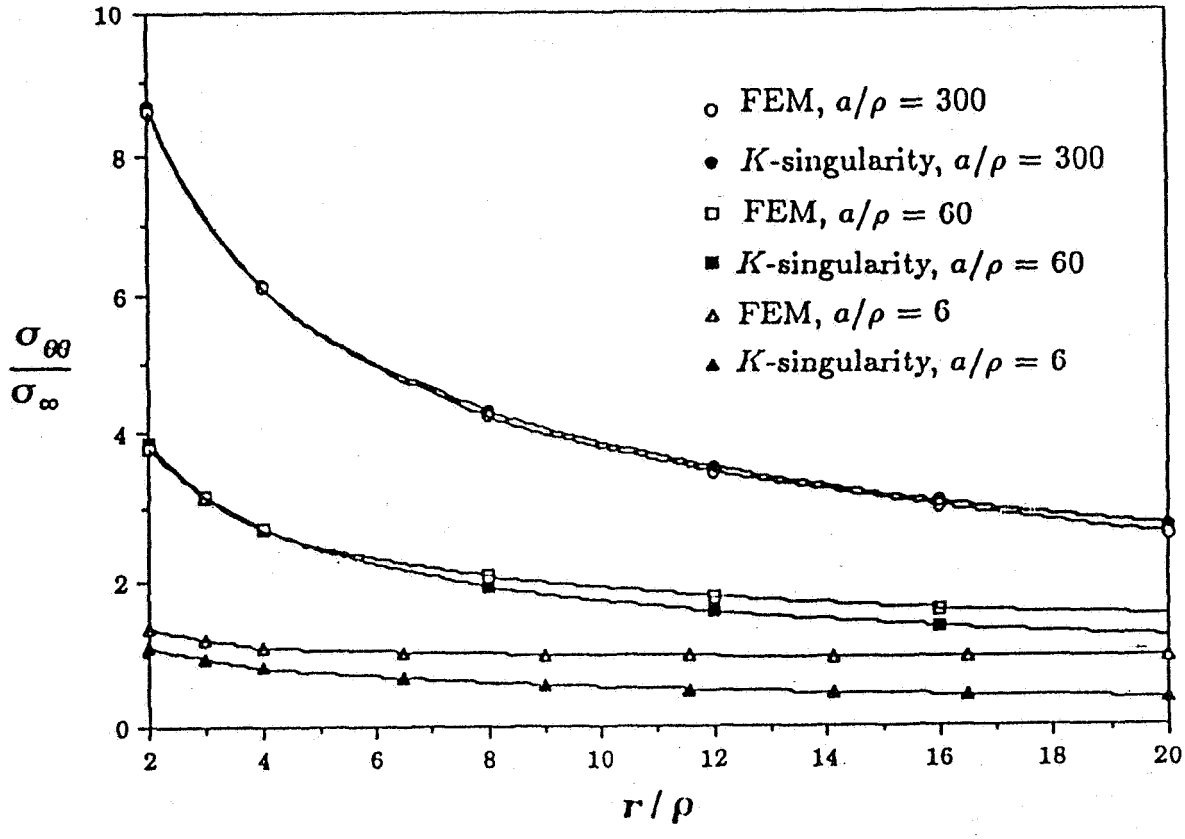

Fig. 5. The stress field $\sigma_{\theta\theta}$ directly ahead of the crack tip for three center-cracked specimens which have the same a/w ratio of 0.02 but different absolute sizes (i.e. a short crack, a/ρ= 6, and two long cracks, a/ρ= 60 and 300).

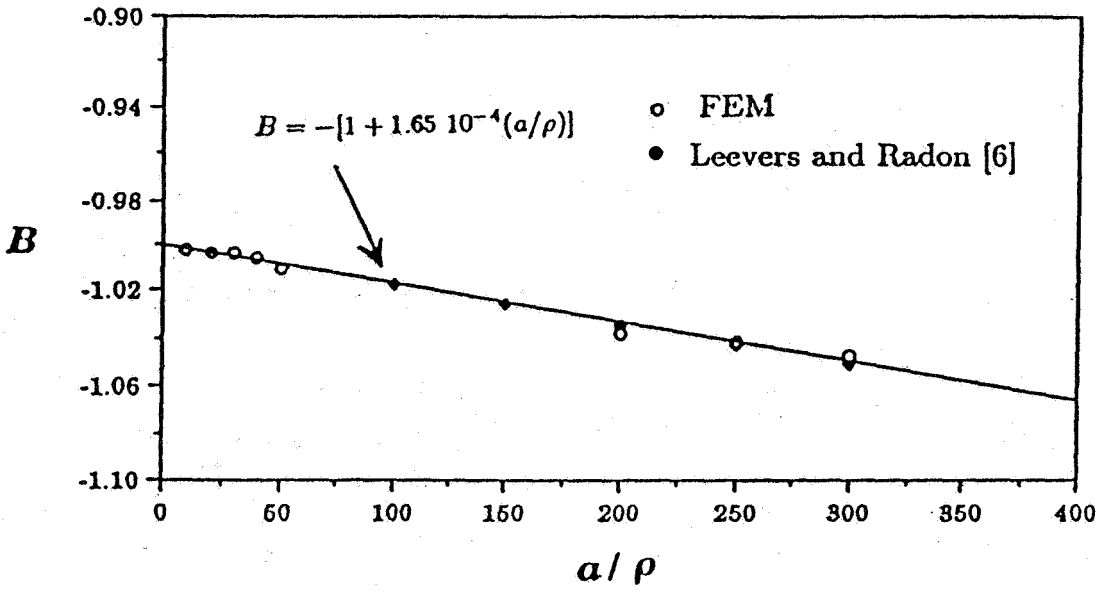

(a)

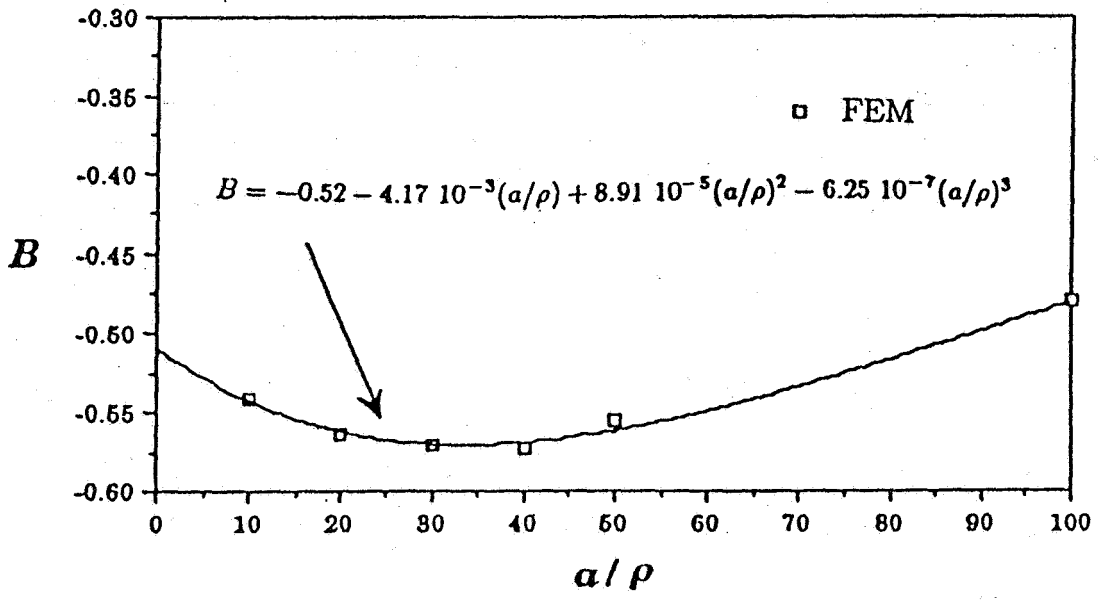

(b)

Fig. 6. The biaxiality ratio, B as a function of crack length a for (a) the center-cracked and (b) the single-edge-cracked specimens.

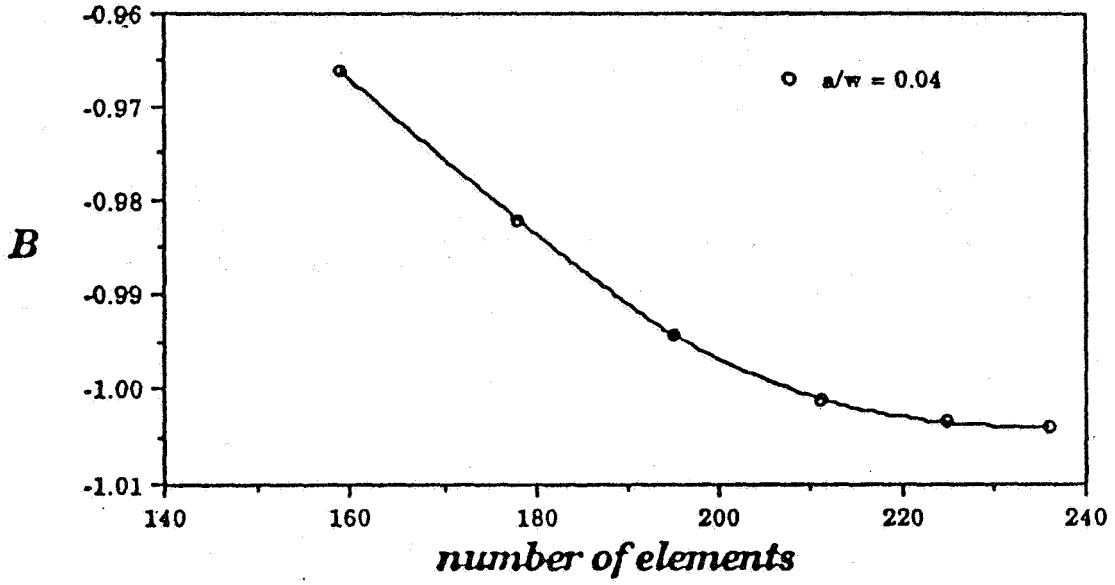

Fig. 7. The biaxiality ratio, B as a function of the number of elements, illustrating the sensitivity of the numerical scheme.

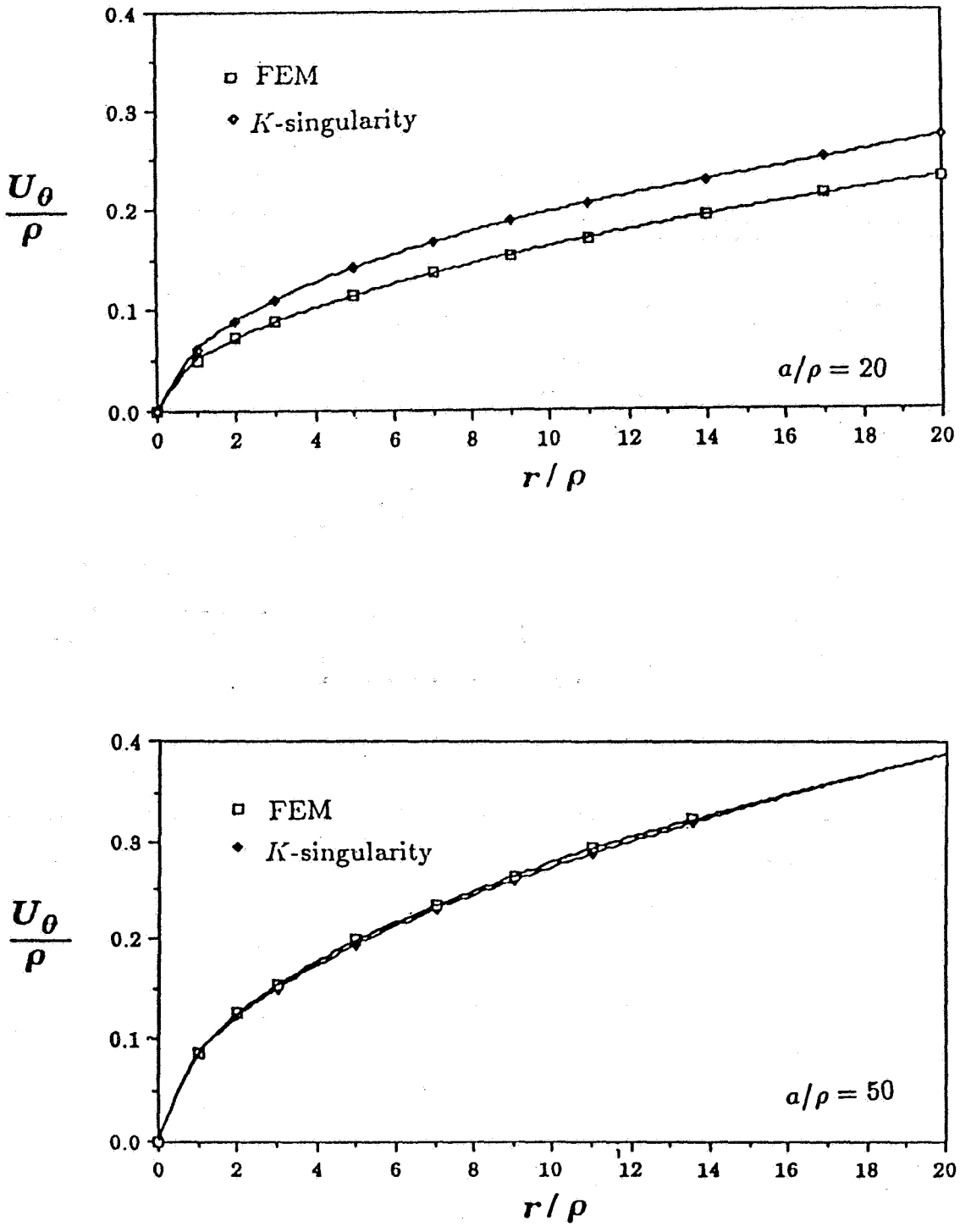

Fig. 8. The displacement field U_θ behind the crack tip for $a/\rho = 20$, 50 in the single-edge-cracked specimen.

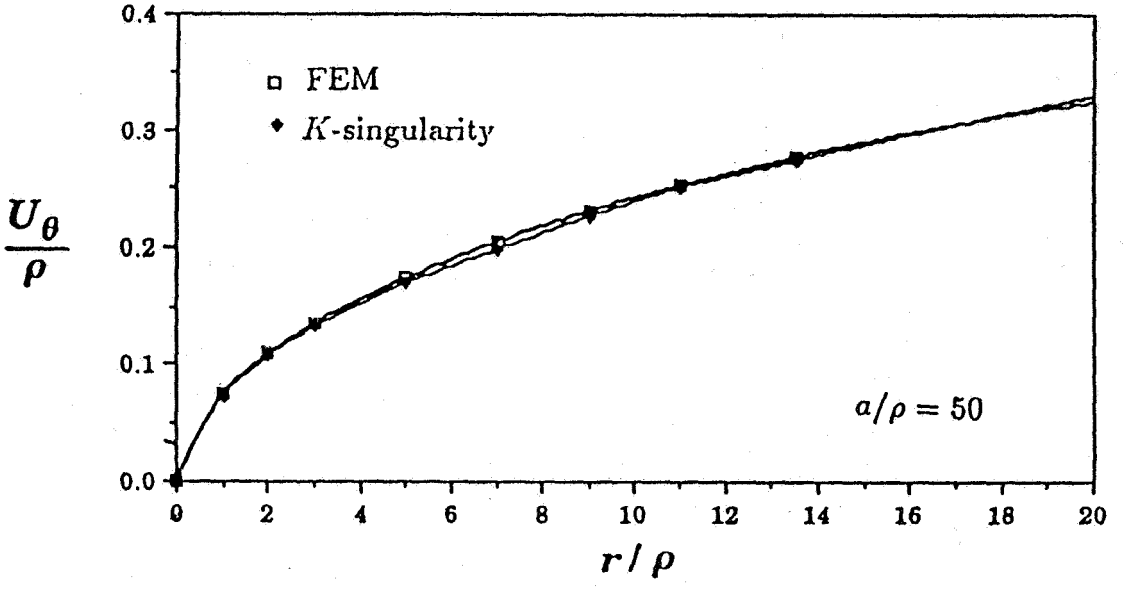

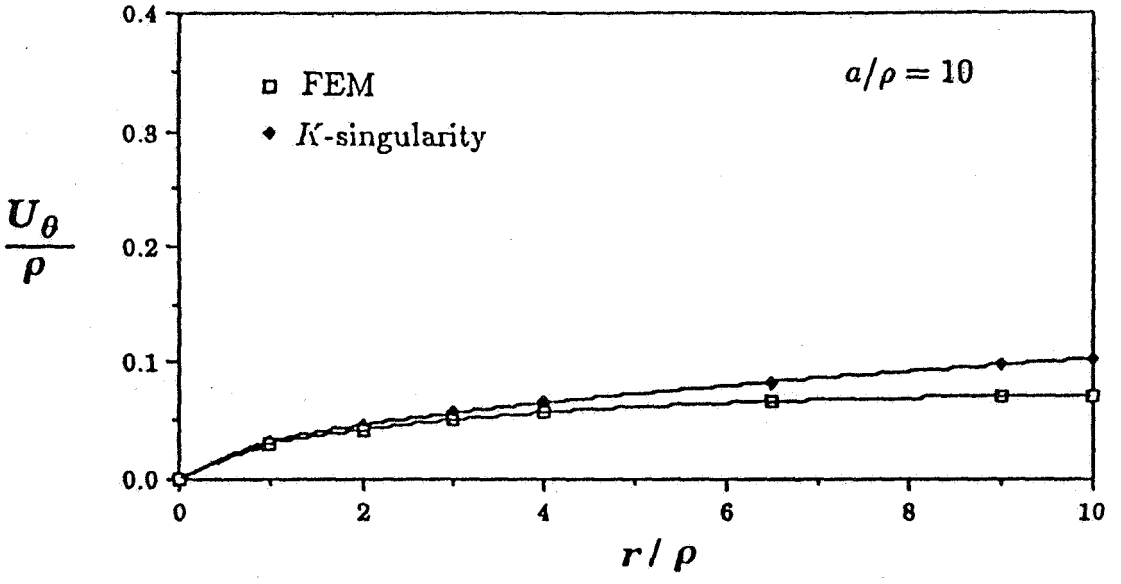

Fig. 9. The displacement field U_θ behind the crack tip for $a/\rho = 10$, 50 in the center-cracked specimen.

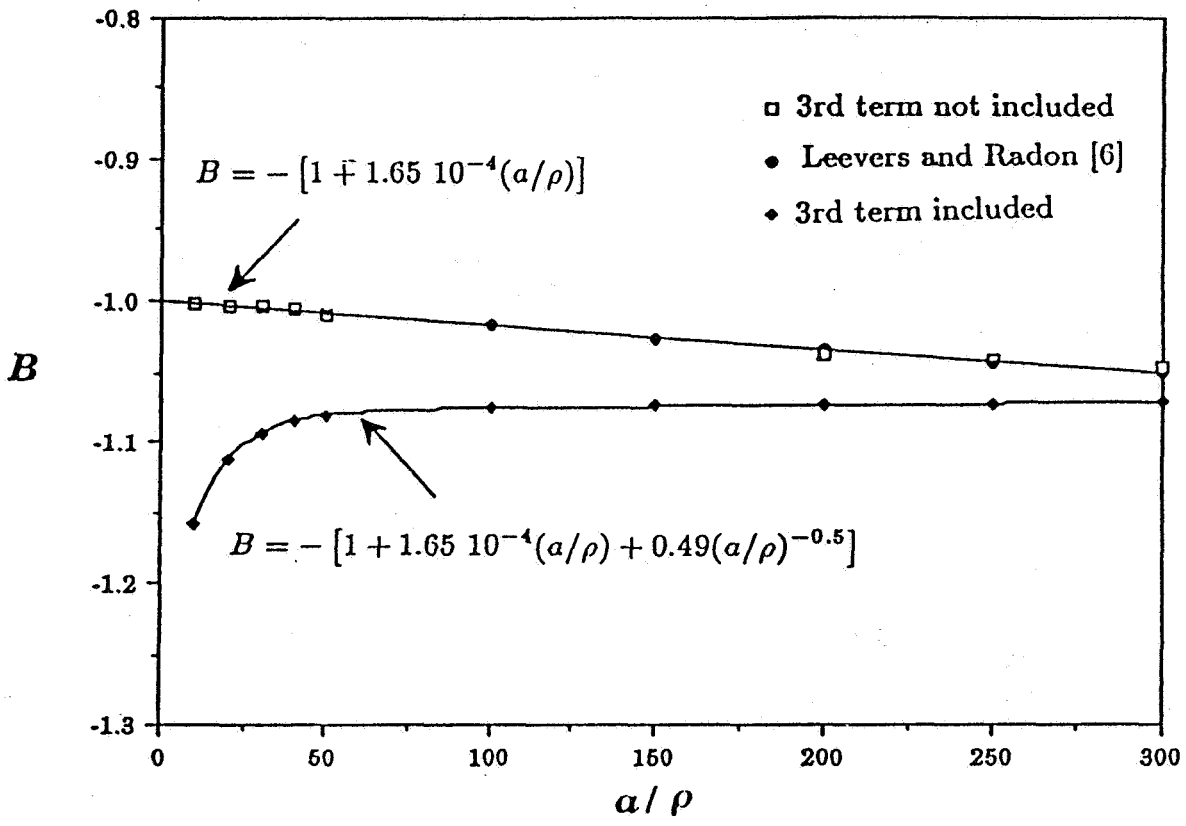

Fig. 10. The effect of the third term on the biaxiality ratio for the center-cracked geometry.

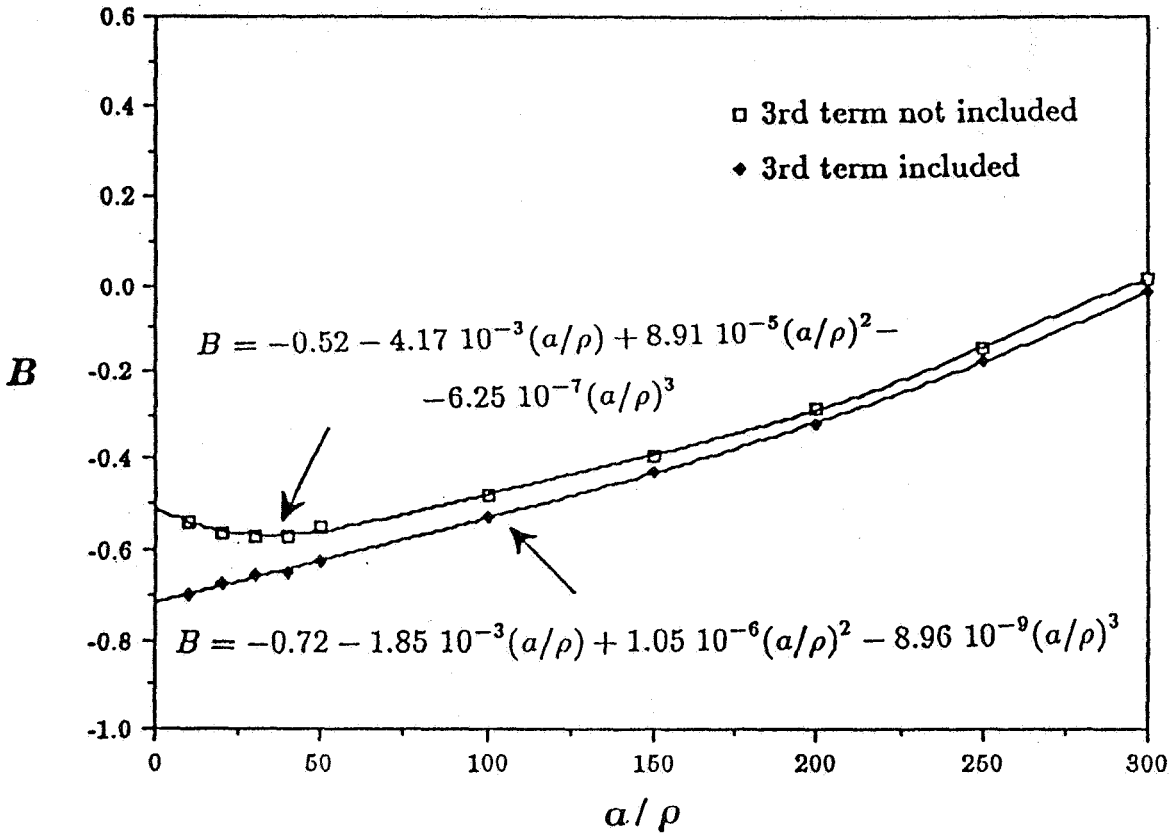

Fig. 11. The effect of the third term on the biaxiality ratio for the single-edge-cracked geometry.

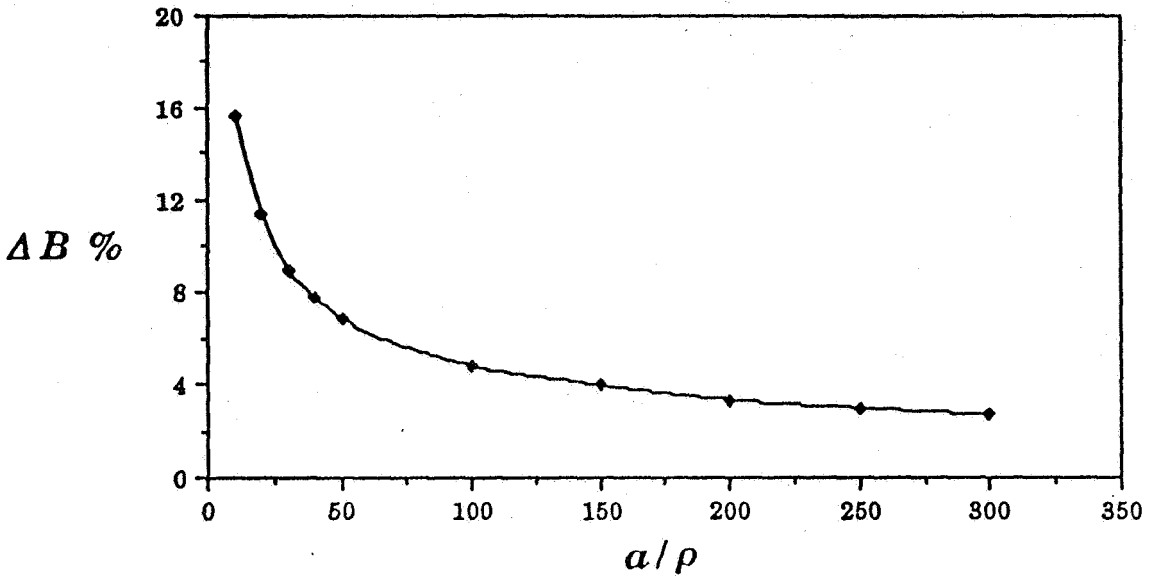

Fig. 12. Percentage increase in B, $\Delta B = (B_{incl} - B_{not\ incl})/B_{not\ incl}$ in the center-cracked case.

WIDESPREAD FATIGUE DAMAGE MONITORING - ISSUES AND CONCERNS*

T. SWIFT

Federal Aviation Administration
3229 East Spring Street
Long Beach, CA 90806-2425

ABSTRACT

This paper is intended to illustrate the considerable effect that small in-service undetectable multi-site-damage (MSD) can have on the residual strength capability of aging aircraft structures. In general, very few people in the industry believe that tiny cracks of undetectable size are a problem because they know that many aircraft have been able to survive much larger damage. In fact they have been certified for this large damage capability. However, this is not the issue. The real issue is the effect the tiny cracks, at multiple sites, have on the large damage capability which the industry has become accustomed to expect and which the aircraft have been certified to sustain. The concern is that this message does not appear to be fully undertood by many people outside the fracture community. The prime purpose of this paper, therefore, has been to convey this message by describing in simple terms the net section yielding phenomenon in ductile materials which causes loss in lead crack residual strength in the presence of MSD. The explanation continues with a number of examples on complex stiffened structures, using the results of previous finite element analyses, which illustrate that the effect of MSD is extremely sensitive to structural configuration. It is hoped that those members of the aviation community who believe that tiny cracks are not a problem will read this paper very carefully.

INTRODUCTION

The ALOHA 737 accident in Hawaii on April 28, 1988 created what may be termed a minor "Structural Integrity Revolution" in the Commercial Transport Industry. This minor revolution can, perhaps, be compared to that existing in the fatigue and fracture community in the aftermath of the F-111 accident on December 22, 1969 at Nellis Air Force Base in Nevada. A few weeks after the Aloha accident the Federal Aviation Administration (FAA) sponsored "The International Conference on Aging Airplanes" held in Washington D.C. in June of 1988. Subsequently, in August of 1988, The Airworthiness Assurance Task Force (AATF), later retitled The Airworthiness Assurance Working Group (AAWG), was formed by The Air Transport Association (ATA) of America and The Aerospace Industries Association (AIA) of America. This group, working in cooperation with FAA and other airworthiness authorities, have made significant contributions to improving the airworthiness of the aging fleet of

* Presented at the 5th International Conference on Structural Airworthiness of New and Aging Aircraft, Hamburg, Germany, June 16–18, 1993.

transport airplanes. Among these contributions are model specific reassessments of Supplemental Structural Inspection programs, incorporation of safety related Service Bulletins not previously mandated and the development of mandatory Corrosion Control programs. This activity is now being extended to the Commuter Fleet of airplanes.

Soon after the ALOHA accident the FAA formulated a draft Special Federal Airworthiness Regulation (SFAR) proposing that older airplanes have, as a minimum, one lifetime of fatigue testing beyond the current fleet lead aircraft. The purpose of this rule was to reduce the exposure to unknown fatigue problems and identify multiple-site-damage (MSD) before it occurred in the commercial fleet. In June of 1990 the AATF/AAWG undertook a review of the proposed SFAR and published a report titled "A Report of the AATF on Fatigue Testing and/or Teardown Issues". This report, [1], outlined alternative means to ensure that widespread fatigue damage would not occur in the transport fleet. This was to be achieved through a structural audit of each of the aging fleets of airplanes. With this in mind a Structural Audit Evaluation Task Group (SAETG) was formed under the umbrella of the Aviation Rulemaking Advisory Committee (ARAC) working through the Transport Aircraft and Engine Sub-Committee (TAES). The charter of this task group was to develop a SFAR titled "Widespread Fatigue Damage Evaluation (Aging Aircraft) with a supporting Advisory Circular having the same title. These documents were intended to provide a common set of guidelines to establish the onset of WFD for the aging fleet of commercial transport airplanes. The Structural Audit Evaluation Task Group has been supported by a further activity under the umbrella of AATF/AAWG conducted by the Industry Committee on Widespread Fatigue Damage (ICWFD). The SAETG includes participating members from the airworthiness authorities while the authorities have participated in the ICWFD as observers only. The SFAR and accompanying AC, produced by the SAETG, are intended to initially address eleven fleets of transport aircraft as follows:- B707/720, 727, 737 (100 and 200 models only), 747 (100 and 200 models only), BAE 1-11, DC-8, DC-9, DC-10, F28, A-300 (B2, B4-100, B4-200, C4 and F4 models only)2 and L-1011.

As can be seen from this introduction major steps have been taken by the so called "Three Legged Stool" (manufacturers, operators and authorities) to improve the structural airworthiness of the aging fleet of airplanes. Notwithstanding this considerable effort there are still outstanding issues and concerns related to the formulation of WFD which is believed to have been a contributing factor in the probable cause of the ALOHA 737 accident.

DEFINITIONS

The two industry activities SAETG and ICWFD, the AIA Structures Technical Subcommittee and the Technical Oversight Group Aging Aircraft (TOGAA) have expended considerable effort defining Widespread Fatigue Damage (WFD) and its two subsets Multiple Site Damage (MSD) and Multiple Element Damage (MED). The definitions

agreed by these groups are:-

Widespread Fatigue Damage (WFD) in a structure is characterized by the simultaneous presence of cracks at multiple structural details that are of sufficient size and density whereby the structure will no longer meet its damage tolerance requirements (e.g., not maintaining required residual strength after partial structural failure).

Multiple Site Damage (MSD) is a type of Widespread Fatigue Damage characterized by the simultaneous presence of fatigue cracks in the same structural element (e.g., fatigue cracks that may coalesce with or without other damage leading to a loss of required residual strength).

Multiple Element Damage (MED) is a type of Widespread Fatigue Damage characterized by the simultaneous presence of fatigue cracks in similar adjacent structural elements.

A further definition for Widespread Fatigue Damage has been proposed by Professor Jim Mar, Chairman of TOGAA. Professor Mar simulates WFD to AIDS in humans. It is a point in the life of an aircraft when the immune system (in this case fail safe or damage tolerance capability) starts to deteriorate. Because WFD in the form of MSD can drastically affect certified levels of residual strength, even when it is so small it is in-service non detectable, Professor Mar believes that either MSD exists or it doesn't. There is nothing in between that can be managed by inspection. Unlike AIDS, however, MSD can be cured by reliably predicting when it is likely to degrade residual strength capability below required levels using the best tools currently available and then modifying the structure in ample time before it has a chance to deteriorate the immune system.

PRIMARY ISSUES AND CONCERNS

As previously mentioned the SAETG supported by the ICWFD are in the process of establishing guidelines to estimate the onset of WFD. It is the intention that the manufacturers provide this estimate based on their knowledge of background fatigue testing and stress analysis of the aircraft. However, the operators have made it clear that they will be reluctant to allocate funds for aircraft modification unless they are sure the estimate is correct. Bearing this in mind the ICWFD has proposed a monitoring period between the first anticipated cracking indications and the onset of WFD where special inspections will be performed of susceptible areas with a view to escalating the manufacturers' estimate of WFD. This monitoring period is illustrated in Figure 1.

Since the ALOHA accident it has been the contention of the airworthiness authorities that managing structural safety in the presence of WFD or MSD is not reliable with current in-service inspection sensitivity. In fact, the FAA no longer allows continued inspection of known problem areas as an alternative to fixing the

problem itself. The issue is, then, how can the monitoring period be technically viable when MSD cannot be reliably found before it has already reduced residual strength capability below regulatory levels.

The concern appears to be confined to just a few people who fully understand the implications of MSD. The others appear to think that small MSD can never be a problem because they have been able to tolerate much larger cracks in the past. This is true but this is not the issue. The issue is that the airplane is designed to tolerate certain lead crack sizes. The inspection program is based on these lead crack sizes and MSD has significant effect on residual strength at these sizes. Further to this the airplane is also designed to sustain a certain degree of discrete source damage due to engine disintegration and other possible sources. MSD can also degrade this discrete source damage capability. It has been pointed out to the operators that the monitoring period will not include "business as usual" inspections but will require finding cracks far below the threshold capability of current Non Destructive Inspection (NDI) used in service. They have chuckled amongst themselves at this and commented that they will need to carry pocket electron microscopes with which to perform the inspections. The truth is that this is what may be required in some areas if the initial estimate made by the manufacturers is to be escalated based on inspections performed during the monitoring period.

It has been stated many times that structure can be made to operate forever with proper inspection and maintenance. The damage tolerance philosophy is supposed to find damage before catastrophe. However, in-service inspections based on a damage tolerance philosophy are designed to find a single lead crack in a structure which is not expected to crack under normal circumstances but may crack within the service life due to initial manufacturing or in-service induced accidental damage. Damage tolerance was not intended as a safety management tool for structures operating beyond their initial design life goals or beyond the point where WFD is likely to occur.

Since the ALOHA accident a large number of researchers have been concerned with predicting the growth of MSD to link-up for what appears to be an endless range of cracking scenarios. This is apparently being considered with a view to managing safety in the presence of MSD. The truth is the range of scenarios <u>is</u> endless, it is impossible to consider all cracking scenarios and it is too late to control when it becomes inspectable.

This author became concerned about the implications of MSD in the early days of the DC-10 development test program in the late sixties where many components were tested to many times the design life goal of the airplane. This concern was expressed in reference [2], presented in Toulouse in May, 1983, where the difficulties of inspecting for MSD and the net section yielding phenomena were pointed out.

Further concerns were expressed in reference [3], presented in Pisa in May, 1985. Reference [3] outlined the fact that residual strength of specimens containing small cracks in 2024-T3 material was limited by typical net section yield stress. That paper also warned that although 2024-T3 material was the most superior alloy for large damage capability its capacity to withstand MSD was limited by low yield strength of the material. Reference [3] also warned that lead crack residual strength could be influenced by fastener holes ahead of the lead crack tip due to plastic yielding between the lead crack tip and the holes. It was pointed out that all residual strength tests performed so far did not consider this phenomenon.

Reference [4] presented in Ottawa in June, 1987, warned that the formulation of MSD may prevent skin "Flapping", a so called safe decompression phenomenon, being depended upon to eliminate the need to perform detailed inspections of lap splices.

As recently as a year ago an explosive decompression failure occurred in the fuselage on a full scale test specimen in Europe. This failure came as a complete surprise to structural engineers who were aware that MSD existed in a lap splice but who were unaware of the serious implications of MSD.

An attempt was made in reference [5] to illustrate the effects of MSD on lead crack residual strength. This paper was, however, presented to a select audience of fatigue specialists at Delft University who it is believed fully understood the implications. However reference [5] is probably not widely publicized among the airline community. At the risk of being criticized for duplication much of the material in reference [5] is again repeated here with the hope that the issues and concerns related to this dreaded disease in aging airframes outlined above will be better understood by a wider audience.

EFFECTS OF WFD/MSD/MFD ON DAMAGE TOLERANCE PHILOSOPHY

The philosophy of damage tolerance assures structural integrity through in-service directed inspections of critical structure. As mentioned earlier the airplane is designed not to crack within one lifetime but may crack due to damage caused during manufacture or during service. The inspection threshold and frequency is determined by engineering evaluation considering the aircraft utilization, material crack growth rates and residual strength capability. A stress spectrum is derived for each principal structural element (PSE) and a safe crack growth period is calculated starting with a single lead crack of a size that is considered to be detectable in-service with a high degree of reliability and confidence and ending with the critical crack size at limit load. This is illustrated by Figure 2. The safe crack growth period is normally divided by a factor of either 2 or 3

depending upon the type of structure. The safety of the airplane depends upon finding cracks before they reach a critical length. The residual strength calculation, supported by tests, normally does not assume the presence of MSD because the airplane is supposed to be designed so that WFD will not occur within the design life goal. However, now that many aircraft are operating beyond this goal the possibility that WFD will occur increases with time. If WFD does occur it can drastically affect the residual strength capability of the single lead crack at limit load. This is illustrated by Figure 3 which shows a typical residual strength diagram for a single lead crack indicated by the upper curve. The lower curve illustrates the effect of MSD ahead of the lead crack tip. As can be seen the effect of the MSD cracks is to decrease the critical crack size at limit load or to decrease the residual strength capability. The effect of decreasing the critical crack size is illustrated by Figure 4. As can be seen this causes a reduction of the safe crack growth period resulting in a much shorter required inspection frequency.

A particularly difficult issue to deal with is the effect of MSD on the discrete source damage capability of the pressure cabin. The airplane is normally designed to sustain damage from discrete sources such as from engine fragments during disintegration. Usually the pressure cabin is certified to a certain level of damage substantiated by discrete source damage tests. For example, in the case of damage from an engine disc fragment, a harpoon blade simulating the disc fragment is fired into the pressurized cabin. This is illustrated by Figure 5. An example of these tests is further illustrated by Figures 24, 25 and 26 of reference [4] for the DC-8 fuselage. Continued operation of the airplane beyond the initial design life goal increases the probability that WFD in the form of MSD will occur in the pressure cabin thus degrading the discrete source damage capability.

As mentioned earlier it is difficult for the layman to appreciate the consequences of extremely small cracks of less than detectable size because aircraft have been able to sustain much larger cracks in the past. However, these extremely small cracks, which develop and become widespread with extended use of the aircraft, have the ability to drastically reduce this large crack residual strength capability which is expected to exist.

EFFECT OF MSD ON LEAD CRACK RESIDUAL STRENGTH

The residual strength of unstiffened panels containing lead cracks can be determined using conventional fracture mechanics principles. For an infinitely wide thin sheet panel the residual strength can be expressed as:

$$\sigma_R = K_c/\sqrt{\pi a} \qquad [1]$$

The value of K_c is the plane stress fracture toughness of the material obtained from unstiffened cracked panel tests and a is half the crack length. For 2024-T3 material, the most common alloy

used for fuselage skins, the full plane stress fracture toughness is not achieved unless the panel width is greater than 50 inches. If critical stress intensity factor is calculated from test results of panels narrower than 50 inches then the resulting values, limited by yielding of the intact ligament on each side of the crack, will be lower than the plane stress fracture toughness. This effect is illustrated by Figure 6 which shows critical stress intensity factor as a function of panel width determined from test results, references[6]and [7]. It can be seen that for panels with widths less than 50 inches the critical stress intensity factor is limited by ligament yielding. This means that failure of 2024-T3 panels with widths less than 50 inches will be governed by net section yielding rather than by stress intensity factors reaching a critical value.

The fracture strength of most aluminum alloys is limited to the typical net section yield strength of the alloy. This phenomenon is best illustrated by considering test results for specimens containing small cracks. Figure 7 shows data for 2024-T351 plate, reference [3], and indicates failure stresses equal to the typical yield strengths for unnotched specimens from the same batch of material. These yield strengths are based on the 0.2% offset strain. Test point A represents a data point for a specimen with an uncracked hole which failed at 59.5 KSI. When this point is compared to the unnotched typical ultimate strength of 73 KSI it is evident that the material is severely notch sensitive, ie., a loss in strength of 18½%.

Feddersen in reference [8] suggested a residual strength criterion for center cracked panels as shown by Figure 8. A residual strength curve is plotted based on $K_c/\sqrt{\pi a}$ or the fracture mechanics mode of failure. A line is drawn from point A, representing typical tension yield strength, tangent to the $K_c/\sqrt{\pi a}$ curve at point B which is at 2/3 the material yield strength. A second line is drawn from point D representing panel width W which in the example shown is 50 inches, tangent to the curve shown by point C, which is at one third the panel width. The residual strength curve is represented by line ABCD. Residual strength is governed by fracture mechanics only between B and C. As illustrated in reference [8] test data falls on this line. For narrower panels fracture is governed by the lines indicated for panel widths W_1, W_2, W_3 and W_4.

For the MSD case shown on Figure 8 the effective panel width is the fastener spacing P or W_1. The residual strength for this case, according to the Feddersen method, is given by the line A W_1. The equation for this line would then be:-

$$\text{Residual Strength } \sigma_R = F_{ty}[P-2a]/P \qquad [2]$$

Where F_{ty} is the typical yield strength, P is the fastener spacing and 2a is the total length of the crack from tip to tip.

Based on this information it appears reasonable to assume that link-up of a lead crack with an MSD crack would occur when the

intact ligament stress between the lead crack tip and the MSD crack tip reached the typical yield strength of the material. This leads one to the intuitive link-up criterion illustrated by Figure 52 of reference [4] and again restated in Figure 21 of reference [5]. As mentioned earlier in this paper it is not clear that the effects of MSD on lead crack residual strength are fully understood by very many people of authority. So this concept will again be repeated in the hope that the old British saying, "Third Time Does It", will apply. Figure 9 restates the link-up criterion. The lead crack plastic zone size R_2 can be calculated using one of the many plastic zone models in the literature. Similarly the MSD crack plastic zone R_1 can be calculated. The interaction between the two crack tips can be determined from Figures 75 and 76 of reference [10]. As the remote stress level increases the plastic zone sizes will increase and it is suggested that the two cracks will link-up when the two plastic zones touch each other as indicated in Figure 9. Thus the entire ligament between the two crack tips has yielded. The net stress at link-up appears to be controversial. As mentioned earlier intuition supported by a considerable background of testing suggests this should be in the neighborhood of the yield stress. It is not yet fully understood whether this is at the 0.1% or the 0.2% offset strain or at some other strain.

Under FAA funded research conducted soon after the ALOHA accident it was determined that the net section stress at failure for 8 inch and 4 inch wide 2024-T3 specimens 0.04 inches thick containing MSD cracks was at least equivalent to the flow stress or approximately $[F_{tu} + F_{ty}]/2$, reference [9]. The flow stress quoted in this case was 65 KSI.

In reference [5] this author used the Irwin plastic zone model with an estimated link-up stress of 50 KSI to illustrate the loss in lead crack residual strength in the presence of MSD. The Irwin plastic zone model does not satisfy equilibrium as pointed out in reference [11]. There are a number of plastic zone models available but not much evidence yet to show that one is better than another.

Other research, reference [12], conducted by CDR Jim Moukawsher of the USCG at Purdue University on 2024-T3 panels 9 inches wide and 0.09 inches thick containing lead cracks under the influence of MSD cracks indicates reasonably good correlation with this link-up criterion using the Irwin plastic zone model and the 0.1% offset yield strength. For these panels this value was 51 KSI.

Research is being conducted under FAA funding to establish a sound link-up criterion. For the purposes of this paper the Irwin plastic zone model combined with a link-up stress of 50 KSI will be used. It is the purpose of this paper to attract more attention and to convince the airline industry of the problem of loss in lead crack strength in the presence of MSD rather than to establish an exact analytical method. It is hoped that this will be achieved in the near future by FAA funded research.

Figure 9 illustrates the intuitive link-up criterion and shows a

lead crack of half length a_2 which has been propagating along a row of holes. A hole containing a MSD crack exists ahead of the lead crack tip. Link-up of the MSD crack with the lead crack will occur when the lead crack plastic zone R_2 touches the MSD plastic zone R_1 as shown in the figure, ie.,

$$R_1 + R_2 = [P-d/2-a_1] \qquad [3]$$

Plastic zone sizes based on the Irwin model are:

$$R_1 = [K_1/\sigma_y]^2/[2\pi] \qquad R_2 = [K_2/\sigma_y]^2/[2\pi]$$

$$K_1 = \beta_h\beta_{I1}\sigma[\pi a_1]^{1/2} \qquad K_2 = \beta_s\beta_{I2}\sigma[\pi a_2]^{1/2}$$

Therefore:

$$[(\beta_h)^2(\beta_{I1})^2\sigma^2\pi a_1 + (\beta_s)^2(\beta_{I2})^2\sigma^2\pi a_2]/(2\pi\sigma_y^2) = P-d/2-a_1$$

Therefore:

$$\sigma_R = \{2\sigma_y^2(P-d/2-a_1)/[\beta_h^2\beta_{I1}^2a_1 + \beta_s^2\beta_{I2}^2a_2]\}^{1/2} \qquad [4]$$

Where:

σ_R = Remote gross stress which causes the plastic zones to touch.

σ_y = Local stress causing link-up. Approx. equal to flow stress or $[F_{tu} + F_{ty}]/2$. (50 KSI assumed in this paper)

β_h = Bowie Factor ref. [13] for cracks at a hole but normalized to crack length measured from hole 1 center, ie., a_1. (see example below).

β_{I1} = Geometric correction factor for crack 1 tip due interaction with lead crack 2. This is determined from reference [10] Figure 75 based on an equivalent lead crack 2 length $a_{e2} = \beta_{s2}^2a_2$ and an equivalent crack 1 length $a_{e1} = \beta_h^2a_1$; ie., it is assumed that the effect of one crack on the other is due to interacting Ks. Equivalent crack lengths are used to calculate interaction accounting for individual crack Ks. This effective crack length philosophy, used here to account for effects of stiffening elements on K, needs further validation.

β_s = Geometric correction factor for lead crack 2. This factor would include the effects of stiffening or any edge effects.

β_{I2} = Geometric correction factor for crack 2 due to interaction of crack 1. This is determined from reference [10] Figure 76 based on an equivalent lead crack 2 length $a_{e2} = \beta_{s2}^2a_2$ and equivalent crack 1 length $a_{e1} = \beta_h^2a_1$.

Consider the MSD cracks in hole 1 of Figure 9 are 0.05 inches at each side of the hole. Assume the hole diameter is 0.19 inches so that a_1 = 0.145 inches. The stress intensity factor for two cracks at a hole under uniaxial loading is given as $K = [\pi L]^{1/2}F(L/r)$ in reference [13] where L is the crack length and r the hole radius. At a value of L/r = 0.05/0.095, F(L/r) = 1.8 [by plotting L/r versus F(L/r)]. The value of β_h can then be obtained as follows:

$$\beta_h = [1.8^2(0.05)/0.145]^{1/2} = 1.057$$

SIMPLE UNSTIFFENED PANEL EXAMPLES

In order to illustrate the link-up phenomenon a simple case of a lead crack in an infinitely wide 2024-T3 unstiffened panel is shown in Figure 10. The curve ABEF represents the residual strength for the lead crack alone uninfluenced by any MSD and is simply based on equation 1 with the plane stress fracture toughness K_c assumed to be 150 KSI $\sqrt{IN}$. Now assume that a pair of 0.19 inch diameter holes containing 0.05 inch long MSD cracks are located ahead of the lead crack tips each at a distance 8 inches from the panel center line as shown on Figure 10. Line HBC is a plot of stress σ_R as a function of lead crack half length a_2 which will cause link-up of the MSD crack with the lead crack tip. Line HBC is based on equation 4 with β_s = 1.0 for the infinite wide unstiffened panel. The term $(P-d/2-a_1)$ in equation 4 is replaced by L, the distance between the lead crack tip and the MSD crack tip.

Therefore: $\sigma_R = \{2\sigma_y L/[\beta_h^2\beta_{11}^2 a_1 + \beta_s^2\beta_{12}^2 a_2]\}^{1/2}$ [5]

For this example β_h = 1.057, σ_y is assumed 50 KSI, β_{11} and β_{12} are obtained from reference 10 Figures 75 and 76 respectively. Referring to Figure 10, imagine this panel in a tensile testing machine with lead crack half length equal to a_{EX} as shown on Figure 10. If the remote stress applied to the panel is increased to σ_{EX} corresponding to point J then link-up of the MSD crack with the lead crack will occur and the effective lead crack length will suddenly increase to point K but will still be stable. The remote stress can now be increased to point E when fast fracture and failure will occur. It can be seen on Figure 10 that the residual strength for lead cracks beyond point B will be reduced to point E.

Now consider two pairs of 0.19 inch diameter holes containing 0.05 inch long MSD cracks at distances 8 and 9 inches from the panel center line as shown on Figure 11. Again line ABGH represents the residual strength for the lead crack uninfluenced by MSD. Line LBC is a plot of remote stress σ_R as a function of lead crack half length a_2 which will cause link-up of the MSD crack, centered at 8 inches from the panel center line, with the lead crack tip. Similarly, line ME is a plot of remote stress σ_R which will cause link-up with the second MSD crack centered at 9 inches from the panel center line. Lines LBC and ME are based on equation 5. Referring to Figure 11, again imagine the panel is in a tensile testing

machine with lead crack length equal to a_{EX}. If the remote stress is increased to σ_{EX} then the MSD crack located at 8 inches will suddenly link-up with the lead crack at point J. The lead crack will now be of half length given by point K and will be stable at remote stress σ_{EX}. If the remote stress is again increased the second MSD crack located at 9 inches will link up with the new lead crack at point E which will suddenly extend to point F. The lead crack will remain stable at this stress. If now the remote stress is increased to point G fast fracture will occur and the panel will fail. Figure 11 illustrates that residual strength of lead cracks beyond point B will be reduced to point G under the influence of the two MSD cracks.

Following this process, Figure 12 illustrates the case when several MSD cracks are located ahead of the lead crack tip. In the example shown five MSD cracked holes were considered. It can be seen that the lead crack does not arrest in a hole which would allow a higher stress to be applied up to curve ABG with no MSD at half lead crack lengths beyond B and stress levels higher than E. For lead cracks with lengths beyond point B the residual strength is reduced to a stress no higher than point E.

The analysis developed to plot Figure 12 was repeated with MSD crack lengths 0.01 inches. The resulting residual strength diagram is shown on Figure 13. The loss in residual strength is not as great as shown by Figure 12 for 0.05 inch MSD cracks but is still substantial as indicated by the drop from point B to point E. It must be remembered that even though the MSD crack of 0.01 inch assumed for this example appears very small it occurs at a fastener hole so the effective length of the crack is 2(0.01) + diameter of the hole in addition to any geometrical effects of the hole itself.

It can be seen from these simple examples of unstiffened panels that extremely small MSD cracks of a size that would be in-service non inspectable could reduce the residual strength of lead cracks used in the evaluation to certify the aircraft. However each area of the aircraft, susceptible to MSD, would need to be reviewed to determine the size of MSD that would reduce the residual strength capability below certification limits.

LARGE DAMAGE SIZE SUBSTANTIATION

Many of the aging fleet of transport aircraft, designed prior to amendment 45 of FAR 25.571, were substantiated for large damage capability. Figure 14 illustrates typical fuselage damage sizes substantiated by both analysis and testing. The example shown happens to be for the DC-10 aircraft (Figure 32 of reference [4]) but other aircraft are capable of similar damage. These damage sizes were used for substantiation of the aircraft to the certifying authorities and also used to market the aircraft to the airlines. The subsequent maintenance and inspection programs reflected a certain level of confidence which directly related to this large damage capability. Without this confidence the inspection program may have been much more demanding in terms of

inspection reliability requirements. As the airplanes age, beyond the time which can be substantiated by fatigue testing, the probability that these damage sizes can be retained at the required load levels will diminish with time. Thus, the fairly comfortable feeling enjoyed by the authorities and the flying public created by this large damage capability will also diminish with time. The manufacturers, having all the design data at their disposal, need to establish the point in the life of the aircraft at which the residual strength at these damage sizes will diminish below the required levels. It is believed this can be done with existing evaluation methods.

COMPLEX STIFFENED FUSELAGE STRUCTURE

The methods used to illustrate the considerable effect of MSD on simple unstiffened panels can be extended to complex stiffened structures. Conventional finite element analyses, normally used to calculate stress intensity factors for stiffened structures, can be used to calculate the term β_s in equation 4. A typical finite element idealization, used to calculate the stress intensity factor and stiffener stresses for the case of a longitudinal crack in a fuselage panel, is shown in Figure 15. This analysis is described in more detail in references [14] and [15]. As illustrated in Figure 15 loads are applied to the top of the panel and reactions at the bottom are disconnected one at a time to simulate the propagating crack. The center frame reactions can also be disconnected to represent a broken frame. The effect of stiffening on the crack tip stress intensity factor is obtained by analysis of the unstiffened panel and again of the stiffened panel. The value of β_s is determined by taking a ratio between the stiffened panel and the unstiffened panel crack tip stresses. Crack tip stresses are considered to be the stresses in the last bar still connected to a reaction as shown in Figure 15. The stress intensity factor K for a lead crack can therefore be calculated for a particular fuselage design. The effect of MSD on the residual strength of this lead crack can be determined through the use of equation 4. For a longitudinal crack case in a pressurized cabin equation 4 in this paper can be modified to include the effects of bulging due to pressure by including an additional bulging factor β_B as shown in equation 4 of reference 5.

DISCRETE SOURCE DAMAGE CASE

As an example, let us first consider a pressurized fuselage panel subjected to discrete source damage. Figure 14 shows this damage size for one aircraft type. Figure 5 illustrates testing normally performed to satisfy the requirements of FAR 25.571 paragraph (e), Damage Tolerance (discrete source) evaluation. Harpoon blades, simulating engine disc fragments, are fired into the pressurized and loaded fuselage. This testing is performed to verify that explosive decompression will be prevented in the event the fuselage sustains damage from a disintegrating engine. Examples of the result of this type of testing are shown in reference [4] for the DC-8 aircraft. As the aircraft ages, particularly beyond the life

substantiated by fatigue testing, the possibility exists that MSD may reduce the residual strength capability demonstrated during certification. The size of MSD which can degrade the residual strength below the certified level will depend on the structural configuration. For example, Figure 16 shows two different fuselage circumferential frame designs. Both of these designs are typical of transport aircraft in service today. One has a titanium crack stopper strap and the other does not. Reference [14] contains the results of finite element analysis which can be used to illustrate the differences in these two design concepts.

The frame cross sections for these two typical examples are shown in Figure 17. The sections were idealized as shown. The idealized areas were chosen to simulate the frame cross sectional area and bending moment of inertia. The idealization on the left considers the case with a 0.025 inch thick titanium crack stopper strap 3.0 inches wide with 3, 3/16 inch diameter rivet holes across the section. The idealization for this element was simulated by an equivalent aluminum area of 0.1035 square inches as shown. The frame for this design concept was idealized by the two elements shown which were equal to the total frame area and set in a location to simulate the bending section properties of the frame. The idealization for the frame without the crack stopper strap is shown to the right in Figure 17. In this case the frame was idealized by three elements as shown.

One of the most important considerations in this analytical method is the correct simulation of the flexibility of the load path from the cracked skin into the frame member. Figure 18 shows how this shear path was idealized for the panels described in reference [14]. The diagram to the left shows the shear clip to frame rivet flexibility represented by springs having the same stiffness as the rivets. A shear panel of length b and height h_1 represents the portion of the shear clip above the longeron cutout. The shear panel of length b_2 and height h_2 represents the portion of the shear clip between the longeron cutouts. The shear flexibility of this system is calculated and simulated to a single shear panel B shown to the right of Figure 18. The thickness of this shear panel is calculated to give the same flexibility as the system to the left. Equations used to make this equivalence are shown in reference [15].

The residual strength of a cracked stiffened panel from a skin fracture viewpoint is given by:

$$\sigma_R = K_c/[(\pi a)^{1/2}\beta_S\beta_B] \qquad (6)$$

Where K_c is the skin material plane stress fracture toughness assumed to be 158 KSI $\sqrt{IN}$ for 2024-T3 for this example, β_S is the effect of geometrical elements such as frames, a is half the crack length and β_B is a geometrical effect caused by crack tip bulging due to pressure and shell radius. Since all of the stiffening material at the center of the crack is assumed failed for the discrete damage case the bulging effect has been assumed to behave

like a one bay crack with the bay equal to two frame spacings. The term β_B used here is based on Paul Kuhn's unstiffened shell data [16] together with a cosine function to damp out the bulging as the crack tip approaches the intact frame. The bulging factor used for this analysis was suggested by Prof. Dr. Lüder Schwarmann [17]. The resulting term is:

$$\beta_B = 1+5(2a)/R[\text{Cos}(\pi a/P] \quad (7)$$

Where a = half crack length
R = shell radius
P = frame spacing

Values of the term β_S, for the frame with crack stopper configuration shown in Figure 17, can be obtained from case 5 on page 180 of reference [14]. The values are given in terms of R_{ct} which is the reciprocal of β_S. The critical stiffening element will be the outer crack stopper. Values of the stress concentration factor for the outer crack stopper are also given as σ_{ocs}/σ for case 5 in reference [14]. However, the gross applied stress σ used to calculate the allowable crack stopper stress should only be based on the skin hoop stress whereas in the case of the skin fracture criterion it is usual to consider the principal stress calculated from the effects of hoop stress and skin shear due to fuselage bending. For the example shown here the skin shear is assumed to correspond to a 1.5g fuselage down bending case and is assumed to be 7.37 KSI. The hoop stress corresponds to 82% PR/t and is assumed to be 12.45 KSI. The principal stress is therefore 15.872 KSI. The ratio between the hoop stress and the shear stress is 0.7844. For purposes of plotting a residual strength curve in the usual way the curve is plotted in terms of principal stress when considering the skin fracture criterion. This is slightly conservative because the principal stress acts at an angle but barrel tests [14] have indicated the conservatism is not great. However, the crack stopper stress is only a function of hoop stress so the crack stopper allowable stress at any one crack length is divided by the ratio of 0.7844 to obtain the corresponding principal stress. This is done solely to plot the crack stopper allowable on the same diagram as the skin fracture criterion. The residual strength from a skin fracture viewpoint is calculated in Table 1. As mentioned previously β_S values are obtained from case 5 of reference [14] and β_B is obtained from equation 7.

The residual strength for the configuration with frames without crack stoppers, as shown to the right of Figures 16 and 17, is calculated in Table 2. The finite element analysis results used for this configuration were taken from Case 1 of reference [2] and modified to include the effects of a broken central frame. The results of these two analyses are compared on Figure 19. For the configuration with crack stoppers the residual strength for the two bay crack condition is given by point B which is at the intersection of the skin fracture and outer crack stopper strength curves. Any fast fracture of the skin crack below point B would be arrested. Any fast fracture above B would not be arrested and

complete failure would be precipitated by outer crack stopper failure. The allowable from a skin fracture viewpoint alone is given by point C. In the case of frames without a crack stopper the residual strength is given by point A at the peak of the skin fracture curve. In this case the frame outer cap stress is low enough to cause the allowable from a frame strength viewpoint to be well above the skin fracture allowable.The reason for this is that the load path from the cracked skin into the frame element is extremely flexible as indicated on Figure 18. The frame acting alone is not as effective as the configuration with crack stoppers and this is illustrated by a comparison of the two peaks of the two fracture curves at points A and C. As in the case of the crack stopper, the frame allowable has been increased by dividing by 0.7844. Again, this is done solely to be able to plot the allowable frame stress on the same diagram as the skin fracture criterion. The frame is only loaded from the effects of hoop stress due to cabin pressure whereas the skin fracture criterion is influenced also by skin shear resulting in a skin principal stress. Figure 19 illustrates that both configurations have crack arrest capability at the typical 1.5g plus 82% PR/t stress expected during the discrete source damage event.

Suppose now the aircraft has aged to the extent that MSD has started to form in the skin at fastener holes. Suppose also that stiffener to skin rivet spacing in a longitudial direction, either a skin splice or at a longeron to skin attachment, is 1.25 inches. During the discrete source damage event assume skin ripping has taken place creating a simulated lead crack with fastener holes containing MSD ahead of this simulated lead crack. In other words suppose discrete source damage has occurred to a structure already damaged by fatigue created by utilization beyond the time supported by fatigue test. The effect of this MSD on the residual strength is illustrated by Figure 20 for the configuration of frames with crack stoppers. The effect of various MSD crack sizes on the skin fracture curve is illustrated. The assumption made here in order to illustrate this effect is that there is always a MSD crack centered 1.25 inches ahead of the lead crack tip. This is a reasonable assumption if the lead crack is propagating along a row of fastener holes. The residual strength is given by points B, C and D for MSD crack sizes 0.05, 0.10 and 0.15 inch respectively. The three curves showing the effect of MSD on skin fracture are based on equation 4 which was modified to include the effects of bulging at the lead crack tip given by equation 7. The resulting modified equation is:

$$\sigma_R = \{2\sigma_y^2(P-d/2-a_1)/[\beta_h^2\beta_{I1}^2a_1 + (\beta_S\beta_B)^2\beta_{I2}^2a_2]\}^{1/2} \qquad (8)$$

The calculation for the configuration with crack stoppers and 0.05 inch MSD cracks is shown in Table 3 as an example. The calculation for the other two MSD cracks is similar. Figure 20 illustrates that even though a considerable loss in residual strength due to MSD occurs as indicated by points B, C and D compared to A the configuration with titanium crack stoppers can tolerate a certain amount of MSD. This is shown by comparing the residual strength at

points B, C and D with the applied principal stress level. The calculation for the configuration without crack stoppers is shown in Table 4 for MSD crack sizes 0.05 inch. The calculation for the other two crack sizes is similar. The effect of MSD for the configuration of frames without crack stoppers is shown on Figure 21. Assuming the skin crack arresting frame member is uncracked its allowable is well above the skin fracture curves. The effect of MSD on skin fracture is shown by the three curves whose peaks are at points B, C and D for MSD cracks 0.05, 0.1 and 0.15 inches respectively. Figure 21 illustrates that 0.05 MSD cracks reduce the residual strength down to just above the required value while 0.1 inch MSD cracks and greater cause the residual strength to drop below the required principal stress.

The calculations made reflect a considerable loss in residual strength with even extremely small cracks and the sensitivity to actual MSD crack sizes appears to diminish to some extent. However, the longitudinal fastener spacing appears to have considerable influence on the resulting residual strength. In order to illustrate this the exercise was repeated for a rivet spacing of 1.0 inches. This is a realistic longitudinal rivet pitch for typical transport aircraft fuselage structure. The calculation for the case with crack stoppers is shown in Table 5 for 0.05 inch MSD cracks and 1.0 inch rivet spacing. For frames without crack stoppers the calculation is made in Table 6 for 0.05 inch MSD. As before the calculations for the other MSD crack sizes are similar. Figure 22 shows the results in the case of frames with crack stoppers. As before a considerable loss in residual strength is shown for the three MSD crack sizes but the allowables for the two bay crack case given by points B, C and D are still above the applied principal stress. These points are shown compared to point A which illustrates the residual strength with no effect of MSD.

For the case with no crack stoppers the original residual strength with no effect of MSD is given by point A on Figure 23 which is above the applied principal stress. However, for all the MSD crack sizes considered from 0.05 to 0.15 inches the allowable for the two bay crack case is below the applied principal stress.

It can be seen from these examples that the size of MSD which could degrade the residual strength capability below the required level is very much influenced by the structural configuration. In some cases the monitoring period, defined in Figure 1, may be useful to verify the onset of WFD because the MSD crack sizes may be in-service inspectable. On the other hand there may be some structural configurations where the residual strength has already become degraded below the required residual strength levels before the MSD is in-service inspectable. In these cases the operators will have a tough time convincing the authorities that the initial manufacturers' estimate of the onset of WFD can be escalated. Figure 24 illustrates that for the case without crack stoppers MSD in the order of 0.032 inches would need to be found to prevent the residual strength from being degraded below the required value.

A school of thought exists that the effect of MSD on the residual strength capability of the pressurized fuselage in the event of discrete source damage from engine disintegration can be managed by risk assessment. The Joint Airworthiness Regulations JAR ACJ No. 2 to JAR 25.903 (d)(1) outlines procedures to minimize the risk in the event damage is sustained by a disc fragment. An evaluation should show that there is more than a 1 in 20 chance of catastrophe created by a one third piece of disc plus one third the height of a blade. This is normally done by limiting the sum of the risk angles to 360/20 = 18 degrees as illustrated by Figure 25. Each critical system and structural element is evaluated and a risk angle θ determined for each. For example, Figure 25 identifies a critical system A the loss of which would cause catastrophic loss of the aircraft. If the loss of this system would occur with disc fragment trajectory between θ_1 and θ_2 then θ_A is the critical risk angle for system A. The sum of all the risk angles including systems and structures should be less than or equal to 18 degrees. However, this procedure does not eliminate the need to consider the effects of MSD on longitudinal damage. If in fact longitudinal damage cannot be contained then the structural angle of risk may already be above the 18 degree limit. This is illustrated by Figure 26 which shows that if the fuselage were pierced between angles θ_1 and θ_2 and the longitudinal damage could not be contained, as illustrated by Figure 23 for the frames without crack stoppers, then the critical structural angle would be 40 degrees for the airplane illustrated. This already exceeds the 18 degree limit without considering any systems. The point here is that risk analysis does not eliminate the need to establish an onset of WFD which would degrade the residual strength capability below required levels in the event of discrete source damage.

A typical residual strength curve for the configuration without crack stopper straps is shown by the lower curve of Figure 19. The structural configuration here involved a fairly substantial frame section as shown by Figure 17. Figure 19 shows that the residual strength peak, given by point A, is above the typical applied principal stress for the discrete source damage case. If the frame member is of lighter construction, however, the peak A could be lower than the applied stress and the damage may not be arrested if fast fracture took place during the discrete source damage event. It may have been demonstrated during certification by harpoon testing that fast fracture would not take place. In fact this would be the case as illustrated by Figure 19. Suppose for example a 12 inch wide blade were used. Figure 19 shows that fast fracture would not occur even allowing for stable growth of say 2 inches making total damage length 14 inches. This would appear to satisfy the discrete source damage requirement. If on the other hand MSD had existed ahead of the lead damage as shown by Figure 27 link up would certainly occur extending the lead damage to a point where fast fracture would occur. If crack arrest capability at the outer frame does not exist, ie., point A of Figure 19 is below the applied principal stress, then explosive decompression would occur. The configuration shown by Figure 27 is particularly

difficult to deal with because crack tip bulging would be nearing a maximum as the tip approaches a point halfway between frames. For example, Table 2 shows for half crack length of 7.5 inches (total 15 inches) the values of β_S and β_B are 1.3779 and 1.526 respectively. β_S is higher than 1.0 because of the broken frame. Multiplying these values in equation 8 gives one of the most critical locations for link up as the crack moves across the bay. It appears that this condition is the most critical for those fuselages not able to contain a two bay crack with a broken frame.

FUSELAGE CIRCUMFERENTIAL CRACK

Probably one of the most critical locations for fuselage cracking is on the crown just over the rear spar of the wing at a location where circumferential frames are attached with shear clips. As indicated by Figure 14 the large damage criterion is to design for a two bay skin crack with a broken central stiffener for limit load. For most commercial transport aircraft the limit stress at this location is about 34 ksi. This damage scenario originates due to the fact that the stiffener, at the attachment to the frame, is critical in bending at the frame due to pressure. In addition, axial stresses are applied from fuselage down bending loads. The stiffener is critical in fatigue and if this cracks and fails and this condition remains undetected the skin becomes highly loaded and eventually cracks. The skin crack propagates into two bays. Figure 28 shows the residual strength curve for a typical location on the crown of the fuselage. The example shown assumes 2024-T3 skin 0.071 inches thick, hat section stiffeners with area 0.3029 square inches and stiffener spacing 8.0 inches. Stiffeners are 7075-T6 extrusions with ultimate tension strength 82 KSI. Skin fracture toughness is assumed 158 KSI $\sqrt{IN}$. The results of finite element analysis for this configuration are contained as case 15 of reference [14]. The residual strength calculation is shown in Table 7. The term R_{ct}, quoted in reference [14], is actually the reciprocal of β_S. The term σ_{OS}, quoted in Table 7, is the stress concentration factor in the stiffener, ie., the stiffener outer fiber stress per KSI of applied gross stress. The residual strength for the two bay crack condition is given by the intersection of the skin fracture and outer stiffener strength curves at point A. Any fast fracture at a gross stress lower than this point would be arrested. Fast fracture at stresses higher than point A would not be arrested and failure would be precipitated by stiffener strength criteria. It can be seen that this configuration is able to tolerate a two bay skin crack at the limit stress of 34 KSI. The effect of MSD is shown and illustrates the considerable loss in residual strength to well below limit capability. The calculations for the 0.05 inch MSD crack configuration, based on equation 5, are shown in Table 8. The calculations for the 0.01 inch MSD crack are similar. Rivet spacing in the circumferential direction is assumed to be 1.0 inches. As mentioned earlier the effect due to a very small crack such as 0.01 inches appears quite severe. One needs to remember that this crack is at both sides of a fastener hole and therefore it is effectively a crack of length 2(0.01) + rivet diameter. This is one area which would need a fairly detailed

investigation to find MSD small enough so as not to degrade the residual strength capability below limit strength.

ONSET OF MSD

Several examples of the effect of MSD in lead crack residual strength have been shown in this paper. It is evident that this analysis, based on the intuitive link up criterion illustrated by Figure 9, indicates considerable effects of structural configuration. The gross applied stress at link up appears to be more sensitive to rivet spacing than the size of MSD once it is assumed that a crack exists in the hole at the tip of the lead crack. Some configurations are able to tolerate much larger MSD sizes than other configurations. This was illustrated by the improvement in capability provided by a configuration with titanium crack stopper straps for the discrete source damage case. Each susceptible area needs to be assessed for the size of MSD which will degrade the lead crack residual strength below limit load. The time in the life of the aircraft at which this occurs will then need to be estimated. One way to obtain this is by a crack growth analysis starting with flaw sizes representative of the initial quality of the structure. This method is described in reference [18] which describes a test program designed to develop equivalent initial flaw sizes for various hole and fastener combinations. Figure 29 shows a typical example of equivalent initial flaw size plotted against cumulative probability. This data, reported in reference[2], was statistically analyzed to obtain a 95% confidence level. The example on Figure 29 shows that it can be assured with 95% confidence that 90% of the flaws would be less than 0.0012 inches. The example shown is for open reamed countersunk holes. Filled holes would most likely indicate a smaller size. This size falls into the well known "short crack problem" area so care would need to be exercised in growth calculations which use large crack da/dN data. Crack growth data would need to be generated at small crack sizes. Some people believe that short crack growth can be accurately calculated using Forman's equation which does not reflect a threshold value. This author has had some success with this as can be seen by Figure 21 of reference [18]. In this case growth rate was simulated by a Forman equation and crack growth started at 0.001 inches. The loading used was for a STOL transport aircraft spectrum and the Generalized Willenborg retardation model was used. Crack size was measured by striation count using an electron microscope on the failed fracture surface.

It is suggested that statistically determined equivalent initial quality flaw data could be used without any additional factors. The reliability would already be included with the flaw size chosen to represent a specific reliability and confidence level. This method would establish a life associated with a specific reliability level providing the time at which the lead damage residual strength level would be degraded below the regulatory level for the specific structural configuration being considered. Obviously, those designs with greater resistance to residual strength loss due to MSD would

provide longer onset times. Further discussion of the Equivalent Initial Quality Flaw concept can be found in a paper by Dr. John W. Lincoln [19].

The proposed monitoring period defined in Figure 1 could probably be reliably used to verify MSD onset prior to residual strength loss in the case where titanium crack stopper straps form a part of the design. However, where the design does not include crack stoppers considerable difficulty would be experienced finding the MSD before residual strength dropped below the required levels.

EFFECT OF EXTERNAL REPAIRS

Figure 30 illustrates a potential problem created by external repair doublers. Many of these repairs to fuselage skins are designed to meet static strength requirements only and virtually no consideration is given to damage tolerance capability. Many of these repairs are too thick causing high load transfer at the first row of fasteners. There is a possibility that hidden MSD in the skin under the doubler may lead to loss in lead crack residual strength as indicated in Figure 30. This problem is discussed in more detail in reference [20].

CONCLUSIONS

1) It has been shown using an intuitive link up criterion that MSD can have considerable effect on lead crack residual strength in complex stiffened structures.

2) The loss in residual strength is extremely sensitive to structural configuration and fastener spacing.

3) Frames with crack stoppers in fuselage structure provide much greater tolerance to MSD than frames without crack stoppers.

4) The industry proposed monitoring period to verify the onset of MSD may be reliable for some structural configurations and unreliable for others.

5) In-service inspection techniques will not be adequate for some structural configurations to validate the onset of WFD established by the manufacturers prior to loss in residual strength below limit.

6) Validation of the onset of WFD during the monitoring period may require local tear down inspection in order to find MSD before certified residual strength is degraded for some structural configurations.

RECOMMENDATIONS

1) It is recommended the FAA continue support for testing required to validate lead crack/MSD link up for complex stiffened structure.

2) It is recommended that the "Equivalent Initial Quality Flaw" concept be investigated to assist in establishing onset of WFD. Further research is needed to improve the reliability of prediction methods to grow short cracks of the order of 0.001 inches up to a size which would cause lead crack residual strength to be degraded below limit values.

3) Recommendation 2 may need further research on crack growth rate da/dN data for short cracks in materials used in the commercial aircraft industry.

4) It is recommended that research for MSD be concentrated on the effects of MSD on lead crack residual strength rather than on crack growth investigations with a view to establishing inspection programs to manage the safety of aircraft in the presence of MSD.

REFERENCES

[1] Air Transportation Association of America Final Report. Airworthiness Assurance Task Force Subcommittee on Fatigue Testing and/or Teardown Issues. February 1991.

[2] Swift, T., "Verification of Methods For Damage Tolerance Evaluation of Aircraft Structures to FAA Requirements". Presented at the 12th Symposium of the International Committee on Aeronautical Fatigue held in Toulouse, France, May 1983.

[3] Swift, T., "The Influence of Slow Growth and Net Section Yielding on the Residual Strength of Stiffened Structure". Presented at the 13th Symposium of the International Committee on Aeronautical Fatigue held in Pisa, Italy, May 1985.

[4] Swift, T., "Damage Tolerance in Pressurized Fuselages". 11th Plantema Memorial Lecture. Presented at the 14th Symposium of the International Committee on Aeronautical Fatigue held in Ottawa, Canada, June 1987.

[5] Swift, T., "Damage Tolerance Capability". Presented at Specialist' Conference on Fatigue of Aircraft Materials. Delft University of Technology, Delft, The Netherlands, October 1992.

[6] Liu, A.F., "Statistical Variation in Fracture Toughness Data of Airframe Materials". Published in Proceedings of the Air Force Conference on Fatigue and Fracture of Aircraft Structures and Materials. AFFDL TR 70-144. September 1970.

[7] Wang, D.Y., "Plane Stress Fracture Toughness and Fatigue Crack Propagation of Aluminum Alloy Wide Panels". Presented to Sixth National Symposium on Fracture Mechanics, ASTM. Philadelphia, Pennsylvania, August 1972.

[8] Feddersen, C.E. "Evaluation and Prediction of the Residual Strength of Center Cracked Tension Panels". Published in "Damage Tolerance in Aircraft Structures ASTM STP 486, 1971.

[9] Private Communication with Dr. Ron Mayville of A.D. Little Inc.

[10] Rooke, D.P. and Cartwright, D.J., "Compendium of Stress Intensity Factors". Published by Her Majesty's Stationary Office, London, England, 1976.

[11] Broek, D., "Elementary Engineering Fracture Mechanics". Published by Martinus Nijhoff Publishers, 1974.

[12] Private Communication : Commander Jim Moukawsher, USCG, Dec. 1992.

[13] Bowie, O.L., "Analysis of an Infinite Plate Containing Radial Cracks Originating from the Boundary of an Internal Circular Hole," Journal of Mathematics and Physics, Vol. 35, 1956.
[14] Swift, T., "Development of the Fail-Safe Design Features of the DC-10. Published in "Damage Tolerance in Aircraft Structures". ASTM STP 486, 1971.

[15] Swift, T and Wang, D.Y., "Damage Tolerant Design-Analysis Methods and Test Verification of Fuselage Structure". Published in Proceedings of the Air Force Conference on Fatigue and Fracture of Aircraft Structures and Materials. AFFDL TR 70-144, September 1970.

[16] Kuhn, P., "Notch Effects on Fatigue and Static Strength". Published in Proceedings of ICAF Symposium held in Rome, 1963.

[17] Private Communication with Prof. Dr. Lüder Schwarmann dated 3 June, 1991.

[18] Stone, M and Swift, T., "Future Damage Tolerance Approach to Airworthiness Certification". Presented at the 10th Symposium of the International Committee on Aeronautical Fatigue held in Brussels, Belgium, May 1979.

[19] Lincoln, J.W., "Assessment of Structural Reliability Derived From Durability Testing". Presented at the 17th Symposium of the International Committee on Aeronautical Fatigue held in Stockholm, Sweden, June 1993.

[20] Swift, T., "Repairs to Damage Tolerant Aircraft". Presented at The International Symposium on Structural Integrity of Aging Airplanes. Atlanta, Georgia, March 1990. FAA-AIR-90-01.

Table 1
Residual Strength Calculation
Two Bay Longitudinal Crack - Frames With Crack Stoppers - Center Frame and Crack Stopper Failed

(1)	(2)	(3)	(4)	(5)
a	β_S	β_B	$\beta_S\beta_B[\pi a]^{1/2}$	σ_R
4.50	1.2870	1.3560	6.5617	24.08
7.50	1.2136	1.5260	8.9895	17.58
10.50	1.1534	1.6020	10.6124	14.89
12.75	1.1161	1.5800	11.1607	14.16
15.50	1.0482	1.4530	10.6280	14.87
17.50	0.9681	1.2880	9.2455	17.09
18.50	0.8993	1.1840	8.1174	19.46
19.50	0.7133	1.0646	5.9436	26.58
20.50	0.5155	1.0646	4.4042	35.87
21.50	0.5200	1.1840	5.0600	31.23

Material 0.071 2024-T3 K_c Assumed 158 KSI $[IN]^{1/2}$

$$\sigma_R = 158/(4)$$

Table 2
Residual Strength Calculation
Two Bay Longitudinal Crack - Frames Without Crack Stoppers - Center Frame Failed

a	β_S	β_B	$\beta_S\beta_B[\pi a]^{1/2}$	σ_R
4.50	1.4741	1.3560	7.5157	21.02
7.50	1.3779	1.5260	10.2065	15.48
10.50	1.3160	1.6020	12.1084	13.05
12.75	1.2707	1.5800	12.7066	13.09
15.50	1.1962	1.4530	12.1268	13.03
17.50	1.1139	1.2880	10.6379	14.85
18.50	1.0541	1.1840	9.5147	16.61
19.50	0.9589	1.0646	7.9901	19.77
20.50	0.8565	1.0646	7.3212	21.58
21.50	0.8005	1.1840	7.7895	20.28

Material 0.071 2024-T3 K_c Assumed 158 KSI $[IN]^{1/2}$

$$\sigma_R = 158/(4)$$

Table 3
Effect of 0.05 Inch MSD on Residual Strength
Two Bay Longitudinal Crack - Frames With Crack Stoppers - Center Frame and Crack Stopper Failed

a_2	β_S	β_B	a_{e2}	a_{e2}/b	β_{I1}	β_{I2}	σ_R
19.5	0.7133	1.0646	11.24	9.73	2.44	1.0	20.34
20.5	0.5155	1.0646	6.17	5.34	2.01	1.0	27.19
21.5	0.5200	1.1840	8.15	7.06	2.12	1.0	23.85

$a_{e2} = (\beta_S\beta_B)^2 a_2$, $a_1 = \beta_h^2 a_1 = 1.057^2(0.145) = 0.162$ (constant)

$b = 1.25-0.095 = 1.155$, $a_{e1}/b = 0.162/1.55 = 0.1403$

$$\sigma_R = \{2\sigma_y^2(P-d/2-a_1)/[\beta_h^2\beta_{I1}^2 a_1 + (\beta_S\beta_B)^2\beta_{I2}^2 a_2]\}^{1/2}$$

$$\sigma_R = \{5050/[0.162\beta_{I1}^2 + (\beta_S\beta_B)^2\beta_{I2}^2 a_2]\}^{1/2}$$

Table 4
Effect of 0.05 Inch MSD on Residual Strength
Two Bay Longitudinal Crack - Frames without Crack Stoppers - Center Frame Failed

a_2	β_S	β_B	a_{e2}	a_{e2}/b	β_{I1}	β_{I2}	σ_R
19.5	0.9589	1.0646	20.32	17.59	3.31	1.0	15.12
20.5	0.8565	1.0646	17.04	14.75	3.01	1.0	16.52
21.5	0.8005	1.1840	19.31	16.72	3.22	1.0	15.50

Reference Table 8 for a_{e2}, a_{e1}, b, a_{e1}/b and σ_R

Table 5
Effect of 0.05 Inch MSD on Residual Strength
Two Bay Longitudinal Crack - Frames With Crack Stoppers -
Rivet Spacing 1.0 Inches

a_2	β_S	β_B	a_{e2}	a_{e2}/b	β_{I1}	β_{I2}	σ_R
19.5	0.7133	1.0646	11.24	12.420	2.80	1.0	17.43
20.5	0.5155	1.0646	6.17	6.820	2.11	1.0	23.48
21.5	0.5200	1.1840	8.15	9.006	2.38	1.0	20.47

$a_{e2} = (\beta_S\beta_B)^2 a2$, $a_{e1} = \beta_h^2 a_1 = 1.057^2(0.145) = 0.162$ (constant)
$b = 1.0 - 0.095 = 0.905$, $a_{e1}/b = 0.162/0.905 = 0.179$
σ_R based on equation 8 with $\sigma_y = 50$ KSI

Table 6

Effect of 0.05 Inch MSD on Residual Strength
Two Bay Longitudinal Crack - Frames Without Crack Stoppers -
Rivet Spacing 1.0 Inches

a_2	β_S	β_B	a_{e2}	a_{e2}/b	β_{I1}	β_{I2}	σ_R
19.5	0.9589	1.0646	20.32	22.45	3.84	1.0	12.94
20.5	0.8565	1.0646	17.04	18.83	3.50	1.0	14.13
21.5	0.8005	1.1840	19.31	21.34	3.76	1.0	13.26

Table 7
Results of Typical Finite Element Analysis
For Circumferential Crack

(1)	(2)	(3)	(4)	(5)	(6)
a	R_{ct}	β_s	σ_r	σ_{os}	σ_{st}
1.5	0.778	1.285	56.64	1.074	76.35
2.5	0.820	1.220	46.21	1.114	73.61
3.5	0.852	1.174	40.59	1.176	69.73
4.5	0.883	1.133	37.09	1.269	64.62
5.5	0.918	1.089	34.90	1.414	57.99
6.5	0.970	1.031	33.91	1.660	49.40
7.5	1.107	0.903	36.05	2.153	38.09
8.5	1.353	0.739	41.37	3.212	25.53
9.5	1.428	0.700	41.32	3.875	21.16

(3) = 1/(2)
(4) = $158/[(\pi a)^{1/2}\beta_s]$
(6) = 82/(5)

K_c = 158 KSI $[IN]^{1/2}$

F_{tu} = 82 KSI

Table 8
Effect of 0.05 inch MSD Crack on Lead Crack Residual Strength
Two Bay Circumferential Crack With Broken Central Stiffener

a_2	β_s	a_{e2}	a_{e1}/b *	a_{e2}/b **	β_{I1}	β_{I2}	σ_R
1.5	1.285	2.477	0.179	2.737	1.50	1.0	36.57
2.5	1.220	3.721	0.179	4.112	1.75	1.0	30.02
3.5	1.174	4.824	0.179	5.330	1.92	1.0	26.48
4.5	1.133	5.777	0.179	6.383	2.05	1.0	24.26
5.5	1.089	6.523	0.179	7.208	2.16	1.0	22.85
6.5	1.031	6.909	0.179	7.634	2.20	1.0	22.22
7.5	0.903	6.116	0.179	6.758	2.10	1.0	23.59
8.5	0.739	4.642	0.179	5.129	1.92	1.0	26.93
9.5	0.700	4.655	0.179	5.144	1.92	1.0	26.90

* 0.162/0.905, ** $a_{e2}/0.905$, $a_{e2} = \beta_s^2 a_2$

$$\sigma_R = \{2\sigma_y^2(P-d/2-a_1)/(\beta_h^2\beta_{I1}^2 a_1 + \beta_s^2\beta_{I2}^2 a_2)\}^{1/2}$$

$$\sigma_R = \{3800/(0.162\beta_{I1}^2 + \beta_s^2\beta_{I2}^2 a_2)\}^{1/2}$$

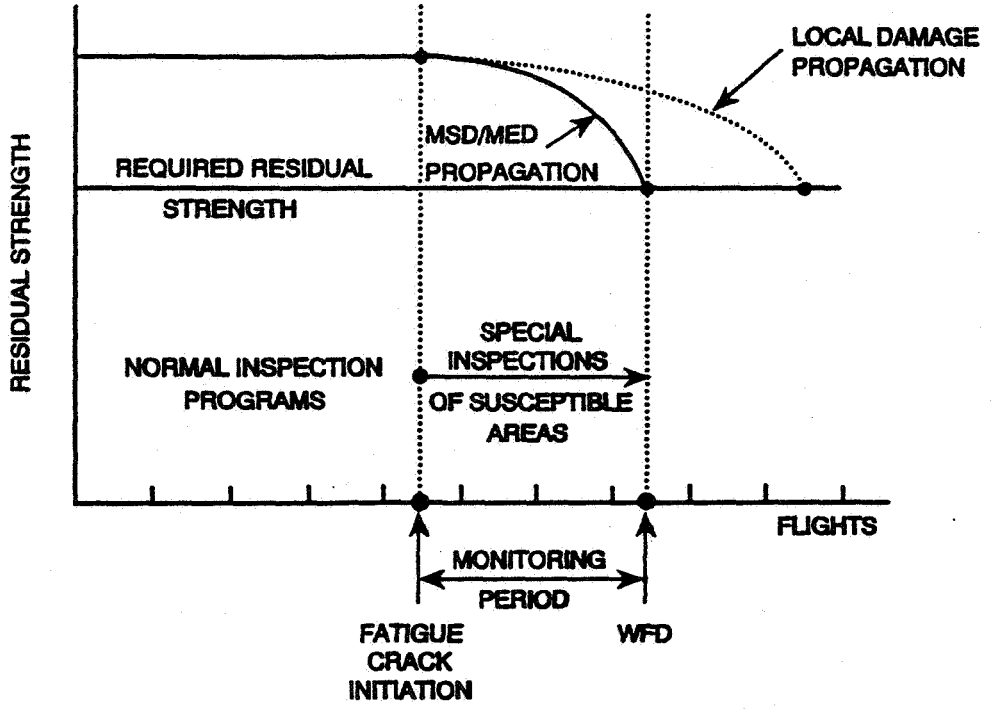

FIGURE 1 RESIDUAL STRENGTH CAPABILITY AND RESULTING INSPECTION ACTIONS

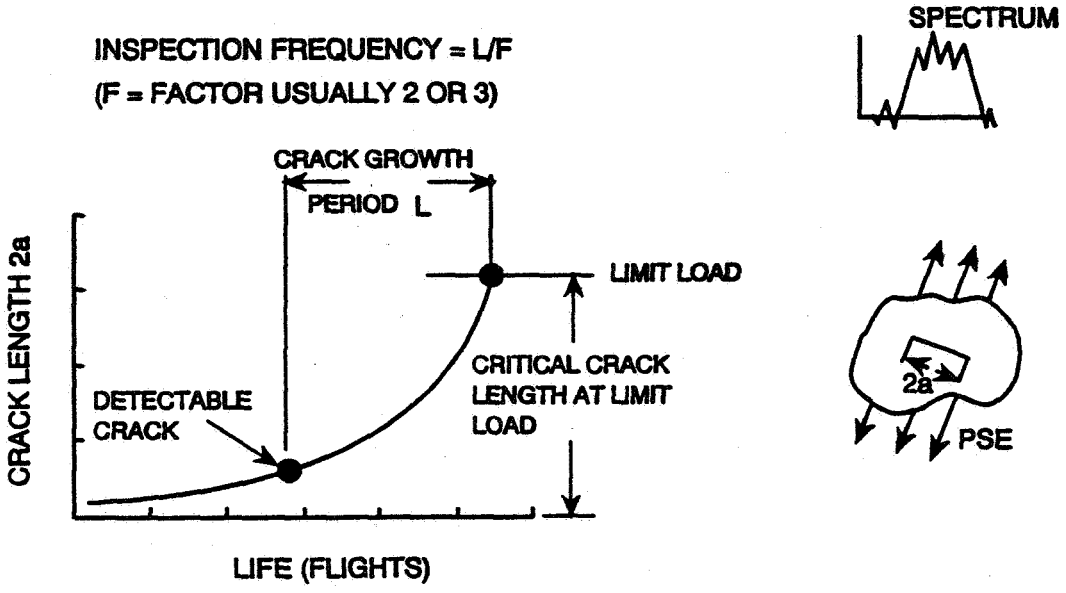

FIGURE 2 INSPECTION FREQUENCY FOR EACH PSE IS RELATED TO CRITICAL CRACK LENGTH

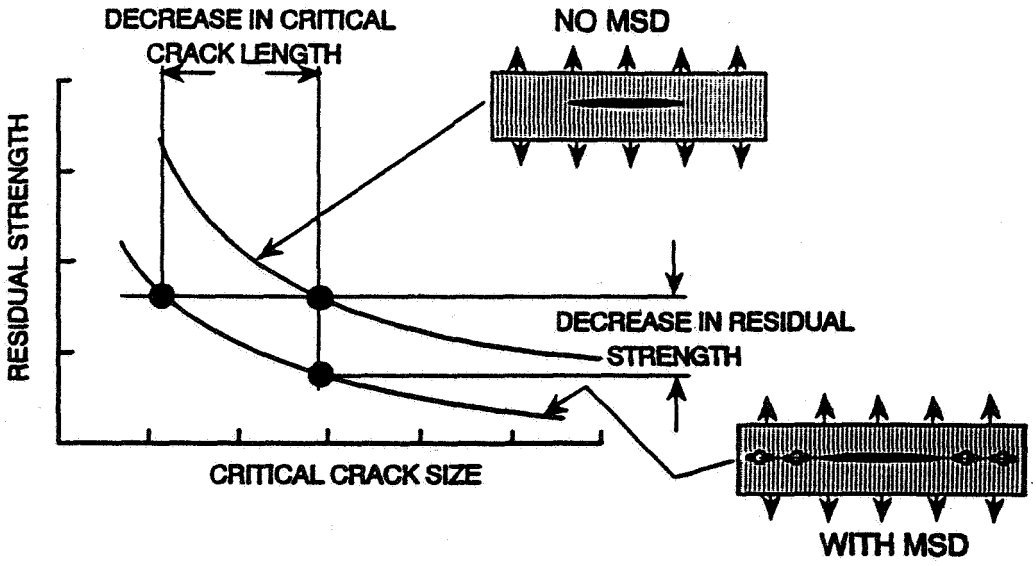

FIGURE 3 EFFECT OF MSD ON CRITICAL CRACK SIZE
AND RESIDUAL STRENGTH

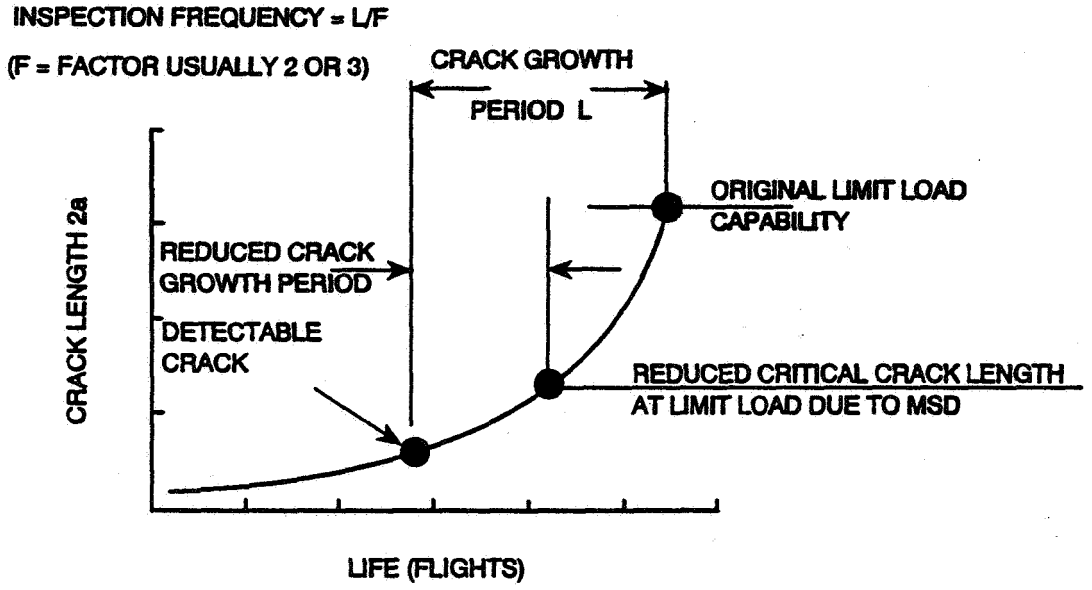

FIGURE 4 REDUCED LEAD CRACK INSPECTION FREQUENCY
RESULTING FROM REDUCED CRITICAL CRACK
SIZE DUE TO MSD

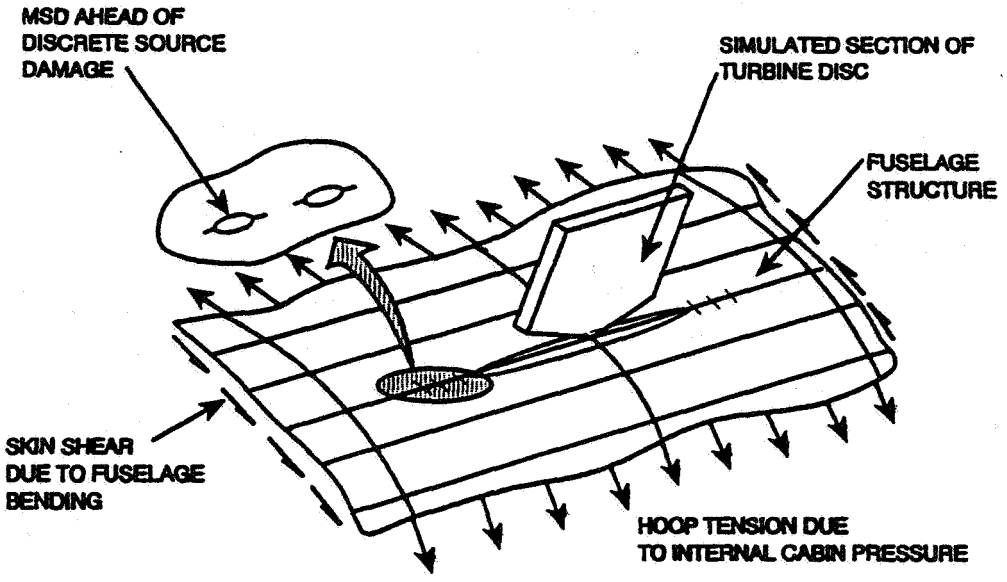

FIGURE 5 EFFECT OF MSD ON RESIDUAL STRENGTH
CAPABILITY DUE TO DISCRETE SOURCE DAMAGE

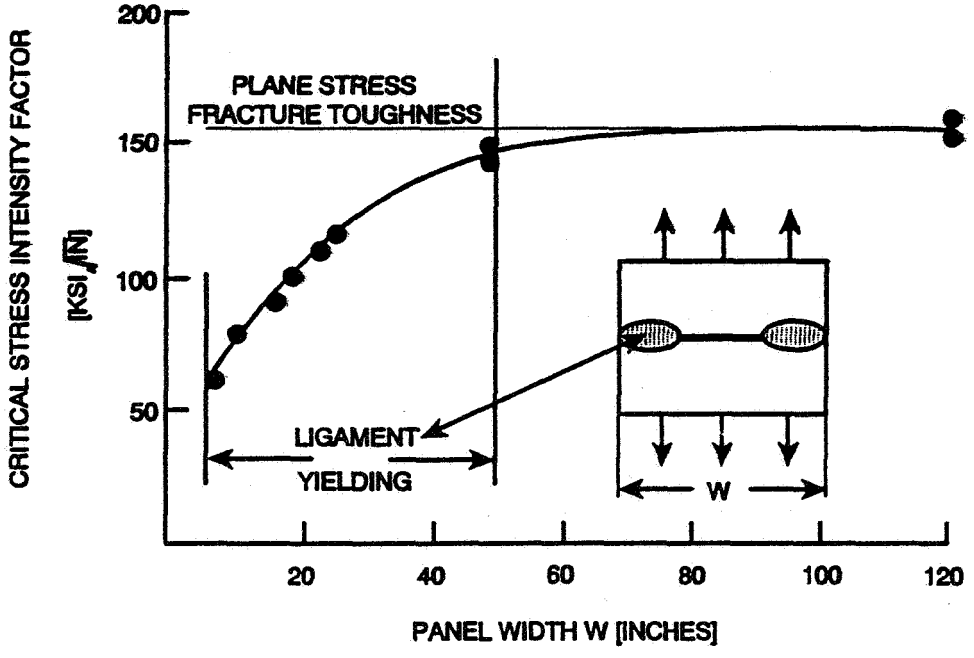

FIGURE 6 CRITICAL STRESS INTENSITY FACTOR VERSUS PANEL WIDTH
FOR LEAD CRACKS IN 2024-T3 SHEET 0.063 INCHES THICK

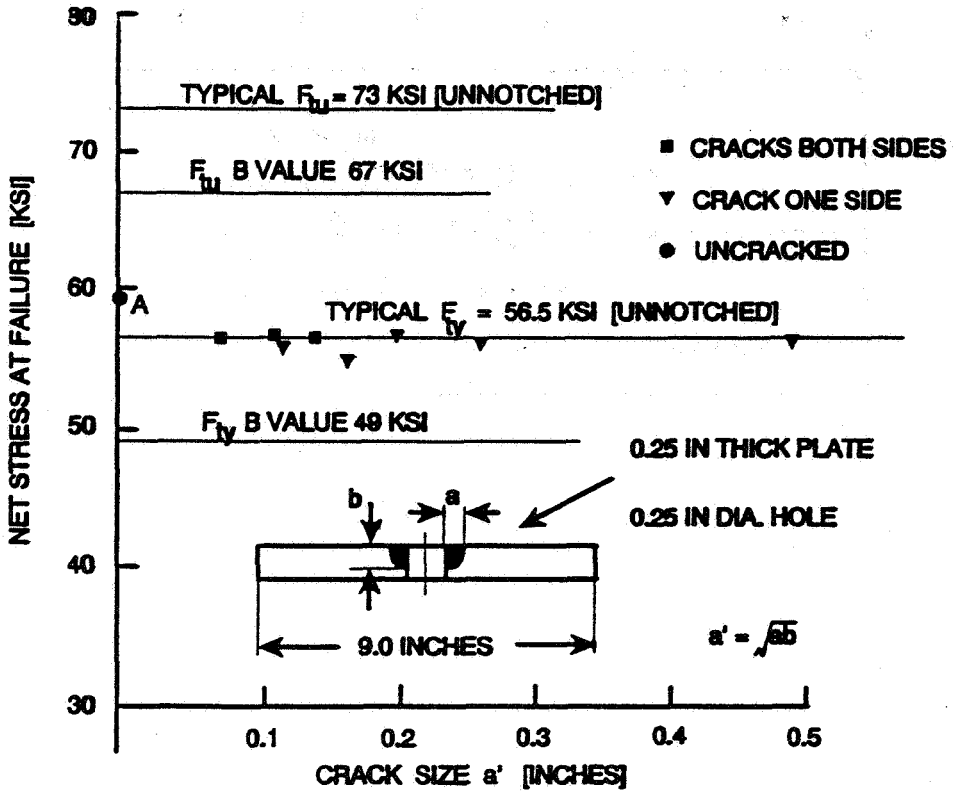

FIGURE 7 RESIDUAL STRENGTH FOR SMALL CRACKS IN 2024-T351 PLATE

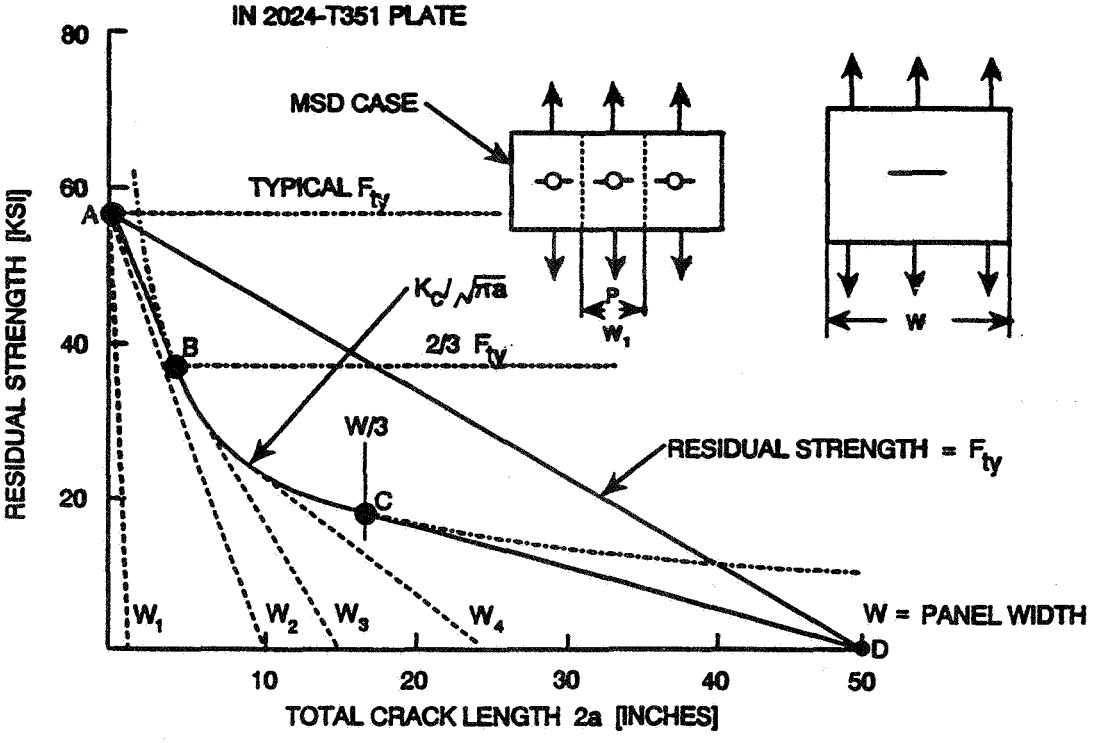

FIGURE 8 TYPICAL UNSTIFFENED PANEL RESIDUAL STRENGTH DIAGRAM BASED ON FEDDERSEN'S METHOD 2024-T351 PLATE

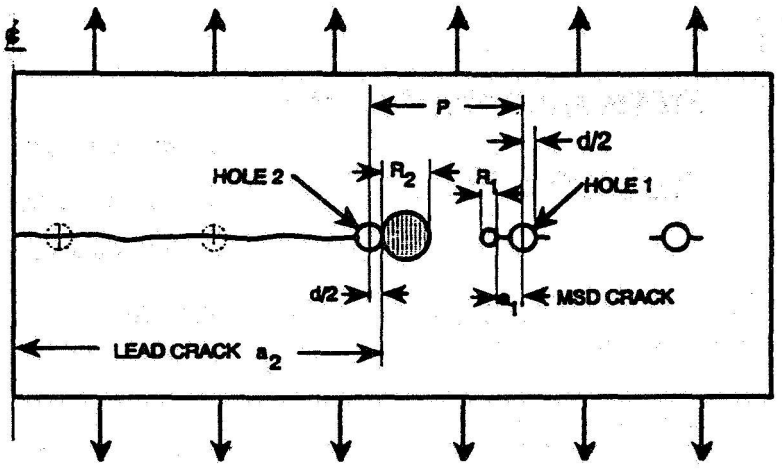

CRITERION FOR LINK-UP WHEN PLASTIC ZONES FROM LEAD CRACK AND MSD CRACK TOUCH

$$R_1 + R_2 = [P-d/2-a_1]$$

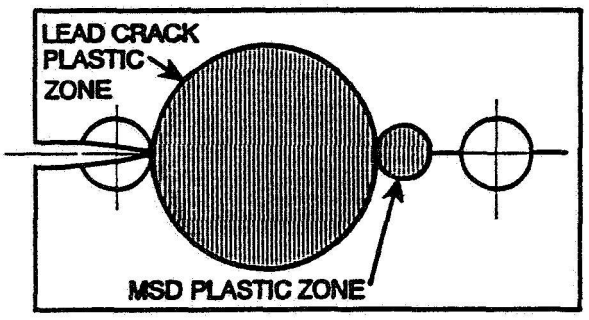

FIGURE 9 LEAD CRACK - MSD CRACK LINK-UP CRITERION

ONE SET OF 0.05 INCH MSD CRACKS

2024-T3 SHEET

NO MSD - RESIDUAL STRENGTH LINE ABEF

WITH MSD - RESIDUAL STRENGTH LINE ABCDEF

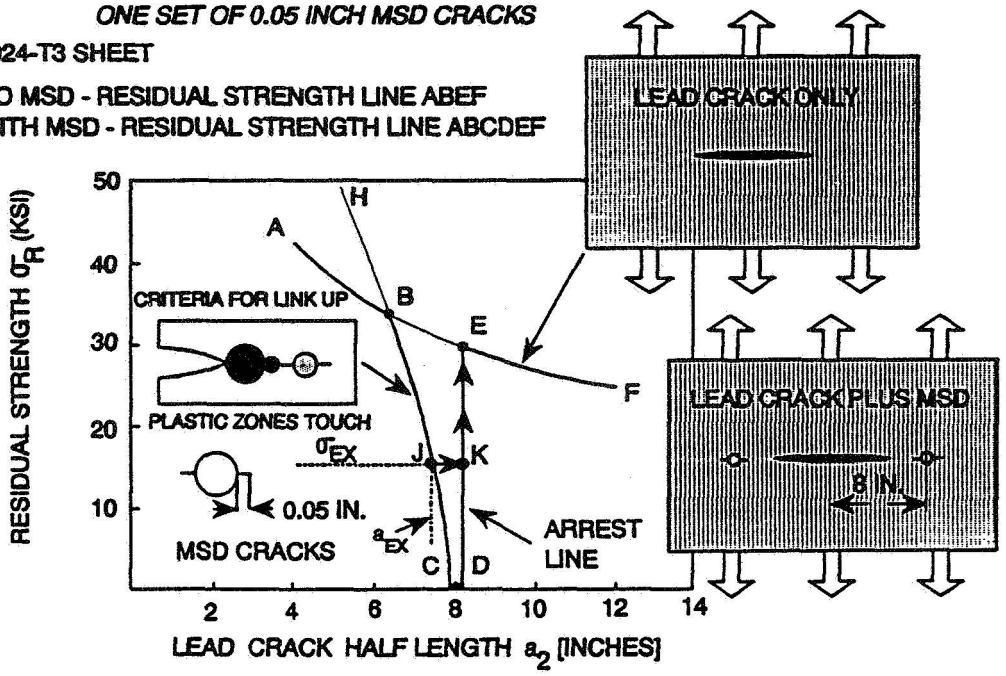

FIGURE 10 EFFECT OF MSD ON LEAD CRACK RESIDUAL STRENGTH
SINGLE 0.05 INCH MSD CRACK EACH SIDE OF LEAD CRACK

TWO SETS OF 0.05 IN.MSD CRACKS

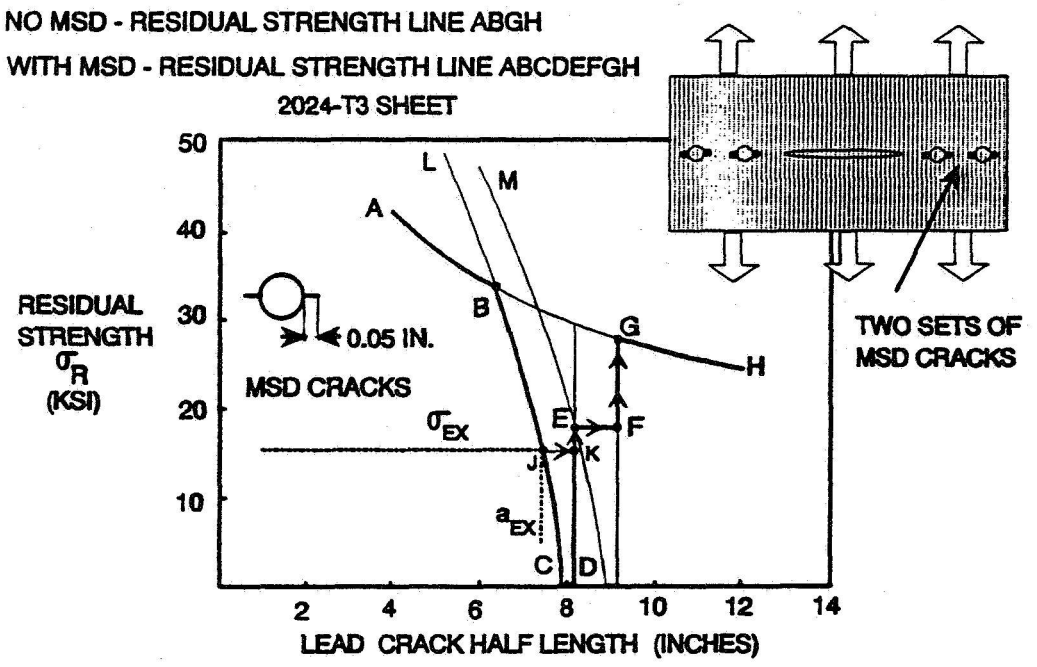

FIGURE 11 EFFECT OF MSD ON LEAD CRACK RESIDUAL STRENGTH
TWO SETS OF 0.05 INCH MSD CRACKS EACH SIDE OF LEAD CRACK

SEVERAL 0.05 IN. MSD CRACKS

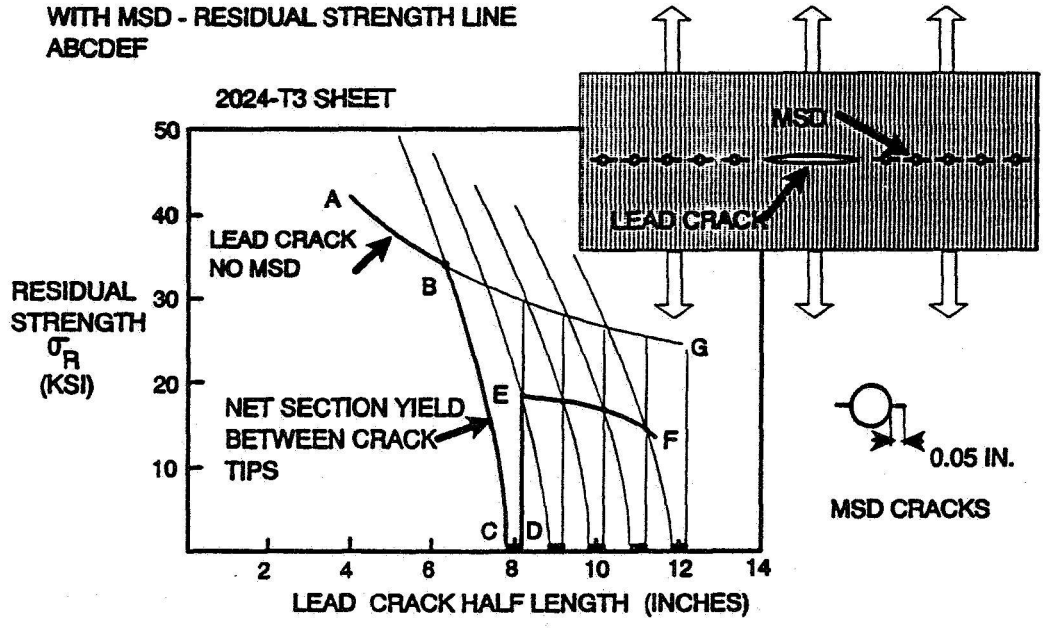

FIGURE 12 EFFECT OF MSD ON LEAD CRACK RESIDUAL STRENGTH
SEVERAL 0.05 INCH MSD CRACKS EACH SIDE OF LEAD CRACK

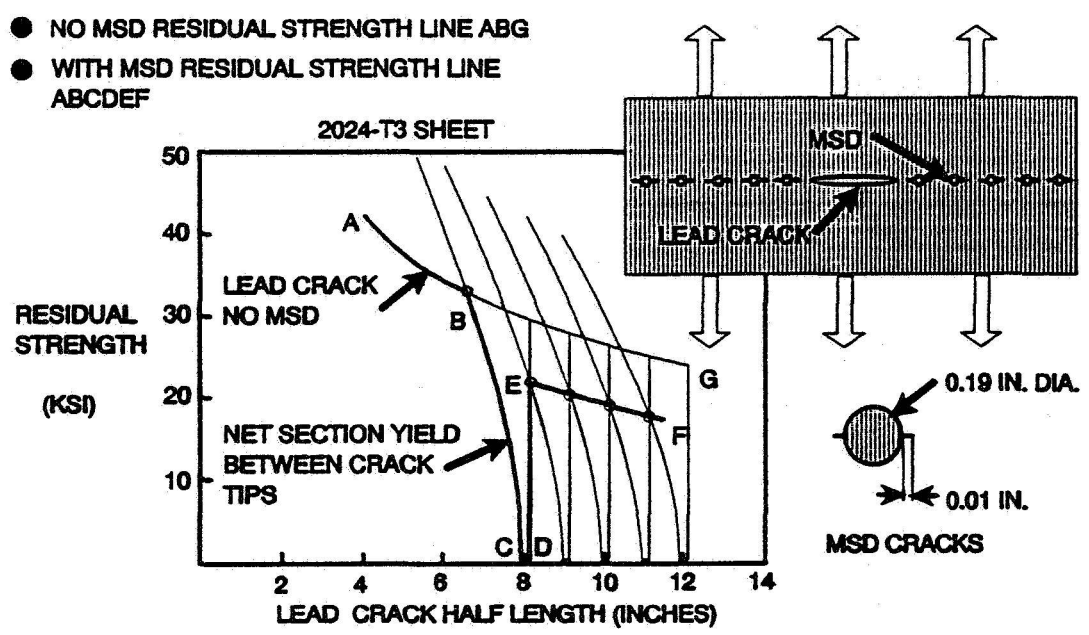

FIGURE 13 EFFECT OF MSD ON LEAD CRACK RESIDUAL STRENGTH
SEVERAL 0.01 INCH CRACKS EACH SIDE OF LEAD CRACK

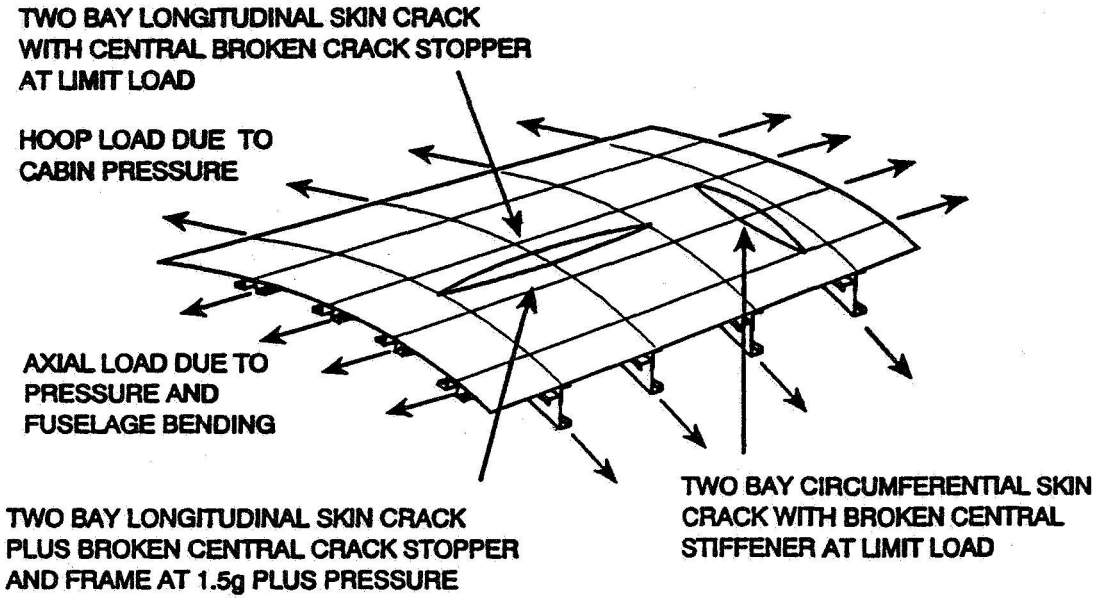

FIGURE 14 FUSELAGE DAMAGE SIZES USED FOR LARGE DAMAGE SUBSTANTIATION

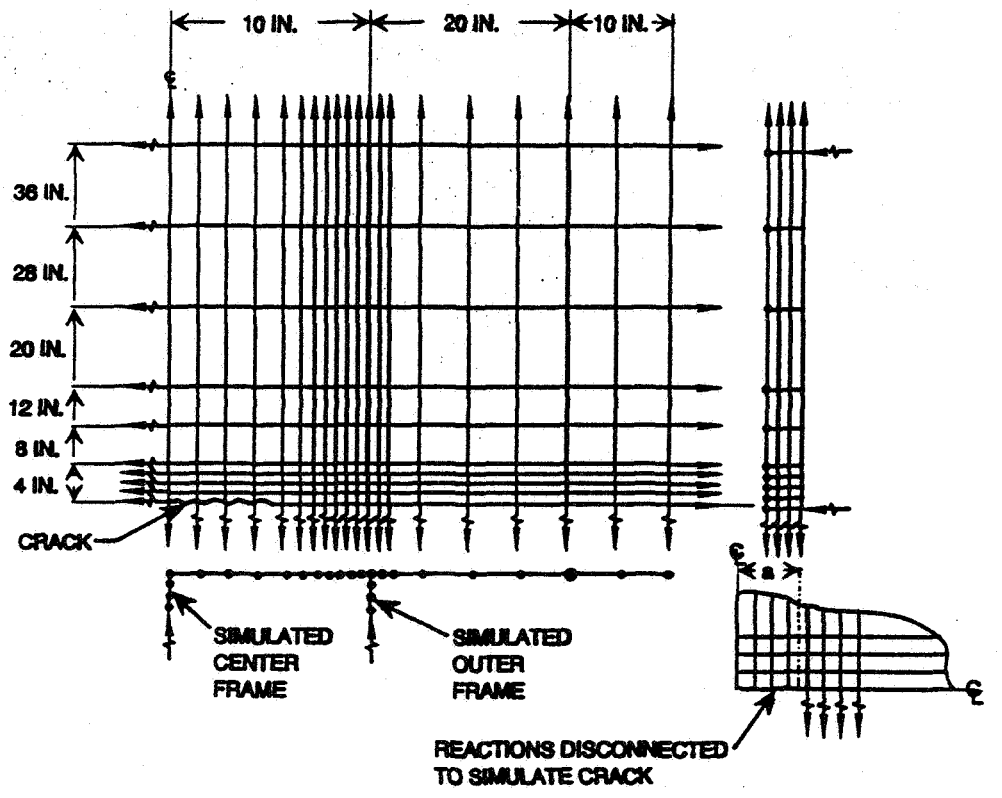

FIGURE 15 IDEALIZATION FOR TWO BAY LONGITUDINAL CRACK

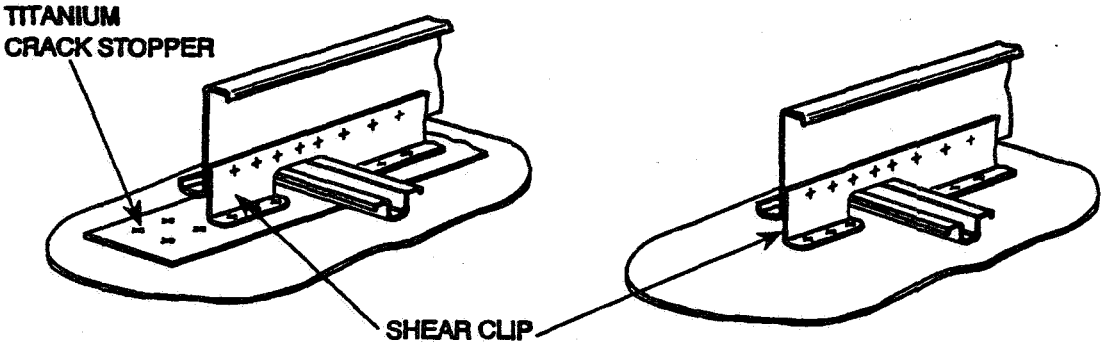

FRAME WITH TITANIUM CRACK STOPPER PLUS SHEAR CLIP ATTACHMENT

FRAME WITH SHEAR CLIP ATTACHMENT ONLY

FIGURE 16 TWO TYPES OF CIRCUMFERENTIAL FRAME DESIGNS IN COMMERCIAL TRANSPORT AIRCRAFT

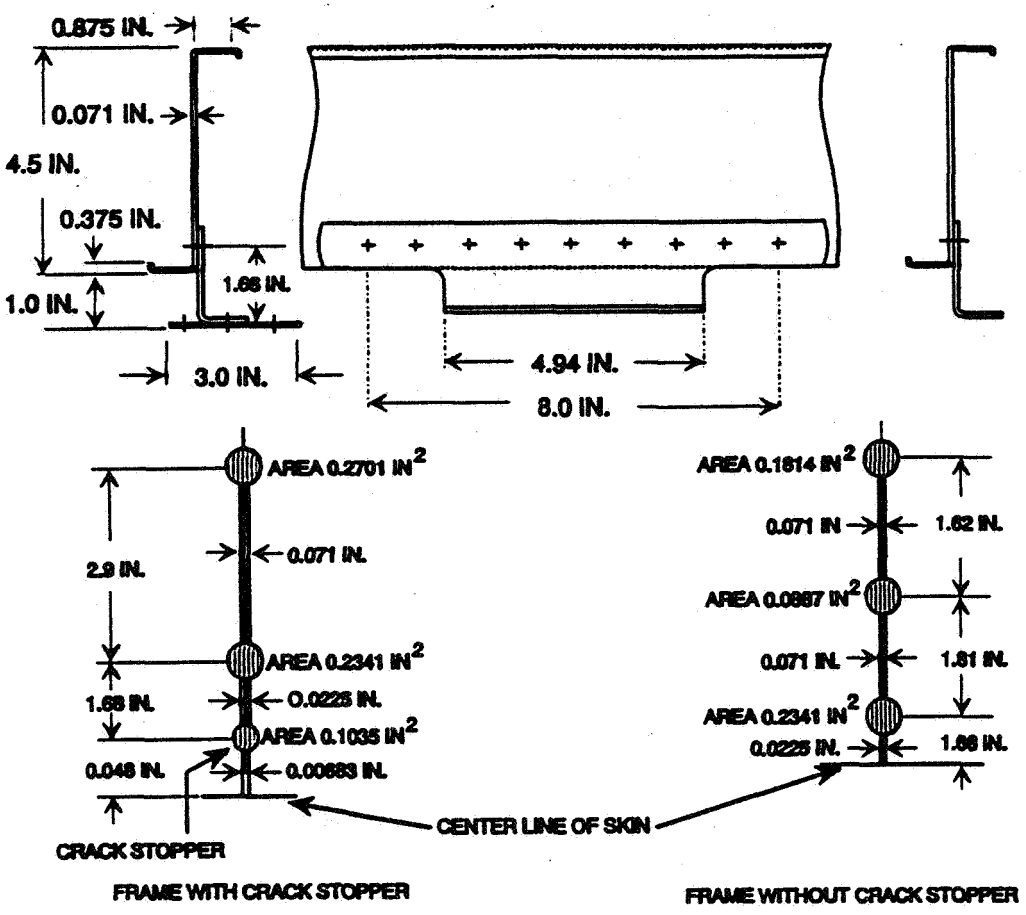

FIGURE 17 CIRCUMFERENTIAL FRAME IDEALIZATION

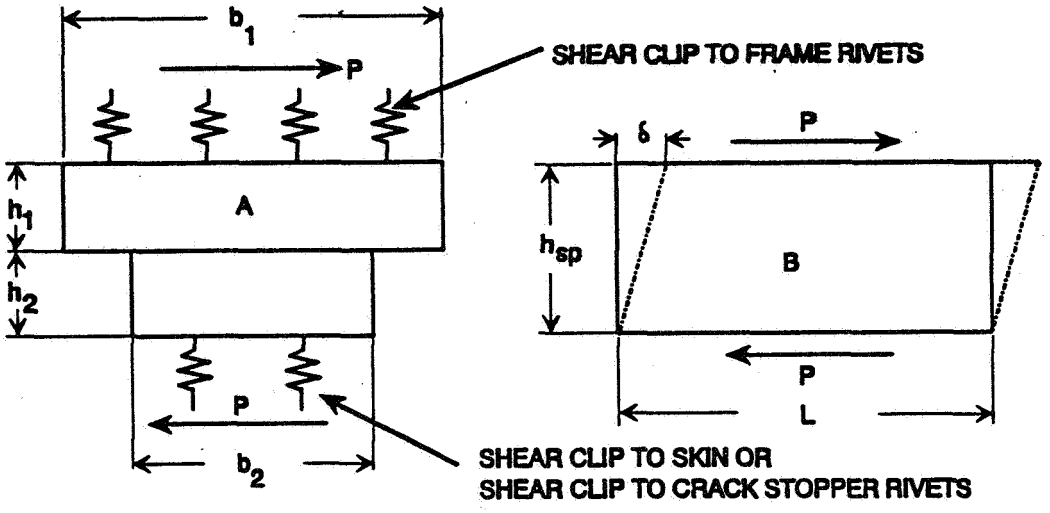

FIGURE 18 SHEAR CLIP IDEALIZATION

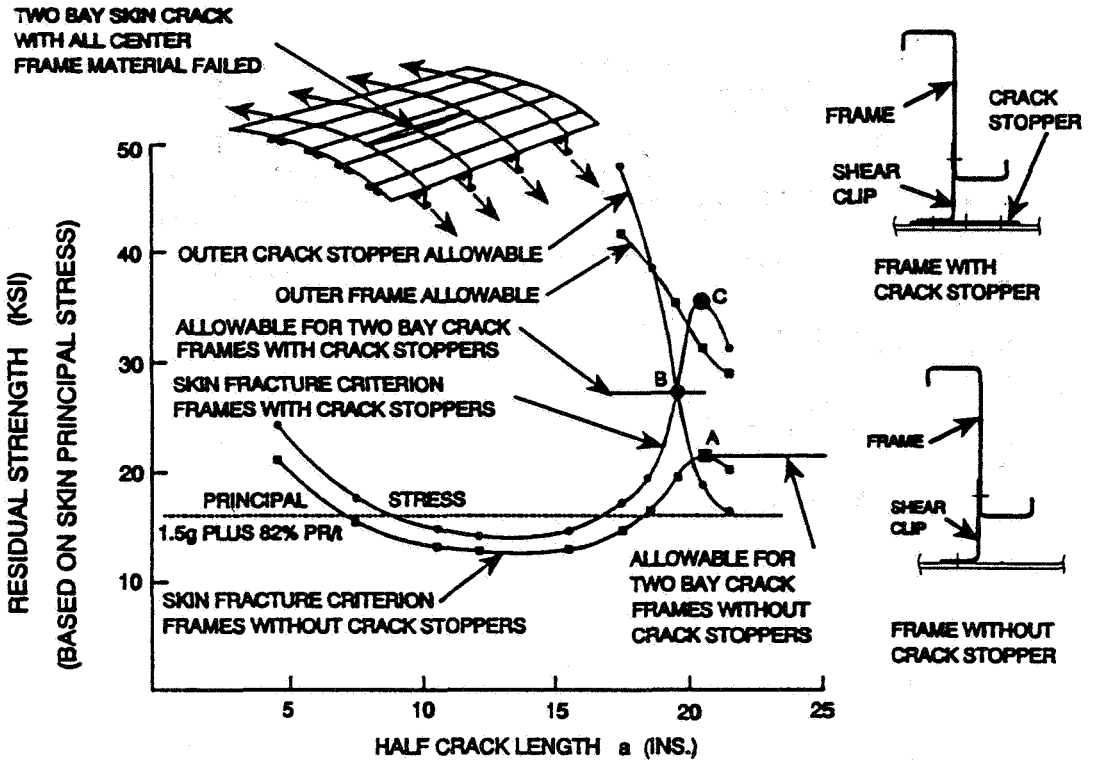

FIGURE 19 RESIDUAL STRENGTH COMPARISON
FRAMES WITH AND WITHOUT CRACK STOPPERS

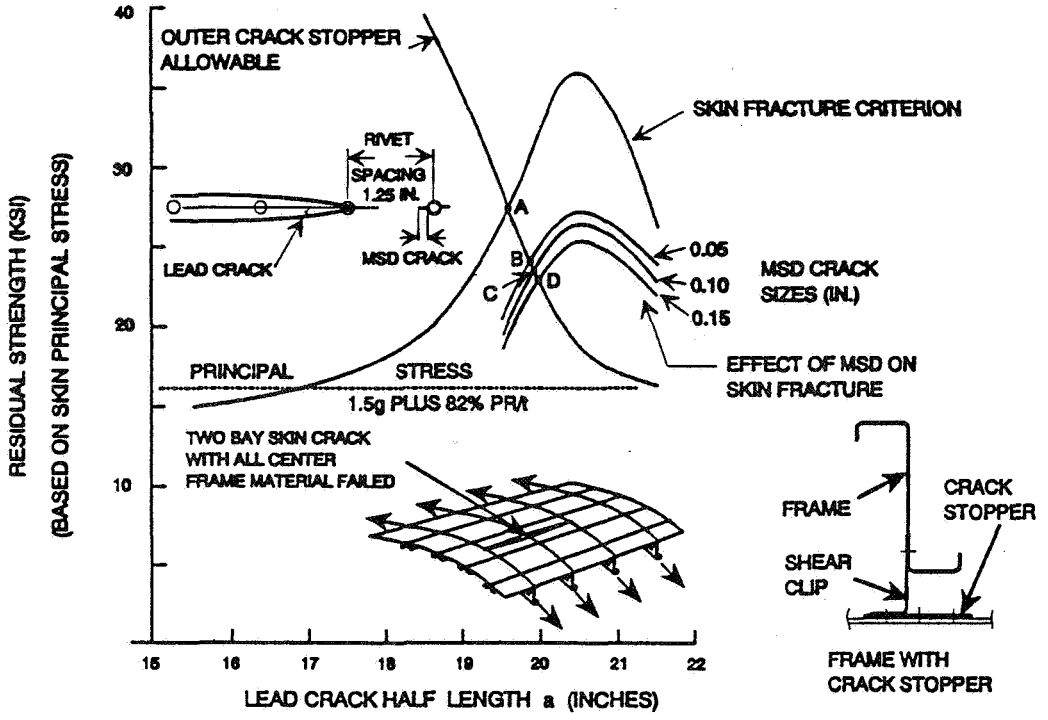

FIGURE 20 EFFECT OF MSD ON LEAD CRACK RESIDUAL STRENGTH
FRAMES WITH CRACK STOPPERS - RIVET SPACING 1.25 IN.

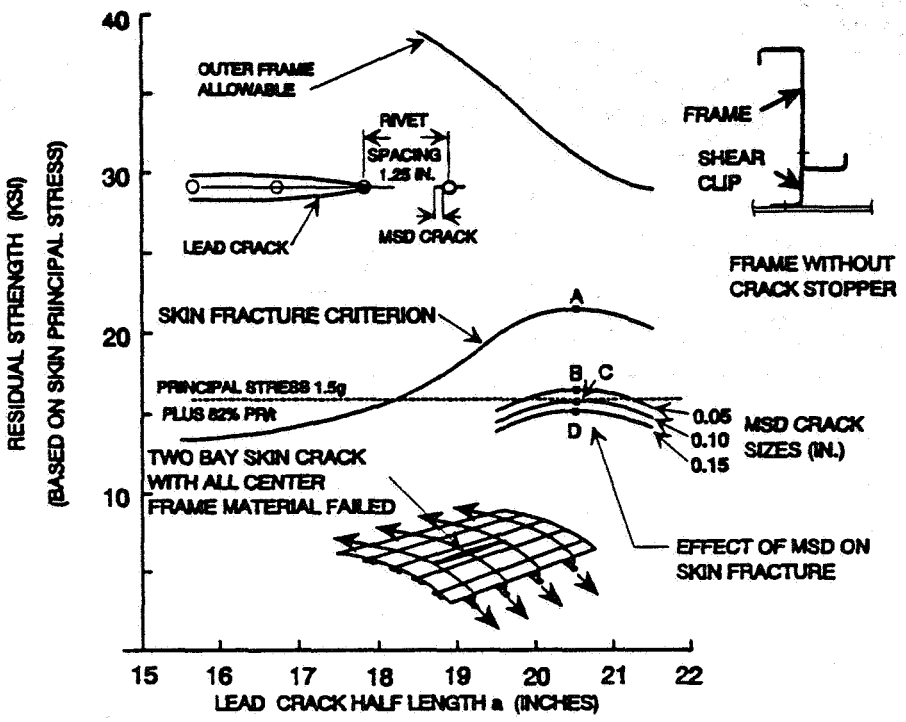

FIGURE 21 EFFECT OF MSD ON LEAD CRACK RESIDUAL STRENGTH
FRAMES WITHOUT CRACK STOPPERS - RIVET SPACING 1.25 IN.

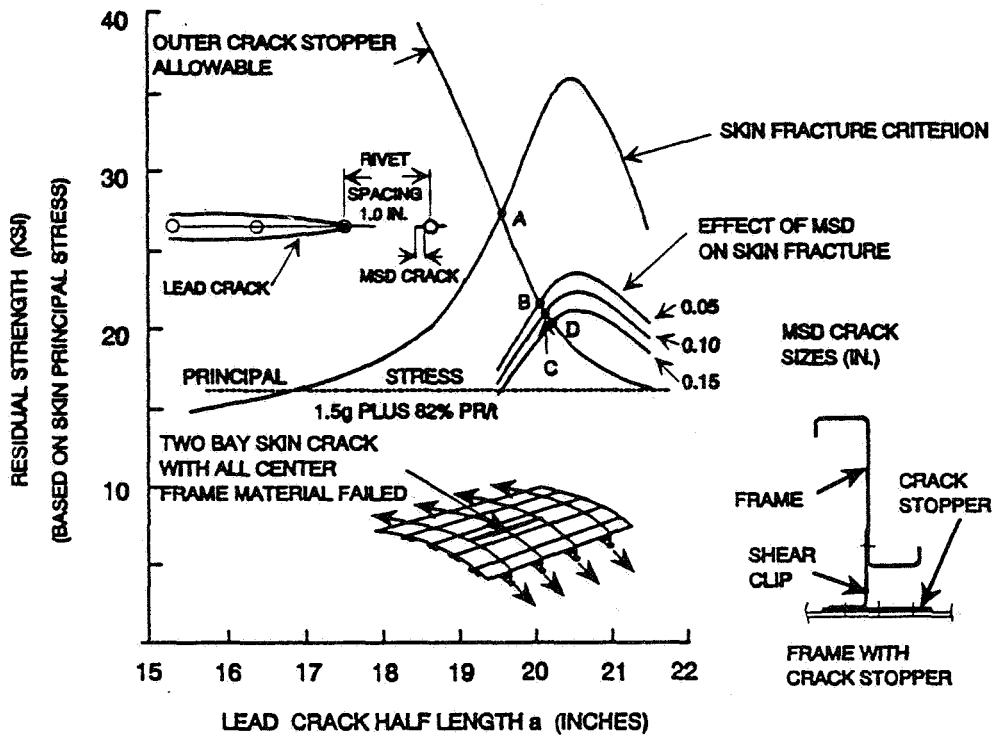

FIGURE 22 EFFECT OF MSD ON LEAD CRACK RESIDUAL STRENGTH
FRAMES WITH CRACK STOPPERS - RIVET SPACING 1.0 IN.

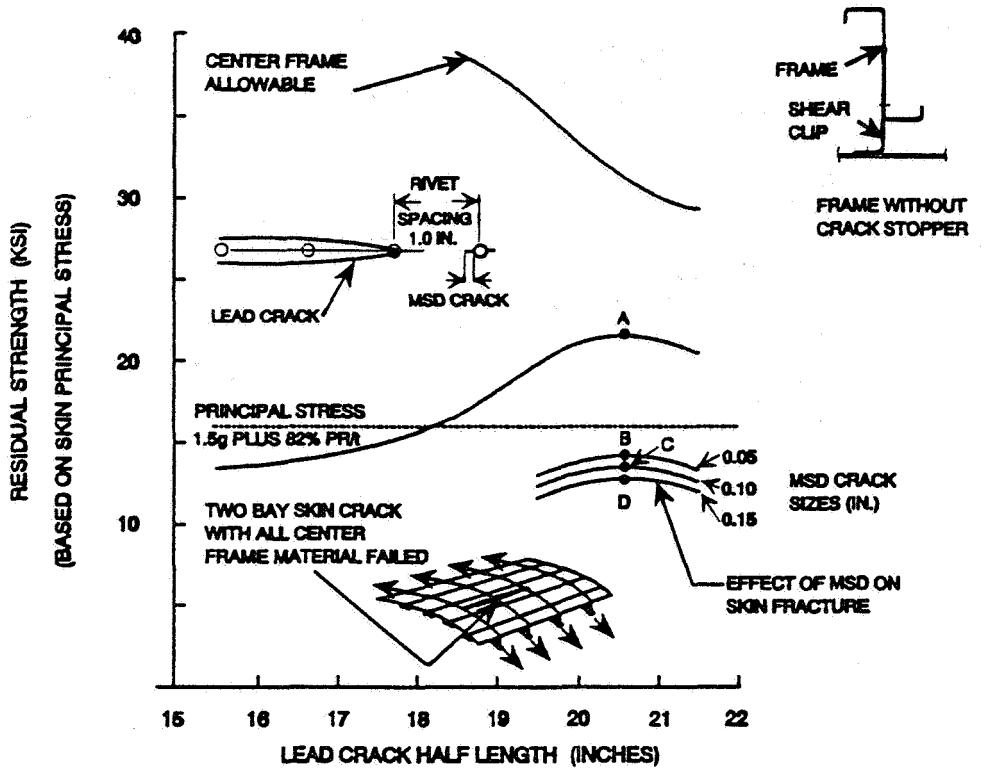

FIGURE 23 EFFECT OF MSD ON LEAD CRACK RESIDUAL STRENGTH
FRAMES WITHOUT CRACK STOPPERS - RIVET SPACING 1.0 IN.

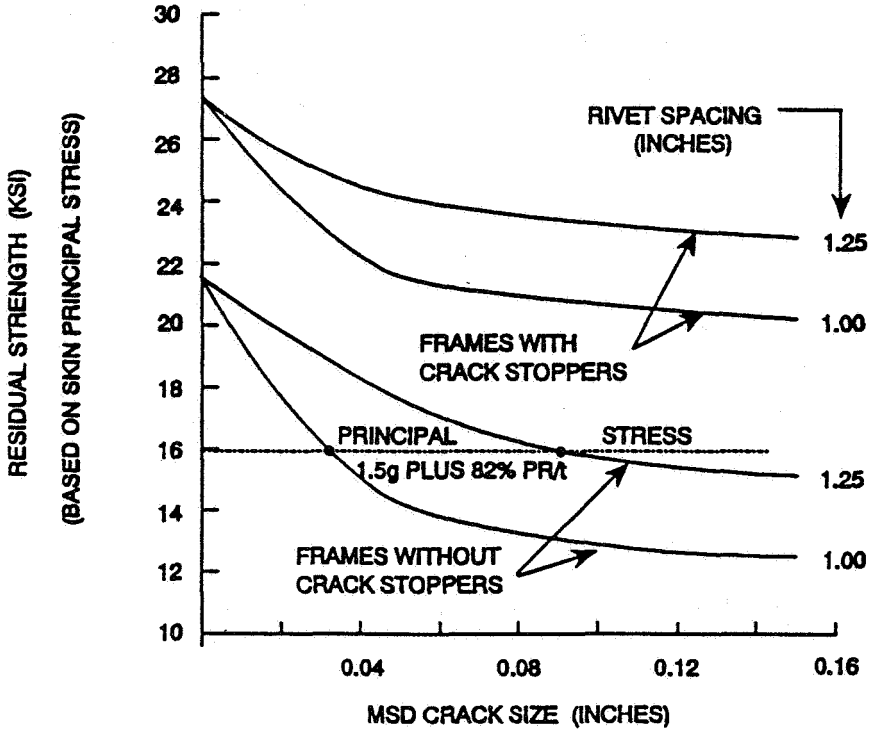

FIGURE 24 EFFECT OF MSD ON LEAD CRACK RESIDUAL STRENGTH FOR
TWO BAY LONGITUDINAL CRACK WITH BROKEN CENTRAL FRAME

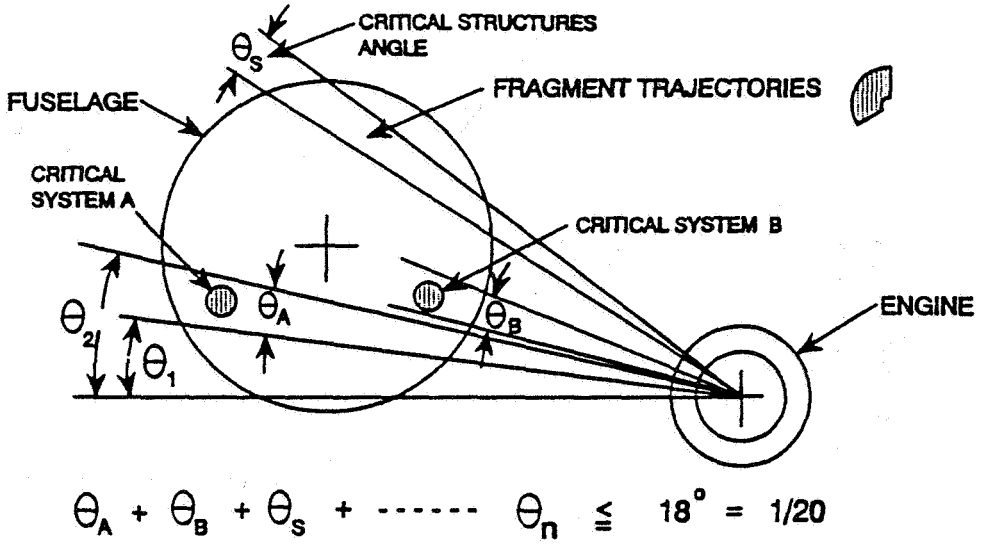

FIGURE 25 RISK EVALUATION - DISCRETE SOURCE DAMAGE

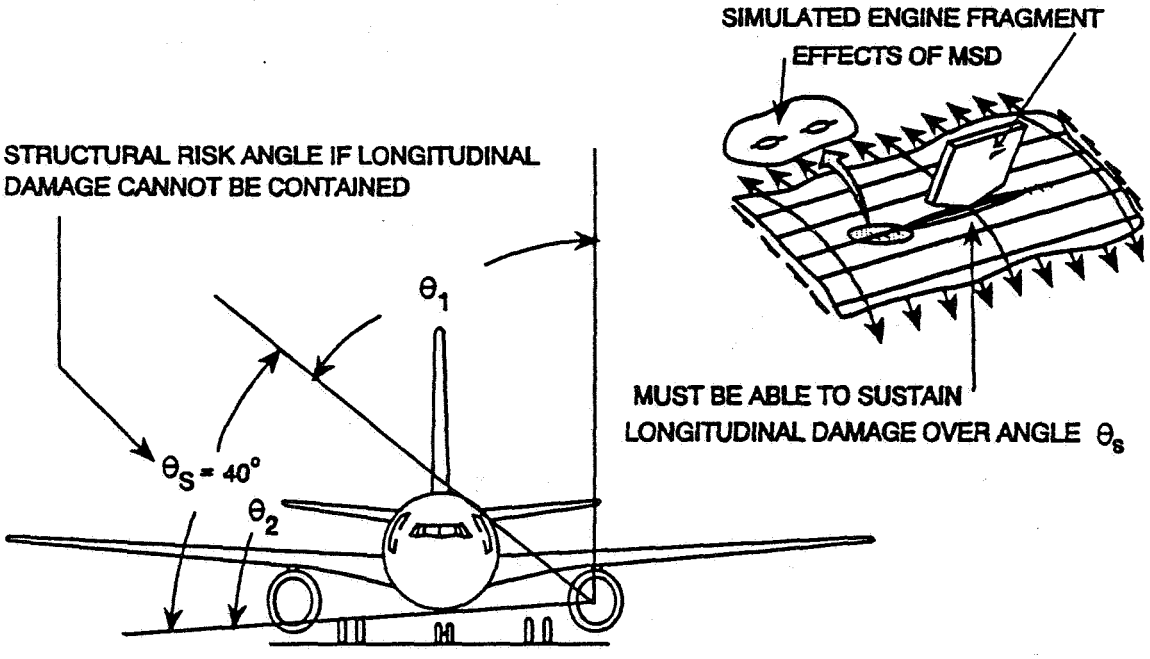

FIGURE 26 EFFECT OF MSD ON LONGITUDINAL DAMAGE CAUSED BY DISCRETE SOURCE DAMAGE MUST BE ACCOUNTED FOR IN ANY RISK EVALUATION

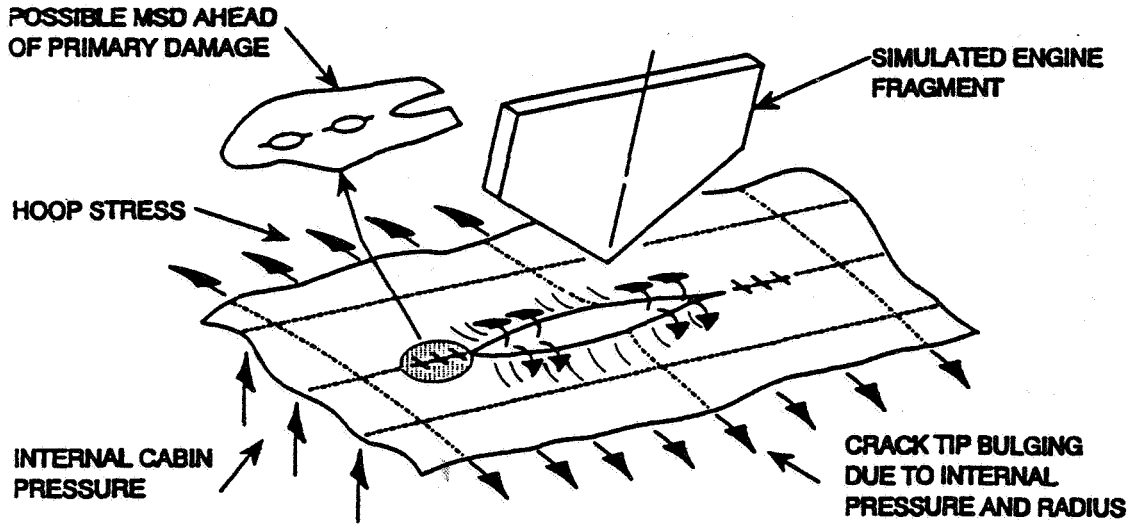

FIGURE 27 EFFECT OF MSD ON LEAD DAMAGE CREATED BY ENGINE FRAGMENT AT DAMAGE LENGTHS WHERE CRACK TIP BULGING DUE TO PRESSURE AND RADIUS IS HIGH

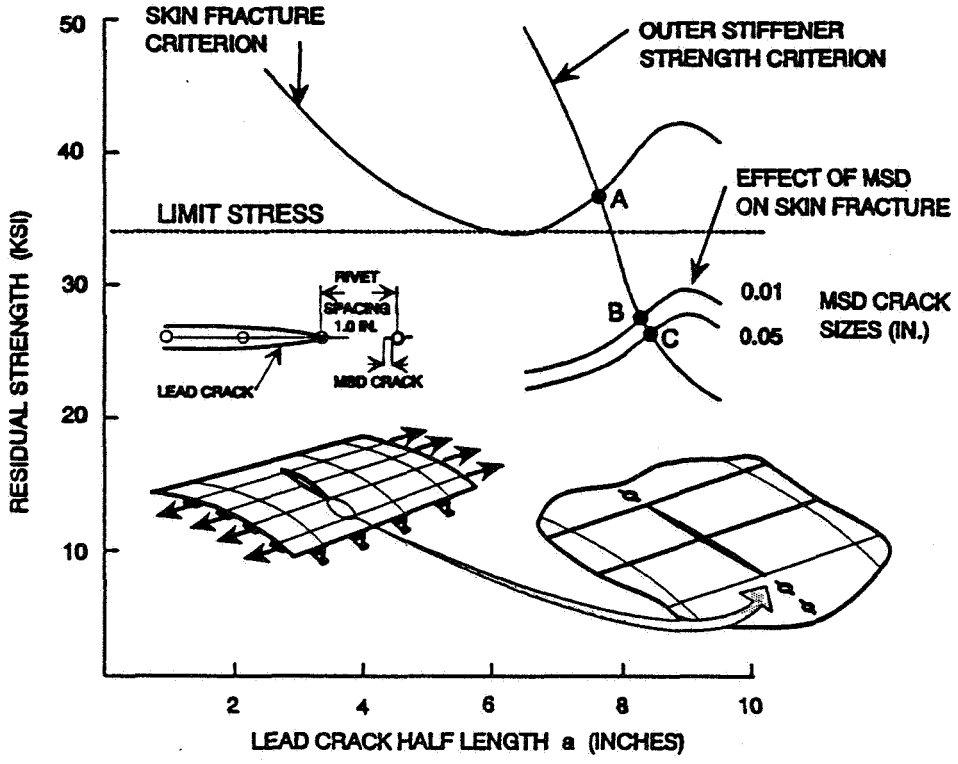

FIGURE 28 EFFECT OF MSD ON LEAD CRACK RESIDUAL STRENGTH TWO BAY CIRCUMFERENTIAL CRACK WITH BROKEN STIFFENER

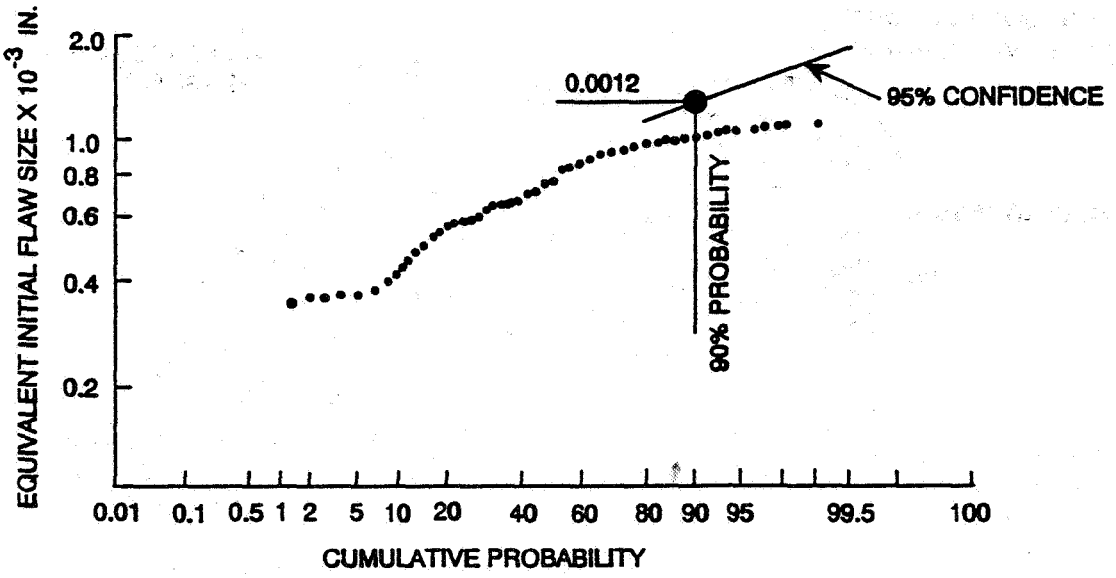

FIGURE 29 EQUIVALENT INITIAL QUALITY FLAW SIZE
EXAMPLE - REAMED COUNTERSUNK HOLES
TEST PANEL DATA

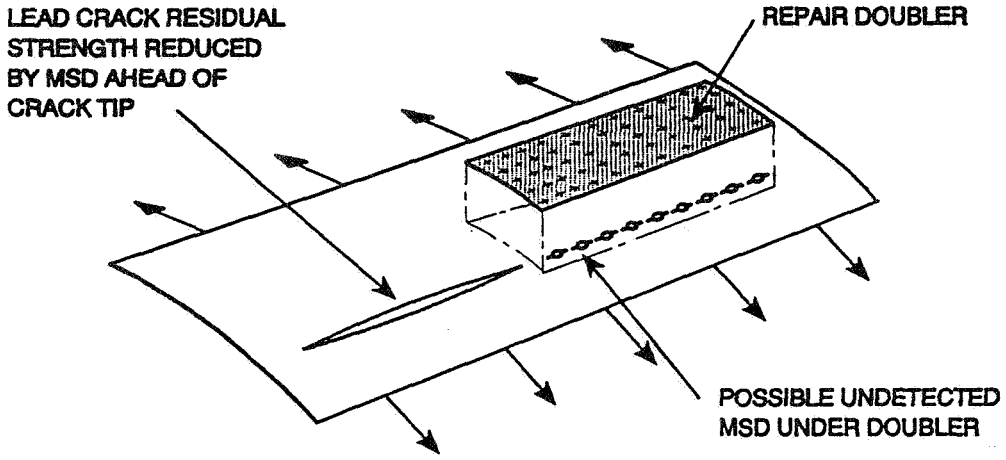

Figure 30 POSSIBLE LOSS OF LEAD CRACK RESIDUAL STRENGTH
DUE TO HIDDEN MSD UNDER REPAIR DOUBLER

MICROSTRUCTURALLY BASED VARIATIONS ON THE DWELL FATIGUE LIFE OF TITANIUM ALLOY IMI 834

Mark L Thomsen
David W. Hoeppner
Quality and Integrity Design Engineering Center
The University of Utah
Salt Lake City, UT

ABSTRACT

An experimental study was undertaken to determine the role of microstructure on the fatigue life reduction observed in titanium alloy IMI 834 under dwell loading conditions. The wave forms compared were a trapezoid with 15 and 30 second hold times at the maximum test load and a baseline, 10 Hertz, haversine. The stress ratio for both loading wave forms was 0.10. The fatigue loading of each specimen was conducted in a vacuum within a scanning electron microscope chamber which minimized the possibility that the laboratory environment would adversely affect the material behavior.

Two microstructural conditions were investigated in the experimental program. The first involved standard "disk" material with equiaxed alpha in a transformed beta matrix. The second material was cut from the same disk forging as the first but was heat treated to obtain a martensitic alpha prime microstructure.

Tensile tests were performed prior to the onset of the fatigue loading portion of the study, and it was determined that the yield strengths of the specimens from both material conditions were within ten percent. The maximum fatigue loads were chosen to be 72 percent of the average yield strength for both materials as determined from the tensile tests. It was found that the cycles to failure from the 10 Hertz loading wave form were reduced by a factor of approximately five when the loading was changed to the trapezoidal wave form for the standard "disk" material. The fatigue life reduction for the martensitic structure under identical test conditions was approximately 1.75. The improvement observed with the martensitic structure also was accompanied by an increase in overall fatigue life for the wave forms tested. This paper will review the results and conclusions of this effort.

INTRODUCTION

Since the development of the gas turbine engine, improvements in engineering alloys, ceramics, and aerodynamics have brought performance levels close to the limits of the materials that are currently available. Because of the wide variety of environmental and loading conditions, various alloy systems are being developed that can withstand very high stresses and high temperatures for an extended period of time. Although the service lives of aeroengines have improved greatly over the past 30 years, life prediction capabilities fall short of maximizing the functionality of critical components [1-5].

In an effort to obtain more service life from the safety critical components in gas turbines, many investigators in the field of fatigue support the use of damage tolerant design [2-6]. Primarily, this involves the use of component life predictions that have been verified by testing. To accomplish this, and get meaningful data, it is necessary to conduct the tests under representative loading and environmental conditions of those experienced in service. Unfortunately, this is costly and time consuming, and in the end, the question of load applicability still exists.

It has been suggested that standardized loading wave forms be used in the testing of components and materials to better characterize their behavior [2,6]. Such programs involve the development of a loading spectrum that is indicative of the actual engine operation. An example of loading spectrum for a military aircraft can be seen in Figure 1 [7]. Although this is much more involved than those for commercial transport aircraft, the concept is the same. Others, however, claim that these spectra may be compressed as shown in Figure 2 which is justified by eliminating the "less severe mission points, e.g. cruise [dwell],..." [1].

The cruise portion of a loading spectrum is important because it requires that the component be under a relatively high load for an extended period of time. Recently, a titanium alloy fan rotor disk failed approximately one hour and seven minutes after takeoff of United Airlines flight 232 [8]. The material the disk was manufactured of contained both the alpha and beta microstructures which have been shown to be sensitive to dwell loading [9-11]. This failure occurred far short of the disk's "rated life" and, ultimately, led to the deaths of 112 people. In sharp contrast to the opinions of some [1,12,13], the importance of the hold time (or dwell period) at some elevated load during operation was shown by this accident.

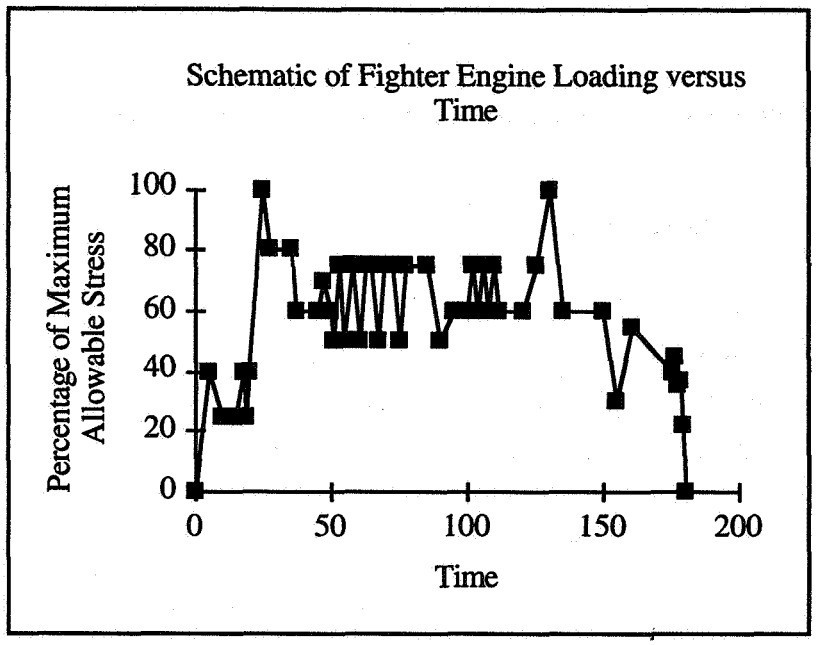

Figure 1. Fighter engine operation spectrum.

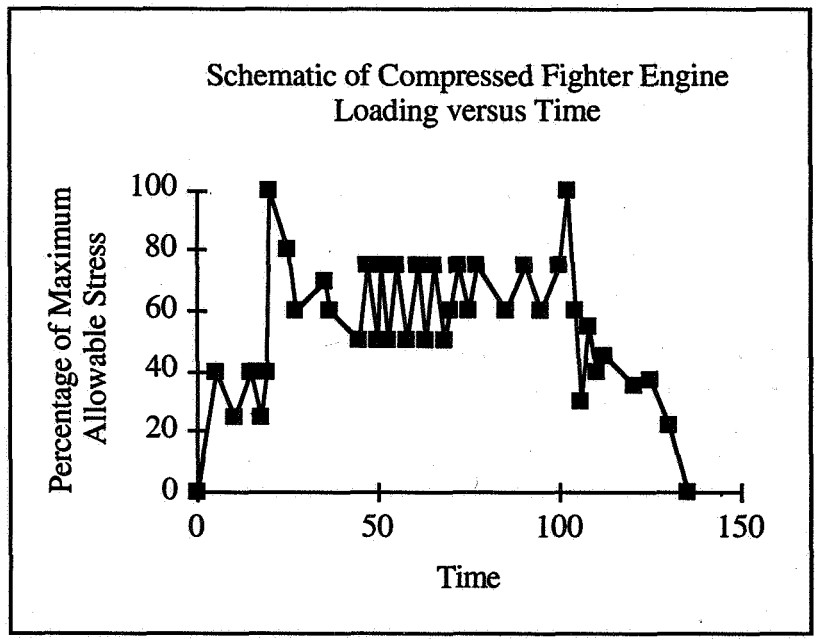

Figure 2. Compressed engine operation spectrum.

EXPERIMENTAL METHODS

The details of this investigation and the approach taken will be described by section.

Microstructural Characterization

Two microstructural conditions of IMI 834 were tested. The first was an equiaxed alpha in a transformed beta matrix (disk) with the equiaxed alpha grain dimensions approximately 50 μm and the transformed beta grain dimensions approximately 70 μm. The second was a martensitic alpha prime with grain dimensions on the order of 600 μm. The target composition of the alloy is given in Table 1 [14].

Table 1
Nominal Composition of IMI 834

Ti	Al	Zr	Sn	Nb	Mo	Si
Balance	5.8	3.5	4.0	0.7	0.5	0.35

In each case the specimen blanks were cut from the bore of the same disk forging. The "disk" specimens then were machined to the specimen geometry with the orientation to the bore of the disk marked for future reference. The specimen blanks from the second microstructural group were cut from the disk forging and then heat treated as to the following schedule: heat 2 hours at 1073 °C, oil quench, age 2 hours at 700 °C, and then air cool. The solution temperature of 1073 °C was chosen since it is 33 °C above the beta transus temperature presented by Bate [15], and complete microstructural transformation was desired. The standard aging temperature and time for the "high alpha-beta" [16] condition was used to allow decomposition of the retained beta phase. Following this heat treatment, the blanks were machined to the specimen geometry to remove the oxygen rich alpha case that often results during heat treating operations [16]. Figures 3 and 4 show the two microstructures used in the study.

Specimen Geometry

The specimen geometry shown in Figure 5 was chosen because the tests were to be conducted in the vacuum chamber of a scanning electron microscope, the details of which are presented by Stephens and Hoeppner [17], to minimize environmental effects. The groove on the top face of the specimen is oriented towards the bore of the disk as signified by the mark made in the specimen blanks mentioned above. The reason for the groove is to provide a stress state that promotes crack nucleation on the top face

C-5

such that it can be viewed in the scanning electron microscope for crack detection and propagation studies. A finite element analysis of the specimen stress state revealed that the presence of the small groove introduced a stress concentration factor of 1.64 near the base of the groove. Since this groove was only on one side of the specimen, the stress concentration diminished to 1.0 at a depth of approximately 0.040 inch.

The surface of the groove was polished to remove any large scratches left over from the final machining operation. This procedure involved a three step wet sanding treatment with 240, 320 and finally 600 grit emery paper. The final polish was with 3 μm diamond paste. This treatment was used for all grooved fatigue test specimens. The tensile test specimens which did not have the groove were tested as received.

Test Matrix

Since the fatigue response of two microstructural conditions were to be compared, tensile tests were conducted to determine some basic material properties. Although the specimen geometry was not of standard configuration [18], comparative tensile data were obtained on specimens similar to those shown in Figure 5, but without the groove. Again, a finite element analysis of this geometry was conducted to verify that no stress concentration existed and, indeed, none did. Once the approximate tensile data were available, the 0.2 percent offset yield strength was determined.

The fatigue test portion of the study involved a 10 Hertz haversine wave form, trapezoidal wave form with a 15 second hold at the maximum load, and a trapezoidal wave form with a 30 second hold at maximum load, all with a stress ratio of 0.1 and σ_{max} = 755 MPa. All fatigue tests were conducted in a vacuum ($\approx 10^{-5}$ torr), the details of which are presented in Table 2.

The tensile tests were conducted using a standard electro-hydraulic servo controlled 100 kilo-Newton MTS load frame and extensometer. The fatigue tests were conducted in a specially designed electro-hydraulic servo controlled 25 kilo-Newton "In-Situ" fatigue loading apparatus controlled with standard MTS components.

Fractography

Fractographic analysis was conducted on the fracture surfaces of the fatigue tested specimens using a Hitachi S-2300 scanning electron microscope operating at 25 kilo-volts. In each case, documentation of the dwell and baseline fracture surface features was made. Comparisons of these features were made and possible reasons for fatigue response variations were drawn.

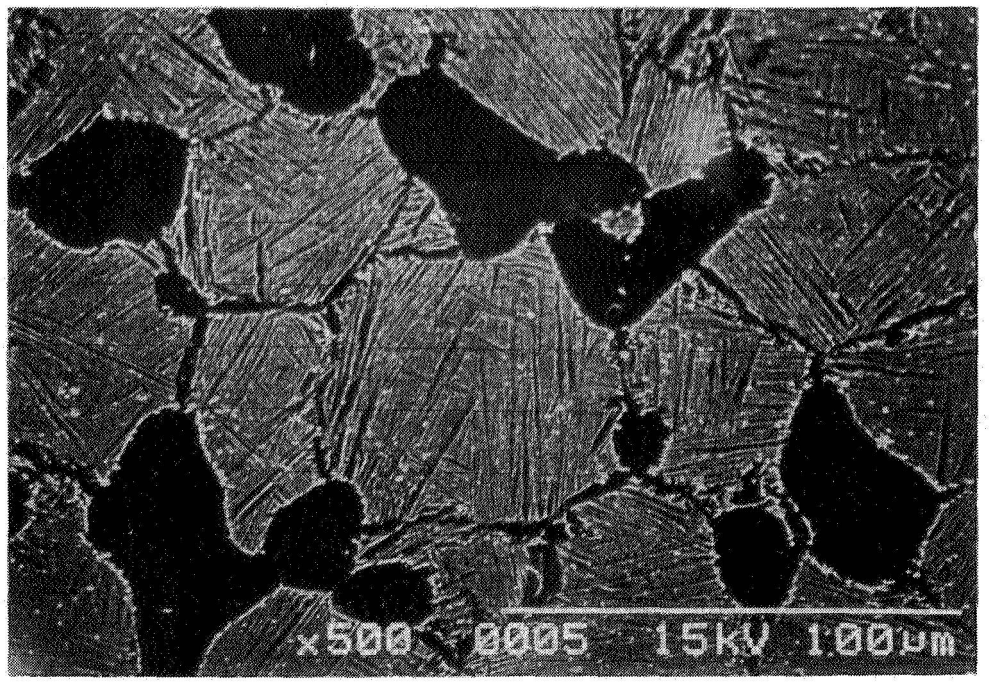

Figure 3. Equiaxed alpha in a transformed beta matrix, "disk" (500X).

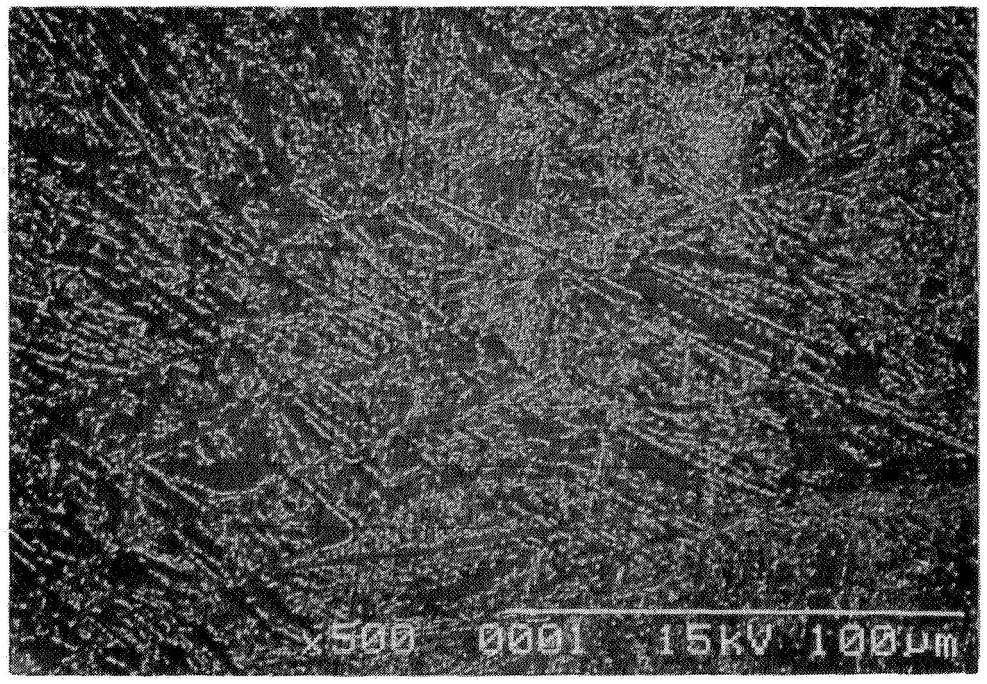

Figure 4. Martensitic alpha prime (500X).

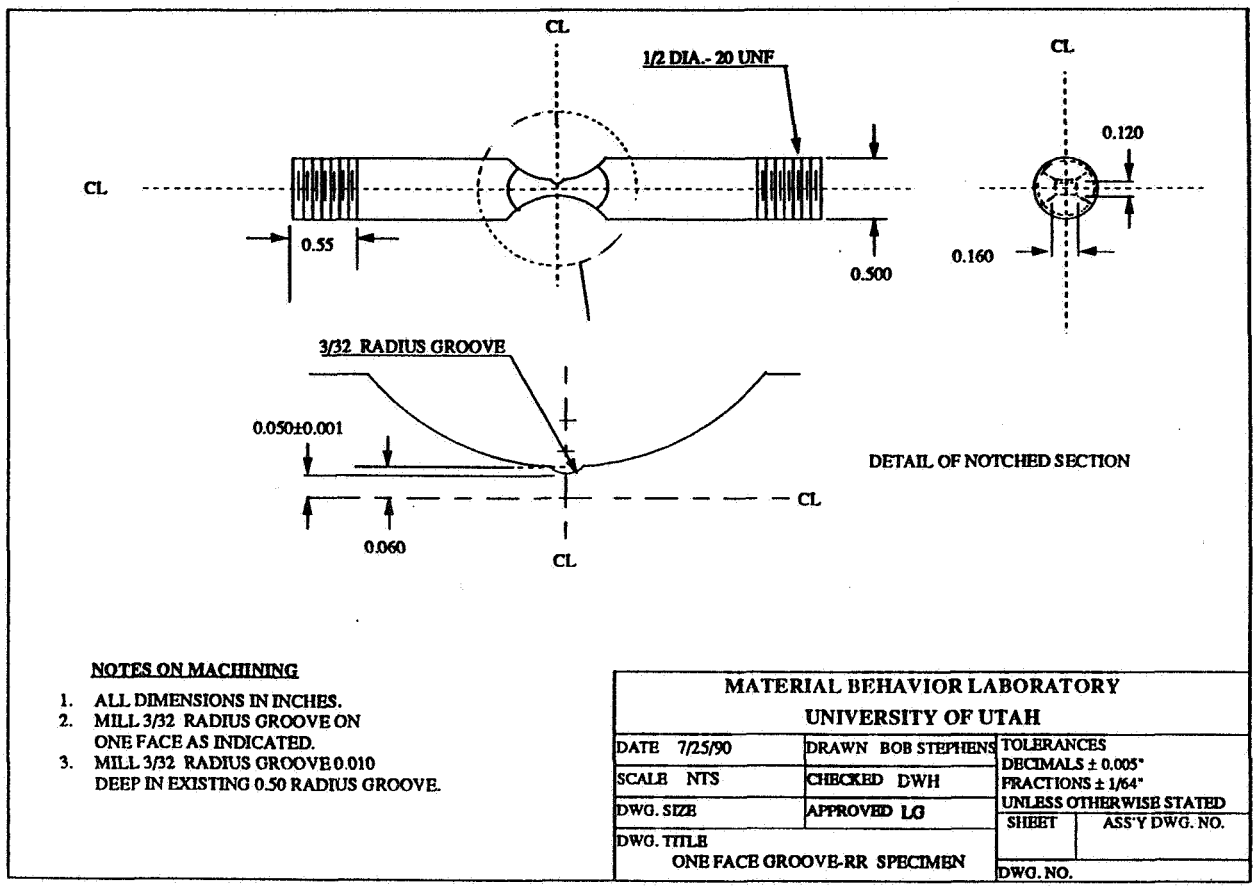

Figure 5. Specimen drawing.

Results

A summary of the tensile data is shown in Table 3 below, and the fatigue data is shown in Table 4. The values for the total cycles to failure, N_f, presented are averages obtained from the number of specimens tested for each condition as listed in Table 2.

Table 2
Overall Experimental Matrix

Test type	Tests	Wave Form and Environment	Microstructural Condition
Tensile	1	N/A Lab Air	Equiaxed Alpha-Transformed Beta
Fatigue	3	10 Hertz Haversine Vacuum	Equiaxed Alpha-Transformed Beta
Fatigue	2	0.065 Hertz trapezoid (15 second hold) Vacuum	Equiaxed Alpha-Transformed Beta
Fatigue	1	0.033 Hertz trapezoid (30 second hold) Vacuum	Equiaxed Alpha-Transformed Beta
Tensile	2	N/A Lab Air	Martensitic alpha prime
Fatigue	2	10 Hertz Haversine Vacuum	Martensitic alpha prime
Fatigue	3	0.065 Hertz trapezoid (15 second hold) Vacuum	Martensitic alpha prime

Table 3
Tensile Test Data

Microstructural Condition	Specimen	0.2 Percent Yield Strength (MPa)	Final Strain at Failure (με)
Equiaxed Alpha-Transformed Beta	1	1,044	51,458
Martensitic Alpha prime	1	999	37,041
Martensitic Alpha prime	2	1,110	34,375

Table 4
Fatigue Test Data

Microstructural Condition	Wave form	Average Cycles to Failure (N_f)
Equiaxed Alpha-Transformed Beta	10 Hertz Haversine	57,372
Equiaxed Alpha-Transformed Beta	0.065 Hertz trapezoid (15 second hold)	13,320
Equiaxed Alpha-Transformed Beta	0.033 Hertz trapezoid (30 second hold)	10,222
Martensitic Alpha prime	10 Hertz Haversine	151,466
Martensitic Alpha prime	0.065 Hertz trapezoid (15 second hold)	88,277

Discussion

The tensile data showed very little difference in the yield strengths between the two microstructures. The strain data of the martensitic specimens, however, was significantly different. This is most likely related to the non-standard heat treatment for this alloy. Typically, solution treating above the beta transus for near alpha alloys results in superior creep resistance at the expense of fatigue properties and deformation characteristics, as shown by the tensile data. However, aging at 700 °C for this particular alloy results in improved fatigue properties while maintaining much of the creep resistance [16] with some loss in total deformation to failure.

From the above, it is expected that the fatigue properties would be comparable between the two microstructures. The advantages of the disk microstructure, equiaxed alpha in a transformed beta matrix, are improved creep resistance, tensile properties, fatigue properties, and fracture toughness [15,19]. Although this was the case, the study shows that for the test conditions employed, the martensitic microstructural condition out performs the disk microstructure.

The observed fatigue life reduction associated with the dwell (hold time) at maximum load has been observed by several others at room temperature. An additional observation associated with this phenomenon is the temperature dependence and the fact that this fatigue life reduction under dwell is diminished as temperature is increased. Reports of this saturation temperature have been from 75-200 °C. Some of the mechanisms that have been proposed are:

- hydrogen embrittlement at, and immediately ahead of, the crack tip by a dislocation locking mechanism which is unlocked at elevated temperature [10],

- hydride formation along the basal planes of the alpha phase and subsequent cracking of these hydrides (related to volumetric misfit between hydride and alpha phase) [20,21],
- hydrogen embrittlement at, and ahead of, the crack tip enhanced by the strain induced increase in the diffusion rate of hydrogen to these zones and subsequent cracking of hydrides that may form [22],
- creep, or strain accumulation, during the dwell period with inclusion of the microstructural "weak link" concept that assists in explaining the effect of specimen size [23], and
- hydrogen assisted grain boundary sliding [24].

Other observations have included that the content of primary alpha influences the degree of the dwell effect [10] on fatigue lives of titanium alloys.

Fractographic observations comparing the fracture surfaces of dwell and non-dwell specimens have noted several features of the dwell specimens. Some of the more prominent observations are [10,23,25]:

- increased faceting oriented approximately normal to the loading axis,
- facet planes are associated with the basal planes of the alpha phase,
- secondary cracking, similar to that observed in embrittled materials, and
- coarsening of the fracture surface features.

With these in mind, it has been reported [25] that a distinct change in crack growth mechanism occurs between dwell and non-dwell specimens.

The degree of fatigue life reduction observed in this study was by a factor of approximately five for the disk specimens and only a factor of 1.7 for the martensitic specimens. Part of this variation can be explained by considering some of the proposed mechanisms.

Each of the specimens are from the same disc, so it is reasonable to assume the internal hydrogen content is similar. Even though subsequent heat treatment was performed to obtain the martensitic specimens, this was done prior to machining. During the machining process, approximately 0.25 inch of material was removed. This would reduce the chance for significant hydrogen pickup during the heat treatment to penetrate to the depth required to influence the behavior of the specimen across the gage section. Therefore, the probability of significant variations in hydrogen content within the two separate microstructural groups is remote.

In examining the fractographic evidence, it is apparent that coarsening of the fracture surface does, indeed, occur as mentioned above. In comparing Figures 6 and 7 to Figures 8 and 9, this coarsening is apparent. Striations were found along the non-dwell fracture surface, Figure 7, that were not observed on dwell fracture surfaces. The secondary cracking associated with the dwell surface was not observed on the non-dwell surface. Increased faceting on the dwell surface is a product of the coarsening mentioned above. The size of the facet planes often corresponded to the size of the near alpha grains. In general, the fracture surface of the non-dwell specimen can be characterized as showing more deformation with some

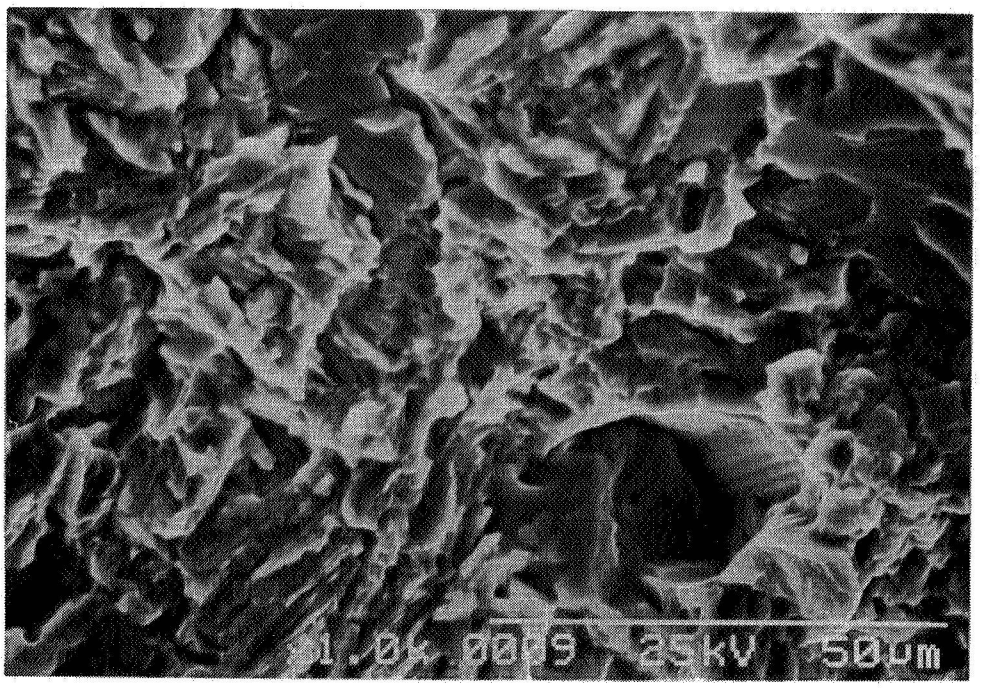

Figure 6. Fracture surface of the Disk specimen with a 10 Hertz haversine fatigue loading wave form (1000X).

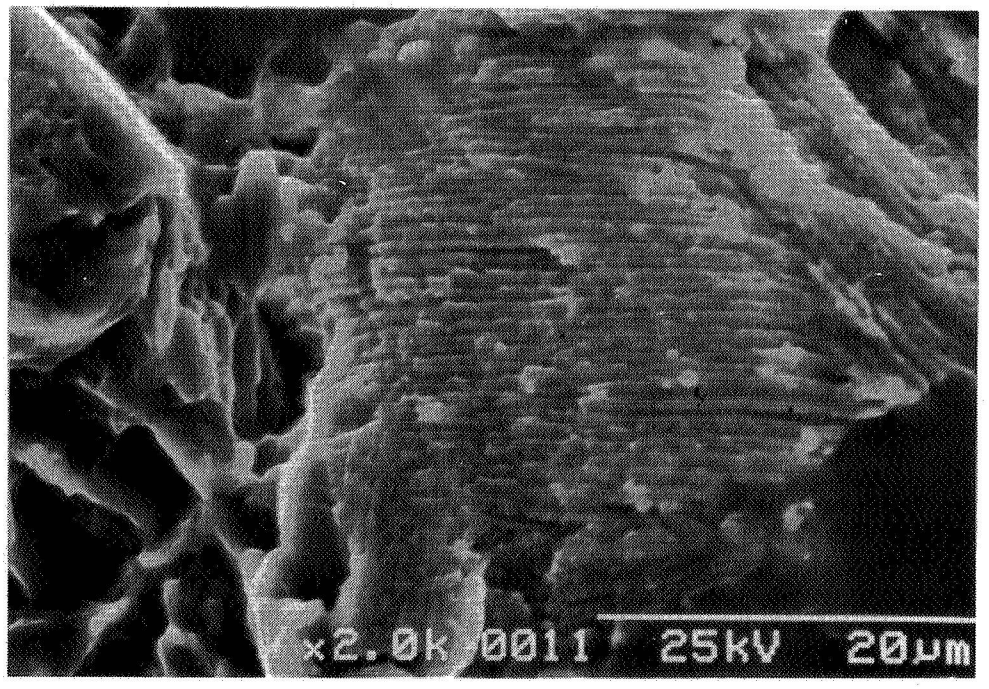

Figure 7. Striation field near the fast fracture zone of the Disk specimen with a 10 Hertz haversine fatigue loading wave form (2000X).

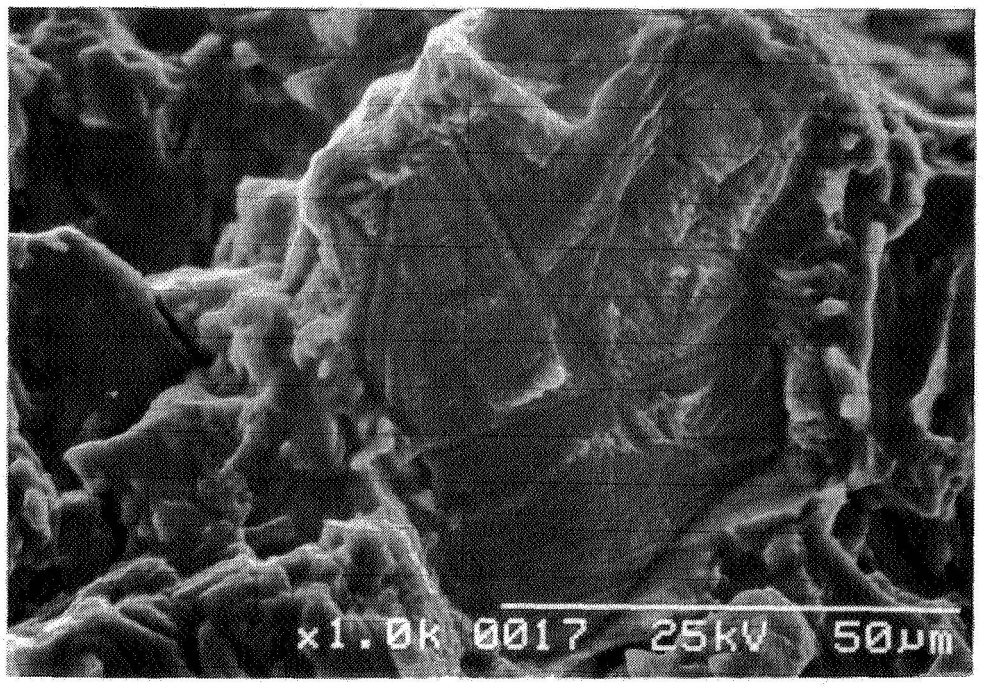

Figure 8. Secondary cracking and cleavage planes on the fracture surface of the Disk specimen tested at 0.065 hertz (Dwell) (1000X).

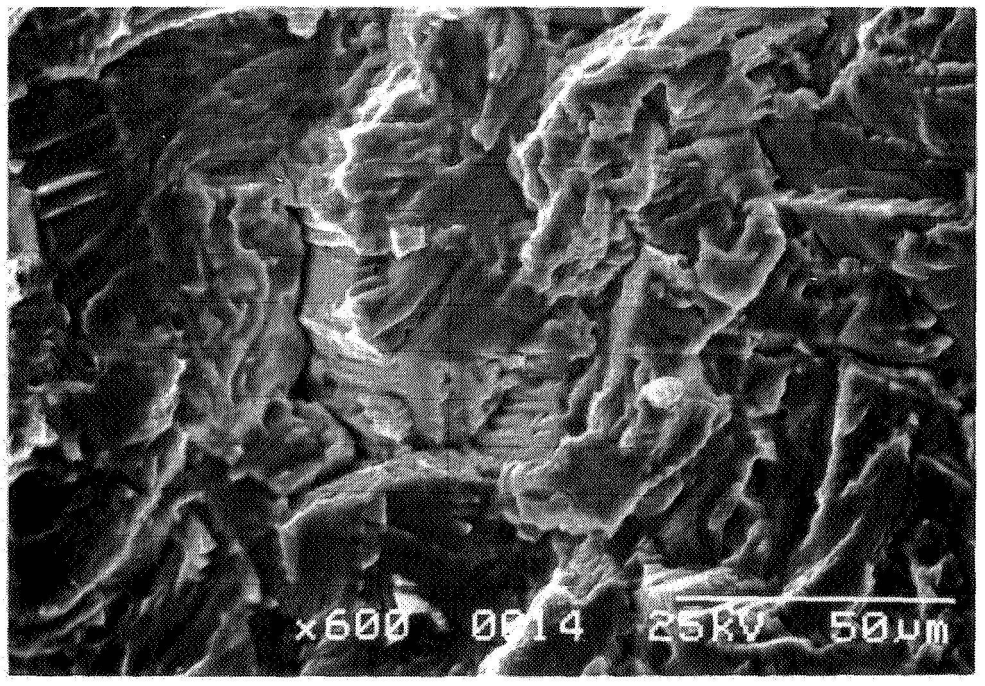

Figure 9. More secondary cracking on the fracture surface of the Disk specimen tested at 0.065 hertz (Dwell) (600X).

striation fields. The dwell specimen surface is predominately quasi-cleavage with very little sign of deformation.

The martensitic fracture surfaces showed distinct microstructural dependence as shown in Figures 10 and 11. The dwell fracture surfaces, Figures 12 and 13, were very similar to the non-dwell surfaces with the exception of numerous craters in the surface associated with very limited secondary cracking as compared to the disk microstructure. In comparison of the fracture surfaces at higher magnification, Figures 11 and 13, very little difference in cracking mechanisms is apparent on the micro-mechanics level. Overall, the fracture surface characterization is predominately transgranular.

An observation made by Song and Hoeppner [26] was that the size of the specimen has an effect on the dwell life reduction observed in other titanium alloys. In this study, three different specimens were tested at three separate stress levels. The findings were that as the specimen size was reduced, a more pronounced dwell life reduction was observed for all stresses tested. The conclusion drawn from this was that dwell effect was related to the degree of coarseness of the microstructure and that the increased prior beta grains tend to impede the deformation under uniaxial loading conditions.

Past In-Situ fatigue crack propagation studies by Stephens and Hoeppner [27] of the disk microstructure has shown an increased tendency for crack nucleation to be associated with the primary alpha grains for non-dwell tests. For the dwell tests, crack nucleation sites were found in both the transformed beta and the alpha phases. Crack growth was found to be planar in the alpha phase and more tortuous in the transformed beta phase. Although an etchant was used, no difference in fatigue life was observed.

In-Situ fatigue crack propagation studies in the martensitic structure were difficult. In comparison to the unetched specimens used for the fatigue study, a pronounced life reduction was encountered when an etchant was used to highlight the microstructural features. This has been observed before by Ryder et. al. [28] and one possible explanation may be related to preferential attack of the alpha prime phase by the etchant. If this occurred, it would be expected that crack nucleation and propagation would be influenced by the orientation of the alpha prime plates with respect to the loading axis. Although the etchant was present, it was observed that crack propagation along the alpha prime plates oriented nearly perpendicular to the loading axis was noticeably faster than those plates oriented nearly parallel to the loading axis. This micro-structurally dependent crack path morphology is shown in Figure 14.

The additional life reduction associated with disk specimens by changing the dwell time at maximum load from 15 to 30 seconds was minimal. This was first noted by Ryder et. al. [28] in 1973. This study mentioned that the maximum effect occurred between 15 seconds and one minute. This would indicate that the mechanisms responsible for this substantial life reduction may be related to dislocation locking, as mentioned above, rather than cold creep. If it was entirely creep related, the tendency for fatigue life reduction would continue with longer periods of hold at maximum load. Therefore, a saturation time would not be achieved, as was shown here and in the work of Ryder et. al.

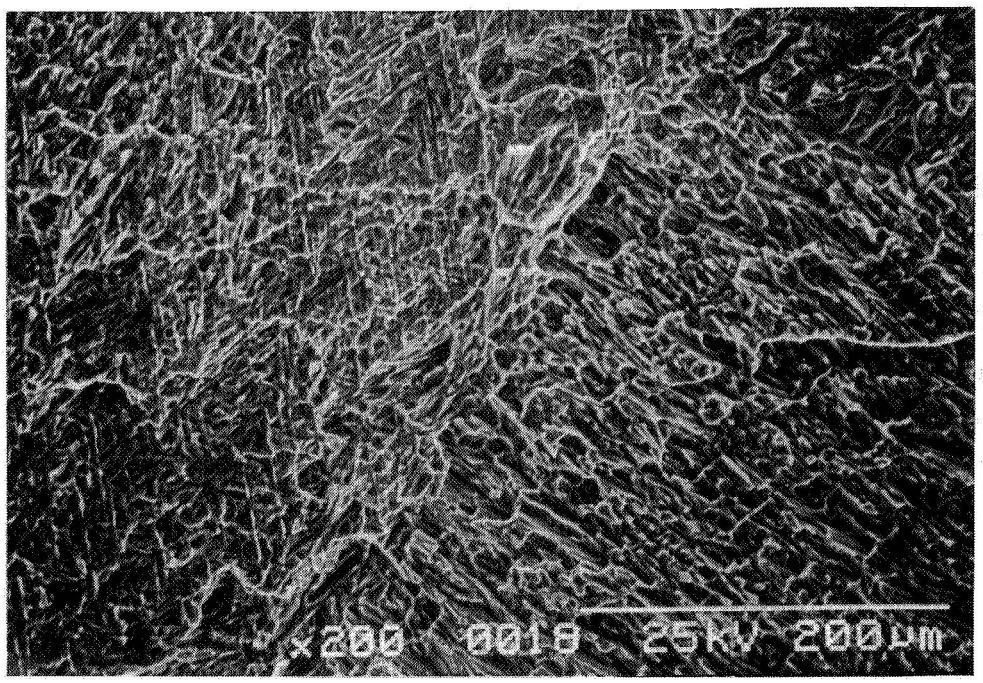

Figure 10. Fracture surface of the martensitic alpha prime condition specimen with a 10 Hertz haversine fatigue loading wave form (200X).

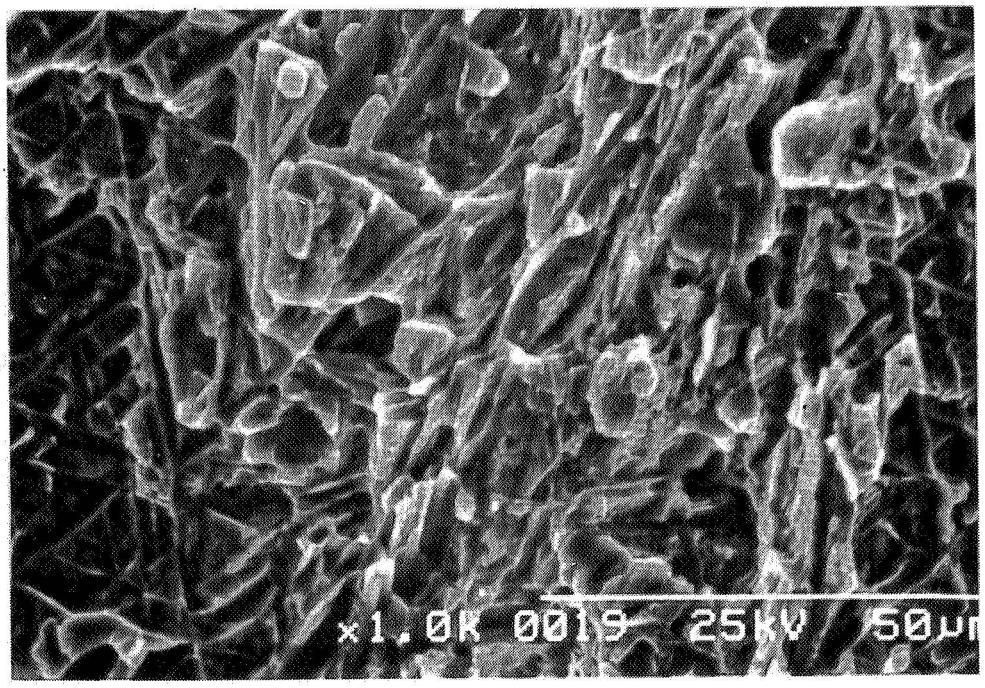

Figure 11. Close up of the martensitic alpha prime fracture surface tested with a 10 Hertz haversine fatigue loading wave form (1000X).

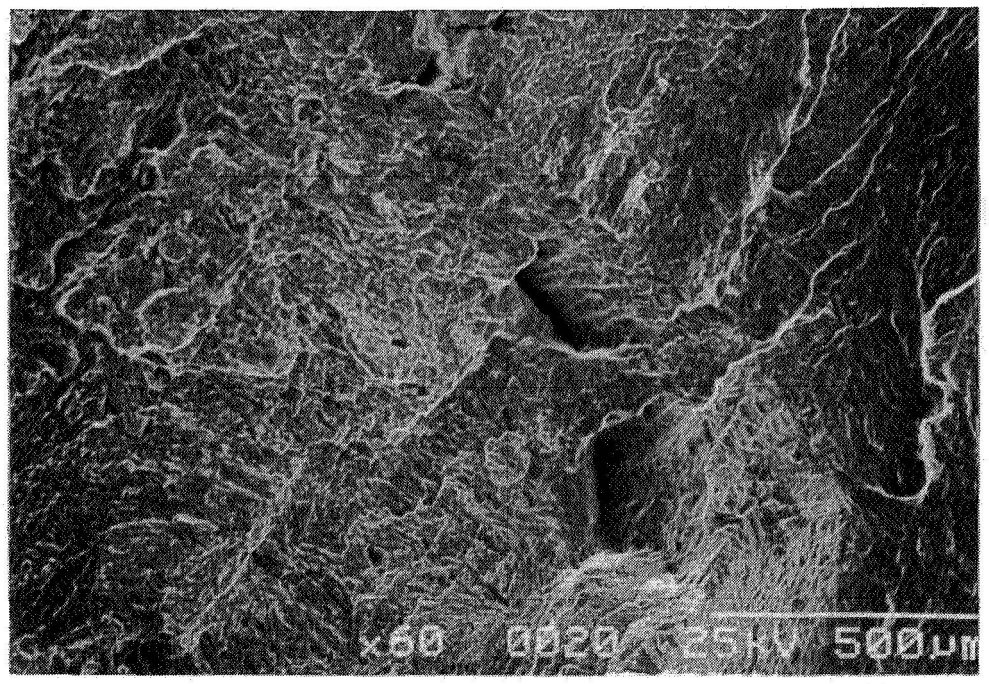

Figure 12. Fracture surface of the martensitic alpha prime condition specimen with a 0.065 Hertz trapezoidal fatigue loading wave form (60X).

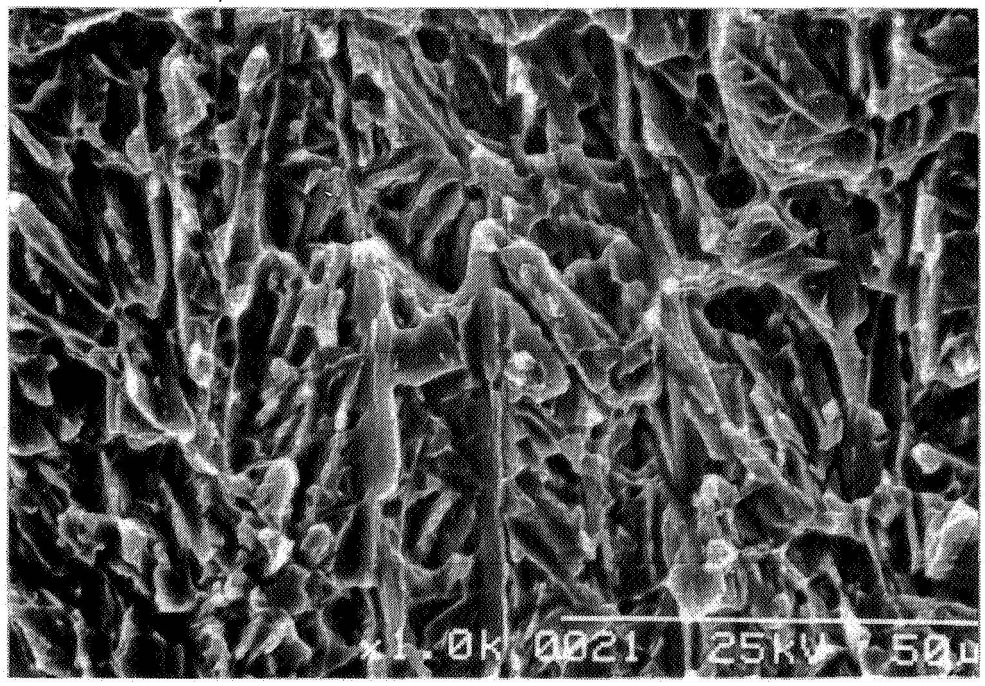

Figure 13. Close up of the martensitic alpha prime fracture surface tested with a 0.065 Hertz trapezoidal fatigue loading wave form (1000X).

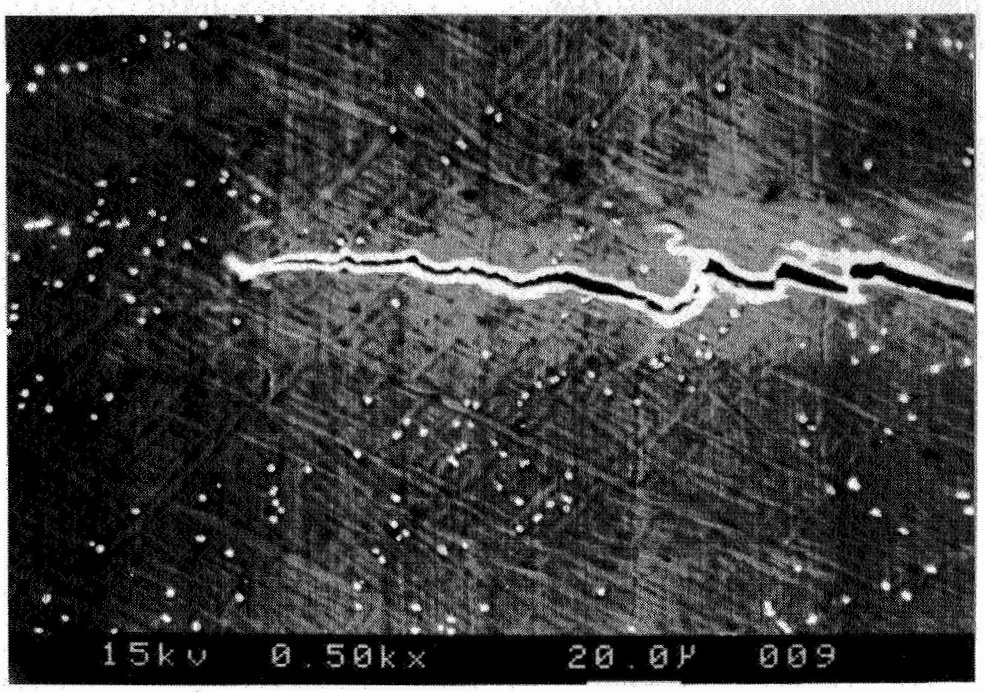

Figure 14. Alpha prime plate orientation influence on the growth of a fatigue crack in an etched specimen (etchant 3 HF-6 HNO_3-100 H_2O at 500X).

Conclusions

The observations made in this investigation are summarized below.

1. Comparable tensile properties to the disk microstructure, equiaxed alpha in a transformed beta matrix, can be obtained from a martensitic microstructure when aged at the "high alpha-beta" aging temperature. Improved fatigue response is achieved, as well, with approximately 30 percent loss in total strain to failure.
2. Martensitic alpha prime showed much less reduction in life compared to the disk microstructure when a dwell time at maximum load was imposed.
3. Very little difference in fracture surfaces was noticed for the two separate loading conditions tested for the martensitic microstructure indicating only subtle changes in crack growth mechanisms.
4. Substantial secondary cracking was found on the fracture surface of the disk microstructure specimens tested with a dwell time at maximum load which was not present in the non-dwell tests.
5. Fatigue life variation between 15 and 30 second dwell tests for the disk microstructure was minimal indicating a saturation time for observation of the dwell induced fatigue life reduction may exist.
6. The mechanisms responsible for the dwell effect in titanium alloys at temperatures less than approximately 200 °C are not entirely related to the room temperature creep, that is also observed in these materials.

Acknowledgments

Thanks are extended to the Quality and Integrity Design Engineering Center and FASIDE International, Inc. for providing equipment and support throughout this research program, Steven Kinyon for assistance during fractographic documentation, and Tom Mills for assistance in preparation. Thanks are also extended to Dr. Leon Grabowski of Rolls Royce plc for his suggestions, comments, and for providing specimens used in this investigation.

References

1. Farmer, T.E.: View of Future Requirements for Engine Cyclic Durability by Analysis and Testing, *AGARD Conference Proceedings n 368 Publ by AGARD*, Neuilly-sur-Seine, Fr Available from NTIS, Springfield, VA, USA, 1984, p 20 1-20 6.
2. Taylor, W.R.: Accelerated Mission Endurance Testing (AMET), *AGARD Conference Proceedings n 368 Publ by AGARD*, Neuilly-sur-Seine, Fr Available from NTIS, Springfield, VA, USA, 1984, p 3 1-3 5.

3. Hoeppner, D.W.: History and Prognosis of Material Discontinuity Effects on Engine Components Structural Integrity, *74th AGARD/SMP Meeting on Impact of Materials Defects on Engine Structures*, Keynote Address , Patras, Greece, May 27-28, 1992, p 1 1-1 8.
4. Jeal, R.H.: Relationship Between Fatigue Modeling and Component Integrity, *Fatigue 84*, Publ by Engineering Materials Advisory Services Ltd, Engl, 1984, p 1865-1879.
5. Evans, W.J.; Smith, M.E.F.; Williams, C.H.H.: Disc Fatigue Life Predictions for Gas Turbine Engines, *AGARD Conference Proceedings n 368 Publ by AGARD*, Neuilly-sur-Seine, Fr Available from NTIS, Springfield, VA, USA, 1984, p 11 1-11 13.
6. Hill, R.J.: Verification of Life Prediction Through Component Testing, *AGARD Conference Proceedings n 368 Publ by AGARD*, Neuilly-sur-Seine, Fr Available from NTIS, Springfield, VA, USA, 1984, p 17 1-17 9.
7. Larsen, J.M.; Nicholas, T.: Cumulative Damage Modeling of Fatigue Crack Growth, *AGARD Conference Proceedings n 368 Publ by AGARD*, Neuilly-sur-Seine, Fr Available from NTIS, Springfield, VA, USA, 1984, p 11 1-11 13.
8. Aircraft Accident Report, PB 90-910406, NTSB/AAR-90/06, [Re:UA Flight 232] Accident July 19, 1989, Report Date November 1990.
9. Evans, W.J.; Smith, M.E.F.; Williams, C.H.H.: Fatigue Performance of Discs and Engineering Specimens, *Fatigue 84,* Publ by Engineering Materials Advisory Services Ltd, Engl, 1984, p 1325-1335.
10. Stubbington, C.A.; Pearson, S.: Effect of Dwell on the Growth of Fatigue Cracks in Ti-6Al-4V, *Engineering Fracture Mechanics*, v 10, p 723-756.
11. Song, Z.; Hoeppner, D.W.: Dwell Time Effects on the Fatigue Behaviour of Titanium Alloys, *International Journal of Fatigue*, v 10 n 4, Oct 1988, p 211-218.
12. Bania, P.J.; Eylon, D.: Fatigue Crack Propagation of Titanium Alloys Under Dwell-Time Conditions, *Metallurgical Transactions A*, 9A, June 1978, p 847-855.
13. Sommer, A.W.; Eylon, D.: On Fatigue Crack Propagation of Titanium Alloys Under Dwell Time Conditions, *Metallurgica Transactions A*, 14A, October 1983, p 2178-2181.
14. Daeubler, M.A.; Walker, N.A.; Cope, M.T.: Influence of Heat Treatment on Microstructure and Properties of an Advanced High Temperature Titanium Alloy, *Sixth World Conference on Titanium*, France 1988.
15. Bate, P.S.; Blackwell, P.L.; Brooks, J.W.: Thermomechanical Processing of Titanium IMI 834, *Sixth World Conference on Titanium*, France 1988, p 287-292.
16. ASM Handbook: Volume 4-Heat Treating, ASM International, 1991, p. 913-923.
17. Stephens, R.R.; Hoeppner, D.W.: A New Apparatus for Studying Fatigue Deformation at High Magnifications, *Review of Scientific Instruments*, Vol. 59, No. 8, August, 1988, p. 1412-1419.

18. Standard Test Method for Tension Testing of Metallic Materials, 1993 Annual Book of ASTM Standards, American Society of Testing and Materials, Vol. 3.01, 1993, p. 130-149.
19. Neal, D.F.: Development and Evaluation of High Temperature Titanium Alloy IMI 834, *Sixth World Conference on Titanium*, France 1988, p 253-258.
20. Numakura, H.; Koiwa, M.: Hydride Precipitation in Titanium, *Acta Metallurgica*, v 32 n 10, Oct 1984, p 1799-1807.
21. Sommer, A.W.; Froes, F.H.; Eylon, D.: On the Incidence of Near Basal Cleavage During the Growth of Fatigue Cracks in Alpha Plus Beta Ti Alloys, Publ by ASM, Metals Park, OH, USA, p 83-87, 1986.
22. Hack, J.E.; Leverant, G.R.: A Model For Hydrogen-Assisted Crack Initiation of Planar Shear Bands in Near-Alpha Titanium Alloys, *Scripta Metallurgica,* v14, 1980, p 437-441.
23. Harrison, G.F.; Trantner, P.H.; Winstone, M.R.; Evans, W.J.: The influence of Low Temperature Cyclic Creep on the Fatigue Resistance of a Near-Alpha Titanium Alloy, *Proceedings of the Second International Conference on Creep and Fracture of Engineering Materials and Structures*, Pt. 1, Pineridge Press, Ltd, Swansea, Wales, 1987 p. 395-406.
24. Margolin, H.: Hydrogen Sliding at Alpha/Beta Interfaces of Titanium Alloys, *Scripta Metallurgica et Materialia*, v 24, 1990, p. 2397-2400.
25. Hoeppner, D.W.: A Fractographic Analysis of Flaw Growth in a High Strength Titanium Alloy, *Metallography*, Vol. 11, 1978, p. 129-154.
26. Song, Z., Hoeppner, D.W.: Size Effect on the Fatigue Behaviour of IMI 829 Titanium Alloy Under Dwell Conditions, *International Journal of Fatigue*, v 11 n 2, Mar 1989, p 85-90.
27. Stephens, R.R.; Hoeppner, D.W.: unpublished work conducted at the Quality and Integrity Design Engineering Center, The University of Utah, Salt Lake City, Utah, 1992.
28. Ryder, J.T.; Pettit, D.E.; Krupp, W.E.; Hoeppner, D.W.: *Final Report: Evaluation of Mechanical Property Characteristics of IMI 685*, Lockheed-California Company, Rye Canyon Laboratory, October 1973.

FATIGUE CRACK GROWTH IN 2024-T3 ALUMINUM UNDER TENSILE AND TRANSVERSE SHEAR STRESSES[1]

Mark J. Viz[2] and Alan T. Zehnder[2]
Department of Theoretical and Applied Mechanics
Cornell University, Ithaca, New York 14853
(607)255-9181, fax: (607)255-2011, email: atz@msc.cornell.edu

SUMMARY

The influence of transverse shear stresses on the fatigue crack growth rate in thin 2024-T3 aluminum alloy sheets is investigated experimentally. The tests are performed on double-edge cracked sheets in cyclic tensile and torsional loading. This loading generates crack tip stress intensity factors in the same ratio as the values computed for a crack lying along a lap joint in a pressurized aircraft fuselage. The relevant fracture mechanics of cracks in thin plates along with the details of the geometrically nonlinear finite element analyses used for the test specimen calibration are developed and discussed. Preliminary fatigue crack growth data correlated using the fully coupled stress intensity factor calibration are presented and compared with fatigue crack growth data from pure ΔK_I fatigue tests.

INTRODUCTION

Recently the problem of a crack near a lap joint (see figure 1) in the pressurized fuselage of an airplane was recognized as a situation in which material near the crack tip is subjected to both tensile and transverse shear (i.e., out-of-plane tearing) stresses. Concern over the effect of tearing stresses on the fatigue crack growth rate prompted researchers at NASA Langley to sponsor a program of analytical, numerical and experimental research at Cornell University aimed at measuring fatigue crack growth rates in such situations and developing the theory and numerical procedures necessary to interpret and to apply the experimental data.

The lap joint problem is illustrated in figure 1. Crack tip tensile stresses arise from the hoop stress in the fuselage skin, while the out-of-plane tearing stresses arise from the pressure difference "pushing out" on the skin. As shown in figure 1, one side of the crack remains riveted to the stringer and to the adjoining skin forming the lap joint. This side of the crack is much stiffer than the other side which is only a single sheet thick. This less stiff side bulges out relative to the stiff side, resulting in tearing stresses at the crack tip.

The stresses at the crack tip resulting from this loading can be described as a combination of membrane stresses constant through the thickness and transverse shear or tearing stresses that have a through the thickness variation. As defined in figure 2, for general loadings of thin, cracked plates under membrane and out-of-plane loads, two fracture modes with corresponding stress intensity factors K_I and K_{II} can be identified with the membrane loads, and two fracture modes with stress intensity factors k_1 and k_2 can be identified with the out-of-plane loads.

[1] This work was performed with support from NASA Langley, under award NAG-1-1311.
[2] Graduate Research Assistant and Assistant Professor, respectively.

Assuming that the crack tip stresses are a superposition of the stresses from the membrane and out-of-plane loads, and that the out-of-plane part can be described using Kirchhoff plate theory, the stresses on a plane ahead of the crack ($\theta = 0$ in the coordinate system of figure 3) are [1-3]

$$\sigma_{22} = \frac{K_I}{\sqrt{2\pi r}} + \frac{k_1}{\sqrt{2r}}\frac{2x_3}{h},$$
$$\sigma_{12} = \frac{K_{II}}{\sqrt{2\pi r}} + \frac{k_2}{\sqrt{2r}}\left(\frac{1+\nu}{3+\nu}\right)\frac{2x_3}{h}, \qquad (1)$$
$$\sigma_{23} = \frac{-k_2 h}{2(2r)^{3/2}(3+\nu)}\left[1 - \left(\frac{2x_3}{h}\right)^2\right],$$

where ν is the Poisson ratio and h is the plate thickness. The in-plane stress components, σ_{12} and σ_{22}, each have a constant and linear thickness variation term resulting from membrane and bending loads. The out-of-plane stress component, σ_{23}, varies parabolically through the thickness of the plate and has an $r^{-3/2}$ singularity, a manifestation of the limitation of Kirchhoff plate theory to satisfy completely the natural boundary conditions occurring at a free crack surface. Note the absence of $1/\sqrt{\pi}$ in the k_1, k_2 terms. This makes the definitions of k_1 and k_2 correspond to those introduced by Sih et al.[3] and is the form adopted by handbooks of stress intensity factors[4]. For more details and references on crack tip fields in plates loaded out-of-plane see [5,6].

Hui and Zehnder[6] argue that crack initiation and growth in thin plates under combined membrane and out-of-plane loads can be correlated with the stress intensity factors K_I, K_{II}, k_1 and k_2 (see eq. (1)). For the lap joint crack it appears that only K_I and k_2 are significant. The other two stress intensity factors are zero or nearly zero in this case. The relative importance of the tension and tearing stresses can be assessed by computing the K_I and k_2 for a crack located along the lap joint and comparing the values. Such a computation was performed by Britt[7] and is summarized here in figure 4 where the geometry of the problem is shown, and the stress intensity factor k_2 is plotted against K_I for a variety of crack lengths. For the crack situated along the stringer k_2 becomes comparable to K_I. A second scenario in which k_2 is relatively large occurs for a curved crack in a fuselage as studied by Potyondy et al.[8]. In this problem, the growth of a curving crack is simulated; high values of k_2 with respect to K_I were found to occur.

In both cases, for longer cracks k_2 becomes significant and thus may be an important factor in determining fatigue crack growth rate. Whether this is true or not is one of the principal subjects of this research. An extensive literature search revealed no data on fatigue fracture under such loadings, thus we are undertaking a series of fatigue crack growth rate experiments such that the K_I and k_2 stress intensity factors are imposed.

NUMERICAL PROCEDURES

To correlate crack growth rate with K_I and k_2, the capability to compute these stress intensity factors for both the test specimen and for the aircraft fuselage structure is needed. Numerical analyses are necessary for this computation since the stress intensity factor handbooks do not contain k_2 solutions for finite dimensional plates that would be used for experimentation. The procedure used here is to compute components of the energy release rate from finite element analyses and then calculate K_I and k_2 from the relations between stress intensity factors and these components of the energy release rate.

The energy released during crack growth is equal to the work done by the tractions acting over the area of crack extension. For a linearly elastic plate of thickness h the energy release rate, G, for self-similar extension of a through crack lying in the x_1, x_3 plane is[9,10]

$$G = \lim_{\Delta L \to 0} \frac{1}{2h\Delta L} \int_0^{\Delta L} \int_{-h/2}^{+h/2} \sigma_{2i}(x_1, \theta = 0) \Delta u_i(\Delta L - x_1, \theta = \pi) dx_3 dx_1, \tag{2}$$

where Δu_i are the components of relative crack tip displacement for a crack extension of ΔL, and the repeated index i implies summation over $i = 1, 2, 3$.

From this statement of the energy release rate the relationship between G and the stress intensity factors can be found[6]. The stress and displacement fields from Williams[1,2] are substituted into eq. 2, and after some manipulation and grouping of the membrane terms and the bending terms, the following relationships between the G components and the stress intensity factors are found

$$\begin{aligned} G_1 &= \frac{K_I^2}{E}, \\ G_2 &= \frac{K_{II}^2}{E}, \\ G_4 &= \frac{k_1^2 \pi}{3E} \left(\frac{1+\nu}{3+\nu} \right), \\ G_3 + G_5 &= \frac{k_2^2 \pi}{3E} \left(\frac{1+\nu}{3+\nu} \right). \end{aligned} \tag{3}$$

For a general loading the total energy release rate is the sum of the above, i.e.,

$$G = G_1 + G_2 + G_3 + G_4 + G_5. \tag{4}$$

The numbering of the components of G is arbitrary; the numbering convention chosen corresponds to the numbering of the degrees of freedom in the finite element program used for the stress intensity factor calculations. If the separate terms of the energy release rate in eq. 3 can be found from a numerical analysis, then eq. 3 can be used to calculate all four stress intensity factors.

To validate the method for the calculation of K_I, K_{II}, k_1 and k_2, six test analyses of finite cracks in infinite plates were conducted. Figure 5 shows these sample problems along with their theoretical solutions taken from refs. 3 and 6. Three of these test cases involve only a single mode; thus, the virtual crack extension technique [11-14] is appropriate to compute the single stress intensity factor in each of these problems. This technique gives only a total G value as its result; consequently, it must be known *a priori* what single mode is present. The other three test cases involve loadings which generate mixed modes at the crack tip. For these cases, the nodal release method [15] is necessary to be able to compute the individual G_is and hence the relevant stress intensity factors. The nodal release method computes the components of G on a nodal degree of freedom basis such that each G_i component is related to one of the four fracture modes shown in figure 2.

The computations of figure 5 as well as the test specimen calibrations discussed later were performed using the STAGS (STructural Analysis of General Shells) code[16]. The plate model

had dimensions of 11.0 by 10.0 by 0.090 thick and contained a centrally located straight crack of length 1.0 oriented parallel to the 11.0 dimension. No special crack tip elements were used. Instead, the STAGS 410 element[17], a four-noded, six degree-of-freedom per node flat plate element, was used for the entire mesh. All elements were square inside a near tip region of mesh refinement that extends a distance $\frac{L}{2}$ above and below the crack line and $\frac{L}{4}$ behind and $\frac{L}{2}$ ahead of the crack tip (L is the crack length). The standard element size in this region was $\frac{L}{64}$.

The results of these sample computations are also given in figure 5. For the three single mode cases the virtual crack extension results were all within 3.6% difference from the theoretical solutions. For the three mixed mode cases the nodal release results were all within 1.3% difference from the theoretical solutions. Based on these results the applicability of these two methods for the calculation of the four stress intensity factors is established.

However, for the stress intensity factor calculations needed for the calibration of the test specimen both the virtual crack extension technique and the nodal release technique have significant drawbacks. The virtual crack extension technique by its nature does not permit the computation of the individual components of the energy release rate, rendering it useless for a mixed mode situation such as our testing configuration. The nodal release method, although applicable to any general mixed mode situation, has the disadvantage of requiring two full finite element analyses to be performed per one G_i computation. This would double the already large number of required analyses. Consequently, a third method, the modified crack closure integral method[18,19], was used. This method approximates the displacement field over a crack advance of ΔL by using the displacement field behind the crack of length L, thus requiring only a single analysis per stress intensity factor calculation. The results already given that relate components of the energy release rate on a nodal degree of freedom basis to the four stress intensity factors can be applied to the modified crack closure integral method.

EXPERIMENTAL METHOD

To determine the fatigue crack growth rate as a function of the two stress intensity factors K_I and k_2, double-edge cracked plates were tested under constant amplitude cyclic tensile and torsional loadings. The test specimens were machined from 2.29mm thick 2024-T3 aluminum plates provided by NASA Langley. This is the same batch of aluminum sheets used by Hudson[20] in his pure mode I fatigue crack growth study in 1969. The test specimen dimensions and geometry are shown in figure 6. On each side of the test specimen a 6.35mm long, 0.18mm wide starter notch was cut using a foil electric discharge machine. The samples were diamond polished to a 3μm finish to improve the optical crack length measurement.

Ideally, the sample loaded into the gripping fixtures is subjected to uniform vertical displacements (in the y direction; see figure 6) and to a rigid rotation about the y axis at the bottom boundary. Any deviation from this condition will change the stress distribution, and consequently the stress intensity factors and rate of crack growth. To prevent any slipping of the test specimen during a fatigue test, the gripping fixtures and face plates each had two channels cut along their wide direction, into which were inserted 1.52mm diameter steel rods, as shown in figure 6. Sandwiching the specimen between fixtures and face plates and tightening the bolts pushes the steel rods into the specimen creating a slight indentation which then ensures a maintainable grip line for the duration of the fatigue test.

All of the tests were performed using an Instron 1321 tension-torsion servohydraulic test frame operating in tension and torque control. The sample, fixtures and part of the testing machine are shown in figure 7. The testing conditions were monitored continuously with an oscilloscope as well as with a computer that digitized the load, stroke, torque and rotation signals. A 2.54mm long fatigue precrack was grown from each starter notch by cycling with a pure tension load at 6Hz with $\Delta K_I \approx 5.5\text{MPa}\sqrt{\text{m}}$ and $R = 0.7$, where $R \equiv P_{min}/P_{max}$, P being the axial tensile load. Typically 100,000 cycles were required for the fatigue precracking.

Testing was performed at $R = 0.7$ for both the tensile and torsional loads. The tensile loads ranged from approximately 2kN to 45kN, and the torques ranged from approximately 11Nm to 110Nm. A thin plate has a relatively low torsional stiffness, thus the specimen experiences large rotations (on the order of 20^o for a torque of 110Nm) severely limiting the testing frequency compared to a pure tension loading test. Above 1Hz the testing machine actuator could not maintain the command signal, thus all of the tests were performed at 1Hz where the loads could be controlled to better than 1.0%.

Crack lengths were measured approximately every 0.5mm of crack growth and were recorded with the corresponding number of elapsed cycles as well as the loading conditions. These crack lengths were measured using two travelling microscopes, one for each crack, mounted to the testing frame. Vertical and horizontal microscope movements were measured with digital travel indicators to give an (x, y) location of the crack tip at each measurement. When setting up the test the microscopes were rotated to be normal to the plane of the center of the specimen when the mean torque was applied. This initial rotation was maintained throughout the test. Fluorescent light reflected onto the specimen surface with a sheet of white card stock was used to illuminate the crack tip region. With this arrangement crack length could be measured to an accuracy of ± 0.05mm.

TEST SPECIMEN CALIBRATION

A calibration is needed to relate experimentally measurable quantities, such as the applied loads and crack length, to the stress intensity factors. For the current experiments, P, the net tension load, T, the net torque and, a, the crack length are inputs to a calibration function with the stress intensity factors, K_I and k_2, as output. What makes the calibration for this testing arrangement difficult is that K_I is not solely a function of P and a and k_2 is not solely a function of T and a; on the contrary, K_I and k_2 are both nonlinear functions of P, T and a. Perhaps a simpler way of stating this disregarding the fracture mechanics is that the axial stiffness as well as the torsional stiffness of the specimen are not just functions of the plate geometry but functions of the plate geometry and the current loading of the plate. To approach this aspect of the experimental work it was deemed early on that a numerical approach would be needed to compute the correct stress intensity factor calibration. The approach thus employed is a fully geometrically nonlinear plate finite element analysis.

The means used to calculate the stress intensity factors from the results of a finite element computation were described in a previous section. Using a half-plate model (see figure 6 for modelling details and boundary conditions) and the modified crack closure integral method to obtain the G_i values, geometrically nonlinear analyses were performed for a grid of P, T values at five discrete crack lengths: 6.35mm, 12.7mm, 19.05mm, 25.4mm and 31.75mm, chosen to span the

experimental results which are for crack lengths from 6.0mm to approximately 32.0mm. The K_I calibration "surface" as a function of P, T for three crack lengths (6.35mm, 19.05mm, 31.75mm) is given in figure 8. The corresponding k_2 calibration for the same crack lengths is given in figure 9.

Although these calibration plots exhibit many interesting features only a few will be discussed here. Notice that for higher torque values K_I becomes less sensitive to increasing axial load (see figure 8). This is especially conspicuous for the shortest crack length. Also notice that k_2 at higher torque levels decreases as the axial load is increased (see figure 9). This effect is a result of the dependence of the torsional stiffness on the axial tension load in that as the axial load is increased, the torsional stiffness of the plate also increases.

Further results from the calibration calculations although not shown in figures 8 and 9 also show that K_{II} and k_1 are small compared to K_I and k_2, respectively, though they are present[7,8]. This result is a welcome one, since the crux of this research depends on the near tip stress field in the test specimen being essentially the same as the near tip field in the actual cracked aircraft fuselage. Simulations of crack growth in fuselage bays show that indeed the K_{II} and k_1 components are small compared to K_I and k_2, respectively.

MIXED MODE FATIGUE CRACK GROWTH RATE DATA

The experiments completed to date cover a wide range of cyclic loadings. The stress intensity factors corresponding to these tests were calculated based on the calibration curves of figures 8 and 9 and the maximum values at the start of a test and the end are plotted as the dashed lines in figure 4. This figure shows that the experiments cover the lower end of the K_I and k_2 range for a crack lying along a stringer in a lap joint.

Results from two of the tests are presented here. Analysis of the remaining twenty tests completed to date is in progress. Figures 10 and 11 show the envelopes of stress intensity factors for test nos. 14 and 18. In both tests the torque range was the same, but the axial load in test no. 14 was ten times larger than the axial load range used for test no. 18. In both tests K_I is larger than k_2 for most of the test except for the longest crack lengths in test no. 18.

Fatigue crack growth rates as well as crack length versus elapsed cycles data for each test are shown in figure 12. Shown on the growth plots are benchmark data from Hudson and Newman for pure mode I fatigue crack growth[20,21].

In each test the crack grew intially at a rate close to the pure mode I rate but slowed down dramatically as the crack grew. Thus the $\frac{da}{dN}$ data fell well below the reference lines for longer crack lengths. This appears to be caused by roughness induced crack closure. During an experiment it is observed (by eye and ear) that the crack faces are in contact as they slide with respect to each other. A scanning electron microscope image of the fracture surface (figure 13) shows the region where crack contact has occurred. In this figure the horizontal direction is parallel to the plate surface; the direction of relative crack face sliding is vertical. The fracture surface is flattened out and scoring in the sliding direction is clearly seen.

However, crack growth rate acceleration does occur towards the end of the test data presented in figure 12. It is thought that the crack surface abrasion just mentioned might wear away

enough of the contacting surface that at some critical point this effect is minimized and the crack growth rate once again increases. If this sort of three-phase behavior (i.e., initial pure mode I type growth, then growth rate decrease followed by an increase) is common to all such loading situations for the testing configuration is still unknown, but should be elucidated after all of the test data is analyzed.

DISCUSSION

The experimental data indicate that in the regime of stress intensity factors for which tests were performed the crack growth rate is initially reduced by the presence of k_2 resulting from crack face contact, but that generally this condition does not persist and crack growth rate does eventually increase. Whether this is true at higher values of K_I and k_2 is unclear at this time. Intuitively it would seem logical that by increasing the value of the stresses at the crack tip the crack would grow faster. This may be the case at the higher levels of K_I and k_2 where the crack faces should separate more and crack face contact should not retard crack growth rate. Thus future experiments may concentrate on higher stress intensity factor levels.

SUMMARY AND CONCLUSIONS

Although it is still unclear as to what systematic role, if any, the presence of a k_2 crack tip fracture mode might have on the overall fatigue crack growth rate of a crack in a stiffened fuselage structure, it is clear that characterizing the problem as one of simple mode I fatigue crack growth resulting from the fuselage hoop stress would greatly underestimate the K_I field at the crack tip. Geometrically nonlinear analyses and resultant stress intensity factor calibrations are necessary to describe properly the crack tip stress field in a cracked fuselage lap joint as well as any test specimen configuration used to examine the fatigue crack growth behavior in such structures. Whether or not the presence of the k_2 mode partially drives the fatigue crack growth or if it is simply the additional K_I supplied by the tearing or bulging aspect of the crack through the geometrically nonlinear effects that drives the crack growth is still not resolved.

However, this investigation has seemingly raised as many questions as it may have answered. The question of how to account for crack face contact effectively and what impact it may have on the local loading or unloading of the crack tip is unresolved. Furthermore, the more basic question of whether or not the same phenomenon occurs when a long crack in a fuselage lap joint is flapping is of primary concern as to the relevance of this work to the actual cracked fuselage problem. To complete some fatigue tests at stress intensity factor levels equal to those experienced by an actual cracked fuselage might be required to answer this question definitively. Finally, a quicker and more accurate method of computing all stress intensity factors from a finite element analysis is required.

REFERENCES

[1] Williams, M.L.: On the Stress Distribution at the Base of a Stationary Crack. *Journal of Applied Mechanics*, vol. 24, 1957, pp. 109-114.

[2] Williams, M.L.: The Bending Stress Distribution at the Base of a Stationary Crack. *Journal of Applied Mechanics*, vol. 28, 1961, pp. 78-82.

[3] Sih, G.C.; Paris, P.C.; and Erdogan, F.: Crack Tip Stress- Intensity Factors for Plane Extension and Plate Bending Problems. *Journal of Applied Mechanics*, vol. 29, 1962, pp. 306-312.

[4] Murakami, Y., ed.: *Stress Intensity Factors Handbook – Vol. 2.* Pergammon Press, 1987.

[5] Sih, G.C., ed.: *Mechanics of Fracture 3, Plates and Shells with Cracks.* Noordhoff Int. Pub. Co., 1977.

[6] Hui, C.Y.; and Zehnder, A.T.: A Theory for the Fracture of Thin Plates Subjected to Bending and Twisting Moments. *International Journal of Fracture*, vol. 61, 1993, pp. 211-229.

[7] Britt, V.O.: personal communication. NASA Langley Research Center, Sept. 1993.

[8] Potyondy, D.O.; Wawrzynek, P.A.; and Ingraffea, A.R.: Discrete Crack Growth Analysis Methodology for Through Cracks in Pressurized Aircraft Structures. *Advanced Structural Integrity Methods for Airframe Durability and Damage Tolerance*, NASA CP-3274, 1994.

[9] Irwin, G.R.: Analysis of Stresses and Strains Near the End of a Crack Traversing a Plate. *Journal of Applied Mechanics*, vol. 24, 1957, pp. 361-364.

[10] Rice, J.R.: Mathematical Analysis in the Mechanics of Fracture. *Fracture*, vol. 2, Academic Press, 1968.

[11] Parks, D.M.: A Stiffness Derivative Finite Element Technique for Determination of Elastic Crack Tip Stress Intensity Factors. *International Journal of Fracture*, vol. 10, 1974, pp. 487-502.

[12] Hellen, T.K.: On the Method of Virtual Crack Extensions. *International Journal of Numerical Methods in Engineering*, vol. 9, 1975, pp. 187-207.

[13] deLorenzi, H.G.: Energy Release Rate Calculations by the Finite Element Method. *Engineering Fracture Mechanics*, vol. 21, 1985, pp. 129-143.

[14] Hellen, T.K.; and Blackburn, W.S.: Nonlinear Fracture Mechanics and Finite Elements. *Engineering Computation*, vol. 4, 1987, pp. 2-14.

[15] Ansell, H.: Bulging of Cracked Pressurized Aircraft Structure. *Ph.D. Thesis No. 138*, Institute of Technology, Linkoping, Sweden, Report No. LIU-TEK-LIC-1988:11, 1988.

[16] Almroth, B.O.; Brogan, F.A.; and Stanley, G.M.: Structural Analysis of General Shells. *User Instructions for STAGSC-1*, vol. 2, Lockheed Missiles and Space Co., Report No. LMSC D633873, 1986.

[17] Rankin, C.C.; and Brogan, F.A.: The Computational Structural Mechanics Testbed Structural Element Processor ES5: STAGS Shell Element. *NASA CR4358*, 1991.

[18] Rybicki, E.F.; and Kanninen, M.F.: A Finite Element Calculation of Stress Intensity Factors by a Modified Crack Closure Integral. *Engineering Fracture Mechanics*, vol. 9, 1977, pp. 931-938.

[19] Viswanath, S.; Lakshminarayana, H.V.; and Ravindranath, D.D.: A Modified Crack Closure Integral Method for Calculating Stress Intensity Factors for Cracked Plates Subject to Bending Loads. *International Journal of Fracture*, vol. 41, 1989, pp. R45-R50.

[20] Hudson, C.M.: Effect of Stress Ratio on Fatigue-Crack Growth in 7075-T6 and 2024-T3 Aluminum Alloy Specimens. *NASA TN D5390*, 1969.

[21] Newman, J.C.: personal communication. NASA Langley Research Center, Sept. 1993.

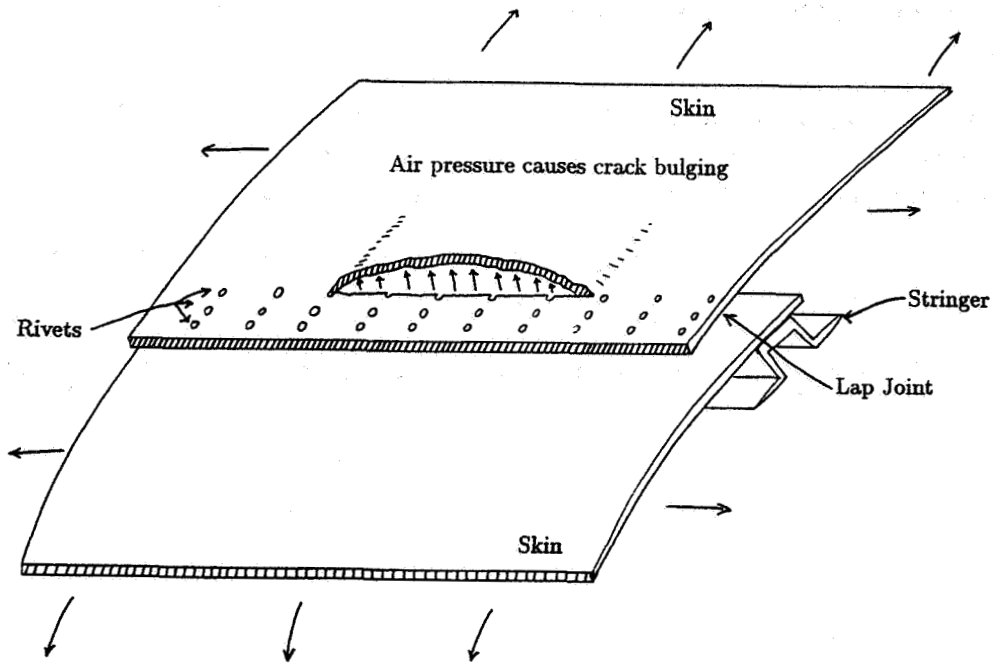

Figure 1. Crack in an aircraft fuselage lap joint along a stringer causing crack face bulging.

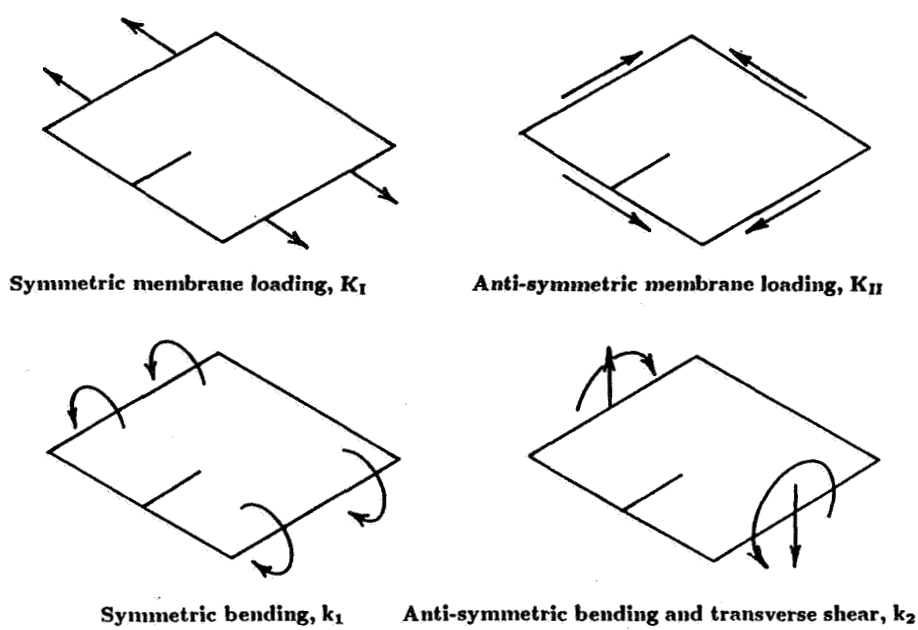

Figure 2. Fracture modes for a thin, cracked plate: K_I, K_{II}, k_1, k_2.

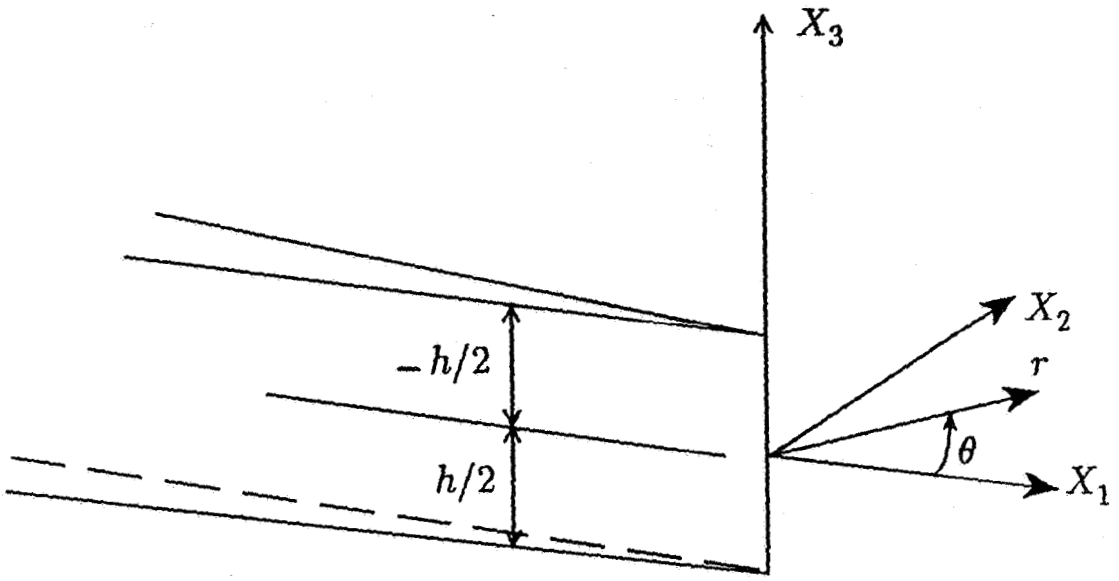

Figure 3. Crack tip coordinate system (see eq. 1).

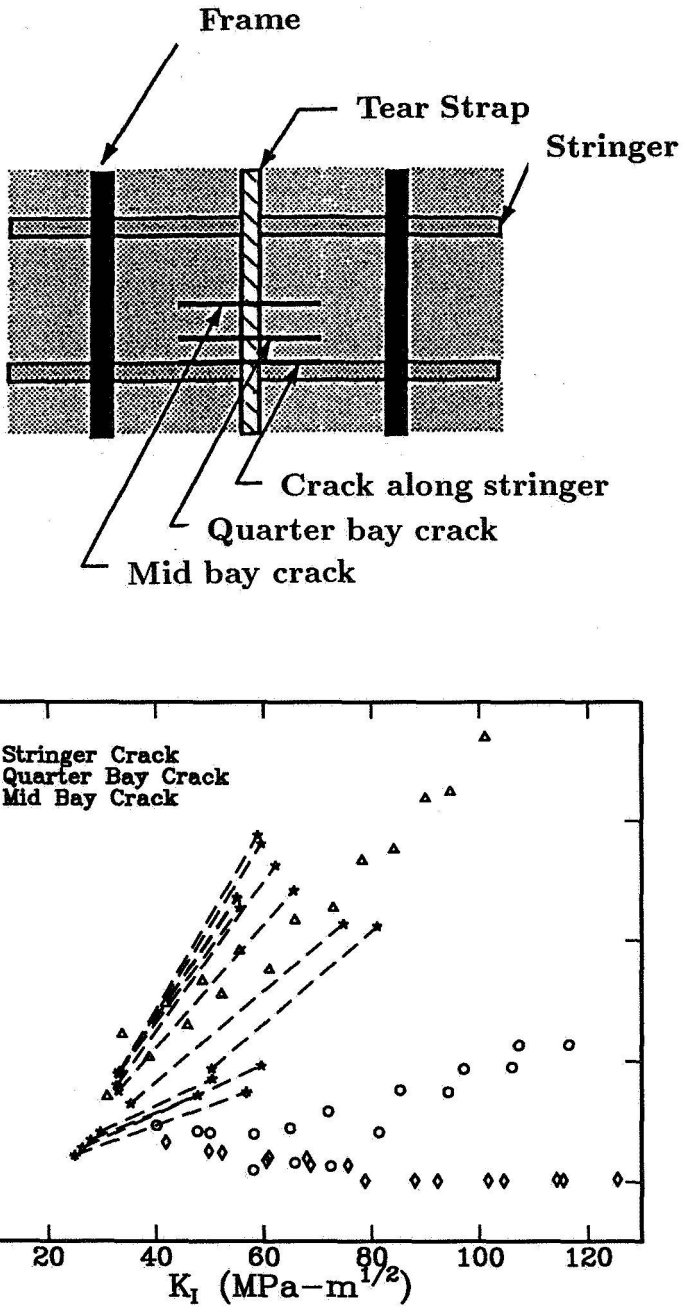

Figure 4. Stress intensity factors, K_I and k_2, for cracks at three positions in a fuselage bay. Points are the computed data from Britt[7]. Dashed lines are the maximum stress intensity factors from the tension-torsion fatigue tests described herein.

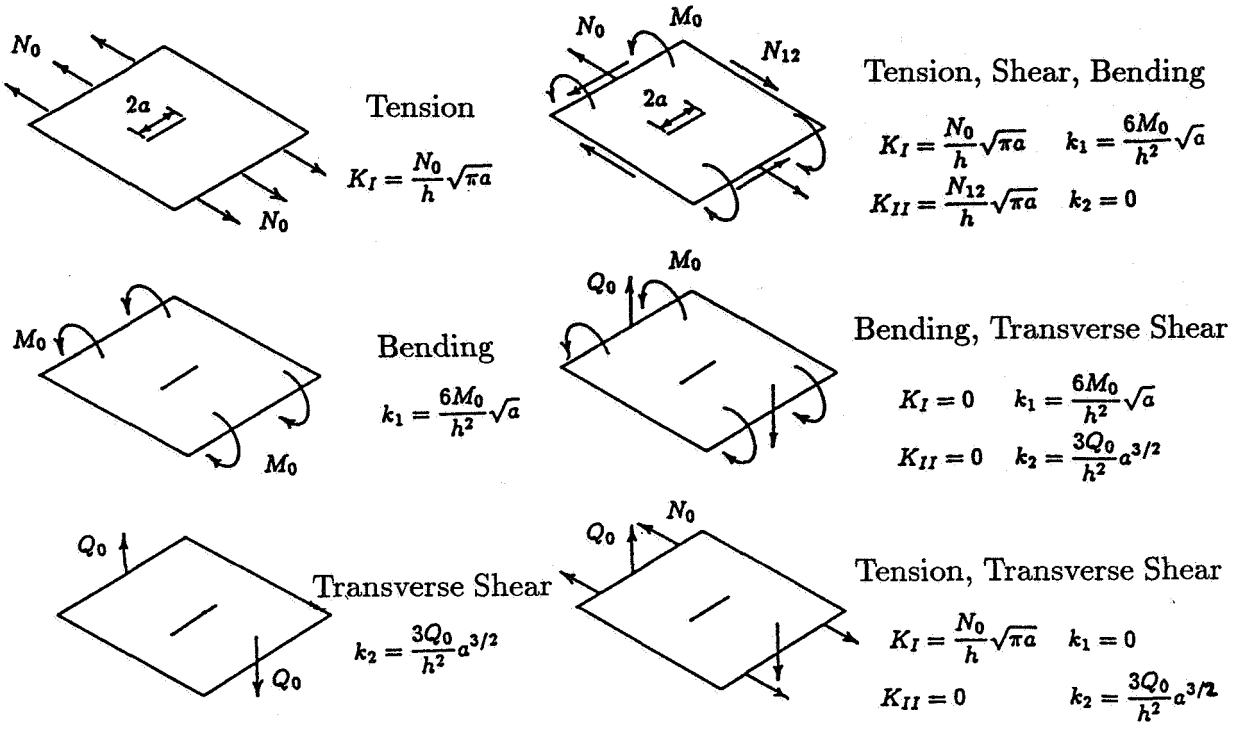

Norm. Theoretical Values	k_1 (6.0)	k_2 (3.0)	K_I (1.7725)	K_{II} (1.7725)
Loading:				
Tension (VCE)[1]	-	-	1.754 (1.0%)	-
Bending (VCE)	5.954 (0.8%)	-	-	-
Transverse Shear (VCE)	-	2.891 (3.6%)	-	-
Tension, Shear & Bending (NR)[2]	5.965 (0.6%)	-	1.765 (0.4%)	1.763 (0.5%)
Bending & Transverse Shear (NR)	5.997 (0.1%)	2.967 (1.1%)	-	-
Tension & Transverse Shear (NR)	-	2.963 (1.3%)	1.760 (0.7%)	-

[1]VCE...virtual crack extension technique
[2]NR...nodal release technique

Figure 5. Six test cases for the validation of the stress intensity factor computation techniques: finite length crack in an infinite plate.

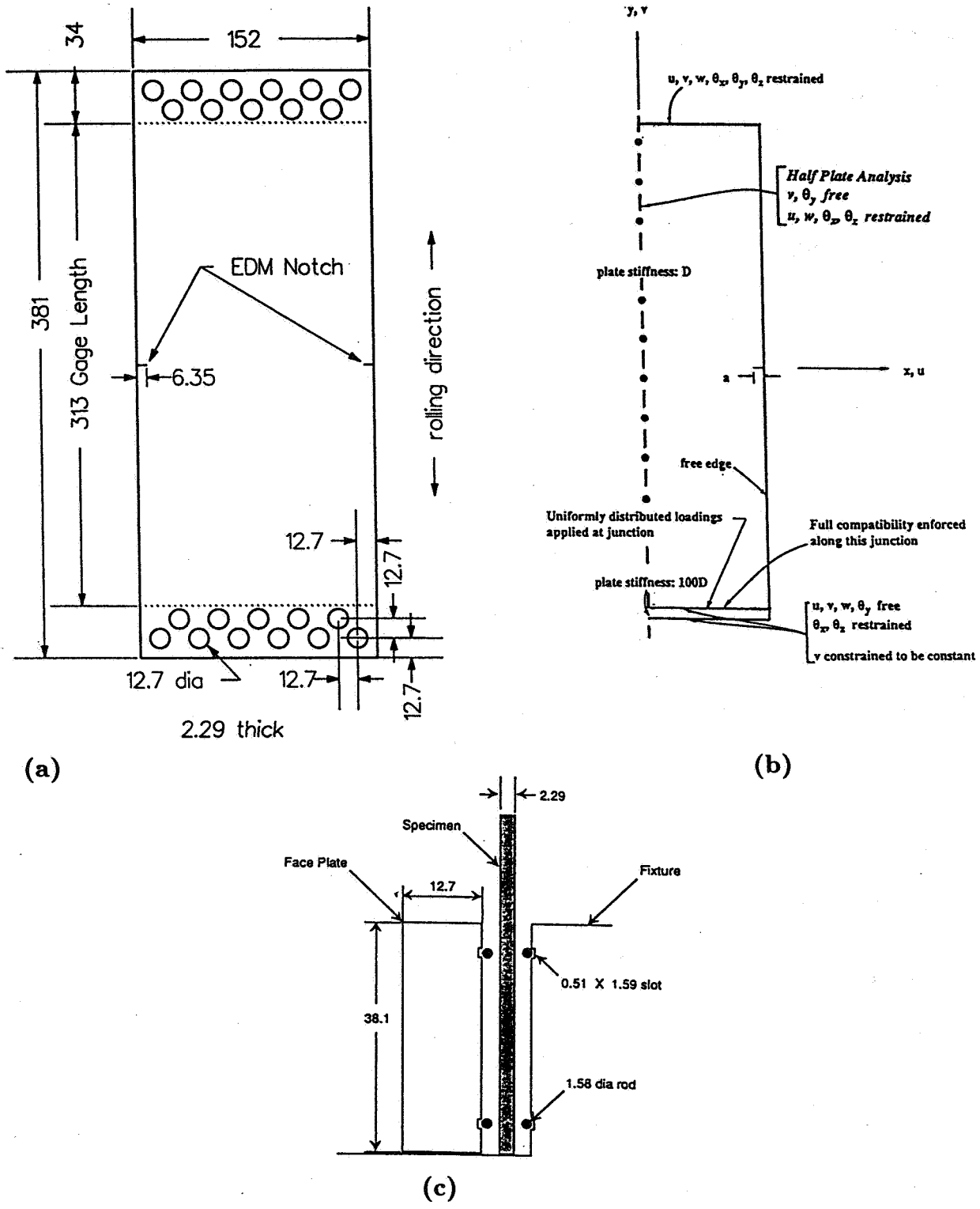

Figure 6. (a) Test specimen, dimensions in mm. (b) Boundary conditions used in finite element model. (c) Detail of specimen gripping fixture.

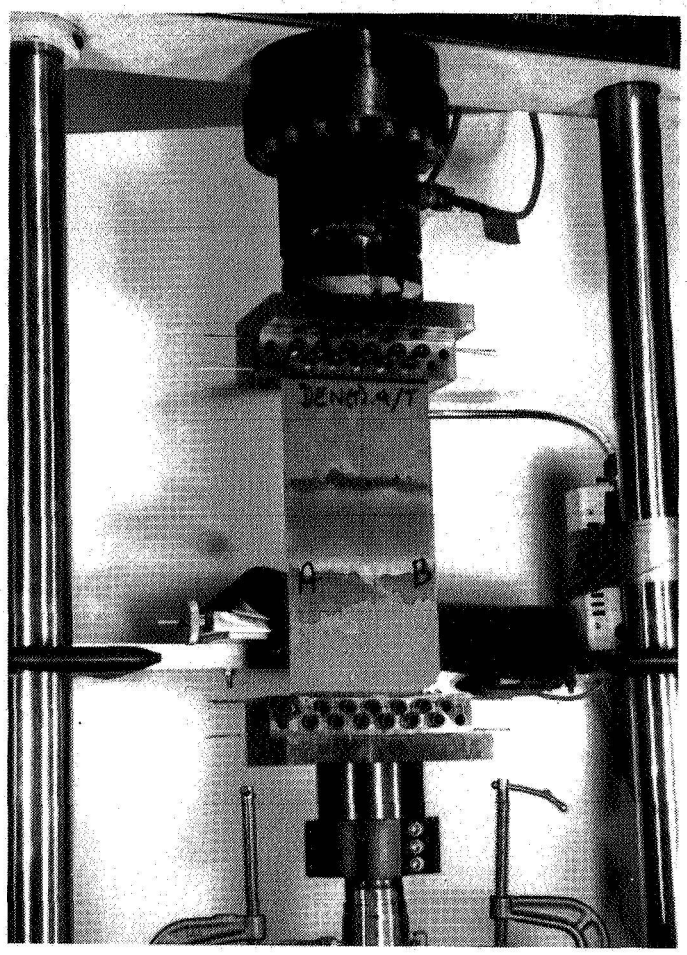

Figure 7. Photograph of the test specimen mounted in the tension-torsion loading frame.

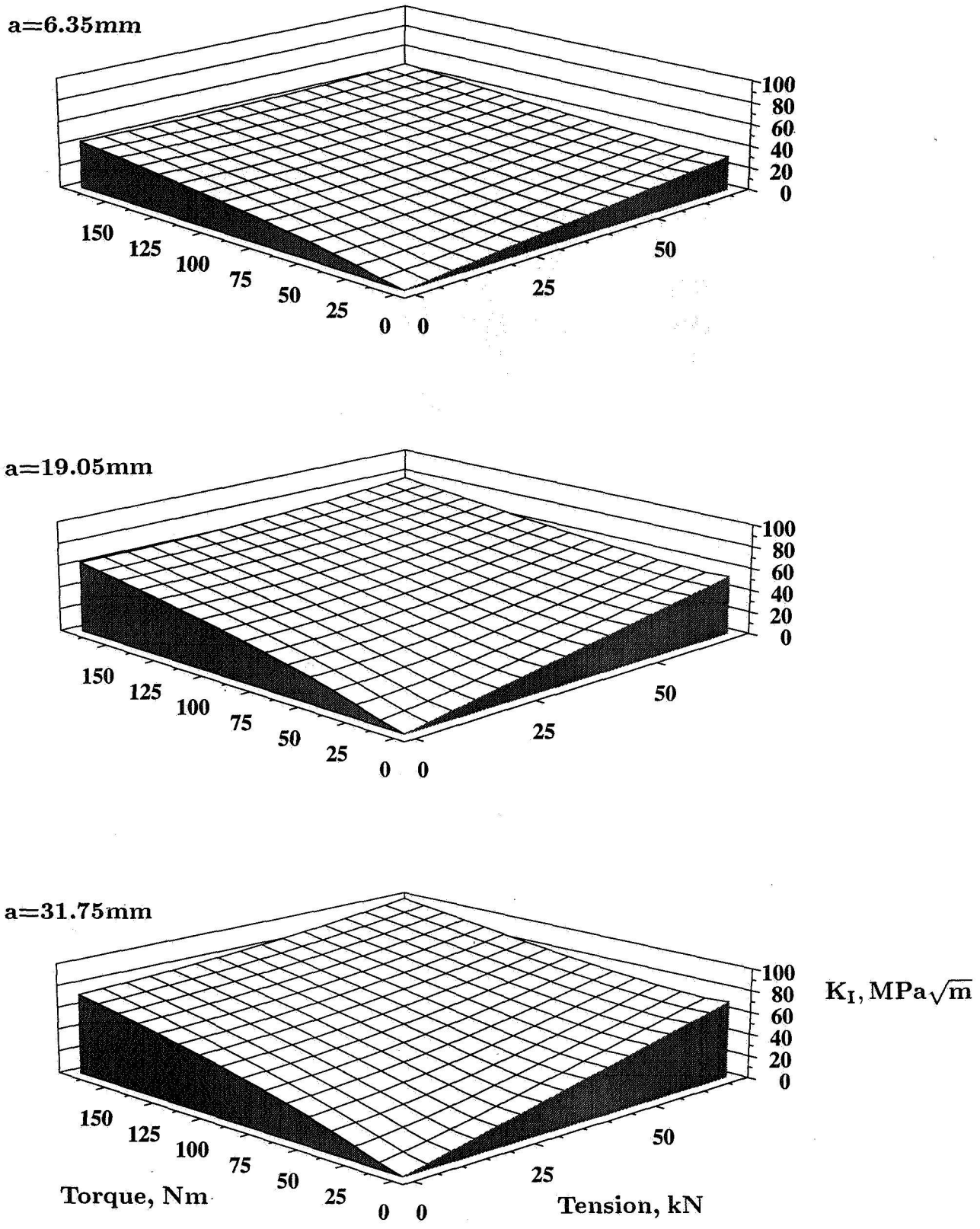

Figure 8. Stress intensity factor K_I versus axial load P and torque T for three crack lengths: 6.35mm, 19.05mm, 31.75mm.

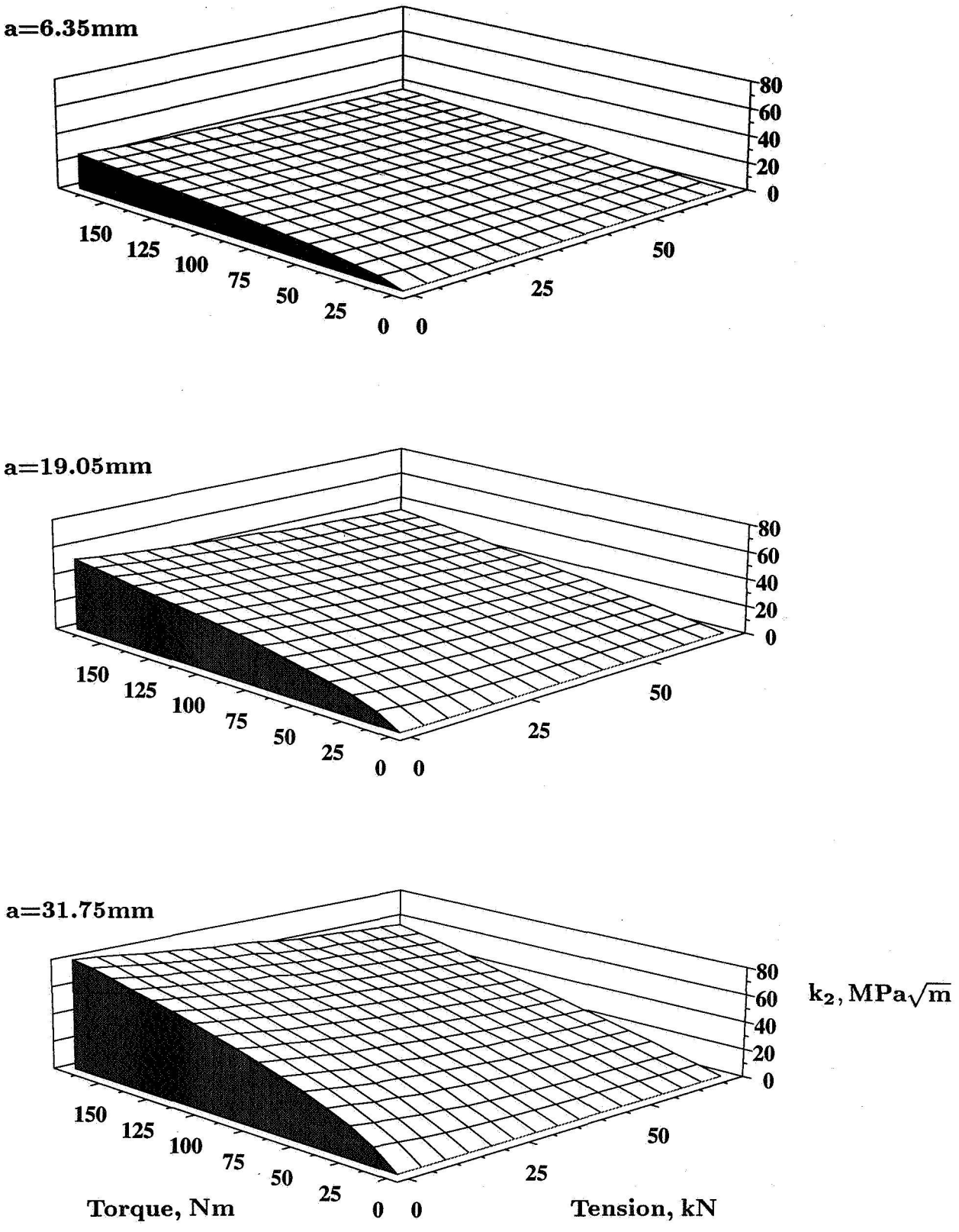

Figure 9. Stress intensity factor k_2 versus axial load P and torque T for three crack lengths: 6.35mm, 19.05mm, 31.75mm.

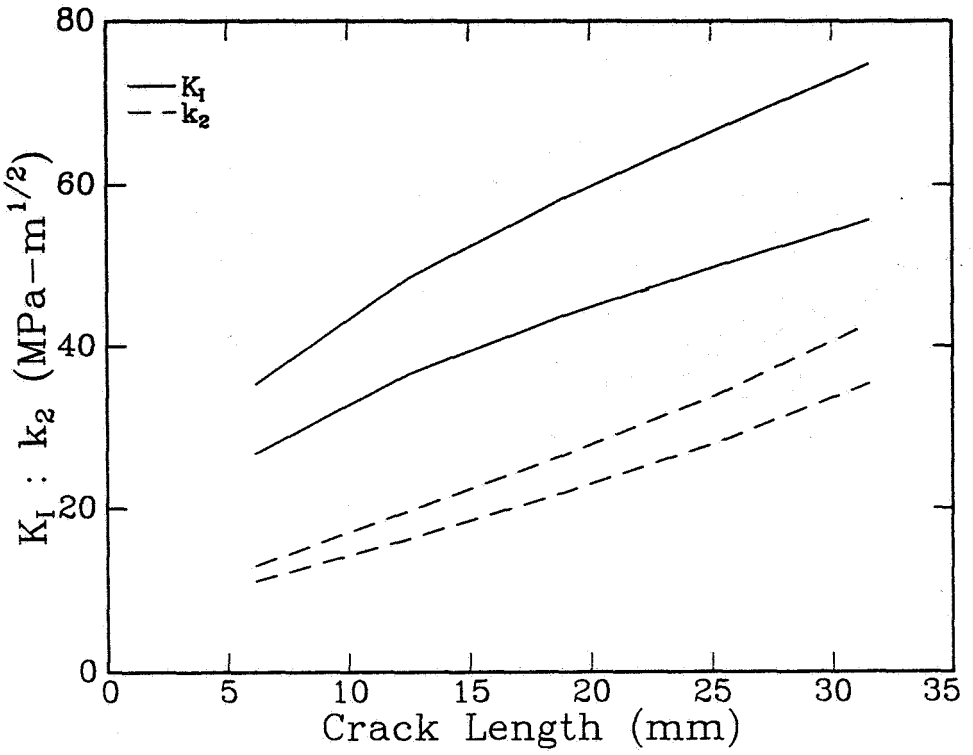

Figure 10. Envelopes of K_I and k_2 versus crack length for test no. 14. (P_{max} =44.5kN, P_{min} =31.2kN, T_{max} =112.0Nm, T_{min} =78.4Nm).

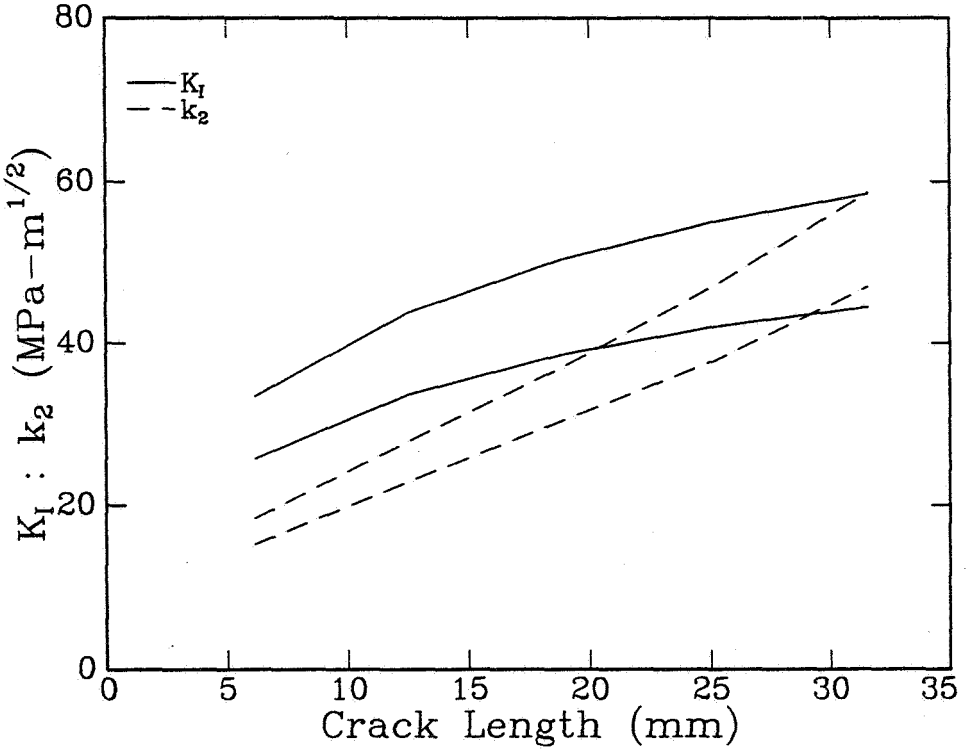

Figure 11. Envelopes of K_I and k_2 versus crack length for test no. 18. (P_{max} =4.5kN, P_{min} =3.1kN, T_{max} =112.0Nm, T_{min} =78.4Nm).

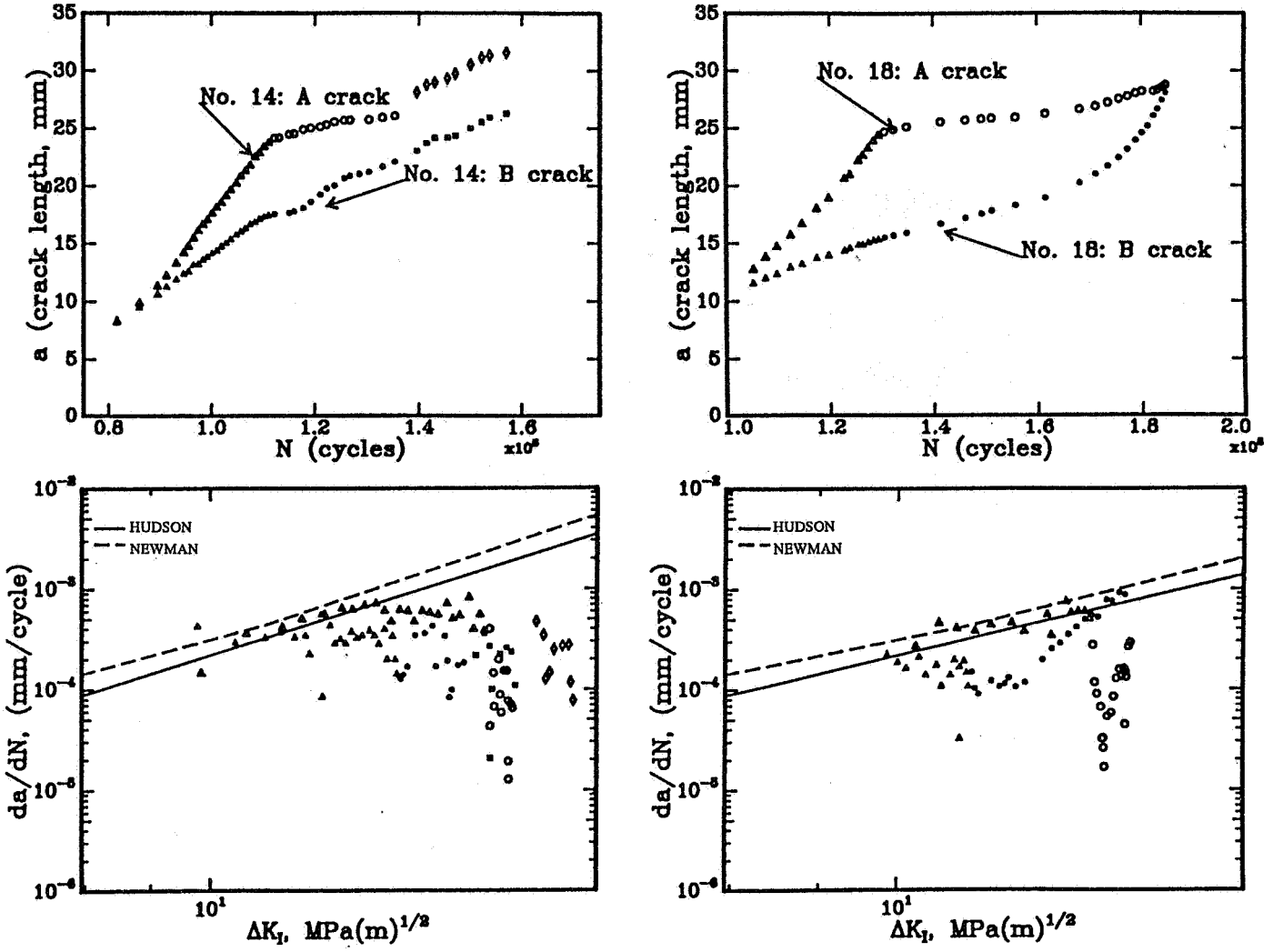

Figure 12. Crack length, a, versus total elapsed cycles, N, and crack growth rate, $\frac{da}{dN}$, versus ΔK_I for test no. 14 (*left*) and test no. 18 (*right*). "A" and "B" designations refer to each of the two cracks in a given specimen. Hudson's[20] pure mode I data is shown by the solid line; Newman's[21] pure mode I data is shown by the dashed line.

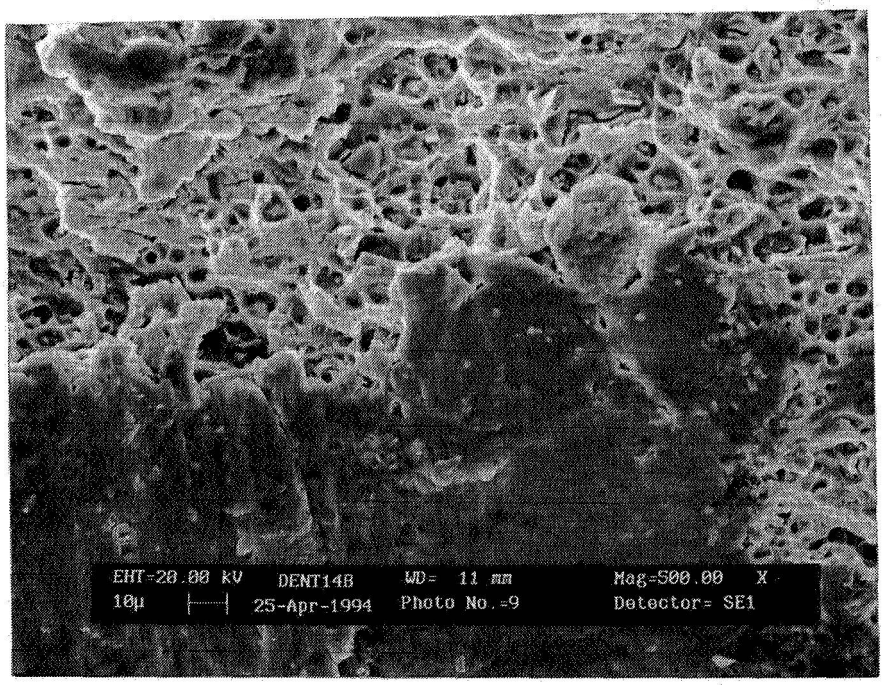

Figure 13. Scanning electron micrograph of the fracture surface in a region where crack contact has occurred. The region in the upper part of the picture shows no contact: the typical ductile fracture surface is seen. In the lower region the ductile fracture surface has been flattened and abraded by the crack surfaces sliding past each other.

RESULTS OF UNIAXIAL AND BIAXIAL TESTS ON RIVETED FUSELAGE LAP JOINT SPECIMENS

H. Vlieger
National Aerospace Laboratory NLR
Amsterdam, The Netherlands

INTRODUCTION

In the USA uniaxial fatigue tests were carried out for the FAA on riveted lap joint specimens to study the effect of various lap joint parameters on fatigue life and the occurrence of MSD. These tests were carried out by Arthur D. Little Co. (ADL) and the Fatigue Technical Institute (FTI). The parameters considered and their levels selected for these tests are shown in Table 1. Figure 1 gives some details of the design of the tested panel configurations. The panels were provided with tear straps and a longitudinal stiffener because the specimens had to be representative for fuselage longitudinal lap joints. The results of these tests are compiled in Ref.1. Considering MSD it was found from these tests that the stress level and the rivet spacing were the most important lap splice parameters.

As part of an FAA-NLR collaborative programme on structural integrity of ageing aircraft NLR carried out fatigue tests on riveted lap joint specimens of similar design as those tested by ADL/FTI, but now both uniaxial and biaxial fatigue tests were performed. The encircled values in Table 1 were chosen for the levels of the parameters in the NLR testing programme. This investigation was sponsored by the FAA. In this paper the experimental results obtained are presented.

DESCRIPTION OF TESTING PROGRAMME

Table 2 shows the matrix of the testing programme carried out by NLR. Two stress levels and two rivet spacings were chosen as parameters in these tests resulting in 4 groups of specimens. All specimens had a skin thickness of 0.05 inch. The other panel characteristics were taken similar to those of the ADL/FTI baseline design (see Table 1). Only the panel widths were taken equal to 14 inches instead of 12 inches (see figure 2) to allow bonding of the clamping arms of the biaxial specimens alongside the tear straps (see next chapter). Further, apart from two specimens in group no 4, the longitudinal stiffener on the lap joint was missing. In each group of specimens the uniaxial tests were carried out in duplicate and the biaxial tests in triplicate. In total 22 specimens were tested (10 uniaxial + 12 biaxial specimens, see Table 2).

The main objective of the biaxial testing programme was to study possible effects of biaxial loading on fatigue life and occurrence of MSD with respect to results of uniaxial tests on lap joints of similar design. Further, comparison of the NLR and the ADL/FTI test results of panels of similar design was an objective.

DESCRIPTION OF SPECIMENS

All specimens were delivered with a length of 36 inches. After delivery at NLR the specimens that were planned for uniaxial testing were provided in the clamping areas with aluminium tabs to prevent clamping failures (at either side of the sheet ends a 1 mm thick sheet was bonded for that purpose). Thereafter the hole pattern being present in the available plate fixtures of the testing machine (see below under Execution of Testing) was drilled in the specimens.

The specimens that were used for biaxial testing required a special treatment. To be able to run biaxial fatigue tests on specimens in which the lap joint is the fatigue critical area, the way of load introduction into the lap joint area is of paramount interest (Ref. 2). Figure 3 shows how this problem was solved: the biaxial loads were applied to the test section by means of load introducing arms consisting of unidirectional Aramid fibres embedded in epoxy raisin. The composite parts of the load introducing arms were made separately by means of a lay-up of aramid prepreg layers. These parts were laid up in a mold and cured in this mold in one autoclave cycle. After curing the aramid parts were cold bonded to the specimen and to the end fixtures. To allow bonding of the horizontal arms to the biaxial specimens the width of all specimens was chosen equal to 14 inches thus leaving 1 inch of material outside of the tear straps free for bonding of the load introducing arms (see Figs. 2 and 3). The exploded view in Fig. 3 clearly shows the complexity of the manufacturing process of the load introducing arms of the biaxial specimens.

With regard to the longitudinal (sheet) stiffener being present on the ADL/FTI specimens (see Fig. 1) the following remarks can be made. It is to be expected that this stiffener will not have a significant effect on fatigue life and/or MSD. Further, in uniaxial testing the loading of this stiffener will not be very realistic: due to the restrained Poisson's constraint, in the tests the stiffener will be loaded in compression and consequently there will be load transfer from the skin to the stiffener. In reality this will hardly be the case. Finally, when considering biaxial testing the presence of this stiffener results in a more complex loading system because load has to be introduced in this stiffener to realise skin-stiffener compatibility during the test. On the basis of these arguments it was decided to omit this stiffener from the specimens in the NLR testing programme. However, in group no 4 (see Table 2) two extra test panels with this stiffener being present were included in the test matrix to study possible effects of this stiffener. These extra panels were tested uniaxially.

To allow comparison of the NLR results with those of Ref. 1 all specimens were manufactured in the USA by the same factory that delivered the specimens of Ref. 1, according to the same production drawings and the same aircraft production standards.

EXECUTION OF TESTING

Uniaxial tests

The uniaxial constant amplitude fatigue tests were carried out in a 900 kN Wolpert Amsler servo-hydraulic (MTS) testing machine. All tests were carried out under load control with an R-value (= ratio of minimum-to-maximum stress in a cycle) of 0.1 and at a frequency of 4 Hz (the same frequency that was used for the tests in Ref. 1). At that frequency no dynamic effects were experienced so that no special fixturing was required.

To check the correct alignment of the specimens during testing in order to obtain a symmetrical stress distribution across the specimen width, all specimens were provided with 4 (end load) strain gauges, i.e. 2 on the front side and 2 on the back side. The positions of these gauges were on the tear strap centrelines, 1 inch above the tear strap ends. After an acceptable alignment of the specimens was reached, prior to test initiation the panels were preloaded up to 1.33 times the maximum test load to simulate proof testing of the fuselage pressure cabin until 133% relief valve setting at delivery of the aircraft.

During the tests all rivet rows (at either side) were inspected frequently by means of a travelling binocular combined with a crack monitoring device (Sony Magnecsale EA-210). When during an inspection a crack was found, then the crosshair of the microscope was positioned successively at the extremities of that crack (i.e. at the rivet head edge and at the crack tip) and the distance between these positions was converted into mm's crack length by means of the displacement transducer in the crack monitoring device. The inspection frequency applied during the tests was based on experience about crack initiation lives gained during the execution of the testing programme. Initially inspections were carried out at rather small inspection intervals (say every 10,000 cycles) but these intervals increased during progress of the testing programme. After cracks were detected in a certain test, the inspections were carried out at smaller intervals to collect as much crack propagation data as possible from the test. Sometimes high frequency eddy current inspections (with a pencil probe) were carried out in support of the visual inspections.

Biaxial tests

The biaxial constant amplitude fatigue tests were carried out in a biaxial fatigue testing frame containing two double-acting hydraulic actuators (see Fig.4). The actuators had a maximum capacity of 200 kN (horizontal actuator) and 100 kN (vertical actuator) and were controlled by close-loop servo systems. At the rod ends of the actuators double-bridge load cells were mounted. During the tests the ends of the four arms of the cruciform specimens were bolted to triangular plate fixtures which in turn were connected to (in length) adjustable tension rods. For each load system one of these tension rods was connected to an actuator load cell and the other to the structure of the test frame. The load systems of the test frame were controlled by a computerized signal generator and control system.

All specimens were subjected to "in-phase" biaxial stresses representing the fuselage pressurisation stress cycles with a biaxiality ratio (= ratio of longitudinal to hoop stress) of 0.5. The synchronisation of the phases of both load systems was controlled by the software of the control system.

All tests were carried out under load control with an R-value of 0.1 and at a frequency of 4 Hz. At that frequency no dynamic effects were experienced so that no special fixturing was required.

In a similar way as described for the uniaxial tests, the correct alignment of the specimens in the test frame during testing was obtained by means of strain gauges, but now in total 8 strain gauges were used, i.e. 4 for each load system. The positions of the strain gauges on the specimen are shown in Fig.4. The strain gauges of each load system were connected in a Wheatstone bridge. The alignment of the specimen in the test frame was carried out as follows. First, a static alignment was performed by adjusting the lengths of the tension rods in such a way that the panel centre was at the

centre of the test frame. Then, in both directions preloads of 1.33 times the maximum test loads occurring in a cycle were applied to the specimen. Finally, the alignment was further fine-tuned dynamically (starting at a low test frequency) by balancing the output of the Wheatstone bridges of both load systems.

The inspections during the tests were carried out in a similar way as described for the uniaxial tests with the exception that no travelling binocular combined with a crack monitoring device was available at the biaxial test frame. Instead the inspections were performed by means of a magnifying glass. In doubtful cases the visual inspections were supported by means of a high frequency eddy current inspection.

TEST RESULTS

Table 3 gives a survey of the uniaxial and biaxial fatigue test results. The biaxial test results are presented in the shaded areas. These results will be discussed in more detail in the following chapter but a few general remarks can be made here on the basis of the data presented in this table.

Table 3 shows the number of kcycles at which the first cracks initiated in the critical (countersunk) rivet row of the lap joint and at the tear strap ends. The values in parentheses represent the percentages of panel failure lives at which this occurred. It is shown here that in almost all panels cracks initiated in the critical rivet row of the lap joint. The crack sizes that were assumed here to define crack initiation are shown at the bottom of the table. Generally also cracks arose in the skin at the tear strap ends due to high secondary bending stresses in these areas.

Further, the table presents the number of kcycles at which the panels failed together with their failure modes. Three panel failure modes are to be distinguished. Figure 5 illustrates how the three failure modes were defined:

- a panel failed in mode A when, after the initiation of cracks in the critical rivet row of the lap joint and linking up of these cracks until a continuous crack of sufficient length, the panel ultimately failed across the critical rivet row.

- failure in mode B occurred when the cracks in the skin at the tear strap ends became unstable before cracks in the lap joint had initiated and developed until a continuous crack of sufficient length. It is shown in Fig. 5 that at the moment of panel failure in the lap joint a crack of only two rivet spacings had developed.

- failure mode C is a combination of failure modes A and B. In this case one of the cracks being present in the skin at the tear strap ends became unstable as a consequence of fracture instability in the rivet row of the lap joint.

DISCUSSION

The test results given in Table 3 were plotted in separate diagrams and will be discussed in more detail in the following sections.

Crack initiation in lap joint area and fatigue lives

The diagram in Fig. 6a shows the crack initiation lives of the lap joints and the panel fatigue lives until failure. Further, the average failure life per specimen group and the failure modes are presented. The shaded bars refer to biaxial test results. The test results of the panels with longitudinal stiffeners were omitted.

It can be concluded from Fig. 6a that for each of the 4 groups of specimens in the uniaxial tests crack initiation in the critical rivet row of the lap joint generally started at a lower percentage of panel failure life than in the biaxial tests (see also data presented in Table 3).

Further, on an average in each group the uniaxially tested specimens showed the shortest failure lives. Finally, for both σ_{max}-levels the specimens with the smaller rivet spacings showed the longest lives. All these observations particularly apply to the test results of groups 1 and 2, i.e. to the specimens tested at the lower σ_{max}-values.

It has to be noted here that the uniaxially tested panels with a .75 inch rivet spacing all failed in mode B (i.e. across the tear strap ends, see Figure 5). This implies that the failure lives presented in Figure 6a for these panels are not representative for the fatigue lives of the lap joints but have to be considered as lower bounds thereof. This aspect has to be accounted for with regard to the conclusions drawn above about the fatigue lives found from the uniaxial and biaxial tests. For the uniaxially tested panels with a 1 inch rivet spacing in almost all cases (except for panel 3b-B; see Figure 6a) the fatigue lives of the lap joints determined the panel fatigue lives.

Crack initiation in the skin at the tear strap ends and measures taken

During the execution of the testing programme both during the uniaxial and the biaxial tests generally cracks initiated in the skin from the rivet holes at the tear strap ends due to high secondary bending stresses in these areas. When this occurred corrective actions were taken in an attempt to increase the life of the panels to such an extent that cracks in the lap joint would have a chance either still to initiate or to develop further during the continuation of the test. This aspect is illustrated in the diagram of Fig. 6b.

At the bottom of the diagram in Fig. 6b the sequence of testing of the panels is shown. It has to be noted here that the biaxial tests were carried out after the uniaxial testing programme was completed.

During the execution of the uniaxial testing programme with the first tested specimen in which cracking at the tear strap ends occurred (specimen 3b-A, see Fig. 6b) no special measures were taken. With the next tested panel (specimen 3b-B, see Fig. 6b) the crack tips were stop-drilled with 5 mm ∅ holes and these holes were cold worked. It has to be noted that such an action could not be applied before the cracks in the skin had passed the tear strap edges, implying that the crack had a length then of about 2 inches. Stop-drilling of these cracks was found to be not very effective: fairly soon after stop-drilling was carried out the panel failed in mode B across the stop-drilled cross section. Therefore with all other panels tested subsequently (both uniaxial and biaxial) the propagation of the cracks at the tear strap ends was stopped by applying a so-called "ball-indentation" process in the crack tip regions. During such a process residual compressive stresses are built up in the material at the crack tip by pressing a steel ball of 8 mm ∅ in the material by means of a riveting hammer, meanwhile supporting the panel at the back side locally by means of a heavy piece of

metal. As is shown in Fig. 6b (see explanation given for specimen 2b-B) this crack arresting process had to be repeated a number of times during the test continuation because new cracks initiated at other locations or reinitiation of cracks at the hammered crack tips occurred later on. It can be seen from Fig. 6b that with the biaxial tests application of the BI-process appeared to be more effective than with the uniaxial tests: although with the biaxial tests the BI-process generally was applied for the first time before any crack initiation in the lap joint was discovered, all biaxially tested panels failed in mode A or mode C whereas in the uniaxially tested panels in which the BI-process was applied, all but one failed in mode B (panel 4c-A failed in mode C).

Failure modes of panels

Comparing the results of the uniaxially and biaxially tested specimens, with regard to crack initiation and propagation in the critical row of the lap joint, a different behaviour was observed for both loading modes. This different behaviour was reflected in the failure modes of the panels.

In the uniaxially tested specimens crack intiation in the critical rivet row generally occurred more or less widespread, resulting in more separate cracks growing simultaneously, without showing obvious interaction.

In the biaxially tested specimens crack initiation in the critical rivet row generally occurred at two or more rivets positioned close together (but not necessarily next to one another) resulting in more cracks growing simultaneously and linking up of these cracks during test continuation. In these panels before panel failure a continuous crack (= a crack extending over one or more rivet spacings) was present in the critical row, extending over a large number (say 10) of rivet spacings.

Fig. 7 illustrates the crack initiation and propagation behaviour being typical for the uniaxially and biaxially tested panels. In the lower half of this figure this behaviour is shown for the critical rivet row as a function of the number of kcycles. It is shown that in the uniaxially tested panels cracks initiated at various locations along the rivet row and just before panel failure (i.e. after 213 kcycles) these cracks still had not linked up. At that moment a photograph was made of the area indicated in Fig. 7. This photograph (see Fig. 8) shows that cracks had propagated from adjacent rivets in opposite directions, more or less parallel to each other without showing linking up.

In the biaxially tested panel shown in Fig. 7 crack initiation remained limited to three adjacent rivets and linking up of these cracks occurred well in advance of panel failure.

Both with the uniaxially and biaxially tested panels, simultaneous with cracking of the critical rivet row of the lap joint, cracks also initiated in the sheet at the tear strap ends. Table 4 gives a survey of the crack lengths that were present in the panels at both locations just before panel failure together with the failure modes of the panels. The results of the biaxial tests are given in the shaded areas. It is clearly shown that all biaxial panels failed in mode A or mode C as a consequence of the large continuous cracks being present in the critical rivet row at the moment of panel failure (generally in these panels also rather large cracks were present at the tear strap ends, see Table 4). On the contrary, of the uniaxial panels that showed cracks at the tear strap ends, all but two (namely panels 3b-A and 4c-A which failed in mode C) failed in mode B because no cracks (or in one case a very small continuous crack) had developed in the critical rivet row during the test. Two of the uniaxial panels which did not show any crack initiation at the tear strap ends failed in mode A (panels 1b-A and 1b-B).

Effect of longitudinal stiffener

The uniaxial specimens tested by ADL/FTI were all provided with a longitudinal stiffener (see Figure 1). In the NLR test programme this stiffener was missing with all specimens but two. These two extra specimens were incorporated in group 4 of the NLR test matrix (see Table 2) to allow examination of possible effects of this stiffener on panel behaviour. These extra specimens were tested uniaxially. The test results of these specimens (specimens 4c-A and 4c-B) are shown in the two lower lines of Table 3 and plotted in Fig. 6b. Apart from the longitudinal stiffener, the design and the test conditions of these panels were similar to those of panels 4b-A and 4b-B. Comparing the test results of the panels with and without this stiffener, no significant effect of the stiffener on panel behaviour could be established.

Development of MSD

Table 5 shows the development of MSD during the last part of the test, i.e. after discovery during inspection of the first continuous crack in the critical rivet row of the lap joint. For obvious reasons only the data of the specimens that failed in mode A or mode C are presented in this table.

Columns 2 and 3 of the table present the number of kcycles tested until the inspection at which for the last time separate cracks were found to be present in the critical rivet row together with the number of rivets at which such cracks were found at that moment. The values in parentheses represent the corresponding percentages of panel failure lives.

The other columns of Table 5 present the number of kcycles at which continuous cracks were found during subsequent inspections together with the lengths of these cracks, expressed in number of rivet spacings. It has to be noted here that in almost all panels crack initiation only was observed in the critical countersunk rivet row. However, two specimens showed a different behaviour (viz., specimens 2a-B and 2a-C, see Table 5). In specimen 2a-B cracks developed in both critical rivet rows simultaneously. In specimen 2a-C crack initiation and propagation remained limited to the critical formed head rivet row, leading ultimately to failure across this row.

The results of Table 5 are plotted in Fig. 9. The moments of inspection are expressed in this figure as percentages of panel failure life. The inspections that represent the last inspection at which separate cracks were found are drawn dotted. The number of cracked rivets being present at that moment are given (see sketches in Fig. 9). The other levels in Fig. 9 represent the levels at which, successively, inspections were carried out and the numbers given at these levels pertain to the number of rivet spacings that were found to be cracked during these inspections.

It can be observed from Figure 9 that the last inspections at which separate cracks were found generally were carried out at levels above 95% of the panel failure lives and consequently development of these cracks across the rivet row ultimately leading to panel failure occurred in less than 5% of the life until failure.

CONCLUSIONS

As part of an FAA-NLR collaborative programme on structural integrity of ageing aircraft, NLR carried out uniaxial and biaxial fatigue tests on riveted lap joint specimens being representative for application in a fuselage. All tests were constant amplitude tests with maximum stresses being representative for fuselage pressurization cycles and R-values of 0.1. The parameters selected in the testing programme were the stress level (σ_{max} = 14 and 16 ksi) and the rivet spacing (.75 and 1.0 inch). All specimens contained 3 rows of countersunk rivets, the rivet row spacing was 1 inch and the rivet orientation continuous.

From the test results the following conclusions can be drawn:

i) Comparing the results of identical specimens it was found that in the uniaxial tests crack initiation in the critical (countersunk) rivet row generally started at a lower percentage of the panel failure life than in the biaxial tests. Further, averaged per group of specimens, the uniaxially tested specimens showed the shortest failure lives.

ii) Independent of the loading mode, for both stress levels the specimens with the smaller rivet spacings showed the longest failure lives.

iii) Crack initiation in the critical rivet row occurred either more or less widespread and crack propagation remained then concentrated around the cracked holes until panel failure (without linking up of cracks) or at two or more rivets positioned close together (but not necessarily next to one another) resulting in more cracks growing simultaneously and linking up of these cracks during test continuation. The former behaviour generally occurred in the uniaxial tests, the latter in the biaxial tests.
In some uniaxial tests crack initiation in the critical row was not found at all.

iv) As a consequence of the large continuous crack (= crack extending over one or more rivet spacings) being present in the critical rivet row at the moment of panel failure (see iii)) all biaxially tested panels failed in mode A (67%) or in mode C (33%); see Figure 5. On the contrary the uniaxially tested panels generally failed in mode B (60%) because no cracks or very small continuous cracks had developed in the critical rivet row during the test. However, sometimes despite this fact uniaxial panels still failed in mode A (20%) or mode C (20%) because during the test no cracks or rather small cracks had developed at the tear strap ends.

v) During the tests generally cracks initiated at the tear strap ends from the rivet holes in the skin due to secondary bending in these areas. Propagation of these cracks was stopped during the test by applying a "ball-indentation" (BI) process in the crack tip region (see text). This crack arresting process had to be repeated a number of times during the test continuation because new cracks initiated at other locations or reinitiation of cracks at the hammered crack tips occurred. The objective of the application of the BI-process was to retard crack propagation at the tear strap ends to such an extent that cracks in the critical row meanwhile would have a chance either to initiate or to propagate with the consequence that panel failure still might occur across the critical rivet row. In this respect the application of the BI-process appeared to be more effective in the biaxial tests than in the uniaxial tests.

vi) It was found from the inspections carried out during the tests that in the panels that failed in mode A or mode C the last inspections at which still separate cracks at rivet holes were found to be present generally were at levels above 95% of the panel failure lives. Consequently, development of these cracks across the rivet row, ultimately leading to panel failure across the cracked row, occurred in less than 5% of the panel lives.

REFERENCES

1. A laboratory study of multiple site damage in fuselage lap splices, ADL report (Draft version) written by Ronald A. Mayville and Milton R. Sigelmann, February 1992.
2. Evaluation of the newly developed NLR biaxial test specimen, NLR report CR 90268 C written by G.J. de Jong, July 1990.

Table 1
ADL/FTI uniaxial fatigue tests on riveted lap joints

important for MSD	Levels selected	
Parameters considered	**original programme 1)**	**additional tests 2)**
stress level (ksi)	12 (14) and (16)	14 18 and 20
rivet type	(flush head) + Briles	flush head
rivet spacing (inches)	(.75) (1.0) and 1.29	1.0
rivet orientation	(continuous) + staggered	continuous
number of rivet rows	(3) + 5	3
skin thickness (inches)	.040 (.050) and .063	.040 .063 and .080
number of specimens →	51	21

1) the encircled values are chosen for the NLR testing programme
2) the underlined levels pertain to the baseline design

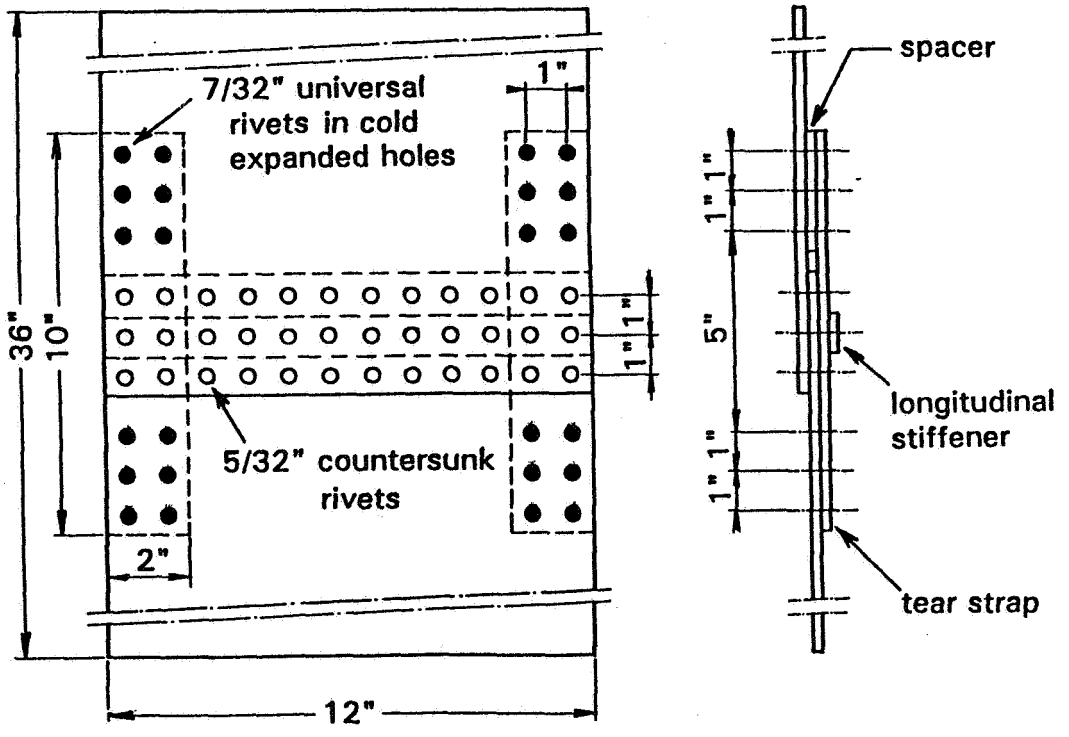

Fig. 1 Geometry and dimensions (inches) of specimens (baseline design)

Table 2
NLR test matrix

Specimen group no 1)	$\sigma_{max}=\sigma_H$ (ksi) 2)	rivet spacing (inch)	skin thickness (inch)
1	14	1.0	0.05
2		.75	
3	16	1.0	
4 3)		.75	

1) Two repeats for uniaxial tests, three repeats for biaxial tests
2) σ_H = hoop stress, σ_L = longitudinal stress, in biaxial tests: $\sigma_L/\sigma_H = 0.5$
3) Only in this group of specimens uniaxial tests were carried out both with and without a longitudinal stiffener (was present in all ADL/FTI specimens)

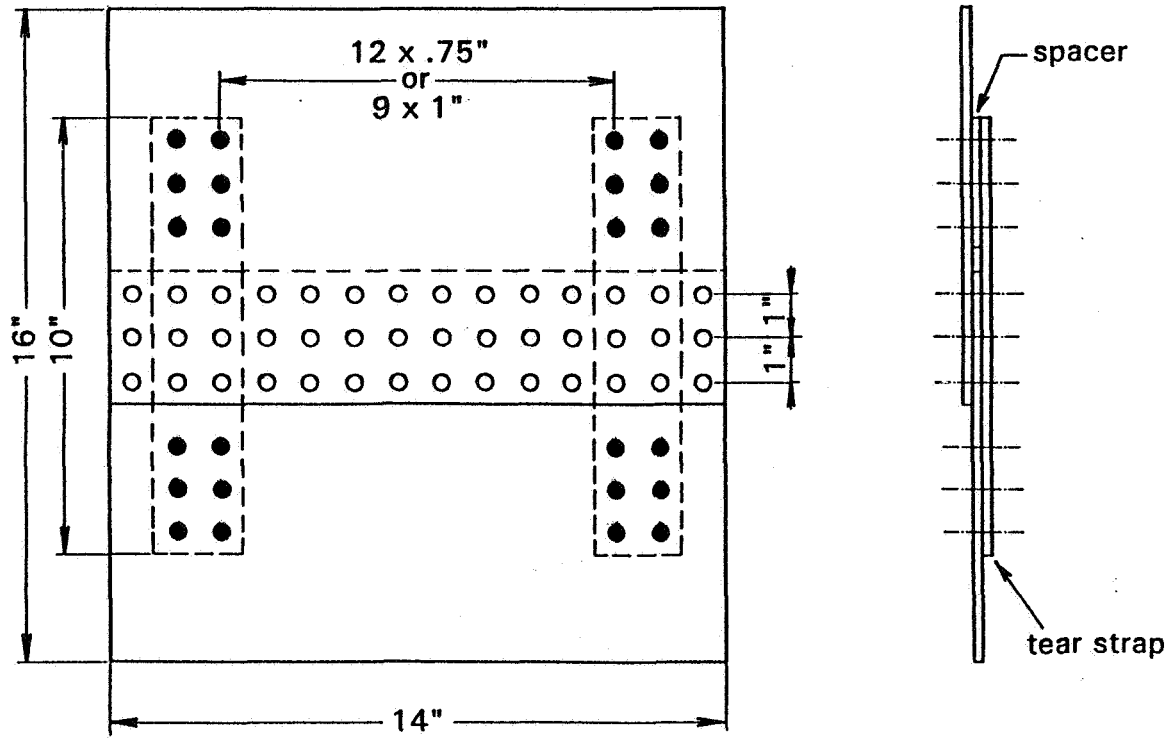

note: All specimens were delivered with a length of 36 inches.
The biaxial specimens were shortened to 16 inches.

Fig. 2 Geometry and dimensions (inches) of biaxial specimens tested by NLR

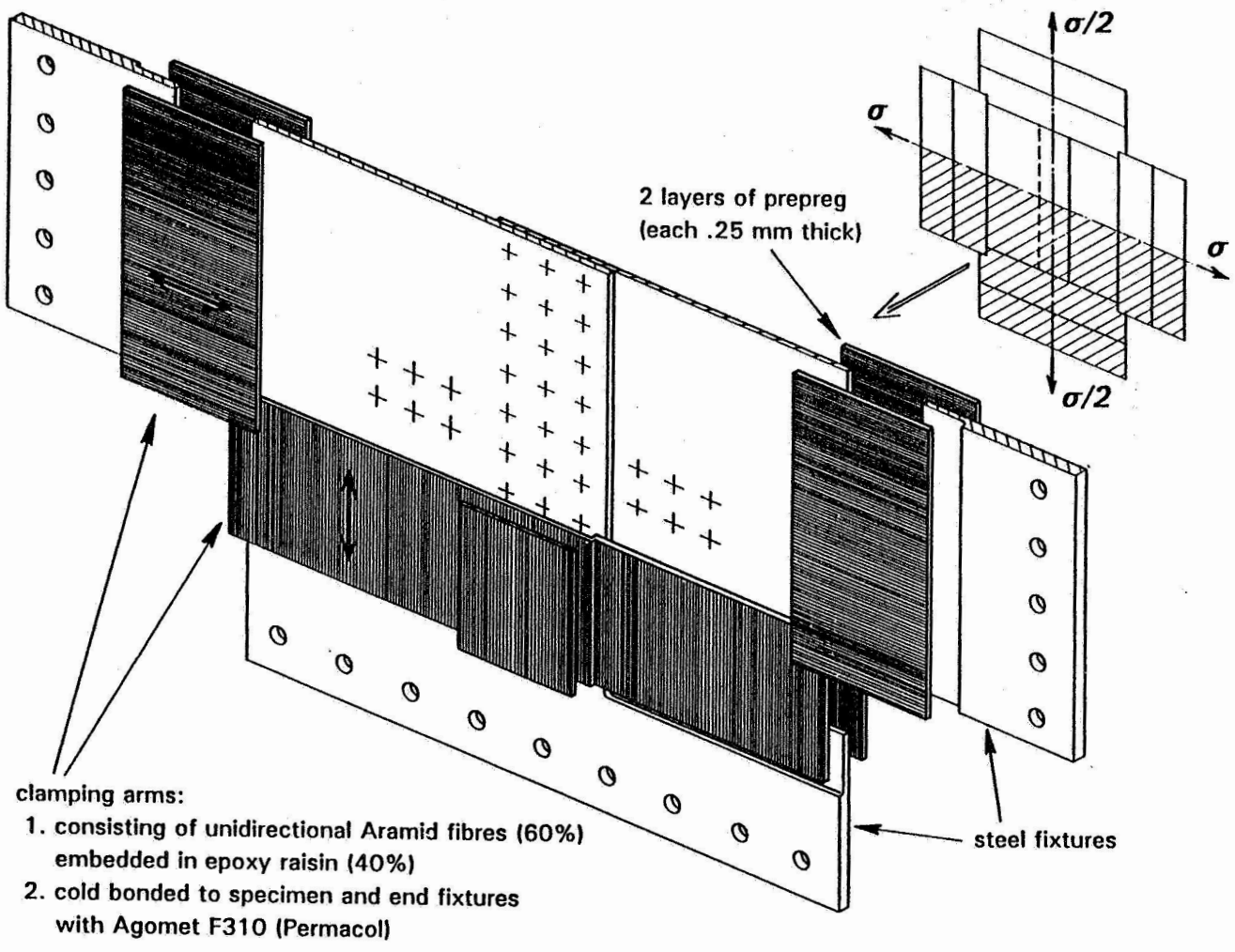

Fig. 3 Exploded view of biaxial lap joint specimen
(half specimen drawn)

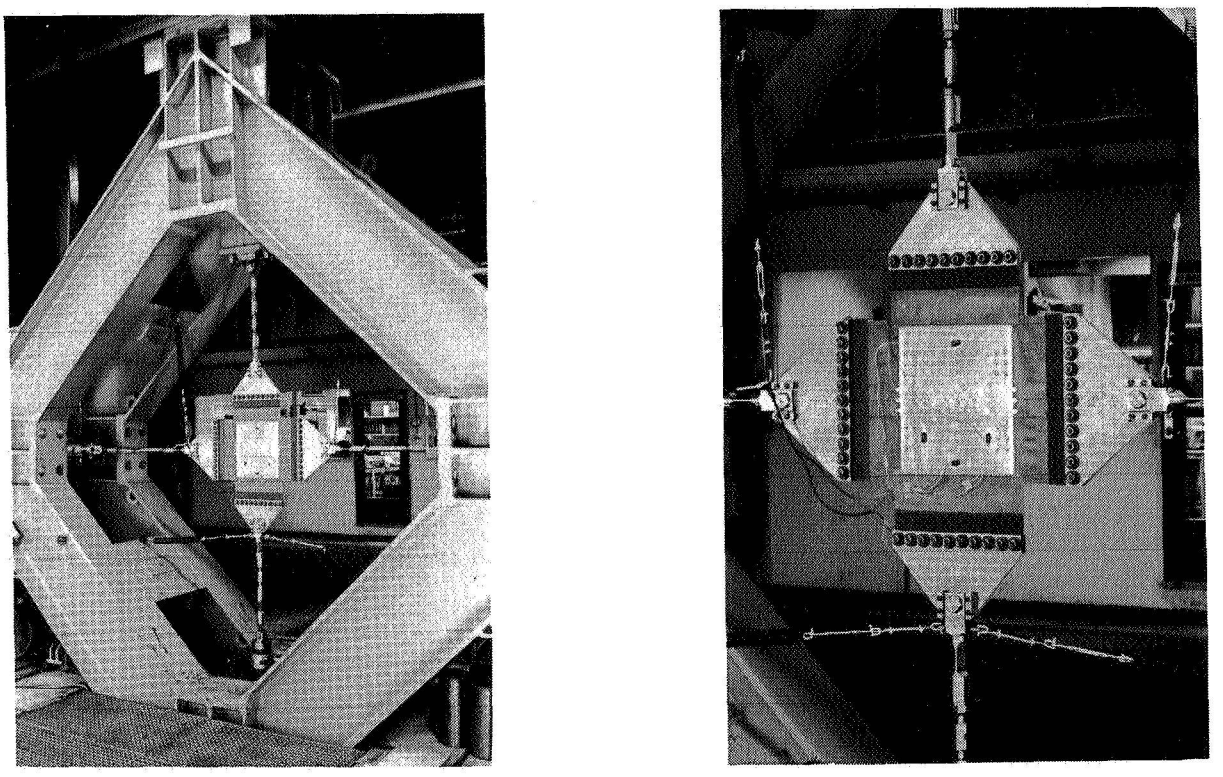

Fig. 4 Biaxial specimen mounted in test frame

Table 3

Survey of uniaxial and biaxial fatigue test results

notes: 1 the results in the shaded areas refer to biaxial tests
2 the values in parentheses represent percentages of panel failure lives

σ_{max} (ksi)	rivet spacing (inch)	specimen identification no		first crack(s) in skin (kcycles)			life until panel failure (kcycles)	failure mode 2)
		group	no	at critical (countersunk) rivet row 1)	at tear strap ends LHS	at tear strap ends RHS		
14	1.0	1a-	A	475 (83)	393 (69)	566 (99)	570	A
			B	613 (89)	525 (76)	525 (76)	691	C
			C	220 (75)	295(100)	-	295	A
		1b-	A	50 (25)	-	-	204	A
			B	120 (55)	-	-	218	A
	.75	2a-	A	485 (85)	485 (85)	-	573	C
			B	750 (63)	475 (40)	900 (75)	1195	C
			C	600 (67)	468 (52)	-	893	A
		2b-	A	120 (18)	357 (53)	470 (70)	672	B
			B	690 (93)	450 (61)	635 (86)	742	B
16	1.0	3a-	A	313 (87)	325 (90)	-	359	A
			B	363 (89)	215 (53)	409(100)	410	A
			C	250 (85)	290 (98)	-	295	A
		3b-	A	230 (78)	260 (88)	-	295	C
			B	120 (36)	300 (90)	270 (81)	334	B
	.75	4a-	A	430 (87)	225 (46)	380 (77)	490	A
			B	475 (92)	413 (80)	488 (95)	515	C
			C	425 (87)	303 (62)	335 (69)	488	A
		4b-	A	281 (89)	175 (56)	254 (81)	315	B
			B	-	263 (62)	342 (81)	422	B
		4c- 3)	A	400 (96)	245 (59)	253 (61)	416	C
			B	-	216 (75)	270 (94)	288	B

1) crack initiation defined by: cracks ≥ 0.5 mm at more than one rivet
or crack > 1 mm at a single rivet

2) panel failure modes: mode A = across critical rivet row
mode B = across tear strap ends
mode C = combination of modes A and B

3) specimens provided with longitudinal stiffener (similar to panels tested by ADL/FTI)

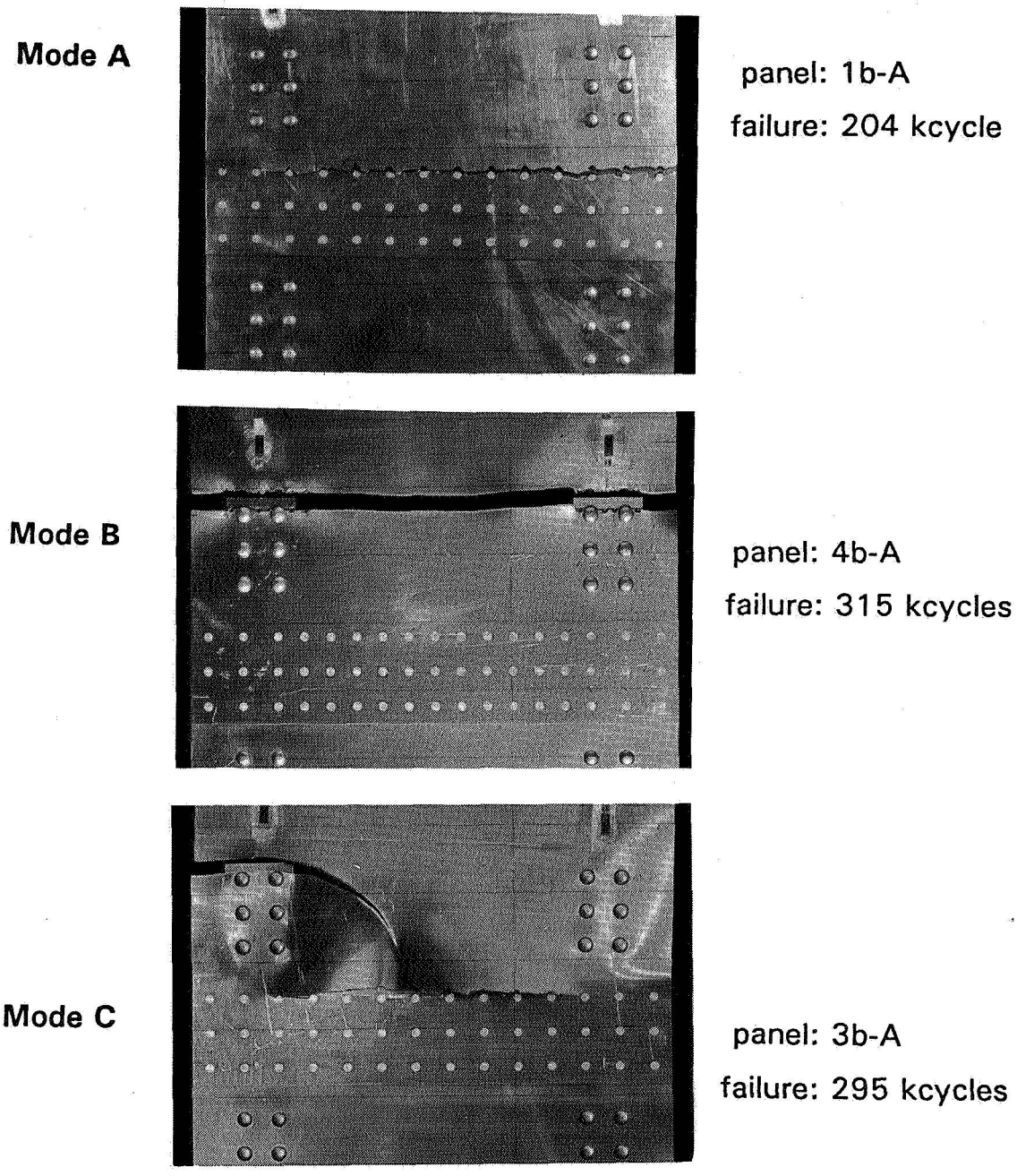

Fig. 5 Panel failure modes

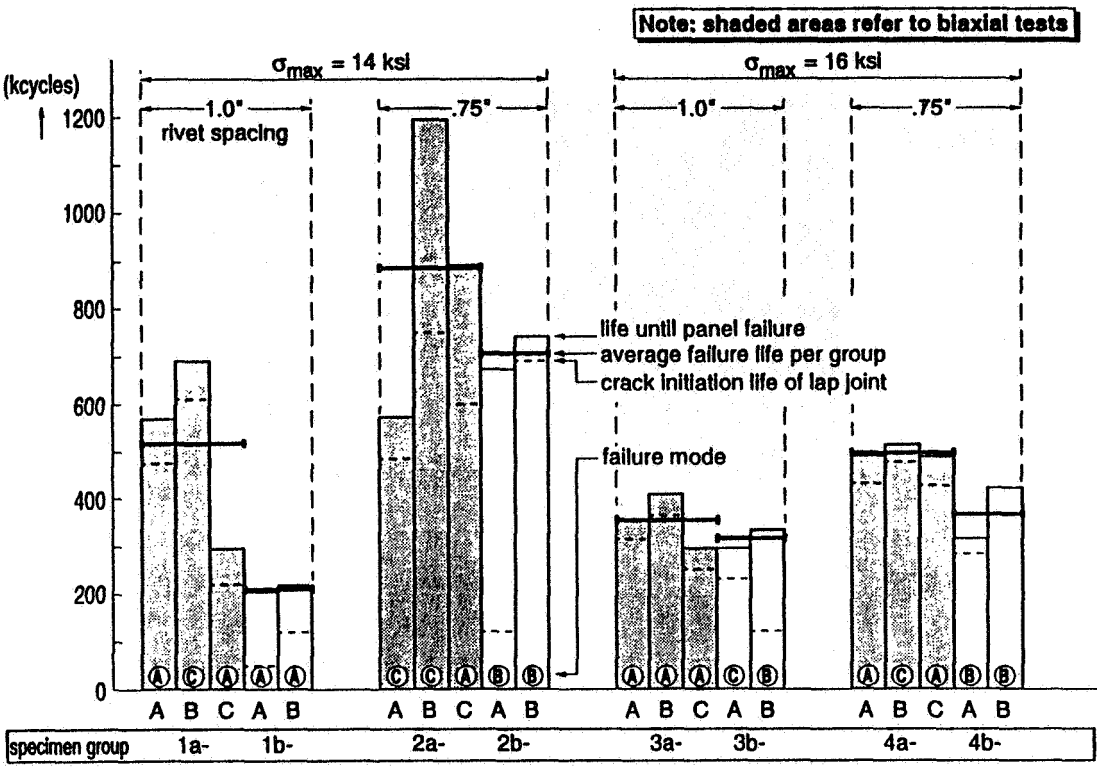

Fig. 6a Crack initiation in lap joints and panel lives until failure (data taken from Table 3)

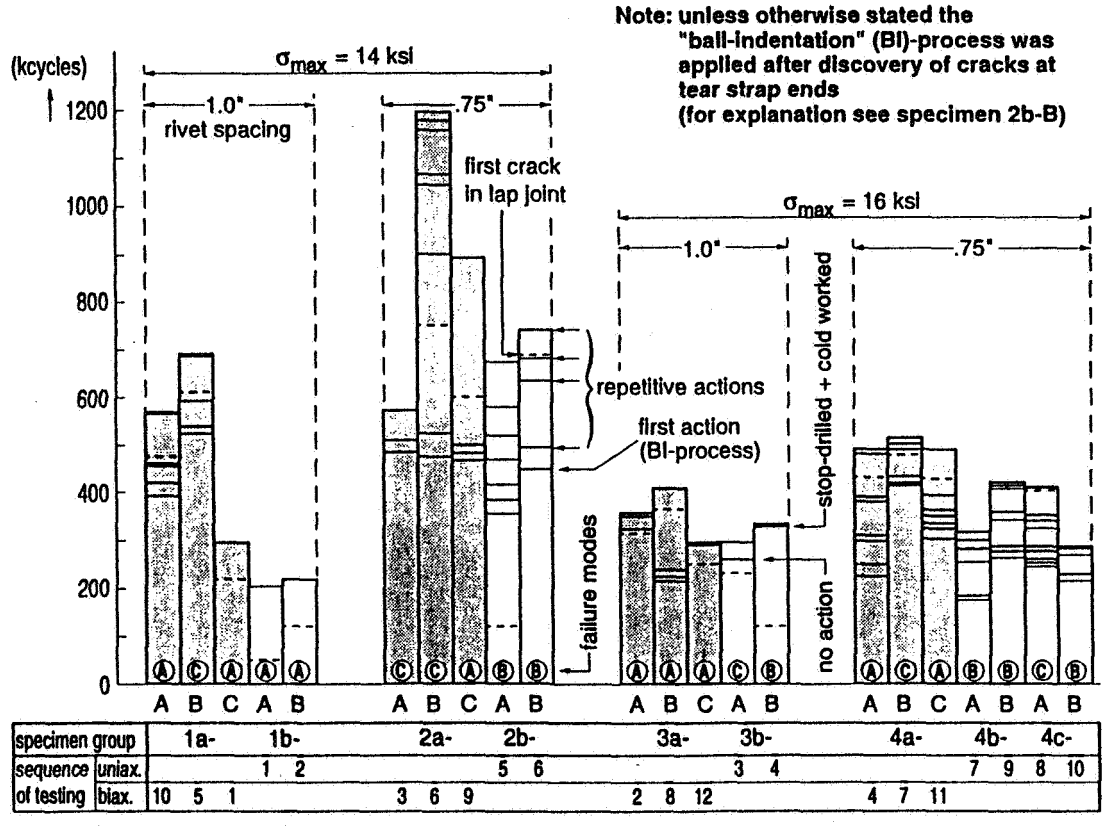

Fig. 6b Crack initiation at tear strap ends and corrective actions taken

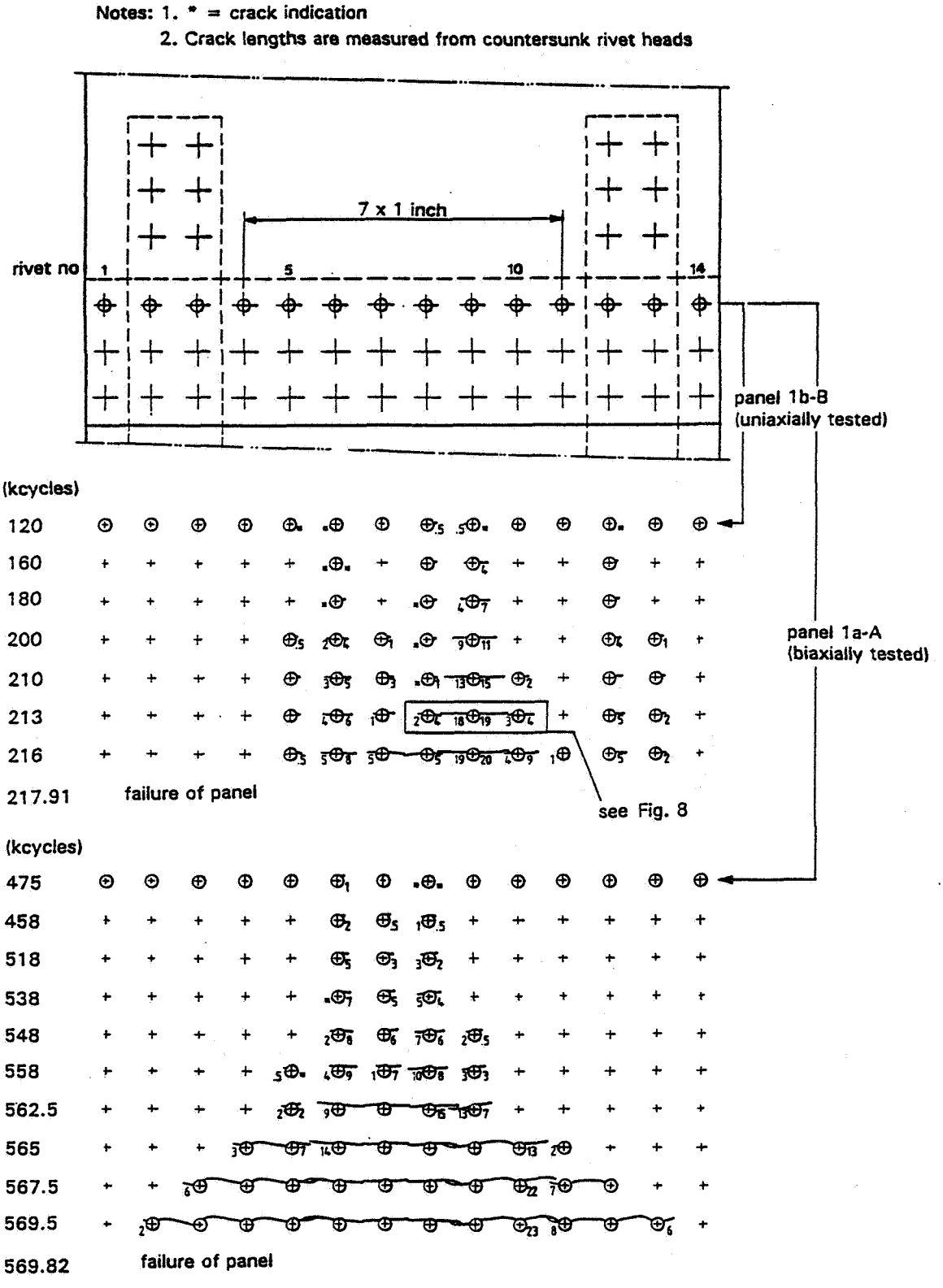

Fig. 7 Crack initiation and propagation in critical rivet row for uniaxial and biaxial specimens (typical)

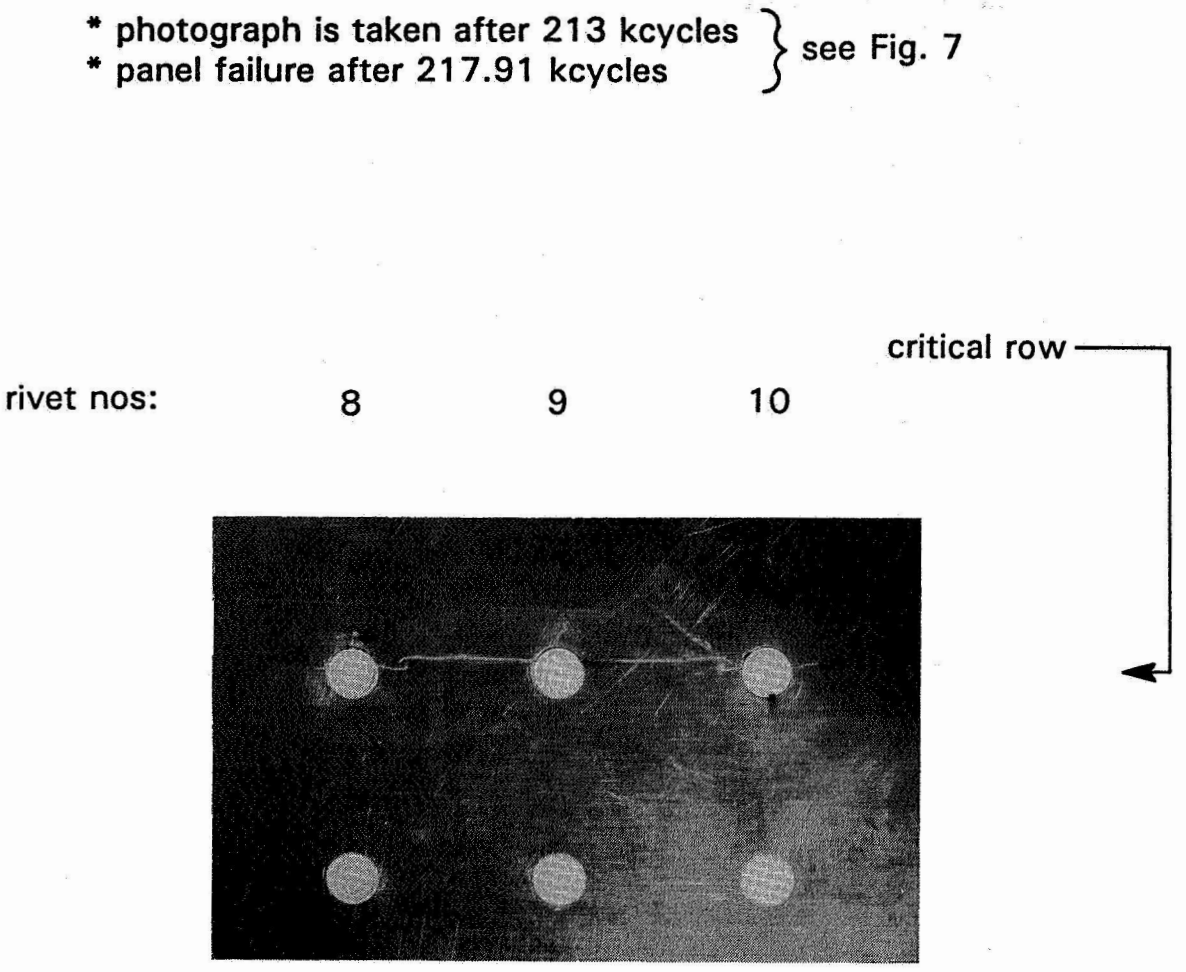

Fig. 8 Photograph of cracks in uniaxially tested specimen 1b-B

Table 4
Crack lengths in skin just before failure + failure modes

σ_{max} (ksi)	rivet spacing (inch)	specimen identification no		life until panel failure (kcycles)	failure mode	present just before panel failure		
		group	no			continuous crack in critical row (no of rivet spacings)	crack length at tear strap ends (mm) 1) LHS	RHS
14	1.0	1a-	A	570	A	11	30	14
			B	691	C	10	48	42
			C	295	A	12	33	none
		1b-	A	204	A	2	none	none
			B	218	A	3	none	none
	.75	2a-	A	573	C	13	53.5	none
			B	1195	C	9	27.5	22
			C	893	A	8	26.5	none
		2b-	A	672	B	none	55.5	39
			B	742	B	none	69.5	16.5
16	1.0	3a-	A	359	A	12	75	none
			B	410	A	11	24.5	12
			C	295	A	11	13.5	none
		3b-	A	295	C	6	29 2)	none
			B	334	B	none	57.5 3)	57 3)
	.75	4a-	A	490	A	13	30.5	26.5
			B	515	C	9	29.5	15
			C	488	A	14	30.5	28
		4b-	A	315	B	2	57.5	42
			B	422	B	none	46	29.5
		4c-	A	416	C	2	47	38.5
			B	288	B	none	53	16

1) unless otherwise stated, these cracks were stopped by applying the "ball indentation" process (see text)

2) no actions taken after discovery of cracks

3) cracks stop-drilled (Ø5 mm and holes cold worked)

Table 5
Development of MSD during the last part of the test

specimen number	separate cracks present at		number of kcycles at which a continuous crack was found														failure (kcycles)
	kcycles	no. of rivets	length of crack found (expressed in number of rivet spacings)														
			1	2	3	4	5	6	7	8	9	10	11	12	13	14	
1a-A	557.5 (97.8)	5		562.5 (98.7)			565 1+4		567	567.5 7+1	568.5 8+1	569 8+2	569.8				569.82
1a-B	675 (97.8)	3	683 (98.9)														690.5
1a-C	277.5 (94.1)	3	279 (94.6)	284 1+1		287 3+1	288 4+1	289 4+2	290		291	293	294	295			295
1b-A	180 (88.4)	6		200 (98.2)													203.64
1b-B	215 (98.7)	5	216 (99.1)				216.5					216.9					217.91
2a-A	522.5 (91.1)	2	537.5 (93.8)		562.5 1+2		567.5						572.5		573.2		573.27
2a-B 1)	1137.5 (95.2)	2	1150 (96.2)	1163				1193	1194	1195							1194.85
2a-B 2)	1175 (98.3)	3		1183 (99)	1188		1193			1195							
2a-C 2)	875 (98)	3			885 (99.1)	887.5		890	892.5	893.2							893.18
3a-A	355 (98.8)	4					356 (99.1)			357	357.5		358.5	359			359.17
3a-B	400 (97.7)	3			406.3 (99.2)	407.5				408		408.5	409.5				409.5
3a-C	285 (96.6)	4	287.5 (97.5)	290	291.3 2+1		292	292.3	292.8	293	293.5	294.3	294.8				294.88
3b-A	285 (96.7)	2	288 (97.7)	289.6	292	293.5		294.6									294.81
4a-A	475 (96.9)	4	480 (97.9)	485			487.5			488.5	489	489.5		490	490.4		490.44
4a-B	508.5 (98.7)	4		511.5 (99.3)				513	513.5	514	514.5						515.33
4a-C	462.5 (94.9)	4	470 (96.4)	477.5						485 4+4		485.5 5+5	486 6+5	487 6+6	487.3 7+6	487.5	487.57
4c-A	412 (98.9)	7		416 (99.9)													416.39

1) cracks in critical countersunk rivet row

2) cracks in critical formed head rivet row

Notes: 1. The shaded areas pertain to biaxial specimens

2. The values in parentheses represent percentages of panel failure lives

3. Unless otherwise stated the cracks were present in the critical countersunk rivet row

4. Only results of specimens that failed in mode A or mode C are presented

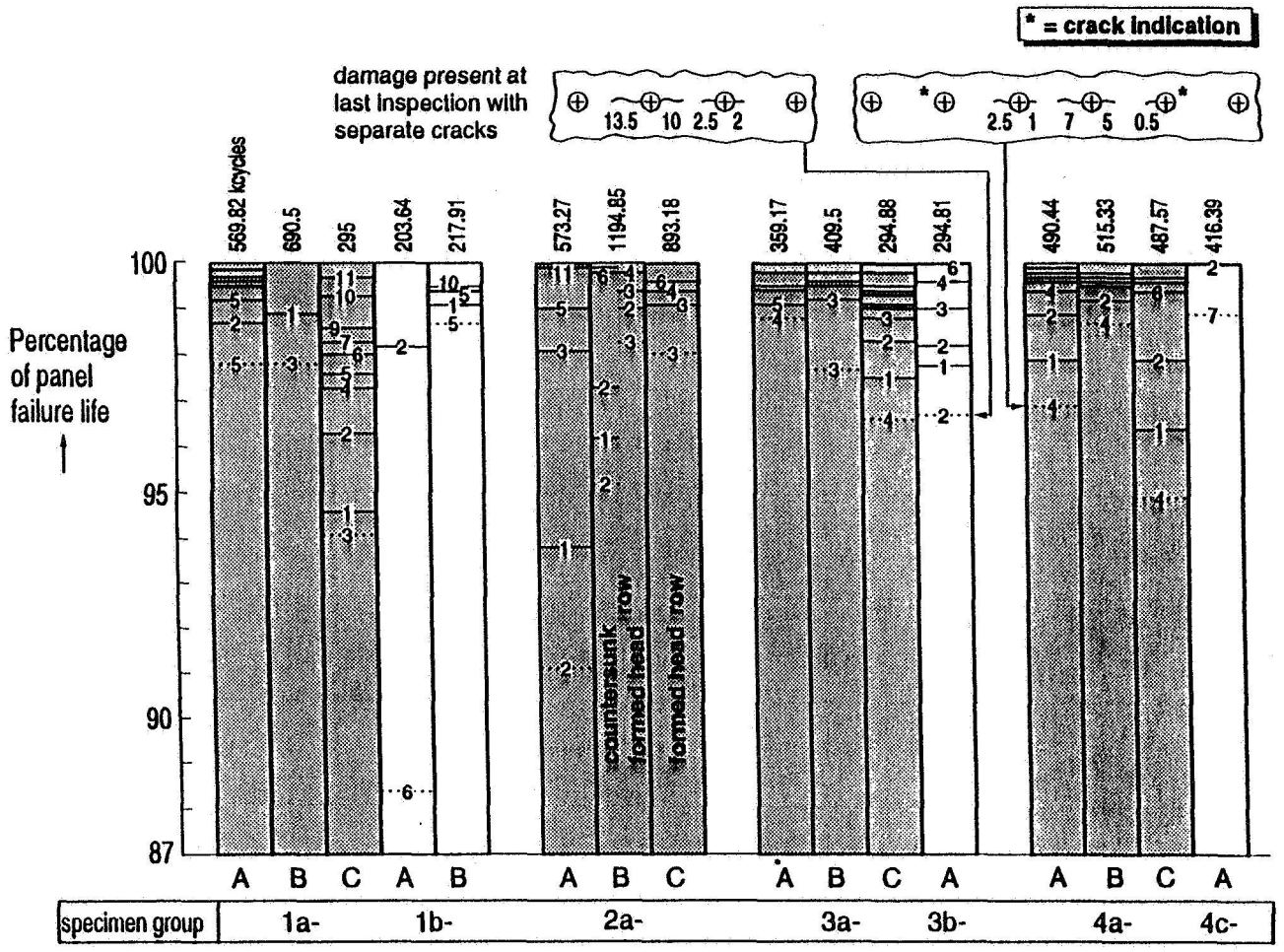

Fig. 9 Development of MSD after the last inspection with separate cracks

ON THE MEASUREMENT OF THE CRACK TIP STRESS FIELD AS A MEANS OF DETERMINING ΔK_{eff} UNDER CONDITIONS OF FATIGUE CRACK CLOSURE

Ian R. Wallhead and Lyndon Edwards
Fracture Research Group, Materials Discipline, The Open University, Milton Keynes, MK7 6AA, UK.

Peter Poole
Structural Materials Centre, Defence Research Agency, Farnborough, Hampshire, GU14 6TD, UK.

SUMMARY

The optical method of caustics has been successfully extended to enable stress intensity factors as low as 1MPa$\sqrt{m}$ to be determined accurately for central fatigue cracks in 2024-T3 aluminium alloy test panels. The feasibility of using this technique to study crack closure, and to determine the effective stress intensity factor range, ΔK_{eff}, has been investigated. Comparisons have been made between the measured values of stress intensity factor, K_{caus}, and corresponding theoretical values, K_{theo}, for a range of fatigue cracks grown under different loading conditions. The values of K_{caus} and K_{theo} were in good agreement at maximum stress, where the cracks are fully open, while K_{caus} exceeded K_{theo} at minimum stress, due to crack closure. However, the levels of crack closure and values of ΔK_{eff} obtained could not account for the variations of crack growth rate with loading conditions. It is concluded that the values of ΔK_{eff}, based on caustic measurements in a $1/\sqrt{r}$ stress field well outside the plastic zone, do not fully reflect local conditions which control crack tip behaviour.

INTRODUCTION

Fatigue crack closure under cyclic tensile loading was discovered by Elber in 1970 [1,2]. Since that time crack closure has been extensively studied and widely used to explain fatigue crack growth behaviour [3]. The most successful fatigue crack growth prediction models are based on crack closure. In these models the rate of crack growth is controlled by the effective stress intensity factor range, ΔK_{eff}, which is defined as:

$$\Delta K_{eff} = K_{max} - K_{cl} \qquad (1)$$

where K_{cl} is the closure stress intensity factor.

Unfortunately, accurate measurement of crack closure has proved difficult, and different measurement techniques have tended to yield different results [4-7]. Although mechanical compliance measurements have been widely used, with crack closure being determined from deviations from linearity of load versus strain gauge or clip gauge readings, various problems still exist and the accuracy of closure stresses determined in this way remains uncertain.

The optical method of caustics is a relatively new technique where the stress intensity factor is determined by measuring out of plane displacements around the crack tip in a K-field well outside the plastic zone [K-field is defined as a stress field where the dominant term at a distance r from the crack tip is proportional to $K/r^{1/2}$].

This paper describes work which was carried out in order to assess the feasibility of using caustics to determine crack closure and ΔK_{eff}, by comparing measured stress intensity factors, K_{caus}, with calculated theoretical values, K_{theo}. Results obtained for centre cracked aluminium alloy panels, containing fatigue cracks grown under various loading conditions are described and discussed.

CRACK CLOSURE AND THE BACKGROUND TO THE STUDY

Crack closure is understood to occur as a result of several mechanisms. The stretch zone in the wake of the crack caused by monotonic plasticity was the first to be discovered (by Elber [1, 2]). In addition, surface roughness and oxidation of the crack flank are known to produce premature crack closure [8, 9]. Regardless of the closure mechanism, the effect is the same: to reduce the strain amplitude at the crack tip so as to reduce the crack growth rate compared to a closure-free crack.

The effects of closure are considered to reduce ΔK_{eff} (see equation 1), which is often expressed in terms of a factor, U, defined as $\Delta K_{eff}/\Delta K$. The assumed stress field for an ideal crack (fully open) and a real crack (with closure) are shown schematically in Figure 1. At K_{max}, where both types of crack are open the stress field ahead of the crack is the familiar $1/\sqrt{r}$ singularity K-field. At K_{min} (R=0) a closure-free crack would exhibit only a small residual stress field resulting from the compression of the stretched monotonic plastic zone by the surrounding elastic material. In contrast, with a real crack the plastically deformed wake first comes into contact at an applied stress intensity factor above K_{min}. As the applied load is further reduced this wake contact increases until the crack is said to be fully closed. At K_{min} the stress/strain state at the crack tip may be considered to be equivalent to that of an ideal crack at a higher stress intensity factor, referred to as K_{cl}. Thus, it is assumed that the stress field ahead of the crack (outside the plastic zone) is a $1/\sqrt{r}$ K-field of intensity K_{cl}. There is some debate, however, as to whether K_{cl} corresponds to the point where the crack starts to close or whether damage still occurs below this point. This is borne out by the fact that many researchers disagree as to whether K_{cl} is determined by the point on the compliance curve where non-linearity first occurs or where two linear portions would intersect.

Thus, fatigue of a real crack is assumed to result in a cyclic crack tip strain amplitude and crack growth rate consistent with a closure-free crack with a ΔK equivalent to ΔK_{eff}.

In order to study crack closure and determine ΔK_{eff}, the stress field ahead of the crack tip provides an alternative source of information to compliance measurements. If the stress intensity factor can be experimentally determined from this stress field then comparison with the applied, theoretical, stress

intensity factor through a fatigue cycle should yield a result as shown schematically in Figure 2. As the applied K is reduced from K_{max} the stress intensity factor experienced by the crack tip falls linearly until the crack starts to close and then decreases non-linearly to K_{cl} at minimum stress.

The optical method of caustics provides a means of experimentally determining the stress intensity factor from the gradient of the stress field ahead of the crack tip.

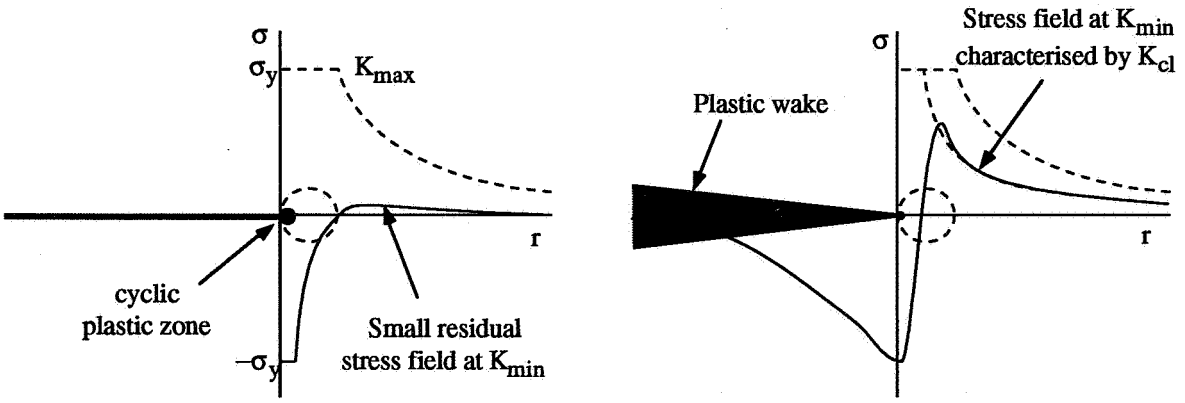

1a. Ideal crack. 1b. Real crack.

Figure 1. Crack tip stress field at the extremes of the fatigue cycle, with and without crack closure.

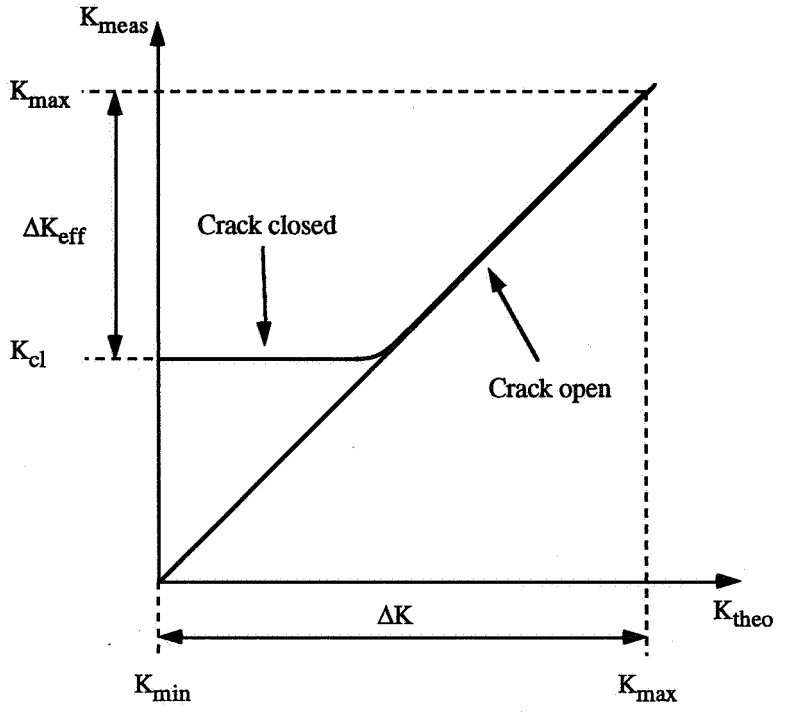

Figure 2. Expected measured K against theoretical K during fatigue.

THE OPTICAL METHOD OF CAUSTICS

A brief explanation of the method of caustics applied to an opaque specimen is as follows. A complete description is found in references [10, 11]. When a plate is subjected to a tensile stress its thickness reduces due to Poisson's effect. If there is a stress gradient the thickness change will be non-uniform, that is, there will be a surface deformation. In the case of a through crack in a parallel sided plate which is subjected to a (mode I) tensile stress, the stress distribution at the crack tip produces a surface deformation as shown schematically in Figure 3. If the surface of the plate is mirrored and illuminated with a spatially coherent beam (such as a laser) then the nature of the surface deformation causes the reflected rays to propagate in a direction as if they had formed a caustic surface behind the specimen as shown in Figure 3.

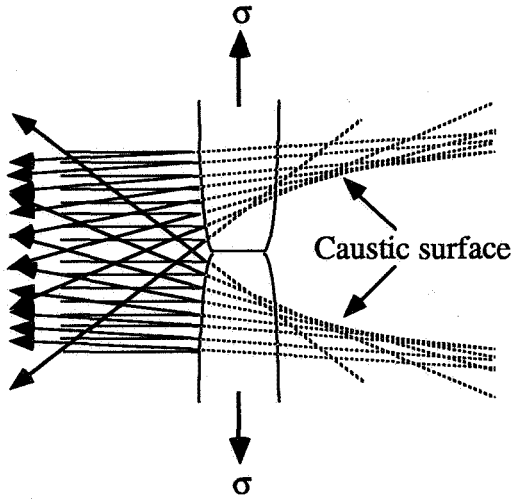

Figure 3. Formation of an optical caustic.

This virtual caustic can be imaged onto a screen in front of the specimen by including a lens in the optical path. The diameter of the caustic, i.e. a cross-section through the virtual caustic surface, for a given specimen is a function of the distance from the specimen surface from which the cross-section is taken (z_0) and the stress intensity factor (K_I) applied to the specimen. The caustic diameter is therefore a measure of the stress intensity factor and, for illumination with a collimated beam, is given by [12]:

$$K_I = \left(\frac{ED^{5/2}}{10.71 z_0 d\nu} \right) \qquad (2)$$

where E and ν are the material's elastic modulus and Poisson's ratio respectively
D is the transverse diameter of the virtual caustic cross-section
z_0 is the distance between the specimen surface and the plane of caustic
d is the specimen thickness.

The diameter, D', of the caustic viewed on the screen is related to D by the magnification of the imaging lens and is given by:

$$D=\frac{f}{v-f}D' \qquad (3)$$

where f is the focal length of the lens

v is the distance between the lens and the screen

Now, each caustic ring is produced from a unique radius, r_0, on the specimen, centred around the crack tip, given by [12].

$$r_0=\left(\frac{3z_0BvK_I}{2\sqrt{2\pi}E}\right)^{\frac{2}{5}} = 0.315D \qquad (4)$$

Manipulation of the optical arrangement (lens focal length and screen position) changes the z_0 and therefore changes the r_0. It is possible, therefore, to choose the measurement radius around the crack tip. Equation (2) is derived assuming the out of plane displacement field is caused by a $1/\sqrt{r}$ plane stress field. By taking a series of measurements at a range of radii from the crack tip the actual stress field's approximation to a K-field can be assessed. It is known that close to the crack tip this assumption breaks down and equation (2) becomes invalid. Within 1.5 times the plane stress plastic zone size plasticity effects impede the measurements [13]. Also, and more importantly, up to a radius of approximately half the specimen thickness the onset of a triaxial stress field affects the measurements [14, 15]. Within the K-dominant zone outside this region the caustic technique can yield accurate stress intensity factor measurements. A $1/\sqrt{r}$ K-field will, therefore, produce caustic measurements which, if presented as a ratio of measured K (K_{caus}) to calculated K (K_{theo}), are shown schematically in Figure 4. Measurements differing from this standard result would indicate a deviation from a K-field.

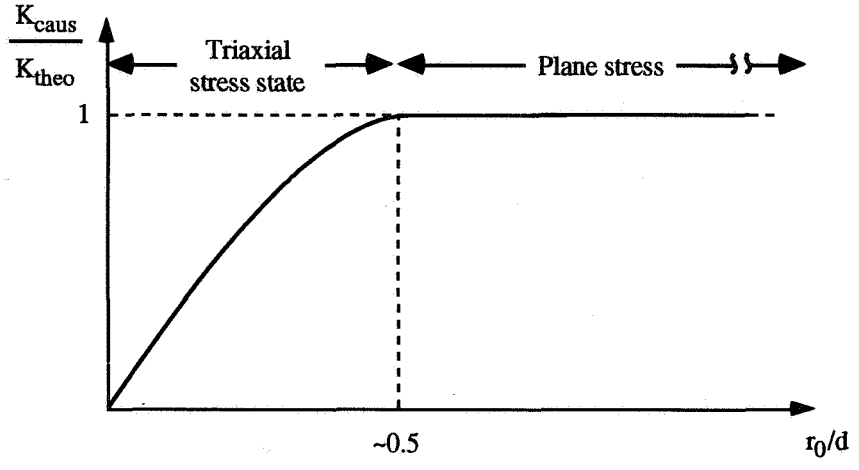

Figure 4. Ideal caustic results for a crack tip K-field.

Despite the fact that the method of caustics has been applied to mode I cracks for almost 30 years surprisingly little research has been conducted on fatigue problems [16-19]. One of the reasons for this is that investigation of fatigue usually requires the measurement of low stress intensity factors where closure is prevalent. The use of caustics at low stress intensity factors is notoriously inaccurate [20] since the Poisson contraction is necessarily very small. However, substantial developments to the technique have been made during this research [20-21] which have facilitated measurements in aluminium alloy at stress intensity factors as low as 1MPa$\sqrt{m}$. These developments have led to a substantial modification of the technique compared with that used by other researchers. Inherent inaccuracies are overcome by using an interferometrically focused laser to simultaneously illuminate both sides of an optically flat single point diamond machined specimen* together with a CCD camera image processing system† to measure the caustic.

EXPERIMENTS

Experiments were conducted on 6mm thick, 300x160mm, 2024-T3 aluminium alloy centre-cracked panel specimens. This widely used aerospace material has been experimentally tested and theoretically analysed extensively over the past two decades since crack closure was discovered and is known to exhibit significant closure.

Variations in the magnitude of crack closure is used to explain stress ratio effects on crack propagation and also load interaction effects. For this reason the specimens were tested at a range of stress ratios, after a single tensile overload, after a single compressive underload and after a high/low block loading sequence as described below.

Stress intensity factors are determined throughout the fatigue cycle by taking the mean of a series of caustic measurements from within the plateau (plane stress) region of Figure 4.

i) Constant Amplitude Fatigue (ΔK=10MPa$\sqrt{m}$, R=0.1, 0.3 and 0.6)

Fatigue cracks grown at the same ΔK, but at a range of stress ratios, were analysed to facilitate comparison between cracks with different levels of crack closure. In addition, a centre-cracked panel was produced by electro-discharge machining a narrow notch (approximately 80μm root radius) into the

---

* The latest developments have recently been submitted for publication in Engineering Fracture Mechanics under the title *High accuracy stress intensity factor measurement using the optical method of caustics* by Wallhead, I.R. and L. Edwards.

† Analysis performed on a Macintosh IIsi computer using the public domain NIH Image program (written by Wayne Rasband at the U.S. National Institutes of Health and available from the Internet by anonymous ftp from zippy.nimh.nih.gov or on floppy disc from NTIS, 5285 Port Royal Rd., Springfield, VA 22161, part number PB93-504868).

specimen. It is assumed that such a narrow notch provides a good approximation to a real crack except that there is no plastic wake behind the crack tip and for this reason it is termed an 'ideal crack'. Stress intensity factor measurements were then taken over the unloading half of a fatigue cycle of ΔK=10MPa$\sqrt{m}$, R=0.1 so as to compare with a real crack over the same loading cycle.

ii) Single Tensile Overload

A crack grown at a ΔK of 10MPa$\sqrt{m}$ (R=0.1) was given a 60% overload in order to induce an increase in closure and consequent crack growth retardation. Measurements were made pre-overload, at two points within the retardation zone and also after the crack had returned to the pre-overload growth rate.

iii) Single Compressive Underload

A crack grown at a ΔK of 10MPa$\sqrt{m}$ (R=0.1) was given a compressive underload of an equal magnitude to the fatigue cycle maximum tensile load. Again, measurements were made pre-compression and at several points post compression.

iv) High/Low Block Loading

Caustic measurements were taken through a fatigue cycle of ΔK=10MPa$\sqrt{m}$, R=0.1 following 5mm of crack growth at ΔK=10MPa$\sqrt{m}$, R=0.6. This load sequence exaggerates the closure effect such that the crack is expected to be closed throughout the whole fatigue cycle of the lower block.

RESULTS AND DISCUSSION

i) Constant Amplitude Fatigue (ΔK=10MPa$\sqrt{m}$, R=0.1, 0.3 and 0.6)

Figure 5 shows the measured (K_{caus}) against calculated (K_{theo}) stress intensity factors for cracks grown at the range of stress ratios shown and also for an electro-discharge machined ideal crack at R=0.1. The dashed 45° line indicates a fully open crack since $K_{caus}=K_{theo}$. Deviation from this line therefore shows that crack closure is occurring.

The most striking feature of Figure 5 is the difference between the real and ideal cracks (R=0.1). The ideal crack shows good agreement with theory over the whole loading range. The real fatigue crack exhibits a marked departure from theory approaching K_{min}. This effect is considered to be caused by crack closure since the main difference between these specimens is the absence of a plastic stretch zone in the wake of the ideal crack.

Figure 5 also shows that crack closure is more pronounced for cracks grown at R=0.1 than at R=0.3. No closure was detected for a crack grown at R=0.6. ΔK_{eff} was calculated from equation 1, using values

of K_{cl} given by K_{caus} measured at minimum stress. Thus, the values of U ($\Delta K_{eff}/\Delta K$) shown in Table 1 were determined.

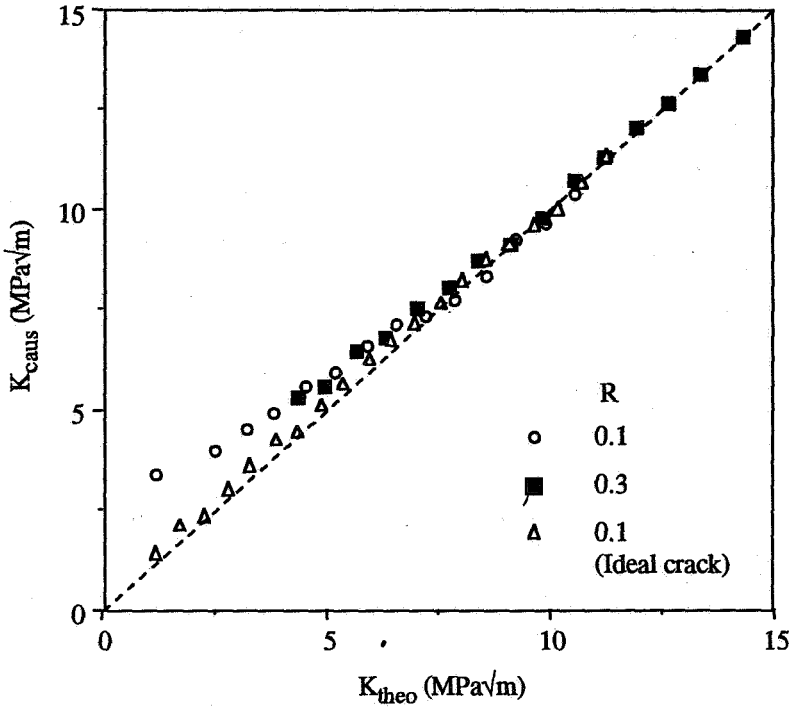

Figure 5 : Constant amplitude fatigue results

Table 1. Calculation of ΔK_{eff} and U

R	K_{max} (MPa√m)	K_{min}(caus) (MPa√m)	ΔK_{eff} (MPa√m)	U (caustic)	U (Newman [23]) α=2.4 (see below)
0.1	11.1	3.5	7.6	0.76	0.77
0.3	14.3	5.5	8.8	0.88	0.88

These values can be compared with theoretical predictions from Newman's analytical model [22]. Based on this model Newman has produced crack opening stress equations [23] which are applicable to centre-cracked tension specimens under constant amplitude loading. In addition he presents closure predictions which collapse da/dN v ΔK plots for 2024-T3 aluminium alloy. These equations, which are derived from polynomial fits to a range of results from the model, are as follows:

$$\frac{S_o}{S_{max}} = A_0 + A_1R + A_2R^2 + A_3R^3 \qquad \text{for } R \geq 0 \qquad (5)$$

and

$$\frac{S_o}{S_{max}} = A_0 + A_1R \qquad \text{for } -1 \leq R < 0 \qquad (6)$$

The coefficients are:

$$A_0 = (0.825 - 0.34\alpha + 0.05\alpha^2)\left[\cos\left(\frac{\pi S_{max}}{2\sigma_o}\right)\right]^{1/\alpha} \quad (7)$$

$$A_1 = (0.415 - 0.071\alpha)\left(\frac{S_{max}}{\sigma_o}\right) \quad (8)$$

$$A_2 = 1 - A_0 - A_1 - A_3 \quad (9)$$

$$A_3 = 2A_0 + A_1 - 1 \quad (10)$$

where S_o is the crack opening stress

S_{max} is the maximum stress in the constant amplitude cycle

(Note S_o/S_{max} could equally be described as K_o/K_{max})

R is the stress ratio

α is a 'constraint factor' (1 for plane stress, 3 for plane strain)

σ_o is the material flow stress (average between the yield stress and ultimate tensile strength)

The ratio S_o/S_{max} can be used to calculate U according to:

$$U = \frac{\Delta K_{eff}}{\Delta K} = \frac{1 - \frac{S_o}{S_{max}}}{1-R} \quad (11)$$

These equations agree with the experimental results provided the (empirically determined) constraint factor, α, has a value of 2.4. In reference [23] Newman identifies a constraint factor of 1.8 for a 2.3mm thick centre-cracked panel specimen. A factor of 2.4 for a 6mm thick specimen, therefore, does not seem unreasonable. However, it is clear that additional data are required, for a range of ΔK and R, in order to establish whether these crack growth data can be explained in terms of ΔK_{eff} measured by caustics.

ii) Single Tensile Overload

Figure 6 shows the plot of crack growth rate against crack length (measured with a travelling microscope) highlighting the familiar overload induced crack retardation. It should be noted that the apparent plateau in the retardation is an anomaly of this particular set of test results and has not been observed in other similar retardation plots. Also shown in the Figure are the points where the caustic measurements were taken.

Figure 7 shows the four sets of caustic measurements over the same fatigue cycle. Remarkably, despite the dramatic retardation, the caustic results exhibit no discernible difference. Any transient change in crack closure caused by the overload did not significantly affect the crack tip stress/strain distribution where the caustics were measured, several millimetres from the crack tip.

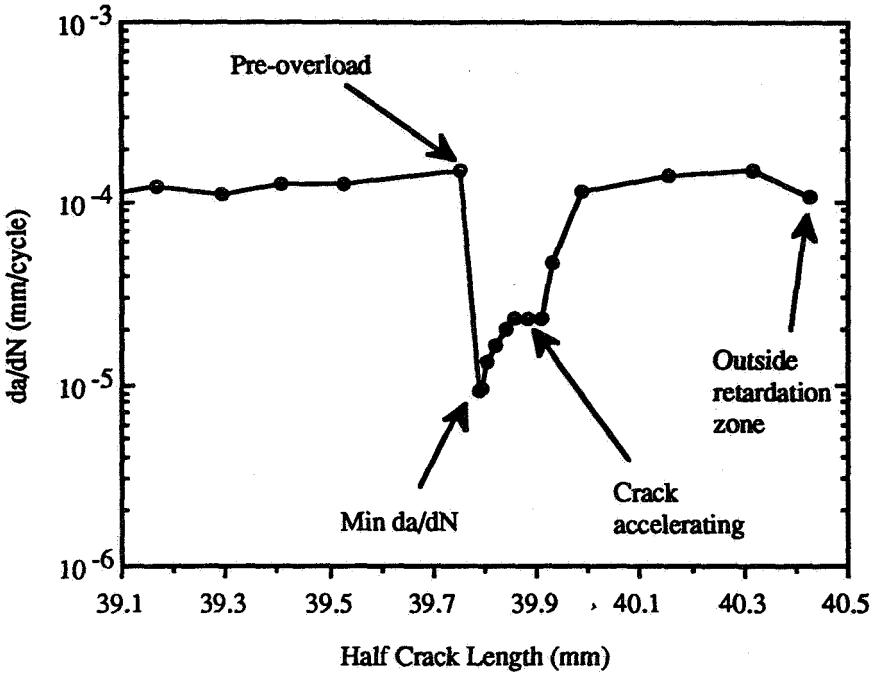

Figure 6. Overload induced crack growth retardation.

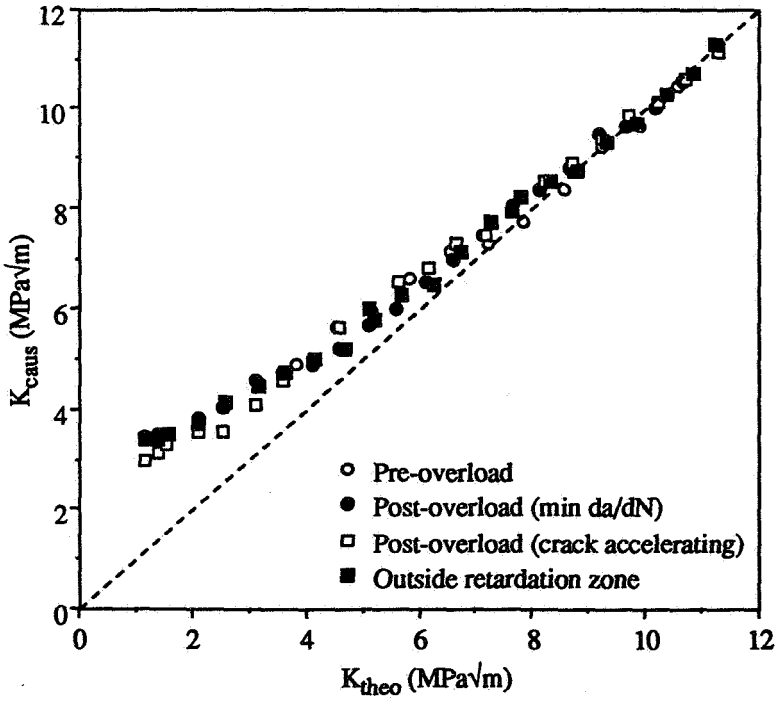

Figure 7 : Results of caustic measurements pre- and post-overload

iii) Single Compressive underload

Figure 8 shows the results following a compressive underload. A notable point is that caustics were observed even under applied compression indicating a tensile field ahead of the crack tip. The first cycle post compression shows a distinct reduction in closure, presumably caused by compressive yielding of the wake during the underload. This level of closure is maintained until over 1mm of crack growth has occurred when the results show a return to the pre-compression level. During the test, however, the crack growth rate showed no discernible change following the compression. This test indicates that the crack tip stress field was modified by a compressive underload but the crack driving force is unaffected.

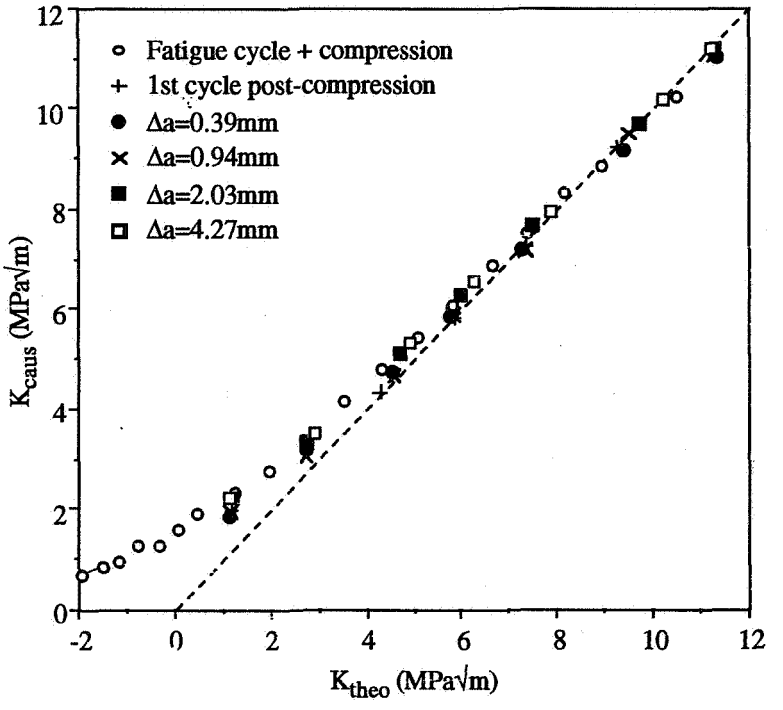

Figure 8 : Caustic results following a compressive underload

iv) High/Low Block Loading

Measurements at a low stress ratio following fatigue at a high stress ratio exaggerate the closure effects. Here, a stress ratio of 0.6 is followed by a ratio of 0.1 which is expected to cause crack closure for the whole of the lower block fatigue cycle. Indeed, the crack arrested for 100,000 cycles after which the test was ceased. Figure 9 illustrates the caustic results at selected stress intensity factors plotted (as in Figure 4) as the ratio of measured to theoretical K against the normalised radius, r_0/d.

Since, under these conditions, crack closure was anticipated to occur at >11MPa$\sqrt{m}$ the caustic curves for the whole lower block fatigue cycle were expected to follow the form of the general curve of Figure 4 (also shown in Figure 9) but with K_{caus}/K_{theo} ratios indicating the same K_{caus} value >11MPa$\sqrt{m}$. The fact that the results do not follow the general curve suggests that the stress field ahead of the crack under these

conditions is not a $1/\sqrt{r}$ K-field. The curves level off at large distances from the crack tip showing the curves asymptote to a $1/\sqrt{r}$ field but closer to the tip the stress gradient is steeper than that for a $1/\sqrt{r}$ field.

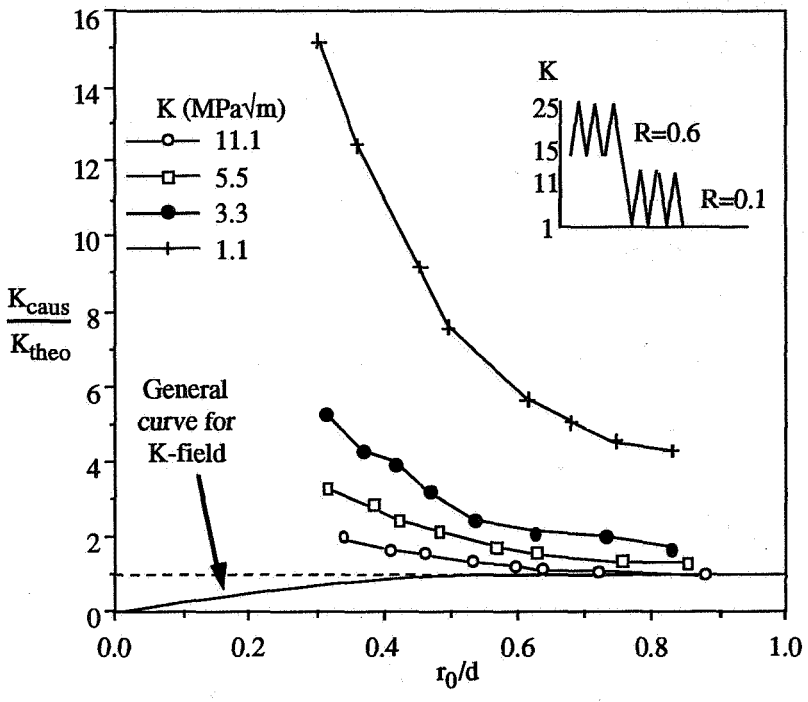

Figure 9. Caustic measurements over a range of radii.

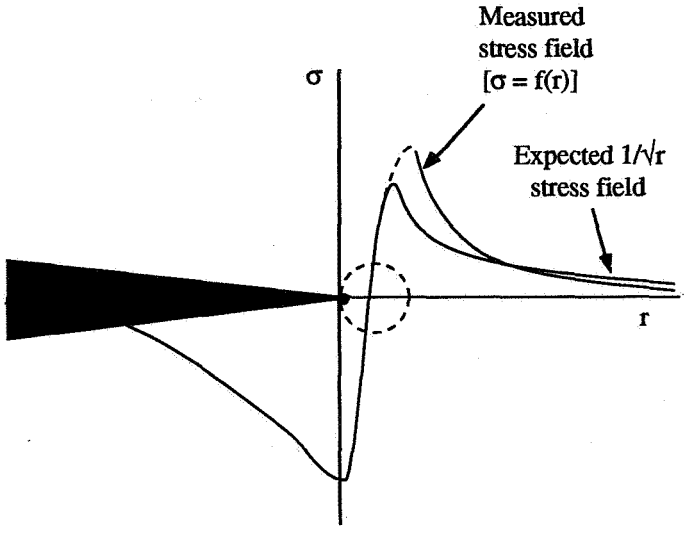

Figure 10. Schematic of the measured and expected closure stress fields

The measured stress field is shown schematically in Figure 10 which may be represented as

$$\sigma = f(r^{-n}) \qquad \text{where } n>0.5 \qquad (11)$$

This strongly suggests that the simple stress intensity factor concept cannot be applied to closed cracks under the conditions investigated.

CONCLUSIONS

The caustic method has been successfully extended to enable stress intensity factors as low as 1MPa$\sqrt{m}$ to be determined accurately for central fatigue cracks in aluminium alloy test panels. Comparisons have been made between measured values of stress intensity factor, K_{caus}, and corresponding theoretical values, K_{theo}, for a range of fatigue cracks grown under different loading conditions. In all cases, the values of K_{caus} and K_{theo} were in good agreement at maximum stress where the cracks are fully open. However, at minimum stress K_{caus} is greater than K_{theo} due to crack closure. For fatigue cracks grown under constant amplitude loading at R ratios of 0.1, 0.3 and 0.6, the difference between K_{caus} and K_{theo} was greatest for R=0.1 and least for R=0.6, in agreement with the widely reported trend that crack closure increases as R decreases. When a tensile overload was introduced during R=0.1 loading, no significant change in K_{caus} was observed, even though the crack growth rate was greatly reduced. In contrast, a compressive underload resulted in a change of K_{caus}, while a high/low block loading resulted in severe crack closure and complex K_{caus} data.

In general the measured values of ΔK_{eff} could not account for the observed variations of crack growth rate with loading conditions. It is concluded that the experimental values of ΔK_{eff}, determined from caustic measurements in a $1/\sqrt{r}$ stress field well outside the plastic zone, do not fully reflect local conditions which control crack growth.

ACKNOWLEDGEMENTS

The authors gratefully acknowledge the Open University for provision of laboratory facilities and the Department of Trade and Industry for the financial support for this project. The work reported in this paper was carried out in collaboration with the Defence Research Agency (Farnborough).

REFERENCES

1. Elber, W.:Fatigue crack closure under cyclic tension. *Engineering Fracture Mechanics*, vol 2, 1970, pp. 37-45.
2. Elber, W.: The Significance of Fatigue Crack Closure, *Damage Tolerance in Aircraft Structures, STP 486*, American Society for Testing and Materials, Philadelphia, 1971, p 230-242.
3. Newman, J.C. and W. Elber, Eds: *Mechanics of Fatigue Crack Closure, STP 982*, American Society for Testing and Materials, Philadelphia, 1988.

4. Abdel Mageed, A.M. and R.K. Pandey: Effect of measurement location and fatigue-loading parameters on crack closure behaviour. *Materials Science and Engineering*, vol A150, 1992, pp. 43-50.
5. Clerivet, A. and C. Bathias: Influence of some mechanical parameters on the crack closure effect in fatigue crack propagation in aluminium alloys. *Mechanics of fatigue crack closure, ASTM STP 982*, J.C. Newman and W. Elber, Editors. American Society for Testing and Materials, Philadelphia, 1988 pp. 583-597.
6. Bertel, J.D., A. Clérivet, and C. Bathias: R ratio influence and overload effects on fatigue crack mechanisms, in *5th International Conference on Fracture : Advances in fracture research*. 1981. Cannes, France: Pergamon Press.
7. Sharpe, W.N.: Applications of the interferometric strain/displacement gage. *Optical Engineering*, vol 21, no 3, 1982, pp. 483-488.
8. Suresh S. and R.O. Ritchie: *Metallurgical Transactions*, 13A, pp 1627.
9. Ritchie R.O. and S. Suresh: *Metallurgical Transactions*, 13A, pp 937-940.
10. Kalthoff, J.F.: Shadow optical method of caustics, in *Handbook on Experimental Mechanics*, A.S. Kobayashi, Editor. Prentice-Hall: New Jersey. 1987, pp. 430-500.
11. Theocaris, P.S.: in *Mechanics of Fracture*, G.C. Sih, Editor. Martinus Nijhoff Publishers: Mass. 1981, pp. 189-252.
12. Beinert, J. and J.F. Kalthoff: in *Mechanics of Fracture*, G.C. Sih, Editor. Martinus Nijhoff Publishers: Mass. 1981, pp. 280-330.
13. Zehnder, A.T. and A.J. Rosakis, *International Journal of Fracture*, vol 30, 1986, pp. R43-R48.
14. Rosakis, A.J. and K. Ravi-Chandar, *International Journal of Solids Structures*, vol 22 no 2, 1986, pp. 121-134.
15. Meletis, E.I., W. Huang, and E.E. Gdoutos, *Engineering Fracture Mechanics*, vol 39 no 5, 1991, pp. 875-885.
16. Hermann, R.: *Scripta Metallurgica*, vol 25 no 1, 1991, pp. 207-212.
17. Leftheris, B.P. and J.M. Papazian: *Journal of Engineering Materials and Technology*, vol 114, 1992, pp. 399-405.
18. S. Güngör, I. R. Wallhead and L. Edwards: Application of the optical method of caustics to fatigue crack growth. Int. Symposium on Non-Destructive Testing & Stress-Strain Measurement, & FENDT '92, Vol 2, pp 598-603, October 12-14, 1992, Tokyo, Japan.
19. I. R. Wallhead, S. Güngör and L. Edwards: Characterisation of fatigue crack growth by the optical method of caustics. Fatigue 93, the Fifth International Conference on Fatigue and Fatigue Thresholds, Vol 3, pp 1863-1868, May 3-7, 1993, Montréal, Canada.
20. I. R. Wallhead and L. Edwards: Letter to the Editor: Comments on 'Techniques of Optical Caustics Photography' by D.A. Meyn. *Engineering Fracture Mechanics*, Vol 46, no 3, 1993, pp 537-540.
21. Wallhead, I.R., S. Güngör, and L. Edwards: Optimisation of the optical method of caustics for the determination of stress intensity factors, *Optics and Lasers in Engineering*, vol 20, pp 109-133, 1994.
22. Newman J.C.: A crack-closure model for predicting fatigue-crack growth under aircraft spectrum loading. NASA TM-81941, January 1981.
23. Newman J.C.: A crack opening stress equation for fatigue crack growth. *Int. J. Fract.* vol 24, R131-135, 1984.

ANALYSIS OF COLD WORKED HOLES FOR STRUCTURAL LIFE EXTENSION

David H. Wieland
Jon T. Cutshall
O. Hal Burnside
Joseph W. Cardinal
Aerospace and Reliability Engineering Department
Southwest Research Institute
San Antonio, TX

SUMMARY

Cold working holes for improved fatigue life of fastener holes are widely used on aircraft. This paper presents methods used by the authors to determine the percent of cold working to be applied and to analyze fatigue crack growth of cold worked fastener holes. An elastic, perfectly-plastic analysis of a thick-walled tube is used to determine the stress field during the cold working process and the residual stress field after the process is completed. The results of the elastic/plastic analysis are used to determine the amount of cold working to apply to a hole. The residual stress field is then used to perform damage tolerance analysis of a crack growing out of a cold worked fastener hole. This analysis method is easily implemented in existing crack growth computer codes so that cold worked holes can be used to extend the structural life of aircraft. Analytical results are compared to test data where appropriate.

INTRODUCTION

Cold working is the process of expanding holes in structural materials to produce residual compressive stresses which reduce the natural tendency of the structure to crack under cyclic load. Simply, the process is accomplished by pulling a tapered steel mandrel through a sleeved hole. The mandrel is tapered to a thickness which, when added to the split-sleeve thickness, causes enough expansion of the hole to produce compressive yielding at the hole. The steel sleeve is utilized as a "sacrificial lamb" to protect the surface of the hole from scoring and tool marks. The split in the sleeve allows for full expansion of the hole. The percentage of applied cold work is calculated by dividing the radial displacement of the hole due to the inserted mandrel, by the radius of the hole before cold working. The percentage of residual cold working is defined by the ratio of the increase of the radius of the hole after mandrel removal, to the radius of the hole prior to cold working.

This process imparts residual compressive stresses around the hole, which tend to impede the advance of fatigue cracking in a similar manner to the compressive residual stress in the plastic zone around a crack tip. In the case of cold working, the magnitude of this compressive stress approaches the yield stress of the material. Since equilibrium must be maintained, the induced compressive stress must be balanced by a residual tension stress field which typically affects free edges of parts or adjacent holes that may not be cold worked. During the course of normal maintenance, these areas are susceptible to nicks, scratches, and other tool marks that on their own are not too serious, but when coupled with the residual tension from cold working, can produce a new breeding ground for fatigue crack initiation and growth.

The first step in analyzing cold worked holes is to perform a stress analysis to determine the applied and residual stress fields. For this purpose the authors used as an analysis model the elastic, perfectly-plastic expansion of a thick-walled tube. Others [1] have proposed using three-dimensional finite element models to determine the stress field due to cold working. While this may give more accurate results, it is not considered practical for use in the production environment where it may be required to analyze hundreds of geometries. Once the applied stress and residual stress fields are determined, the information can be used to determine the amount of cold working to use for various edge distances. Validation of the stress analysis is performed by comparison to finite element analysis and measured strains in test specimens.

Knowing the residual stress field for the uncracked geometry, the stress intensity factors (SIF) for various crack lengths emanating from the cold worked hole can be determined using a Green's function. This approach for calculating stress intensity factors is sometimes referred to as an indirect method for SIF computation. It is a generally acceptable method in the presence of complicated stress distributions. The SIF for the cold worked hole can then be superpositioned with the SIF factor computed for each individual load cycle to determine crack growth during cyclic loading. Crack growth results are presented for constant amplitude and random cyclic loading conditions.

STRESS ANALYSIS OF COLD WORKED HOLES

Stress analyses of fastener hole cold-expansions were performed due to concern regarding the cold working of short edge-distance holes and to determine residual stress fields of cold worked holes. The primary concerns were fracture during cold working and the damage tolerance life of cold worked holes. Additionally, concerns arose about the residual tension stresses at the free edge nearest to cold-expanded holes. This tension field could accelerate crack growth from the edge to the hole if cracks or surface flaws were present or initiated on the free edge. This paper does not address the free edge residual tension stress issue. The purpose of this examination was to determine the induced and residual stress distribution through the ligament around cold worked holes.

Examination of the cold working process began with a survey of documented experimental results showing the beneficial effects of cold working on fatigue life enhancement. Next, a classical analytical model was used to approximate the plastic deformation of a hole with applied internal pressure [2]. The expected induced and residual stress distribution through the ligament thickness can be seen in Figures 1 and 2, respectively. The constant k used to nondimensionalize the stresses in these plots is the value of the yield stress in pure shear. The Tresca yield criterion was adopted for this solution.

Mathematical plasticity calculations based on the model are made to determine the induced and residual stress field around cold worked holes. A diagram of the plasticity model geometric configuration is shown in Figure 3. The methodology approximates a cold worked hole geometry by a thick walled cylinder having an internal radius equal to the hole radius, a, and the distance to the nearest free edge equal to the external radius, b. The other parameters shown in Figure 3 are the plastic yield radius, c, and the reverse yield radius, ρ.

The equations for the mathematical model from Reference [2] which predict the induced stresses are:

$$\sigma_r = -\frac{kc^2}{b}\left(\frac{b^2}{r^2} - 1\right), \qquad \sigma_\theta = \frac{kc^2}{b^2}\left(\frac{b^2}{r^2} + 1\right) \qquad c \le r \le b$$

$$\sigma_r = -k\left(1 - \frac{c^2}{b^2} + \ln\frac{c^2}{r^2}\right), \qquad \sigma_\theta = k\left(1 + \frac{c^2}{b^2} - \ln\frac{c^2}{r^2}\right) \qquad a \le r \le c \tag{1}$$

In these equations, σ_r is the induced radial stress, σ_θ is defined as the induced circumferential stress and k is the yield stress in pure shear. The zone from c to b is the elastic region while the zone from a to c is the plastic region. The variable c is thus defined as the yield radius. The internal pressure, p, is

$$p = k\left(1 - \frac{c^2}{b^2} + \ln\frac{c^2}{a^2}\right) \tag{2}$$

and the displacement at the inner radius due to the applied pressure is

$$u_a = a\left[\frac{v^2 p}{G(1+v)(b^2/a^2 - 1)} + (1-v)\frac{kc^2}{Ga^2} - (1-2v)\frac{p}{2G}\right] \tag{3}$$

The value of the plastic zone size, c, is still indeterminate from the above equations. The imposed radial displacement u_a is known from the cold working tool geometry so that c can be solved for in an iterative manner until the proper displacement at the inner radius is achieved.

Since the cold worked fastener holes were determined to undergo reverse yielding after removal of the mandrel, the residual stresses were determined by adding the following equations to those noted above.

$$\sigma_r' = 2k\frac{\rho^2}{b}\left(\frac{b^2}{r^2} - 1\right), \qquad \sigma_\theta' = -2k\frac{\rho^2}{b^2}\left(\frac{b^2}{r^2} + 1\right) \qquad \rho \le r \le b$$

$$\sigma_r' = 2k\left(1 - \frac{\rho^2}{b^2} + \ln\frac{\rho^2}{r^2}\right), \quad \sigma_\theta' = -2k\left(1 + \frac{\rho^2}{b^2} - \ln\frac{\rho^2}{r^2}\right) \qquad a \le r \le \rho \tag{4}$$

where the radius ρ is determined from the boundary condition $\sigma'_r = p$ at $r = a$. In these equations, the residual radial stress is defined as σ'_r, and σ'_θ represents the residual circumferential stress. For a more detailed discussion of this solution see Reference [2].

Model Validation

In order to validate the use of the plasticity model for decisions concerning cold working, comparisons to finite element models and USAF experimental results were made. First, a two dimensional non-linear analysis for investigation of a hole with 2.8 percent interference was performed by Crows [3]. Next, a three-dimensional NASTRAN lug model was developed for an investigation of cold working effects at Kelly AFB [4]. Finally, experimental data was obtained from strain gaging and cold working T-37 "302" attachment fitting lugs at Randolph AFB [5]. Graphical representations of these comparisons appear in Figures 4 through 7.

Figure 4 gives Crows' finite element results [3] for a 7075-T6 rectangular sheet with an interference fit hole. Results are given for the interference stress in both the hoop and radial directions together with the present solutions for a thick walled tube under applied pressure with the same b. It can be seen that a good agreement exists between them.

A three dimensional non-linear material NASTRAN analysis was performed to investigate to effects cold working at Kelly AFB[4]. The lug geometry analyzed had a hole radius of 0.438 inches and an edge distance of 1.093 inches. The material of the model was 7075-T6 die forging. Figure 5 shows comparisons for the residual hoop stresses through the ligament, i.e., the material from the edge of the hole to the free edge. This figure shows a favorable comparison between the results from the NASTRAN model and the plasticity model for 4.0 percent cold work. Figure 5 also shows that

the plasticity model is predicting reverse yielding while the NASTRAN results are not given at a fine enough resolution to determine if reverse yielding occurred.

Figures 6 and 7 show comparisons between the plasticity model and the USAF "302" lug experimental data [5]. The strain gage data was obtained from the free edge of the lugs. The geometry of the lugs is the same as the above NASTRAN model. Figure 6 shows the plasticity model to be an upper bound for the experimental data. The data in Figure 7 shows that the retained expansion can also be calculated accurately. The comparison of the plots supports the validity of the model for the ranges of cold work from 2.8 to 4.0 percent.

DAMAGE TOLERANCE ANALYSIS OF COLD WORKED HOLES

Damage tolerance analysis of cold worked holes is performed so that realistic crack growth lives for cold worked holes can reliably be predicted. To perform DTA of cold worked holes, the effect of the residual stress field on the stress intensity factor must be determined. After determining the SIF due to cold working, this value is superpositioned with the SIF due to the applied spectrum load. After superpositioning the SIFs, the growth increment due to the load cycle is calculated using standard linear elastic fracture mechanics (LEFM) crack growth rate models.

Determination of Stress Intensity Factors

The residual stress intensity factors were determined using Shaw's Green's function for a radially cracked hole[6] and the residual stress distribution as determined from the above equations. Shaw's Green's Function for a diametrically cracked hole is:

$$K_I = \frac{M_f}{\sqrt{\pi l}} \int_{-l}^{l} \sigma_x \left[\frac{l+x}{l-x}\right]^{1/2} dx \qquad (5)$$

where M_f is a free surface correction given by

$$M_f = 1.0 + 0.12\left(\frac{0.3 - l/R}{0.3}\right), \text{ for } 0 \le \frac{l}{R} \le 0.3 \qquad (6)$$

and

$$M_f = 1.0, \text{ for } \frac{l}{R} > 0.3 \tag{7}$$

The stress intensity factor for one crack is given by Shah as

$$(K_I)_{\text{one crack}} = \sqrt{\frac{2R+l}{2R+2l}}\,(K_I)_{\text{two cracks}} \tag{8}$$

The ratio of the geometry factor for a Newman/Raju corner crack at a hole [7] to the NASA FLAGRO [8] solution for a radial through crack at a hole was used to account for the flaws being corner cracks rather than through-the-thickness cracks. The determination of the residual stress intensity factor was performed using a spread sheet. The stress intensity factor for a corner crack at a cold worked hole is:

$$K_{cold} = \frac{\beta_c}{\beta_t}(K_I)_{one\ crack} \tag{9}$$

where β_c is the Newman/Raju corner crack geometry factor and β_t is the geometry factor for a through crack. Figure 8 compares the stress intensity factor for a 0.31 inch open hole with a edge distance of 0.75 inches under 35 ksi far field stress to that of a 4.8 percent expanded cold worked hole in 7075-T6511 extrusion. It can be seen in this figure that the stress intensity for the cold worked hole is much less than the open hole case for a large portion of the crack length. The stress intensity factors for cold worked holes are larger than the stress intensity factor for an open hole at larger crack sizes due to residual tension stress at larger crack sizes.

Crack Growth Analysis Method

Spectrum fatigue crack growth predictions were made using the applied stress intensity range, ΔK, for each cycle in the flight by flight spectrum. The stress intensity factors were calculated by the superposition of the residual stress intensity factor due to cold working with the stress intensity from the cyclicly applied load. The calculated values of ΔK are used to determine the crack growth increment for that cycle. The method can be used with any of the standard crack growth rate equations. The authors modified a version of the Cracks III computer code[9] to perform the superposition on a cycle-by-cycle basis. The authors' work used the Walker equation for stress ratio adjustments in crack growth rates. The form of the Walker equation used is:

$$\frac{da}{dN} = C\left(\frac{\Delta K}{(1-R)^{1-M}}\right)^n \qquad \text{for } R \geq 0.0 \tag{10}$$

and in the form

$$\frac{da}{dN} = C\left[\left(1 + R^2\right)^q \cdot K_{max}\right]^n \qquad \text{for } R < 0.0 \qquad (11)$$

where R is the stress ratio, ΔK is the stress intensity range and C, M, n, q are material constants. The residual stress intensity is very important for determining the stress ratio adjustments in that most of the cycles have large negative stress ratios, and thus the crack growth rates are decreased significantly.

Validation of Crack Growth Analysis

The crack growth analyses of cold worked holes are validated with constant amplitude and random cycle loadings. The first case analyzed is a 0.31 inch hole in a 7075-T6511 aluminum alloy extruded panel, under constant amplitude far field stress of 35 ksi and an R ratio of 0.1[10]. Figure 9 presents the test results for cold worked and non cold worked holes compared to the crack growth analysis. Figure 10 compares similar test results for R=0.8 to crack growth analysis results.

The final case analyzed was a 100 percent pin load 0.5616 inch fastener hole in 7075-T651 extrusion 1.067 inches wide and 0.09 inches thick [11]. The test spectrum was a cycle-by-cycle bearing stress spectrum for the T-37 horizontal stabilizer. The maximum spectrum bearing stress was 30.6 ksi. The fastener hole was expanded 3.64 percent. Crack growth retardation was predicted using the Wheeler plastic zone model [12]. The magnitude of the retardation parameter M was determined to be 4.0. Figure 11 presents the results of two tests specimens and the damage tolerance analysis.

DISCUSSION

While initially evaluating the effects of cold worked holes, the authors were concerned with the wide variation in applied expansion using standard tools. Due to hole and cold working tooling tolerances for a normal 0.25 inch hole, the applied expansion can vary from 2.5 percent to 6 percent. Figure 12 shows a calculation demonstrating how this variation in applied expansion can affect the damage tolerance life.

It is also possible to use this analysis to predict the amount of cold working required to stop a crack of a specified length from growing under spectrum loading. This is done by calculating the SIF for a cold worked hole with a crack length of x and super-positioning it with the SIF for a

cracked hole of length x at maximum spectrum stress. If the combined SIF is less than zero then no crack growth will occur. If the SIF is greater than zero, then the amount of cold working can be increased until the SIF becomes less than zero. Obviously there is a limit to the amount of cold working that may be applied.

In conclusion, a method for performing stress analysis and damage tolerance analysis of cold worked holes has been presented. The method has been validated to the extent possible with existing test data. The method is simple and does not require a nonlinear finite element analysis to obtain accurate results. The method lends itself to inclusion of computer programs to analyze damage tolerance lives of cold worked holes.

REFERENCES

1. Forgues, S. A.; Bernard, M.; and Bui-Quoc, T.: "3-D Axisymmetric Numerical Analysis and Experimental Study of the Fastener Hole Coldworking Process," *Computer Methods and Experimental Measurements for Surface Treatment Effects*, M.H. Alibadi and C.A. Breddia, eds., Computational Mechanics Publications, Southampton, U.K., 1993.

2. Chakrubarty, J.: *Theory of Plasticity*. McGraw-Hill Book Company, New York, 1987, pp. 316-334.

3. Crows, J. H., Jr.: An Elastoplastic Analysis of a Uniaxially Loaded Sheet with an Interference-Fit Bolt. NASA TN D-7748, 1974.

4. Wieland, D.H.: Undocumented NASTRAN Model of Wing Attachment Fitting Lugs for Analysis at Kelly AFB MMEOD, June 1989.

5. Uhuad, G. C.: Untitled Memorandum from USAF MMETT to MMEOD and MMSRA; Subject: T-37 302 Spar Fitting Strain Gage Project Report, Directorate of Material Management, Kelly AFB, Sept. 7, 1989.

6. Rooke, D. P.; Baratta, F. I.; Cartwrught, D. J.: Simple Methods of Determining Stress Intensity Factors. *Engineering Fracture Mechanics*, vol. 14, 1981, pp. 397-426.

7. Newman, J. C., Jr.; Raju, I. S.: Stress Intensity Factor Equations for Cracks in Three-Dimensional Finite Bodies Subjected to Tension and Bending Loads. NASA TM 85793.

8. NASA/FLAGRO Fatigue Crack Growth Computer Program. National Aeronautics and Space Administration, JSC-22267, Revised Dec. 1988.

9. Engle, R. M., Jr.: CRACKS III - A Digital (FORTRAN) Computer Program for Crack Propagation Analysis. AFFDL Version 1, July 10, 1975.

10. Toor, Pir M.: "Cracks Emanating from Precracked Coldworked Holes." *Engineering Fracture Mechanics*, 1976, vol. 8, pp. 391-395.

11. Wieland, D. H.; FitzGerald, J. H.: "Damage Tolerance Testing of T-37 Horizontal Stabilizer," Final Report, SwRI Project 06-3775, Prepared for San Antonio Air Logistics Center, Kelly Air Force Base, TX, Jan. 1992.

12. Wheeler, V. E.: Transactions. American Society of Mechanical Engineers, *Journal of Basic Engineering*, vol. 94, March 1972, pp. 181-186.

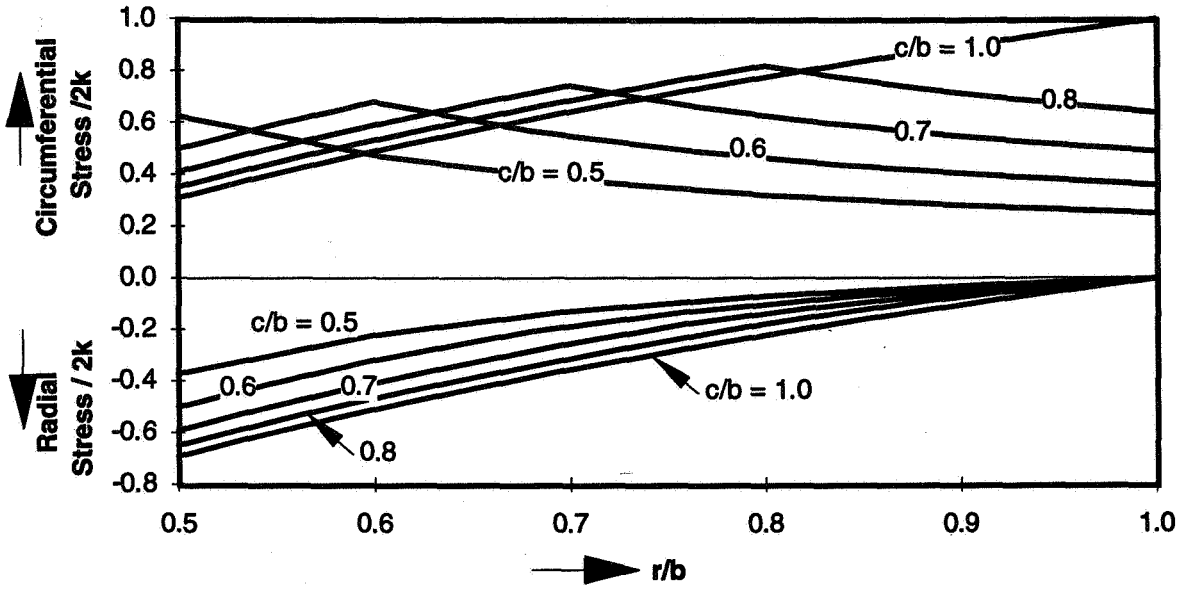

Figure 1. Typical nondimensional radial and circumferential stress in an elastic/plastic thick walled tube subjected to internal pressure.

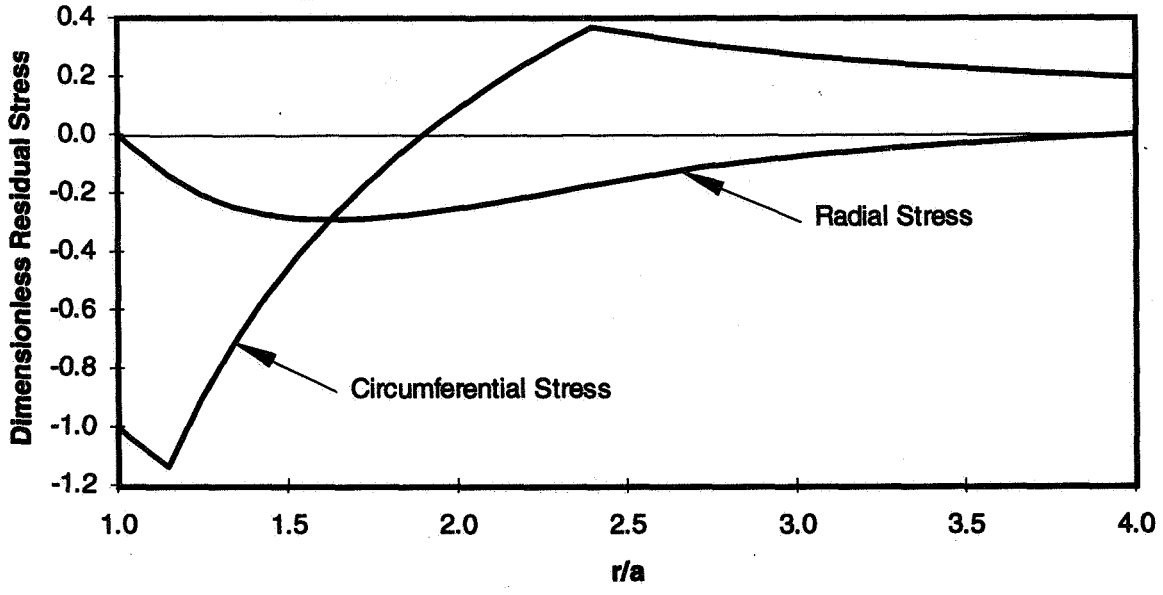

Figure 2. Typical residual stress distribution in a thick walled tube unloaded from an elastic/plastic state.

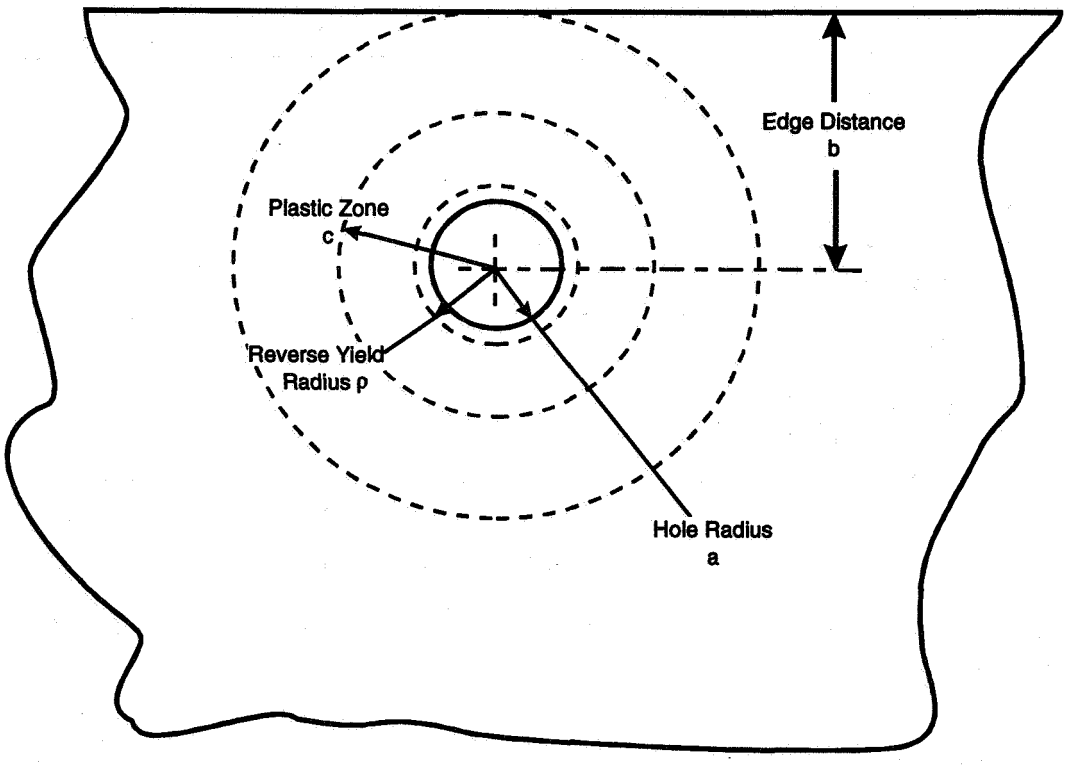

Figure 3. Idealized plasticity model geometric configuration.

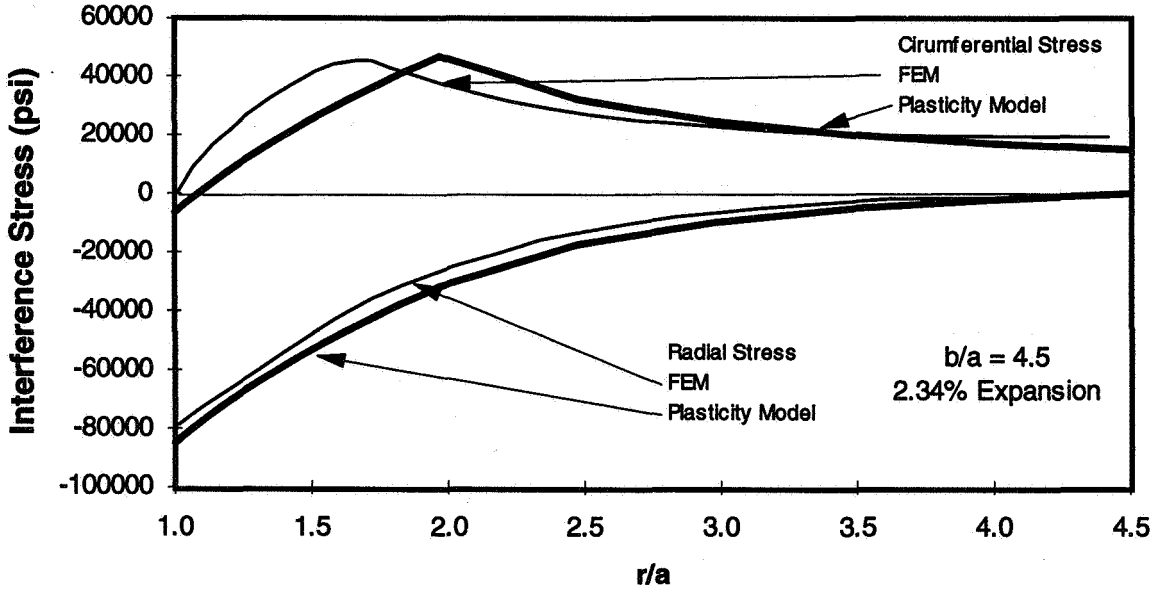

Figure 4. Comparison of results between plasticity model and finite element analysis[3].

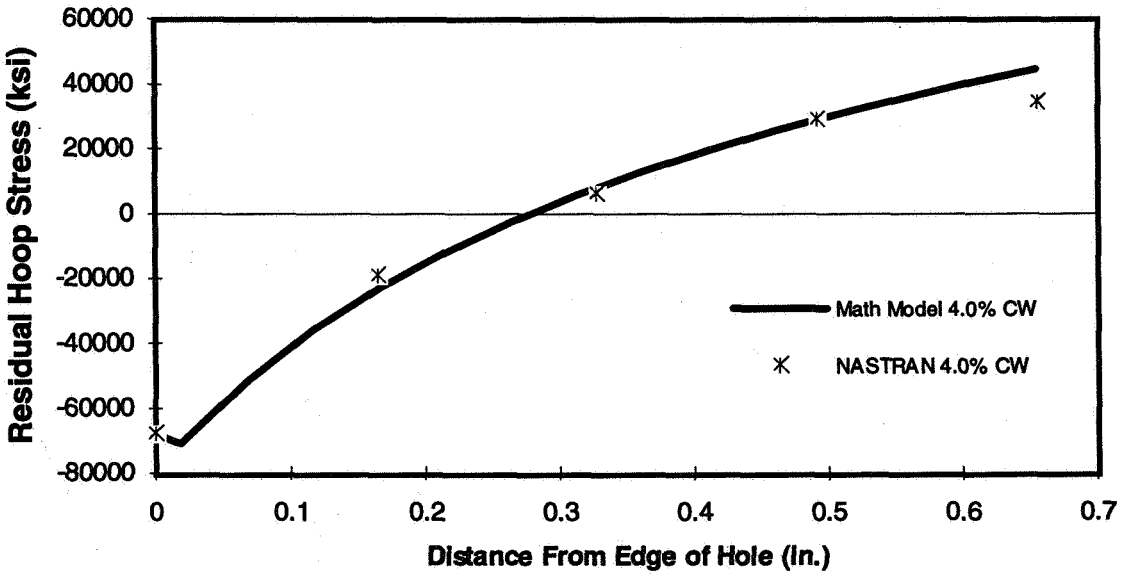

Figure 5. Comparison of results between plasticity model and USAF NASTRAN model of "302" lug.

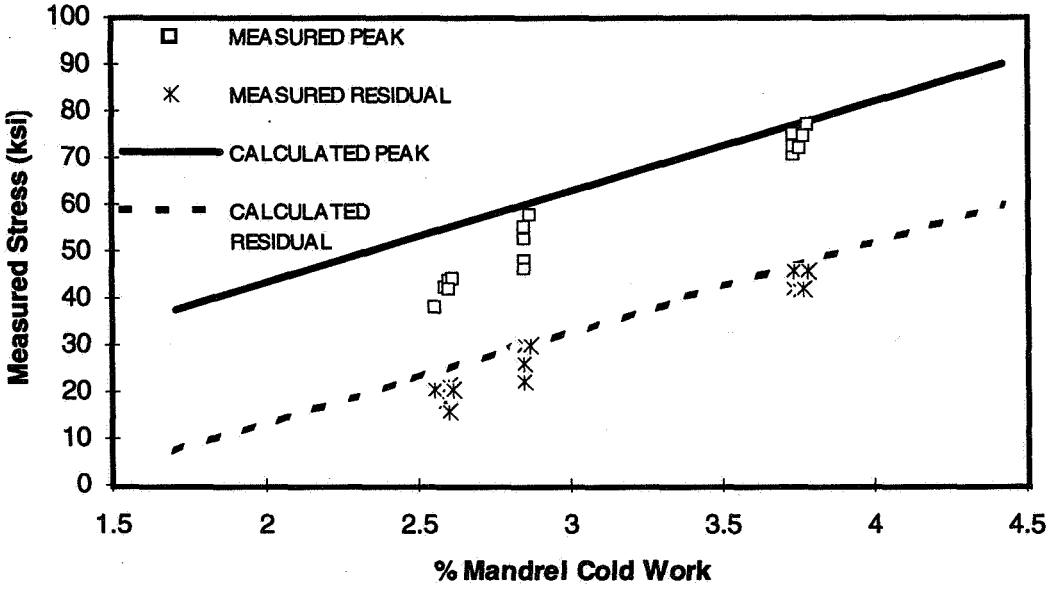

Figure 6. Comparison of stress results between plasticity model and USAF experimental results.

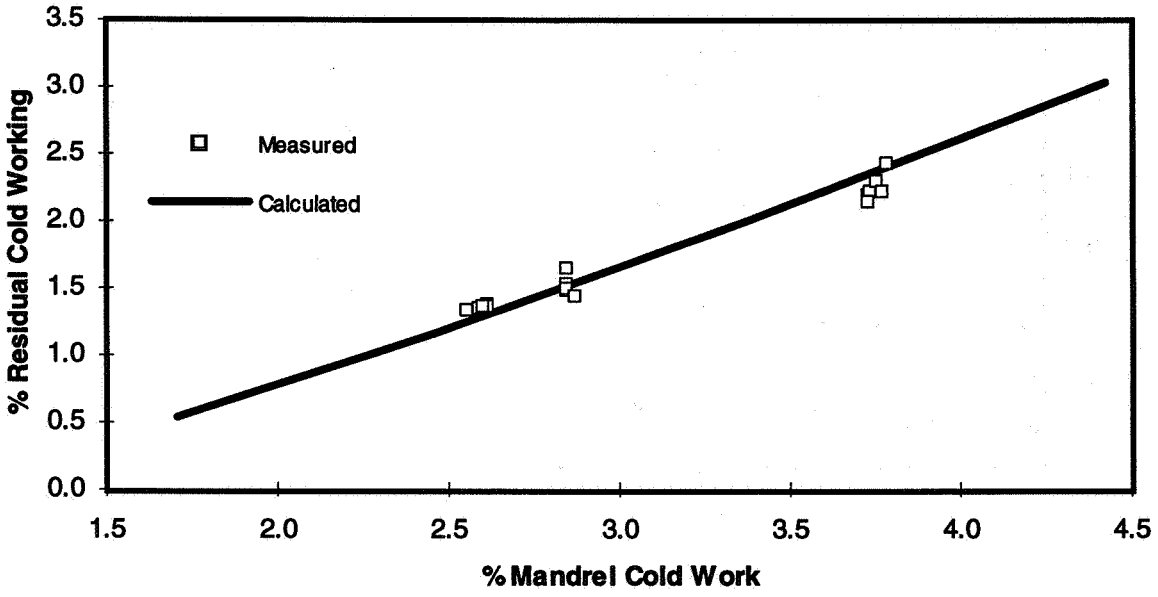

Figure 7. Comparison of percent residual cold working between plasticity model and USAF experimental results.

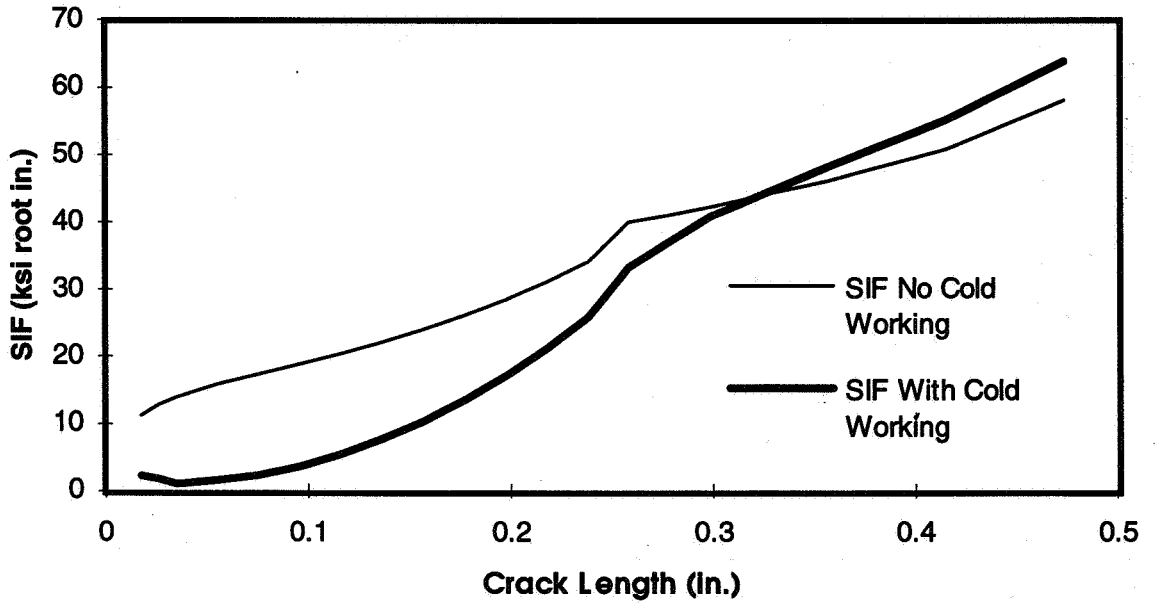

Figure 8. Comparison between the stress intensity factor for a cold worked hole and a normal hole.

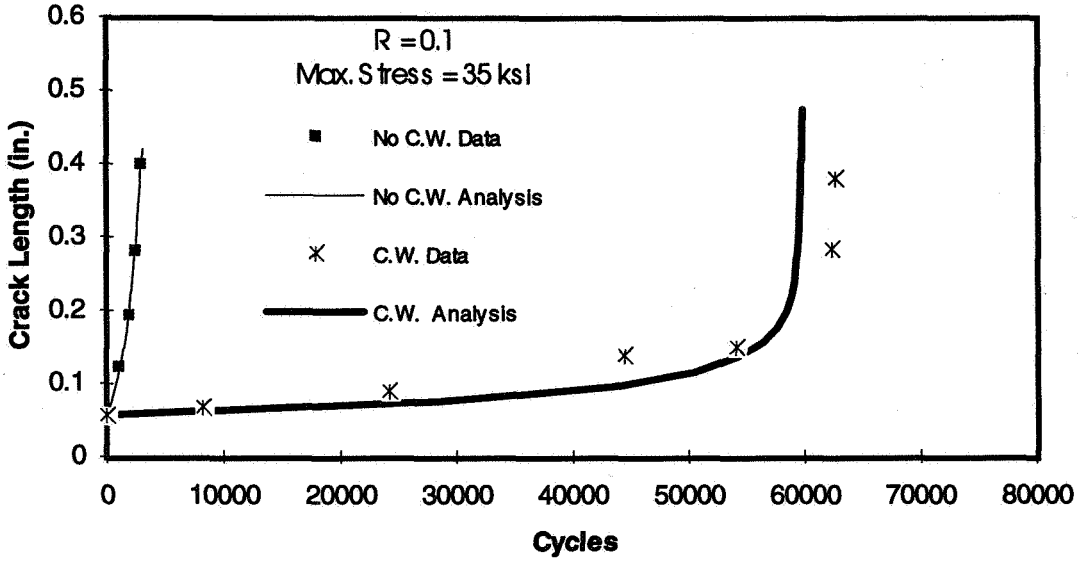

Figure 9. Comparison of constant amplitude damage tolerance analyses to test data for R =0.1 and maximum stress of 35 ksi.

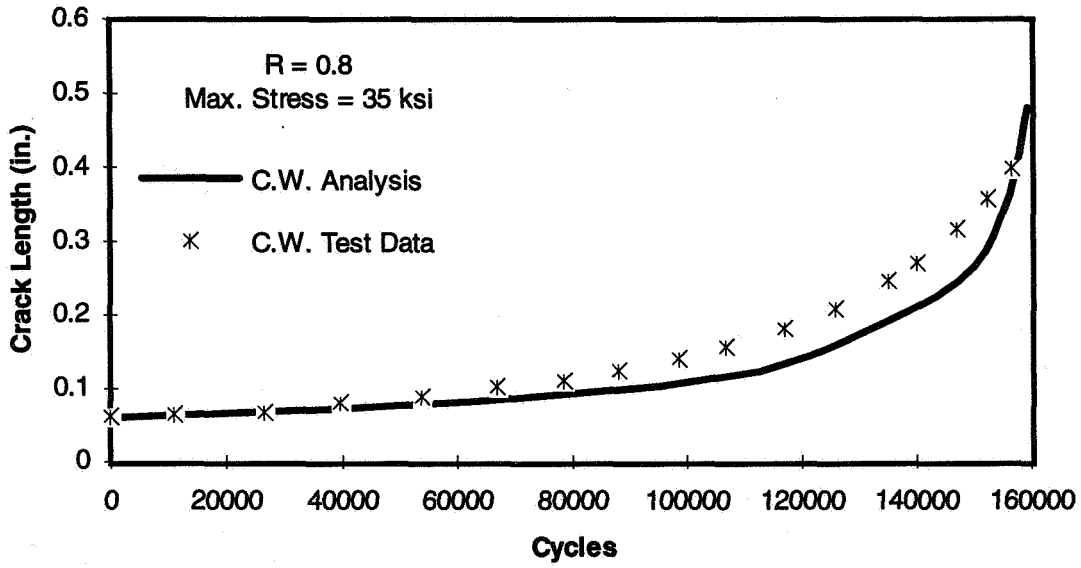

Figure 10. Comparison of constant amplitude damage tolerance analyses of a cold worked hole to test data for R =0.8 and maximum stress of 35 ksi.

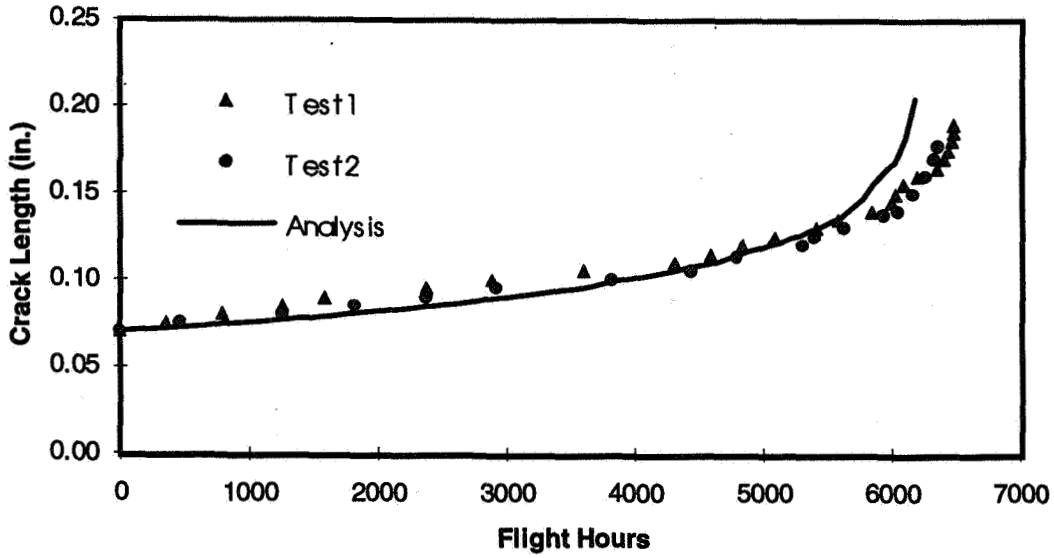

Figure 11. Spectrum crack growth analysis comparison of cold worked fastener hole to spectrum test data.

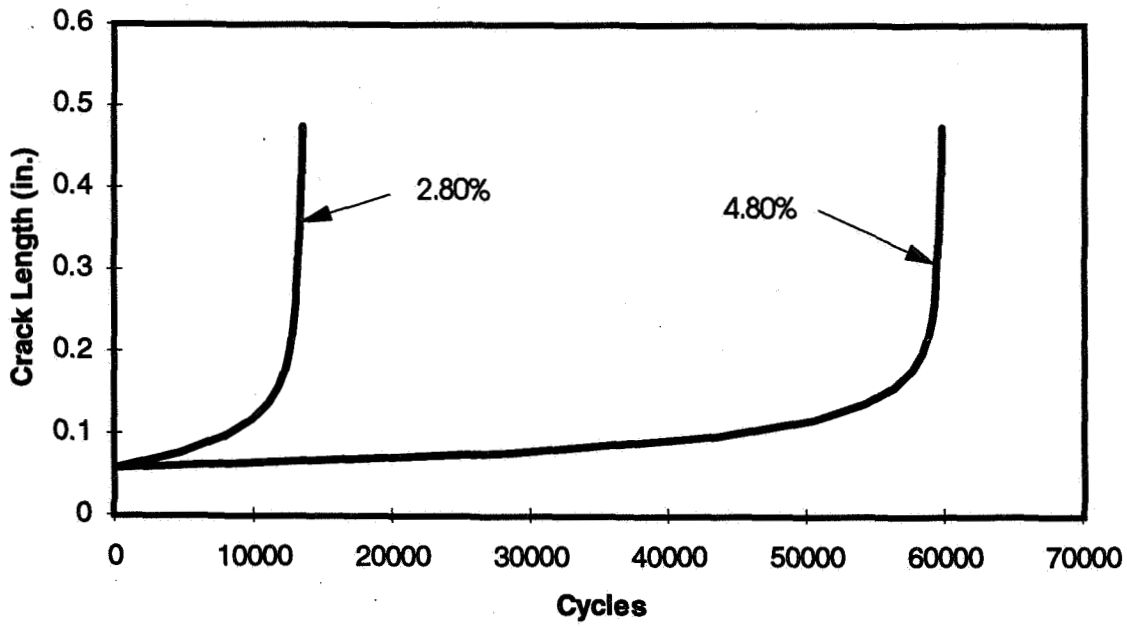

Figure 12. Variation in cold worked fastener hole damage tolerance life due to allowable tooling tolerance build up.

FRACTURE BEHAVIOR OF LARGE-SCALE THIN-SHEET ALUMINUM ALLOY*

Roland deWit, Richard J. Fields, Leonard Mordfin,
Samuel R. Low, and Donald Harne
Mechanical Properties and Performance
National Institute of Standards and Technology
Gaithersburg, MD 20899

ABSTRACT

A series of fracture tests on large-scale, pre-cracked, aluminum alloy panels is being carried out to examine and to characterize the process by which cracks propagate and link up in this material. Extended grips and test fixtures were specially designed to enable the panel specimens to be loaded in tension, in a 1780-kN-capacity universal testing machine. Twelve panel specimens, each consisting of a single sheet of bare 2024-T3 aluminum alloy, 3988 mm high, 2286 mm wide, and 1.016 mm thick are being fabricated with simulated through-cracks oriented horizontally at mid-height. Using existing information, a test matrix has been set up that explores regions of failure that are controlled by fracture mechanics, with additional tests near the boundary between plastic collapse and fracture. In addition, a variety of multiple site damage (MSD) configurations have been included to distinguish between various proposed linkage mechanisms. All tests but one use anti-buckling guides. At this writing seven specimens have been tested. Three were fabricated with a single central crack, three others had multiple cracks on each side of the central crack, and one had a single crack but no anti-buckling guides. Each fracture event was recorded on film, video, computer, magnetic tape, and occasionally optical microscopy. The visual showed the crack tip with a load meter in the field of view, using motion picture film for one tip and SVHS video tape for the other. The computer recorded the output of the testing machine load cell, the stroke, and twelve strain gages at 1.5 second intervals. A wideband FM magnetic tape recorder was used to record data from the same sources. The data were analyzed by two different procedures, (1) the plastic zone model based on the residual strength diagram, and (2) the R-curve. The first three tests were used to determine the basic material properties, and these results were then used in the

---

*Work done under Interagency Agreement No. DTFA03-92-Z-00018, Task Number 4, with the Federal Aviation Administration, U.S.Department of Transportation.

analysis of the two subsequent tests with MSD cracks. There is good agreement between measured values and results obtained from the model.

KEY WORDS: aluminum, crack, fracture mechanics, multiple site damage, plastic zone, R-curve, toughness

INTRODUCTION

The aging of the commercial transport fleets around the world is of constant concern because of the loss of structural integrity through fatigue cracking. In one design approach for aircraft fuselages using semi-monocoque construction, circumferential rings or frames are intended to steer dangerous longitudinal cracks—if they appear—in the less threatening circumferential direction around the fuselage. It has been hypothesized, however, that in the case of aging aircraft in which multiple site damage, such as short fatigue cracks emanating from rivet holes, is present, cracks that start running longitudinally may continue to do so because the cracked rivet holes may provide a path of lesser resistance. Our research is intended to provide some of the information needed to better understand this crack propagation process. In this work we were greatly aided by the advice of David Broek. Also a team from NASA Langley under leadership of James C. Newman assisted with additional measurements.

The specialized facilities and capabilities at NIST are being used to carry out a series of fracture tests on twelve large-scale, 2286-mm wide, pre-cracked, aluminum alloy panels to examine and to characterize the process by which cracks propagate and link up in this material. The tests are sponsored by the Federal Aviation Administration (FAA) as part of its National Aging Aircraft Research Program. The current tests were deemed necessary by the FAA because in previous work [1] only 508-mm wide flat panels were tested, while all other tests were performed on 2286-mm wide curved panels loaded by pressure, both with and without frames and tear straps. The results of these previous tests were predicted very well with a plastic zone model, but showed that the main mode of failure was plastic collapse. In the current program the wide plates failed under conditions closer to fracture mechanics and R-curve behavior.

Using existing information obtained from the tests with smaller specimens, we set up a test matrix that explores regions of failure that are controlled by fracture mechanics, with additional tests near the boundary between plastic collapse and fracture. In addition, a variety of multiple site damage (MSD)

configurations have been included to distinguish between various proposed linkage mechanisms. All tests but one are planned with the use of anti-buckling guides. The one without anti-buckling guides was recommended by NASA Langley to help assess the effect of buckling.

At this writing seven specimens have been tested. Three were fabricated with a single central crack. Three others had multiple cracks on each side of the central crack. One had a single crack with no anti-buckling guides. Each fracture event was recorded on film, video, computer, magnetic tape, and the NASA team occasionally also added optical microscopy. Using flat sheets without stringers to stiffen the panels, these are uncomplicated tests aimed more at obtaining basic material properties than simulating fracture in an airplane fuselage. The material properties sought are the basic fracture properties and linkage criteria for the MSD cracks.

The data were analyzed by two different procedures, (1) the plastic zone model based on the residual strength diagram, and (2) the R-curve. The plastic zone model is an engineering approach which takes the plasticity into account by using an effective fracture toughness, which is less than the true fracture toughness of the material. The basic concept is that the residual strength in the presence of MSD depends on the criterion that an MSD crack will be absorbed by the main crack when their two plastic zones meet, so that the ligament then fails by collapse. It has been a very good predictor of the test results. The R-curve uses a more fundamental approach but requires more data collection and analysis. It accounts directly for the plasticity by the R-curve behavior, and gives more detailed information of the fracture event, such as the amount of crack growth before instability.

The first three tests each contained a single crack and the collected data were used to determine the basic material properties, namely the collapse strength and the effective fracture toughness for the residual strength diagram, and an analytic expression for the R-curve. These results were then used in the analysis of the two subsequent tests with MSD cracks. The results show good agreement between measured values and results obtained from the two independent analyses.

DESCRIPTION OF TESTS

Since this effort uses 90 inch (2286 mm) wide panels, some with multiple site damage (MSD), it has been named the "90 MSD" program. The planned test matrix is shown in Table 1. The

quantities that appear in this table are defined in Figure 2. The individual tests are labeled MSD-1, MSD-2, etc.

Twelve panels were procured, each consisting of a single sheet of bare (not clad) 2024-T3 aluminum alloy, 3988 mm high, 2286 mm wide, and 1.016 mm thick. The specimens are being fabricated with simulated through-cracks oriented horizontally at mid-height. The simulated cracks are saw cuts, ending with the sharpest jeweller's saw cuts available, having a final tip radius of 0.076 mm. The first three tests each had a single central crack. Subsequent tests will also have multiple small cracks on each side of a larger central crack to simulate multiple site damage (MSD). Each MSD crack had a circular 5.6 mm diameter hole in its center to simulate a rivet hole, as shown schematically in Figure 1.

A review of the literature suggests that the specimens tested in this program are the largest structural panels that have been tested in tension. The great size necessitated special design and testing considerations in order to introduce the test loads uniformly along the panel widths. A whiffle-tree approach was ruled out by the height limitations of the 1780-kN-capacity 4-screw-powered universal testing machine (UTM) that was used. As it was, 76 mm had to be cut from the specimens reducing their height to 3912 mm, and only 30 to 50 mm of the testing machine's stroke remained at specimen failure. The machine is one of the largest electro-mechanical testing machines in the world. In its unaltered state, with power screws in all four corners of the 1068 mm x 1524 mm testing table, loads to 448 kN can be applied up to 914 mm off-center, and up to full capacity at 152 mm off-center.

However, to accommodate our large panels, the heads of the testing machine were effectively enlarged with pairs of wide flange structural steel beams (W8x40), 2286 mm long, bolted together. The grips consisted of 2286-mm-long, thick-walled aluminum-alloy extrusions bolted to the steel beams. Each end of the panel specimens was fastened between the grips with forty-five 15.875-mm high-strength steel bolts, fully tightened. The length of the panel between the top and bottom rows of bolts was 3810 mm. Abrasive cloth was inserted between the specimens and the grips to maximize the transfer of load by shear and thereby avoid pin bearing failures of the thin panel material.

The uniformity with which the load was introduced was monitored in the first test with 20 strain gages and in subsequent tests with 10 strain gages mounted on each panel about 406 mm from the grips at each end. These are called the far field strain gages. The strain distribution was measured at low loads, prior to each test, and, if necessary, thin metal shims were inserted between the steel beams and the grips in order to achieve a more uniform distribution. Uniformities within ±10 percent were obtained in

all cases.

Anti-buckling guides, consisting of four aluminum channels, were used to restrain out-of-plane buckling of the panel. The beams were placed horizontally about 12 mm above and below the crack on both sides of the specimen. In the first test a 12 mm thick felt pad was used between the guides and the specimen to facilitate smooth sliding. In subsequent tests rubber was used. Test MSD-6 was performed without the anti-buckling guides to ascertain their effect.

The tests were highly instrumented. Eight additional strain gages (12 for the first test) were placed near the crack tips or MSD cracks. The strain gage signals were run through wide band strain gage conditioning amplifiers. A displacement gage was installed at the bottom of the cross head to measure the total displacement. For specimens MSD-4 and MSD-5 a clipgage was also mounted at the middle of the central crack. The signals of all these gages were recorded by a computer. A SVHS video camera was mounted to view the right crack tip and a motion picture camera viewed the left. For tests MSD-2, 3, 4 and 6 a team from NASA Langley also used high resolution optical microscopy at the left crack tip from the backside. Test MSD-6, which had no anti-buckling guides, used thirteen 3-element rosette strain gages. Seven of these were in the two crack paths and four were near the center of the crack.

The tests consisted of pulling the specimen to fracture under displacement control. The displacement was generally applied at load intervals of 20 to 45 kN and held for one to four minutes at each load level. The whole test lasted from 15 to 20 minutes. Link-ups to MSD cracks occurred in a fraction of a second. Towards the end of the test there was a large amount of crack growth with very small increase of load. After 50 to 100 mm of such tearing instability occurred and the load started to drop. Final fracture occurred with an audible rip.

DATA COLLECTION

The data collection had some built-in redundancy and consisted of up to five components: manual, visual, computer, magnetic tape, and occasionally optical microscopy. The signals from various gages were recorded as a voltage and therefore prior to each test various calibrations were performed to be able to convert these voltage readings to the appropriate physical quantities.

Manual Recording

During the test at each load level the load was noted from the dial of the universal testing machine (UTM). The strain at these loads was read with a bridge amplifier at some of the far field gages near the top and bottom of the specimen. For tests MSD-1 and 7 all the far field strain gages were manually recorded and for MSD-6 none were manually recorded. These recordings provided a record of the average strain and its uniformity across the panel. When the final fracture occurred the fracture load was also recorded from the dial of the UTM.

Visual Recording

The visual recording consisted of showing a voltmeter with a crack tip and the MSD cracks (when present) in the field of view, using SVHS video tape for right tip and motion picture film for the other. The two voltmeters were connected to the UTM load cell and showed a voltage proportional to the load. A calibration was run for the voltmeters prior to the test. The SVHS recording could be observed live on a TV screen. Thus the progress of the crack growth could be monitored during the test. After the test the visual recordings were used to determine the crack extension as a function of the load.

Computer Recording

A personal computer was set up to collect data from various sources. These included the current time, the load obtained from the UTM load cell, the displacement, the strains from the far field gages that were not taken manually, the gages near the crack, and for tests MSD-4, 5, and 7 the clipgage. Each data set was taken at 1½ second intervals, was shown live on the monitor screen, and could be stored in a file.

As mentioned the input data were read as a voltage. Therefore, calibrations were run prior to each test. For the load calibration a simulated load was generated at the UTM console with 22.2 kN intervals from zero up to 200 or 450 kN. The displacement gage was calibrated at 0.254 and 0.635 mm intervals over a range of 20 mm. The strain gages had a resistance of 350 Ω and a gage factor of 2.135. They were calibrated using the

strain gage conditioning amplifiers, which also contained bridge resistances of 350 Ω. With a switch a shunt resistance of 174.8 kΩ could be shorted across the bridge, which corresponded to a simulated strain change of 936 microstrain. The above calibrations resulted in linear conversions. The clipgage worked on the capacitive principle and was calibrated at 0.635 mm intervals from zero to 15 mm. It resulted in a nonlinear conversion of the form $a+bx+cx^2/x+d/x$.

Tape Recording

A wideband FM magnetic tape recorder was used to record data from the same sources as the computer recording. The tape recorder was set to IRIG I and run at 30 inch per second, which provides a distortion free signal (1 dB) from DC to 20 kHz. These recordings are fast enough to show dynamic effects. These data have not yet been analyzed.

Optical Microscopy

For tests MSD-2, 3, and 4 a team from NASA Langley collaborated with high resolution optical microscopy (OM) at one crack tip. For test MSD-6 they additionally recorded the signals from the 3-element rosette strain gages. Their optical microscopy apparatus was used to observe the growing crack. A photographic technique was developed to measure the crack tip opening angle during crack initiation and stable tearing. The OM apparatus consisted of a computer controlled, long focal length microscope fitted to a video camera. The field of view of the microscope was a square with sides approximately 1.8 mm long. The field of view was centered on the crack tip and advanced as the crack grew. The results from this analysis will be reported elsewhere by NASA Langley.

R-CURVE ANALYSIS

The crack extension that occurred as the load increased was measured with the SVHS video tape, the movie film, and the OM apparatus. The results for tests MSD-1, 2, 3 and 6 are shown in Figure 3. These tests all had a single central crack, see Table

C-6

1. Specimen MSD-6 had no anti-buckling guides and the data for this test fall below those for MSD-3, which had the same crack size. This shows that the lack of guides and consequent buckling acted as a stress intensification at the crack tips.

We have used the R-curve concept [2] to analyze some of the data. First, we show here how to find the crack-extension force, G, from the slow stable crack growth data. This quantity is related to the stress-intensity factor, K, by

$$G = K^2/E \tag{1}$$

where E is Young's modulus. The stress-intensity factor is generally given by the generic expression

$$K = \beta\sigma\sqrt{(\pi a)} \tag{2}$$

where the function β is used to describe the effect of the shape and size of the crack and the specimen. For the center crack specimen we then have

$$G(a) = (\sigma^2\pi a/E)\beta^2(\pi a/W) \tag{3}$$

where σ is the applied stress, a the half-crack size, and W the panel width. For the stress-intensity factor of a center-notch specimen with sharp crack tips Feddersen [3] discovered that

$$\beta(\pi a/W) = \sqrt{\sec(\pi a/W)} \tag{4}$$

gives an approximation that is accurate to 0.3 percent for $2a/W<0.7$. The stress is given by

$$\sigma = P/(WB) \tag{5}$$

where P is the load and B is the panel thickness. For our panels we have

$$W = 2286 \text{ mm}$$
$$B = 1.016 \text{ mm}$$
$$E = 71 \text{ GPa}$$

Using these values and Equations (3)-(5), the movie film and video tape data from Figure 3 were converted into the crack-extension force data shown in Figure 4. We see that for small crack-extensions the data from the tests with the anti-buckling guides collapse nicely into a master curve, but without anti-buckling guides the data are distinctly different. Now, according to the R-curve concept the crack-extension resistance, R, equals the crack-extension force, G, for slow stable crack growth with a sharp crack tip. We wish to identify those points for tests MSD-1, 2, and 3, shown solid in Figure 4, that qualify as R-curve data. The data with no crack-extension represent the

original blunt notch and so do not yet represent crack growth along the R-curve. For short crack-extensions up to about 75 mm there is slow stable crack growth, while for larger crack-extensions there is unstable dynamic crack growth. Initially we do not yet know the critical point of instability that separates the stable from the unstable data for each test. We therefore used an iterative procedure and started with an initial guess for the critical crack-extension. To represent the R data by a universal R-curve, a power law was fitted to them, giving

$$R = 75.9\ da^{0.28} \tag{6}$$

where R is measured in kN/m and da in mm. With an analytic expression for the R-curve the point of instability can be found. The stability diagram in Figure 5 illustrates this for test MSD-1. A crack-extension force line or G-line is drawn and the control parameter is adjusted until the line is tangent to the R-curve when it becomes the G_c-line. For simplicity we can take for G the expression for the infinite plate with a single crack (β=1) under load or stress control

$$G = \sigma^2 \pi a/E \tag{7}$$

because for cracks under 500 mm in our panels this equation does not differ much from the correct expression below. Equation (7) gives a straight line in Figure 5. Tangency is achieved by adjusting the stress until a critical value of σ_c=146 MPa is obtained, which then gives a critical crack-extension of da_c=69.3 mm and a critical crack-extension force of G_c=249 kN/m. Hence, the data points for which 0<da<69.3 mm are stable for MSD-1 and those points were used for the curve fit in Figure 4. The same procedure was applied to the data of tests MSD-2 and 3. If it is found that the initial guess for da_c was wrong the procedure is repeated until all the fitted points lie below the points of tangency. Figure 5 shows that for da>da_c the unstable points lie closer to the G_c-line than the R-curve.

Actually the testing machine was operated under displacement control so that the displacement, δ, is the control parameter. This quantity is related to the stress by

$$\sigma = \delta/(BWC_t) \tag{8}$$

where C_t is the total compliance of the testing system, which can be decomposed into the machine, panel, and crack compliance, as follows

$$C_t = C_m + H/(EBW) + 4/(\pi EB)\ I(\pi a/W) \tag{9}$$

where H (150 in) is the panel height and

$$I(x) = \int x\beta(x)dx \tag{10}$$

The total compliance was found for each test from the slope of the measured total displacement versus load curve. Using the slope before any crack extension occurred, Equation (9) was used to deduce the machine compliance. The average for the first three tests was $C_m = 1.082 \times 10^{-5}$ m/kN (± 4%). The complete expression for the G-line under displacement control is then given by combining Equations (3), (8), and (9) into

$$G(a) = E\delta^2 \pi a \, \beta^2(\pi a/W) \; / \; [EBWC_m + H + 4W/\pi \; I(\pi a/W)]^2 \qquad (11)$$

To find the critical point of instability, as was done in Figure 5, the displacement is adjusted in this equation until tangency to the R-curve is achieved. In this way critical values are found for the displacement, δ_c, crack-extension, da_c, and crack-extension force, G_c. The critical stress, σ_c, is found by Equation (8) or (3), the load, P_c, by Equation (5), and the toughness, K_c, by Equation (1). The results for the first three tests are summarized in Table 2. This table also includes measured values and results from the residual strength diagram discussed in the next section. There is good agreement.

RESIDUAL STRENGTH DIAGRAM

The residual strength diagram is used in an engineering approach to determine how the residual strength of a structure depends on the crack geometry and the specimen size. It is shown schematically for a center cracked sheet structure in Figure 6. The dotted line represents the residual strength assuming linear elastic fracture mechanics for an infinite sheet. The straight line shows the residual strength assuming net section collapse of a sheet of width W. For small and large crack sizes, near the intersections of these two curves there is a region of transition from one failure mode to the other. Feddersen [4] argued that two linear tangents to the idealized K curve can be used to establish a smooth and continuous curve for the residual strength. One tangent to the K curve is drawn from the point $\sigma=\sigma_Y$, where σ_Y is the stress at which the structure without crack collapses. The other tangent is drawn from the point 2a=W that represents the width of the structure. The fracture toughness is customarily determined from the crack size at the failure stress by Equation (2). However, in thin sheets where crack extension occurs before failure, the final crack size is generally not known. Therefore the data points plotted in the residual strength diagram usually are the initial crack size and the final failure stress, i.e. the crack extension and plasticity are ignored. To compensate for this inconsistency, an effective value of the toughness is used, denoted by K_e, which is lower than the true toughness, such as that obtained e.g. by the R-

curve. A slight improvement to the analysis can also be made by taking the finite width of the panel into account, i.e. by using

$$K_e = \sigma_c[\pi a_i \sec(\pi a_i/W)]^{1/2} \quad (12)$$

In this way a value of K_e=111 MPa$\sqrt{m}$ was obtained as the average of the first three tests. Application of the residual strength diagram to the first three tests is shown in Figure 7. The predicted fracture paths are shown and the measured data points are plotted as solid circles. The results for all three tests fall in the fracture mechanics region of the diagram. They are summarized in Table 2. There is good agreement between the measured data, the predictions from the R-curve and the residual strength diagram for these single crack specimens.

THE LINK-UP CRITERION

For the panels with multiple site damage (MSD) we have used the analysis of Broek [1]. Here we have a situation where small cracks exist ahead of the large central crack. The first link-up is governed by the stress-intensity factor of the combination of the main crack and the first MSD crack. The geometry factors of the two cracks must therefore be compounded by the effect of crack interaction. As the ligament undoubtedly will fail by plastic collapse or net section yield, the compounded stress intensity factor can be used to calculate the plastic zone of both cracks and used with the criterion that link-up occurs when the two plastic zones meet. Broek found that the best estimate of the plastic zone size for this application was given by the Irwin expression

$$r_p = (K/\sigma_Y)^2/2\pi \quad (13)$$

where σ_Y is the collapse strength. This expression represents the plastic zone at the tip of the main crack and a similar expression holds for the plastic zone at the MSD crack. Here the stress-intensity factor is still given by Equation (2), but with the MSD crack nearby the function β that takes the crack interaction into account is much more complicated than Equation (4). To model the first link-up Broek assumed that the main interaction was between one tip of the central crack and the first MSD crack in front of it, ignoring all the other MSD cracks. Thus β will depend on the central crack size, a, the MSD crack size, a_{MSD}, and the ligament L between them, Figure 2, so that Equation (2) becomes

$$K = \beta(a, a_{MSD}, L)\ \sigma\sqrt{(\pi a)} \quad (14)$$

A similar expression holds for the stress-intensity factor to use in the plastic zone at the MSD crack. For these β functions Broek has derived approximations based on published expressions for the stress intensity factors of two unequal length collinear cracks, which we have used. The link-up criterion between the central and first MSD crack now is

$$r_p + r_{pMSD} = L \tag{15}$$

or, from Equations (13) and (14)

$$\sigma = \sigma_Y[2L/(a\beta^2 + a_{MSD}\beta_{MSD}^2)]^{1/2} \tag{16}$$

For test MSD-4 this expression is plotted as the first dashed curve in Figure 8. Though it is not shown explicitly in Equation (16) this curve represents the final failure stress as a function of initial crack size, in the same sense as was discussed for Equation (12). The x-axis in Figure 8 represents the central crack size, a. For the curves that are plotted the MSD crack size, a_{MSD}, and the position of the MSD crack, d_{MSD}, are kept constant. However, as may be clear from Figure 2, the ligament L varies with a. For the central crack with size a=177.8 mm, Equation (16) predicts the first link-up at σ=81 MPa. This is shown by the intersection of the fracture path line with the first dashed curve in Figure 8. After the first link-up the central crack has absorbed the first MSD crack and it is assumed that we now have a larger central crack, a=195.58 mm, that interacts with the second MSD crack. Equation (16) is again used with these new parameters and plotted as the second dashed curve in Figure 8. The predicted stress for the second link-up then is σ=117 MPa. This procedure is then repeated for the third link-up and we find σ=111 MPa at a=220.98 mm. Since this stress is lower than for the second link-up, we conclude that the panel is super-critical and the fracture will run straight through after absorbing the second MSD crack at 117 MPa, as shown by the fracture path in Figure 8. When all three MSD cracks have been absorbed by the central crack, it behaves as a large single crack of size a=246.38 mm in the panel. Failure is then predicted by the simpler Equation (12), as also shown in Figure 8. The results of this analysis for tests MSD-4, 5, and 7 are summarized in Table 3 and compared with the measured values.

R-CURVE AND MSD

We now apply the R-curve to the failure prediction of a panel with MSD cracks. We assume that an R-curve emanates from each MSD crack as well as the main central crack, as shown by the solid lines in Figure 9. Each R-curve is given by Equation (6).

We then draw G_c-lines tangent to each R-curve to determine the link-ups and final instability. The G-lines are still given by an expression similar to Equation (3), but now the β function for the central crack must also take the interaction with the MSD crack into account

$$G(a) = (\sigma^2 \pi a/E)\beta^2(a, a_{MSD}, L) \quad (17)$$

For a given stress this equation gives the G-line under load control. Using the appropriate parameters, the stress was adjusted until tangency was achieved for each of the R-curves, as shown by the dashed lines in Figure 9. The final fracture at 246.3 mm uses the same procedure as discussed before. With the MSD cracks the G-lines have quite a bit of curvature just before the instability point. The link-up stress for the third MSD crack is less than for the second. This indicates that, after link-up of the second MSD crack, the panel is super-critical and the fracture will run straight through after absorbing the second MSD crack. The results for tests MSD-4, 5, and 7 are summarized in Table 3. There is good agreement with the measured values and also with the results predicted from the plastic zone model. However, for MSD-5 and 7 the prediction from both the R-curve and the plastic zone model is that the final fracture will occur with the second and third link-up, whereas actually the load had to be raised from 375 to 407 kN for MSD-5 and from 205 to 214 kN for MSD-7 after the second and third link-ups for the final fracture.

CONCLUSION

Analysis appears to provide good predictions of the residual strength, link-ups, and fracture of panels with multiple site damage (MSD) of different size and spacing. The critical fracture stress can be predicted by using either the plastic zone criterion or the R-curve, and the results are virtually the same. Several improvements to the analysis are being considered. Notwithstanding the large widths of the panels the MSD cracks are quite small and closely spaced so that small discrepancies in these dimensions may affect the results. Therefore more accurate measurements of the MSD configurations are currently being made under a microscope. The plastic zone analysis uses guestimates for the effective fracture toughness, K_e, and the collapse strength, σ_y. The values of these two quantities can be optimized when the data from all the tests are in. In the R-curve analysis load control was used and the backward growth of the MSD crack was ignored. Improvements in this analysis are quite complex, but we think possible. Displacement control would allow the load to drop as in fact it did in MSD-5 and 7.

REFERENCES

1. Broek, D., "The effects of multi-site damage on the arrest capability of aircraft fuselage structures," FractuREsearch TR 9302, June 1993

2. Broek, D.: Elementary Engineering Fracture Mechanics. Martinus Nijhoff Publishers, 1987

3. Feddersen, C. E.: "Discussion," Plane Strain Crack Toughness Testing of High Strength Metallic Materials, ASTM STP 410, by William F. Brown, Jr., and John E. Srawley, American Society for Testing and Materials, Philadelphia, 1966, p. 77

4. Feddersen, C. E.: "Evaluation and prediction of the residual strength of center cracked tension panels," ASTM STP 486, American Society for Testing and Materials, Philadelphia, 1971, pp. 50-78

Table 1. Planned Test Matrix for 90 MSD Program

Test No	Main crack		MSD cracks				Date of test
	2a (mm)	a (mm)	d_{MSD} (mm)	s_{MSD} (mm)	$2a_{MSD}$ (mm)	number per side	
MSD-1	355.6	177.8				0	7/23/93
MSD-2	203.2	101.6				0	8/25/93
MSD-3	508.0	254.0				0	9/13/93
MSD-4	355.6	177.8	190.5	25.4	10.16	3	11/29/93
MSD-5	142.24	71.12	88.9	38.1	15.24	3	12/1/93
MSD-6[A]	508.0	254.0	(no anti-buckling guides)				4/12/94
MSD-7	508.0	254.0	266.7	38.1	12.7	5	4/20/94
MSD-8[B]	355.6	177.8	190.5	25.4	10.16	3	
MSD-9	482.6	241.3	266.7	38.1	12.7	10	
MSD-10	254.0	127.0	165.1	25.4	10.16	10	
MSD-11	(to be defined)						
MSD-12	(to be defined)						

[A] This test was recommended by NASA Langley
[B] This test is a repeat of MSD-4

Table 2. Measured Data and Failure Predictions for the First Three 90 MSD Tests

	Half-Crack Size			Stress (MPa)	Load (kN)	Displacement (mm)	
	Initial (mm)	Final (mm)	Extension (mm)				Date
MSD-2							8/25/93
Measured	101.6			184	428	16.1	
RSD		142	40.4	196	454		
R-curve		141.1	39.5	183	424	14.5	
MSD-1							7/23/93
Measured	177.8			148	343	12.6	
RSD		244.3	66.5	146	340		
R-curve		247.1	69.3	146	340	11.9	
MSD-3							9/13/93
Measured	254.0			124	289	12.2	
RSD		340.4	86.4	121	280		
R-curve		353.1	99.1	125	289	10.5	

Table 3. Link-up and Failure Predictions from the Residual Strength Diagram and the R-curve for tests 90 MSD-4, 5, and 7

	Link-up 1		Link-up 2		Link-up 3		Fracture	
	Load (kN)	Stress (MPa)	Load (kN)	Stress (MPa)	Load (kN)	Stress (MPa)	Load (kN)	Stress (MPa)
MSD-4								
Measured	196	84	227	98	227	98	307	132
RSD	188	81	272	117	(258)	(111)	285	123
R-curve	240	103	274	118	(258)	(111)	294	126
MSD-5								
Measured	320	138	375	161	375	161	407	174
RSD	329	142	445	191	(392)	(169)	(346)	(149)
R-curve	388	167	403	174	(347)	(149)	(344)	(148)
MSD-7								
Measured	133	57	205	88	205	88	214	92
RSD	134	57.8	268	116	(249)	(107)	(204)	(88)
R-curve	183	78.9	255	110	(239)	(103)	(213)	(92)

The numbers in parentheses are lower than for a previous link-up, thus failure will precede the link-up

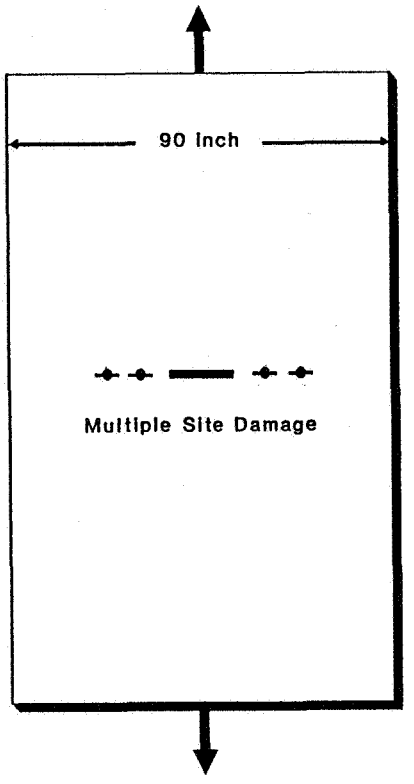

Figure 1. Typical 90 MSD test panel

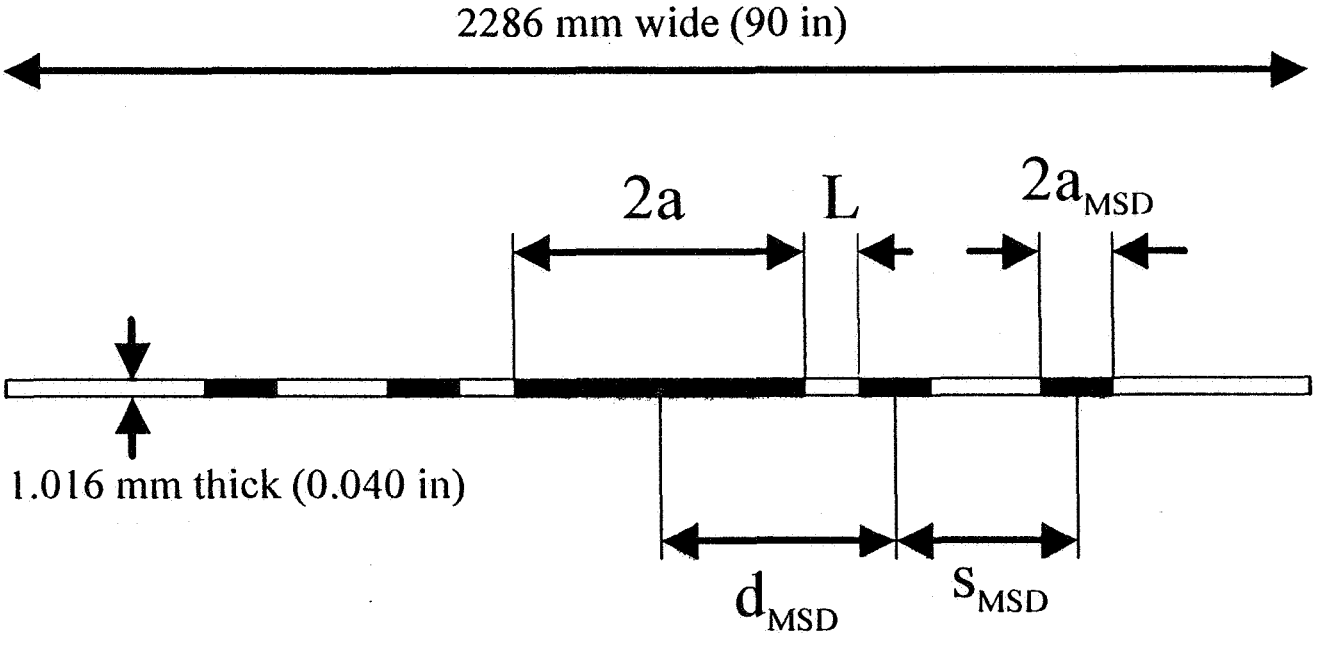

Figure 2. Definitions of 90 MSD crack configurations and dimensions

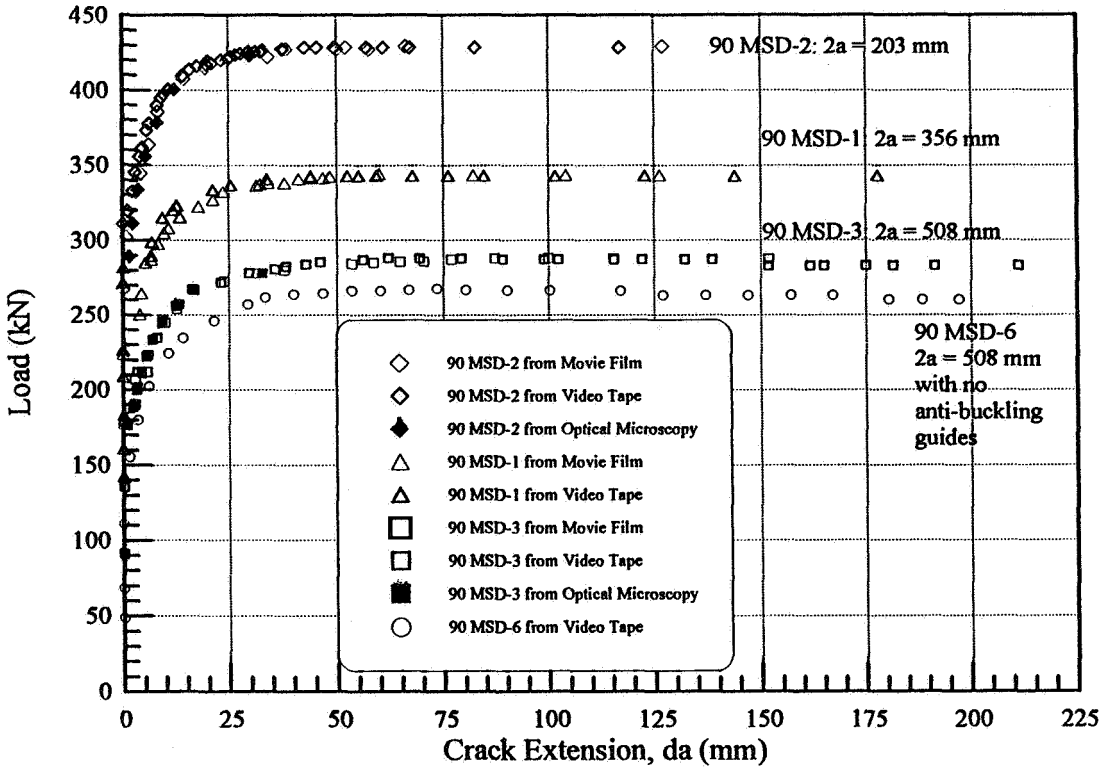

Figure 3. Crack growth measurements for tests 90 MSD-1, 2, 3 and 6

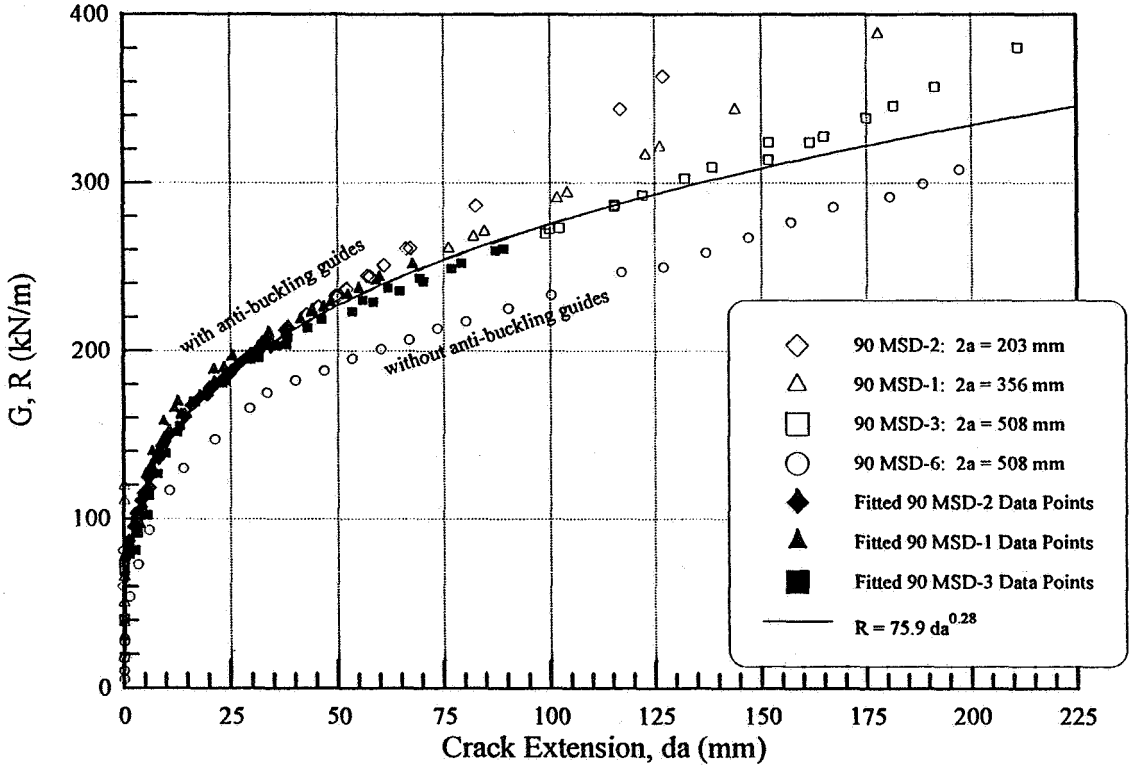

Figure 4. Crack-extension force data and analytic R-curve for 90 MSD tests

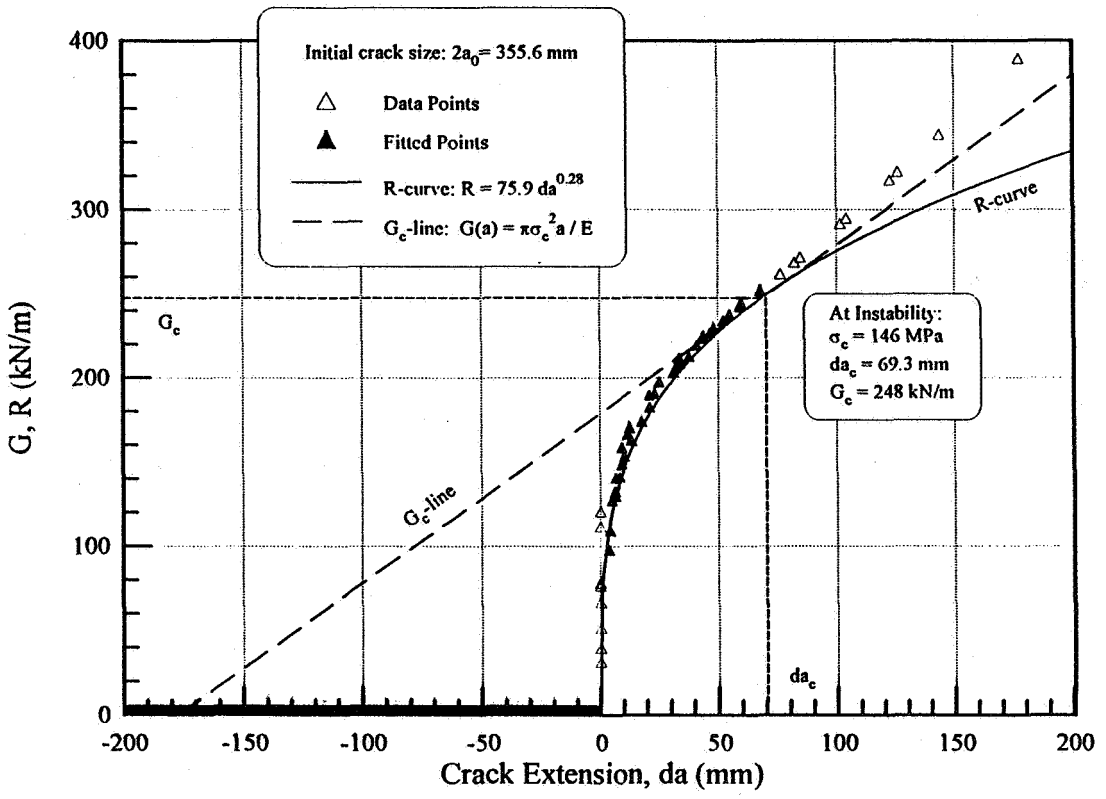

Figure 5. Stability diagram for test 90 MSD-1

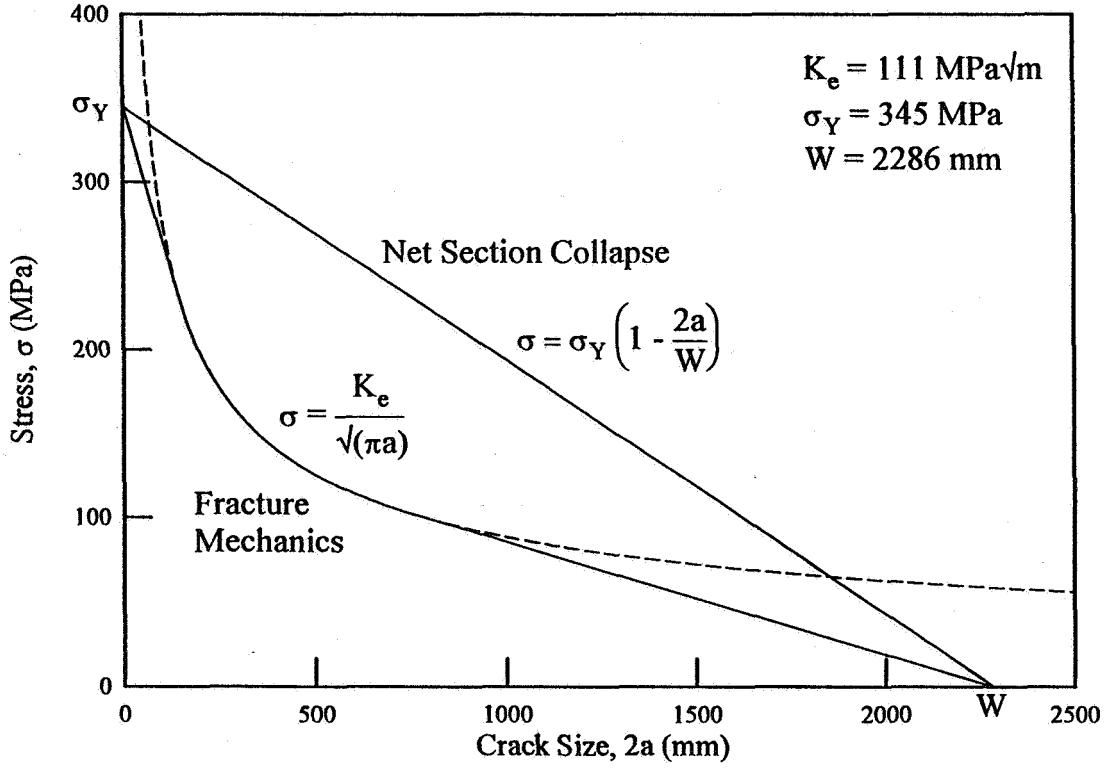

Figure 6. Residual strength diagram with analysis of Feddersen

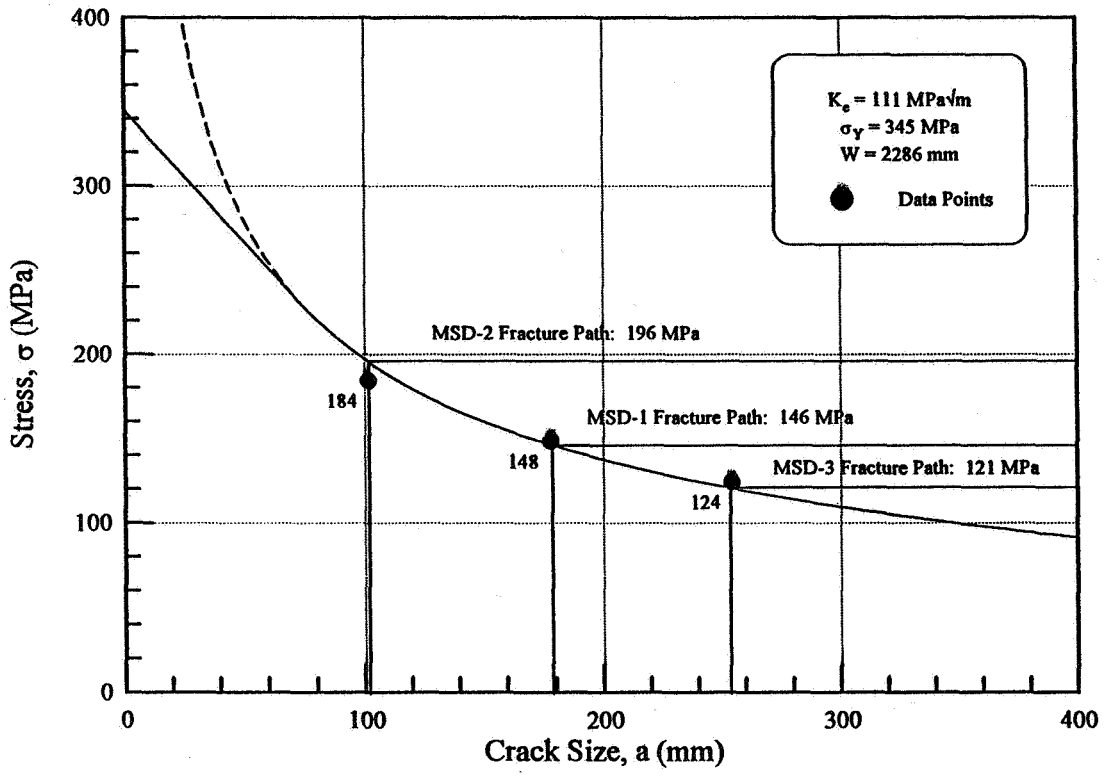

Figure 7. Residual strength for tests MSD-1,2, and 3 with measured data points and predicted fracture paths

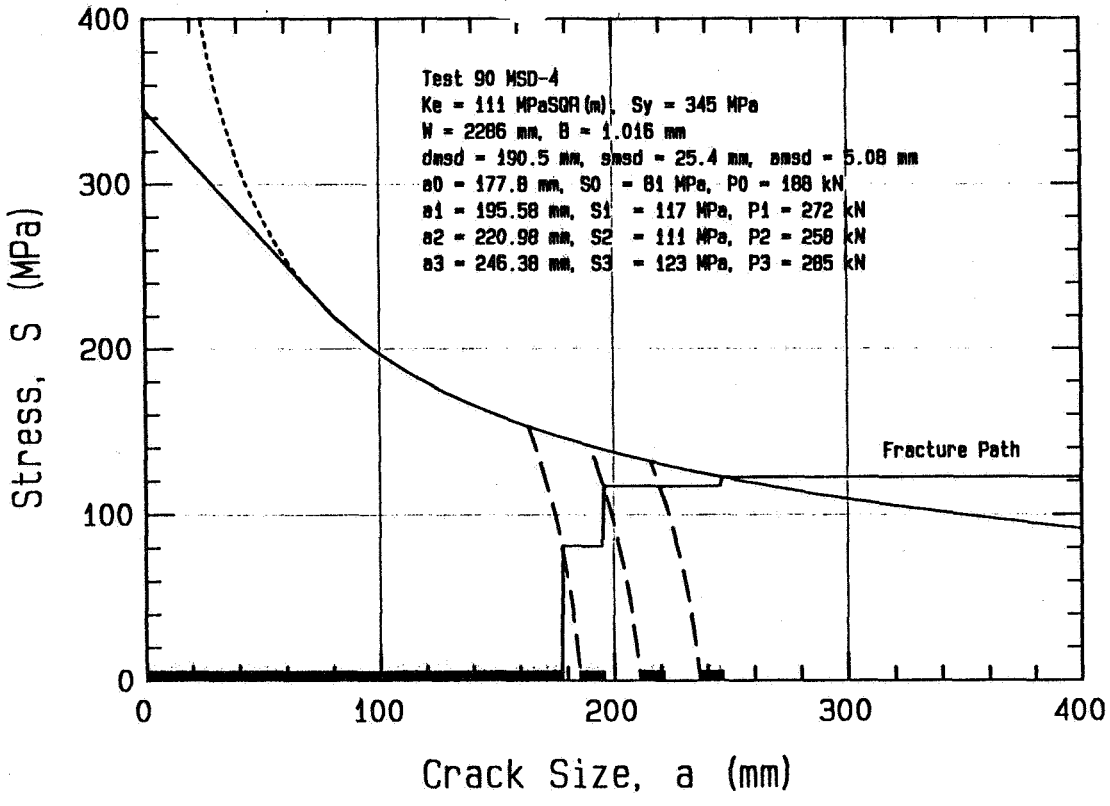

Figure 8. Residual strength diagram for test MSD-4 with plastic zone criteria and predicted fracture path

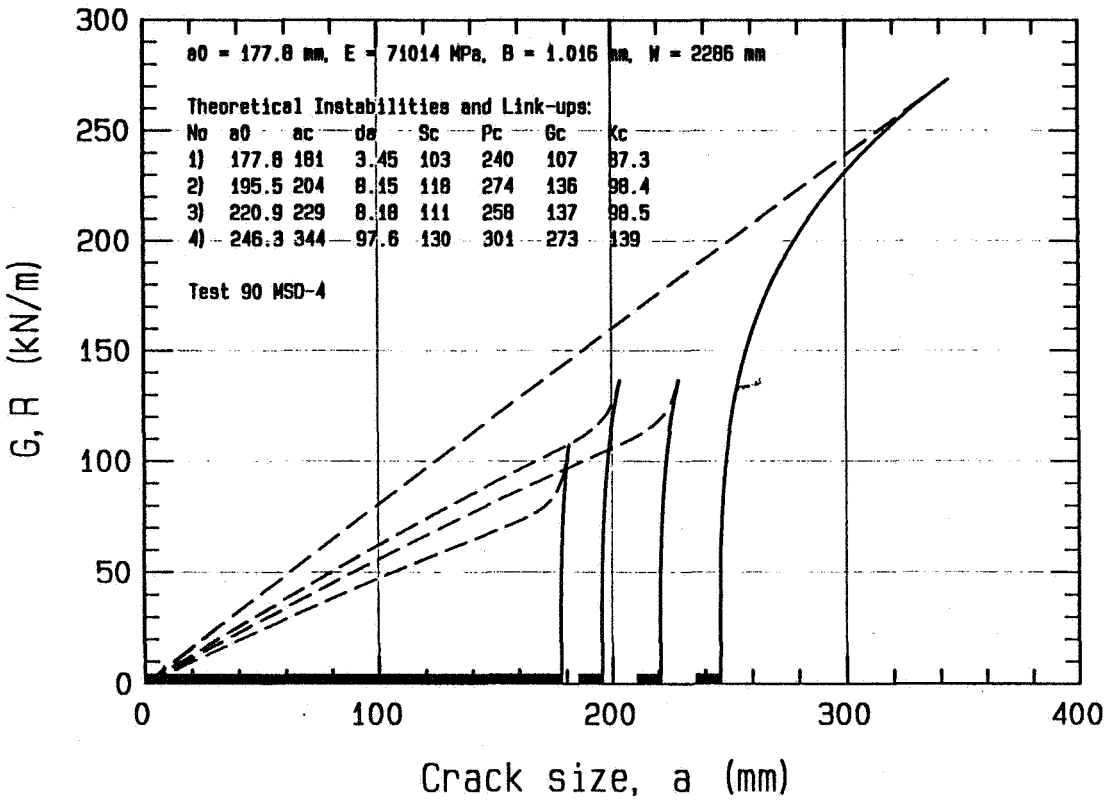

Figure 9. Stability diagram for test 90 MSD-4

FATIGUE AND RESIDUAL STRENGTH INVESTIGATION OF ARALL®-3 AND GLARE®-2 PANELS WITH BONDED STRINGERS

Ming Wu, Dale A. Wilson
Tennessee Technological University
Cookeville, TN

S.V. Reddy
Textron Aerostructures
Nashville, TN

SUMMARY

Stiffened panels were fabricated from ARALL-3 and GLARE-2 laminates for the purpose of providing improved structural performance of lower wing panels for aircraft. To verify the designs fatigue crack growth and residual strength tests were conducted and compared to those for conventional monolithic aluminum panels.

INTRODUCTION

The development of a new aircraft is significantly influenced by the introduction of new structural materials. The driving force behind such development is the everlasting incentive to reduce aircraft operating costs. Future operating costs will incur even greater fuel and maintenance costs, making it cost effective for aircraft structures to be designed with new materials to obtain a lower weight and to require less maintenance. Maintenance is directly related to durability and damage tolerance. ARALL (Aramid Fiber Aluminum Laminate) and GLARE (Glass Fiber Aluminum Laminate) laminates, illustrated in Figure 1, were designed to combine the high static strength of fibers with good crack growth resistance and impact tolerance of aluminum alloys. The excellent fatigue strength of the laminates is unique due to the bridging effect of the crack tip fibers in the prepreg layer of the laminates.

ARALL and GLARE laminates were originally developed by Delft University. They incorporate adhesively bonded laminates which are built up as laminated sheet materials with thin high strength aluminum alloy sheets and strong unidirectional or woven aramid or glass fibers, impregnated with a thermoset or thermoplastic resin followed by (if desired) post-stretch of the material after curing, which results in a compressive residual stress in the metal sheets. ARALL and GLARE laminates are a new family of structural composite materials. The final properties are highly dependent on the variables of the material. They can be tailored for many different applications by varying fiber-resin systems, aluminum alloys, sheet gauges, stacking sequences, fiber orientations (such as uniaxial and cross-ply), surface preparation techniques, and by the degree of post-cure stretching and rolling. Several ARALL and GLARE laminates are listed in Table 1.

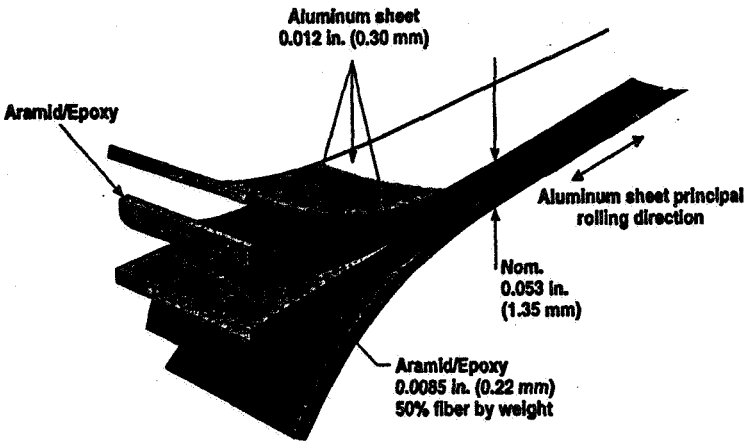

Figure 1: 3/2 ARALL-1 Laminate Layup.

Table 1: ARALL and GLARE Laminates [1]

Laminates	Alloy	Composition	Orientation	Post stretched
ARALL-1	7075-T6	Aramid/epoxy	U.D.*	None
ARALL-2	2024-T3	Aramid/epoxy	U.D.	None
ARALL-3	7475-T76	Aramid/epoxy	U.D.	0.4%
ARALL-4	2024-T8	Aramid/epoxy	U.D.	None
GLARE-1	7075-T6	Glass/epoxy	U.D.	0.4%
GLARE-2	2024-T3	Glass/epoxy	U.D.	None
GLARE-3	2024-T3	Glass/epoxy	Cross ply (50/50)	None
GLARE-4	2024-T3	Glass/epoxy	Cross ply (70/30)	None

* U.D. stands for unidirectional.

Developing a new aircraft structure is a complicated and lengthy process due to the high safety requirements of the airplane. Every aspect of the new material must be fully tested and analyzed. Fatigue and residual strength are two of the most important aspects of damage tolerance evaluation of the material. The primary objectives of this investigation were to build the stiffened center notched panel specimens using ARALL and GLARE laminates based on the existing lower wing cover design, conduct fatigue crack growth tests under constant amplitude loading, conduct residual tension strength tests, and compare the test results with those from the conventional 2024 aluminum structures.

SPECIMEN DESIGN AND EXPERIMENTAL PROCEDURES

Test Specimens

Two stiffened test panels (one of ARALL-3 and one of GLARE-2) were designed based on a 2024-T351 panel that was tested during Gulfstream Aerospace's G-IV wing program. The panels were fabricated at Textron Aerostructures. The original ARALL-3 and GLARE-2 sheets were manufactured by Structural Laminates Company of ALCOA. The cross-sectional area of the panel was kept the same to enable a direct comparison of these two different types of materials. The panels were 28.0 inches wide and 75.9 inches long with three Z-shaped stringers and two simulated beam caps bonded to the composite skins. A sketch of the fatigue panel is shown in Figure 2 (The crack size shown in the Figure is not the actual size). The skin pads were used between the stringers and the panels. The 1.4 inch initial crack, $2a$, was induced by sawcut. The sawcut was through the middle stringer and skin. The cut plane was perpendicular to the skin surface within $\pm 2^o$ (Figure 3).

Z-shaped stringers, made of 7075-T6511 aluminum extrusions, were bonded to ARALL and GLARE panels with AF163 film adhesive. The ARALL-3 and GLARE-2 panels (anodized at Structural Laminates Company) were primed with corrosion inhibiting primer and then dried in oven at 250^oF. The stringers were first anodized and primed like the panels. The stringers and panels were then vacuum bagged and cured in an autoclave with 40 *psi* pressure at 250^oF for 90 minutes to achieve the optimum bonding. The material properties used in this investigation are tabulated in Table 2 [2].

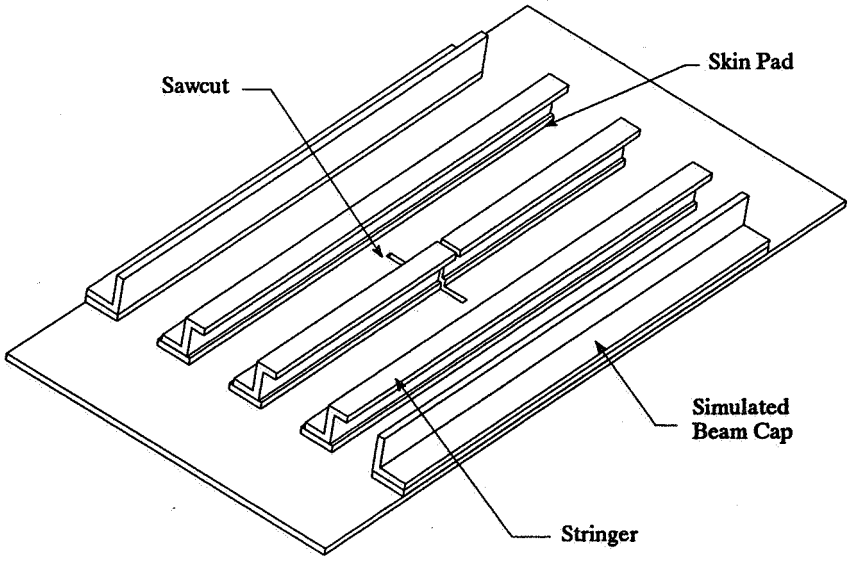

Figure 2: Design of Stiffened Center Notched Laminate Panel.

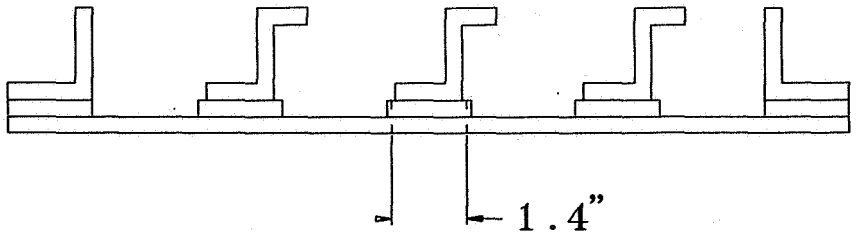

Figure 3: Sawcut Location and Size for Fatigue Tests.

Test System and Experimental Procedures

The testing of these two panels was conducted at Alcoa Technical Center. An MTS servo-hydraulic testing machine with 250 *kips* dynamic loading and 400 *kips* static loading capacity was used to apply the cyclic and static tension load to the panels. The test system is shown in Figure 4.

The test panel was first mounted on the testing machine with upper and lower ends clamped by the gripping fixture as shown in Figure 4. A constant amplitude load spectrum of 10.0 *kips* to 47.3 *kips* was applied to both test panels for 85000 cycles at 5 Hz frequency. The crack length measurements were recorded every 5000 cycles with optical magnifying device.

The cracks were sawcut to 9.73 inches (dimension between first pair of out stringers) after 85000 cycles of fatigue crack growth tests (Figure 5). This crack length was to be the initial crack extension for the residual strength tests. Since the fatigue crack growth for the ARALL-3 and GLARE-2 stiffened panels was much lower than that for the 2024 stiffened panel due to the excellent fatigue resistance of these fiber/metal laminates, sawcut was introduced to extend the initial crack to the same length as for the 2024 stiffened panel. Both ARALL-3 and GLARE-2 test panels were then loaded till fracture in the same testing machine.

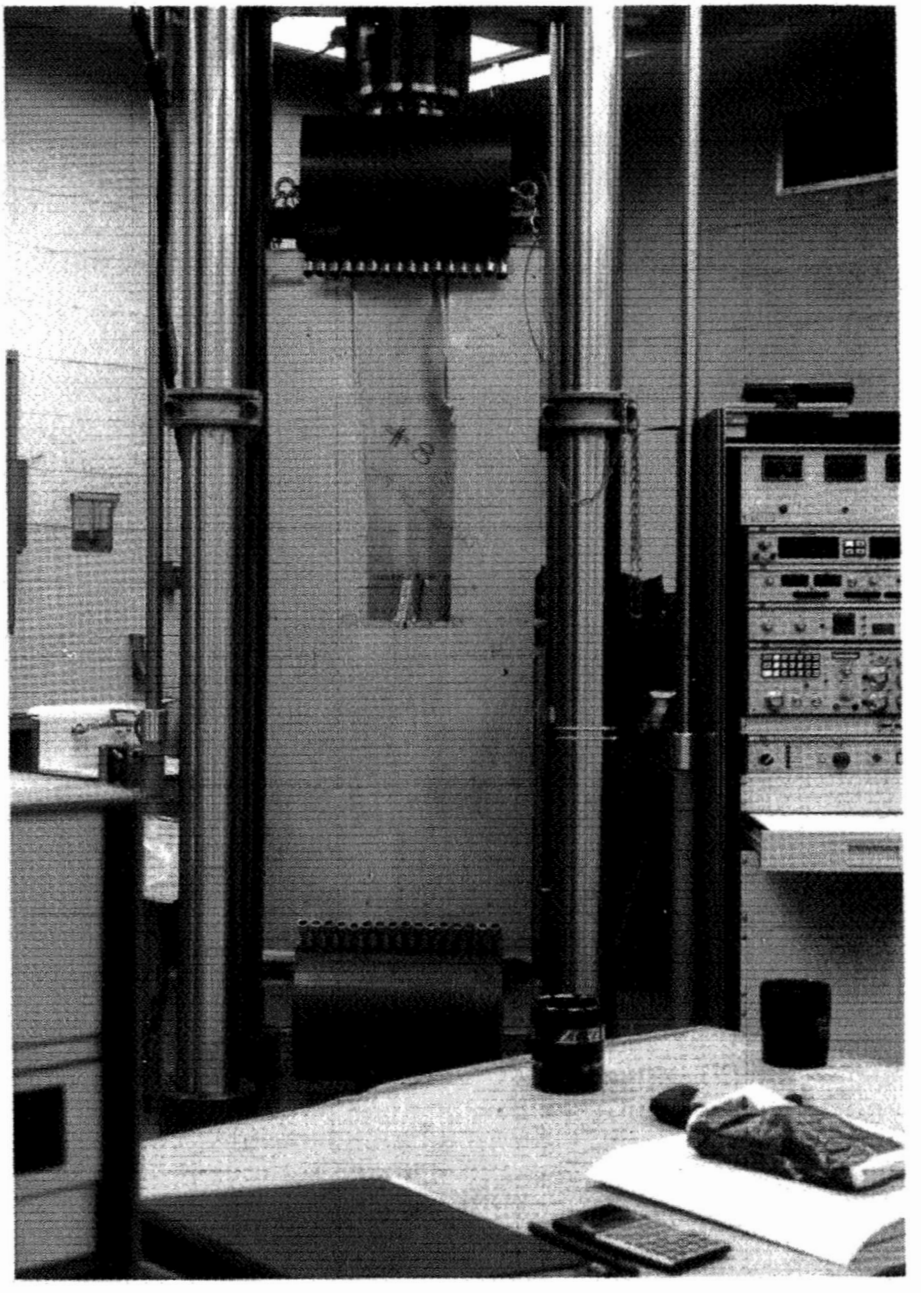

Figure 4: Test System Set-Up.

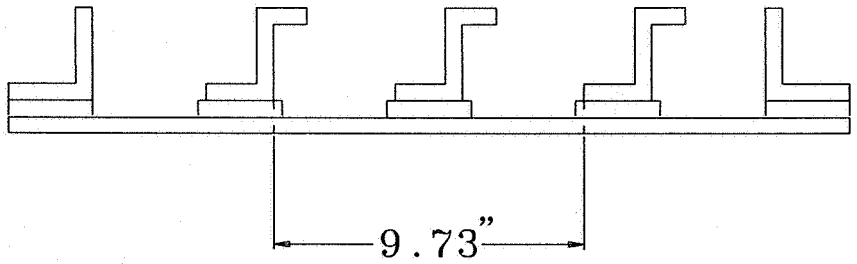

Figure 5: Sawcut Location and Size for Residual Strength Tests.

Table 2: Mechanical Properties of Materials

		STRINGER	UPPER SKIN		LOWER SKIN		
		7075 T6511 extr QQ-A-200/11 0.750"-1.490"	7075 T7351 plate QQ-A-250/12 0.500"-1.000"	2090 T83 sheet AMS 4251 0.126"-0.249"	2024 T351 plate QQ-A-250/4 0.500"-1.000"	ARALL-3 5/4 sheet AMS 4302A 0.094"	GLARE-2 4/3(5/4) sheet 0.078"(0.100")
F_{tu}, ksi	L	94.7	70	84.8	65	123.9	173.3
F_{ty}, ksi	L	84.7	59	79.2	50	89.7	56.1
F_{cy}, ksi	L	87.7	58	71.3	41	47	59.1
F_{su}, ksi		49	39	41.9	38	34.2	-
F_{bru}, ksi e/D=1.5 e/D=2.0		 122 152	 106 136	 100 126	 98 120	 82 84	 - 103
E_t, msi	L	10.4	10.3	11.3	10.7	9.2	9.4
E_c, msi	L	10.7	10.6	10.6	10.9	9.2	9.4
G, msi		4	3.9	-	4	2.3	-
μ		0.33	0.33	-	0.33	0.35	-
n		26	20	20	9	5.8	-
w, lb/in^3		0.101	0.101	0.093	0.1	0.081	0.09
t, in		-	-	-	-	0.094	0.078(0.100)
cost, \$/lb		2.5	4	15	3	58	56

TEST RESULTS AND DISCUSSIONS

The fatigue crack growth tests for both stiffened center notched ARALL-3 and GLARE-2 panels show considerable reduction of crack growth rate compared to 2024 aluminum stiffened panels. The test results are tabulated in Table 3. For ARALL-3 panel, $P_{max} = 51$ *kips*, $P_{min} = 11$ *kips*, and frequency = 7 *Hz*. For GLARE-2 panel, $P_{max} = 48$ *kips*, $P_{min} = 10$ *kips*, and frequency = 5 *Hz*. The comparison of fatigue crack growth curves between stiffened ARALL-3 and GLARE-2 laminated panels and stiffened 2024 aluminum panel is shown in Figure 6.

Table 3: Fatigue Crack Growth Test Results for ARALL-3 and GLARE-2 Stiffened Panels

	ARALL-3		GLARE-2	
No. of Cycles	a, left	a, right	a, left	a, right
0	0.70	0.70	0.70	0.70
5000	0.73	0.72	0.78	0.74
10000	0.75	0.74	0.84	0.79
15000	0.76	0.75	0.87	0.82
20000	0.78	0.76	0.90	0.83
25000	0.79	0.76	0.92	0.84
30000	0.80	0.78	0.95	0.86
35000	0.81	0.78	0.97	0.88
40000	0.82	0.78	0.99	0.89
45000	0.83	0.79	1.01	0.90
50000	0.84	0.80	1.02	0.91
55000	0.84	0.80	1.04	0.92
60000	0.84	0.81	1.06	0.92
65000	0.85	0.82	1.07	0.94
70000	0.86	0.82	1.08	0.94
75000	0.87	0.82	1.09	0.94
80000	0.87	0.82	1.10	0.96
85000	0.88	0.83	1.11	0.96

The higher fatigue crack growth resistance of ARALL-3 and GLARE-2 laminate panels is due to the bridging mechanism of fibers at the crack tips which prevents the crack from further opening. The cyclic crack closing fiber stresses, due to crack bridging, are partly transferred into the aluminum across the adhesive. This causes delamination in the adhesive behind the crack tip due to cyclic shear loading of the adhesive interface between the fibers and the aluminum sheets. If this delamination is assumed to be absent and the adhesive exhibits an infinite shear modulus, the crack bridging of the fibers will be perfect. The crack can not open. Consequently the stress intensity factor at the crack tip is zero,

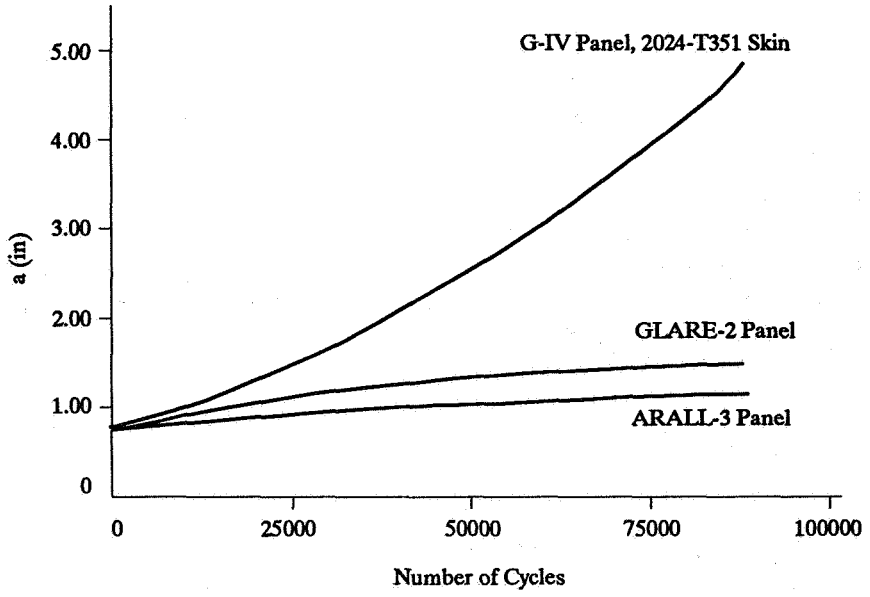

Figure 6: Crack Extensions vs Number of Cycles.

and the fatigue crack growth will not occur. The load transmission "through" the crack occurs by the fibers only. Due to the stress concentration caused by the notch, the fiber loads will become high, especially at the end of the starter notch. This could cause fiber failure, which implies a complete loss of crack bridging effect. Therefore, a perfectly stiff adhesive between the layers and a zero delamination are not an optimum condition for the ARALL and GLARE laminates. In reality, there is some adhesive shear deformation which allows some crack opening. Further, some delamination will occur around the crack, especially at locations where the fiber stresses are high. As a consequence, a redistribution of the fiber stresses along the crack occurs. Because the redistribution of the fiber stress along the crack implies a much lower peak load value at the notch root, fiber failure behind the crack tip can be avoided. However, the amount of adhesive shear deformation and delamination should remain within certain limits. Otherwise, the crack bridging efficiency would become too small. Fortunately, for ARALL and GLARE laminates, these aspects are not critical.

The crack growth rates of ARALL-3 and GLARE-2 panels decreased with increasing crack length as demonstrated in Figure 6. This is due to the increasing amount of crack bridging fibers with increasing crack length.

The residual strength test of both ARALL-3 and GLARE-2 stiffened panels demonstrated an increase of strength over 2024 aluminum stiffened panel with the same initial crack size (9.73 inches) as shown in Figure 7. This is due to the high tensile strength aramid or glass fibers in these laminates. Buckling and bending were observed during the residual strength tests. The buckling was caused by compressive stress in the direction perpendicular to the loading direction and the bending was due to the off-centroid loading

of the panels. Severe buckling around the initial crack was the reason that shearing occurred at the crack tip. The gripping fixture used for these tests was smaller than the panel width. This was the other reason that caused the shearing, which could have affected the true strength results of these laminate panels. The failed ARALL-3 and GLARE-2 panels are shown in Figures 8 to 11.

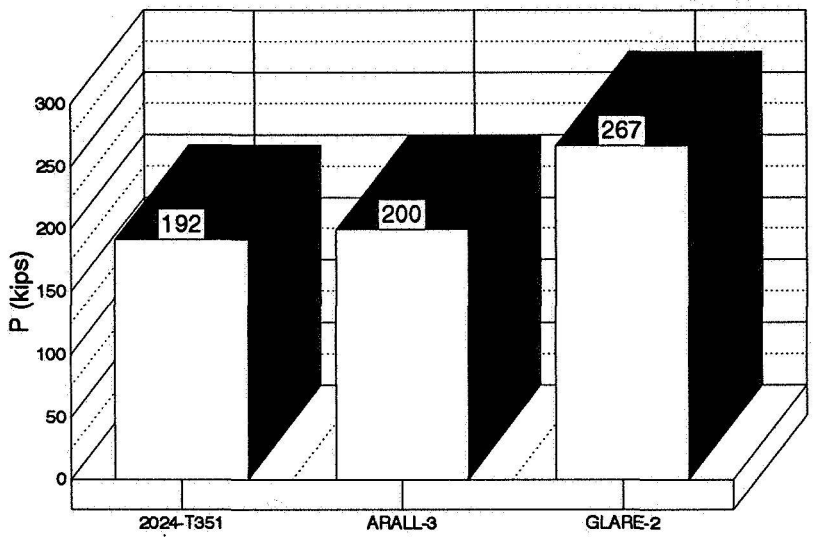

Figure 7: Residual Strength Test Results for a 9.73 in. Initial Crack Length.

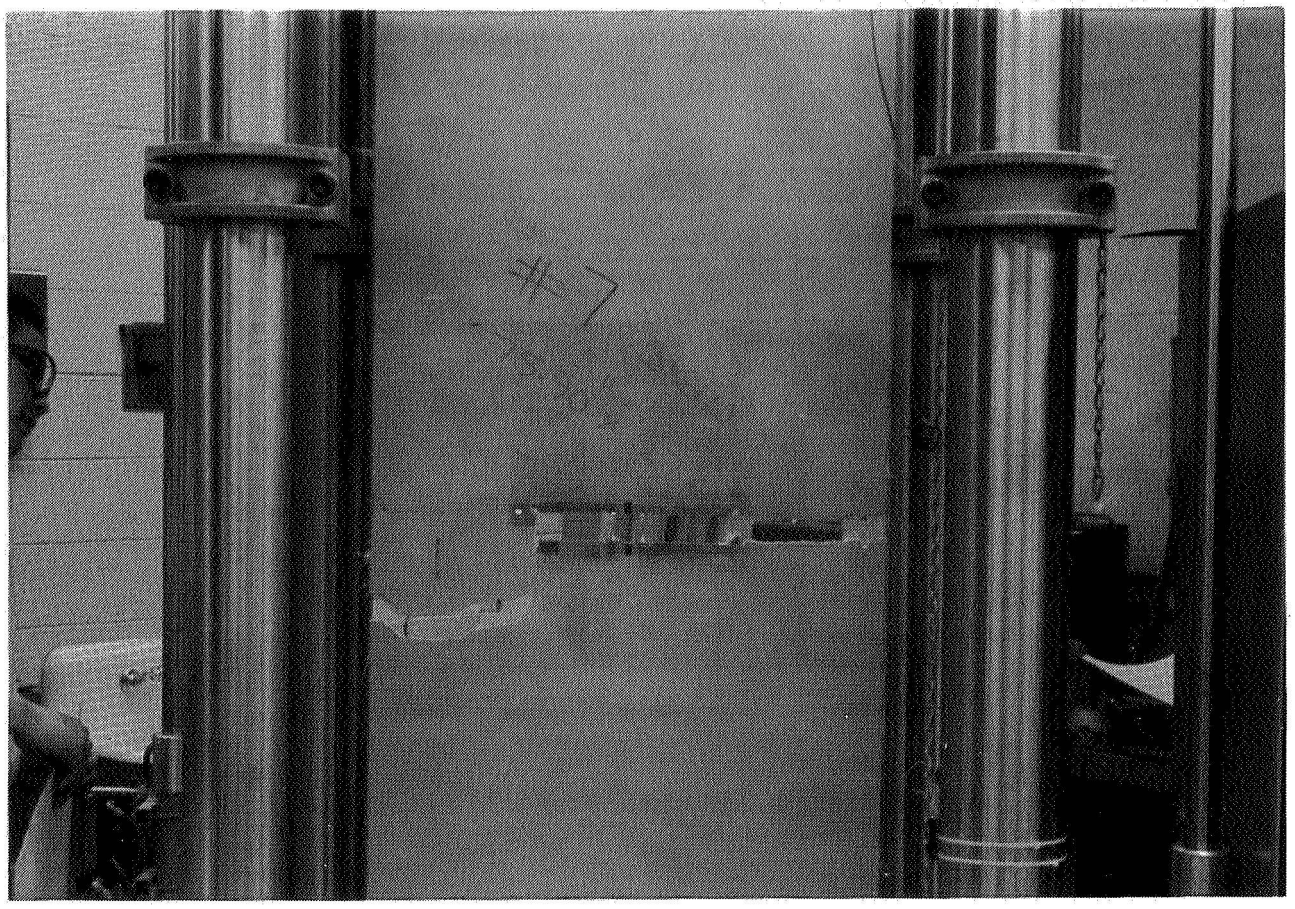

Figure 8: Skin Side of Failed ARALL-3 Stiffened Panel.

Figure 9: Stringer Side of Failed ARALL-3 Stiffened Panel.

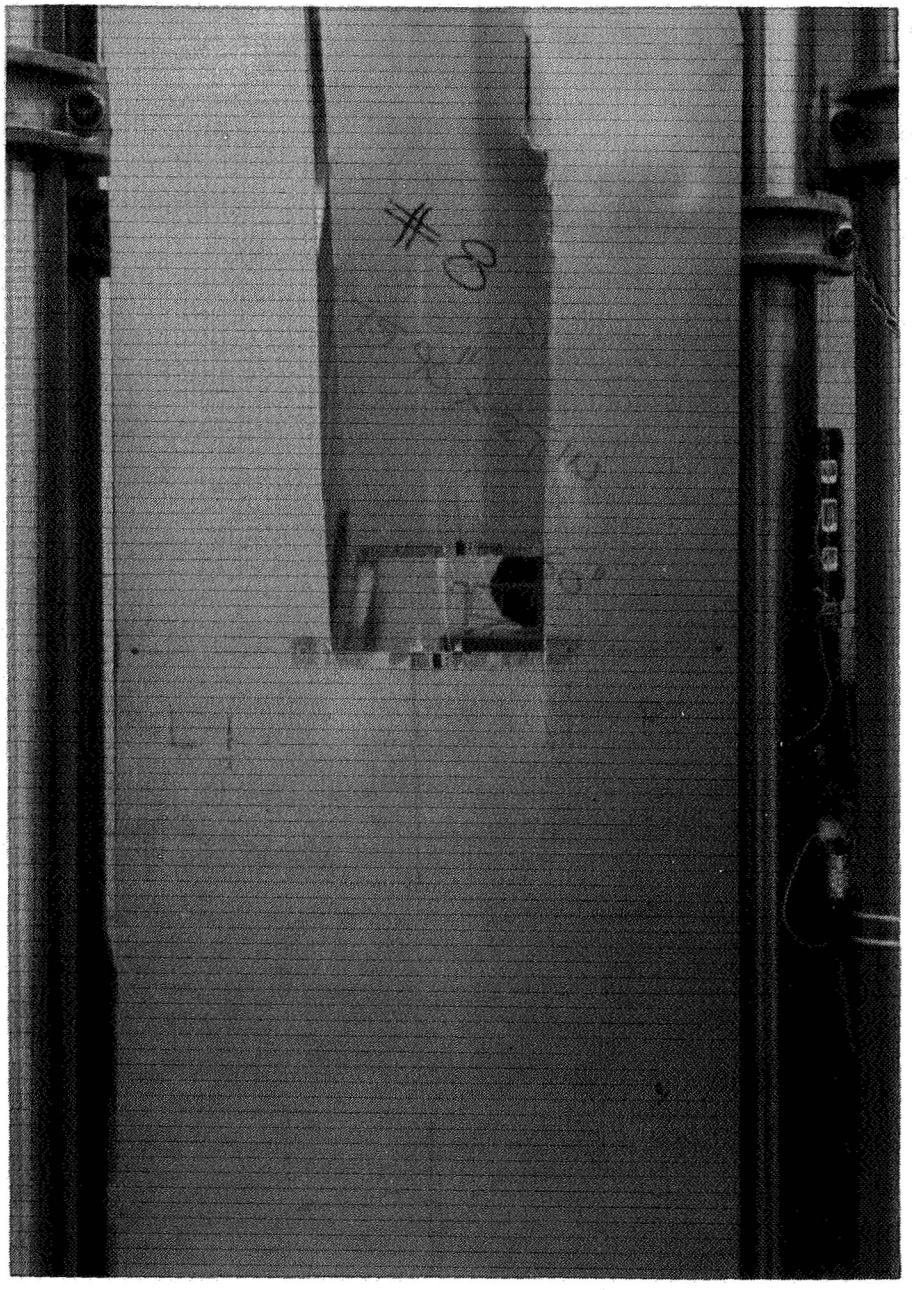

Figure 10: Skin Side of Failed GLARE-2 Stiffened Panel.

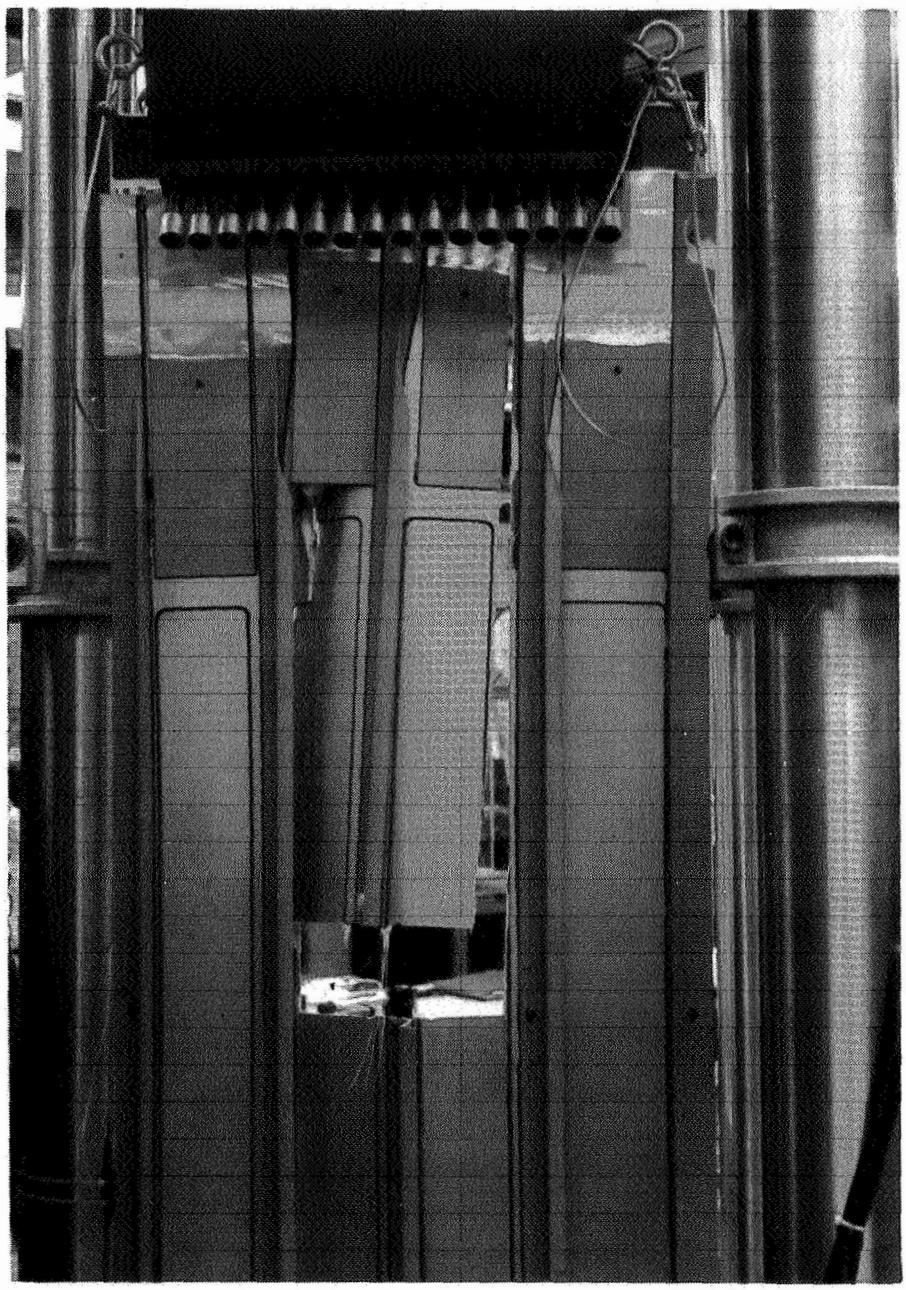

Figure 11: Stringer Side of Failed GLARE-2 Stiffened Panel.

CONCLUSIONS

The fatigue crack growth tests showed that the ARALL-3 and GLARE-2 panels have a much lower crack growth rate than that of an equivalent 2024 stiffened panel which was tested for the G-IV wing program. These laminated panels were sized to have the same cross sectional areas and initial crack lengths as the 2024 panel. The residual strength of ARALL-3 and GLARE-2 panels was higher than that of the 2024 panel due to the high strength aramid and glass fibers in the laminates. The improvement of fatigue and residual strength over aluminum, combined with lower density, gives these fiber/metal laminates a potential application in future aircraft structures.

REFERENCES

1. Bucci, R. J., Mueller, L. N., Vogelesang, L. B., and Gunnick, J. W., "ARALL Laminates Properties and Design Update," Proceedings, Thirty-third International SAMPE Symposium on Materials—Pathway to the Future, Anaheim, CA, 1988.

2. Ming Wu, Reddy, S. V., and Dale Wilson, "Design and Testing of Z-Shaped Stringer Stiffened Panels – Evaluation of ARALL, GLARE, and 2090 Materials," Proceedings, ASM/TMS Material's Week, to be Published, October, 1994.

PREDICTION OF R-CURVES FROM SMALL COUPON TESTS

J.R. Yeh, G.H. Bray, R.J. Bucci
Aluminum Company of America
Alcoa Center, PA 15069

P.15

Y. Macheret*

P.

SUMMARY

R-curves were predicted for Alclad 2024-T3 and C188-T3 sheet using the results of small-coupon Kahn tear tests in combination with two-dimensional elastic-plastic finite element stress analyses. The predictions were compared to experimental R-curves from 6.3, 16 and 60-inch wide M(T) specimens and good agreement was obtained. The method is an inexpensive alternative to wide panel testing for characterizing the fracture toughness of damage-tolerant sheet alloys. The usefulness of this approach was demonstrated by performing residual strength calculations for a two-bay crack in a representative fuselage structure. C188-T3 was predicted to have a 24% higher load carrying capability than 2024-T3 in this application as a result of its superior fracture toughness.

INTRODUCTION

The R-curve approach to fracture toughness evaluation can be advantageously applied to thin, ductile materials where slow, stable tearing is likely to precede rapid fracture. The R-curve portrays toughness development, or resistance to crack extension, as a crack extends under continuously increasing applied load or displacement. In thin, ductile materials, the toughness increases with crack extension until a plateau is reached beyond which the toughness remains essentially constant. The R-curve is a function of material and thickness and is essentially independent of planar geometry within reasonably broad limits. These are very important attributes because they enable residual strength predictions to be made for complex structural configurations using R-curve data from much simpler test specimen geometries.

R-curves for sheet products are typically obtained from center-cracked M(T) panels. For tough sheet materials like 2024-T3, panel widths in excess of 48 inches are required to obtain the complete R-curve measurement (i.e., up to the plateau). Testing this size specimen is often not feasible due to limited material quantities, test machine and setup limitations, or high cost. For this reason, tests on small M(T) panels or toughness indicator tests such as Kahn tear or notched tensile are often used to characterize toughness. These tests are inexpensive and require only small amounts of material. However, the fracture toughness data obtained are geometry dependent, provide only relative rankings of fracture toughness, and may be of little or no use for predicting fracture behavior and residual strength in actual structures.

Thus, there is a need to develop methods to predict structural component performance from small test-coupon data. One such method developed at the Alcoa Technical Center allows a complete R-curve to be predicted from results of a Kahn tear test (ref. 1). This method has the advantages of a

---

* Formerly at Aluminum Company of America, Alcoa Center, PA.

small-coupon indicator test while preserving the true property measurement capabilities of wide-panel R-curve tests.

The prediction method is based on two fracture parameters derived from a Kahn tear test record using finite element analysis: the J-integral for crack initiation, J_i, and the critical crack-tip opening area for propagation for a given distance behind the crack tip, A_p (Figure 1). The latter criterion assumes that the area under the crack profile near to the crack tip is constant during crack extension. J_i is assumed to control crack initiation and A_p is assumed to control crack extension. The crack-tip opening area criterion is similar to a crack tip opening angle (CTOA) criterion which has been the subject of several recent studies (refs. 2 and 3). These studies indicate that CTOA is nearly constant after a small amount of crack growth . Newman et al. (ref. 4) used the CTOA criteria in combination with finite element analysis to predict the load-load line displacement response for various M(T) panels, and found good agreement between the predictions and test data.

A_p was selected over CTOA or CTOD in the current method because it proved less sensitive to changes in finite element mesh size. This is illustrated schematically in Figure 2 which shows a critical crack profile plotted after crack extensions to **a** and **b** during crack propagation. The element size behind the crack tip at **a** is half that at **b**. By fitting the critical crack-tip opening area at crack tip **a,** the critical line **b-e** is predicted at crack tip **b**. Similarly, CTOA(α_c) and CTOD (δ_c) from crack tip **a** yield critical lines **b-d** and **b-f,** respectively. It can be seen that applying the CTOD criterion from one element size to a larger element size under predicts the critical line, while the CTOA criterion overpredicts the critical line. The A_p criterion enables the element size to be changed along the line of crack extension and for different panel sizes while the CTOA and CTOD criteria require an absolute element size and arrangement along the line of crack extension and for every panel size. The ability to change element size becomes important for large panel predictions since it is very computer time consuming to make wide panel predictions using the same element size as for the small Kahn tear specimen.

In the current study, the method was applied to predict the R-curves of two damage-tolerant aluminum sheet alloys: 2024-T3 and C188-T3. C188 is a new alloy with improved toughness and fatigue crack growth resistance intended to replace 2024 in aircraft skin sheet applications. The predicted and experimentally-obtained R-curves were used to make residual strength predictions for a two-bay crack in a representative fuselage structure.

EXPERIMENTAL PROCEDURES

Materials and Mechanical Testing

Alclad 2024-T3 and C188-T3 sheet with a nominal thickness of 0.063 inch were obtained from NASA and Boeing Commercial Airplane Group, respectively. The panels were remnants of 60-inch wide M(T) specimens previously tested at Boeing. The load-COD curves from these tests were also provided by Boeing. Both materials were produced by Alcoa and were of recent vintage.

A single tensile specimen in the L direction was tested from each material in accordance with ASTM E8. The specimens were standard sheet type with a gage length of 2 inches and a uniform gage width of 0.5 inch. The extensometer remained on the specimen to failure to obtain the full stress-strain curve.

Duplicate Kahn tear specimens (Figure 3) in the L-T orientation were tested from each material using standard practices in place at the Alcoa Technical Center (ref. 5). The specimens were pulled to

failure at a crosshead speed of 0.1 inch/min. Load versus load-line displacement was acquired digitally by computer.

R-curve tests on M(T) specimens in the L-T orientation were performed in accordance with ASTM E561. A single 6.3-inch wide specimen was tested for 2024-T3 and single 6.3 and 16-inch specimens for C188-T3. The specimens were fatigue precracked at R=0.1 at a maximum net section stress of 25 to 35% of the yield strength. The precrack was extended approximately 0.125" from each side of the machined slot to an initial crack length $2a_o$ of approximately 0.25 the panel width, W. After precracking, anti-buckling restraints composed of rigid face plates were attached to the specimen. The specimens were pulled to failure under displacement control. The displacement rate was approximately 0.3 inch/min. for the 2024-T3 specimen and 0.1 inch/min. for the C188-T3 specimens. Load versus crack opening displacement (COD) was acquired digitally by computer. R-curves were calculated from the load-COD curves using the secant compliance method of ASTM E561. R-curves were also determined by this same method for the 60-inch wide specimens from the load-COD curves provided by Boeing.

Prediction of R-Curves

R-curves for 6.3, 16 and 60-inch wide M(T) specimens were predicted for C188-T3 and 2024-T3 using a method developed at Alcoa Technical Center (ref. 1). The first step in the method is to obtain the J-integral for crack initiation, J_i, and the critical crack-tip opening area for propagation area, A_p, from the Kahn tear test results. The true stress-strain curve and initial estimates of J_i and A_p are input into a 2-D finite element model of the Kahn tear specimen (Figure 3). Because of symmetry, only half the specimen is considered. A displacement is imposed on the model at the loading pin and nodes in the model along the line of crack extension are disconnected to simulate crack growth. The first node is released when the J-integral at the notch tip exceeds the initial estimate of J_i. Subsequent nodes are released when the crack-tip opening area exceeds the initial estimate of A_p. J_i and A_p are adjusted iteratively to obtain the best possible agreement between the model response and the experimental response of the Kahn tear test specimen. The force on the first node at release, F, is also noted after the final values of J_i and A_p are obtained.

The values of J_i and A_p obtained by fitting the Kahn tear test specimen response are subsequently input into a 2-D finite element model of an M(T) specimen (Figure 4). In this case, only one quarter of the specimen is considered because of symmetry. A uniform displacement is imposed on the top edge of the model. Crack extension is simulated by releasing the first node when the J-integral exceeds J_i. The finite element mesh size for the first few nodes is identical to that in the Kahn tear model. However, it is found that the force on the first node at release, F, depends on panel width and differs from that in the Kahn tear simulation. The assumption is made that the product of the force at node release and the critical crack-tip opening area is constant (i.e., geometry independent), and the critical crack-tip opening area, A_p, for the M(T) panel is determined from the relationship:

$$(F^*A_p)_{\text{Kahn tear}} = (F^*A_p)_{\text{M(T)}} \qquad (1)$$

Subsequent nodes are released when the crack opening area exceeds the calculated A_p for the M(T) specimen. The mesh size is increased after the first few nodes in order to reduce computation time. The load-COD curve predicted by this procedure is analyzed using the secant compliance method of ASTM E561 to obtain the predicted R-curve.

The need to adjust A_p using Equation 1 is not completely understand at this time. Without this adjustment (i.e., A_p held constant), the applied load is consistently over predicted by the method and

the magnitude of this over prediction increases with increasing panel size. One possibility is that the experimental loads are reduced by panel buckling. Unloads during the tests of the 16 and 60-inch wide panels in this study indicates that buckling was occurring even though anti-buckling guides were applied to the specimens. A finite element model is currently being developed that incorporates buckling effects. Once buckling effects are incorporated it may be possible to obtain good predictions with a constant value of A_p.

Prediction of Residual Strength for Two-Bay Crack

The experimental and predicted R-curves of 2024-T3 and C188-T3 from a 60-inch wide specimen were used to predict the residual strength of a two-bay crack in a representative fuselage structure (Figure 5). A common design policy is to ensure that structure can sustain a two-bay under the severest anticipated operating conditions. The crack was assumed to extend entirely across two bays ($2a_o$=40 inches) with the center stiffener (i.e., frame) failed. The stiffener material was assumed to be 7075-T6. The crack drive or K solution derived by Yeh (ref. 6) was used in the analysis. This solution is for a flat, stiffened panel subjected to uniform axial loading and does not include possible rivet or stiffener failure. It does account for shear deformation of the fasteners and bending deformation of the sheet and stiffeners.

RESULTS

Tensile Properties and Kahn Tear Results

The engineering stress-strain curves of the clad 2024-T3 and C188-T3 sheet are shown in Figure 6. True stress-strain curves were derived from these curves and used as inputs into the R-curve prediction method. The yield strength, ultimate tensile strength and total strain at failure are given in Table I. The tensile properties of the two alloys were nearly the same. The C188-T3 had a slightly higher yield strength and 2024-T3 had a slightly higher ultimate tensile strength. The total strain at failure was nearly identical in both materials.

The experimental and predicted Kahn tear test records are shown in Figure 7. The experimental responses of the 2024-T3 and C188-T3 were significantly different. The peak load and area under the curve of C188-T3 was greater than that of 2024-T3. The area under the load-displacement curve represents the energy required to fail the specimen.

Good agreement was obtained between the predicted and experimental Kahn tear test records. The values of J_i and A_p obtained from the finite element analysis are given in Table II. J_i was 34% greater and A_p 50% greater in C188-T3 than in 2024-T3 indicating the former had higher initiation toughness and better crack extension resistance. J_i is found to be primarily controlled by the peak load and A_p by the slope of the test record beyond peak load. The serrated appearance of the predicted test record after peak load is a consequence of discrete node release in the model.

Comparison of Experimental and Predicted R-curves

The experimental and predicted load-COD records and R-curves for the 6.3, 16 and 60-inch wide M(T) specimens are shown for 2024-T3 and C188-T3 in Figures 8, 9 and 10, respectively. The values

of J_i and A_p used in the predictions are given in Table II. Experimental and predicted R-curve data in Figures 8 through 10 are shown only up to the point where the net section stress in the uncracked specimen ligament based on physical crack length exceeds 100% of the material's yield strength. Experimental and predicted values of crack extension resistance, K_R, just prior to net section yielding are compared in Table III. The comparisons are at effective crack extensions of Δa_{eff}=0.4, 0.8, and 5 inches for the 6.3, 16, and 60-inch wide specimens, respectively.

The load-COD response of the 6.3-inch wide specimen was over predicted for both 2024-T3 and C188-T3 resulting in an over prediction of the R-curves (Figure 8). The difference between predicted and experimental K_R at Δa_{eff}=0.4 was 11% for the 2024-T3 and 4.4% for C188-T3. The agreement between experiment and prediction for C188-T3 was nearly perfect for the 16-inch wide specimen (Figure 9). The difference between predicted and experimental KR was less than 1%. There was no 16-inch wide specimen tested for 2024-T3. For the 60-inch wide specimen, the agreement between experiment and prediction for 2024-T3 was excellent, while the load-COD response and R-curve for C188-T3 were again over predicted (Figure 10). The difference between predicted and experimental K_R at Δa_{eff}=5 inches was 1.4% for 2024-T3 and 9.1% for C188-T3. Figure 10 also shows the R-curves from other lots of Alclad 2024-T3 and Alclad C188-T3 in the thickness range 0.036 to 0.249 inch. Comparison shows that the lots in this study are typical of production material.

Residual Strength Predictions for a Two-Bay Crack

The residual strength predictions for the representative fuselage structure obtained from the experimental and predicted R-curves from 60-inch wide panels are shown in Figure 11. The crack drive curves reflect a decrease in stress intensity factor as the crack approaches the intact stiffeners (i.e., frames). Failure occurs at the applied stress where the crack drive curve becomes tangent to the R-curve. This stress defines the maximum residual strength capacity of the structure with a two-bay crack. The residual strength prediction for the structure with Alclad 2024-T3 fuselage skin was 37 ksi using either the experimental or predicted R-curve. The prediction for a Alclad C188-T3 skin was 46 ksi using the experimental R-curve and 50 ksi using the predicted R-curve, a difference of 8%.

The extent of valid R-curve data from the 6.3 and 16-inch wide specimens are also shown in Figure 11. Beyond these values the 6.3 and 16-inch wide specimens exhibit net section yielding in violation of ASTM E561 validity requirements. Thus, the 6.3 and 16-inch wide specimen R-curves are clearly inadequate for predicting residual strength of the fuselage structure. The tangency point occurs at a much greater crack extension than can be obtained in these size panels. Residual strengths predicted from the predicted R-curves, while up to 8% higher than residual strengths predicted from the experimental R-curves obtained from 60-inch wide panels, are clearly more reliable than those that would be predicted using R-curves obtained from 6.3 or 16-inch wide specimens. The latter would significantly underestimate the residual strength of the structure.

DISCUSSION AND CONCLUSIONS

Experimental and predicted R-curves correlate reasonably well for the specimen geometries and alloys considered. The fact that reasonable R-curve predictions were obtained for a 60-inch wide M(T) specimen is especially encouraging, since R-curves from this size panel or larger are often needed to predict the fracture response of actual structural components. This was certainly the case for the two-bay crack in the representative fuselage structure in Figure 5.

The results indicate that the prediction method is a viable alternative to wide panel testing for material development and preliminary design. The problem of having insufficient R-curve for a residual strength prediction of a structural component is overcome by this method, since the finite element model can be adjusted to obtain an R-curve from any size wide panel specimen. The residual strength predictions for the two-bay crack in the fuselage structure using experimental and predicted R-curves were in reasonable agreement demonstrating the validity and usefulness of this method. However, it should be noted that none of the predictions were verified by testing actual structural components.

The method has several other advantages over wide-panel tests. The Kahn tear test is inexpensive, requires a minimal amount of material, and can be performed on almost any load frame. These are particularly advantageous in alloy development programs where there are a large number of variants and the amount of material for characterization is often limited. The prediction method will allow selection of alloys based on their predicted fracture behavior in intended structural applications, rather than on the basis of small-panel or toughness indicator results which may have little relevance to actual structural response. The Kahn tear test can also be performed in or after exposure to various environments or temperatures representative of service conditions. Testing of wide panels under these conditions may be impractical or prohibitively expensive.

However, additional work is needed to establish the generality of this approach and validate the method for a broader range of alloys and products. In particular, its applicability to thicker products needs to be explored. Since the R-curve is influenced by stress state, it is desirable to establish the validity of this approach over a full range of thickness encompassing plane stress to plane strain behavior. The sensitivity of the method to the input parameters (i.e., J_i, A_p, and stress-strain curve) also requires further investigation.

Both the experimental and predicted R-curves show the superior fracture toughness of C188-T3 sheet relative to 2024-T3. Residual strength calculations using the experimental R-curves indicate that the superior toughness yields a 24% higher load carrying capability for C188-T3 sheet in a representative fuselage structure.

ACKNOWLEDGMENTS

The authors would like to acknowledge the interest and encouragement provided by the Boeing Commercial Airplane Group. In particular we would like to thank Matt Miller, Sven Axter and Ken Barlow of Boeing for providing the 60-inch wide M(T) panel data and C188-T3 specimen remnants. The authors also thank fellow Alcoans Mark Mahler, Dick Rolf, Mike Kulak and Brian Cheney for their contribution to this effort.

REFERENCES

1. Macheret, J. and Yeh, J.R.: Aluminum R-Curve Estimated from Small Coupon Test Data. PDM Report No. 57-93-15, Alcoa Technical Center, Aluminum Company of America, 1993.

2. Luxmoore, A., Light, M.F. and Evans, W.T.: A Comparison of Energy Release Rates, the J-Integral and Crack Tip Displacements. *Int. J. Fracture,* vol.13, 1977, pp. 257-259.

3. Kobayashi, T., Irwin, G.R. and Zhang, X.J.: Topographic Examination of Fracture Surfaces in Fibrous-Cleavage Transition Behavior. *ASTM STP 827*, 1989, pp. 234-251.

4. Newman, J.C., Dawicke, D.S. and Bigelow, C.A: Finite-Element Analyses and Fracture Simulation in Thin-Sheet Aluminum Alloy. NASA TM-107662, 1992.

5. Kaufman, J.G. and Reedy, J.F.: Description and Procedure for Making Kahn-Type Tear Test. Alcoa Research Laboratories Report No. 9-M-681, Aluminum Company of America, 1966.

6. Yeh, J.R.: Fracture Analysis of a Stiffened Orthotropic Sheet. *Engineering Fracture Mechanics*, vol. 46, 1993, pp. 857-866.

Table I. Longitudinal Tensile Properties for 0.063-inch Alclad Sheet (1 lot each alloy)

Alloy	TYS (ksi)	UTS (ksi)	Total Strain at Failure (%)
2024-T3	50.7	66.0	17.6
C188-T3	52.6	64.8	17.3

Table II. Fracture Parameters for 0.063-inch Alclad Sheet (1 lot each alloy)

Alloy	Geometry	Fracture Parameter (L-T orientation)			
		J_i (ksi-in.)	A_p (in.^{2})*	F (kip)	F*A_p (kip-in.^{2})
2024-T3	Kahn Tear	0.35	8.00E-4	0.119	9.52E-5
	W=6.3 in. MT	0.35	7.87E-4	0.121	9.52E-5
	W=16 in. MT	0.35	7.21E-4	0.132	9.52E-5
	W=60 in. MT	0.35	6.14E-4	0.155	9.52E-5
C188-T3	Kahn Tear	0.47	1.20E-3	0.120	1.44E-4
	W=6.3 in. MT	0.47	1.18E-3	0.122	1.44E-4
	W=16 in. MT	0.47	1.08E-3	0.133	1.44E-4
	W=60 in. MT	0.47	9.23E-4	0.156	1.44E-4

* for d=0.2 inch

Table III. Comparison of Experimental and Predicted K_R at Discrete Δa_{eff} (1 lot each alloy)

MT Width (inch)	Δa_{eff} (inch)	Alclad 2024-T3 (0.063 in.)			Alclad C188-T3 (0.063 in.)		
		K_R, Exp (ksi$\sqrt{in.}$)	K_R, Pred (ksi$\sqrt{in.}$)	Δ%	K_R, Exp (ksi$\sqrt{in.}$)	K_R, Pred (ksi$\sqrt{in.}$)	Δ%
6.3	0.4	72.6	80.5	+11	81.4	85.0	+4.4
16	0.8	---	109.0	---	118.7	117.8	-0.8
60	5.0	188.4	185.6	-1.4	229.0	249.8	+9.1

Kahn Tear Test Model (J.R. Yeh, Y. Macheret)

Two Fracture Criteria:

J_i = Energy for Crack Initiation

A_p= Critical Crack-tip Opening Area for Propagation

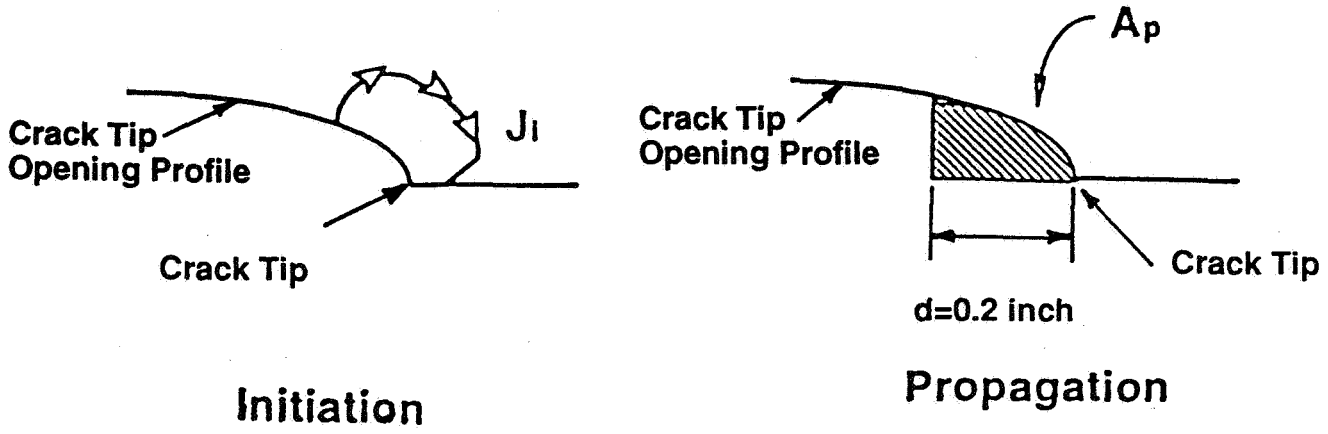

Figure 1. Fracture criteria used in R-curve prediction method.

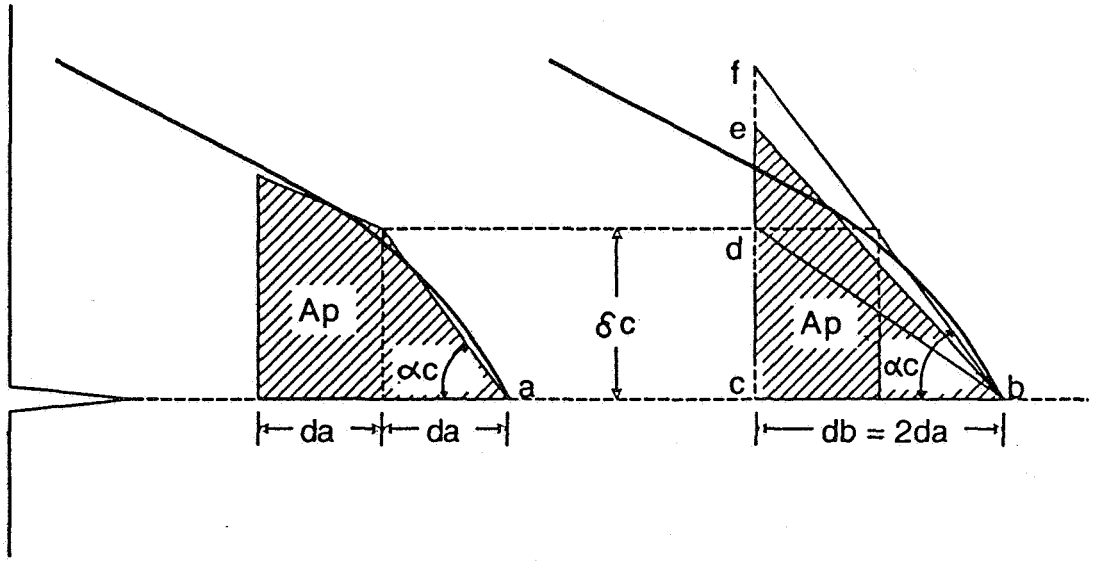

Figure 2. Schematic showing effect of element size for Ap, CTOA, and CTOD criteria.

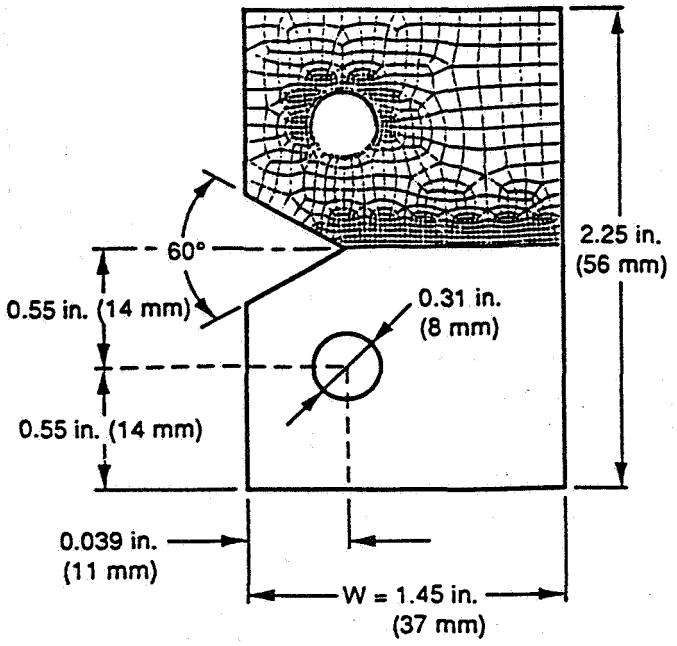

Figure 3. Kahn tear specimen and its finite element model.

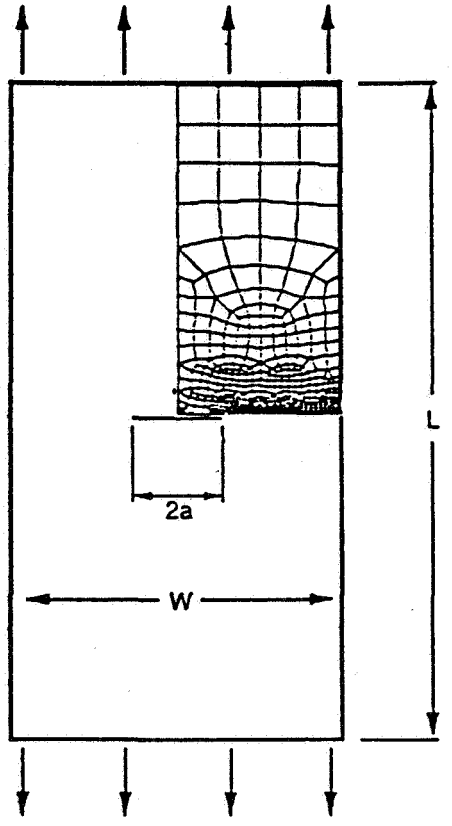

Figure 4. M(T) panel and its finite element model.

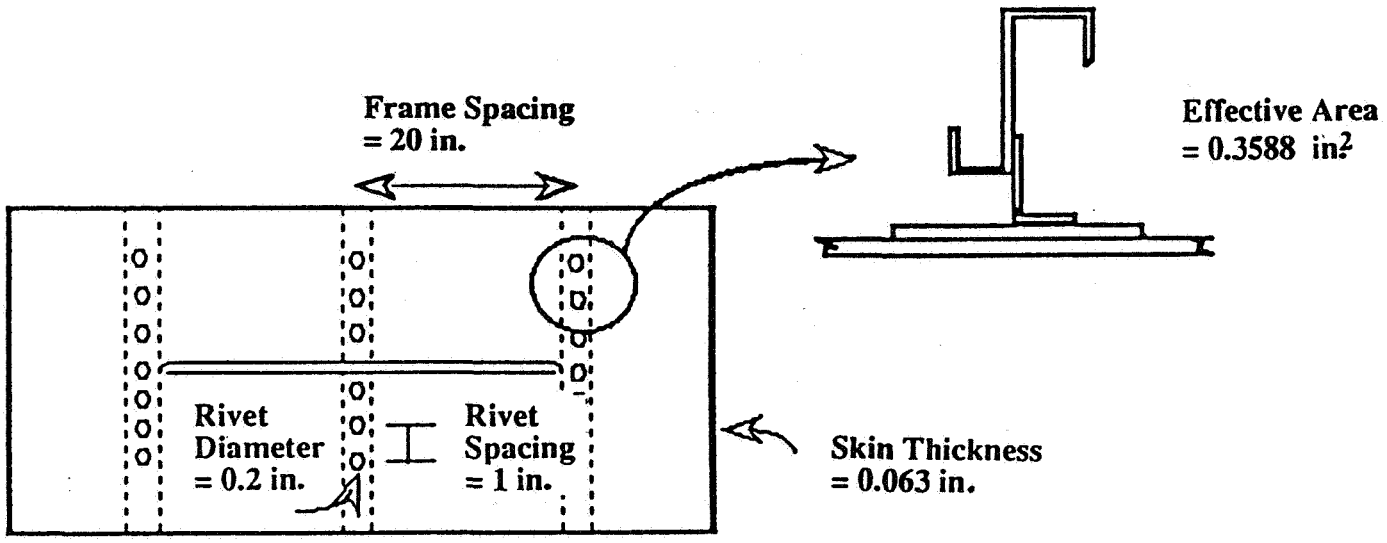

Figure 5. Representative fuselage structure with two-bay crack.

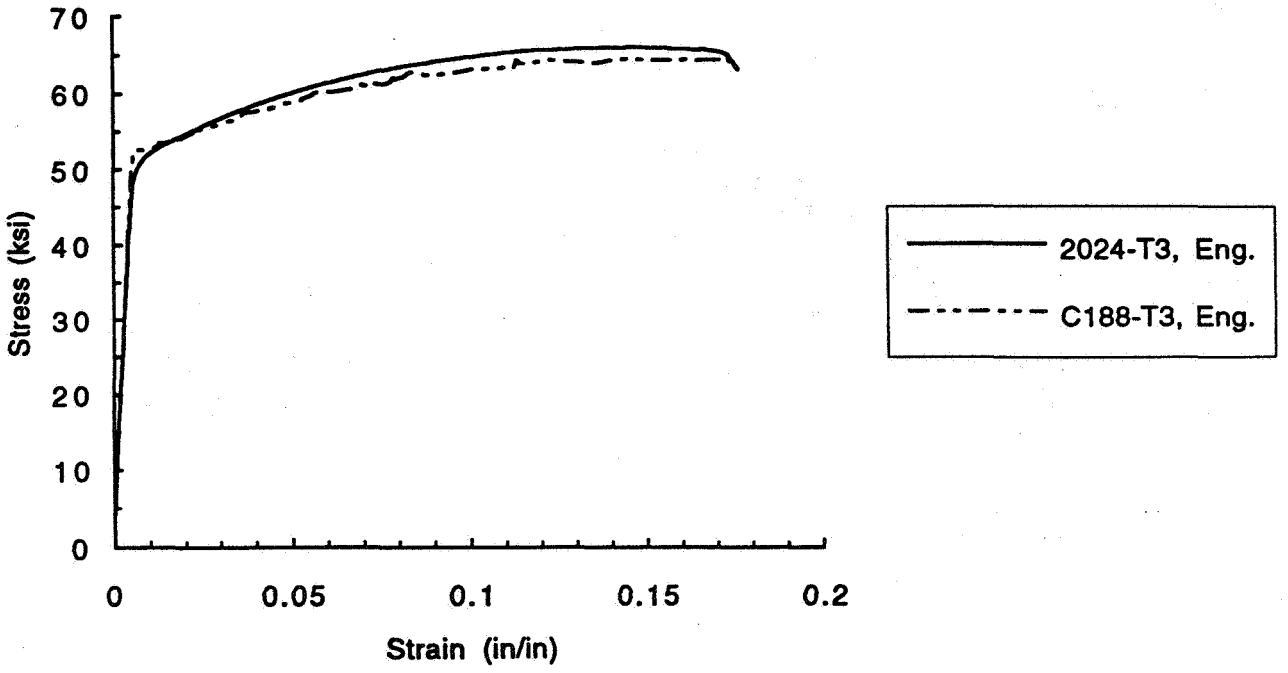

Figure 6. Engineering stress-strain curves for 0.063-inch Alclad 2024-T3 and Alclad C188-T3 sheet (1 lot each alloy).

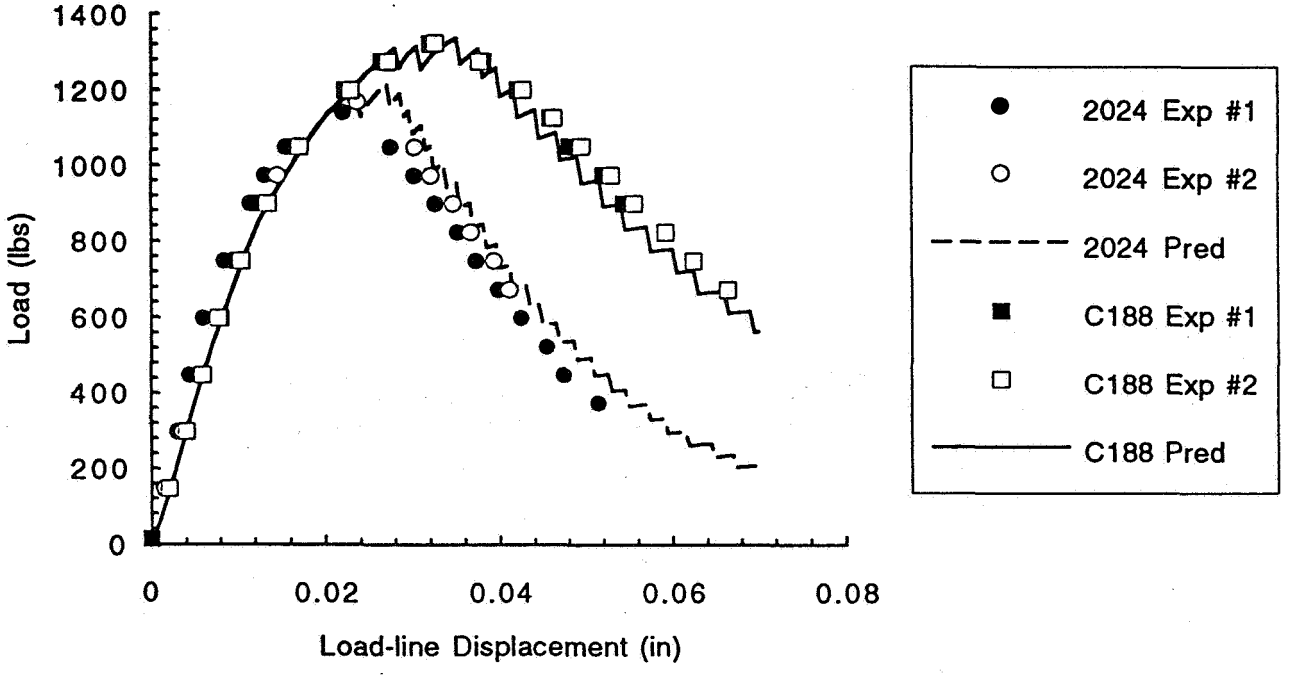

Figure 7. Predicted and experimental Kahn tear test records for Alclad 0.063-inch 2024-T3 and Alclad C188-T3 sheet (1 lot each alloy).

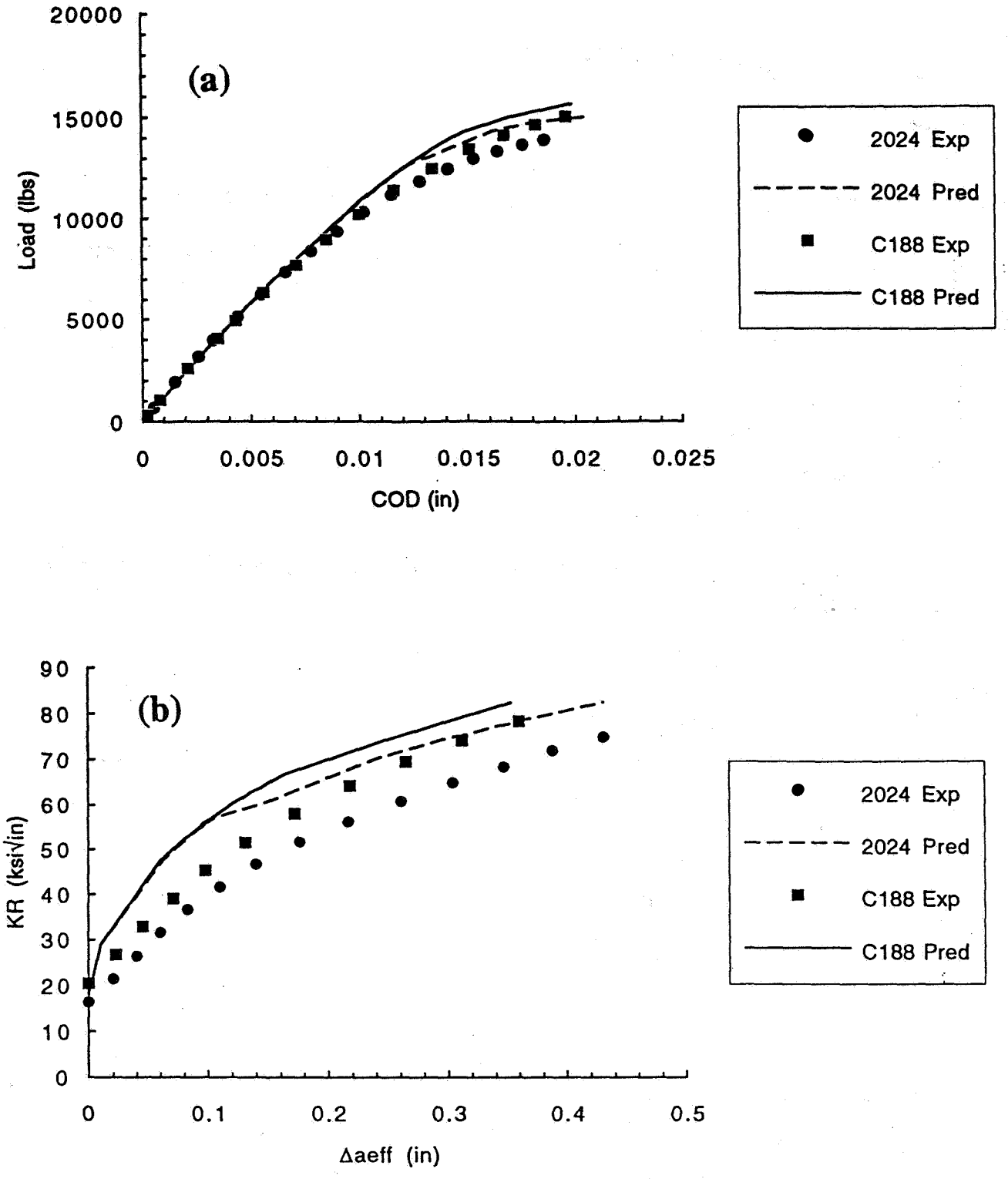

Figure 8. Predicted and experimental load-COD response (a) and R-curves (b) for 6.3-inch wide M(T) specimen.

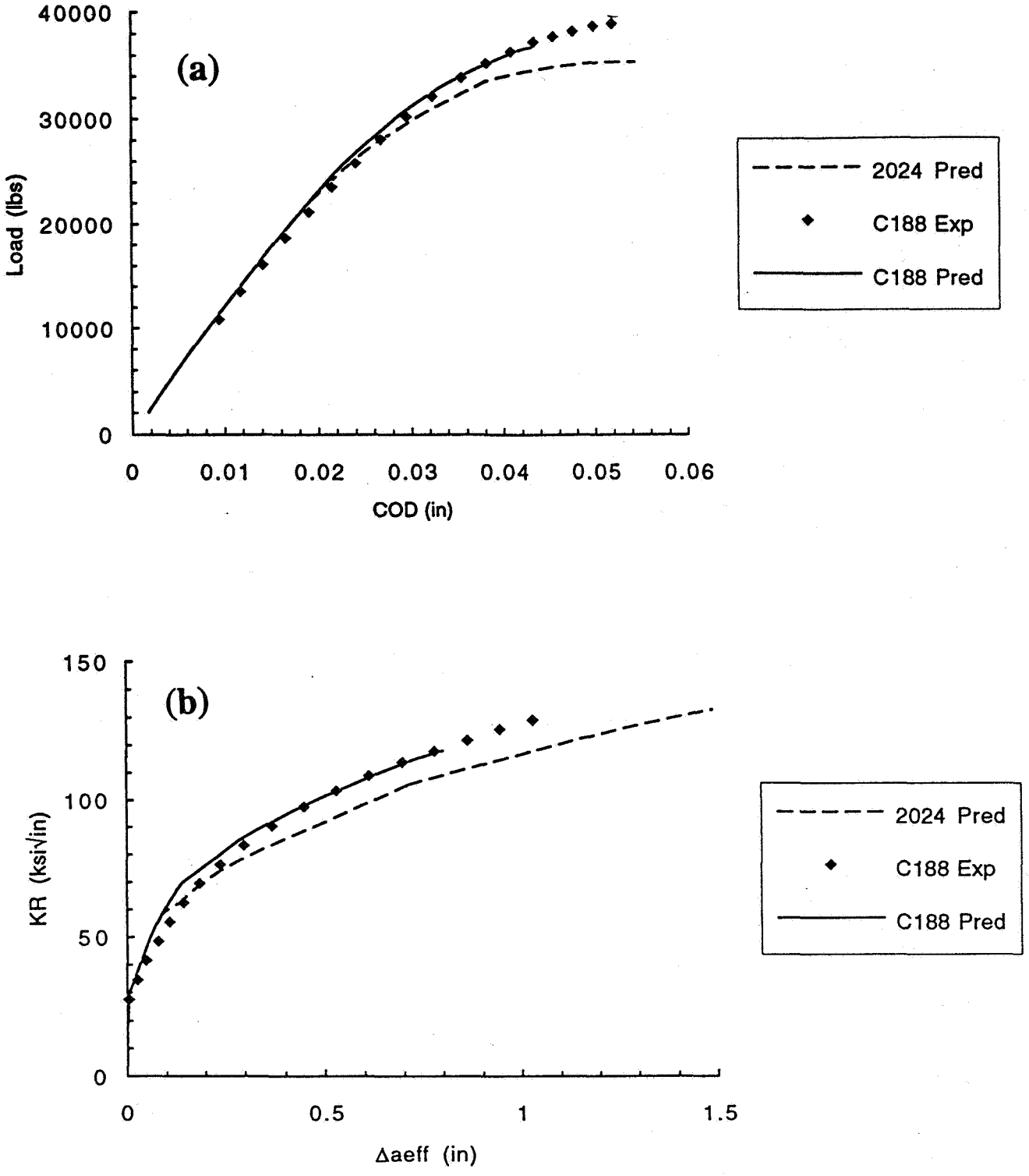

Figure 9. Predicted and experimental load-COD response (a) and R-curves (b) for 16-inch wide M(T) specimen.

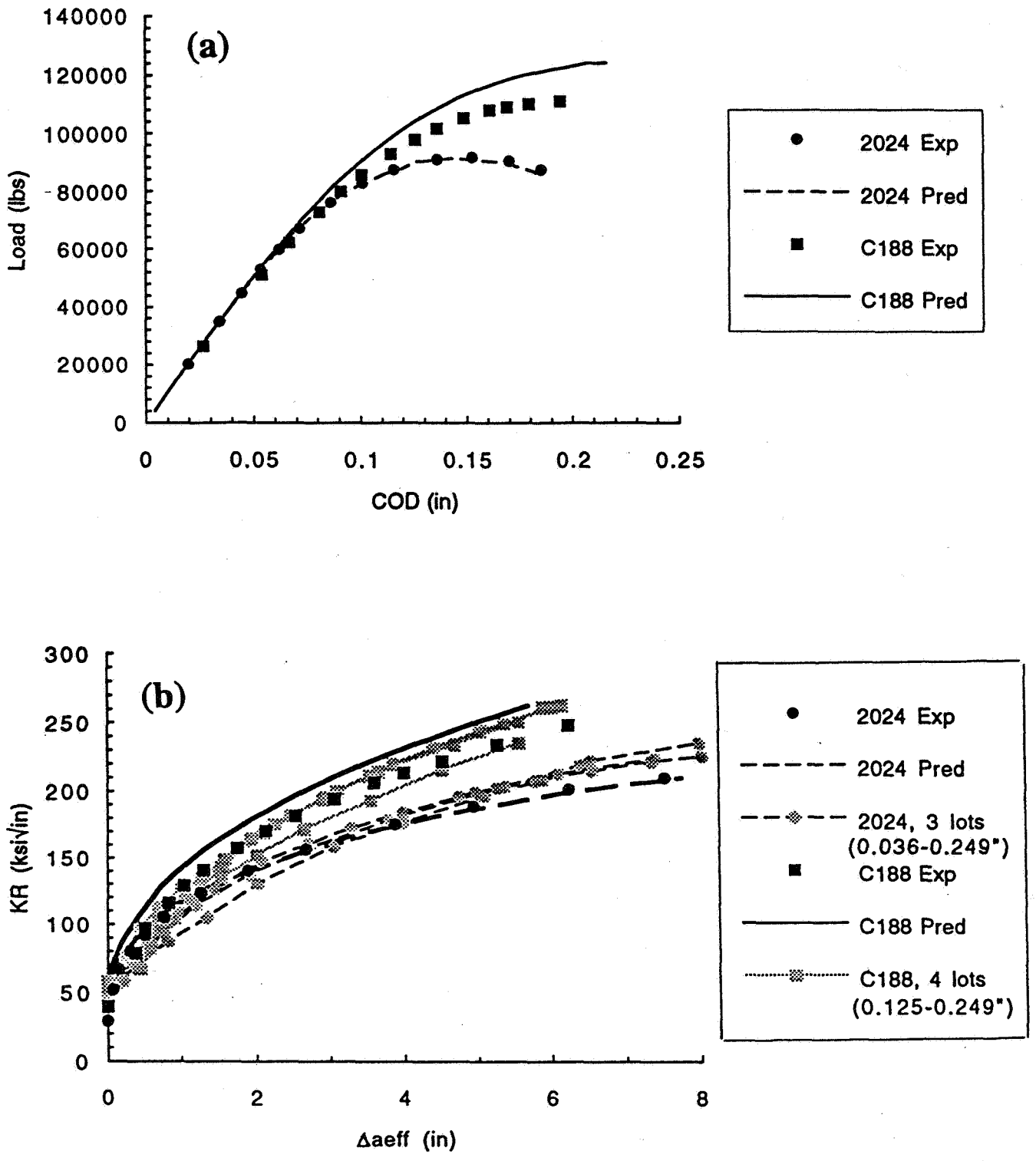

Figure 10. Predicted and experimental load-COD response (a) and R-curves (b) for 60-inch wide M(T) specimen

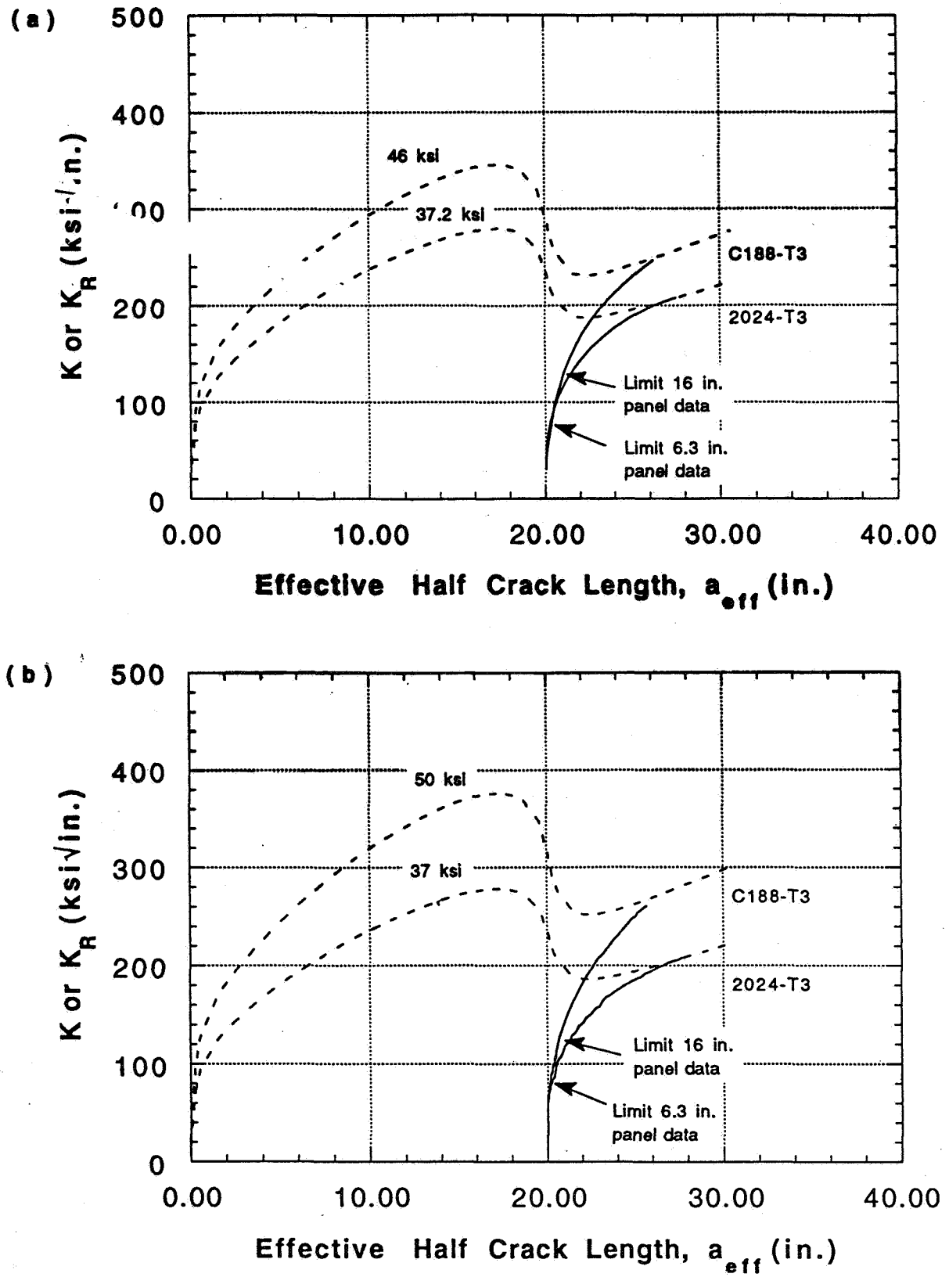

Figure 11. Residual strength prediction for two-bay crack in fuselage skin using experimental R-curves (a) and predicted R-curves (b) for Alclad 2024-T3 and Alclad C188-T3 0.063-inch sheet (1 lot each alloy).

AIRCRAFT FATIGUE AND CRACK GROWTH CONSIDERING LOADS BY STRUCTURAL COMPONENT

J. D. Yost
DPRO–Bell Helicopter Textron, Inc.
Fort Worth, TX

SUMMARY

The indisputable 1968 C-130 fatigue/crack growth data is reviewed to obtain additional useful information on fatigue and crack growth. The proven Load Environment Model concept derived empirically from F-105D multichannel recorder data is refined to a simpler method by going from 8 to 5 variables in the spectra without a decrease in accuracy. This approach provides the true fatigue/crack growth and load environment by structural component for both fatigue and strength design. Methods are presented for defining fatigue scatter and damage at crack initiation. These design tools and criteria may be used for both metal and composite aircraft structure.

INTRODUCTION

The main objective is to provide the best methods for fatigue/crack growth and load environment prediction. In most cases only one full scale fatigue test is conducted per aircraft type. The local loading on component elements can not be simulated even though shear, torsion and bending moment at a station may be in good agreement with theoretical or flight test values.

In 1967 many C-130 aircraft were flying in Southeast Asia with fatigue cracks (Yost, Ref. 1) at low risk due to their damage tolerant structural design. Aircraft were sent to be repaired when the cumulative cracks' length at a surface wing station was 10 inches or more. In about 1970 the aluminum 7075T6 center wing sections on the C-130s were replaced with a new structure due to many fatigue cracks in fleet aircraft. Wing station (WS) 120 center section crack data are used to give a better understanding of structural fatigue in aircraft.

The primary elements of the load environment may be broken down into ground-air-ground (GAG), gust, maneuver, buffet, taxi, jump takeoff and landing. Buffet loads may be superimposed on gust or maneuver and sometimes on both. Load spectra of most concern for fighter aircraft (Yost and Johnson, Ref. 2) are maneuver loads. Both gust and maneuver are very important for transport design for the flight domain. Current civil transport aircraft fly at higher speeds than earlier prop aircraft, thus they respond to a lower frequency portion of the gust Power Spectral Density or longer wavelength higher magnitude gusts (Yost et al., Ref. 3). Comparison of current versus past NASA *VGH* data shows this trend. Also, severe turbulence is avoided and the normal load factor (Nz) spectra contain buffet, gust, and maneuver. Military specifications in the MIL-A-8860 series have been updated as new data became available from test programs and fleet aircraft load recorder programs. Even though

these data are *Nz* spectra which include buffet, gust, and maneuver, the breakdown to mission segment is of great value.

Ground operations are centered on landing gear design for sink rate, taxi response for usage and gear dynamic magnification factor (DMF). DMF for spin-up and spring-back loads may be greater in the Drop-Tower certification than during aircraft landings, so fatigue and strength design is conservative. Fatigue is accumulated on other aircraft components besides the landing gear and backup structure during ground operations.

A new method is presented for defining scatter in fatigue failures (Yost, Ref. 4). It is believed that the methods for prediction of loads (Ref. 2 and Yost, Ref. 5) and fatigue failures in metal structure are the same for composite structure.

SYMBOLS USED

Aa = angle of attack (deg)

AC = aerodynamic center (in)

Ax = roll acceleration (deg/s^2)

Ay = pitch acceleration (deg/s^2)

Az = yaw acceleration (deg/s^2)

B = sideslip angle (deg)

CG = center of gravity (in)

CL = crack length (in)

D = Miner's damage equation: $\Sigma(n/N) = 1$

Da = aileron position (deg)

De = elevator position (deg)

Di = damage at crack initiation

Dr = rudder position (deg)

FW = fuel weight (lb)

g = acceleration due to gravity (ft/s^2)

Ixx = roll moment of inertia (lb-s^2-ft)

Iyy = pitch moment of inertia (lb-s^2-ft)

Izz = yaw moment of inertia (lb-s^2-ft)

Kt = stress concentration factor

n = structure stress cycles

N = cycles read on S/N curve

Ny = lateral load factor (g)

Nz = normal load factor (g)

Q = dynamic pressure (psf)

Sa = stress amplitude (ksi)

Sm = mean stress (ksi)

S/N = stress versus cycles curve

STW = store weight (lb)

V = variation coefficient

VGH = velocity, g, altitude

W = gross weight (lb)

C-130 CRACK GROWTH DATA BASE

The C-130 data (Ref. 1) from 1967 and 1968 is the best, most complete large statistical sample source for fatigue and crack growth by mission of documented data for upper and lower wing surface. The in-flight fatigue test data cover nine different missions. These included a mild load environment long range cargo mission. One of the most severe load environment missions was low altitude with gust loads superimposed on the maneuvers. A very high percentage of these fleet aircraft had fatigue cracks as shown in Table 1.

The crack growth was monitored by measuring the crack length every two weeks. Accumulated crack growth data was added to the data base. The past history of individual aircraft was defined by taking records of missions flown per base and the flight hours accumulated at assigned bases.

Table 1. C-130 Fleet Aircraft Cracks in 1968

Total aircraft	619
Aircraft with fatigue cracks	345
Aircraft with fatigue cracks at WS 120	289
Aircraft repaired	81

A crack growth curve was derived from documented data with crack length on the ordinate and fatigue damage on the abscissa. This crack growth curve was used to convert the total crack length per upper or lower surface at WS 120 to fatigue damage on the left or right side. A new crack growth curve was obtained by least squares curve fit of fleet crack growth data and is presented in Figure 1 for upper and lower surfaces.

The actual fatigue damage on individual aircraft was obtained by taking the crack growth curve in Figure 1 and cumulative crack length per surface for converting to actual damage. Next a regression analysis was conducted using actual damage as the dependent variable and flight hours for each of the nine missions as independent variables. These analyses produced coefficients that were damage per flight hour for upper and lower surfaces at WS 120 for each of the nine missions. Validation of these coefficients was accomplished by using crack growth data from aircraft which had most or all of their usage on only one mission.

The actual damage per mission flight hour was used as a dependent variable to interrogate the fleet data with regression analysis for the damage source. Statistical sound parameters were used as independent variables in this analysis. These variables were: (% time in turbulence) (gust intensity factor)/ (mission/hour) for gust, (GAG/mission/hour) for GAG, (ratio of paved to unpaved runway roughness standard deviation) (number of landings/ mission/hour) for taxi. To define maneuver damage per hour, the missions having very low time in turbulence gave maneuver contribution as the equation constant, so this one unknown resulted in some iteration.

These empirical relations allow a definitive look at aircraft structural fatigue that is not available for any other aircraft.

AIRCRAFT FATIGUE LIFE

In order to define what portion of the aircraft life that is available after crack initiation we selected a 0.5-inch crack as the actual total life for our analysis. The two crack growth equations in Figure 1 were used in computing the actual damage per 0.03-inch and 0.5-inch crack lengths for the crack growth portion. This produces a crack growth portion of 26.7% for lower surface and 18.6% for upper surface. The average portion of fatigue life that is crack growth is about 23%. Since this statistical sample is so large, this information provides a better understanding of structural fatigue. One point we must make is that these aircraft

had flaws which required the use of stress concentration factors (Kt) in fatigue analysis of 8 and 10.

C-130 SCATTER FACTORS

The Long Range Cargo was selected as the mildest and Sky-Hook as one of the most severe load environment missions to study scatter. Data was available on these two missions for crack initiation where the aircraft were almost single mission usage aircraft. Then 10,000 flight hours were computed as the mean flight hours to crack initiation from Figure 1 and the damage per flight hour, for the Long Range Cargo mission at WS 120 on the lower surface. The first crack initiations were about 5,000 flight hours, which allowed the calculation of 2 for the scatter factor. Using this same procedure on Sky-Hook the mean flight hours to crack initiation were 1,400 and first crack initiation was about 950 flight hours, so the computed scatter factor is 1.47. The crack initiation and crack growth curve for the first aircraft on each of these two missions are shown in Figure 2.

The more severe load/stress cyclic environment has less scatter, which is the same trend in stress versus cycles (S/N) curve raw data points. In an earlier paper (Ref. 4), we derived an equation to represent the scatter in S/N raw data points as a function of stress amplitude, mean stress and stress concentration factors. The natural log of the variation coefficient (Ln V) as the dependent variable in Equation 1 represents the scatter.

$$\mathrm{Ln}V = 1.56 + \frac{9.57}{Sa} + \frac{2.53}{Kt} - 0.0255Sm \qquad (1)$$

Data for this equation derivation was a very large number of 2024T3 and 7075T6 aluminum specimens. This coefficient is computed from Miner's Damage Equation (SUM $[n/N] = 1.0$) values.

THEORETICAL FATIGUE SCATTER ($\Sigma[n/N]$)

To help keep scatter to a minimum relative to the S/N curve effects, it is suggested that good statistical coverage of mean stress (Sm), stress amplitude(Sa), and stress concentration factors is needed for small specimens. The next step we propose is to derive an equation for these type data to represent the complete family of S/N curves for each material, as we have done. Other variables should be added to the equation for component specimens, loading complexity, and specimen size. Thus six component specimens per helicopter S/N curve and a large scatter factor would not be needed. Accurate load spectra are needed to reduce scatter in fatigue predictions. These spectra should be per mission segment for structural component location.

For each analysis location, the design stress concentration factor must be defined from use of finite element model and/or detailed stress analysis.

THEORETICAL CRACK GROWTH ANALYSIS SCATTER

The same accurate load spectra for fatigue analysis are needed for crack growth analysis predictions. The design stress concentration factors are also needed with detailed information about the analysis locations. Structural inspection of fleet aircraft is required to validate the crack growth predictions.

AIRCRAFT FATIGUE PREDICTIONS

Some of the many parameters to be considered for fatigue analysis are listed in Table 2. A scatter factor of about 40 is common for helicopter parts and 4 is used on most airplanes. The main objective is to keep the scatter to a minimum. Critical crack length is the best selection for fatigue to avoid high risk. Miner's damage equation is the best fatigue damage method to define crack initiation when corrections are included for scatter. The selection of the most severe mission for fatigue life calculations allows adequate life on any mission.

Table 2. Aircraft Fatigue Predictions

Scatter range:		
S/N curves	–	1 to 40
Loads	–	1 to 3
Design *Kt*	–	1 to 10
Define Fatigue Life:		
Select crack length		
Critical crack length		
Crack initiation		
Method of fatigue prediction:		
Miner's Damage Equation SUM(*n/N*)		
Crack growth analysis		
Select load environment:		
Most severe mission		
Mission mix		

A method is desired that provides the positive and negative load peaks for any selected location on the aircraft for design strength or fatigue analysis. The Load Environment Model (2) concept is capable of doing these things and has been computer programmed for the F-106, F-111, and A-7D aircraft. The initial model was eight variables and was derived with F-105D multichannel recorder data. The new method uses all the proven features of the above model minus the aircraft angular velocities and without any decrease in accuracy.

This new model has five variables and may need to go to six variables if the longitudinal load factor is important for the aircraft being analyzed. A step-by-step description of model derivation starts with a good statistical normal load factor spectra per mission segment that the model aircraft is expected to be flying during its usage life. The next requirement is multichannel recorder data from a similar type of aircraft, which includes angular acceleration about each of the three axes, plus *Nz* and lateral load factor (*Ny*). Then derive probability curves for *Ny*, roll acceleration (*Ax*), pitch acceleration (*Ay*), and yaw acceleration (*Az*) versus *Nz*. These probability curves are used to expand the *Nz* spectra per mission segment to a five-variable Load Environment Model per mission segment. Table 3 is taken from MIL-A-8866A (USAF) to show an example of *Nz* spectra per mission segment.

Table 3. Maneuver–Load–Factor Spectra A, F, TF Classes, Cumulative Occurrences per 1,000 Flight Hours by Mission Segment

Nz	Cruise	Air–Ground	Air–Air	
				Positive
2.0	10,000	175,000	300,000	
3.0	2,500	100,000	150,000	
4.0	400	40,000	50,000	
5.0	1	10,000	13,000	
6.0		1,500	2,500	
7.0		200	900	
8.0		15	180	
9.0		1	60	
10.0			15	
				Negative
0.5			44,000	
−0.5			1,200	
−1.5			60	
−2.5			1	

To make use of the model, regression equations are needed for control surface positions and load/stress regression equations for selected structural component locations. Next, use the most severe mission to compute load spectra with the load equations and the Load Environment Model. These location spectra are to be used to compute strength required and fatigue analysis for design. Each component spectrum will be different and will allow the minimum structural weight to be defined for strength and fatigue. Strength design limit loads are the maximum values for one life on the spectra. The flowchart in Figure 3 shows how the Load Environment Model fits in with other tasks.

LOAD REGRESSION EQUATIONS

Load equations are required to go from a Load Environment Model to a structural component location spectrum. Load equations for the F-111 were complex due to the wing variable sweep, but were high-quality since they were derived from recorded flight test data. The tiltrotor on the V-22 presented a different set of problems in obtaining valid load equations even before flight test. Data for the F-106 equations were very limited. Equations for the A-7D were very good, but consideration of Buffet was not included.

Detailed stress analysis and finite element models (FEM) must be validated, plus all critical control points for strength and fatigue must be correctly selected.

The independent variables must be logical for the component analysis locations selected. Goodness of fit for the computed equations is best measured with the standard error and correlation coefficient. Two independent variables which have high correlation with each other should not be used in the same equation. The maximum number of variables per equation should be about ten. As variables enter an equation, the standard error decreases and the correlation coefficient increases to approach 1. The point in equation derivation where the correlation coefficient does not increase when a new variable is added may be the stopping place for that equation. Also, another stopping point is when the standard error does not decrease when a new variable is added to the equation.

A short list of independent variables is as follows: *Nz*, *Ny*, *Ax*, *Ay*, *Az*, *Q*, *W*, *Iyy*, *Izz*, *Ixx*, *STW*, *FW*, *AC*, and *CG*. A list of control surface equations and other dependent variables with their crossproduct variables are listed in Table 4.

A minimum of thirty theoretical conditions are needed to cover the edges of the aircraft operational envelope and have a good statistical base for regression analysis.

COMPUTING WEIGHTED SCATTER FACTORS

It was shown earlier that scatter increases as N goes to the higher values on an *S/N* curve. So the scatter should be multiplied by damage at *N* values as a weighting consideration. This process is shown best by Equation 2.

Table 4. Key Regression Equation Variables

	Independent Variable			
Dependent Variable	1	2	3	4
Aileron position (*Da*)	*NyW/Q*	*IxxAx/Q*	*IzzAz/Q*	
Rudder position (*Dr*)	*IxxAx/Q*	*B*	*IzzAz/Q*	*NyW/Q*
Elevator position (*De*)	*IyyAy/Q*	*NzW(AC−CG)/Q*	*NzW/Q*	
Sideslip angle (*B*)	*NyW/Q*	*IzzAz/Q*		
Angle of attack (*Aa*)	*NzW/Q*	*NzW(AC−CG)*		
Wing stress	*NzW*	*NzSTW*	*NzFW*	
Vertical stab. stress	*BQ*	*DrQ*	*Ax*	
Horizontal stab. stress	*AaQ*	*DeQ*	*Ay*	
Wing/fuselage lug stress	*DaQ*	*BQ*	*NzW*	*Ay*

$$Vt = \frac{\sum\left[\left(\frac{n}{Nj}\right)Vj\right]}{\sum\left(\frac{n}{Nj}\right)} \tag{2}$$

The total weighted variation coefficient (Vt) is computed for the analysis locations on the S/N curve at j values.

FATIGUE LIFE EQUATION

The fatigue life damage at crack initiation (Di) is defined with Equation 3.

$$Di = \sum\left(\frac{n}{N}\right) - \frac{3Vt}{100} \tag{3}$$

An adjustment factor for crack initiation should be obtained from the full-scale cyclic test and is identified as Fc. When cracks start showing up in fleet aircraft, Fc should be replaced with Ff, which represents the adjustment factor for crack initiation in the fleet.

For all locations or elements with no alternate load path, not damage tolerant, noninspectable joints, critical crack length is so short it cannot be seen by visible inspection and helicopter rotor system parts, then use a safety factor ($Fs = 2$) for these designs. In addition, a safety factor of 1.5 should be used for the complete aircraft when using a low-confidence load environment, to help prevent fatigue modifications.

Weight reductions during design could affect fatigue life. The most common problem is an aircraft which is operated in a more severe load environment than that for which it was designed. In computing upper surface damage for flight, change the mean stress from negative to positive to agree with C-130 fleet damage data and to allow use of current *S/N* curves. Fatigue prediction correction factors are presented in References (1) and (4).

CRACK GROWTH ANALYSIS

Any fleet aircraft with cracks should be inspected periodically to validate crack growth predictions and define its location on the damage versus crack growth plot. The damage versus crack growth plot is the best way to define where individual aircraft are in the scatter distribution and their *Ff*. Residual strength for cracked structure is very important and analysis/test at the end of the full-scale cyclic test is required to define risk of aircraft flight with cracks. Crack growth analysis should begin on a fleet airplane when cracks are found during inspection.

The *Kt* of a crack is about 18, so crack growth is predictable and high loads cause retardation as they do in fatigue. Critical crack length is defined as the length at which theoretical failure will occur when limit load is applied. The crack growth analysis and fatigue analysis can be used as tools to define inspection requirements. Repair of areas which have cracks approaching critical length and their total number is basic data for defining the aircraft economic life. These methods provide a direct path for updating design criteria for strength and fatigue.

FLIGHT LOADS RECORDING

A large sample of fleet *Nz* recorder data is needed with altitude and airspeed to allow breakdown to mission segment spectra per aircraft type and mission. Also, a smaller sample of five-variable (*Nz, Ny, Ax, Ay,* and *Az*) multichannel recorder data is needed to expand mission segment *Nz* spectra to a five-variable spectra for the same or similar aircraft type.

HUMAN FACTORS

The current design of aircraft to a normal load factor is not good when fleet aircraft exceed this limit value more than once per each aircraft's life. The normal load factor limit value is mainly important for wing design. The methods presented in this paper allow the design per

fleet aircraft usage for crew and passenger safety, since about 80% of accidents are related to human factors. This method will greatly decrease risk by designing all structural components for the load environment experienced during the fleet usage.

AGING AIRCRAFT

The C-130 data gives a detailed view of what is occurring in aging aircraft structure and how inspections are needed to avoid unacceptable risks. These inspections allow those aircraft which do not have high risk cracking to be used much longer, even though they may have high flight hours.

CONCLUSIONS

In review of the interrogation of the C-130 fleet damage sources, ground-air-ground was almost twice as great for the lower surface as it was for the upper surface. Taxi damage was high for only the upper surface on the Shuttle mission, which included operations on unpaved runways. Gust damage was about the same for upper and lower surfaces for all nine missions. Missions with a high percentage of maneuver damage were Sky-Hook, Support, and Proficiency Training where the upper surface damage was a little higher than the lower surface damage. However, the damage rate per flight hour on the Support mission was low, thus the evasive maneuvers for missiles and ground fire would account for this maneuver damage.

The most extreme case is finding the 2–4*g* maneuvers on the Air Drop mission caused a small percentage of maneuver negative damage for the lower surface. Keep in mind the C-130 has a 2.5*g* design limit load factor. Extremely high loads such as C-130 air drops changed the shape of flaws and reduced the Kt only in the wing lower surface.

Compression load cycles on the wing upper surface must be considered during design. Actual damage in the C-130 fleet was linear and had low scatter.

The methods for design loads in this paper are needed to prevent pilots from taking their airplanes to nearly twice the design limit load, as occurred with the F-86's in Korea. Thus the load limiter concept may put the pilot in great danger in air-to-air combat.

Strength and fatigue design for composite structure can make use of these methods with consideration that flaws exist and in some cases they can be removed. In addition, the damaged hot wet specimens represent the worst case for structural conditions in the fleet. Risk of adhesive and resins to debond with age, temperature, and humidity effects is another problem designers must face.

Most of the NASA-airplane large statistical samples of normal load factor data include maneuvers with gust cycles superimposed on them. USAF recording programs for aircraft response also do not separate gust from maneuver, but do have a wider range of aircraft types.

There are many advantages for deriving one equation per material type and its family of *S/N* curves. First, the scatter and error due to interpolation are cut to a minimum. Also, high-cycle conditions such as buffet and helicopter rotor loads can be easily handled.

REFERENCES

1. Yost, J. D.: Correction Factors for Miner's Fatigue Damage Equation Derived From C-130 Fleet Aircraft Fatigue Cracks. AIAA-86-2684, Oct. 1986.

2. Yost, James D.; and Johnson, Guinn S.: Strength and Fatigue Loads Computed with a Load Environment Model. *AIAA J. of Aircraft*, vol. 9, no. 3, March 1972.

3. Yost, James D.; Jackson, Wayne B.; and Salter, L. Wayne: Improved Methods of Atmospheric Turbulence Prediction for Aircraft Design and Operation. *AIAA J. of Aircraft*, vol. 9, no. 4, April 1972.

4. Yost, James D.: Parameters Affecting Structural Fatigue Scatter Factors with Fatigue Life Defined as Critical Crack Length. Copyright James D. Yost, February 1972.

5. Yost, James D.: Reduction of Pressure Survey Data with Regression Analysis. SAE 760451, April 1976.

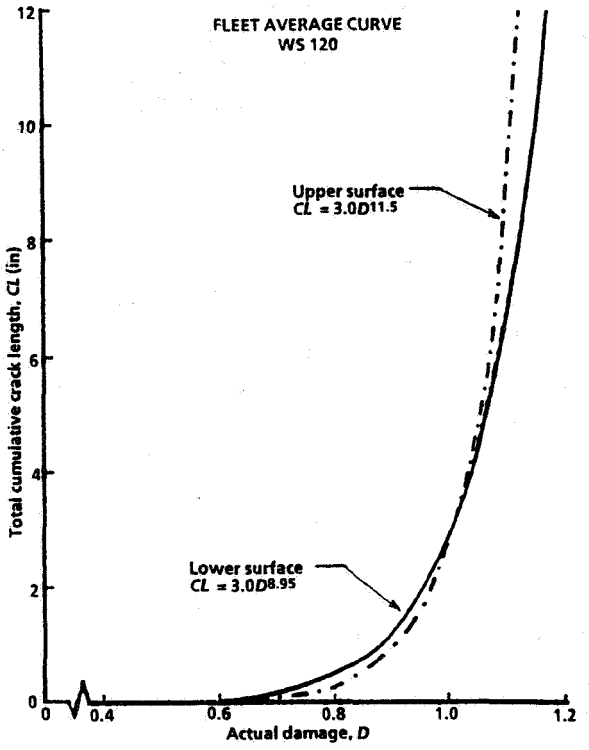

Figure 1. C-130 fatigue crack propagation.

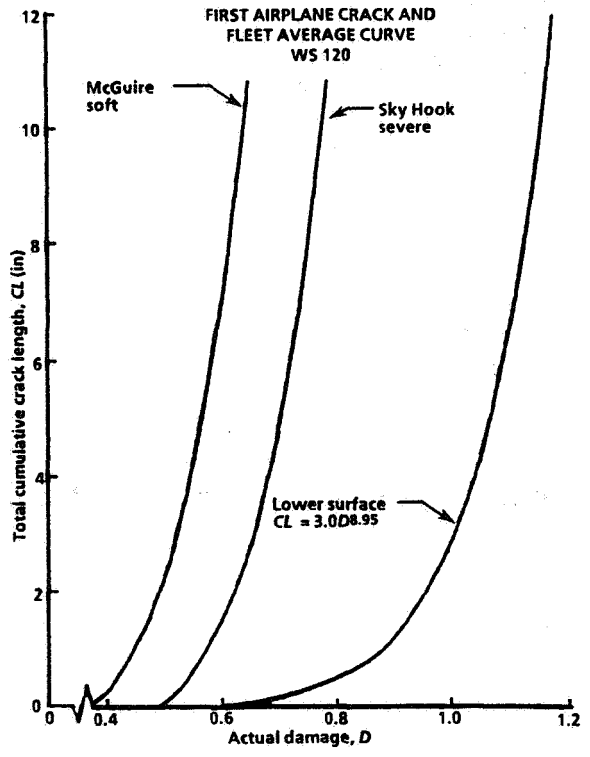

Figure 2. C-130 fatigue crack propagation: 1st aircraft on two missions.

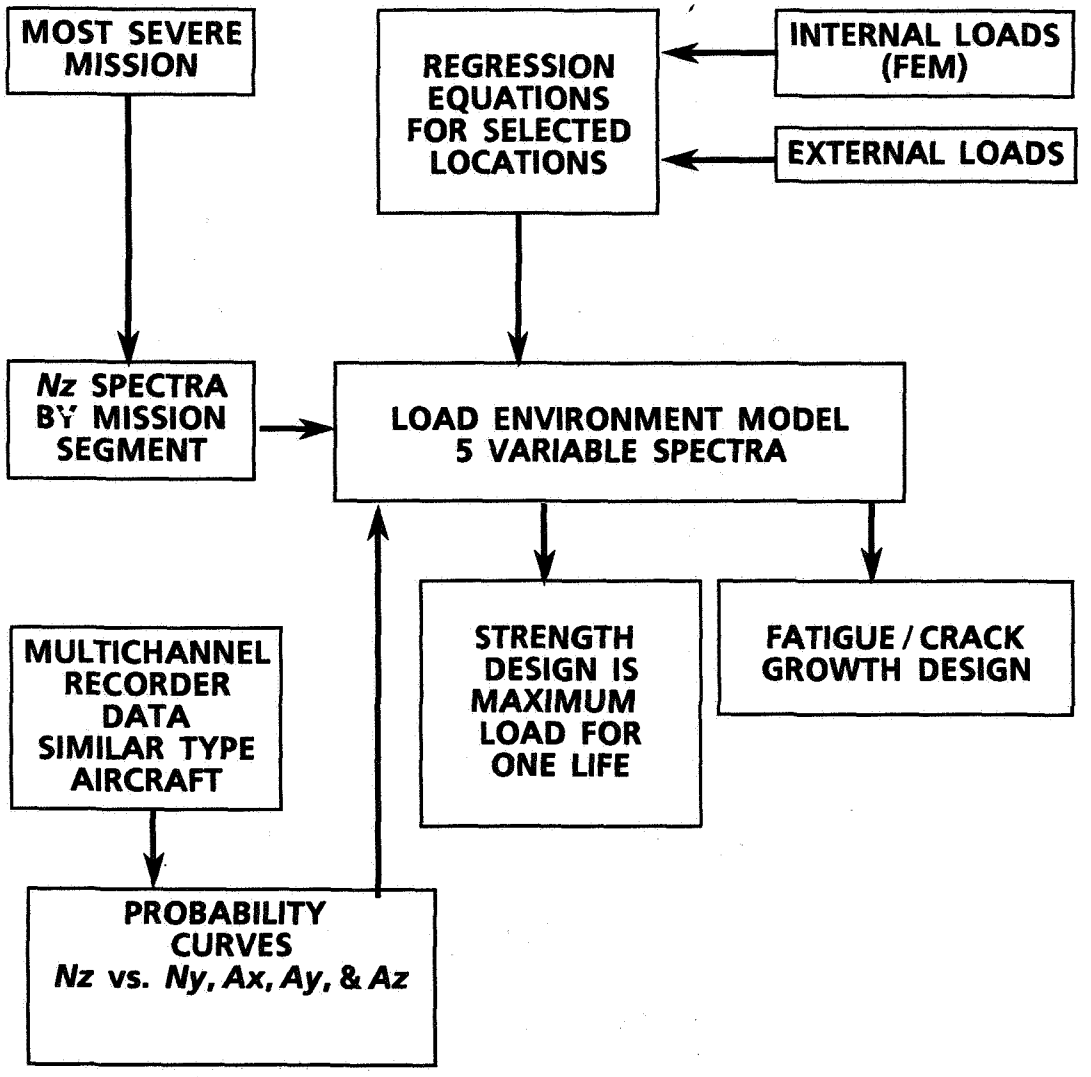

Figure 3. Design loads per structural component.

STRESS INTENSITY FACTORS FOR SURFACE AND CORNER CRACKS EMANATING FROM A WEDGE-LOADED HOLE[1]

W. Zhao and M.A. Sutton
University of South Carolina
Columbia, SC 29208

K.N. Shivakumar
North Carolina A & T State University
Greensboro, NC 27410

J.C. Newman, Jr.
NASA Langley Research Center
Hampton, VA 23681-0001

ABSTRACT

To assist analysis of riveted lap joints, stress intensity factors are determined for surface and corner cracks emanating from a wedge-loaded hole by using a 3-D weight function method in conjunction with a 3-D finite element method. A stress intensity factor equation for surface cracks is also developed to provide a closed-form solution. The equation covers commonly-encountered geometrical ranges and retains high accuracy over the entire range.

INTRODUCTION

Current damage tolerance analysis of aircraft structures is mainly based on linear elastic fracture mechanics, where the stress intensity factor is a key parameter. Surface and corner cracks emanating from circular holes are among the most common defects occurring in aircraft structures. Stress intensity factor solutions for these cracks are available in the literature for remote tension and remote bending [1-5]. Based on three-dimensional finite element solutions, the corresponding stress intensity factor equations were also developed [3], and are being used in a variety of applications. However,

---

[1] Work done on contract at University of South Carolina, NAG-1-1489.

for another important category of loading conditions (i.e. wedge loading of a cracked hole) very limited solutions [1,4] exist in the literature for corner cracks, and no solution is available for surface cracks. The primary interest in the wedge loading case lies in the fact that solutions for commonly encountered pin-loading case, such as the riveted lap joints shown in Fig.1, can be obtained by superposing solutions for remote tension, remote bending and wedge loading. The objective of this paper is to provide stress intensity factor solutions for surface and corner cracks emanating from a wedge-loaded hole, which can be used to obtain solutions for rivet loading. This is accomplished in two ways. First, an accurate and efficient 3-D weight function method [5] is extended to solve the problems by using stress distributions from a 3-D finite element analysis of the same, but otherwise uncracked, configuration. The weight-function analysis code covers a wide range of geometrical parameters and various loading conditions, and produces accurate solutions on Personal Computers. Second, a stress intensity factor equation for surface cracks is developed by curve-fitting procedures. This latter effort is to facilitate the determination of stress intensity factors for commonly-encountered surface cracks in damage tolerance analysis.

METHODS OF ANALYSIS

The crack configurations to be considered are shown in Fig.2 together with the definition of relevant parameters (infinite plate width and height assumed). The 3-D weight function method is used in combination with the 3-D finite element method to solve these problems. This combined approach takes optimal advantage of both methods. The weight function method is accurate and efficient in solving 3-D crack configurations. However, its accuracy can not be guaranteed without using, as input, an accurate stress solution for the same, but otherwise uncracked, configuration. For crack configurations involving stress concentrations (such as a hole or notch), the stress distribution in the region of uncracked configuration where cracks will occur has a fully 3-D nature, the stress varies not only in plate-width direction but also in thickness directions, even though the applied load does not change through the plate thickness. This 3-D effect manifests itself most near the intersection of the hole with the plate surface for small r/t ratios (see for example [6,7]). Therefore, to account for this 3-D nature, a 3-D finite element analysis was performed [7] to provide the normal stress distributions. Because the finite element analysis involves no cracks, only one finite element calculation is required for each r/t ratio. The normal stress distribution obtained from the finite element analysis is then fitted into the following equation:

$$\sigma(x,y)/\sigma_0 = \sum_{i=1}^{I}\sum_{j=1}^{J} C_{ij}\left(\frac{x}{r}\right)^{2-2i}\left(\frac{y}{t}\right)^{2j-2} \qquad (1)$$

Equation (1) is used in the following weight function equations:

$$K_a(x,a_x) = \int_0^{a_x} [\sigma(x,y) - P(x,y)]\, W_a(a_x,y)dy \tag{2a}$$

$$K_c(y,c_y) = \int_0^{c_y} P(x,y)\, W_c(c_y,x)dx \tag{2b}$$

where $K_a(x,a_x)$ and $K_c(y,c_y)$ are, respectively, stress intensity factors for a-slice and c-slice, intersecting at point (x,y) on the crack front (see Fig. 2 (d) and (e)), and W_a and W_c are the weight functions. The stress intensity factors for the 3-D crack, $K(\varphi)$, are then obtained by eq.(3):

$$K(\varphi) = \frac{(-1)^n}{1-\eta^2(\nu, a/c, \Delta\varphi)} \left\{ K_a^4(x,a_x) + \left[\frac{E}{E_s} K_c(y,c_y) \right]^4 \right\}^{\frac{1}{4}} \tag{3}$$

For further details of the weight function method, please refer to [5].

RESULTS AND COMPARISONS

The stress intensity factors are presented in a dimensionless form defined as:

$$F(\varphi) = K(\varphi)/(\sigma\sqrt{\pi a/Q}) \tag{4}$$

in which σ is a reference stress, and equal to remote uniform stress for remote tension, and $\sigma=P/(2rT)$ for wedge loading, where P is the total applied force along the bore of the hole.

Corner Cracks

Reference [1] provides stress intensity factors for wedge loading with a cosine squared pressure distribution, while the present weight function solutions are for wedge loading with a cosine pressure distribution. However, the difference caused by the different pressure distributions will be negligible, as long as the c/r ratio of cracks exceeds about 0.8. The following comparisons are made for such cases. Figure 3 shows the comparison of the weight function results with the finite element solution [1]. Very good agreement is observed. Figure 4 (a) shows the difference between a single corner crack and double corner cracks. Figure 4 (b) gives the stress intensity factor ratio of double corner

cracks over single corner cracks. The corresponding estimate by using Shah's empirical formula [8] and the ratios for through-the-thickness cracks [9] are also shown in Fig. 4 (b).

Surface Cracks

The comparison with finite element solution [3] for surface cracks is made for remote tension, since no solution is available for surface cracks under wedge loading in the literature. Figure 5 shows the comparison. Again, very good agreement is observed. To examine the behavior of the weight function method, some limiting cases are also considered as $a/c \to 0$ and ∞. Figures 6 (a) and (b) show these limiting cases. It is clear that the appropriate 2-D limits are reached under the limiting conditions.

STRESS INTENSITY FACTOR EQUATION FOR SURFACE CRACKS

In many situations, a closed-form solution is desirable, as evidenced by the popularity of the previous stress intensity factor equations for other cases [3]. Therefore, an effort is made to develop an equation for double surface cracks under wedge loading based on the weight function solutions. The applicable range of the equation is chosen to be $1 \le r/t \le 5$, $0.5 \le a/c \le 2$ and $0.005 \le a/t \le 0.9$. This range is believed to cover most cases encountered in practice. If a problem does go beyond this range, then the weight function code is directly used. The equation is developed separately at 0° and 90° only, so as to reduce the number of independent variables from 4 to 3 (r/t, a/c and a/t). The general form of the equation is:

$$K(\varphi) = \sigma\sqrt{\pi a/Q}F(\varphi) \quad \varphi = 0°, 90° \tag{5}$$

The developments for F(90°) and F(0°) are described in the following sections.

Development of F(90°)

The form of F(90°) is:

$$F(90°) = (\frac{a}{c})^{\gamma} f_9(\frac{r}{t}, \frac{a}{c}, \frac{a}{t}) \tag{6}$$

where $\gamma=0$ for $a/c \leq 1$, and $\gamma=-1$ for $a/c > 1$. The f_9 function is given below:

$$f_9(\frac{r}{t}, \frac{a}{c}, \frac{a}{t}) = g_9(\frac{r}{t}, \frac{a}{c}, \frac{a}{t}) f_{sa}(\frac{x}{r}, \frac{a}{t}) \tag{7}$$

where g_9 is a fitting function, and f_{sa} is a combination of the two functions $f_s(x/r)$ and $f_a(a/t)$.
The $f_s(x/r)$ is the dimensionless normal stress distribution along the x-axis for a wedge loaded hole in an infinite plate. According to Rooke & Tweed [10], $f_s(x/r)$ is expressed as:

$$f_s(\frac{x}{r}) = \frac{\sigma(x)}{\sigma} = \frac{4}{\pi}\left\{3 + \frac{1}{(1+\frac{x}{r})^2} + \frac{1+2(1+\frac{x}{r})^2 - 3(1+\frac{x}{r})^4}{2(1+\frac{x}{r})^3} \ln\left[\frac{2+\frac{x}{r}}{\frac{x}{r}}\right]\right\} \tag{8}$$

The $f_a(a/t)$ is the dimensionless stress intensity factor for collinear cracks, and given as [11]:

$$f_a(\frac{a}{t}) = \left[\tan(\frac{\pi a}{2t})/(\frac{\pi a}{2t})\right]^{\frac{1}{2}} \tag{9}$$

The introduction of f_s and f_a is based on the consideration that $F(90°)=f_s(0)*f_a(a/t)$ as $a/c \to 0$. Using f_s and f_a, f_{sa} is defined as:

$$f_{sa}(\frac{c}{r}, \frac{a}{t}) = \frac{1}{4}\left[3 f_s(0) f_a(\frac{a}{t}) + f_s(\frac{c}{r}) f_a(0)\right] \tag{10}$$

The use of f_{sa} is to bring in some of the contributions of the rest of the crack to F(90°). The use of these functions is believed to be very helpful in fitting complicated functions involving multiple variables in a wide range. The g_9 is fitted in the following form:

$$g_9(\frac{r}{t}, \frac{a}{c}, \frac{a}{t}) = \alpha_1(\frac{r}{t}, \frac{a}{t}) * (\frac{a}{c})^{\alpha_2(\frac{r}{t}, \frac{a}{t})} \tag{11}$$

The functions $\alpha_1(r/t,a/t)$ and $\alpha_2(r/t,a/t)$ are expressed as:

$$\alpha_1(\frac{r}{t},\frac{a}{t})=\left\{\alpha_{11}(\frac{r}{t})+\alpha_{12}(\frac{r}{t})*(\frac{a}{t})^3\right\}*\exp\left[\alpha_{13}(\frac{r}{t})*(\frac{a}{t})\right]$$

$$\alpha_{11}(\frac{r}{t})=\alpha_{111}*(\frac{r}{t})^{\alpha_{112}}$$

$$\alpha_{12}(\frac{r}{t})=\alpha_{121}+\alpha_{122}*(\frac{r}{t}) \tag{12}$$

$$\alpha_{13}(\frac{r}{t})=\alpha_{131}+\alpha_{132}*(\frac{r}{t})+\alpha_{133}(\frac{r}{t})^2$$

$$\alpha_2(\frac{r}{t},\frac{a}{t})=\left\{\alpha_{21}(\frac{r}{t})+\alpha_{22}(\frac{r}{t})*(\frac{a}{t})+\alpha_{23}(\frac{r}{t})*(\frac{a}{t})^2\right\}*\cos\left[\alpha_{24}(\frac{r}{t})*(\frac{a}{t})^3\right] \tag{13}$$

$$\alpha_{2i}(\frac{r}{t})=\alpha_{2i1}+\alpha_{2i2}*(\frac{r}{t})+\alpha_{2i3}*(\frac{r}{t})^2+\alpha_{2i4}*(\frac{r}{t})^3,\quad i=1,2,3,4.$$

The α parameters with 3-digit subscripts are constants, and listed in Table 1.

Development of F(0°)

The functional form of F(0°) is given as:

$$F(0°)=(\frac{a}{c})^{\lambda}f_0(\frac{r}{t},\frac{a}{c},\frac{a}{t}) \tag{14}$$

where λ=1/2 for a/c≤1, and λ=-1/2 for a/c>1. The f_0 function is given below:

$$f_0(\frac{r}{t},\frac{a}{c},\frac{a}{t})=g_0(\frac{r}{t},\frac{a}{c},\frac{a}{t})f_c(\frac{c}{r})t_0(\frac{r}{t},\frac{a}{c},\frac{a}{t}) \tag{15}$$

where g_0 and t_0 are fitting functions, and f_c is a weighted average of $f_{c0}(c/r)$. The latter is the dimensionless stress intensity factor for through-the-thickness cracks under the same loading, and given as:

$$f_{c0}(\frac{c}{r})=1.788-4.935(\frac{c}{r})+8.527(\frac{c}{r})^2-7.790(\frac{c}{r})^3+3.450(\frac{c}{r})^4-0.5832(\frac{c}{r})^5 \tag{16}$$

Then, f_c is defined as:

$$f_c(\frac{c}{r}) = \frac{1}{4}\left[3f_{c0}(\frac{c}{r}) + f_{c0}(0)\right] \tag{17}$$

Similarly to F(90°), the introduction of f_{c0} is based on the consideration that $F(0°)=f_{c0}(c/r)$ as $a/c\to\infty$. And f_c is used to bring in some of the contributions of the rest of the crack to F(0°). The g_0 is fitted in the following form:

$$g_0(\frac{r}{t},\frac{a}{c},\frac{a}{t}) = \beta_1(\frac{r}{t},\frac{a}{t}) * (\frac{a}{c})^{\beta_2(\frac{r}{t},\frac{a}{t})} \tag{18}$$

The functions $\beta_1(r/t,a/t)$ and $\beta_2(r/t,a/t)$ are expressed as:

$$\begin{gathered}
\beta_1(\frac{r}{t},\frac{a}{t}) = \beta_{11}(\frac{r}{t}) * Exp\left[\beta_{12}(\frac{r}{t}) * (\frac{a}{t}) + \beta_{13}(\frac{r}{t}) * (\frac{a}{t})^3\right] \\
\beta_{11}(\frac{r}{t}) = \beta_{111} + \beta_{112} * (\frac{r}{t}) \\
\beta_{12}(\frac{r}{t}) = \beta_{121} + \beta_{122} * (\frac{r}{t}) + \beta_{123} * (\frac{r}{t})^2 + \beta_{124} * (\frac{r}{t})^3 \\
\beta_{13}(\frac{r}{t}) = \beta_{131} + \beta_{132} * (\frac{r}{t}) + \beta_{133}(\frac{r}{t})^2
\end{gathered} \tag{19}$$

$$\begin{gathered}
\beta_2(\frac{r}{t},\frac{a}{t}) = \left\{\beta_{21}(\frac{r}{t}) + \beta_{22}(\frac{r}{t}) * (\frac{a}{t})^{\frac{1}{2}}\right\} * Exp\left\{\beta_{23}(\frac{r}{t}) * (\frac{a}{t}) + \beta_{24}(\frac{r}{t}) * (\frac{a}{t})^2\right\} \\
\beta_{2i}(\frac{r}{t}) = \beta_{2i1} + \beta_{2i2} * (\frac{r}{t}) + \beta_{2i3} * (\frac{r}{t})^2 + \beta_{2i4} * (\frac{r}{t})^3, \quad i=1,2,3. \\
\beta_{24}(\frac{r}{t}) = \beta_{241} + \beta_{242} * (\frac{r}{t}) + \beta_{243} * (\frac{r}{t})^2
\end{gathered} \tag{20}$$

The β parameters with 3-digit subscripts are constants and listed in Table 2. The t_0 is a fine-tuning function and equal to 1 for $a/t<0.2$, and fitted as follows for $a/t\geq 0.2$:

$$t_0\left(\frac{r}{t},\frac{a}{c},\frac{a}{t}\right)=p_1\left(\frac{r}{t},\frac{a}{t}\right)+p_2\left(\frac{r}{t},\frac{a}{t}\right)*\left(\frac{a}{c}\right)^{\frac{1}{4}}+p_3\left(\frac{r}{t},\frac{a}{t}\right)*\left(\frac{a}{c}\right)^{\frac{1}{2}}$$

$$p_i\left(\frac{r}{t},\frac{a}{t}\right)=p_{i0}\left(\frac{a}{t}\right)+p_{i1}\left(\frac{a}{t}\right)*\left(\frac{r}{t}\right)+p_{i2}\left(\frac{a}{t}\right)*\left(\frac{r}{t}\right)^2+p_{i3}\left(\frac{a}{t}\right)*\left(\frac{r}{t}\right)^3 \quad i=1,2,3. \tag{21}$$

$$p_{ij}\left(\frac{a}{t}\right)=p_{ij0}+p_{ij1}*\left(\frac{a}{t}\right)+p_{ij2}*\left(\frac{a}{t}\right)^2 \quad j=0,1,2,3.$$

The constants p_{ijk} for t_0 are given in Table 3.

Comparison of Equation with Weight Function Data

The accuracy of the equation is examined by comparing it with the original weight function data. Figures 7 (a) and (b) give F(90°) and F(0°) versus a/t, respectively. The variations of F(90°) and F(0°) with a/c are shown in Figs. 8 (a) and (b), respectively, which are for a/t=0.9, the largest a/t ratio considered. The largest deviation of the equation with the weight function data occurs at this a/t ratio for F(90°). From Fig. 8 (a) the maximum deviation is within 3%. Figures 9 (a) and (b) show F(90°) and F(0°) versus r/t, respectively. It is seen that the equation is generally within 2% of the weight function data, with maximum error of about 3% in the whole range considered.

CONCLUSIONS

Based on the above analysis and results, the following conclusions can be made:

1. The combination of the 3-D weight function method and the 3-D finite element method is an efficient approach to solve 3-D crack problems involving stress concentrations.

2. Accurate stress intensity factors are provided for surface and corner cracks emanating from a wedge-loaded hole.

3. A stress intensity factor equation is developed for double surface cracks. The equation covers commonly-encountered geometrical ranges and retains very good accuracy.

REFERENCES

1. Raju, I.S.; and Newman, J.C.,Jr.: Stress intensity factors for two symmetric corner cracks. ASTM STP 677, C.W. Smith, Ed., pp.411-430, 1979.

2. Grandt, A.F., Jr.; and Kullgren, T.E: Stress intensity factors for corner cracked holes under general loading conditions. J. Engng. Materials Technology 103, pp.171-176, 1981.

3. Newman, J.C., Jr.; and Raju, I.S.: Stress intensity factor equations for cracks in three-dimensional finite bodies. ASTM STP 791, Lewis, J.C. and Sines, G., Ed., pp.I-238-256, 1983.

4. Nishioka, T.; and Atluri, S.N.: Integrity analysis of surfaced-flawed aircraft attachment lugs: a new, inexpensive, 3-D alternating method. Paper 82-0742, AIAA/ASME/ASCE/AHS 23rd Structures, Structural Dynamics and Materials Conference, May 10-12, pp.287-300, 1982.

5. Zhao, W.; Wu, X.R.; and Yan, M.G.: Weight function method for three dimensional crack problems-II. Engng. Fracture Mech. Vol.34, No.3, pp.609-624, 1989.

6. Folias, E.S.: Some remarks on three-dimensional fracture. ASTM STP 969, T.A. Cruse, Ed., pp.56-72, 1988.

7. Shivakumar, K.N.; and Newman, J.C. Jr.: Stress concentrations for straight-shank and countersunk holes in plates subjected to tension, bending, and pin loading. NASA-TP-3193, 1992.

8. Shah, R.C.: Stress intensity factors for through and part-through cracks originating at a fastener hole. ASTM STP 590, pp.429-459, 1976.

9. Wu, X.R.; and Carlsson, J.: Weight functions and stress intensity factor solutions. Pergamon press, 1991.

10. Rooke, D.P.; and Tweed, J.: Stress intensity factors for a crack at the edge of a loaded hole. Int. J. Engng. Sci. 18, pp.109-121, 1980.

11. Sneddon, I.N.; and Srivastav, R.P., The stress in the vicinity of an infinite row of collinear cracks, Proc. R. Soc. Edinb., Section A, Vol.67, p.39, 1963-64.

Table 1. Coefficients of g_9 function

	1	2	3	4
α_{11i}	1.292	-0.02280		
α_{12i}	-0.6158	0.03094		
α_{13i}	-0.3834	0.1790	-0.02065	
α_{21i}	0.06285	0.01986	-0.008287	0.0009832
α_{22i}	0.1827	-0.2219	0.08763	-0.01045
α_{23i}	0.09046	-0.02106	-0.02337	0.005125
α_{24i}	1.871	-0.7457	0.4400	-0.05090

Table 2. Coefficients of g_0 function

	1	2	3	4
β_{11i}	0.9708	-0.005293		
β_{12i}	-1.415	0.7752	-0.1815	0.01502
β_{13i}	0.4926	-0.1570	0.01652	
β_{21i}	0.0007527	0.05418	-0.02149	0.002344
β_{22i}	0.4667	-0.4266	0.1586	-0.01709
β_{23i}	3.345	0.04976	-0.6747	0.1018
β_{24i}	-3.626	1.941	-0.2248	

Table 3. Coefficients of t_0 function

	1	2	3
p_{10i}	6.89367	-53.6151	50.8248
p_{11i}	-4.08538	40.9391	-46.3484
p_{12i}	0.677014	-9.35989	12.1718
p_{13i}	-0.0226694	0.668142	-1.00152
p_{20i}	-12.0523	108.472	-102.842
p_{21i}	8.63812	-84.3581	94.9457
p_{22i}	-1.60061	20.0463	-25.5194
p_{23i}	0.0778192	-1.51170	2.15760
p_{30i}	5.83664	-53.1766	50.5411
p_{31i}	-4.20676	41.6555	-46.9805
p_{32i}	0.801768	-10.0724	12.7830
p_{33i}	-0.0421292	0.778241	-1.09613

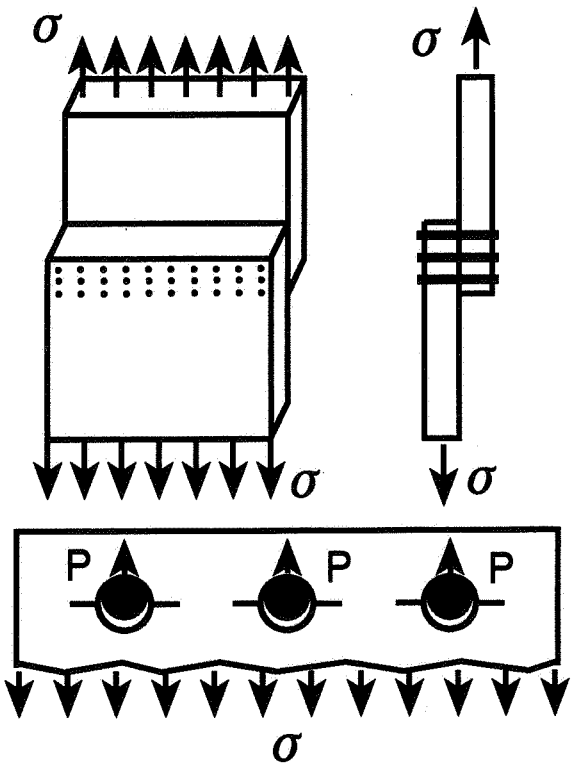

$$K_{pin} = (K_{tension} + K_{wedge})/2 + K_{bending}$$

Fig.1 Riveted lap joints with cracks.

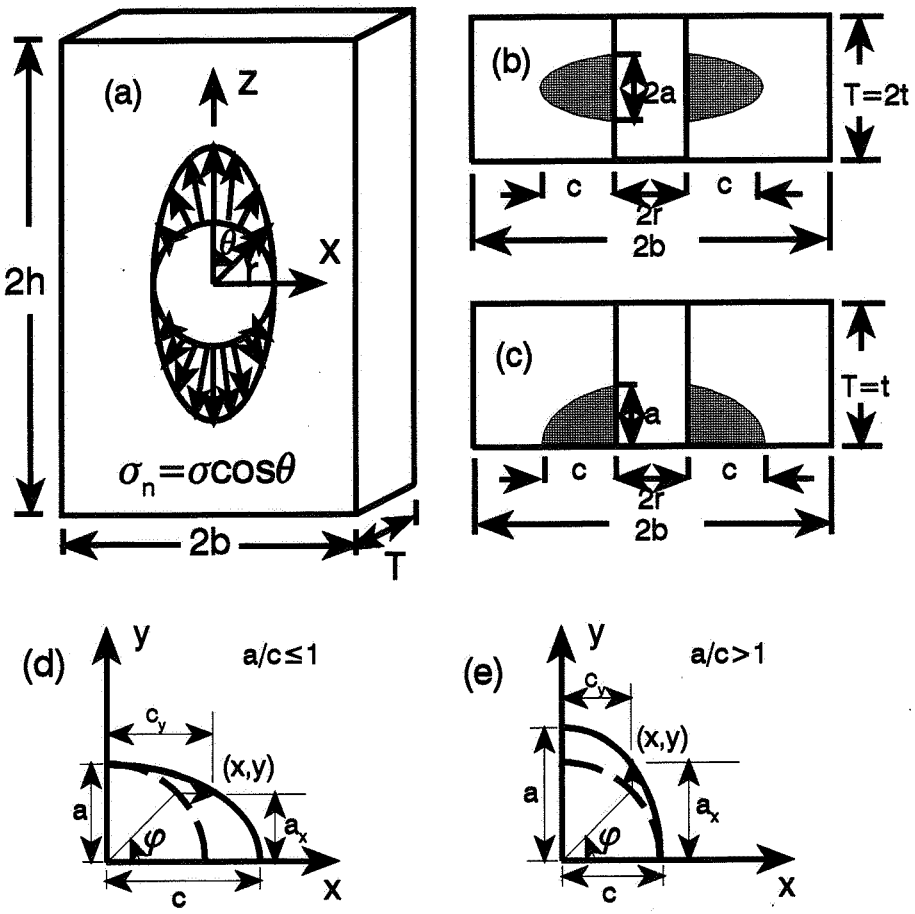

Fig.2 (a) wedge-loaded hole, (b) surface cracks, (c) corner cracks, (d) & (e) crack front coordinates.

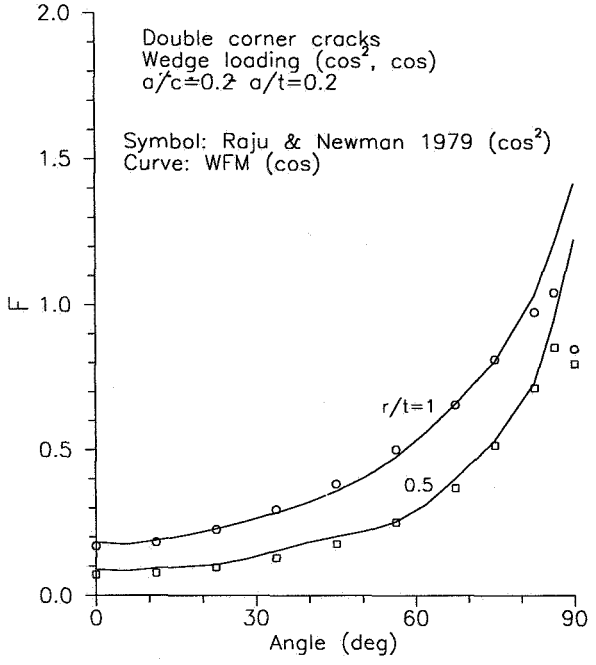

Fig.3 Comparison of dimensionless stress intensity factors with finite element solutions.

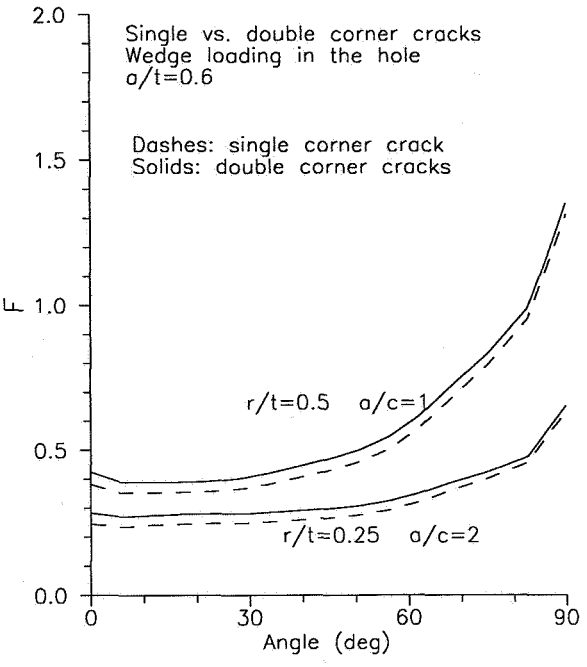

Fig. 4 (a) Comparison between single crack and double cracks.

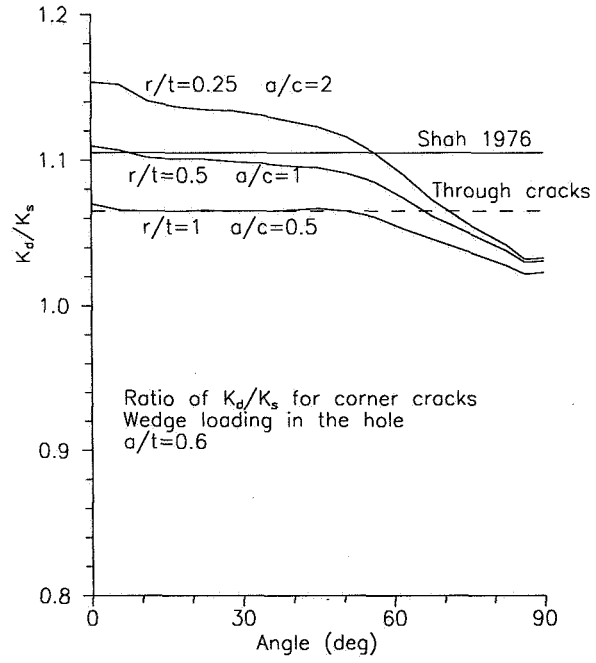

Fig. 4 (b) Ratios of stress intensity factors of double cracks to single cracks.

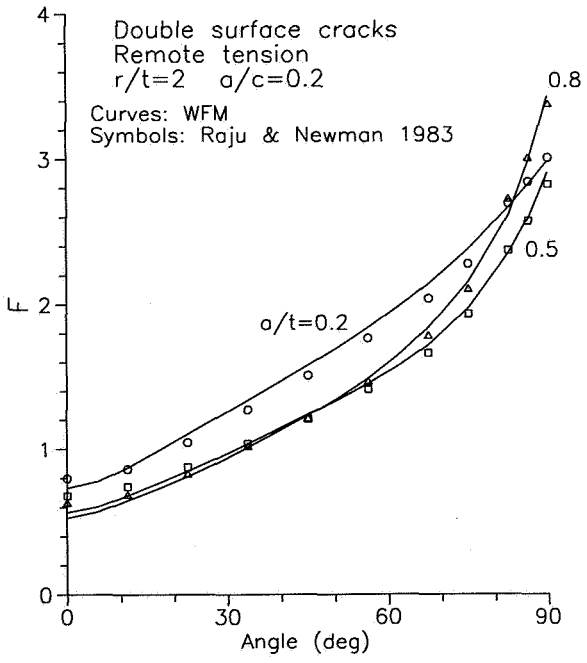

Fig. 5 Comparison with finite element solutions for surface cracks under remote tension.

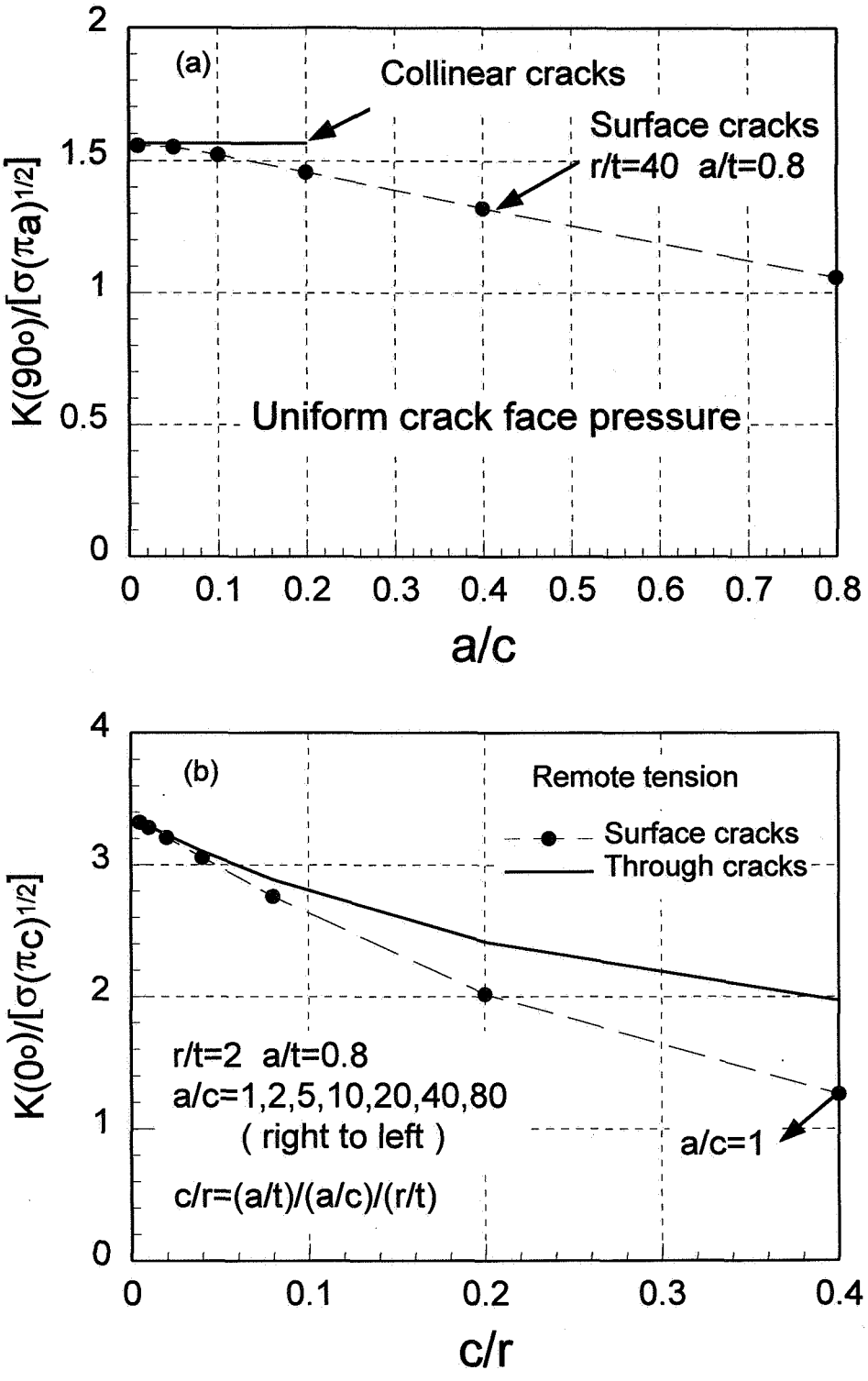

Fig. 6 Limiting behavior as (a) a/c tends to 0, (b) a/c tends to infinity.

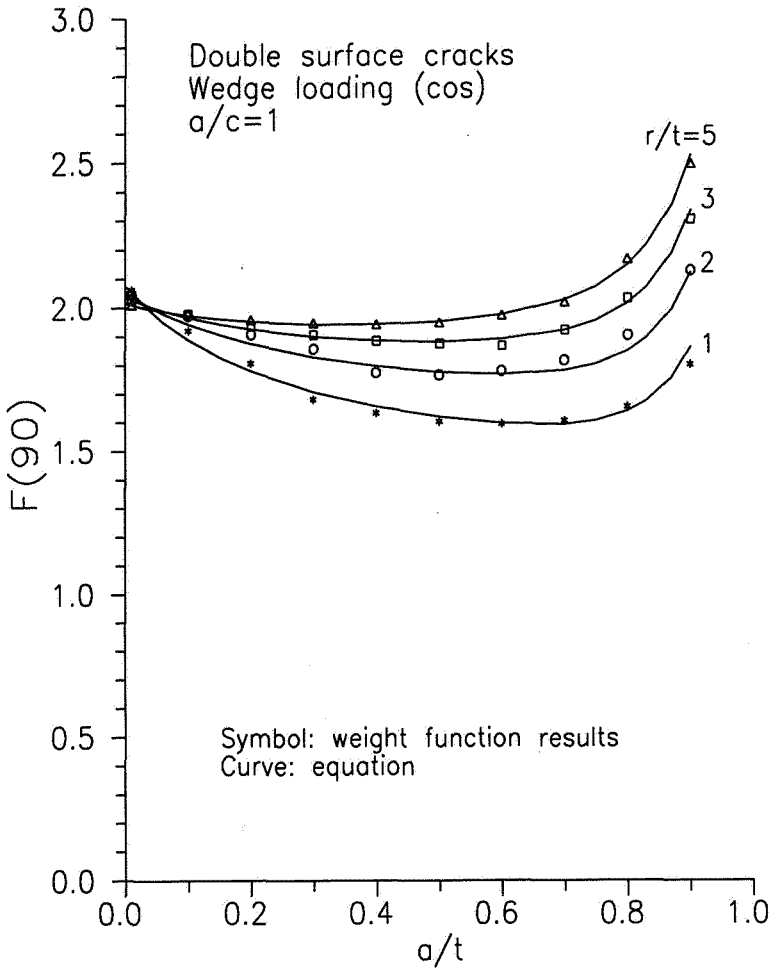

(a)

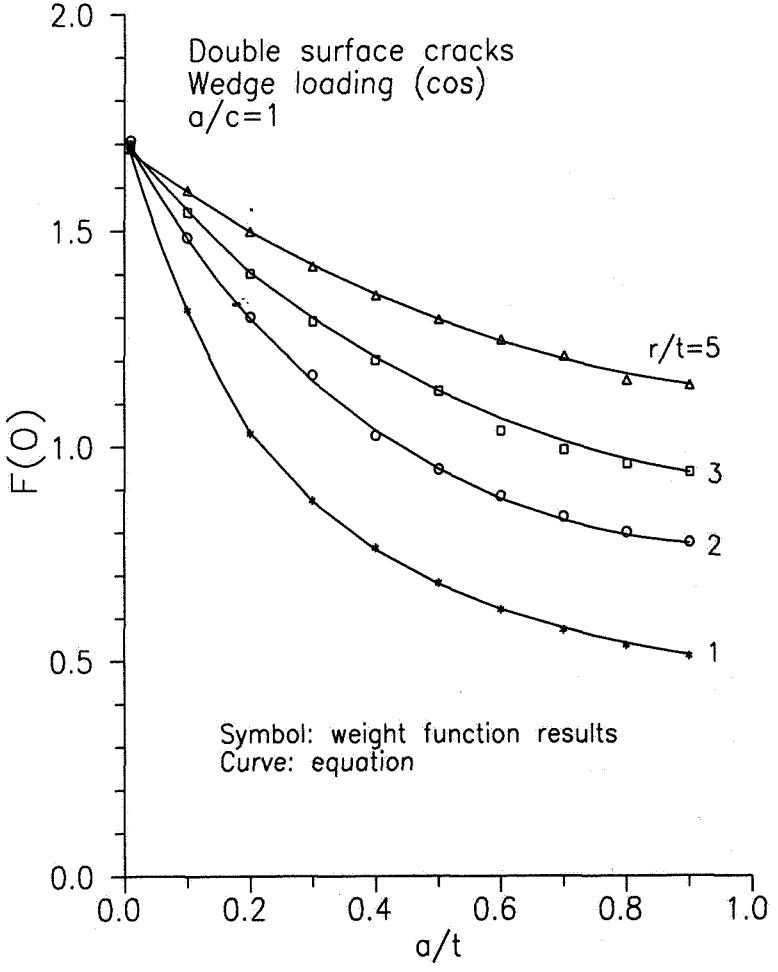

(b)

Fig. 7 Comparison of the equation with original data, (a) at 90 degree, (b) at 0 degree.

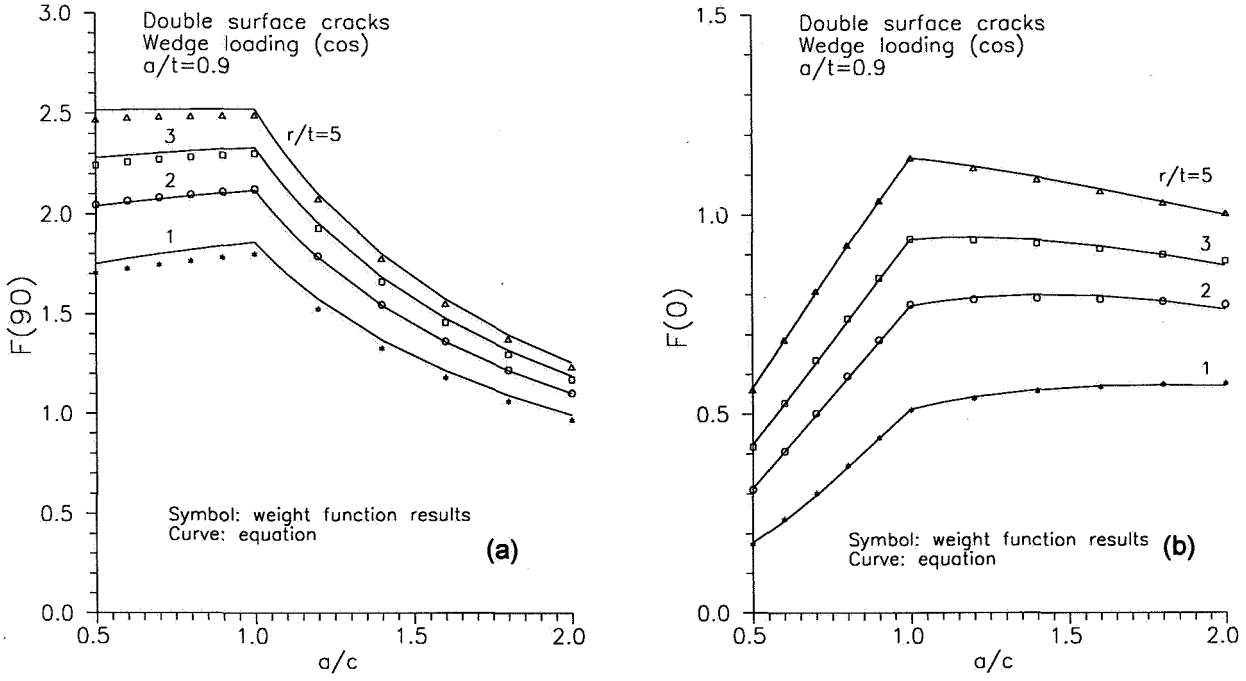

Fig. 8 Comparison of the equation with original weight function data, (a) at 90 degree, (b) at 0 degree.

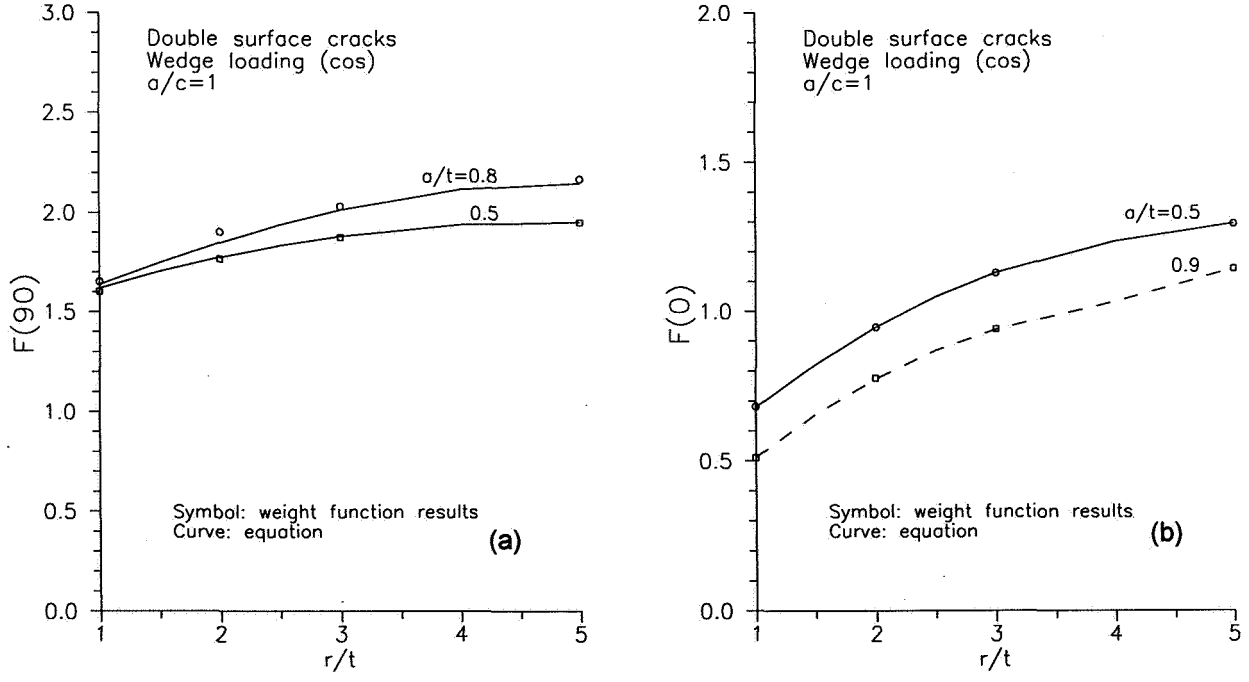

Fig. 9 Dimensionless stress intensity factor as a function of r/t ratio, (a) at 90 degree, (b) at 0 degree.

Nonlinear Analysis of Damaged Stiffened Fuselage Shells Subjected to Combined Loads

James H. Starnes, Jr.[1], Vicki O. Britt[1], Richard D. Young[2], Charles C. Rankin[3], Charles P. Shore[1] and Nancy Jane C. Bains[1]

[1]NASA Langley Research Center
Hampton, VA

[2]Lockheed Engineering and Sciences Company
Hampton, VA

[3]Lockheed Palo Alto Research Laboratory
Palo Alto, CA

Abstract

The results of an analytical study of the nonlinear response of stiffened fuselage shells with long cracks are presented. The shells are modeled with a hierarchical modeling strategy that accounts for global and local response phenomena accurately. Results are presented for internal pressure and mechanical bending loads. The effects of crack location and orientation on shell response are described. The effects of mechanical fasteners on the response of a lap joint and the effects of elastic and elastic-plastic material properties on the buckling response of tension-loaded flat panels with cracks are also addressed.

Introduction

Transport fuselage shell structures are designed to support combined internal pressure and mechanical flight loads which can cause a geometrically nonlinear response of the shell. The structural response of a stiffened fuselage shell with one or more local cracks is influenced by the local stress and displacement gradients near the cracks and the internal loads in the shell. The response of a stiffened fuselage shell with a crack must be understood to determine the structural integrity of the fuselage and to predict its residual strength. As a crack grows in a stiffened shell, the stiffness and internal load distributions change, and these changes affect the local stress and displacement gradients near the crack in a manner that may cause additional crack growth. The structural integrity of a stiffened fuselage shell that has a crack and that is subjected to combinations of internal pressure and mechanical flight loads can be studied analytically with a nonlinear structural analysis procedure that models crack growth in the shell.

The present paper describes the results of an analytical study of the nonlinear response of stiffened fuselage shells that are subjected to combined

internal pressure and mechanical loads and that have long cracks. A hierarchical modeling strategy is used to represent the global and local response characteristics of stiffened shells with long cracks. This modeling strategy uses sufficient modeling detail to predict accurately the local stress and displacement gradients in a shell. These local gradients are caused by cracks in the shell and by structural details such as frames, stringers, failsafe straps, and joints. The STAGS (STructural Analysis of General Shells) nonlinear shell analysis code (Ref. 1) is used to predict the geometrically nonlinear response of the shells studied. The hierarchical global-local modeling strategy allows the internal load distribution and local stress and displacement gradients to be simulated accurately as the loads are increased and the crack grows.

The nonlinear analysis procedure and the modeling approach used in the present study are described herein. The analysis procedure used in the present study maintains the shell in a nonlinear equilibrium state while a crack is grown in the shell. Analytical results are presented for stiffened shells of practical interest that are subjected to combined internal pressure and mechanical bending loads. These results demonstrate the effects of combined loads on the global response of shells with longitudinal and circumferential skin cracks and on the local stress and deflection gradients near the cracks. The effects of changing crack length and other geometric parameters on nonlinear response for different loading conditions are also discussed.

Nonlinear Analysis and Modeling Procedures

A nonlinear shell analysis procedure combined with a hierarchical modeling strategy is used in the present study to analyze the nonlinear response of stiffened fuselage shells with long skin cracks and subjected to combined internal pressure and mechanical loads. The analysis procedure simulates crack growth within a shell that is in a nonlinear equilibrium state. The analysis procedure includes the capability to examine local response phenomena, such as local stress and displacement gradients, in critical areas of a fuselage where cracks may be growing. The analysis procedure accurately models frame and stringer cross-sectional distortion and rolling and predicts the nonlinear interactions that occur between individual structural elements and larger subcomponents that result from these deformations. The details of this analysis and modeling procedure are discussed subsequently.

Nonlinear Analysis Procedure

The STAGS (STructural Analysis of General Shells) nonlinear finite element analysis code (ref. 1) is used in the present study to conduct the nonlinear structural analyses of stiffened shells with long cracks. STAGS is a finite element code for analyzing general shells that includes the effects of geometric and material nonlinearities in the analysis. STAGS is capable of conducting strength, stability and collapse analyses for general shell structures. The code uses both the modified and full Newton methods for its nonlinear solution algorithms and accounts for large rotations of a shell by using a co-

rotational algorithm at the element level. STAGS has static and transient analysis capabilities that can be used to predict local instabilities and modal interactions that occur due to the addition of destabilizing mechanical loads such as an applied bending moment. The Riks arc-length projection method is used in STAGS to continue the solution past the limit points of a nonlinear response. A boundary constraint function, based on a least-squares analysis, is used in STAGS to apply equivalent beam loads to the boundary of the thin shell finite element model. By using this least-squares constraint function, flight loads can be extracted from a global aircraft structural model and then applied as edge loads on the boundaries of a refined finite element model of a fuselage shell section as shown in figure 1.

STAGS can perform crack-propagation and residual-strength analyses and can represent the effects of crack growth on nonlinear shell response. A virtual crack extension method and a load relaxation technique are used in STAGS to extend the length of a crack while the shell is in a nonlinear equilibrium state. With this method, the forces necessary to hold the nodes together along the path of new crack growth are calculated. These forces are then released and a new equilibrium state is calculated which corresponds to the additional crack growth. The changes in the stiffness matrix and internal load distribution that occur during crack growth are accounted for in the analysis, and the nonlinear coupling between internal forces and inplane and out-of-plane displacement gradients that occurs in a shell is properly represented. STAGS has an adaptive mesh refinement capability that models self-similar and non-self-similar crack-growth trajectories and can model changes in shell response due to a change in the direction of crack growth. Non-self-similar crack growth, which is determined by using an adaptive mesh refinement technique, is modeled using the crack simulation code FRANC3D (ref. 2). FRANC3D includes an automatic mesh generator that can model an arbitrary region surrounding a crack. When modeling non-self-similar crack growth, FRANC3D is used as a graphical interface between the user and STAGS. Cracks in structural elements, such as frames, stringers, and tear straps, can also be modeled by STAGS. Results from STAGS calculations include strain energy release rates and stress intensity factors which can be used to calculate the residual strength of a damaged shell.

Hierarchical Modeling Procedure

A hierarchical stiffened-shell modeling strategy is used herein for the analysis of stiffened fuselage sections as shown in figure 2. The hierarchical modeling strategy begins with a global nonlinear analysis of a large stiffened fuselage section that is subjected to combined internal pressure and mechanical loads. The mechanical loads are applied to the ends of the fuselage section and can include axial and vertical shear loads, torsion, and bending moments. The global model includes structural details such as frames, stringers, tear straps, shear clips, and floor beams. The frames, which have a nonsymmetric cross section, are modeled with beam and shell elements in order to represent accurately the cross-sectional bending of the frame. The stringers, shear clips, tear straps, and floor beams are modeled with beam elements. Damage is included in the model in the form of longitudinal or circumferential cracks and

may also include broken frames, stringers, and tear straps. Displacements and internal forces are obtained from the analysis of the global model and are then used as boundary conditions in the next level of modeling detail used in the hierarchical modeling strategy.

The second level of modeling detail used in the hierarchical modeling procedure is a stiffened-panel structural model (see figure 2). This stiffened-panel model has a higher degree of mesh refinement and structural detail than the global model previously described in order to characterize the structural response more accurately. Frames, stringers, and shear clips are modeled as branched shells in the stiffened-panel model, and the tear straps are modeled using shell elements. Distortion of structural elements, such as frames and stringers, is accounted for at this modeling level, and a mesh with sufficient refinement around the crack tip is used to calculate some crack-growth parameters.

Displacements and forces obtained from the stiffened-panel model, or second level of modeling detail, are used as boundary conditions for a third level of modeling detail that includes smaller, more-detailed local-panel models. These detailed local models include a damaged area of the shell and may also include such structural details as lap joints and fasteners which STAGS models using nonlinear springs. Finally, a fourth level of local modeling detail is used to represent accurately the shell response in the area near the crack tip. A detailed fracture mechanics analysis is performed at this modeling level to determine crack growth and propagation characteristics. As a crack grows, changes occur in the stress and displacement fields of the local models. These changes are accounted for in the more global models by reanalyzing these models with the new crack configuration. This procedure is repeated for all levels of modeling detail at each stage of crack growth.

Results and Discussion

The results of an analytical study of the nonlinear response of stiffened fuselage shells with long cracks are presented herein. Results are presented for fuselage shells subjected to internal pressure and mechanical bending loads that show the effects of crack location and orientation on shell response. Results that indicate the effects of mechanical fasteners on the response of a lap joint are also presented. In addition, results are presented that account for yielding that occurs in the crack tip region during crack growth. These results are used to demonstrate the effects of elastic and elastic-plastic material properties on the buckling and postbuckling response of tension-loaded flat panels with cracks and also to indicate the consequences of neglecting the out-of-plane deflections in a fracture mechanics analysis of a thin-walled structural element.

Shell with Internal Pressure Load

An example of the hierarchical modeling strategy described herein and the corresponding analysis results for a stiffened shell subjected to 8 psi of internal

pressure are shown in figure 3. A global fuselage model that characterizes a typical stiffened fuselage shell section is shown in the upper right of the figure. Contour plots of the hoop stress resultants in the shell are shown on the corresponding deformed shapes in the figure for all models. There is a 10-inch-long longitudinal skin crack located between two stringers and two frames in the crown of the fuselage. The crack length is extended to 20 inches using the load relaxation technique while the shell is in a nonlinear equilibrium state. Displacements obtained from the analysis of this global model for various crack lengths are applied as boundary conditions to the second level of modeling detail which is represented by the six-bay by six-bay crown-panel section model shown in the upper left part of the figure. At this level of refinement, the stress gradients are more localized in the area of the frame than for the larger, less-refined global fuselage model. Displacements obtained from the crown-panel section model are applied as boundary conditions to a two-bay by three-bay local-panel model that is centered around the crack. This third level of modeling detail is referred to in the figure as the crack extension model and has a higher level of mesh refinement than the second level of modeling detail, or the panel model, in order to represent the behavior of the crack region more accurately. The crack length is grown from 10 inches to 20 inches during the analysis using the load relaxation technique while maintaining equilibrium in the nonlinear state for both the second and third levels of modeling detail. The panels at the bottom of figure 3 represent the changes in the hoop stress and normal deflection gradients that occur as a result of crack growth.

Shell with Internal Pressure and Bending Loads

The effects of combined internal pressure and mechanical bending loads on the response of a stiffened fuselage section with a 10-inch-long longitudinal crack located in the fuselage crown are illustrated in figures 4, 5, and 6. The axial stress resultants are shown in figure 4 for three load cases: an internal pressure load; an internal pressure load plus a down-bending moment; and an internal pressure load plus an up-bending moment. An up-bending moment is defined as shown on the global shell model in figure 2. The axial stress resultants for the internal pressure load case are distributed uniformly around the circumference of the shell except where the floor beams are attached to the frames. For the case where the shell is subjected to internal pressure and a down-bending moment, the axial stress resultant contours indicate that the crown is in tension and the keel is in compression. For the case where the shell is subjected to internal pressure and an up-bending moment, the axial stress resultants in the keel are in tension and those in the crown are in compression except for the local region near the crack. The skin at the edge of the crack is in tension in the axial direction due to the bulging deformation that occurs in the local region of the crack which is caused by the internal pressure load.

Axial stress resultants for a two-bay by three-bay local model with a crack are shown in figure 5 for the three load cases shown in figure 4. The changes in the axial stress resultant fields are shown in this figure as the crack length grows from 10 to 20 inches. For the case when the fuselage crown is in compression, axial tension stress resultants exist at the edge of the crack due to the bulging of

the skin surrounding the crack. As the crack length grows to 15 and then to 20 inches, axial tension stress resultants develop in the skin bays adjacent to the skin bay with the crack due to the deformation of the stringers on each side of the crack.

The strain energy release rate G_1 that corresponds to a crack opening mode for a straight crack located at panel midbay is shown in figure 6 as a function of crack length for the three load cases. The results indicate that the strain energy release rates for combined internal pressure and axial tension stress resultants due to the down-bending moment are lower in value than the strain energy release rates for internal pressure acting alone. The results also indicate that the strain energy release rates for combined internal pressure and axial compression stress resultants due to the up-bending moment are higher in value than the strain energy release rates for internal pressure acting alone. These results suggest that the addition of an axial compression load in the area of a longitudinal crack would cause the crack to grow at a lower value of applied load than for the addition of an axial tension load. The axial compression load couples with the out-of-plane displacements at the edge of the crack to increase the magnitudes of the skin displacements near the crack.

Stiffened Panels with Different Damage Conditions

The effects of different damage locations and different types of structural element damage were studied in the present investigation at the stiffened-panel modeling level. A detailed six-bay by six-bay stiffened panel model with a 14-inch-long longitudinal skin crack is shown in figure 7. The panel is subjected to an internal pressure load and the stress resultants corresponding to an up-bending moment. A view of the concave side of the panel is shown at the bottom of the figure and indicates how the structural elements are modeled. Shell elements are used to model the frames as Z sections and the stringers as inverted hat sections. The shear clips and tear straps are also modeled with shell elements.

Contour plots of the hoop stress resultants for different crack locations are shown on the deformed shapes of the panel in figure 8 for an internal pressure load. The figures on the left side of figure 8 represent the shell as viewed from the convex side of the shell, and the figures on the right represent the shell as viewed from the concave side. The crack is centered over an undamaged circumferential tear strap that is located midway between two frames. Results for three crack locations are shown in the figure. The cracks are located at the edge of the tear strap that lies beneath a stringer, at the 1/4-bay location between the stringers, and at midbay between the stringers. The stress intensity factors K_I and K_{II} corresponding to the crack locations shown in figure 8 are shown in figure 9 as a function of crack length. The stress intensity factor K_I, which corresponds to a crack opening mode, has the highest value when the crack is located at midbay. The crack located adjacent to the edge of the stringer has the lowest value of K_I. The trends for the stress intensity factor K_{II}, that corresponds to a crack shearing mode, are opposite to the trends for the stress intensity factor K_I.

The effect of a broken tear strap on the hoop stress resultants for the panel are shown in figure 10 for the same three crack locations shown in figure 8. When the tear strap is broken and the crack lies adjacent to the edge of the stringer, the stringer rolls away from the center of the skin bay where the crack is located. However, when the crack is located at midbay, the stringer rolls toward the skin bay where the crack is located. The stress intensity factors for the panel with the broken tear strap are shown in figure 11. The trends for the stress intensity factors are the same as for the panel with the undamaged tear strap, but the values of the stress intensity factors for the panel with the broken tear strap are twice as large as those for the panel with the undamaged tear strap.

Shells with Circumferential Cracks

The effects of a circumferential crack on the response of a subscale pressurized aluminum cylindrical shell with spherical end-caps have also been studied in this investigation. Contour plots of the axial stress resultants are shown on the deformed shape of the unstiffened cylindrical shell subject to 8 psi of internal pressure in figure 12. The shell has a 14.4 inch radius and a 0.015 inch wall thickness. A 10-inch-long circumferential crack is located at the midlength of the shell. The internal pressure load causes the center of the edge of the crack to deflect outward, and causes the surface of the shell at the crack tips to deflect inward. This response is due to a nonlinear effect associated with the curvature of the shell. Contour plots of the axial stress resultants for a stiffened aluminum cylinder subject to 8 psi of internal pressure are shown on the shell deformed shape in figure 13. The stiffened shell has the same radius and thickness as the unstiffened shell and has rings and longitudinal stringers and a 10-inch-long circumferential crack at shell midlength. The results indicate that the stringers do not restrain the inward bending of the shell at the crack tip.

Panel with a Lap Joint

The effects of discrete fasteners on the response of a cylindrical panel with a lap joint have been studied in the present investigation using the local panel model shown in figure 14. The model represents a lap joint in one half of a single skin bay between the frames and stringers of a typical fuselage shell. The model consists of two skin elements and an inverted hat stringer at the lap joint. The elements of the joint are connected by three rows of fasteners in a staggered pattern. An expanded view of the model shows the elements or layers of the lap joint and is used to display the results for each joint element. The panel is loaded by internal pressure, and symmetry conditions and displacement constraints are applied to simulate the effects of the adjacent structure which is not modeled. The left edge of the model is clamped to simulate the influence of a frame. The right edge of the model is midway between two frames and is constrained by enforcing symmetry conditions. A comparison of the undeformed and deformed cross sections of the panel is also shown in figure 14. The local bending of the skin and stringer, and the rolling and distortion of the stringer cross section that occurs in the lap joint are indicated in the figure. These stringer cross-sectional

deformations would not be represented in a model using a conventional discrete beam model for the stringer.

Contour plots of the surface hoop strains for each skin element of the joint are shown in figure 15. Results are shown for two types of joint connections. The skin elements in the model on the right are continuously attached along the length of the joint in a manner that is similar to an adhesively bonded joint. The model on the left has discrete fasteners connecting the skin elements to form the joint. The outer-surface hoop strains of the joint skin elements are shown in figure 15a as viewed from the convex side of the shell. The view of each model is rotated in figure 15b to show the inner-surface hoop strains of the joint skin elements as viewed from the concave side of the shell. For both types of joint connections, the maximum surface hoop strain occurs on the inner surface of the outer skin element near the edge of the attachment between the inner and outer skin elements. The hoop tension loads and the eccentricity of the inner and outer skin elements couple to cause local bending in the joint which adds to the skin bending associated with the internal pressure load. For the model with the continuous attachment, this bending occurs in a region visible from the inner or concave surface of the joint. The discrete fasteners cause maximum bending to occur adjacent to the top row of fasteners, which is in a region hidden from view by the inner skin element. This location on the inner surface of the outer skin element at the top row of fasteners has been identified as a critical crack initiation site for lap joints. Crack initiation often occurs at this location because the fasteners are often countersunk into the outer skin element.

The model with the discrete fasteners was modified to study the effect of a skin crack at this critical crack-initiation site by introducing a 3-inch-long half crack along the top row of fasteners. Contour plots of the stress resultants for the undamaged panel and the panel with the 3-inch-long half crack are shown on the deformed shapes of the panels in figures 16 and 17. The hoop and axial stress resultant contours shown in figure 16 demonstrate the effects that introducing the crack have on the stress distribution, on the stress concentration at the crack tip, and on the bending of the stringer. The transverse shear stress resultant contours shown in figure 17 indicate the presence of the fastener pull-through forces at the fastener locations. Deformed shapes of three cross sections of the panel with the 3-inch-long half crack are shown in figure 18. One cross section is located ahead of the crack, one is located at the crack tip, and one is located at crack mid length. These deformed shapes demonstrate the stringer rolling and cross-section distortion that occur as a result of the deformations in the region of the crack.

Tension-Loaded Panel with a Crack

A tension-loaded flat panel with a central transverse crack was modeled as shown in figure 19 to study the effect of the transverse compression stresses on panel buckling near the crack. These transverse compression stresses are induced by the Poisson effect that occurs in plates and shells. When these compression stresses reach a critical value for a given crack length, the panel buckles into a local mode that extends above and below the crack. The mode

has one half-wave in the longitudinal and transverse directions. The finite element discretization of the panel used for the nonlinear analysis is shown in figure 19. The panel is 24 inches long, 12 inches wide, and 0.090 inch thick. The crack lengths considered are 4, 5 and 6 inches. The material is 2024-T3 aluminum alloy. The finite element model shown in figure 19 models only one half of the plate and uses 5-node transition elements for mesh refinement.

Nonlinear static analyses were conducted for each crack length using either elastic or elastic-plastic material properties. The results of these analyses are shown in figures 20 and 21. Nonlinear solutions were obtained in the prebuckling and postbuckling load range for each crack length. The shape of the first buckling mode was used as a geometric imperfection in the analysis to continue the solution onto the initial postbuckling branch of the solution. The out-of-plane displacement at the center of the crack is shown as a function of the applied tension load in figure 20 for each crack length. The results obtained using elastic material properties are shown by the solid lines, and results obtained with elastic-plastic material properties are shown by the dashed lines. The panel with the 4-inch-long crack has the highest buckling load and has the greatest reduction in buckling load and postbuckling stiffness when elastic-plastic material properties are included in the analysis. The panel with the 6-inch-long crack buckles at a substantially lower value of applied tension load than the corresponding panels with the other two crack lengths, and its buckling load and initial postbuckling response are not significantly affected by elastic-plastic behavior.

The results presented in figure 20 indicate that the buckling load is dramatically affected by the length of the crack. The buckling load is influenced by the increase in local panel flexibility near the crack as the crack length increases. The results also indicate that the stress level in the panel at the onset of buckling is higher for the shorter crack lengths than for the longer crack lengths since the buckling load increases as crack length decreases. These results suggest that buckling of the panels with the shorter crack lengths occurs at general stress levels that are high enough to yield the panel locally. The local bending stresses associated with the buckling response also add to the general stress level in the panel and can cause enough reduction in stiffness due to yielding to reduce the magnitude of the postbuckling loads to values below the elastic response curves as shown in figure 20.

Contour plots of the axial stress and strain results for the panels with 4- and 6-inch-long cracks are shown in figure 21. Results are shown for tension loads that are 20 percent greater than the buckling loads of the corresponding panels with elastic material properties. The applied tension load that is 20 percent greater than the buckling load for the panel with the 4-inch-long crack is 35,000 lbs. The axial stress resultants from the analysis with elastic material properties are significantly different from those obtained from the analysis with elastic-plastic material properties because a relatively large area of material near the crack tip has yielded. In contrast, the applied tension load that is 20 percent greater than the buckling load for the panel with the 6-inch-long crack is only 13,500 lbs. The axial stress resultants for the panel with the 6-inch-long crack

are much lower in value than the corresponding results for the panel with the 4-inch-long crack, and are essentially not affected by including elastic-plastic material properties in the analysis. In addition, the size of the area of material at the crack tip that exhibits inelastic strain is much smaller than that for the panel with the 4-inch-long crack.

Concluding Remarks

The results of an analytical study of the effects of long cracks on the nonlinear response of stiffened fuselage shells subjected to combined internal pressure and mechanical loads are presented. The results suggest that nonlinear stiffened-shell analyses provide accurate predictions of the global and local responses of stiffened shells that have cracks and are subjected to combined loads. The results of nonlinear analyses show that the response of a damaged stiffened shell subjected to combined internal pressure and mechanical loads is different from the response of the shell subjected to an internal pressure load acting alone. Structural details and built-up structures with fasteners are included in the nonlinear analyses to provide an accurate representation of practical stiffened-shell structures. In addition, crack growth is predicted in a stiffened shell while the shell is in a nonlinear equilibrium state. Large local stress and out-of-plane deflection gradients that exist near cracks in stiffened shells are predicted accurately with a nonlinear stiffened-shell analysis. The results of the analysis indicate that curvature may affect the response of a shell with a circumferential crack more than it affects the response of a shell with a longitudinal crack. It is shown that both geometric and material nonlinear effects can be important for accurately predicting crack growth in stiffened shells. As an example of the importance of these nonlinear effects, the buckling load of a tension-loaded panel with a transverse crack was found to depend on the length of the crack. The results indicate that, if the crack is short enough for the panel to have a relatively high buckling load, the stresses in a tension-loaded panel with a transverse crack can be high enough to yield the panel near the crack tip.

References

1. Almroth, B. O.; and Brogan, F. A.: The STAGS Computer Code. NASA CR-2950, 1980.

2. Potyondy, David O.: A Software Framework for Simulating Curvilinear Crack Growth in Pressurized Thin Shells. School of Civil and Environmental Engineering Report 93-5, Cornell University, August 1993.

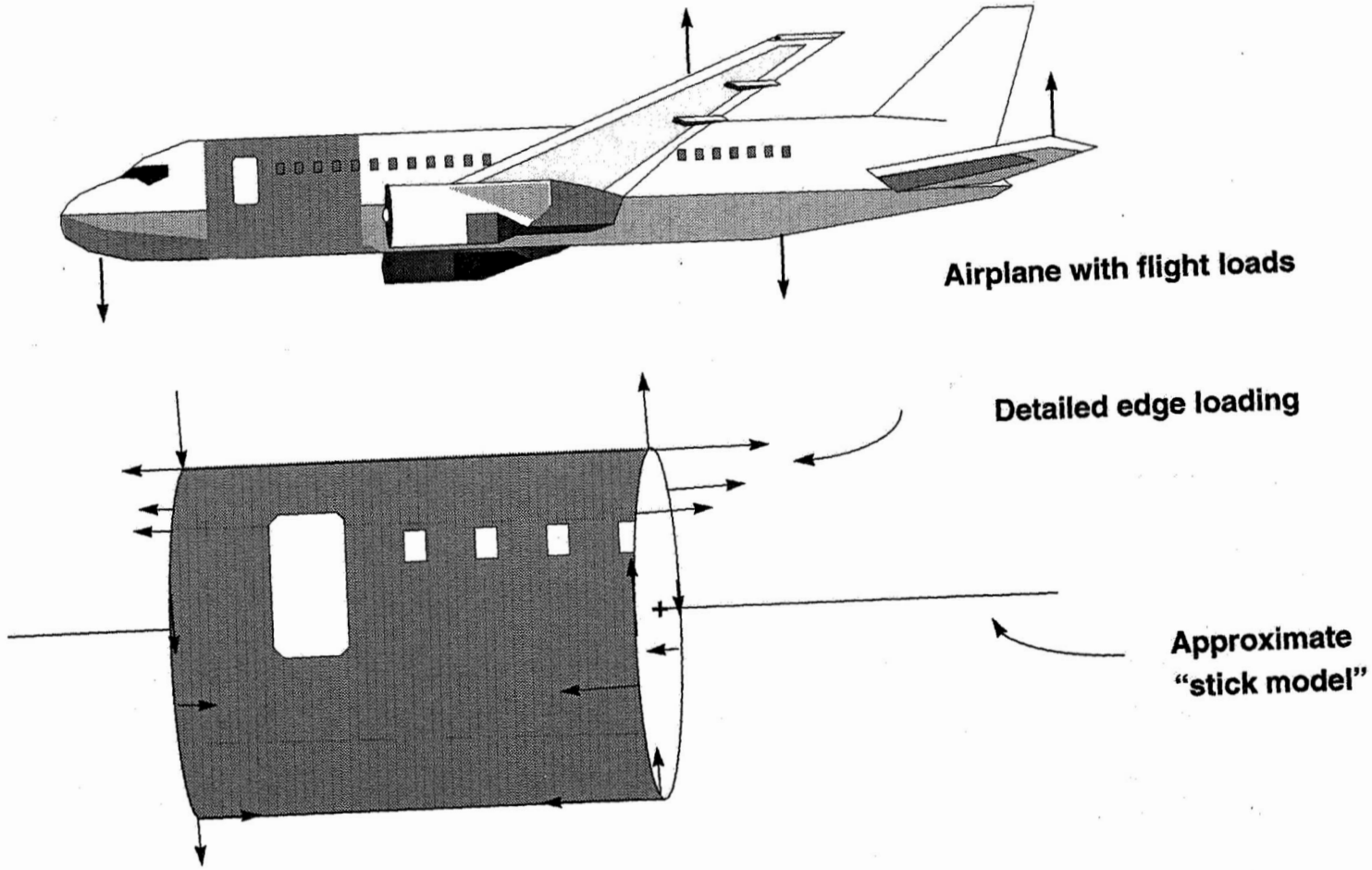

Fig. 1 Flight loads transformed to fuselage shell loads.

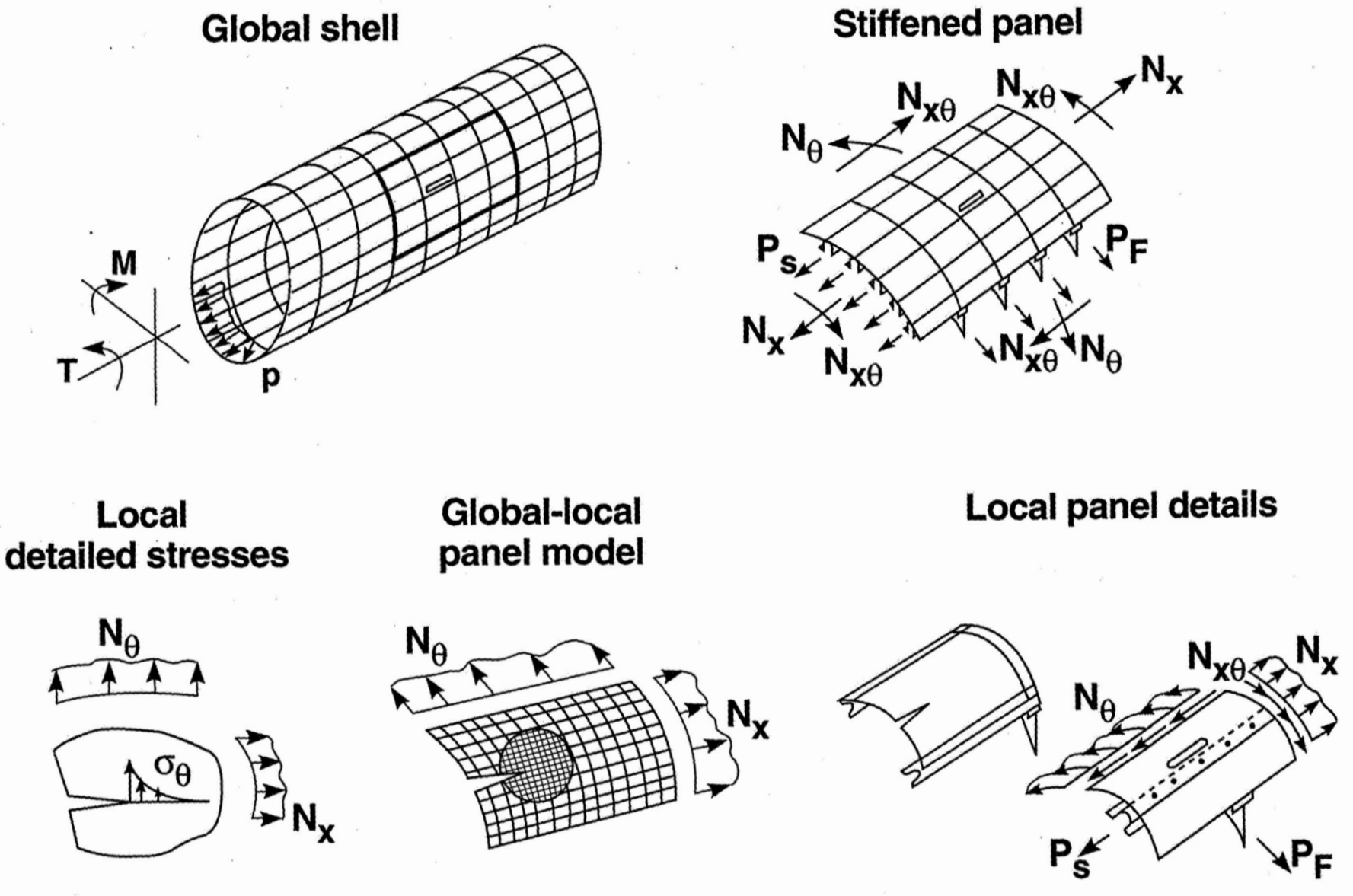

Fig. 2 Hierarchical nonlinear stiffened-shell models.

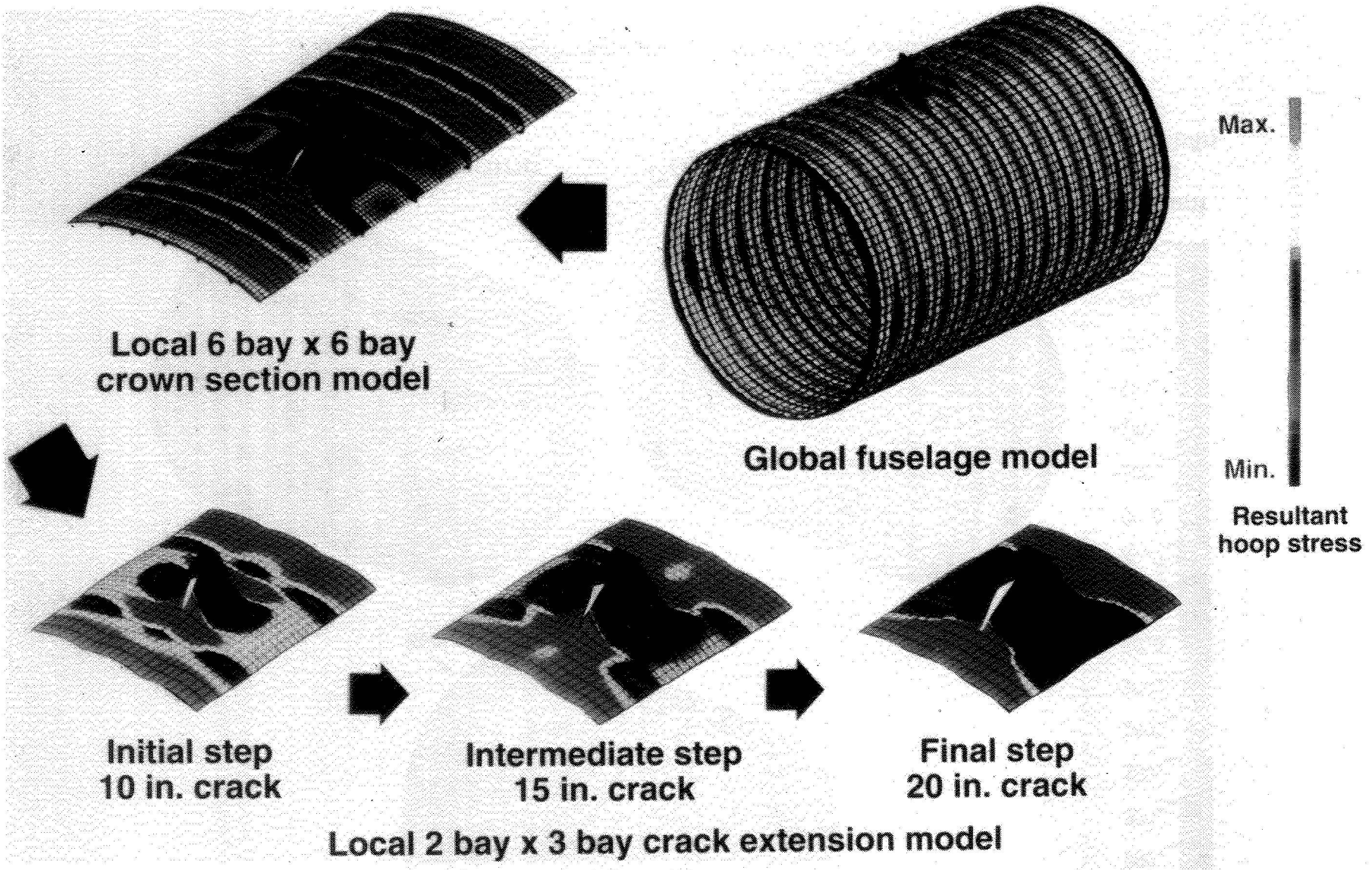

Fig. 3 Nonlinear crack growth in an aircraft fuselage structure using a hierarchical modeling strategy.

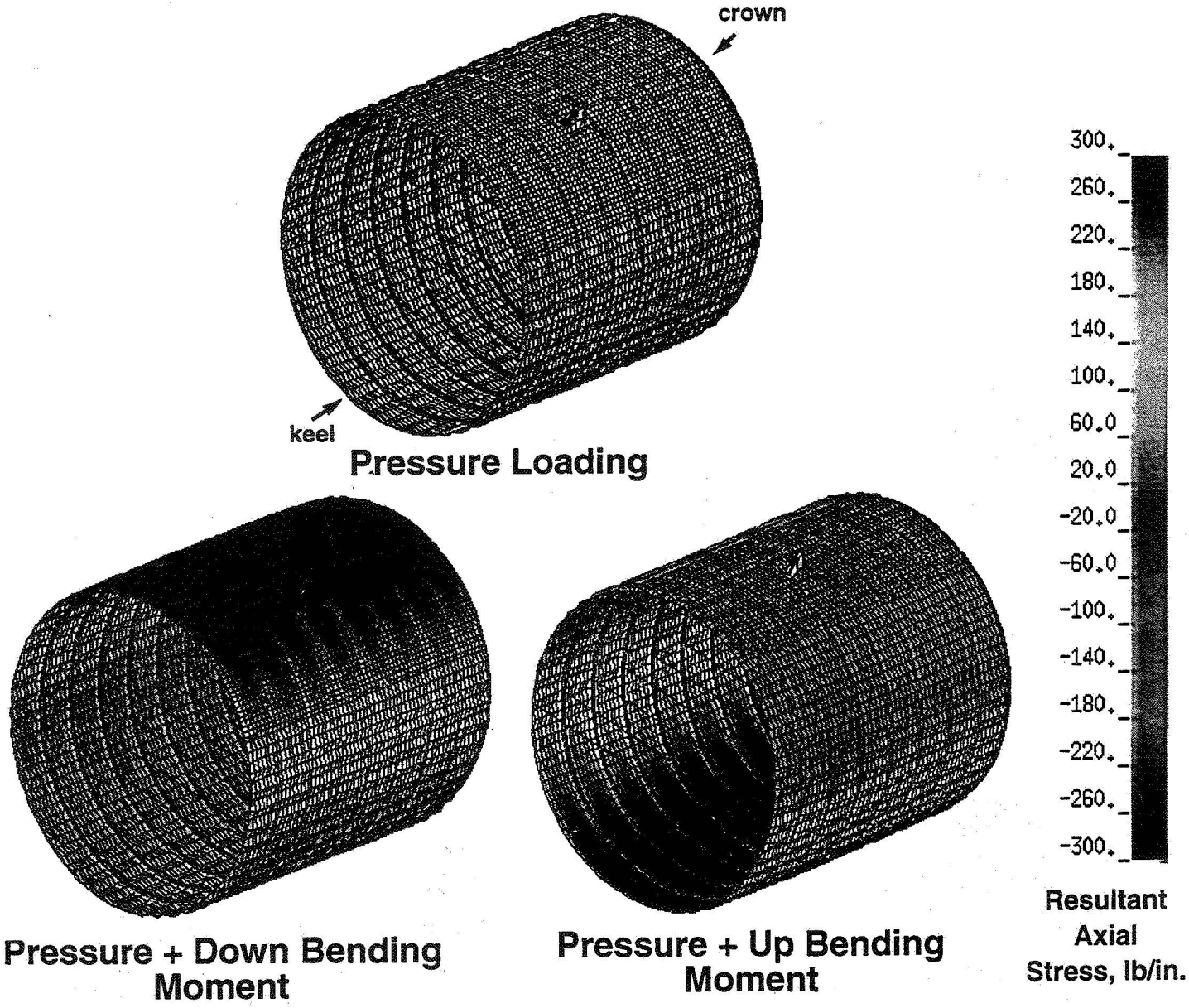

Fig. 4 Stiffened aluminum fuselage shell with a 10-inch-long skin crack.

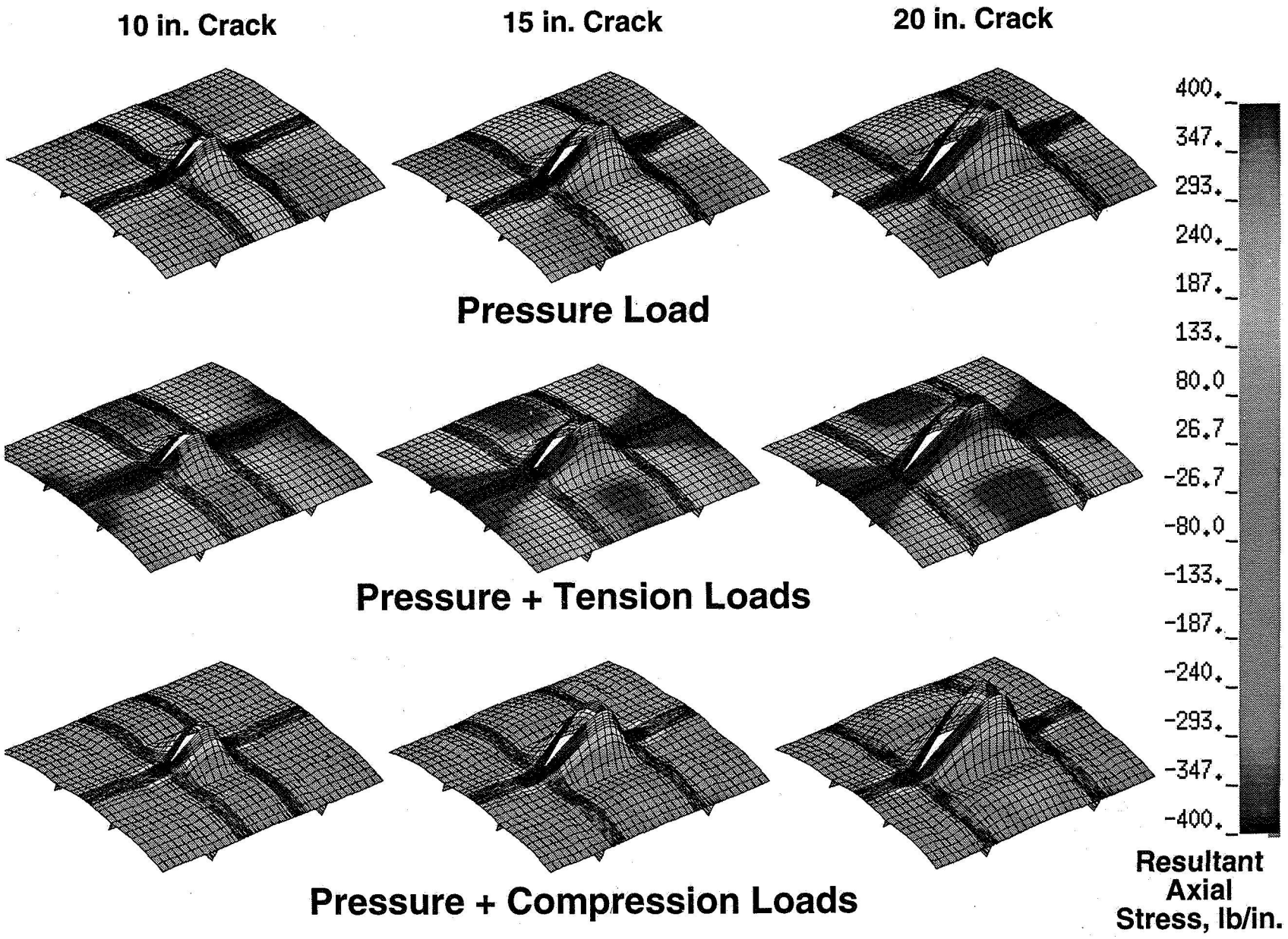

Fig. 5 Two-bay by three-bay stiffened aluminum fuselage panel model with a skin crack.

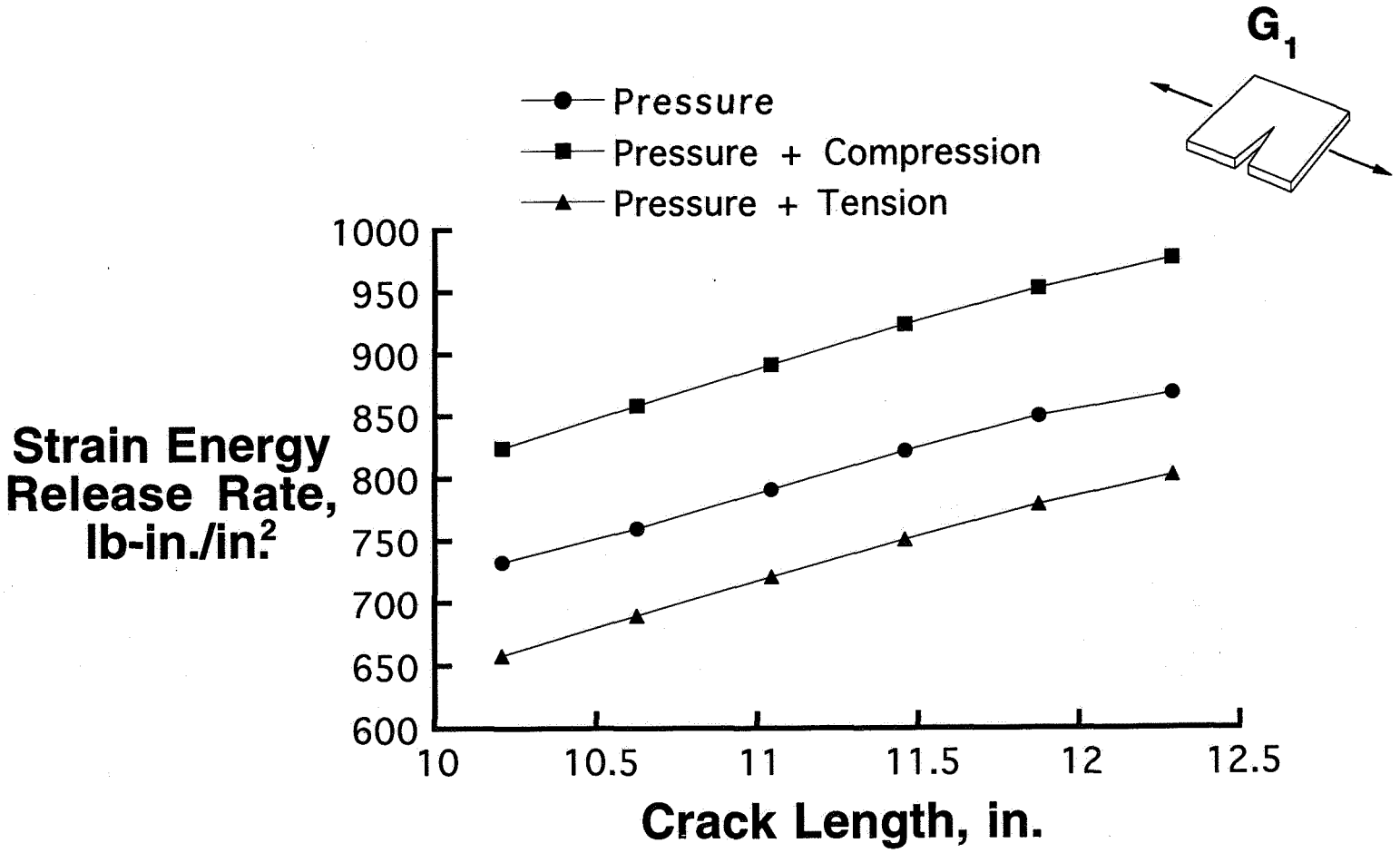

Fig. 6 Strain energy release rate for a two-bay by three-bay stiffened aluminum fuselage panel model with a skin crack.

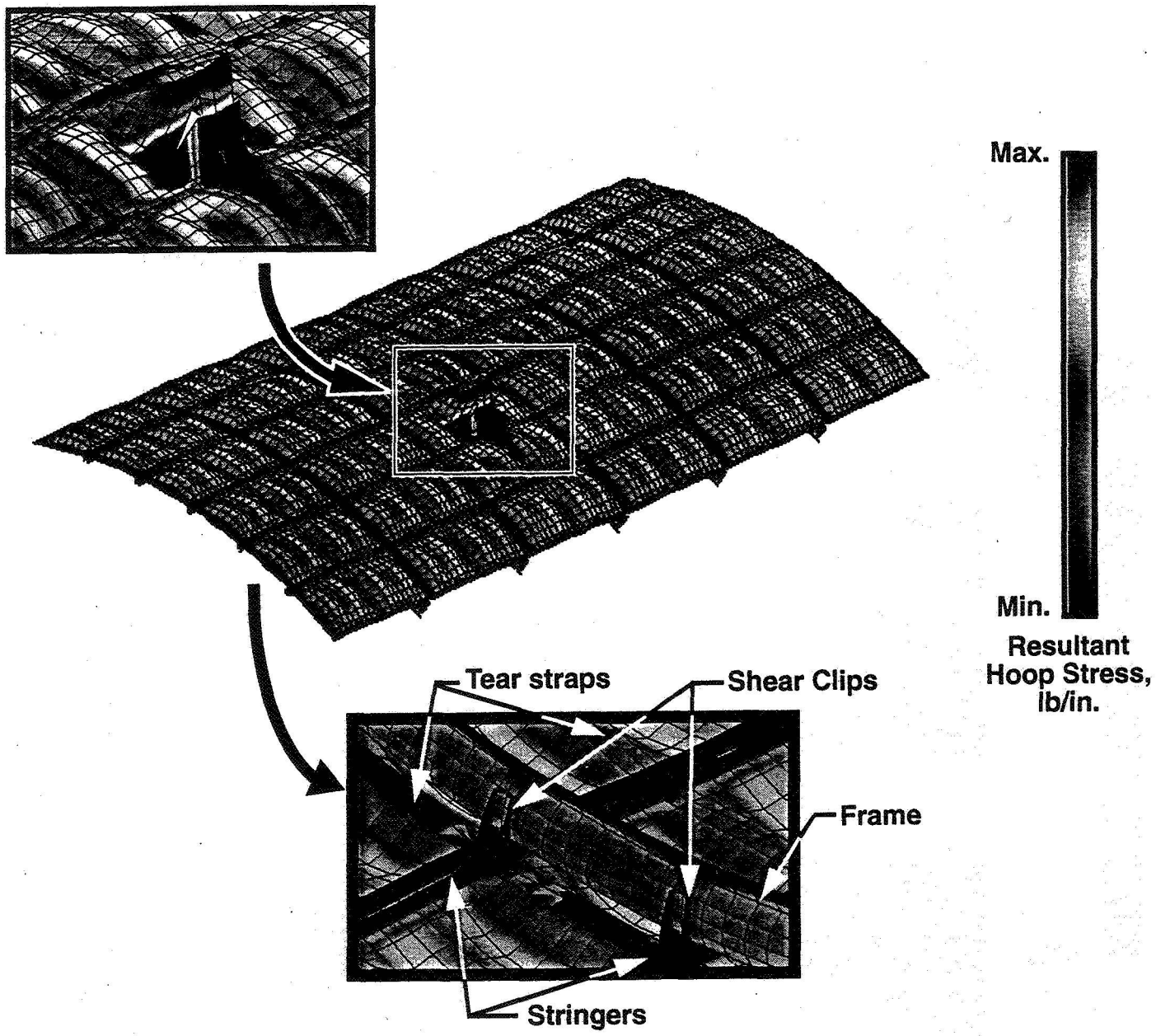

Fig. 7 Structural details of a local six-bay by six-bay stiffened-panel model subjected to internal pressure and an up-bending moment.

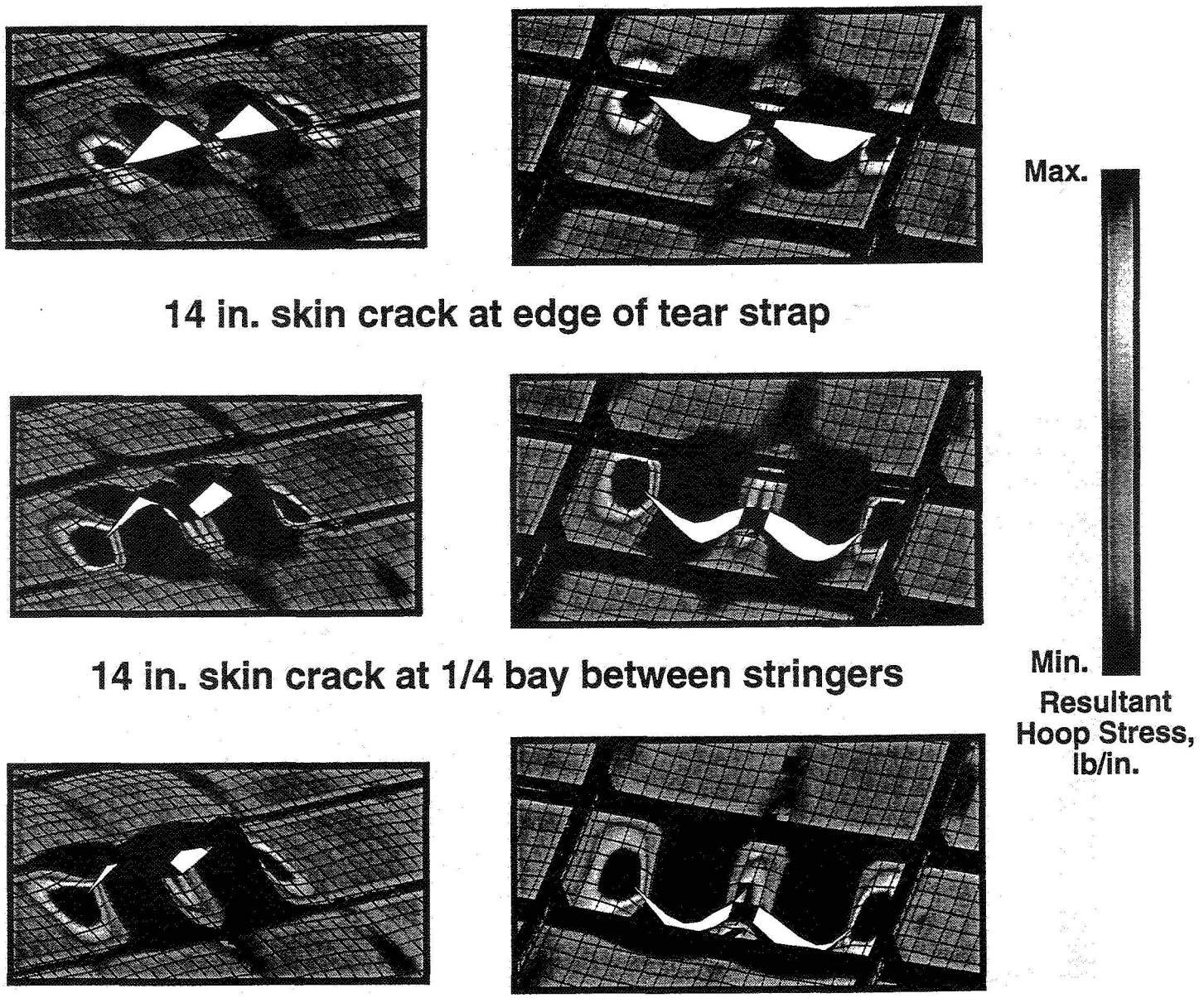

Fig. 8 Six-bay by six-bay stiffened panel with a skin crack and subject to internal pressure.

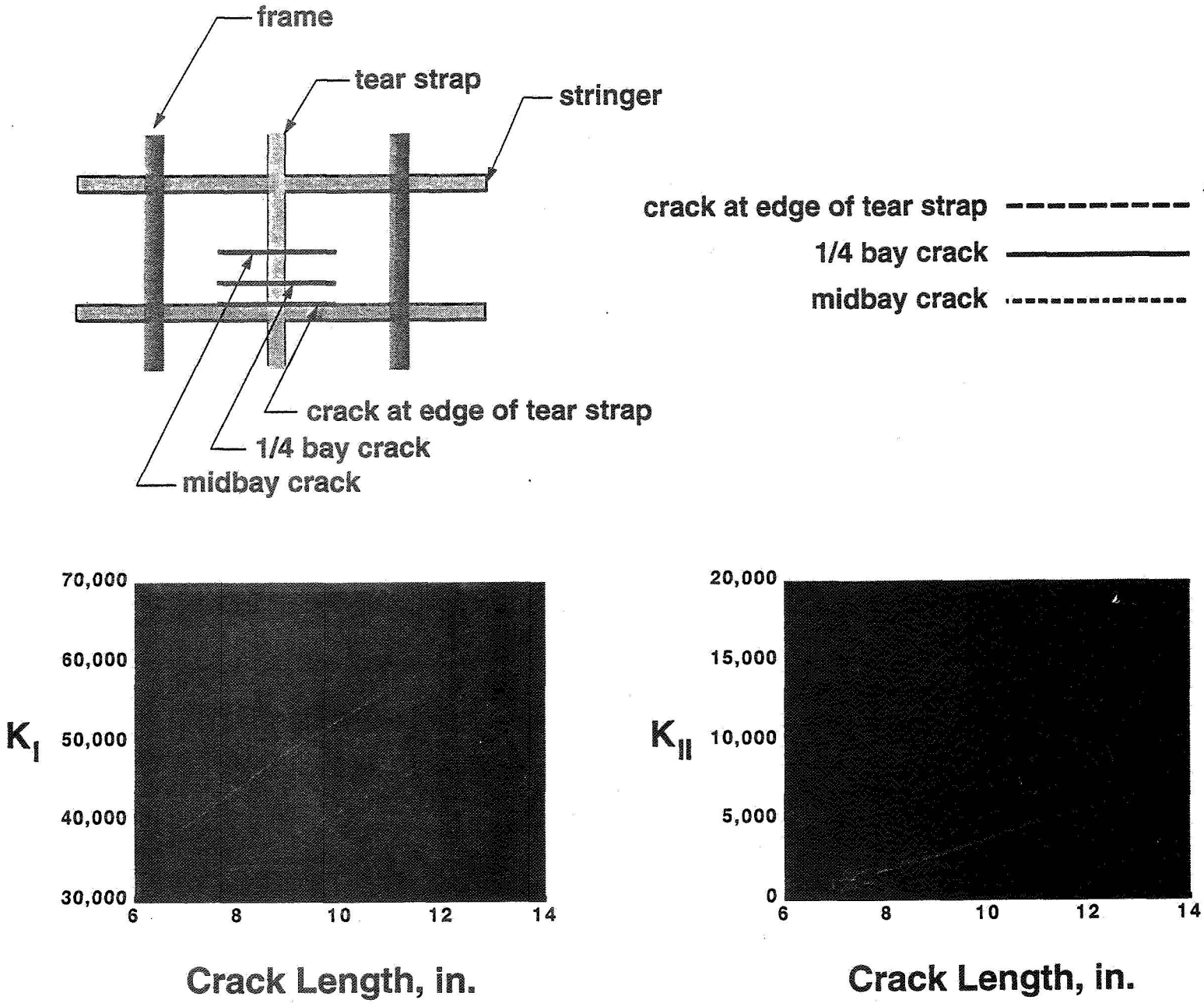

Fig. 9 Stress intensity factors for a six-bay by six-bay stiffened panel with a skin crack and subject to internal pressure.

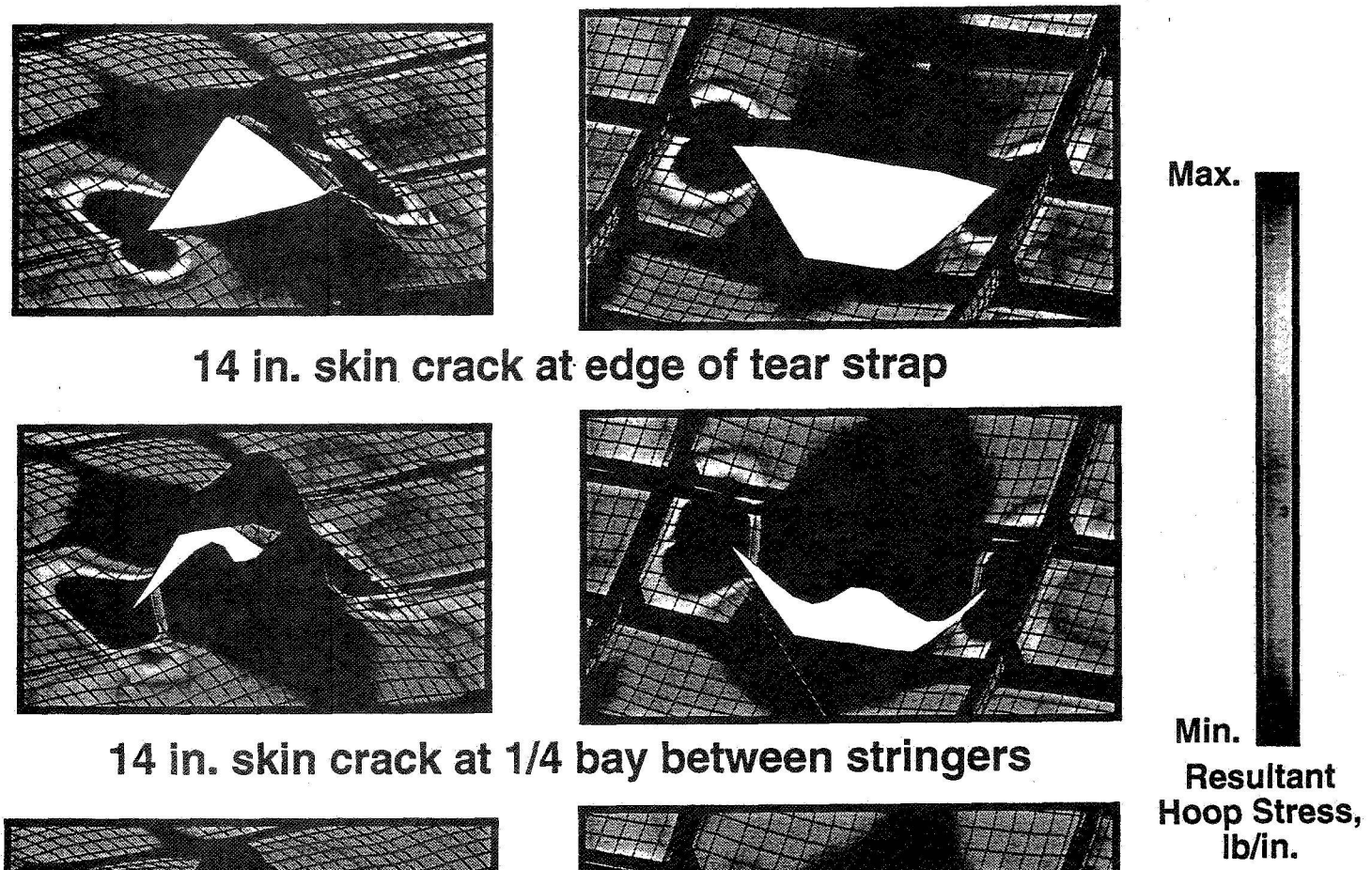

Fig. 10 Six-bay by six-bay stiffened panel with a skin crack and broken tear strap and subject to internal pressure.

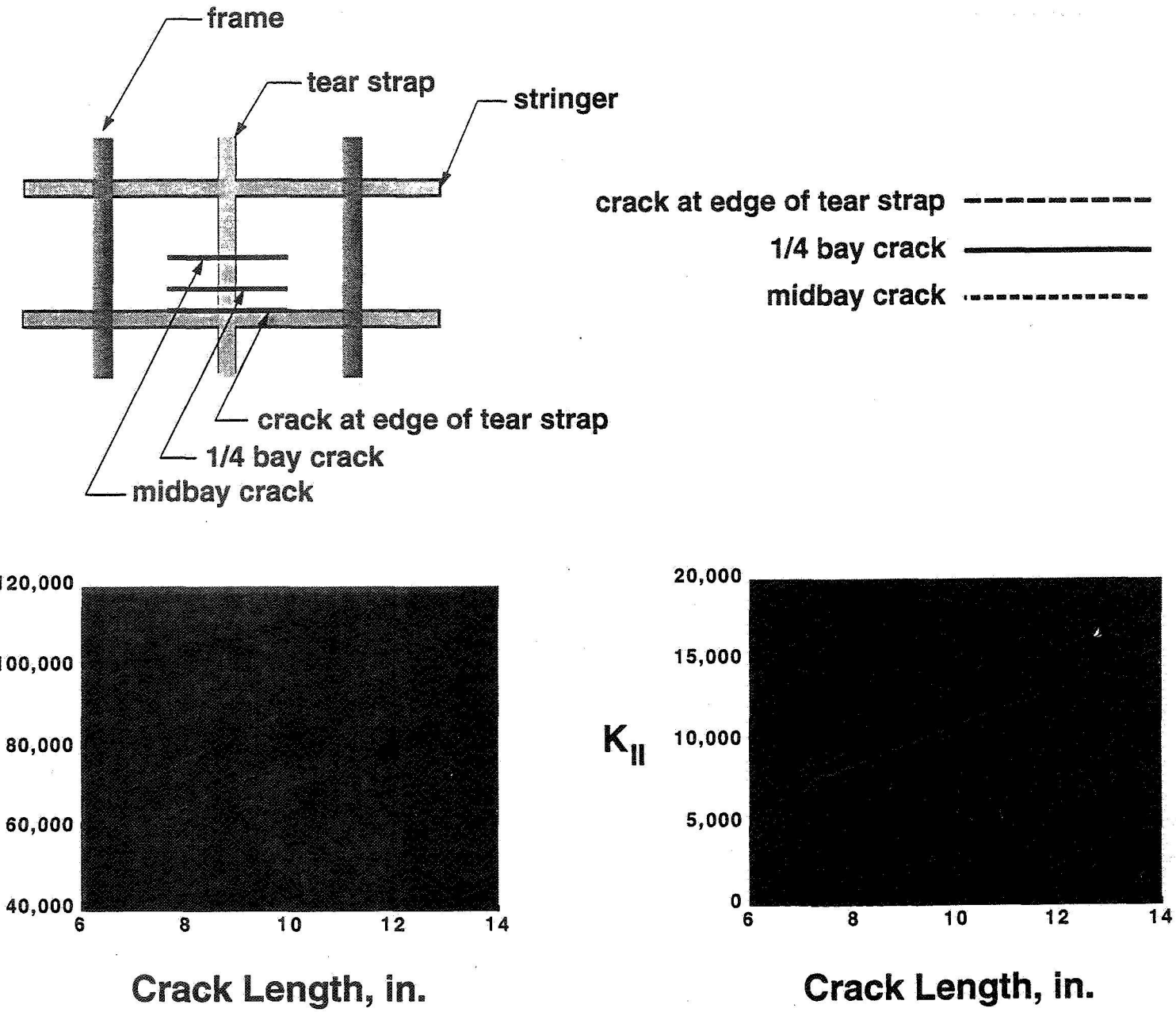

Fig. 11 Stress intensity factors for a six-bay by six-bay stiffened panel with a skin crack and a broken tear strap and subject to internal pressure.

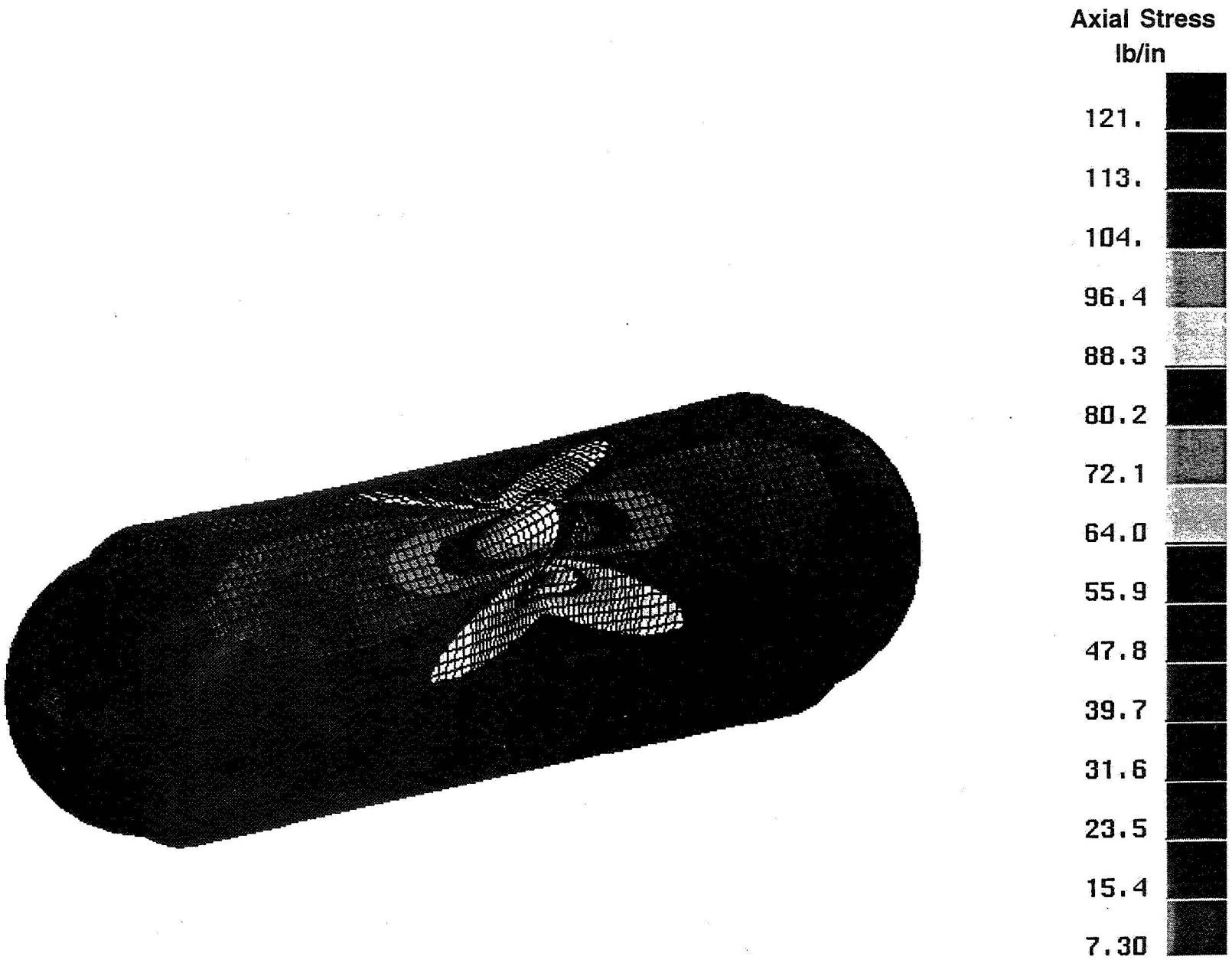

Fig. 12 Effect of a circumferential crack on the axial stress resultant distribution in a pressurized unstiffened aluminum shell.

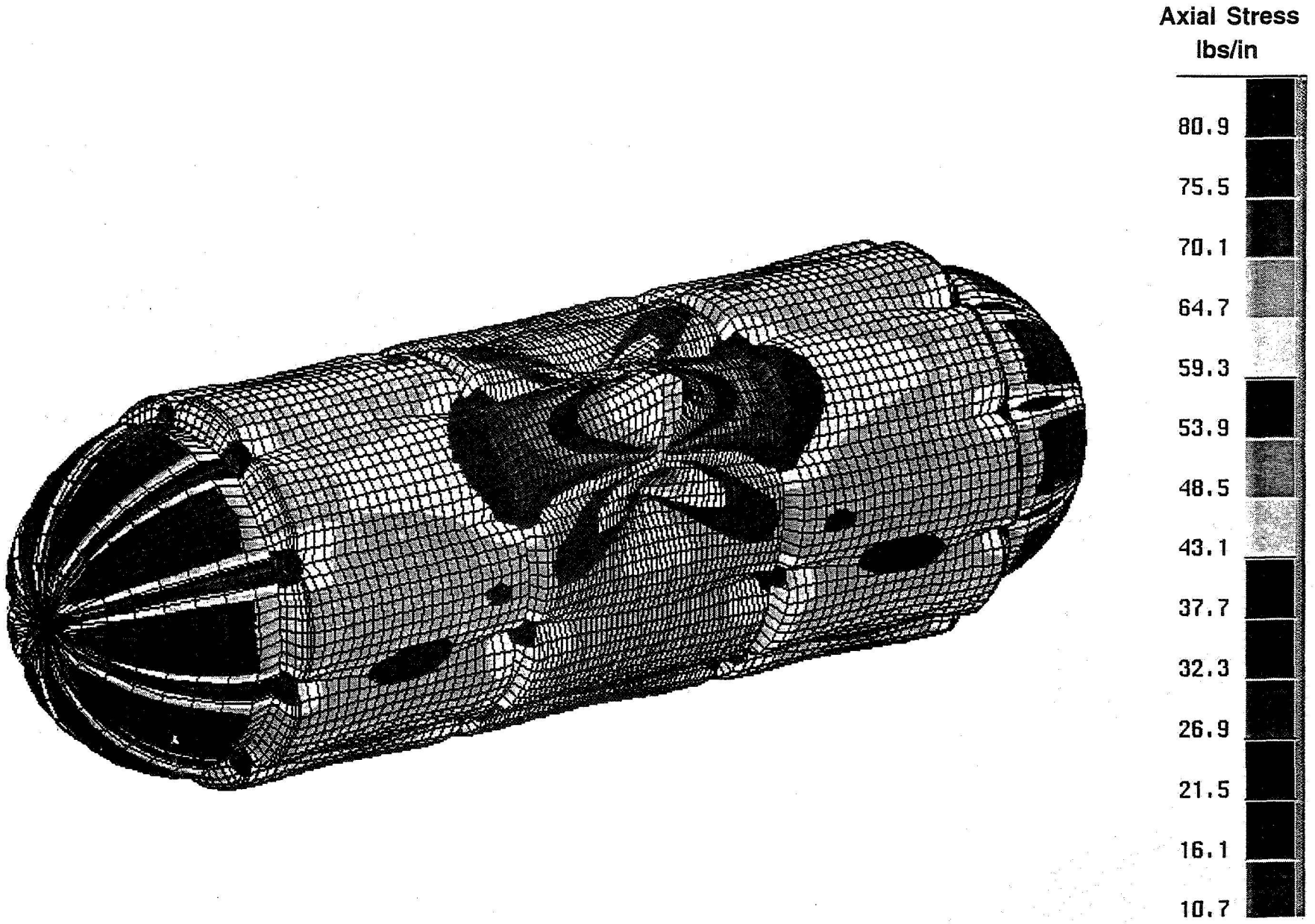

Fig. 13 Effect of a circumferential crack on the axial stress resultant distribution in a pressurized stiffened aluminum shell.

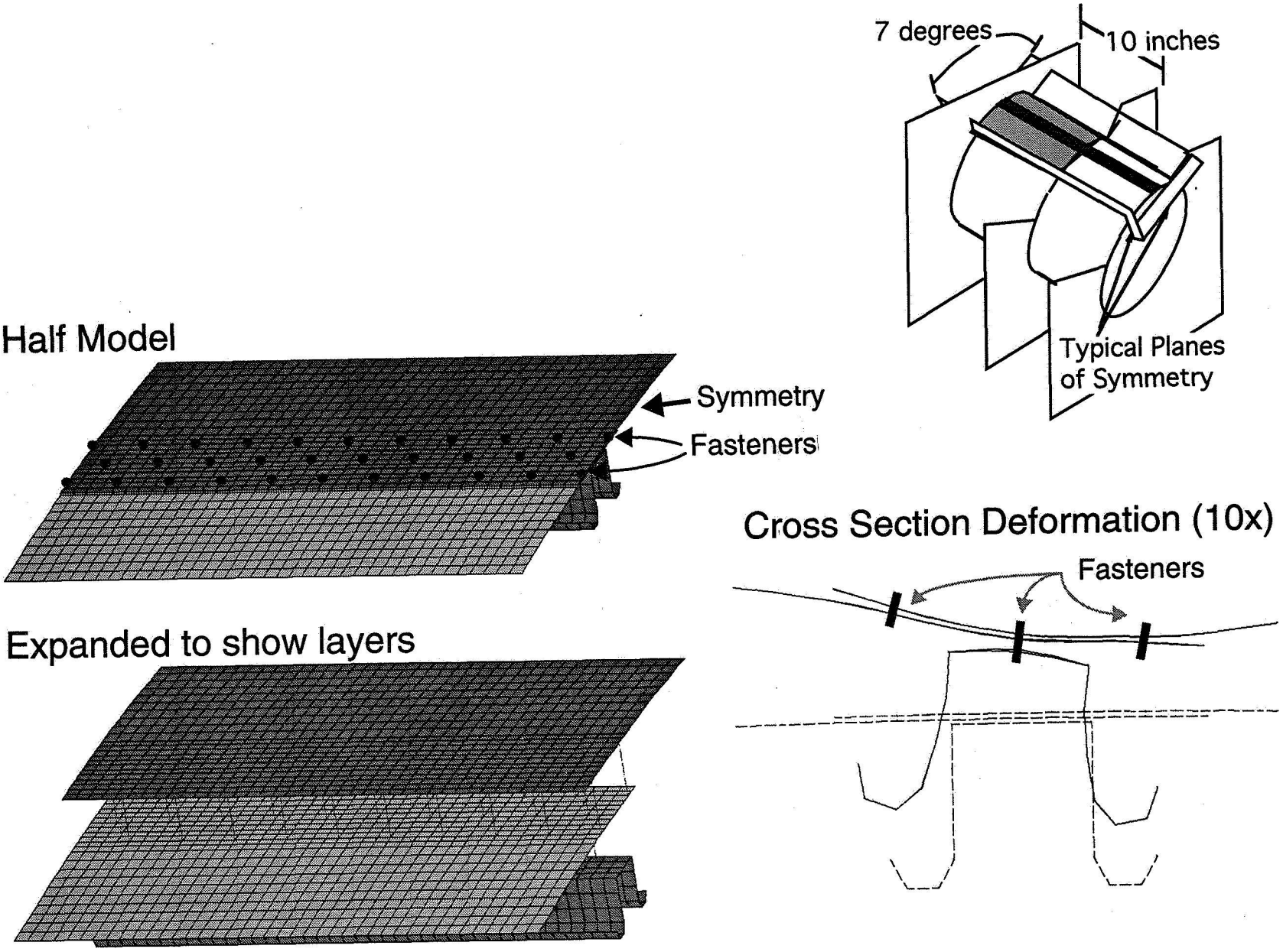

Fig. 14 Stiffened aluminum lap joint with discrete fasteners.

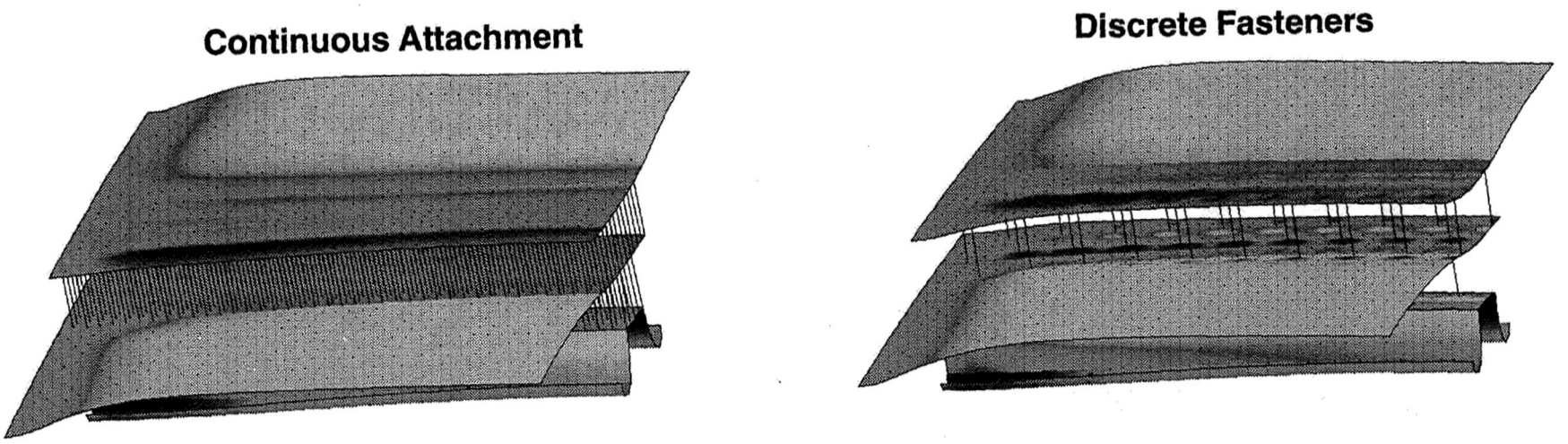

(a) Outside surface

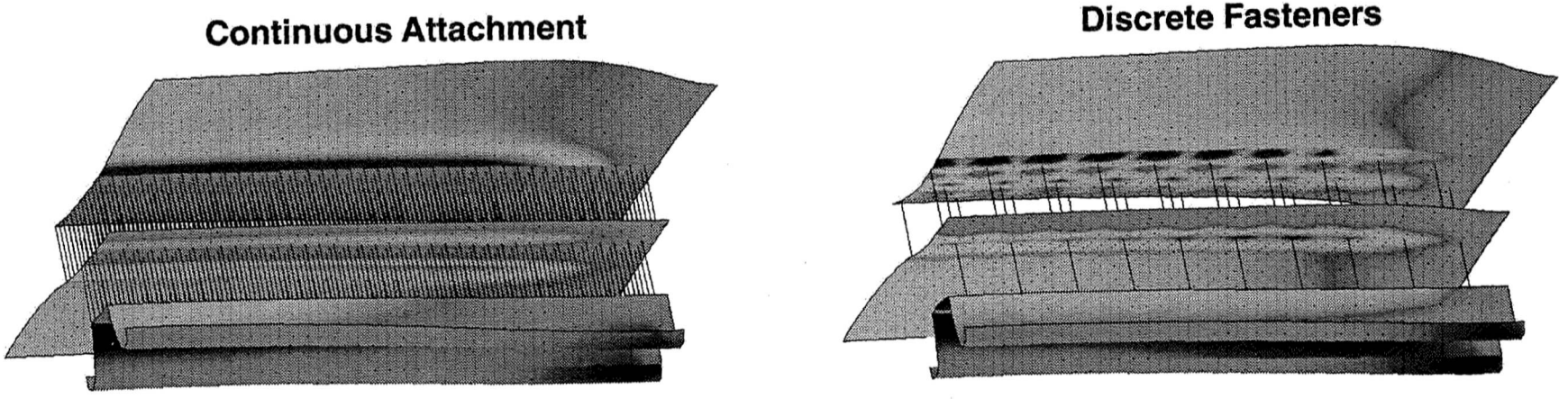

(b) Inside surface

Max. surface strain: inside surface of outer skin near top row of fasteners

Fig. 15 Surface hoop strains in lap joints that are continuously attached and have discrete fasteners.

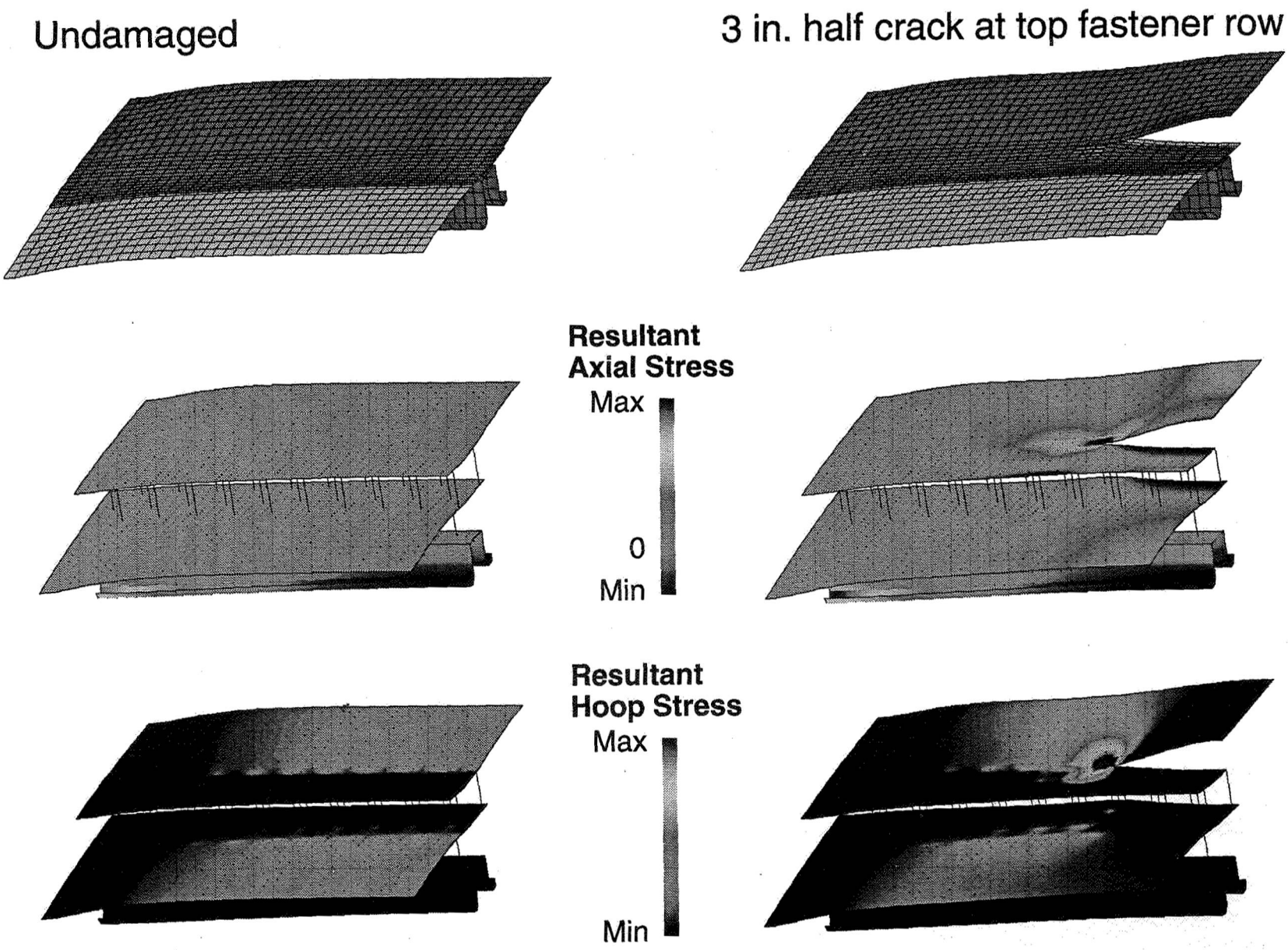

Fig. 16 Deformed shape, and axial and hoop stress resultants for an undamaged lap joint and a lap joint with a 3-inch-long half crack along the top fastener row.

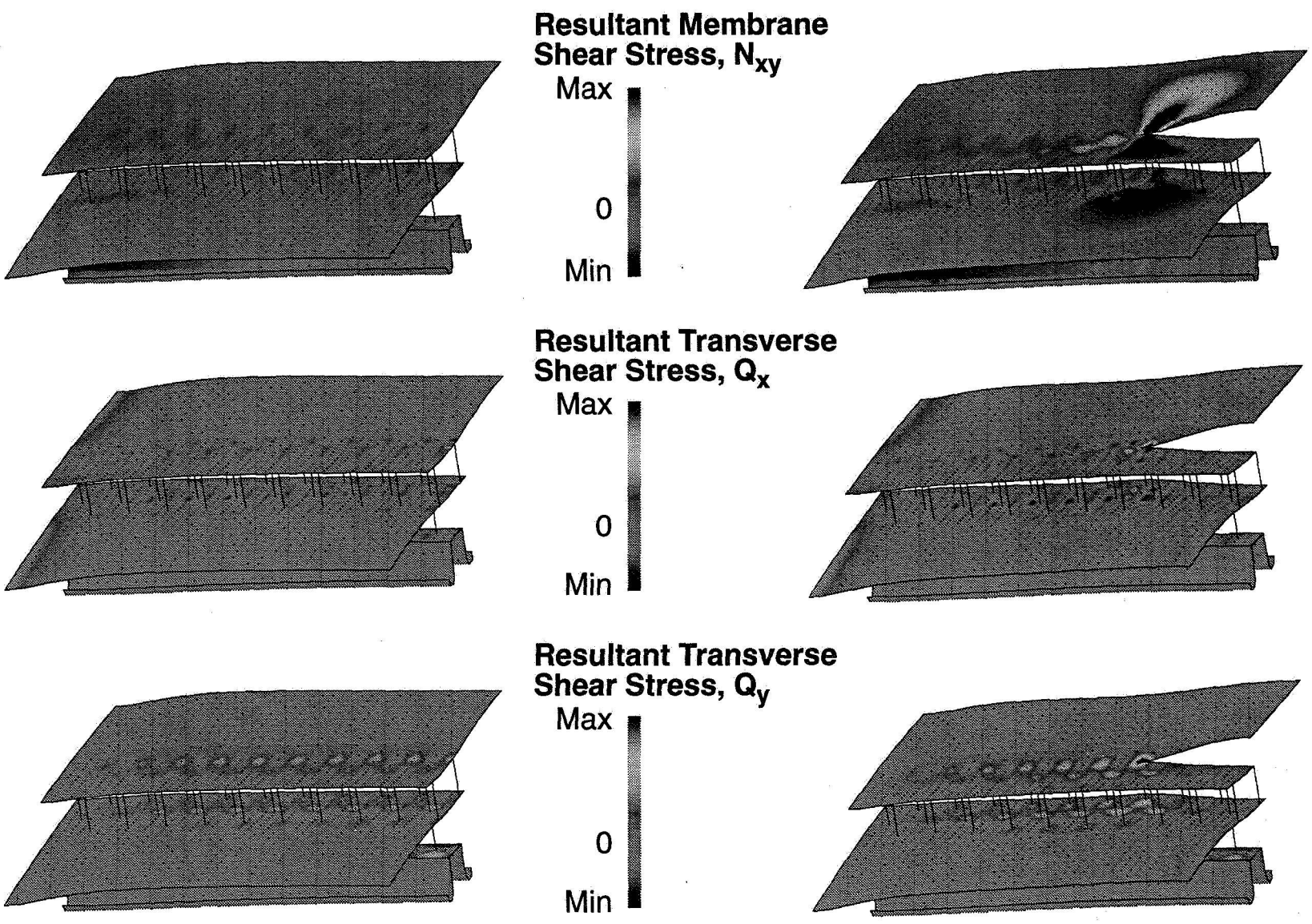

Fig. 17 Inplane and transverse shear stress resultants for an undamaged lap joint and a lap joint with a 3-inch-long half crack along the top fastener row.

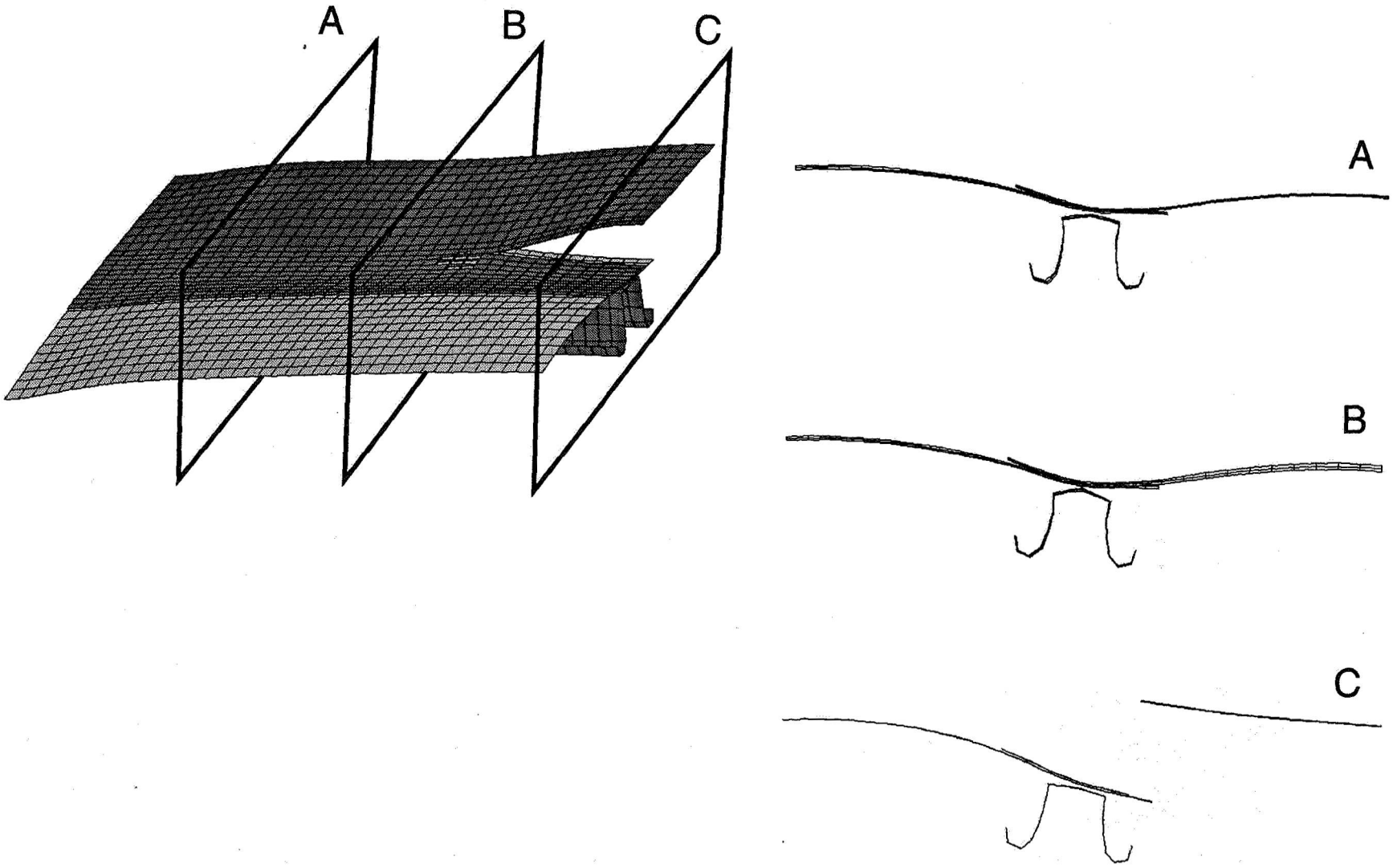

Fig. 18 Stiffener cross-section deformations for a lap joint with a 3-inch-long half crack along the top fastener row.

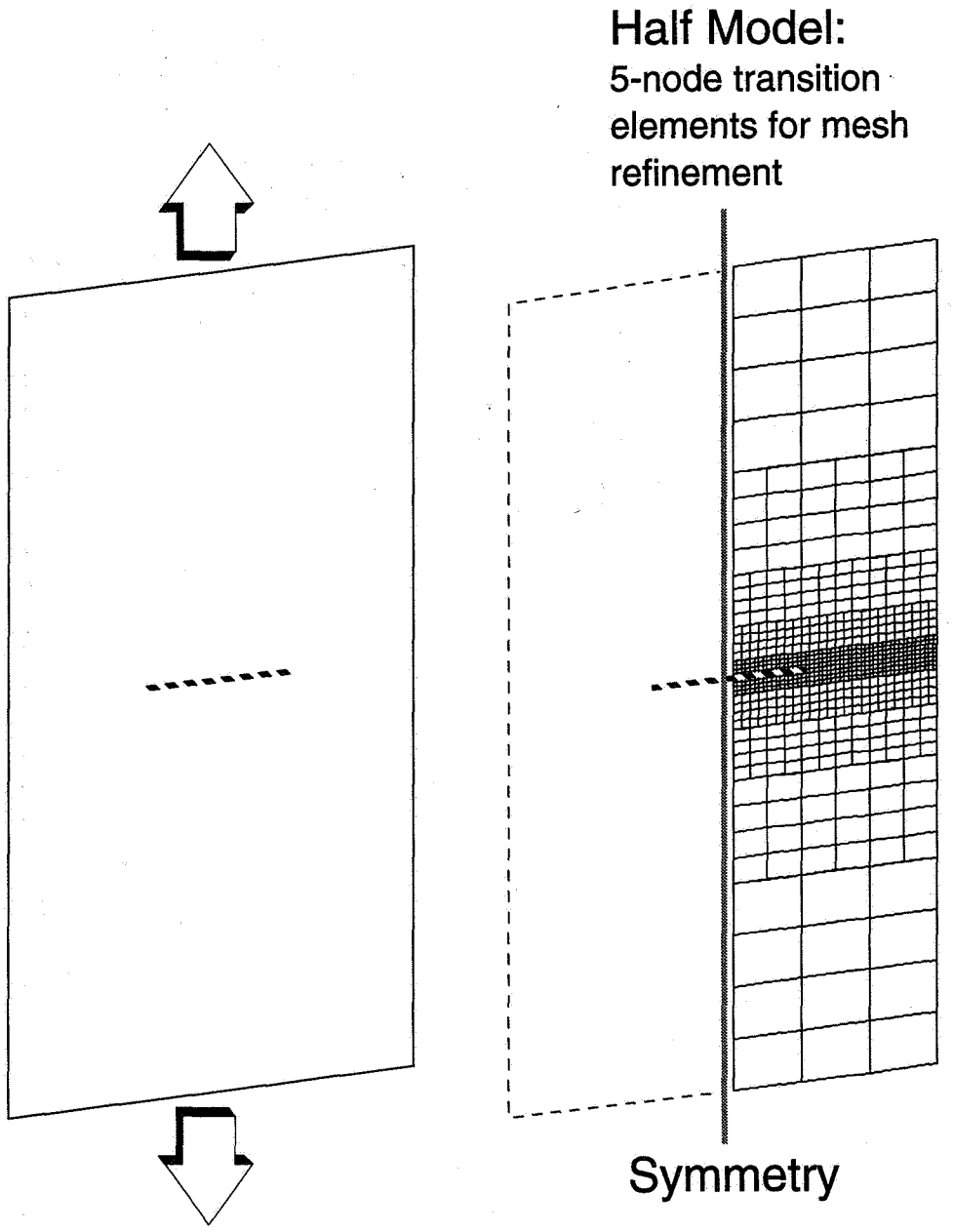

Fig. 19 Finite element model of a flat aluminum panel with a transverse center crack.

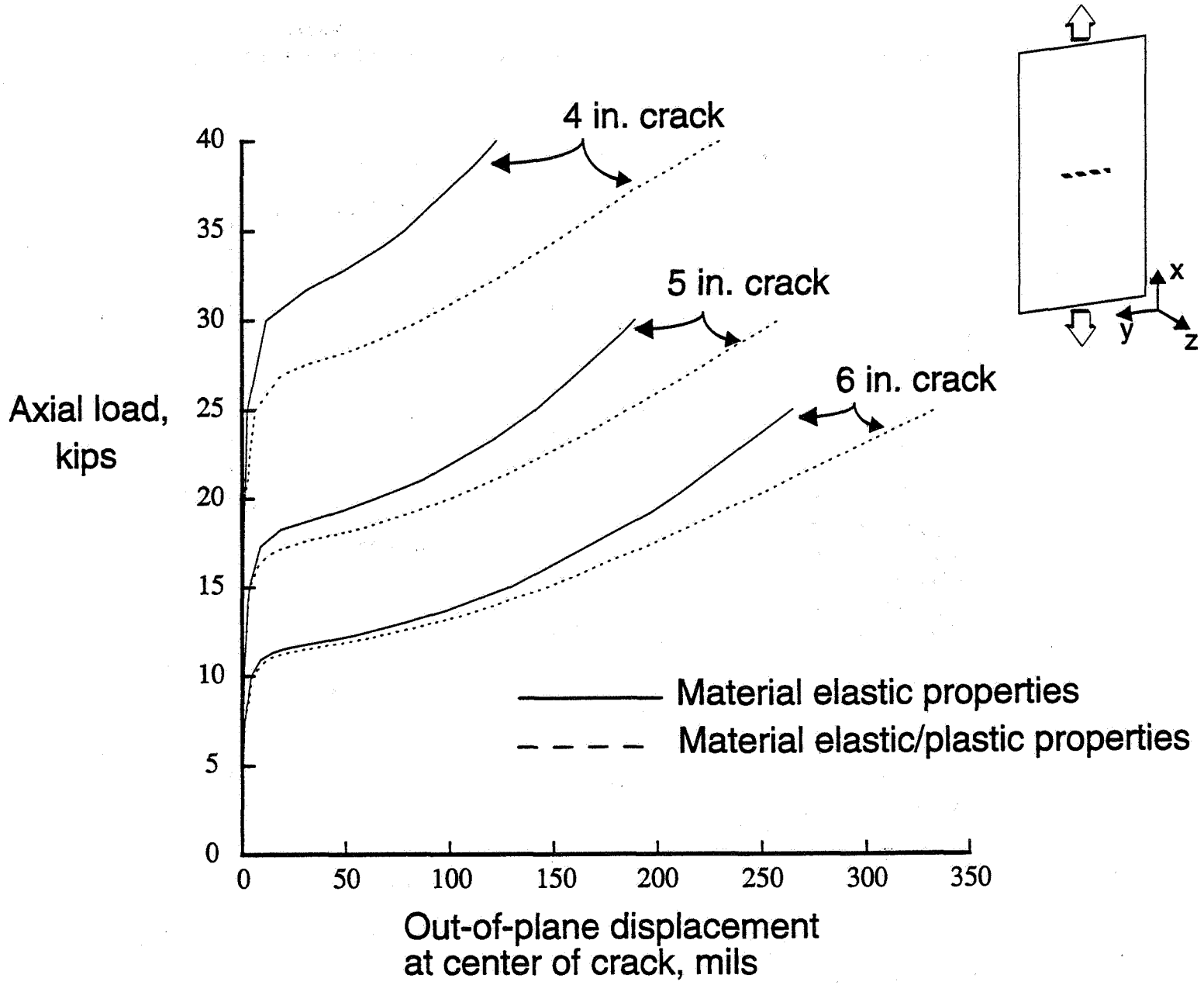

Fig. 20 Out-of-plane displacements at the crack center for tension-loaded panels with elastic and elastic-plastic material properties.

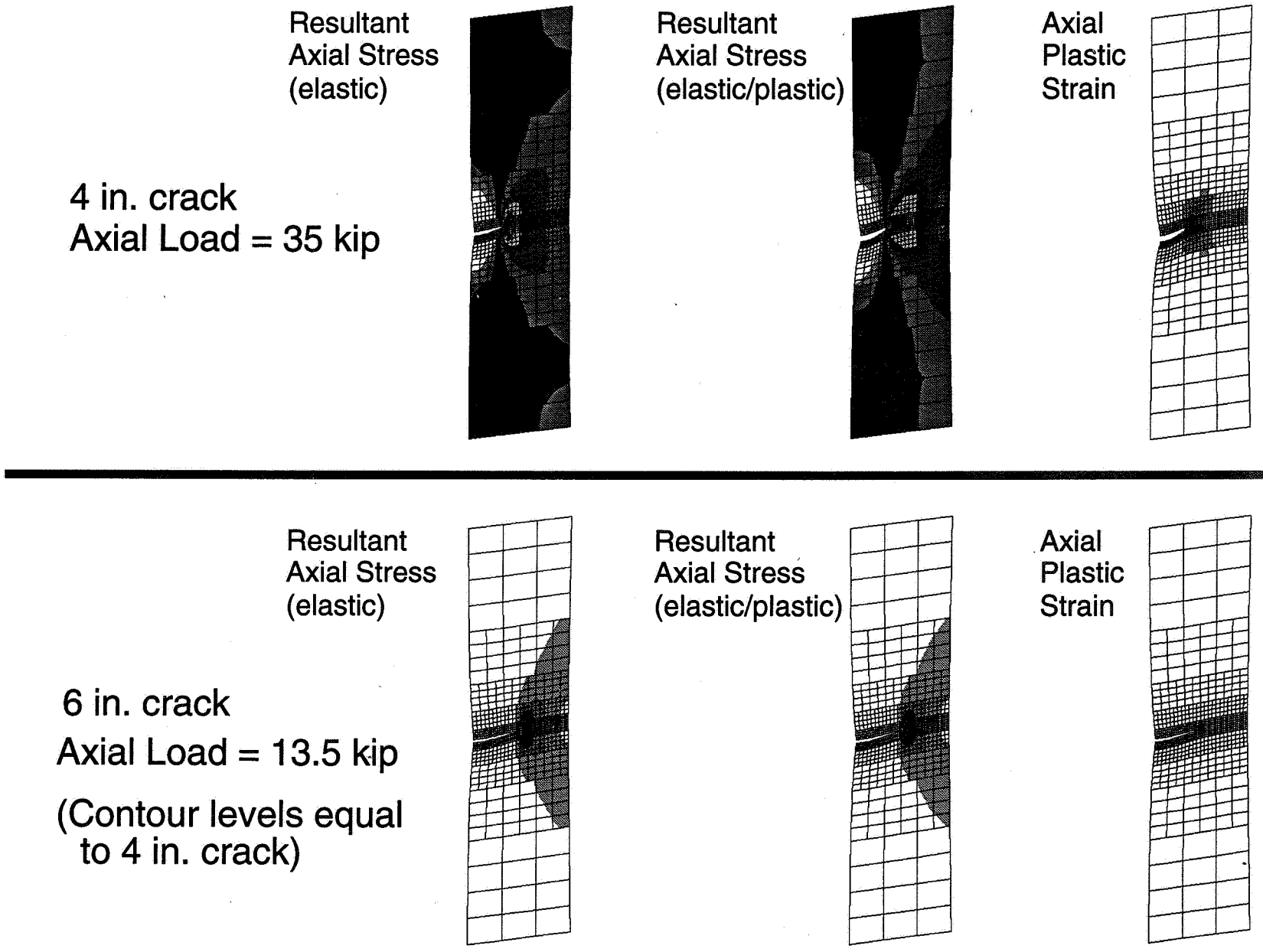

Fig. 21 Axial stress resultants and plastic strains for panels with applied tension loads that are 20 percent greater than the panel buckling loads.

SPLIT MANDREL VS. SPLIT SLEEVE COLDWORKING: DUAL METHODS FOR EXTENDING THE FATIGUE LIFE OF METAL STRUCTURES

Geoffrey A. Rodman
West Coast Industries, Inc.
Seattle, Washington 98133

Matthew Creager
Structural Integrity Engineering
Chatsworth, California 91311

ABSTRACT

It is common practice to use split sleeve coldworking of fastener holes as a means of extending the fatigue life of metal structures. In search of lower manufacturing costs, the aerospace industry is examining the split mandrel (sleeveless) coldworking process as an alternative method of coldworking fastener holes in metal structures. The split mandrel process (SpM) significantly extends the fatigue life of metal structures through the introduction of a residual compressive stress in a manner that is very similar to the split sleeve system (SpSl). Since the split mandrel process is significantly less expensive than the split sleeve process and more adaptable to robotic automation, it will have a notable influence upon other new manufacture of metal structures which require coldworking a significant number of holes, provided the aerospace community recognizes that the resulting residual stress distributions and fatigue life improvement are the same for both processes. Considerable testing has validated the correctness of that conclusion. The findings presented in this paper represent the results of an extensive research and development program, comprising data collected from over 400 specimens fabricated from 2024-T3 and 7075-T651 aluminum alloys in varied configurations, which quantify the benefits (fatigue enhancement and cost savings) of automating a sleeveless coldworking system.

SPLIT MANDREL VS. SPLIT SLEEVE COLDWORKING:
DUAL METHODS FOR EXTENDING THE FATIGUE LIFE OF METAL STRUCTURES

INTRODUCTION

In light of today's emphasis on economy, engineers must make informed decisions that influence the costs associated with the manufacture of new, and retrofit modification of aging aircraft structures. The manufacturing costs associated with such programs often drive decisions to sacrifice long term design life in order to minimize short term costs associated with manufacturing or repair. One classical fatigue problem has been that associated with the stress concentration found at fastener holes. For several decades, the aerospace industry has utilized numerous techniques to introduce a beneficial compressive residual stress at the hole in order to minimize the effects of the discontinuity. Many of these methods, including roller burnishing, ballizing, mandrelizing, ring coining, and shot peening, have enjoyed varying levels of success in providing the required life improvement. However, these systems have limitations which can only be overcome by the high interference coldworking processes available today.

Boeing's (BCAC) Materials Research & Development has developed two high interference coldworking systems which provide significant life improvement at holes in metal structures exposed to cyclic loading. The split sleeve process, developed in the early 1970's, has gained acceptance by the aerospace industry as a valuable tool for fighting fatigue [1-3]. The main drawback of the sleeve system has been the high cost associated with disposable perishable tooling (split sleeves). A solution for this problem was the sleeveless split mandrel system developed by Boeing in the early 1980's [4-5].

As sometimes occurs with any newly developing technology, the fatigue life benefits obtained during the developmental phase were somewhat disappointing. In 1983, an evaluation [6] compared the split sleeve process with the new sleeveless system, using an early developmental mandrel. The results of this program concluded that the sleeveless system, though cost effective, provided somewhat less fatigue life improvement (Figure 1) than that provided by the sleeve system. It was proposed that "the higher retained expansion found in the holes coldworked with the sleeveless system may have been due to plastic flow into the mandrel slots" [6]. The results obtained in that program were indicative of the state of the art at that time. The tooling used in that program is no longer used for split mandrel coldworking. The tooling system in use today produces fatigue life results substantially different from that published in the 1983 study. Although no data has been published in the open literature, significant data exists at Boeing, Bristol Aerospace (under oversight of Canadian Air Forces), U.S. Air Force (Wright Laboratories), and WCI, demonstrating similar life improvement for both the split mandrel and split sleeve processes. As a result of this data, the sleeveless system has been incorporated into the Boeing 777, Automated Spar Assembly Tool (ASAT), and in a similar robotics environment at Bristol Aerospace (F-5 re-wing program).

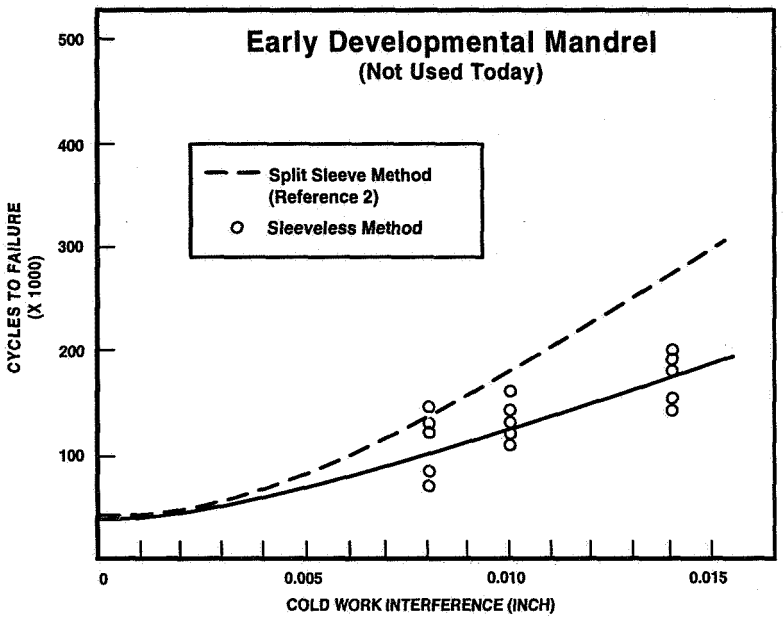

Figure 1. Test results using early developmental mandrel [6].

PROCESS DESCRIPTION

The mechanism by which fatigue life gain is achieved, by any coldworking process, is due to the introduction of compressive residual stresses in the material surrounding the hole. These stresses are created by the radial expansion of material (plastically), as the mandrel is drawn into the hole and the creation of a large compressive hoop stress adjacent to the hole ($\approx$ equal to the yield strength of the material), in combination with a tensile stress (required for equilibrium of forces) located some distance away from the hole after the mandrel is withdrawn. The net effect of the residual compressive stress is to lower the stress ratio (σ min/σ max) and the resulting damage associated with predominantly tensile cyclic loads.

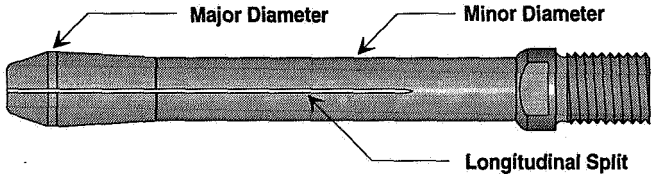

Figure 2. Split mandrel.

The only difference between the split mandrel (SpM) and split sleeve (SpSl) system for coldworking holes is the design of the tooling system utilized in performing the work. The split mandrel process

utilizes a collapsible mandrel (Figure 2) with a sliding pilot shaft extending through the mandrel which serves to solidify the mandrel prior to coldworking a hole. With the pilot retracted, the mandrel is partially collapsible, allowing insertion into the hole. When the puller unit is actuated, the pilot extends and solidifies the mandrel. The mandrel is then pulled through the hole (Figure 3). Boelube, a Boeing developed lubricant, is used to lower the frictional forces resulting from the mandrel sliding against the hole during the coldworking process. The proper amount of lubrication (approximately one drop) is automatically applied to the mandrel after each cycle as it re-extends. Boelube is a lubricant used in other machining steps such as pre- and post-reaming of coldworked holes. Clean-up is minimized, since less than one drop is required per hole,.

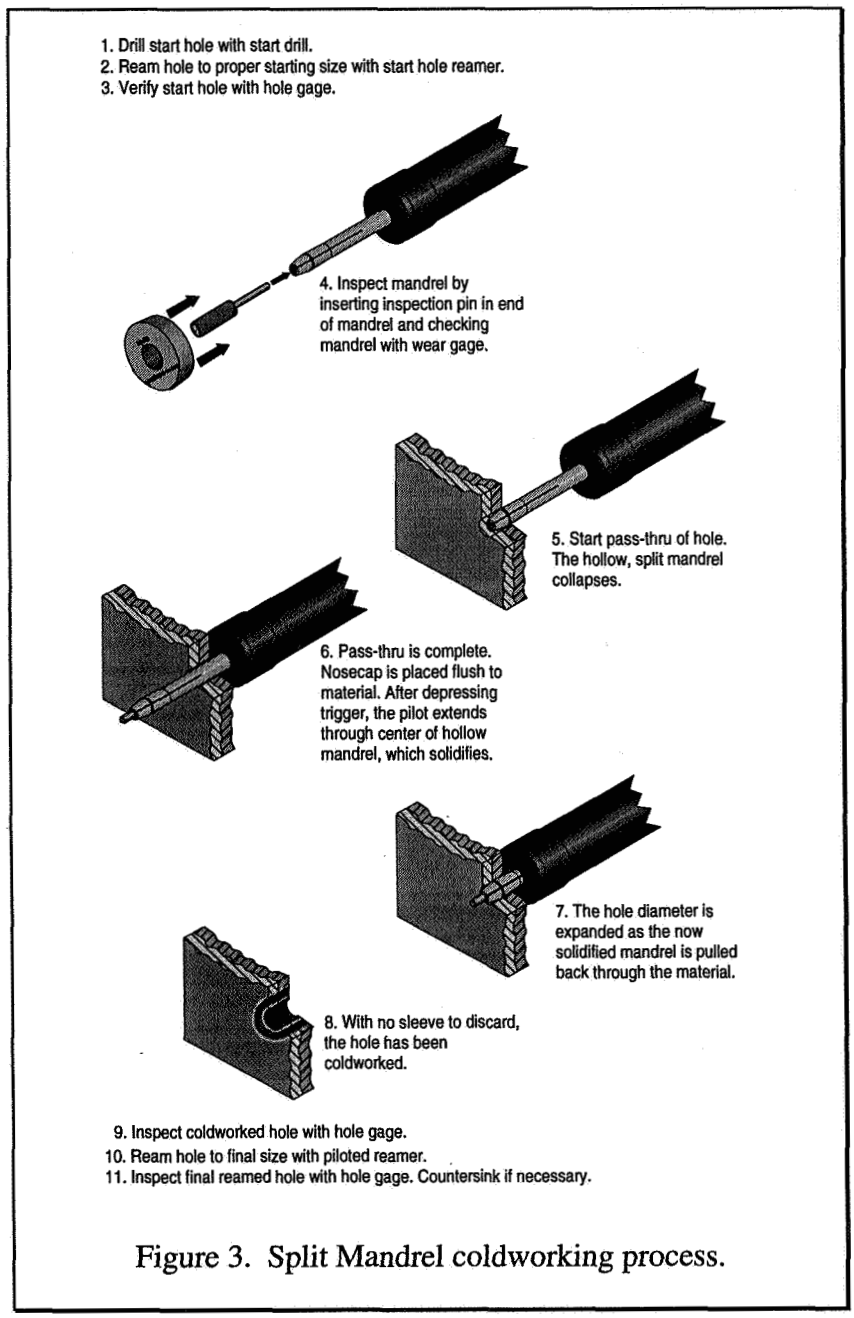

Figure 3. Split Mandrel coldworking process.

TEST PROGRAM

Two groups of experiments were performed in order to quantify the fatigue life benefits obtained when using either coldworking process, and facilitate a comparison of these systems. The open hole specimens used in these experiments were manufactured from 2024-T3 and 7075-T6 aluminum plate, double disk ground to a material thickness of 0.250. One group of tests (Table 1) was performed under cyclic load control, at constant amplitude, with a gross maximum stress level of 30 ksi and a stress ratio of 0.1. The process parameters examined included the minimum and maximum applied expansion levels following the established applicable process standard. In the second group of tests, similar specimens were tested (1/4" diameter hole) at differing maximum stress levels (R=0.1), to obtain information regarding process performance under a range of load conditions.

Table 1. Specimen Configuration

	Hole Size			
Material	**5/32**	**3/16**	**1/4**	**17/64**
2024-T3 [10]			0.250" x 1.50"	
7075-T651 [9]	0.250" x 1.0"	0.250" x 1.0"	0.250" x 1.50"	0.250 x 1.50"

RESULTS AND DISCUSSION

In order to objectively compare the SpM and SpSl coldworking processes, it is necessary to compare fatigue life test results at identical test conditions. Obviously, specimen material, test geometry, machining quality, and applied loads, need to be the same. Additionally, the amount of coldwork applied to each specimen should be the same.

The amount of coldwork performed on a hole is controlled by the amount of applied expansion (E_a) used to work the hole. Since the split sleeve experiences a great deal of deformation during the coldworking process, the "applied expansion" used in the split sleeve process is not necessarily the true expansion that is delivered to the hole. This does not hold true for the SpM system, since there is no sleeve to deform. E_a is calculated by:

$$E_a = \frac{A - B}{B} x100$$

A = Mandrel Major Diameter + 2 x sleeve thickness *(Split Sleeve)*

or:

Mandrel Major Diameter *(Split Mandrel)*

B = Start Hole Diameter

Retained expansion (E_r), a ratio of the post coldwork hole diameter to the initial hole diameter, is also a measure of the amount of coldwork performed on the hole. This value measures the actual material response to the coldworking process and is unaffected by different coldworking processes. The equation for evaluating the amount of retained expansion (for any process) is as follows:

$$E_r = \frac{C - B}{B} x100$$

C = Measured Hole Diameter After Coldworking

B = Start Hole Diameter

Due to the deformation of the split sleeve during the coldworking process, the relationship between E_a and E_r is generally different for each coldworking process. Consequently, the retained expansion is a more fundamental and appropriate measure to use in evaluating the efficacy of any coldworking process and in comparing the split mandrel and split sleeve processes.

The 2024-T3 and 7075-T651 coldworked specimen life data presented in Figure 4 has been normalized by the non-coldworked (NCW) baseline life for each material and hole size. Unlike the data from the 2024 material (containing one hole size), the data from the 7075-T651 material was generated at four hole diameters. Normalizing of the 7075 data at the corresponding hole diameter decreases any effect of hole diameter on the observed data trends. All of the data presented clearly reflects a trend of longer fatigue life with increased retained expansion. The data also clearly shows an increase in fatigue life for the split mandrel process, over the split sleeve process. Above an E_r level of approximately 2.5%, there is a clear discernible increase in life due to split mandrel coldworking over that due to split sleeve coldworking. Note that there is a marked similarity in the relationship between normalized life and retained expansion for both materials. Figure 5 shows the ratio of SpM life based upon the Figure 4 linear regression lines (log life versus retained expansion) for both coldworking processes. This allows quantification of the life improvement benefits for either system. The resulting graphic demonstrates a somewhat higher ratio for the 7075-T6 material, but the difference between the two materials is not large.

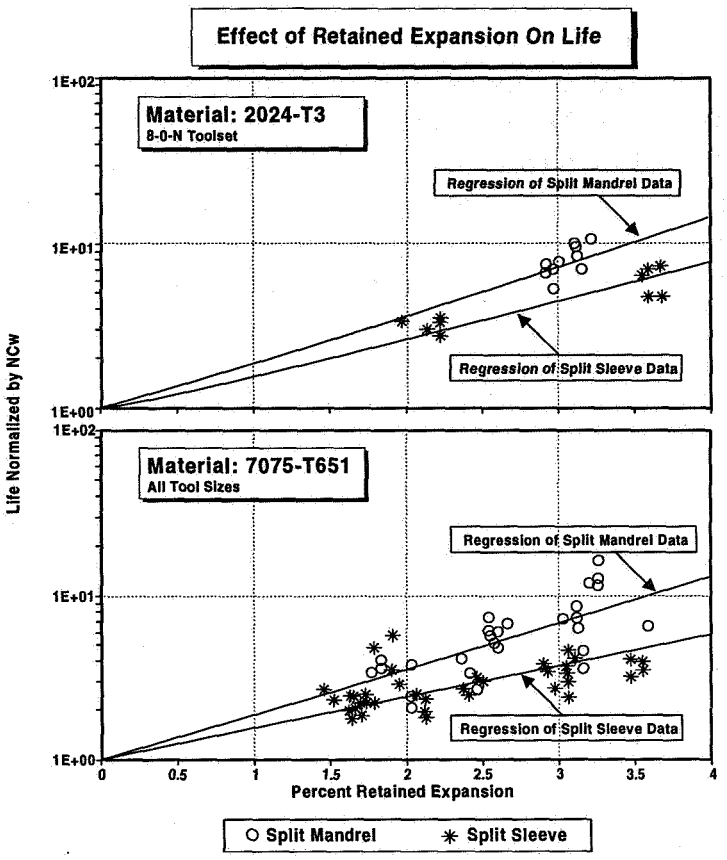

Figure 4. Regression analysis of split mandrel and split sleeve data. *7075 data [9], 2024 data [10].*

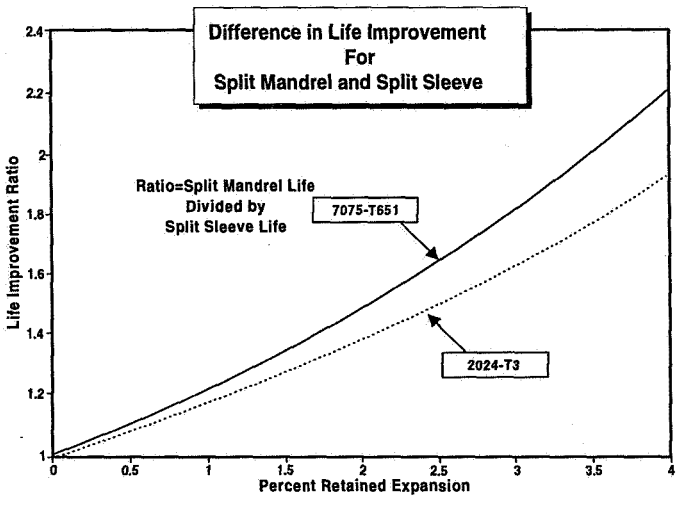

Figure 5. Differences in life improvement for the two systems and materials. *7075 data [9], 2024 data [10]*

Additional tests were run at stress levels above and below 30 ksi for 0.250" diameter holes with the applied expansion levels at or near the maximum specification values. The resulting data are plotted in Figure 6 (2024-T3) and Figure 7 (7075-T6) along with regression analysis curves for the data sets of the split sleeve process, split mandrel process, and non-coldworked specimens. Again, the data reflect an increased effectiveness of the split mandrel as compared to the split sleeve process. The increased effectiveness, although not as distinct in the 2024-T3 material, is observed at all stress levels and serves to demonstrate that the SpM process is equal or superior to the split sleeve coldworking process for all loading levels.

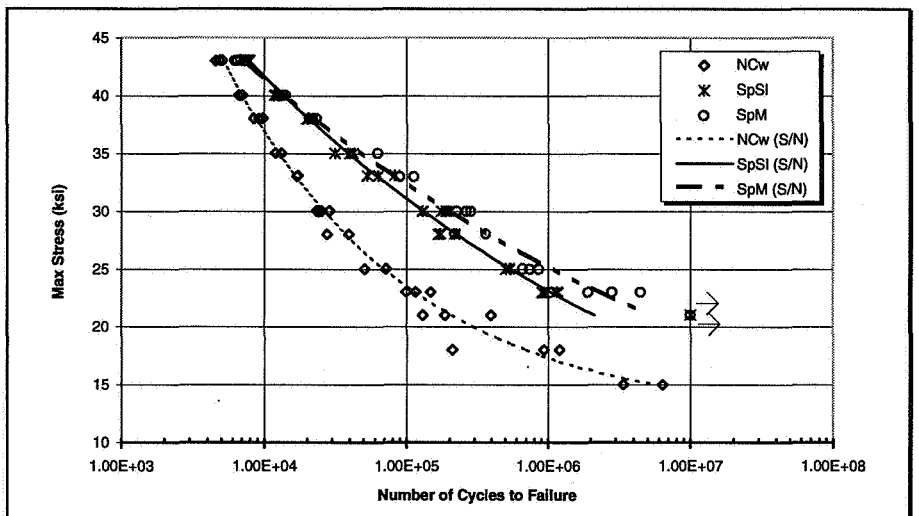

Figure 6. S/N Curve for 2024-T3 [10]

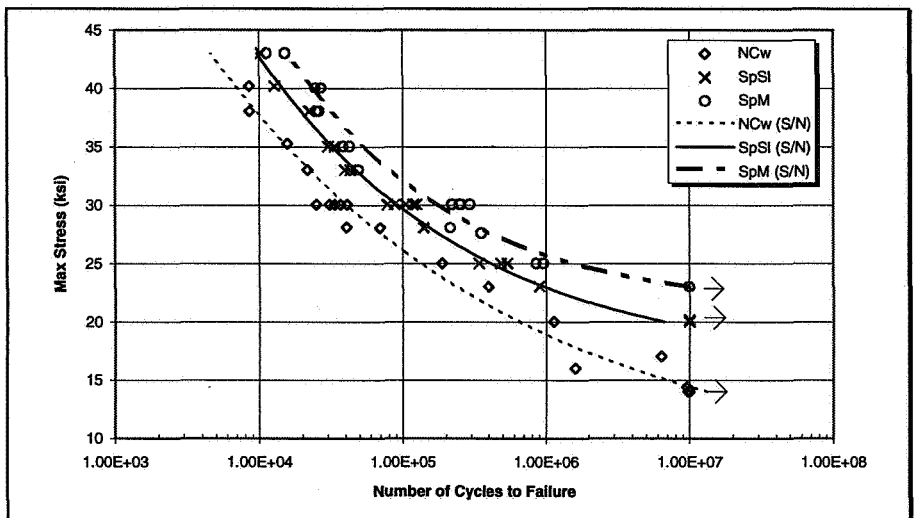

Figure 7. S/N Curves for 7075-T651 [9]

MANUFACTURING CONSIDERATIONS

In addition to the fatigue life benefits obtained with any fastener hole coldworking system, another facet of importance is the cost (time and materials) of implementing the process. Boeing developed the sleeveless process as a means to lower manufacturing costs. The split mandrel system has been used in production on every Boeing produced hardware system since 1983, and has been chosen for use in an automated environment on the new ASAT (Automated Spar Assembly Tool) machine for the manufacture of the new 777 wing. Additionally, Bristol Aerospace has recently begun the manufacture of improved wing sets for the F-5 using automated split mandrel coldworking. In each case, economic considerations were the basis for the choice of the split mandrel system, since both the split mandrel and split sleeve systems provide comparable life improvement. Both companies had investigated the sleeve process in automated and non-automated environments and found it to be impractical and cost prohibitive. This was mainly due to the deceptively simple task of selecting, orienting, placing and removing the disposable sleeve.

The cost of coldworking a hole using the split sleeve system varies from 0.50¢ to $17.00, depending upon sleeve size, length, etc. In deleting the sleeve cost, the split mandrel system will coldwork a hole at 0.05¢ per hole, without the burden of expensive supporting capital equipment. The only difference in the capital equipment between either process is the automatic lubricator and puller unit utilized in the split mandrel system. The split mandrel capital tooling detail parts are interchangeable (in many cases) with those of the sleeve system. This allows the capital equipment costs for either system to be virtually the same due to economy of scale.

Additional cost savings when using the SpM system are realized by reducing the amount of processing time required for each hole. Roughly four seconds are required for a robot, or operator, to coldwork a hole and move to the next. With the split sleeve process, there is the additional processing time required for installing and disposing of the split sleeve (multiplying the time by a factor of 3).

CONCLUSIONS

Through its simplicity of design, the split mandrel process is an efficient, cost effective system for high interference coldworking of holes. The data collected in this research program demonstrate that the split mandrel and split sleeve processes increase the fatigue life of holes significantly, and that the life improvement obtained with the split mandrel process is at least as good as that provided by the split sleeve process. The combination of effectiveness and economic advantages of the split mandrel process over other coldworking processes should serve as a driving force for the aerospace community to turn to the split mandrel system as the preferred solution to high manufacturing costs, in both time and materials, often associated with the coldworking of critical holes in aircraft metallic structures.

REFERENCES

1. J.L. Phillips, "Sleeve Coldworking of Fastener Holes," *AFML-TR-74-10, Vol. 1*, Air Force Materials Laboratory, Wright-Patterson AFB, February 1974.
2. "Sleeve Cold Working of Holes in Aluminum Structure," *BAC 5973,* Boeing Aircraft Co., Process Specification, 1975.
3. "Split Sleeve Coldworking–Holes (Aluminum, Steel & Titanium)," *Process Specification WCI-9201*, West Coast Industries, Inc., 1992.
4. "Mandrel Cold Working of Holes in Aluminum," *BAC 5768,* Boeing Aircraft Co., Process Specification, 1983.
5. "Split Mandrel Coldworking–Holes (Aluminum)," *Process Specification WCI-9202*, West Coast Industries, Inc., 1992.
6. M.W. Ozelton and T.G. Coyle, "Investigation of Fatigue Life Improvement By Cold Working Of Holes In Aircraft Materials," *NOR 83-191,* Northrop Corporation, 1983.
7. "Standard Practice for Conducting Constant Amplitude Axial Fatigue Tests of Metallic Materials," *ASTM E466-82, Vol. 03.01, Metals—Mechanical Testing*, 1982.
8. "Standard Practice for Statistical Analysis of Linear or Linearized Stress-Life (S/N) and Strain-Life (ε-N) Fatigue Data," *ASTM E739-91, Vol. 03.01, Metals—Mechanical Testing*, 1991.
9. G.A. Rodman and M. Creager, "Split Mandrel vs. Split Sleeve Coldworking: A Comparison of Two Manufacturing Processes," *Laboratory Technical Report, LTR-9308*, West Coast Industries, 1993.
10. G.A. Rodman and M. Creager, "Split Mandrel vs. Split Sleeve Coldworking: Comparing Fatigue Life Improvement in 2024-T3," *Laboratory Technical Report, LTR-9403*, West Coast Industries, 1993.

REPORT DOCUMENTATION PAGE

Form Approved
OMB No. 0704-0188

1. AGENCY USE ONLY *(Leave blank)*	2. REPORT DATE	3. REPORT TYPE AND DATES COVERED
	September 1994	Conference Publication

4. TITLE AND SUBTITLE
FAA/NASA International Symposium on Advanced Structural Integrity Methods for Airframe Durability and Damage Tolerance

5. FUNDING NUMBERS
WU 538-02-10-01

6. AUTHOR(S)
Charles E. Harris, Editor

7. PERFORMING ORGANIZATION NAME(S) AND ADDRESS(ES)
NASA Langley Research Center
Hampton, VA 23681-0001

8. PERFORMING ORGANIZATION REPORT NUMBER
L-17432

9. SPONSORING/MONITORING AGENCY NAME(S) AND ADDRESS(ES)
Federal Aviation Administration Technical Center
Atlantic City International Airport Center, NJ 08405
and
National Aeronautics and Space Administration
Washington, DC 20546-0001

10. SPONSORING/MONITORING AGENCY REPORT NUMBER
NASA CP-3274, Part 2

11. SUPPLEMENTARY NOTES

12a. DISTRIBUTION/AVAILABILITY STATEMENT
Unclassified–Unlimited

Subject Category - 03, 26, 39

12b. DISTRIBUTION CODE

13. ABSTRACT *(Maximum 200 words)*

The international technical experts in the areas of durability and damage tolerance of metallic airframe structures were assembled to present and discuss recent research findings and the development of advanced design and analysis methods, structural concepts, and advanced materials. The principal focus of the symposium was on the dissemination of new knowledge and the peer-review of progress on the development of advanced methodologies. Papers were presented on the following topics: structural concepts for enhanced durability, damage tolerance, and maintainability; new metallic alloys and processing technology; fatigue crack initiation and small crack effects; fatigue crack growth models; fracture mechanics failure criteria for ductile materials; structural mechanics methodology for residual strength and life prediction; development of flight load spectra for design and testing; and advanced approaches to resist corrosion and environmentally assisted fatigue. About 300 people attended the symposium.

14. SUBJECT TERMS
Fatigue; Fracture mechanics; Metals; Airframe; Durability

15. NUMBER OF PAGES
578

16. PRICE CODE
A25

17. SECURITY CLASSIFICATION OF REPORT	18. SECURITY CLASSIFICATION OF THIS PAGE	19. SECURITY CLASSIFICATION OF ABSTRACT	20. LIMITATION OF ABSTRACT
Unclassified	Unclassified	Unclassified	